Dissertation

Interaction of Terahertz Radiation with Semiconductor Nanostructures and Quantum Systems

Wladislaw Michailow
Trinity College
Cavendish Laboratory
University of Cambridge

August 2021

This thesis is submitted for the degree of
Doctor of Philosophy.

Preface

This thesis is the result of my own work carried out in the Semiconductor Physics Group at the Cavendish Laboratory from October 2017 to June 2021 and includes nothing which is the outcome of work done in collaboration except as declared in the acknowledgements and specified in the text. It is not substantially the same as any work that has already been submitted, or, is being concurrently submitted for any such degree, diploma or other qualification at the University of Cambridge or any other University or similar institution. The thesis word length, as described by the Degree Committee for the Faculty of Physics and Chemistry, does not exceed the prescribed limit of 65,000 words, including abstract, tables, and footnotes, but excluding table of contents, photographs, diagrams, figure captions, bibliography, and acknowledgements.

Readers of the electronic version of this document may click on the titles of the referenced works in the bibliography to visit the corresponding website and on the purple-coloured links in the text for navigation within the document.

Wladislaw Michailow, August 2021.

Interaction of Terahertz Radiation with Semiconductor Nanostructures and Quantum Systems

Wladislaw Michailow

Abstract

Terahertz (THz) waves constitute radiation with frequencies around 10^{12} Hz, lying between the microwave and infrared regions. For a long time, the THz range has been one of the less explored areas of research in contemporary physics, owing to the fact that physical principles used in both the higher and the lower frequency ranges no longer work in the THz range, a phenomenon known as the "Terahertz gap". Although progress over the recent decades has considerably reduced the Terahertz gap, the technology in the THz region is not yet sufficiently developed for practical applications because of a lack of efficient, inexpensive, and easy-to-use sources and detectors operating in this range.

Nowadays, THz science is an actively developing research area, with still many open questions. THz radiation could have numerous technological applications, ranging from non-damaging methods of visualising cancerous tissue in medicine over the detection of hidden weapons and illegal drugs in security applications to ultrafast data communication beyond the era of 5G wireless networks. This showcases the wide range of opportunities that THz science provides and highlights the need for the development of devices operating in the THz range and for research on the physics of THz interaction with various structures and materials, including semiconductor nanostructures and quantum systems.

This is the topic that this thesis is dedicated to. In this work, I demonstrate a highly sensitive THz detector based on a new physical principle of operation which was called the "in-plane photoelectric effect", show the realisation of the Talbot effect in the THz range for focusing of THz radiation using waveguides, and describe the work towards developing devices bridging the terahertz and visible/near-infrared frequency ranges, such as THz-to-Optics interfaces based on quantum dots.

In chapter 1, a brief overview of state-of-the-art terahertz technology is given. A number of sources, detectors, and measurement systems operating in the THz range are reviewed.

To carry out the subsequent measurements, an experimental setup is required that makes

it possible to study electrically contacted samples at liquid helium temperatures with simultaneous optical and terahertz access. For this purpose, I designed and constructed a unique system, described in chapter 2, which solves this ambitious task using cryogenically compatible terahertz waveguides. The waveguide system has a high transmission and exhibits a number of advantages compared to free-space setups. It enables the determination of the frequency of the THz source and allows accurate measurements of the power, as well as of the spatial distribution of the intensity and electric field polarisation directly at the position of the sample.

As part of the characterisation of the experimental setup, the THz mode profile (i.e., the spatial intensity distribution) at the end of the THz waveguide system was measured. The results revealed highly focused radiation with a complicated pattern. Its exact origin was unknown, since a comprehensive theory describing propagation after the end of cylindrical waveguides was lacking in literature. To explain the observed mode profiles, I developed a ray-optical theory of cylindrical multimode waveguides, described in chapter 3. It predicts the beam profile both within the waveguide and in the free space after its end. Remarkably, this theory also predicts that a waveguide itself can be used to focus radiation, without any additional lenses or parabolic mirrors. I show that the waveguide can be understood as an interferometric system and that its output beam profile is a "two-dimensional interferogram" of the input beam. It contains information about the input electric field, such as its direction of polarisation and the angles of angular misalignment of the source.

To check the predicted focusing effect, I fabricated waveguides of the geometrical sizes expected to yield optimal focusing. Measurements of the beam propagation at the waveguide end showed the expected pattern, confirming the theory and proving the focusing effect of multimode cylindrical waveguides. At terahertz frequencies, this effect combines the advantage of low losses of multimode waveguides with the ability of free-space setups to focus radiation to a tight spot. Physically, the phenomenon is related to the Talbot or self-imaging effect, and the constructed waveguided experimental setup represents its first practical realisation in circular waveguides at THz frequencies.

In chapter 4, I describe the design, fabrication, and measurements of a THz detector based on a two-dimensional electron gas (2DEG). It is based on a novel antenna-coupled, dual-gated device architecture. After simulation of the antenna design, the fabrication procedure is developed and successfully processed samples are demonstrated. Then the journey of searching for and finding a THz response is described. After a number of improvements of the setup, I demonstrate a highly efficient direct detector of THz radiation, that shows a giant photocurrent and photovoltage response.

The origin of the THz photoresponse was unclear. The electron transport in the 2DEG was analysed in a variety of aspects and additionally characterised using supporting measurements of the Hall effect and Shubnikov-de Haas oscillations in a magnetic field. The experimentally measured THz response was compared with existing theories, and it was found that they could not explain the observed effect. For example, the demonstrated THz detector exhibits a response more than an order of magnitude larger than expected from the common interpretation by the classical plasmonic mixing mechanism. I found that the observed phenomenon is due to a new, quantum-mechanical effect, which I called the “in-plane photoelectric effect”. This phenomenon, which is described in chapter 5, is observed under conditions where the conventional, three-dimensional photoelectric effect cannot be observed and has a number of crucial features that make it superior to the three-dimensional photoelectric effect. In collaboration with a theorist, a quantitative theory was developed, which describes the measured data very well. The experimental results demonstrate the great potential of the in-plane photoelectric effect, which makes it possible to create a new class of highly sensitive, ultrafast THz detectors. Theoretically, the effect is expected to provide efficient THz detection across the entire THz range.

In chapter 6, I describe the work carried out in parallel towards studying the interaction of THz radiation with optically active semiconductor quantum dots. These small, quasi-zero-dimensional objects are often called artificial atoms and can be used as a “box” to store one or several electrons. The spin of the captured electrons represents a unit of quantum information – a qubit. Thus, quantum dots can be used as a physical implementation of quantum memory. In the area of quantum computation, qubits in quantum dots are initialised, manipulated and read out using infrared or visible light. However, to date, there are no reports where all-optically controlled quantum states were manipulated by THz photons. If THz photons could be used to switch optically written and read states of a quantum dot, this would represent a quantum interface between THz and optics – a breakthrough in the field of quantum computing and THz technology. This challenging task requires careful experimental preparation to ensure optimal coupling of the dots to both THz and optical (visible/near-infrared) photons. For this purpose, various material systems and different growth methods of quantum dots and quantum dot molecules (coupled pairs of quantum dots) have been studied together with a molecular beam epitaxy grower and checked for their suitability for this task. In addition, I have proposed and simulated a bandstructure that aims to enable all-optical readout of the quantum states over a wide range of both positive and negative applied electric fields.

Finally, in chapter 7 the main results are summarised, and an overview of potential future research directions is given.

Contents

1 An overview of terahertz technology

The terahertz (THz) region of the electromagnetic spectrum refers to electromagnetic waves with frequencies between approximately 0.1 THz and 10 THz (Figure 1.1, Table 1.1). For a long time, it has been difficult to access due to a lack of suitable sources and detectors [1, 2].

Terahertz photons are due to their low energy not ionising. They are strongly absorbed by water and moisture in air. Large molecules, such as those making up proteins and deoxyribonucleic acids, exhibit intramolecular vibration modes in this frequency region. [3]

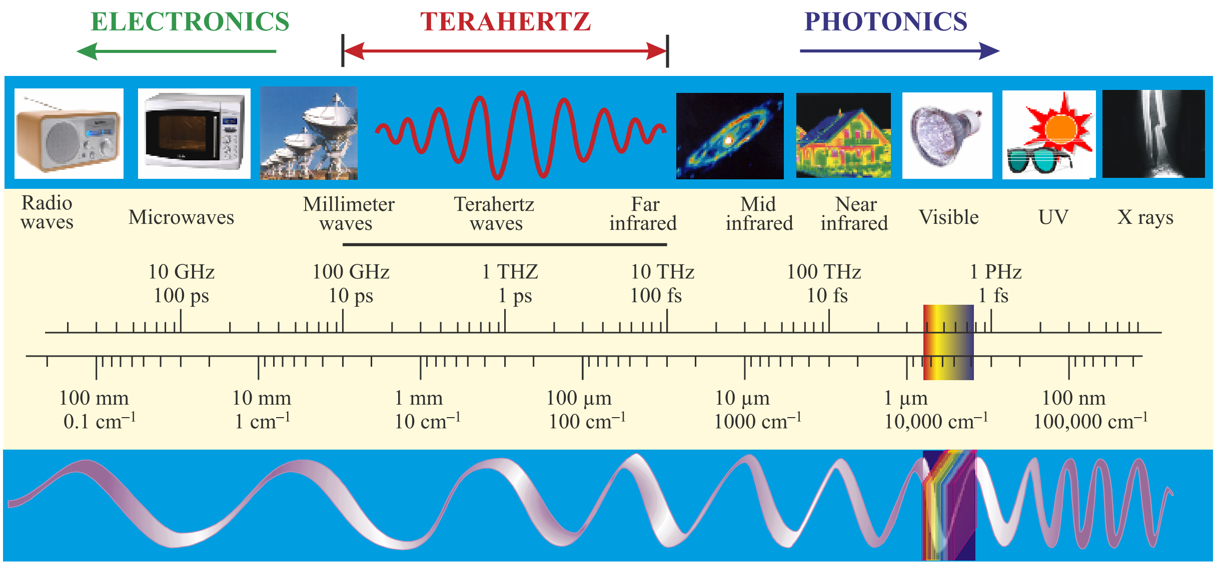

Figure 1.1: **The terahertz region in the electromagnetic spectrum.** This graphics, published by De Gruyter, is licenced under the Creative Commons licence CC BY-NC-ND 3.0 and is from Ref. [1].

Frequency	Time scale	Photon energy	Wavelength	Wavenumber
0.1 THz	10 ps	0.4 meV	3 mm	3.3 cm^{-1}
0.3 THz	3.3 ps	1.2 meV	1 mm	10 cm^{-1}
1 THz	1 ps	4.1 meV	300 µm	33 cm^{-1}
3 THz	0.33 ps	12 meV	100 µm	100 cm^{-1}
10 THz	0.1 ps	41 meV	30 µm	333 cm^{-1}

Table 1.1: **Characteristic energy scales in the THz region:** comparison of different units of typical photon energy values.

Developments in the field of terahertz sources, detectors and spectroscopy over the last decades have led to a new area of applications [4]. For example, it is possible to distinguish between healthy and damaged cells (e. g. cancerous) by studying the response of human tissue to terahertz radiation [5]. Another application is non-destructive testing of materials and molecular spectroscopy [3]: With terahertz radiation, it is possible to “see through” optically opaque materials such as paper, cardboard and many plastics [6] and detect non-destructively their contents [7]. Such imaging techniques [6] have applications in security such as screening for drugs [8] and explosives [9]. Short-range communication via terahertz radiation may facilitate further increase in data transmission rates in wireless networks (e. g. beyond 10 Gigabit per second) [10].

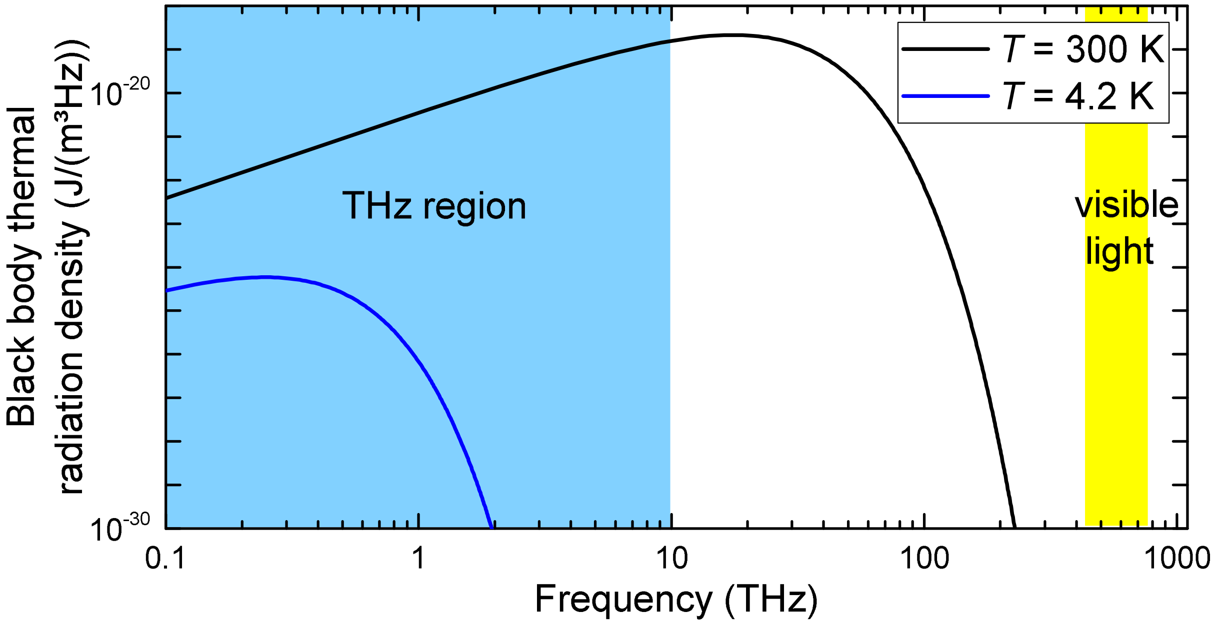

Figure 1.2: **Thermal radiation density** according to Planck’s law for room temperature (300 K) and liquid helium temperature (4.2 K) on a double-logarithmic scale. The higher contribution of thermal radiation density in the THz region as compared to the visible range can be reduced by cooling to cryogenic temperatures.

For a general understanding of terahertz radiation it is useful to compare the energy ranges involved with thermal radiation. Ambient room temperature, $T\sim$300 K, corresponds to around 26 meV by $\hbar\omega = hf \approx k_B T$. As seen from Table 1.1, this is commensurate with photon energies in the terahertz region. In Fig. 1.2, the black body thermal radiation density according to Planck’s law [11],

$$g(f) = \frac{8\pi}{c^3} \cdot \frac{hf^3}{\exp\left(\frac{hf}{k_B T}\right) - 1}, \tag{1.1}$$

is shown for room temperature (300 K) and for liquid helium temperature (4.2 K; [12, 13]).

Here, $h = 2\pi\hbar$ is the Planck constant, c the speed of light, k_B the Boltzmann constant, and $f = \omega/(2\pi)$ the frequency. It can be seen that ambient black body radiation is much more pronounced in the THz region than in the visible range. The thermal radiation density in the terahertz region can be substantially reduced by cooling to 4.2 K.

For these reason, most solid state terahertz sources based on quantum mechanics have to be cooled for efficient operation, since thermal filling of states by the Fermi function $1/\{1 + \exp[(E - \mu)/(k_B T)]\}$ limits device efficiency. It also means that ambient thermal radiation provides an always-present background noise that can only be eliminated by cryogenic cooling. Therefore, experiments in the terahertz region often make use of the lock-in measurement technique, which allows to filter away noise at any frequencies except the frequency of interest [14, 15].

1.1 Terahertz sources

Fig. 1.3 illustrates the lack of suitable, i. e. cheap, compact, frequency-tunable sources operating at room temperature with high power output in the THz region. Gunn-diodes [17]

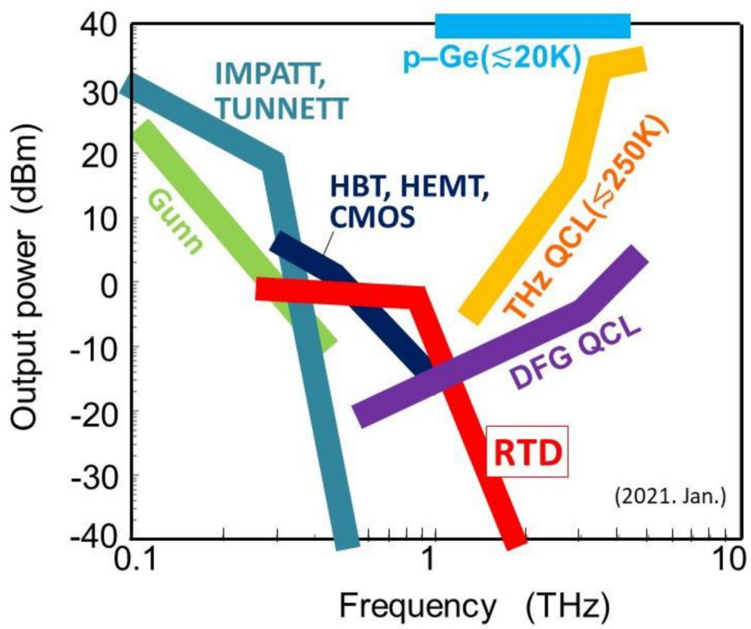

Figure 1.3: **Solid state sources in the THz region:** most of the commonly used devices from both the high and low ends cannot be used for generation around 1 THz. Among them are shown: resonant tunneling diodes (RTD), impact ionisation avalanche transit-time diodes (IMPATT), tunnel injection transit time diodes (TUNNETT), THz quantum cascade lasers (THz QCLs), p-Germanium emitters (p-Ge), transistor-based sources (HBT, HEMT, CMOS), difference frequency generation quantum cascade lasers (DFG QCLs). Reprinted from Ref. [16] under the Creative Commons licence CC BY 4.0.

have been pushed into the sub-THz region [18] and were demonstrated at around 300 GHz [19]. IMPATT-diodes [20] work up to around 300 GHz as well, yet work on IMPATT-diodes operating at higher frequencies ($\sim$ 1 THz) is mostly theoretical [21]. Another source is a gas laser which can provide up to 30 mW power at discrete frequencies corresponding to transitions in the gain medium (e. g. methanol), which is pumped by a CO_2 laser [2].

In the following, common sources of THz radiation are reviewed.

1.1.1 Globar

One of the simplest light sources for the far-infrared or terahertz region is a thermally heated object emitting black body radiation. A globar [22, 23] is such an electrically heated object, commonly made out of silicon carbide [24], that has been used for a long time (since about 1925 [25]) in far-infrared spectroscopy [26].

1.1.2 Vacuum electronic devices

Vacuum based sources of microwave and terahertz radiation use the electromagnetic interaction of accelerated electrons moving in vacuum with magnetic or electric perturbations. A review can be found in Ref. [27]. Being a classical source of radiation, they can operate at room temperature and do not require temperatures below $\hbar\omega/k_{\mathrm{B}}$.

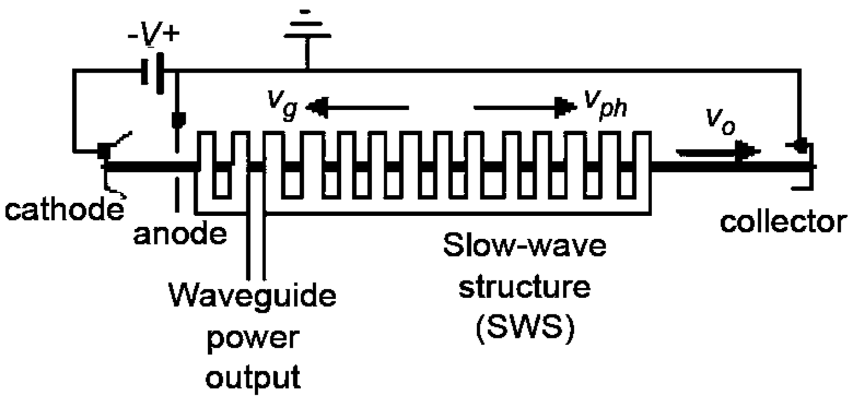

Figure 1.4: **Vacuum circuit design of a backward wave oscillator.** Electrons are accelerated from cathode to anode and interact with a slow-wave structure (a periodic metallic structure), generating radiation. From Ref. [27], © 2011 IEEE.

In a typical vacuum electronic device such as the backward wave oscillator (Fig. 1.4), electrons are emitted by a heated cathode and accelerated in the electric field generated by the voltage applied to the anode. They then pass a periodic metallic structure, inducing an oscillating electric field in the structure. A magnetic field parallel to the direction of electron motion is needed to confine the electron beam and prevent the electrons from escaping. For very high frequencies up to the THz region, the electrons have to be guided very closely to the metallic structure, whose transverse dimensions have to be less than the free space wavelength (i. e. < 1 mm) [3]. The metallic structure itself needs to have small features < 100 µm with surface finish < 20 nm which requires sophisticated microfabrication techniques. [3, 27]

Backward wave oscillators for 1.2–1.4 THz with 2 mW output power, operating at room temperature, are currently commercially available [28], however they require a high magnetic field ~ 1 T. With frequency multiplication, radiation up to 2.1 THz can be achieved, yet with very low powers (25 µW) [29].

An important high-power source of THz radiation is the free electron laser. Electrons are accelerated to high energies of a few MeV and pass periodic magnetic fields, which causes them to “wiggle” and emit electromagnetic radiation. Average powers of up to 500 W and peak powers up to 500 kW are possible [3]. However, a free electron laser is a very large facility, and there are only a few of those in the world. [27]

1.1.3 p-Germanium emitter

A tunable, high-power source of THz radiation is p-doped germanium. If p-doped germanium cooled to liquid helium temperatures is placed in crossed electric and magnetic fields, a population inversion can occur between the light- and heavy-hole bands [31]. This can lead to stimulated emission of electrons relaxing from the light- into the heavy-hole band, having a smaller curvature and thus smaller energy at the same momentum, see Fig. 1.5 [30]. Radiation in the region of 1–4 THz can be obtained, depending on suitable electric and magnetic fields, with powers up to 10 W at 4.2 K temperature [30, 32, 33].

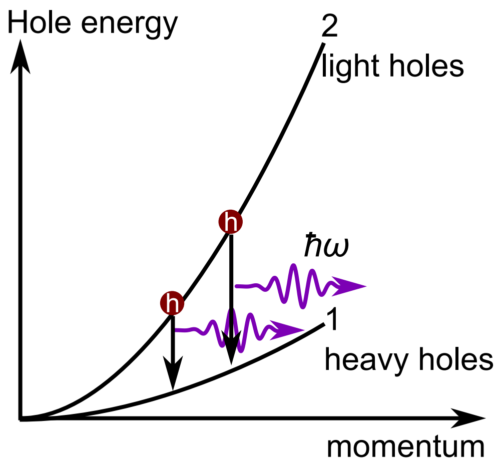

Figure 1.5: **Stimulated emission in a p-Germanium emitter.** Electrons relax from the light hole band into the heavy hole band by emission of a THz photon. With information from Ref. [30].

1.1.4 Quantum cascade laser

A quantum cascade laser (QCL) is a semiconductor device capable of emitting radiation in the region of mid-infrared to terahertz frequencies. During molecular beam epitaxy (MBE) growth of a QCL, a semiconductor superlattice is deposited, which yields a sequence of quantum wells and barriers with precisely controlled thicknesses. In the superlattice, a sequence of quantum wells and barriers, called period or active region design, is repeated multiple times. When a certain voltage is applied to the heterostructure, the superlattice forms a “ladder”. Injected electrons that tunnel through the structure undergo intersubband transitions, emitting photons. [34]

Following the idea that intersubband transitions in a semiconductor superlattice can yield a negative differential resistance and lead to light amplification [35], concepts of a laser based on intersubband transitions were developed [36, 37]. The first QCL, demonstrated in 1994, was based on InGaAs and worked at 70 THz [38]. In 1998, an AlGaAs-based QCL working at 32 THz was shown [39], and in 2002, the first THz-QCL operating at 4.4 THz was demonstrated [40]. The working principle is illustrated in Fig. 1.6.

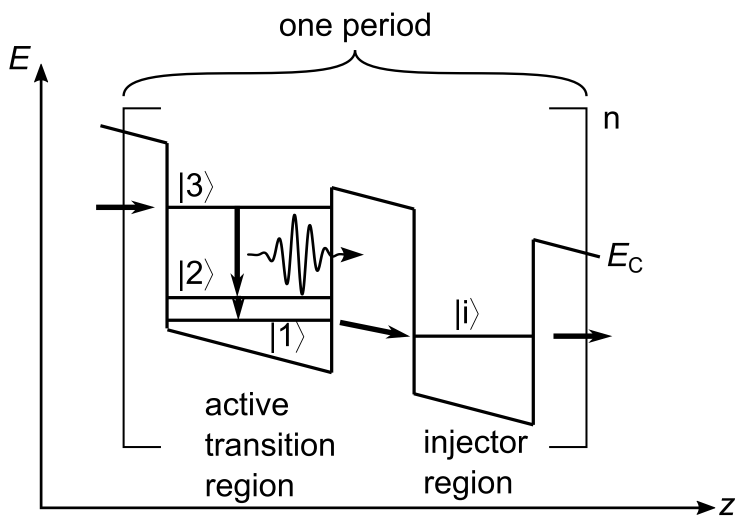

Figure 1.6: **The period of a quantum cascade laser in a simple model.** The tilted conduction band edge under the presence of an electric field is shown. The period consists of an injector region and an active optical transition region and is repeated 100–200 times [41]. Based on Ref. [36].

Electrons accumulate in the injector region and tunnel into an excited state of the active transition region quantum well. This causes the excited level $|3\rangle$ to have a population inversion with respect to $|2\rangle$. The electrons relax into the second excited level under emission of a photon. Subsequently, they relax into the ground state level and tunnel into the injector states of the next period. [36]

In order to get lasing action, a population inversion must exist between the lasing energy levels [42]. This requires that the lifetime of the upper state is longer than the lifetime of the lower lasing state [34].

In real quantum cascade lasers, the period is more complicated than shown in Fig. 1.6. Both the active transition region and the injector region consist of multiple quantum wells [39]. They form “mini-bands”, since any additional periodicity superimposed on the atomic lattice periodicity creates bands and gaps in the energy structure [43]. Numerical simulations are used to optimize the heterostructure sequence [44].

Apart from the heterostructure design, for a functioning laser there needs to be a waveguide that confines the lasing mode, which should overlap with the active region, i. e. the heterostructure containing the approximately 100 – 200 periods. For terahertz quantum cascade lasers, there are two main types of waveguides, see Fig. 1.7 [34, 45].

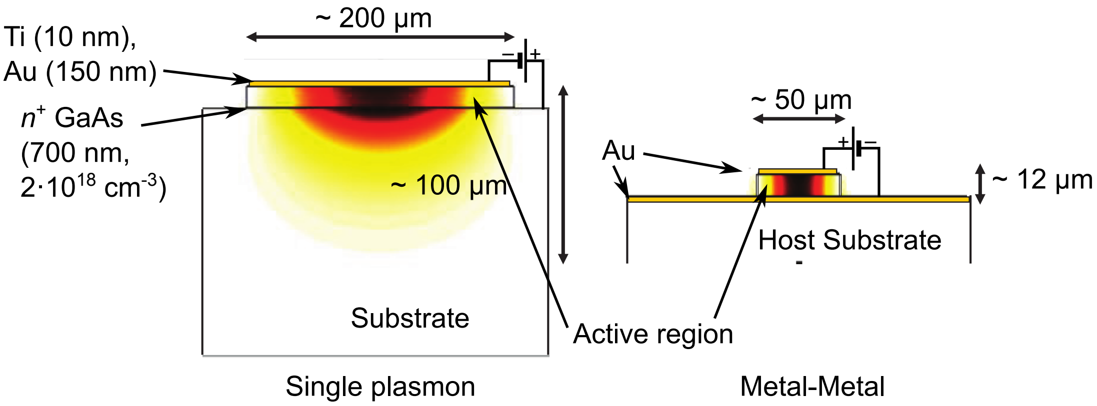

Figure 1.7: **Waveguide designs: single plasmon (left) and metal-metal (right).** The active regions and optical modes are shown. This figure from Ref. [3], published by IOP Publishing Ltd., is used under the Creative Commons licence CC BY 3.0, and has been adapted with information from Refs. [41, 45, 46].

In the *single plasmon* configuration, the active region is between the top metal contact and a thin doped layer. This waveguide exhibits relatively low losses and yields an almost Gaussian, single-lobed far field by coupling into free space modes. However, for low photon energies, this waveguide becomes less efficient, since then the optical mode becomes larger in size and gets pushed out into the substrate, which reduces the overlap with the active region. [34, 45, 46]

In the *double metal* configuration, the active region is quenched between two metallic layers. This yields a high overlap of the mode field with the active region for a large range of frequencies [34]. Confining the optical mode between the metallic layers allows to use thin and narrow ridges (< 100 µm), which contributes to improved thermal management with a reduced power dissipation [46]. However, the fabrication of metal-metal waveguides is more complicated since it requires thermo-compression bonding techniques [46]. The output beam profile has a lower quality and a much larger divergence angle (typically >50°) as compared to single plasmon waveguides [3, 34, 45, 46].

Quantum cascade lasers work most efficiently at low temperatures and are often operated using liquid helium cooling [40, 46]. Output powers above 1 W have been demonstrated at 10 K [47]. The operating temperature can be further increased by optimising the QCL active region, and recently, a QCL operating at 250 K has been demonstrated, although with sub-mW output power [48].

1.1.5 Difference frequency generation

THz radiation can be generated by combining the radiation of two higher frequency radiation sources and extracting the difference frequency. This can be achieved e. g. using mid-infrared quantum cascade lasers operating at slightly different wavelengths [49, 50]. In contrast to THz QCLs, mid-infrared QCLs have higher output power and operate at room temperature. If one of the mid-infrared QCLs is tuned in output frequency, the THz difference frequency is tuned accordingly. This way, a continuously tunable source between 1.7 THz and 5.25 THz was demonstrated [50]. However, this approach suffers from the low conversion efficiencies of the difference frequency generation.

1.1.6 Photoconductive antenna

Photoconductive antennas [51, 52] are metallic dipole antennas that are deposited on a photoconductive substrate. Upon illumination with a femtosecond optical pulse, they emit a terahertz pulse [53]. The principle of operation is shown in Fig. 1.8.

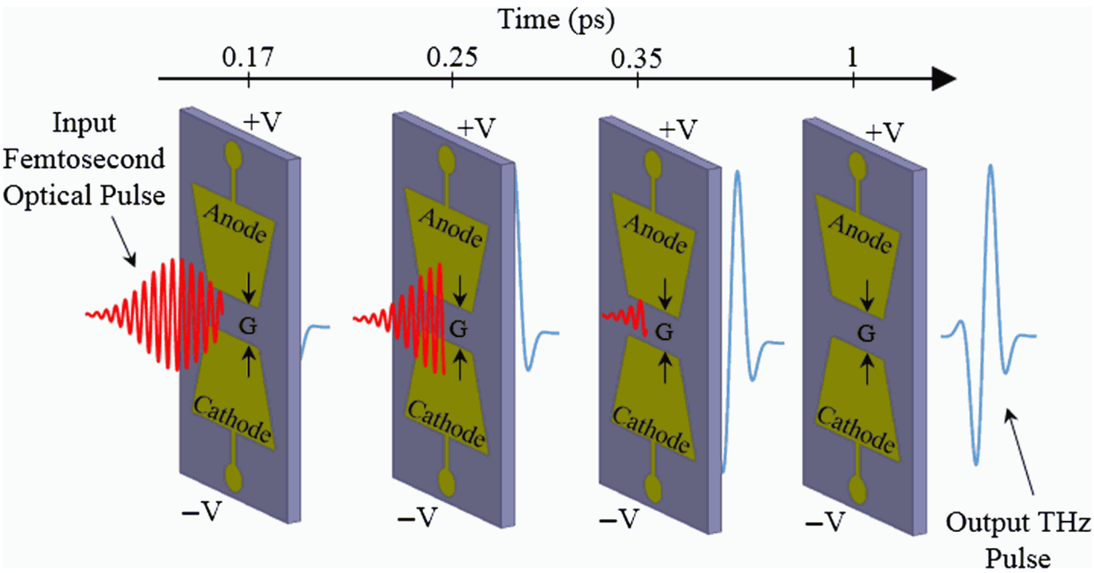

Figure 1.8: **Operating principle of a photoconductive antenna generating THz pulses.** An incident optical pulse is converted to a THz pulse. Reprinted with permission of SPIE from Ref. [53].

A high voltage (~ 120 V [54]) is applied to the photoconductive antenna. The incident optical/infrared pulse generates electron-hole pairs in the photoconductive substrate, such as GaAs or InGaAs, which are then accelerated by the applied electric field. This creates a time-varying photocurrent that couples to the dipole antenna. As a result, the dipole antenna re-emits a short pulse on the order of a picosecond at terahertz frequencies. [53]

A THz photoconductive emitter is most efficient when a large temporal change in photocurrent is induced [55, 56], which makes materials with small effective mass and large carrier mobility the best candidate [55]. To achieve a large acceleration of charge carriers, a strong electric bias has to be applied to the material. This requires the material to exhibit a high breakdown field as well as a high resistivity, to avoid thermal heating deteriorating the device's efficiency or even damaging it [57]. A suitable material is semi-insulating GaAs [55, 58, 59]. The bandwidth of the THz pulse is limited by the duration of the exciting infrared pulse which determines the electric field rise time [60]. The THz bandwidth can be further increased using a material with carrier lifetimes shorter than the length of a THz cycle ($\lesssim$ 1 ps), such as low temperature grown GaAs, or by deliberately introducing carrier trapping centers in the crystal structure by ion implantation [54, 59–61].

1.2 Terahertz detectors

After an overview of the key figures of merit for detectors, important mechanisms of THz detection are reviewed in this section. For exemplary direct detectors, an overview of the relevant parameters is given in Table 1.2.

1.2.1 Detector characteristics and figures of merit

To compare different types of detectors with each other, some figures of merit are necessary to quantify their performance. These are presented in the following (according to references [62–65]).

Responsivity is the ratio of the root-mean-square values of the electrical output signal to the incident input power P. For detectors generating a photocurrent I or a photovoltage U, it is given by

$$R_{\mathrm{I}} = \frac{I}{P} \quad \text{and} \quad R_{\mathrm{U}} = \frac{U}{P}\,, \tag{1.2}$$

respectively. The units are A/W and V/W.

Measurement bandwidth B defines over which timescale a measurement value is taken. Integration over a larger time (i. e. with a reduced bandwidth) decreases the noise level.

Noise equivalent power (NEP) is the amount of input power that generates an output signal equal to the root-mean-square noise signal output, normalised to a bandwidth of

Detector	NEP ($pW/\sqrt{Hz}$)	Temperature	Responsivity	Response time	Frequency	Reference
Thermal detectors						
Bolometer	2.0	4.2 K	15 000 V/W	3.3 ms	(broadband)	[66]
Golay cell	140	room	100 000 V/W	30 ms	0.04–750 THz	[67]
Pyroelectric	1000	room	70 000 V/W	200 ms	0.1-30 THz	[68]
Thermopile	38 000	room	35 V/W	25 ms	(broadband)	[69, 70]
Semiconductor-based detectors						
GaAs FET	10 000	room	0.008 V/W	–	1.63–2.54 THz	[71]
	28700	room	0.167 V/W	–	0.7 THz	[72]
Bow-Tie diode	6 000	room	0.1 mA/W	7 ns	0.7 THz	[73]
	–	room	5 V/W	–	0.01-1 THz	[74]
	4000	room	6 V/W	–	0.591 THz	[75]
	60	room	220 V/W	–	0.26–0.4 THz	[76]
Si FET (CMOS)	487	room	30 V/W	–	0.2-4.3 THz	[77]
	100	room	115 000 V/W	–	0.7-1.1 THz	[78]
	66	room	800 V/W	–	0.6-1.1 THz	[79]
	400	room	50 000 V/W	–	0.6 THz	[80]
GaAs point contact	–	4.2 K	1 000 000 V/W	–	0.11-0.17 THz	[81]
Single photon detectors						
Electrostatic QDs	10^{-9}	70 mK–4.2 K	10^{6}-10^{10} A/W	–	0.5, 1.43–2.14 THz	[82]
CSIP	$8.3 \cdot 10^{-7}$	$\lesssim$2.3 K	$4 \cdot 10^{6}$ A/W	–	6–30 THz	[83]
Novel materials						
hBN-BP-hBN	100	4 K	20 V/W	–	0.27-0.63 THz	[84]
	–	room	~ 1 V/W			[84]
Graphene bow-tie array	150 000	room	34 µA/W		2 THz	[85]
InAs nanowire	2 000	room	1 V/W	–	0.3 THz	[86]
Graphene FET	515	room	14 V/W	–	0.6 THz	[87]

Table 1.2: Comparison of parameters of direct detectors in the THz frequency range.

1 Hz. If U_n is the noise voltage output, then the noise equivalent power is

$$NEP = \frac{U_\mathrm{n}}{R_\mathrm{U} \cdot \sqrt{B}}\,. \tag{1.3}$$

The unit is W/$\sqrt{\text{Hz}}$. An input signal with power equal to the NEP value yields a **signal-to-noise ratio (SNR)** of 1.

Detectivity is the reciprocal of the noise equivalent power:

$$D = \frac{1}{NEP} \tag{1.4}$$

The **Specific Detectivity** is useful for those sorts of noises where the noise scales with the square root of the detector area A:

$$D^* = \frac{\sqrt{A}}{NEP} \tag{1.5}$$

This allows to compare the performance of detectors of the same type having different areas. The unit is cm$\cdot\sqrt{\text{Hz}}$/W.

Response time characterises the typical timescale over which the detector is able to respond to the signal. For input signals that change on time scales faster than the response time of the detector, the detector output will be strongly reduced and become useless. Thus, the response time defines the maximum measurement bandwidth.

1.2.2 Thermal detectors

In general, thermal detectors are composed of an absorbing element, that is attached to a heat sink over a thermal conductance. Absorbed incident radiation is converted to heat. This increases the temperature of the absorbing element, which will eventually reach a steady-state value. [88]

For a temperature measurement, the absorbing element has to reach thermal equilibrium. Therefore, thermal detectors are rather slow as compared to other types, with response times being typically $>$ 1 ms, but they have the advantage of spanning a broad range of frequencies with a flat response [3, 4].

There are many ways of how the temperature change is read out. Bolometers detect the change in temperature over a change in electrical resistance of a material, typically heavily doped silicon or germanium [4]. They are often operated at cryogenic temperatures and can also be fabricated in focal plane arrays [1].

Thermopiles, one of the oldest thermal radiation detectors, work on the Seebeck thermoelectric effect [89–91]. To increase the output impedance, many thermocouples are connected in series, with the cold junctions mounted on the heat sink, and the hot junctions mounted on the absorbing material. [88, 92]

Pyroelectric detectors use the strong dependence of the dielectric function of a material (e. g. a ferroelectric material) on temperature. This can be detected in a capacitance measurement circuit. [88, 93, 94]

A Golay cell [95–97] is a pneumatic detector of infrared and terahertz radiation. Its working principle is illustrated in Fig. 1.9: incident radiation is absorbed in an absorbing film. The generated heat is transferred to a gas chamber, which has a flexible, reflective film. The gas heats up and causes the reflective film to bend. The change can be detected optically: a lamp illuminates the reflective foil, and tiny changes in reflection due to expansion of the gas can be registered with a photodetector. [96]

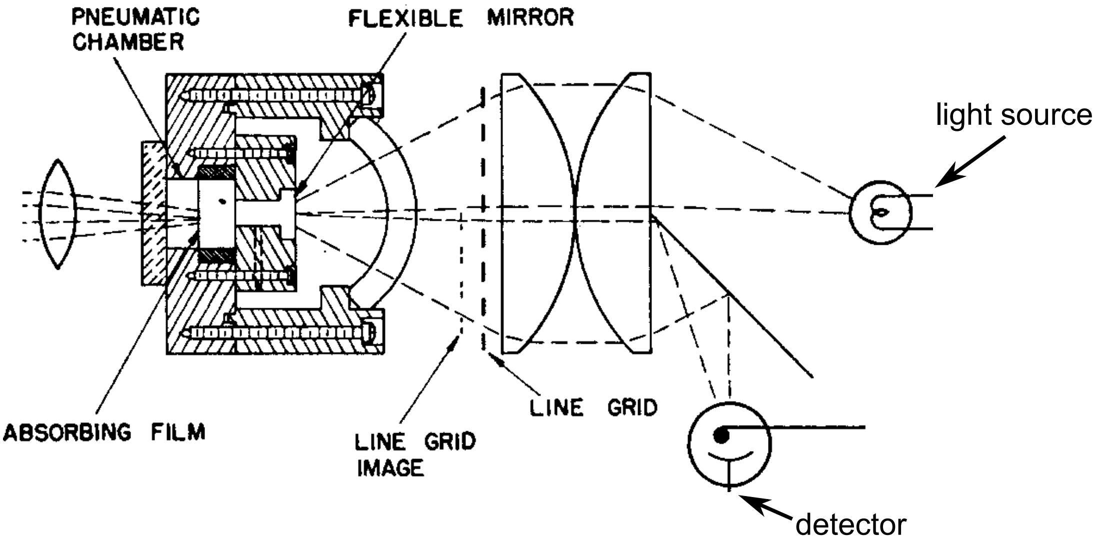

Figure 1.9: **Working principle of a Golay cell**, reproduced from Ref. [97], with the permission of AIP Publishing. The arrows show the light source and optical detector used to optically detect bending of the flexible mirror as a result of THz-induced temperature changes of the gas in the pneumatic chamber.

1.2.3 Schottky barrier diodes

A basic element of solid-state THz technology is the Schottky barrier diode. Due to its nonlinear current-voltage characteristic it is able to rectify incident THz radiation, which at the maximum of an electric field oscillation accelerates electrons and enables them to overcome the Schottky barrier [64]. The responsivity of these diodes rapidly falls off towards the THz range when the frequency is increased. The limiting factor is the series resistance and the junction capacitance, whose inverse product defines the cut-off frequency of the Schottky diodes [64, 98, 99]. Attempts to improve sensitivity in the THz range have focused on reducing both of these values. A typical THz Schottky diode is shown in Fig. 1.10.

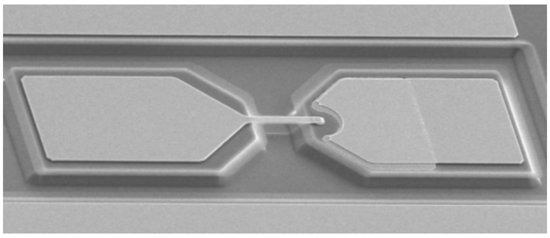

Figure 1.10: **A planar Schottky diode,** scanning electron microscope image. Reprinted from Ref. [99], with the permission of AIP Publishing.

1.2.4 Semiconductor detectors based on a two-dimensional electron gas

A wide range of research is devoted to terahertz detectors using standard semiconductor devices. Amongst them are field-effect transistors (FETs), in which a two-dimensional electron gas is controlled using gate electrodes. Typical figures of merits of such devices are overviewed in Table 1.3. In the following, the physical mechanisms giving rise to a photoresponse in such devices are reviewed.

1.2.4.1 Detection exploiting plasma waves or resistive mixing

One of the first and simplest methods to utilise a FET for power detection is resistive mixing [100]. This early concept was developed with MHz–GHz frequencies in mind. In this detection principle, an AC signal $u_{\mathrm{ac}}(t) = u_{\mathrm{ac}} \sin(\omega t)$ is applied to both gate and drain contacts. The source-drain current is proportional to the applied source-drain voltage $U_{\mathrm{SD}}(t)$ and channel conductance $g(t)$. The channel conductance is proportional to $u_{\mathrm{ac}}(t)$ since the AC signal is applied to the gate. The source-drain voltage has a component proportional to $u_{\mathrm{ac}}(t)$ as well. As a result, the source-drain current gets a component proportional to u_{ac}^2 – a rectified DC output voltage proportional to the input AC power [80].

As the frequency grows, this simple electrostatic picture breaks down. The application of a high-frequency electric field on a 2D conducting channel launches plasma waves (or plasmons), i. e. collective excitations of charge carriers, and this should be considered in FETs at THz frequencies. The dispersion relation for plasmons in an ungated 2D electron gas is [101, 102]:

$$\omega_{\mathrm{P}}^2(q) = \frac{e^2 n_{\mathrm{s}}}{2\varepsilon_0 \varepsilon_{\mathrm{r}} m_{\mathrm{eff}}} q \sim n_{\mathrm{s}} q \, . \tag{1.6}$$

Here, ω is the frequency, q the wavevector, e the elementary charge, n_{s} the surface density, $\varepsilon_0\varepsilon_{\mathrm{r}}$ the dielectric permittivity of the medium, and m_{eff} the effective mass of the particle. It can be seen that ω_{P}^2 is proportional to the electron density n_{s} and the wavevector q, hence $\omega_{\mathrm{P}} \sim \sqrt{q}$.

Under a gate, the plasmon dispersion relation is different. For $qd \ll 1$, where d is the

Type	Bandwidth	Frequency	Comments, figures of merit	Ref.
THz room-temperature FET detectors				
Si CMOS FET		0.216 THz	NEP: 59 pW/$\sqrt{\text{Hz}}$	[104]
		0.59 THz	NEP: 20 pW/$\sqrt{\text{Hz}}$	
		2.52 THz	NEP: 63 pW/$\sqrt{\text{Hz}}$	
		3.11 THz	NEP: 85 pW/$\sqrt{\text{Hz}}$	
		4.25 THz	NEP: 110 pW/$\sqrt{\text{Hz}}$	
Si CMOS FET		0.595 THz	350 V/W; NEP: 42 pW/$\sqrt{\text{Hz}}$	[77]
		0.763 THz	550 V/W	
		1.4 THz	132 V/W	
		1.75 THz	55 V/W	
		2.9 THz	30 V/W; NEP: 478 pW/$\sqrt{\text{Hz}}$	
		4.1 THz	4.6 V/W	
Si CMOS FET	< 20 MHz	3.1 THz	230 V/W; NEP: 85 pW/$\sqrt{\text{Hz}}$	[105]
Si CMOS FET		4.75 THz	NEP: 370 pW/$\sqrt{\text{Hz}}$	[106]
Si CMOS FET		4.75 THz	75 V/W; NEP: 404 pW/$\sqrt{\text{Hz}}$	[107]
Si CMOS FET		0.25–2.2 THz	220 V/W, 45 mA/W, NEP: 70 pW/$\sqrt{\text{Hz}}$ at 1.5 THz	[108]
GaAs FET	33 GHz	1.2–5 THz	30 ps response time, for FEL characterisation, responsivity 0.03–1 V/µJ	[109]
InAlAs/InGaAs/InP HEMT		1 THz	2.2 kV/W; NEP: 15 pW/$\sqrt{\text{Hz}}$	[110]
Graphene FET	180 MHz	3.4 THz	50 V/W; NEP: 120 pW/$\sqrt{\text{Hz}}$	[111]
Sub-THz room-temperature FET detectors				
InAlAs/InGaAs HEMT		280 GHz	1.5 A/W – 5 A/W	[112]
InAlAs/InGaAs/ InP HEMT		200 – 300 GHz	22.7 kV/W; NEP: 0.48 pW/$\sqrt{\text{Hz}}$ 520 V/W at 2 THz	[113]
InP double-heterojunction bipolar transistors	10 GHz	300 GHz	2 kV/W at 0.3 THz, 80 µV/W at 3 THz (decays with frequency as ω^{-6})	[114]
Si, GaAs FET	18 GHz	310 GHz	8.2 Gbit/s data rate; Responsivities of detectors used: Schottky diode few kV/W, 1pW/$\sqrt{\text{Hz}}$ NEP, 20 GHz BW Si MOSFET 5 kV/W, 1 pW/$\sqrt{\text{Hz}}$ NEP (with antenna) GaAs HEMT 10 V/W, 10 nW/$\sqrt{\text{Hz}}$ NEP, few GHz BW	[115]
GaAs FET	18 GHz	310 GHz	8.2 Gbit/s data rate	[116]
GaN/AlGaN HEMT		0.7–0.925 THz	NEP: 30 pW/$\sqrt{\text{Hz}}$ [NEP: 1 pW/$\sqrt{\text{Hz}}$ at T=77 K]	[117]
GaN/AlGaN HEMT		0.65 THz	325 mA/W; NEP: 3.7 pW/$\sqrt{\text{Hz}}$	[118]

Table 1.3: **Overview of some room-temperature semiconductor THz and sub-THz detectors based on field-effect transistors reported in the literature.**

distance between 2DEG and gate, it is [103]:

$$\omega_{\mathrm{P}}^2(q) = \underbrace{\frac{e^2 n_{\mathrm{s}}}{2\varepsilon_0\varepsilon_{\mathrm{r}} m_{\mathrm{eff}}} d}_{s^2} \cdot q^2 = s^2 q^2 \,. \tag{1.7}$$

In this case, the dispersion relation is linear, $\omega_{\mathrm{P}} \sim q$, and the plasma wave velocity s can be introduced.

The utilisation of plasma waves in FETs was proposed as a method for terahertz detection in 1996 [119]. Here, electrons in the conducting channel of a high electron mobility transistor are modelled using the continuity equation and the hydrodynamic Euler equation of motion, which takes into account the Coulomb force acting on the electrons from the charge density fluctuations [119, 120]:

$$\frac{\partial v}{\partial t} + v\frac{\partial v}{\partial x} + \frac{v}{\tau} + \frac{e}{m_{\mathrm{eff}}}\frac{\partial U}{\partial x} = 0\,, \tag{1.8}$$

$$\frac{\partial n}{\partial t} + \frac{\partial (nv)}{\partial x} = 0\,. \tag{1.9}$$

Here, n is the electron sheet density, and v is the mean electron velocity, both of which depend on the time t and coordinate x along the channel. e is the electron charge, m_{eff} the effective electron mass, and τ the scattering time. The rectification of plasma waves has its origin in the non-linear terms $\partial(nv)/\partial x$ and $v\partial v/\partial x$. The photovoltage U_{ph} resulting from these equations can be written in the form [119]:

$$U_{\mathrm{ph}} = \frac{1}{4}\frac{u_{\mathrm{ac}}^2}{U_{\mathrm{G}} - U_{\mathrm{th}}} f(\omega\tau, s\tau/l)\,, \tag{1.10}$$

where U_{G} is the gate voltage and U_{th} the threshold voltage of the transistor. The frequency response is determined by the function f that depends on two parameters: $\omega\tau$ and $s\tau/l$, where $\omega = 2\pi f$ is the angular frequency, s the plasmon velocity and l the channel length. $s\tau/l$ determines how quickly plasma waves decay spatially over the length of the channel, and $\omega\tau$ – how fast they decay in the time domain.

For $s\tau/l \gg 1$ and $\omega\tau \gg 1$, the channel length is small compared to the plasmon decay length. This corresponds to the resonant case, plasma waves are launched along the channel and lead to oscillations of the charge density and photovoltage response along the channel [119, 120]. The function f displays resonant enhancement of the photoresponse.

For a very long channel $s\tau/l \ll 1$, any plasmonic oscillations are damped along the channel, and with $\omega\tau \gg 1$, $f(\omega\tau, s\tau/l) \rightarrow 3$.

Later, researchers have been working on unifying the physical picture of plasmonic mixing with the concept of resistive self-mixing known from electrical engineering [77, 120].

The case $\omega\tau \gg 1$ corresponds to the plasmonic mixing regime. The lower-frequency non-resonant case of $\omega\tau \ll 1$ is often separated in two regimes. The first is the quasistatic limit of resistive self-mixing at very low frequencies, when the size of the channel is small compared to the plasmon wavelength. When the plasmon wavelength becomes smaller than the channel wavelength, the gate and the channel cannot be considered as a single element, and instead, the position dependence of the time dependent gate-to-channel voltage needs to be considered. This is the second case, called distributed resistive self-mixing.

Eq. (1.10) diverges when the gate voltage appoaches the threshold regime. In this situation the equation is not valid, and the response for this regime has been considered in Ref. [121] for the non-resonant case $\omega\tau < 1$. Near the threshold voltage, the photoresponse reaches a maximum of the value

$$U_{\mathrm{ph,max}} = \frac{e u_{\mathrm{ac}}^2}{4\eta k_{\mathrm{B}} T} \,. \tag{1.11}$$

Here, η is an ideality factor describing the fact that for real FETs the conductance changes smoother near the threshold regime than expected theoretically.

Since the plasma wave velocity can reach $\sim 10^7$ m/s, a value much higher than the typical Fermi velocity in two-dimensional electron gases, $\sim 10^5$ m/s, devices utilising plasma waves are supposed to operate up to $\sim$ 10 THz, as opposed to typical $\sim$ 100 GHz transit-time limited performance [119, 122]. In practice, when approaching THz frequencies, the required channel lengths to observe resonant plasmonic enhancement of the photoresponse are very small, in the sub-micron region. Therefore at THz frequencies usually non-resonant detection is observed [121, 123], e. g. in terahertz imaging demonstrations with GaAs transistors [71, 72], and with integrated antennas in the FET [112]. Considerable progress has also been made in the area of silicon-based detectors on CMOS technology [77, 80, 124]. In the last years, focal plane arrays using this principle were demonstrated [78, 79]. Recently, the plasmonic mixing principle has also been exploited in novel two-dimensional graphene-related materials [84, 87, 125, 126].

By fixing the wave vector q of plasma waves, frequency-sensitive detectors can be fabricated. They display a resonant response if the incident radiation frequency matches the plasma wave frequency defined by the wavevector q. This can be achieved by depositing a grating on top of the conducting FET channel, that is simultaneously used as a gate to control the charge density. This mechanism was described on double quantum well structures [127], and later also on single quantum well devices [128, 129] at liquid helium temperatures. This way, a grating induces an in-plane wavevector q, and n_{s} can be controlled by an applied gate voltage, so that a resonant photoresponse is obtained when the frequency of the incident radiation matches the frequency of the plasmon.

1.2.4.2 Photon-assisted tunneling

The concept of photon-assisted tunneling was first introduced in a superconductor-insulator-superconductor system [130] (a Josephson junction, [131]).

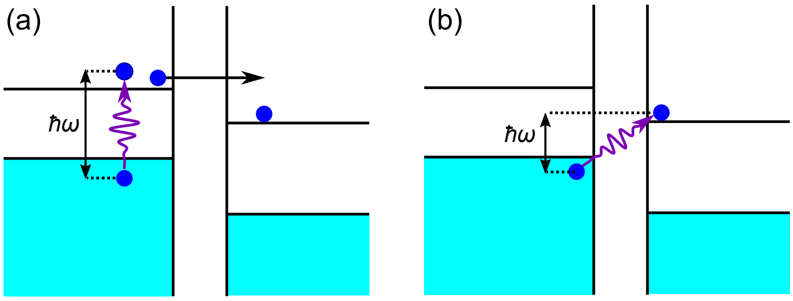

Figure 1.11: **The observation of photon-assisted tunneling.** (a) Normal tunneling after absorption of a photon; (b) Photon-assisted tunneling: for a photon $\hbar\omega$ less than the gap energy this process would be impossible, but is observed – a tunneling electron absorbs a photon. Based on information from Ref. [130].

"Normal" tunneling describes the quantum-mechanical process when a particle passes a potential barrier higher than the particle's energy, which is possible if the barrier is sufficiently thin. This process is shown in Fig. 1.11 (a): once a photon has excited the electron into the upper band, it tunnels through the insulating barrier into the other superconductor. A process in Fig. 1.11 (b) would be impossible by tunneling alone, since the electron does not have sufficient energy to reach the free state in the right superconductor, but it is observed under incident radiation with photon energies less than the gap energy. That means, the photon enables the electron to tunnel into the other material without the intermediate step of first being absorbed within the material – this is photon-assisted tunneling. [130]

This process was later observed in other material systems with tunneling barriers, such as in electrostatic quantum dots [132–134], in self-assembled quantum dots at THz frequencies [135, 136], in resonant tunneling diodes [137] and in 2D gated devices with thin gates [138]. It has also been used to interpret the photoconductance of quantum point contacts formed on a GaAs-AlGaAs 2DEG [139, 140].

1.2.4.3 Thermal effects in gated 2D electron systems

There are several effects that can be understood more generally as thermal effects occuring within the 2D electron gas.

Some detectors use the bolometric effect: incident radiation heats up the temperature of the electrons, which changes the conductance. Bolometric effects dominate in the pinch-off regime, where conduction is sensitive to small temperature changes [141], and commonly give rise to photoconductance, rather than a zero-bias photocurrent or -voltage [81, 141, 142].

The (photo-)thermoelectric effect can give rise to a zero-bias photocurrent in the case of a broken symmetry [143, 144]. In this mechanism, incident radiation locally heats up the charge carriers in a material, which creates a temperature gradient. The observed photocurrent or photovoltage is due to the Seebeck effect. The Seebeck coefficient for a conducting channel is often written in terms of the conductivity using the Mott relation [144, 145]:

$$S = \frac{\pi^2 k_B^2 T}{3e} \left. \frac{\mathrm{d}\ln(\sigma(E))}{\mathrm{d}E} \right|_{E=E_F} . \tag{1.12}$$

As in a thermocouple, a temperature difference at the junction of two materials with Seebeck coefficients S_1 and S_2 induces a thermovoltage of

$$U_{\mathrm{ph}} = \Delta T (S_1 - S_2) . \tag{1.13}$$

The materials do not have to be chemically different; in the case of semiconductor 2DEGs, they can be made dissimilar by gating which changes their conductivity [84, 111, 144–146].

The mechanisms above, the bolometric and photothermoelectric effects, arise from a local increase of the temperature of charge carriers in the sample. These mechanisms are relevant when electrons are excited and very quickly, on a picosecond time scale, thermalise with each other, but not necessarily with the lattice, which results in a locally higher electron temperature.

On the other hand, in clean samples with a high mobility, there are few scattering processes. In this case, electron "heating" can also occur in a collisionless way, in the sense that the incident radiation increases the mean electron energy. The increase in the mean energy of the electrons can be estimated as

$$\frac{\mathrm{d}p}{\mathrm{d}t} = eE_{\mathrm{ac}} \cos(\omega t) \;\Rightarrow\; p = p_0 + \frac{eE_{\mathrm{ac}}}{\omega} \sin(\omega t) \;\Rightarrow\; \langle E_{\mathrm{kin}} \rangle = \left\langle \frac{p^2}{2m_{\mathrm{eff}}} \right\rangle = E_{\mathrm{kin},0} + \frac{e^2 E_{\mathrm{ac}}^2}{4 m_{\mathrm{eff}} \omega^2} . \tag{1.14}$$

Such a collisionless mechanism has been used to explain the photoconductance of a quantum point contact in Ref. [81].

1.2.4.4 Photovoltaic effect

In gapless materials such as graphene, where both electrons and holes can be present simultaneously, a THz photoresponse can arise due to the photovoltaic effect [85]. This is shown in Fig. 1.12.

The material contacting graphene was Ti on one half of the antennas, leading to n-type doping in the graphene, and Pd on the other half of the antennas, giving rise to p-type doping. This leads to an internal electric field which separates photogenerated electron-

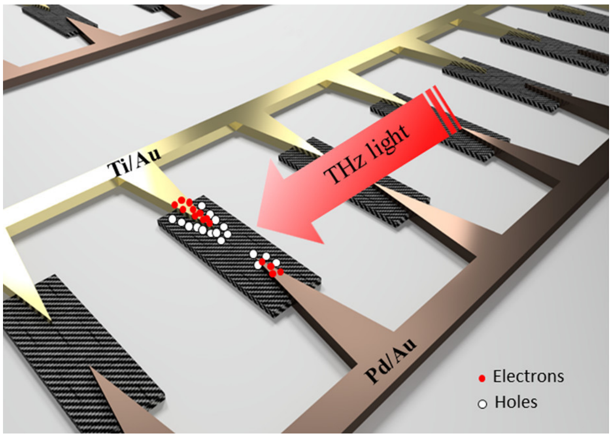

Figure 1.12: **Photovoltaic THz detection.** An array of THz antennas, made from different materials, is placed on top of graphene flakes. The resulting internal electric field in the graphene draws apart photoexcited electrons and holes due to the photovoltaic effect. This graphics, published by the American Chemical Society, is licenced under the Creative Commons licence CC BY 4.0 and is from Ref. [85].

hole pairs by the photovoltaic effect. The mechanism is most efficient when the graphene layer is tuned to the Dirac point using the back gate. [85]

1.2.5 Photoemissive detectors

Another class of detectors operates on internal photoemission. A photocurrent is generated by the internal photoelectric effect: electrons are photoexcited above a workfunction barrier formed at the interface between two semiconductors [147]. A DC bias is applied to extract the photoexcited carriers, i. e. such detectors usually operate in the photoconductive regime. An example is shown in Fig. 1.13.

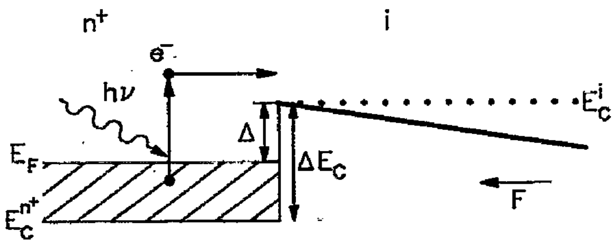

Figure 1.13: **Working principle of a homojunction internal photoemission detector.** Reprinted from Ref. [147], with the permission of AIP Publishing.

If the two semiconductors are chemically different, the devices are called heterojunction internal photoemission detectors. If the same semiconductor material is used, the workfunction is created by different doping densities – these are homojunction internal photoemission detectors [147, 148]. These devices work well in the mid-infrared and the lower-wavelength end of the far-infrared, but their responsivity rapidly falls off towards the THz range [149]. The physics of these devices will be explained in more detail in the introduction to chapter 5. Internal photoemission is also the underlying principle of quantum well infrared photodetectors and blocked impurity band detectors [98, 148].

1.2.6 Non-uniform carrier heating in asymmetrically shaped diodes

Another concept of terahertz radiation detection is based on non-uniform carrier heating in diodes [150, 151]. The diodes (often called bow-tie diodes) have an asymmetrical shape, so that under incident radiation, this gives rise to different gradients of the electric field. This generates a measurable photoresponse. These experiments were performed on GaAs diodes; later experiments implemented InGaAs-based diodes, and imaging of objects was demonstrated [73–76].

1.2.7 Single-photon infrared photodetectors

To achieve single photon sensitivity in the mid- and far-infrared ranges, very low (milli-Kelvin) temperatures are required. Prominent examples are charge-sensitive infrared photodetectors and coupled electrostatic quantum dots.

Charge-sensitive infrared photodetectors (CSIP, Fig. 1.14) are single-photon detectors for the range of 10 – 50 µm (6 – 30 THz). They are based on a double quantum well structure. The upper quantum well is isolated from the lower quantum well by negatively biased top gates. When an infrared photon is absorbed by an electron in the top quantum well via

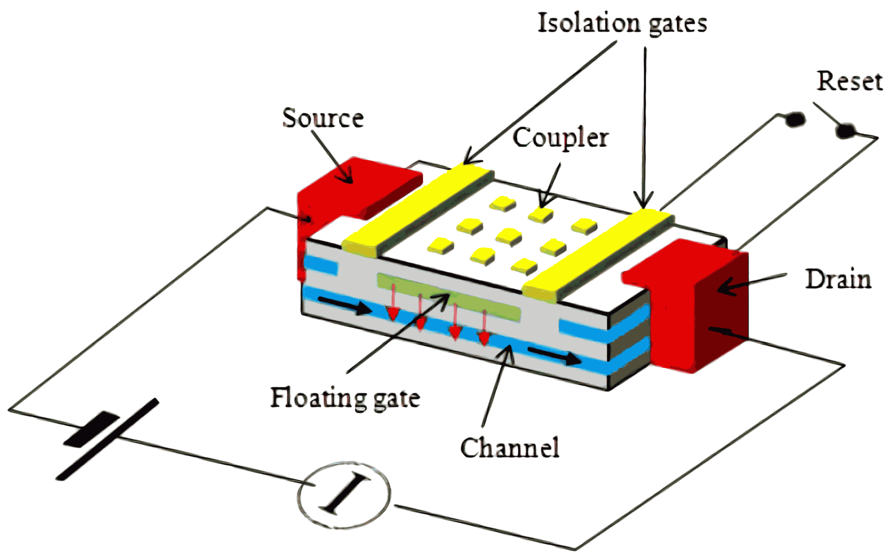

Figure 1.14: **A charge-sensitive infrared photodetector.** Charge that is generated by incident light accumulates in the isolated upper quantum well and changes the conductance of the bottom quantum well. This graphics, published by MDPI, is licenced under the Creative Commons licence CC BY-NC-SA 3.0 and is from Ref. [83].

an intersubband transition, the electron tunnels to the lower quantum well, leaving a hole behind. The presence of charge in the upper quantum well changes the conductance of the lower quantum well channel. With time, charge in the upper quantum well accumulates. The detector can then be reset to its initial state by sending a voltage pulse to a reset gate. [83]

Another detection mechanism involves coupled electrostatic quantum dots, see Fig. 1.15. By applying a negative voltage to the gates (yellow in Fig. 1.15), the underlying 2DEG is depleted, and two coupled electrostatic quantum dots are formed. The electrostatic quantum dot on the left acts as a single-electron transistor. If an absorbed photon ionizes the quantum dot on the right, its charge can be sensed by measuring the transport characteristics of the single electron transistor: the conductance-vs-gate voltage curves shift depending on the charge state of the quantum dot. [82, 152]

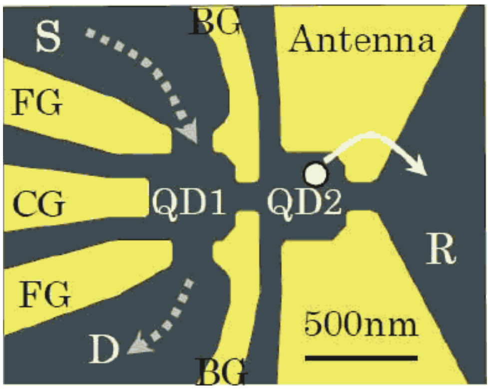

Figure 1.15: **A single electron transistor sensing a nearby electrostatic quantum dot.** From Ref. [82], © 2011 IEEE.

1.2.8 Self-mixing in lasers

Another radiation detection technique uses the laser source itself both for generation and detection. The concept is based on the fact that the operation parameters of a laser depend on the amount of light coupled back into the cavity. The reason is that the electric field back-reflected into the laser cavity adds phase-sensitively to the lasing field [153]. This interference or mixing results in variations in output power, gain, lasing spectrum, and operating voltage [154].

One of the first demonstrations was a laser Doppler velocimeter [155]. Light from a helium-neon laser reflected from a moving target is reflected back with a slight shift in frequency. Instead of using an external interferometer such as the Michelson interferometer, in reference [155] the light is backreflected into the laser cavity, as shown in Fig. 1.16. Thus, the laser output itself is modulated with the Doppler frequency, which can be detected with a photodetector.

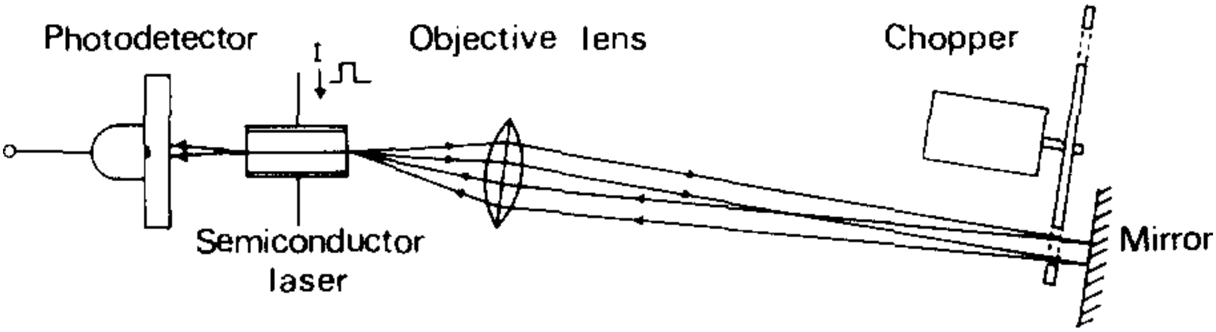

Figure 1.16: **A laser self-mixing setup.** The laser output, modulated with an optical chopper, is backreflected into the laser cavity. Reprinted from Ref. [156], with the permission of AIP Publishing.

Later experiments with semiconductor lasers (AlGaAs) [156–158] have demonstrated how light coupled back into the laser cavity changes the laser operation: either by reducing its output power [156], changing the voltage across the laser or creating oscillations of the operating voltage [157], or generating hysteresis phenomena in the light-current characteristics [158].

This effect was later also observed with QCLs [159], which allowed them to be used in imaging applications [154, 160]. Here, as a self-mixing signal, the change in voltage across the laser is used, when the laser beam is focused on an object. Scanning the laser beam, or scanning the object with a fixed laser beam, allows the creation of an image of the target, which contains information about the spatial dependence of its reflectivity in the terahertz range [154, 160]. In references [46, 160] a silicon lens with an antireflection coating made out of Parylene C was mounted on the facet of the QCL. This reduces the reflectance of one of the laser facets, which suppresses lasing. This turns the quantum cascade laser into a quantum cascade amplifier, which is very sensitive towards reflections from an external mirror or object coupled back into the laser cavity that can reinstate the lasing action [46, 160].

1.2.9 Photoconductive sampling

Detection of a THz pulse by photoconductive sampling allows to measure the temporal dependence of the electric field E, unlike other detectors, that measure intensities $I \sim E^2$. This can be accomplished by photoconductive antennas (see 1.1.6) [53].

For detection, photoconductive antennas do not have any external bias applied. The THz radiation is focused on the antenna together with an optical pulse, that is used for switching the photoconductive antenna. The optical pulse generates photoexcited electrons and holes, that are accelerated by the electric field of the incident THz beam. This way, a photocurrent can be detected, and by adjusting the delay between optical pulse and THz beam, the THz electric field can be probed [53, 161]. For photoconductive detection, a short sub-picosecond optical excitation pulse as well as short carrier lifetimes in the semiconductor material are essential, as they directly relate to the time window in which the charge carriers sample the electric field and hence define the THz bandwidth of the detector [161, 162].

1.3 Terahertz spectroscopy and near-field imaging

By combining detection and generation, techniques for studies of materials and devices in the THz frequency range have emerged. Three important techniques are reviewed in the following.

1.3.1 Fourier-transform infrared spectroscopy

A widely used technique for spectroscopy in the infrared is Fourier-transform infrared spectroscopy (FTIR) [163]. An FTIR usually contains a Michelson interferometer (Fig. 1.17).

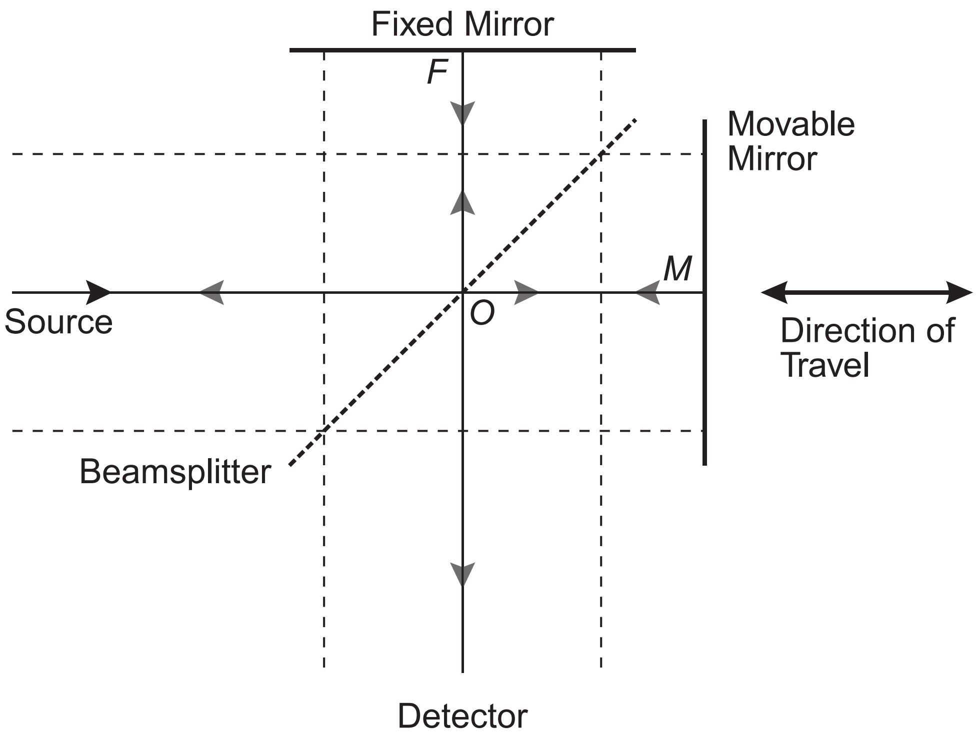

Figure 1.17: **Beam paths in the Michelson interferometer.** Reproduced from Ref. [163] with permission; figure copyright: © 2007, John Wiley and Sons.

The input beam is separated on a 50:50 beamsplitter. One beam is reflected on a fixed mirror, while the other beam is reflected on a movable mirror. At the beamsplitter, each of the reflected beams are separated into another two beams, respectively. This way, there are two beams incident on the detector. The electric fields of the beam reflected on the fixed mirror $E_1(t)$ and of the beam reflected on the movable mirror $E_2(t)$ interfere with each other phase-sensitively, i. e. constructively or destructively, dependent on the respective phase or travel distance difference. [163]

With the electric fields for monochromatic radiation

$$E_1(t) = Ae^{i\omega t} \text{ and } E_2(t) = Ae^{i\omega t + i\delta} \tag{1.15}$$

we get for the detector intensity $I(\delta)$, where δ is the phase delay:

$$I(\delta) = [E_1(t) + E_2(t)] \cdot [E_1(t) + E_2(t)]^* = 2A^2[1 + \cos(\delta)] \,. \tag{1.16}$$

The phase delay δ is related to the wavelength of the radiation λ and the mirror displacement Δs:

$$\delta = 4\pi \cdot \frac{\Delta s}{\lambda} \,. \tag{1.17}$$

For monochromatic radiation, the periodicity of $I(\delta)$ allows to extract the wavelength of the radiation. For a spectrum consisting of multiple frequencies, the spectrum is obtained by Fourier transformation.

FTIRs can be used from the terahertz to the near-infrared ranges, depending on the choice of the source, beamsplitter and detector. For terahertz measurements, a Mylar beamsplitter can be used together with a liquid-helium cooled bolometer as detector. [46, 164]

1.3.2 Terahertz time-domain spectroscopy

By combining photoconductive antennas for generation and for detection, a terahertz time-domain spectroscopy (TDS) setup (Fig. 1.18) can be created [165–167].

Femtosecond laser pulses are divided into two beams. One of them is used to create terahertz pulses on a photoconductive antenna. The other beam can be time-shifted by a delay line and is used for sampling of the terahertz signal on the other photoconductive antenna. Silicon lenses on the antennas are used to focus the THz radiation. By scanning the time delay, the waveform of the electric field, $E(t)$, can be recorded. [53, 168]

The Fourier transform of $E(t)$ yields both amplitude and phase information. This way, THz-TDS can be used to study both the real and imaginary part of the dielectric function of a material in the terahertz frequency range. [53, 168]

1.3.3 Terahertz scanning near field optical microscope

There is a well-known limit to the minimal size of objects that can be imaged in an optical system – the diffraction limit. Features that are smaller than about half the wavelength in a medium, $\lambda_0/(2n)$, where λ_0 is the vacuum wavelength and n is the refractive index of the

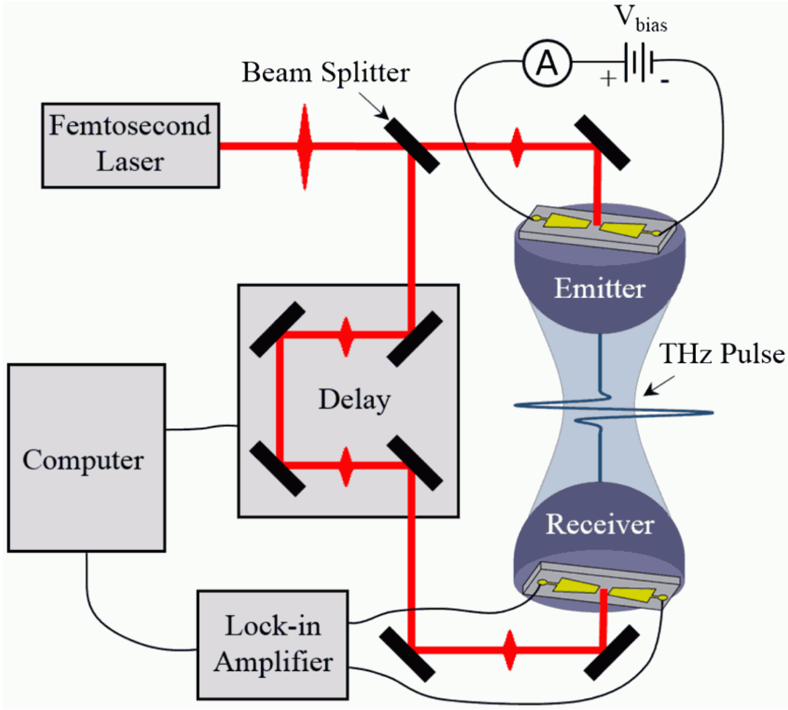

Figure 1.18: **Schematics of a terahertz time-domain spectroscopy setup.** Reprinted with permission of SPIE from Ref. [53].

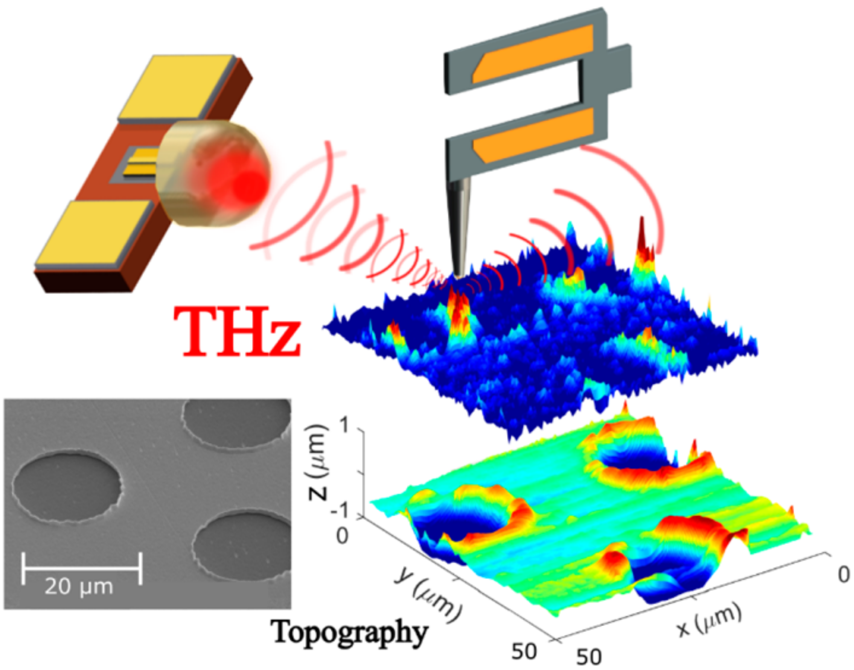

Figure 1.19: **Sub-wavelength imaging with a Terahertz scanning near field optical microscope.** Reprinted with permission from Ref. [170]. Copyright 2017 American Chemical Society.

medium, cannot be resolved by optical systems [169]. This limits the resolution to hundreds of microns in the THz frequency range.

However, this limit can be overcome by using near-field techniques. This is used in the scanning near field optical microscope, an imaging technique that has been transferred into the terahertz domain [170–180]: incident THz radiation is focused on a sharp metallic tip with < 50 nm radius [170] (see Fig. 1.19). The tip concentrates the electromagnetic field in a small region. The scattered light is collected by a detector and contains information about the material close to the tip at a resolution orders of magnitude better than the wavelength, such as 40 nm or $\lambda/3000$ [175].

2 Combining terahertz, optics, and cryogenics using a waveguided system

As a prerequisite for the following experiments, a setup is needed that is capable of performing measurements of electrically contacted samples at liquid helium temperatures with simultaneous optical (visible and near-infrared) access and terahertz excitation. This chapter describes the setup I designed and constructed to meet these requirements, as well as the resulting performance of the setup, which formed the basis for experiments presented in subsequent chapters.

Given the constraints of the cryogenic environment, it is a challenging task to realise a dual-access terahertz and optical system, ensuring at the same time a good thermal contact to the sample for cooling down. Many materials transparent to visible radiation are absorbing in the terahertz region, and vice versa, except for some as e. g. polymethylpentene (TPX) [181]. Both terahertz and optical access from one side of a cryogenically cooled sample would require use of such a material for the cryostat window. However, the desired capability of high-efficiency diffraction-limited optical microphotoluminescence requires a microscope objective with a short working distance on the order of a few millimeters, which precludes the simultaneous free-space access for a terahertz beam. The issue can be resolved by exciting a sample from the bottom with terahertz radiation focused by a parabolic mirror, and using the top side of the sample for optical access.

A free-space configuration using components such as lenses or parabolic mirrors, which is the common design of terahertz setups, has several downsides. To achieve the tightest focal spot on a sample, a high numerical aperture is required [182], which makes it difficult to quantify the incident intensity, and makes the setup prone to small changes in the focal position. A beam of low divergence requires a low numerical aperture $n \sin \vartheta$ and will result in reduced focusing capability (larger beam waist Δx) by Abbe's diffraction limit [182], which states that the resolution Δx inversely scales with numerical aperture, $\Delta x = \lambda/(2n \sin \vartheta)$ [183]. Such a system will be difficult to align and will be prone to angular misalignment, since susceptibility to misalignment increases with the total path length. In addition, the optical components are expensive, their bulkiness complicates usage in scenarios where purging is required, and their use is particularly challenging in difficult-to-access environments such as cryostats.

These issues could be eliminated by the use of waveguides. Metallic single-mode waveguides are common in microwave technology, and single-mode dielectric optical fibers are a routine tool in infrared and visible optics. In the terahertz range, single-mode waveguides become increasingly impractical with rising frequency [184], due to prohibitively high losses [185, 186] and difficulty in coupling and fabrication. In dielectric terahertz fibers, losses per lengths are substantially higher than in their optical counterparts [187]. The losses of multi-mode hollow metal waveguides are proportional to λ^2/R^3, where λ is the wavelength and R the radius of the waveguide [188]. This makes multimode waveguides with $R \gg \lambda$ attractive. Therefore, I decided to design and construct a system that delivers terahertz radiation to the bottom of a sample using a multimode waveguide, while optical microphotoluminescence can be performed from the top.

In multimode waveguides, mixing of modes may result in a large size of the output beam with a poor profile, which will be impractical for further focusing by lenses or parabolic mirrors. However, as will be shown, by exploiting multimode interference and the self-imaging phenomenon, the waveguide itself can be designed to serve as a focusing element providing a tight spot at its output, which is how the waveguide system presented here works. In this chapter, I will describe the design and the performance of the waveguided delivery system, while in chapter 3, the physics behind the focusing effect will be explained.

2.1 Operation of the quantum cascade laser

The THz source used throughout this work is a THz quantum cascade laser (QCL) [38, 40]. This source needs to be cooled to liquid helium temperatures, and thus has to be operated in a cryostat. The THz radiation needs to escape from the cryostat, and for this purpose, a high-density polyethylene (HDPE) window is used. HDPE is amongst the materials with lowest losses in the terahertz region, and its complex dielectric function is approximately constant across the range of 0.8–2.7 THz [189].

The HDPE window has a cylindrical form and separates ambient room pressure from the vacuum in the cryostat. The coldfinger is made out of oxygen-free high conductivity copper

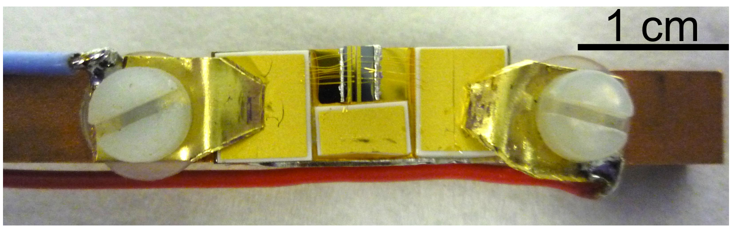

Figure 2.1: **Photo of the coldfinger assembly with the QCL.** The QCL chip is held in place by two brass clamps, that act as the two electrical contacts. They are screwed in place by plastic screws and washers that isolate the brass clamps from the conducting copper coldfinger. Everything has to fit into the 12 mm diameter inner bore of the cylindrical HDPE window.

by electrical discharge machining and sticks out in the cylindrical HDPE window of the vertical continuous-flow Janis ST-300 cryostat. With the THz QCL mounted, the coldfinger assembly looks as shown in Fig. 2.1.

Although this thin coldfinger design, similar to the one described in Ref. [46], does not provide maximum thermal cooling power, it was chosen as it allows the copper waveguide used in subsequent experiments to be brought as close as 2–3 mm to the QCL facet. A photo of the HDPE window of the coldfinger is shown in Fig. 2.2 (a). In Fig. 2.2 (b), the same HDPE window is photographed in the infrared range using a FLIR thermal camera from Thorlabs during cooldown of the QCL using liquid helium. Since HDPE is partially transparent to thermal radiation, the coldfinger with the QCL can be observed through the HDPE window. The coldfinger assembly, being substantially cooler than room temperature, emits orders of magnitude less thermal radiation in the infrared range. The lack of thermal radiation coming from the coldfinger, superimposed on the HDPE's own thermal emission, appears as a cooler area on the thermal camera image. This see-through effect enables diagnosis of thermal issues during cooldown, such as parts of the coldfinger touching the inside of the HDPE window.

To drive the QCL, a high current pulsed width modulation (PWM) signal is used (similar to [46]). The reason is that QCLs dissipate a lot of power (e. g. around 9 W for the laser, as will be seen), and when driving the QCL by a direct current, the cryostat coldfinger would not be able to manage the heat dissipation and maintain the required temperature. Therefore,

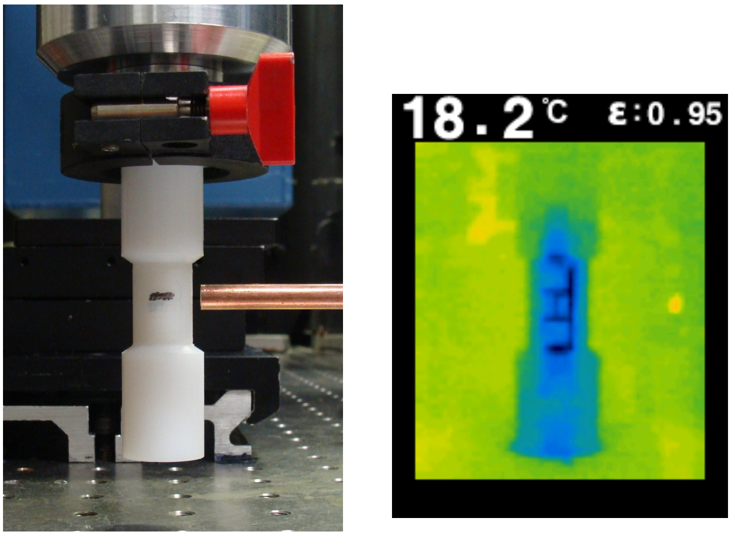

(a) (b)

Figure 2.2: **Photo of the HDPE window with the coldfinger assembly inside.** (a) Photo in the visible range with a copper waveguide on the right-hand side, (b) Photo in the infrared range with cooling of the coldfinger, made with a FLIR camera from Thorlabs. The see-through effect obtained thanks to the partial transparency of the HDPE window is useful for diagnosis of thermal problems during liquid helium cooling.

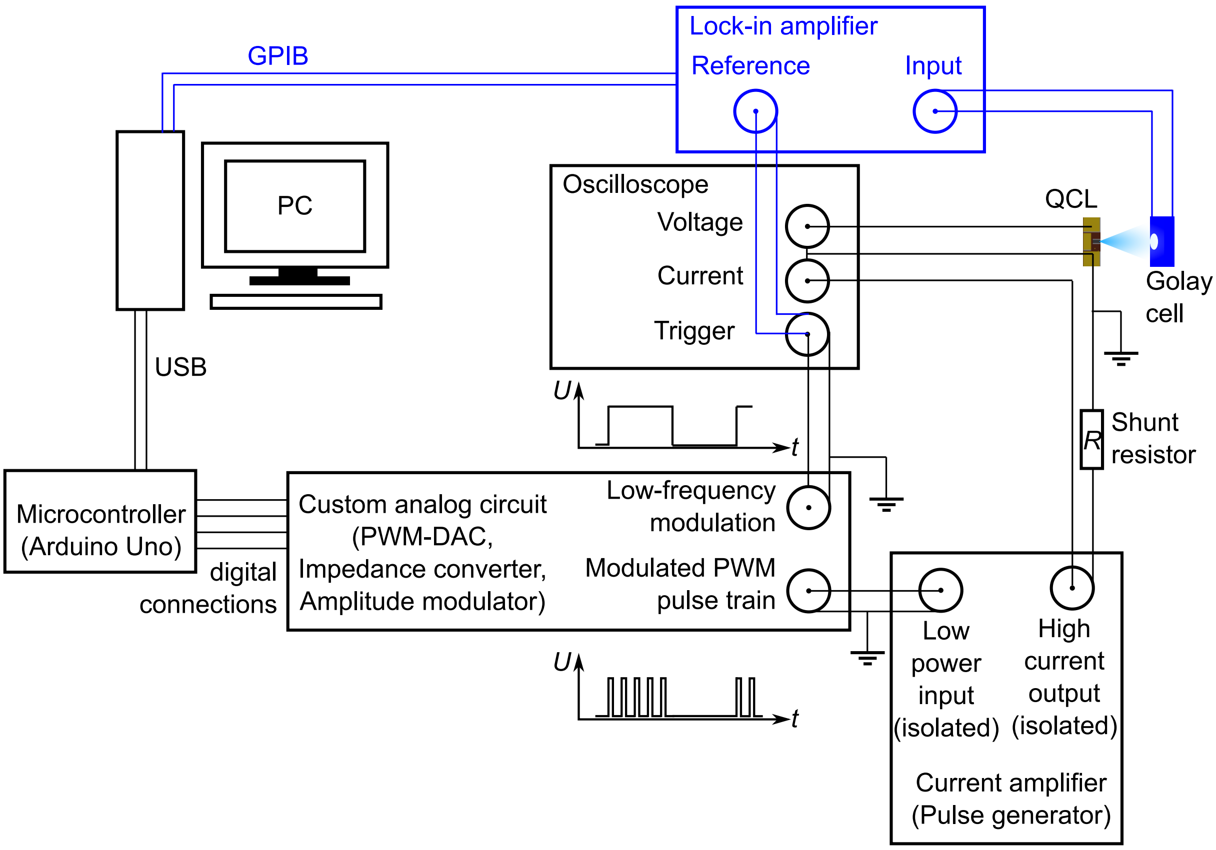

Figure 2.3: **Experimental setup to power the QCL.** The digital waveforms synthesized on an Arduino microprocessor controlled from a computer are converted into analog waveforms and sent to an oscilloscope and a current amplifier to power the QCL, respectively. For a power measurement, shown in blue, the QCL output signal is measured by a Golay cell, whose output signal is demodulated by a lock-in amplifier at the slow modulation frequency and acquired by the computer.

the QCL is driven with a PWM/square wave signal with a low duty cycle (typically 0.1–2 % for the QCL used, and >500 Hz frequency).

The THz output of the QCL is measured with a Golay cell. These detectors are AC coupled, i. e. they react to a change in incoming radiation, and have a very slow response time, with the best responsivity being around 10 Hz. Therefore, a double-modulation technique is employed, that consists of two signals: the PWM pulse train described above is gated with a low-frequency modulation signal. The Golay cell then reacts to this low-frequency modulation, which is used as a reference in measurements with a lock-in amplifier [14, 15]. In Fig. 2.3, the electrical setup that was built is shown.

The QCL has a low resistance of a few Ohms at its operating point and thus has to be driven using a low-impedance, high-current pulsed source. To generate the signals, I wrote a custom firmware for an Arduino microcontroller, and designed and fabricated an analog circuit to convert the digital signal output of the microcontroller to analog signals.

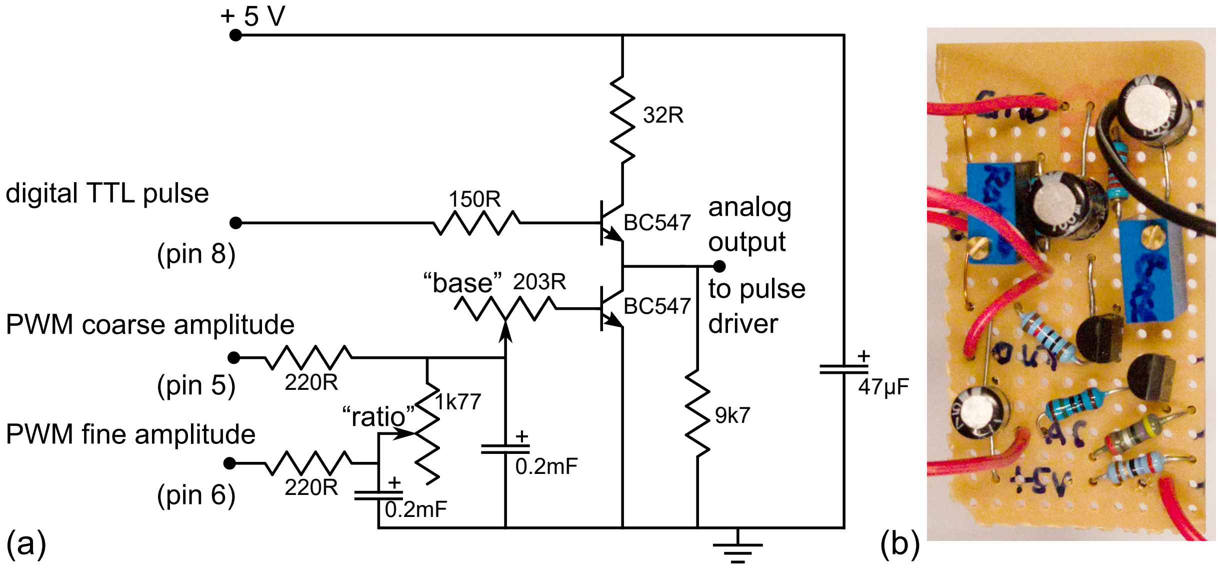

Figure 2.4: **Circuit of the custom-made analog circuit used to drive the pulse amplifier of the QCL.** (a) Diagram of the digital-to-analog converter and impedance matching circuit, (b) finished device soldered on a circuit board.

These analog signals of the desired amplitude and timing are then sent to the current pulse amplifier J517 built by the Cavendish Electrical Workshop, which has a low impedance output.

This approach using a custom-developed circuit was chosen instead of commercially available devices for a variety of reasons. One way of generating the double-modulation signal is to use standard function generators. This requires two coupled devices, where one function generator is gated by the other. This setup may have issues with pulse synchronisation: depending on the ratio of duty cycles and frequencies, some pulses may be "cut short" at the end of a slow modulation pulse in a practical realisation. Also, many simple function generators do not have a gating input, and their duty cycle control has a lower limit of 10 %, which is too high. Alternatively, instead of using a pulse amplifier after the two coupled function generators, a commercial high current pulsed voltage source could be used as one of the function generators. However, tests with commercial HP/Agilent 8114A high current pulsers showed considerable timing jitter on the order of 50 ns, and long-term temporal drifts of the pulse lengths in excess of 200 ns. While this is not relevant for a simple power measurement of the QCL, it can be an issue for more advanced experiments involving synchronisation of pulsed sources, as those used for self-mixing measurements. Another possibility to generate the double-modulation waveform would be to use an arbitrary waveform generator, but this is already a much more advanced device than what is needed to synthesize the desired waveform.

Therefore in this work, an Arduino microcontroller together with a custom-made analog circuit is used to create the double-modulation waveform. The microcontroller is connected to the measurement computer via USB and is controlled over a virtual COM port. A custom firmware was written using a combination of the Arduino libraries and the low-level commands of the AVR Atmega 328P microcontroller. The microcontroller synthesizes the TTL timing waveforms and two PWM signals for amplitude control.

The developed analog circuit is powered by the 5 V USB voltage. It modulates the amplitude of the digital signal and converts its impedance to match the input of the current amplifier. The circuit, shown in Fig. 2.4, was first simulated in LTSpice, later assembled and tested on a breadboard, and finally soldered and fine-tuned.

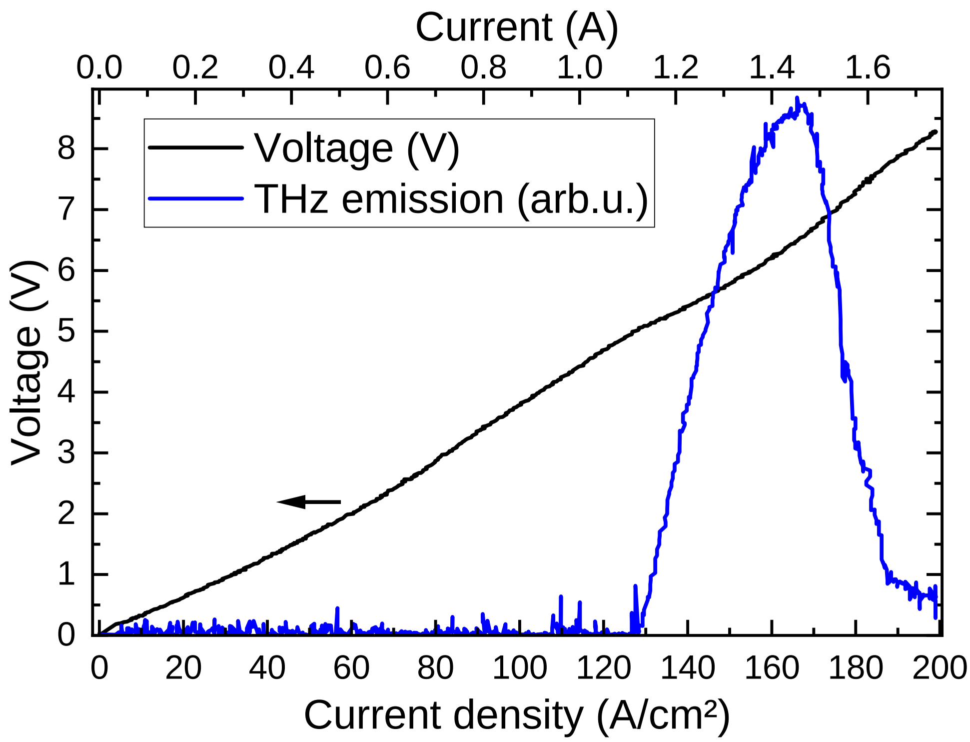

Figure 2.5: **Electrical and optical characteristics of a quantum cascade laser.** Voltage across a 1.9 THz single-plasmon QCL (black) and THz output power measured with a Golay cell (blue) as a function of the current (top axis) and current density (bottom axis) flowing through the QCL.

The waveform parameters such as timing and amplitude are set by byte and integer values and can be changed programmatically on the Arduino microcontroller. Using communication over the virtual COM port, one can change the duty cycle, frequency, and amplitude of the desired waveform. With the 16 MHz intrinsic clock, on-times as short as 250 ns (corresponding to 4 clock cycles) have been achieved. The miniature-sized portable microcontroller replaces two coupled function generators that would otherwise have been needed to synthesize the desired waveform. It can generate short pulses with sharp edges and has a stable time base thanks to its intrinsic clock. Compared to commercial function generator units, this solution is also orders of magnitude less expensive and provides much more flexibility.

Thus generated double-modulated pulse train of the desired pulse height is sent to the QCL after being amplified with the current pulse amplifier. The current is read as a voltage falling across a shunt resistor with a low resistance of 0.1 Ω, digitally on the oscilloscope.

As an example, a typical measurement of the current-voltage characteristic of a QCL combined with its lasing output power is shown in Fig. 2.5. To measure it, a Golay cell was mounted in front of the QCL cryostat at a distance of 9 cm. A lock-in amplifier then reads the optical power from the Golay cell, using the low-frequency modulation signal as output.

The QCL used throughout this work is a high-power single-plasmon laser (ridge length 3.5 mm, ridge width 250 µm) operating at a frequency of about 1.9 THz (~ 160 µm wavelength). This QCL with wafer number V308 is based on a bound-to-continuum design [190], where one period of the active region consists of the following layer sequence in nanometers: **4.4**/12.6/**4.4**/12/**3.2**/$\underline{12.4}$/**3**/$\underline{13.2}$/**2.4**/14.4/**1**/11.8/**1**/14.4. Here, the bold values are $Al_{0.1}Ga_{0.9}As$-barriers and the non-bold values are the GaAs quantum wells. The two underlined quantum wells are n-doped with silicon at a density of $1.3 \cdot 10^{16}/cm^3$ [190].

At the threshold of around 1.1 A, energy levels in the active region periods start to become aligned and lasing operation starts to take place. The maximum output power is seen around 1.45 A, and for even higher currents, output power drops as the energy levels become misaligned again. Current-voltage curves of quantum cascade lasers often exhibit larger nonlinearities [46] than in this measurement, where the current-voltage curve is nearly Ohmic. This may be due to the additional contact resistances added in series to the resistance of the active region due to the 2-terminal measurement configuration, which would diminish non-linear effects arising from the semiconductor heterostructure.

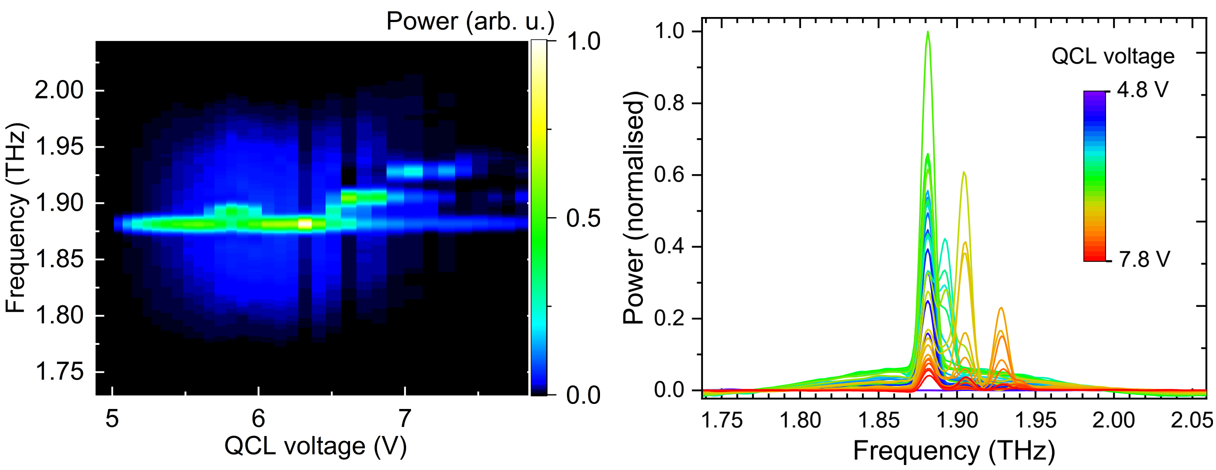

Figure 2.6: **Spectrum of the QCL.** For different voltages across the QCL shown at the horizontal axis, the spectra are shown colour-coded as vertical lines, with the frequency values indicated on the vertical axis.

Using a Fourier-transform infrared spectrometer, the emission spectrum of the QCL was measured at different voltages across the QCL. The result is shown in Fig. 2.6. It shows that the QCL emission is mostly single-mode, although multi-mode behaviour can be found particularly at the higher voltages. The maximum power is achieved in single-mode emission at 1.881 THz.

The QCL emits predominantly linearly polarised light, with polarisation in growth direction of the QCL. The degree of polarisation of the QCL is measured by placing the Golay cell with a polariser directly in front of the QCL and measuring the minimum and maximum power values when rotating the polariser. A response of 24.0 mV is found in co-polarised direction and 0.98 mV in cross-polarised direction. Assuming that the cross-polarised signal originates from unpolarised light, the degree of linear polarisation of the QCL is 92.2 %.

2.2 Design of the waveguide-coupled system

Experiments combining terahertz radiation with optical spectroscopy and cryogenic temperatures are likely to give access to a new field of physical phenomena. The challenges faced during the realisation of such a system have their origin in the following competing requirements:

- Electrical contacts to the sample;
- Access for optical radiation;
- Access for terahertz radiation;
- Low temperatures (around 4.2 K), i. e. cryogenic cooling with a proper thermal contact to the sample;
- Magnetic fields.

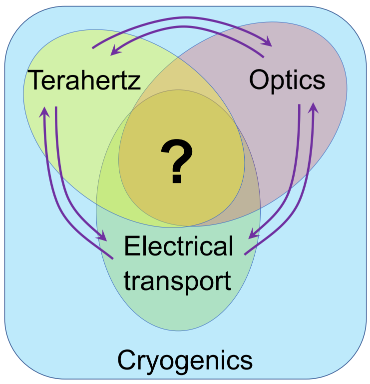

A waveguided THz delivery system was designed that addresses these issues. The system is shown in Fig. 2.7. It consists of two liquid helium continuous-flow cryostats, a vertical one on the left, and a horizonal one on the right, that are coupled together by a copper waveguide. The THz source is located in the left cryostat (Janis ST-300). The emitted THz radiation enters a copper waveguide. After being reflected upwards on a 45° polished aluminium mirror, it then enters the coldfinger in the right cryostat, which has an axial bore *that acts itself as a waveguide*, until it finally hits the sample. The ready-built setup is shown in Fig. 2.8.

The THz source is the single-plasmon quantum cascade laser described in section 2.1. It is cooled to ca. 18 K. The coldfinger assembly and the QCL are shown in Fig. 2.1. The copper waveguide is made out of annealed copper and has an inner diameter of 4.6 mm. This type of cylindrical hollow metal waveguide has been shown to exhibit very low losses at THz frequencies, <3 dB/m [191], compared to other types of hollow-metal waveguides

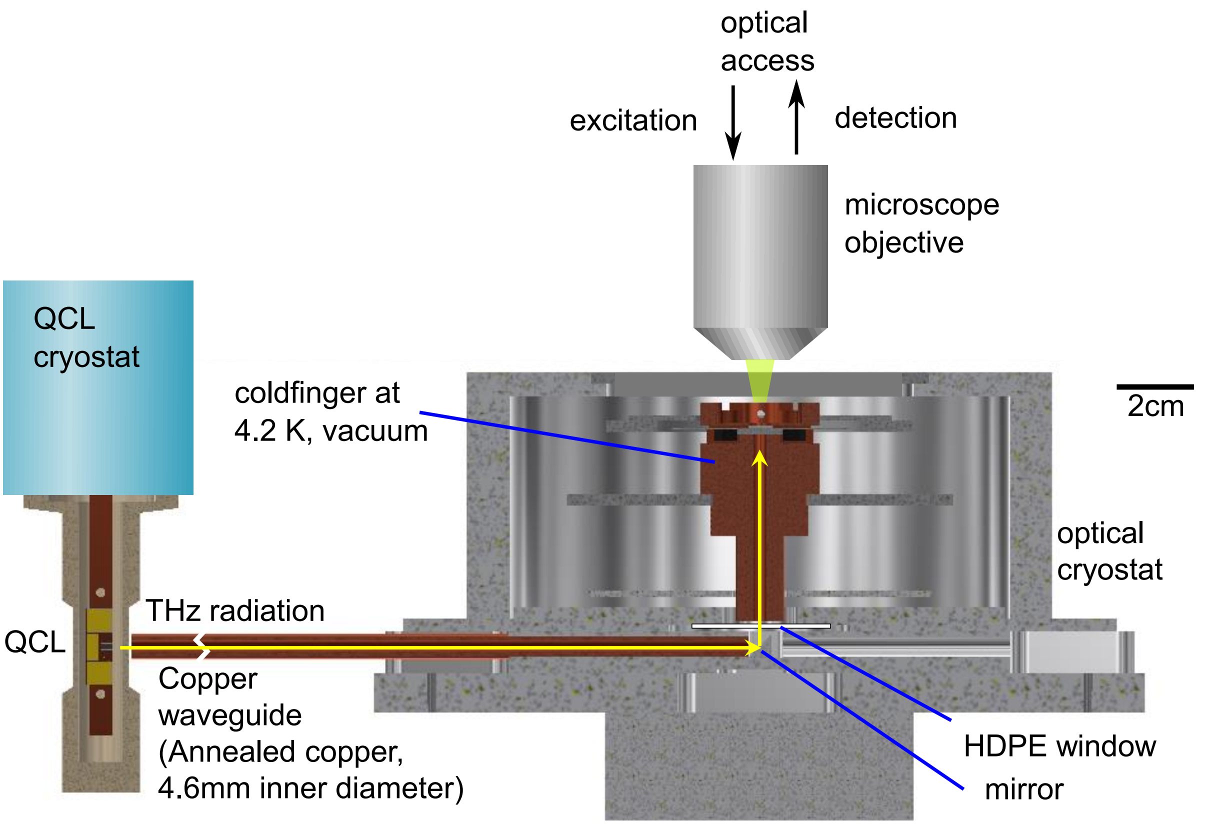

Figure 2.7: **Waveguide-coupled cryogenic THz delivery system combining optical and terahertz access.** Cryostat with QCL (left-hand side) emits radiation that is guided through a copper waveguide, reflected upwards at a mirror, and guided into the cryostat on the right-hand side, where the coldfinger itself acts as a waveguide. Optical access from the top and the possibility of electrical measurements is preserved. Terahertz access is done via multimode waveguides exploiting the focusing effect.

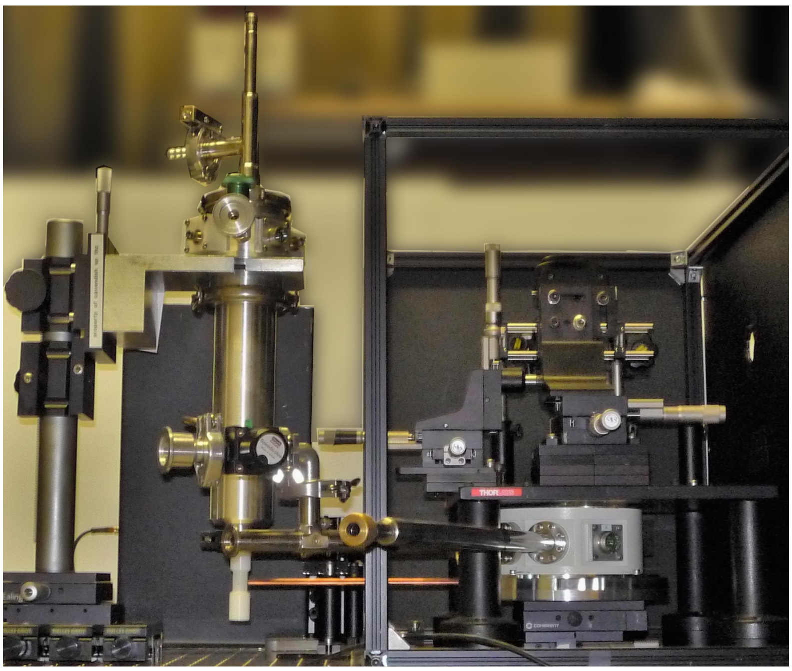

Figure 2.8: **Photo of the constructed setup.**

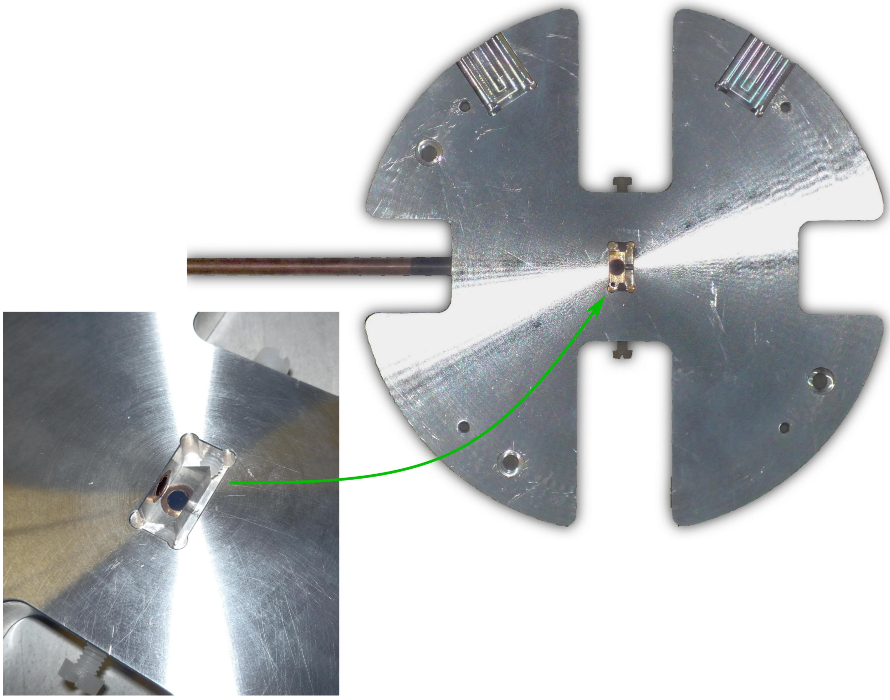

Figure 2.9: **Waveguide baseplate,** the extension to the optical cryostat at the bottom. The copper waveguide is inserted from the left. At the top, two milled cut-outs can be seen: clamps can be inserted there to aid with alignment of the horizontal optical cryostat (with the vertical coldfinger waveguide) with the horizontal waveguide. In the inset, the 45° mirror can be seen that is held by two plastic screws.

(un-annealed copper, stainless steel metal waveguides with smaller diameters) [46]. The same diameter has been used for the inner bore of the coldfinger, which is fabricated out of oxygen-free high conductivity copper. The horizontal waveguide is 30.2 cm long, the coldfinger waveguide 4.6 cm long, and the free-space length between coldfinger and waveguide 1.2 cm.

The horizontal, right cryostat is based on a commercially available cryostat for optical measurements. Thus this setup inherits the capability of performing any kinds of optical experiments in the near-infrared and visible ranges. The baseplate of the right cryostat was replaced by a custom version with a high-density polyethylene (HDPE) window glued in. This window is transparent to THz radiation and, at the same time, decouples the outer ambient air pressure and room temperature from the vacuum environment inside the cryostat. On the right of the mounting plate for the right cryostat, a bore was added for nitrogen purging purposes. The waveguide mounting plate is shown in Fig. 2.9.

There are two possible measurement configurations: one for measurements with both optical and terahertz excitation, see Fig. 2.10 on the left, and another one for terahertz-only measurements, as shown in Fig. 2.10 on the right.

In the first configuration, Fig. 2.11 (a), the sample is mounted face-upwards on a chip

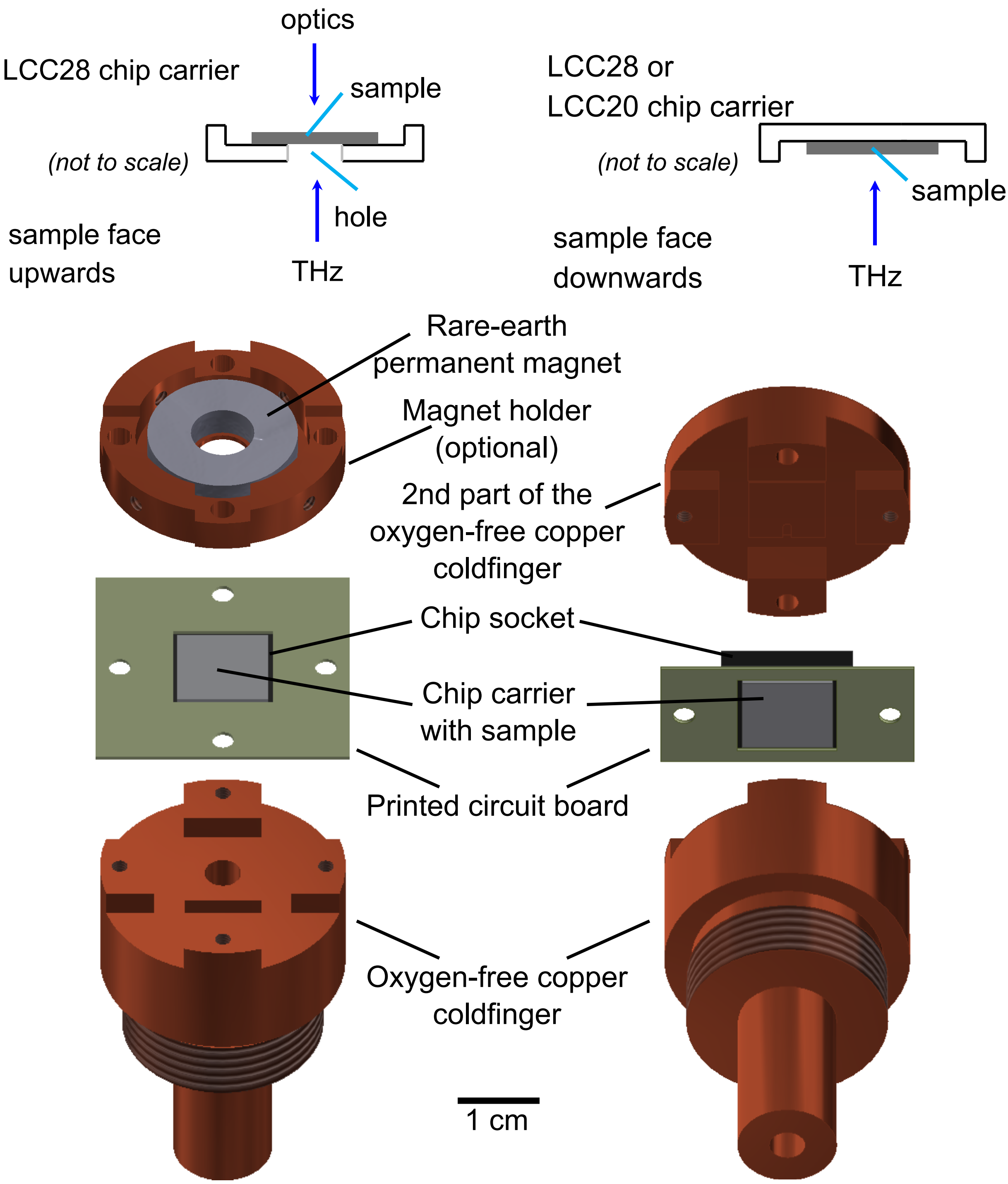

Figure 2.10: *Left: Configuration for optical and THz measurements.* The sample is mounted in a LCC28 chip carrier that has a hole in the center for access with THz radiation. The chip carrier is inserted into a socket that is soldered on a PCB. Optionally, a permanent ring magnet can be mounted on top. *Right: Configuration for THz-only measurements.* The sample can be mounted in a LCC20 or LCC28 chip carrier. The PCB with the socket is mounted on a second copper part, which is then mounted with the sample facing downwards on the coldfinger.

(a) LCC28 in optical configuration:

(b) LCC20 on 2nd part of cold-finger: THz-only configuration:

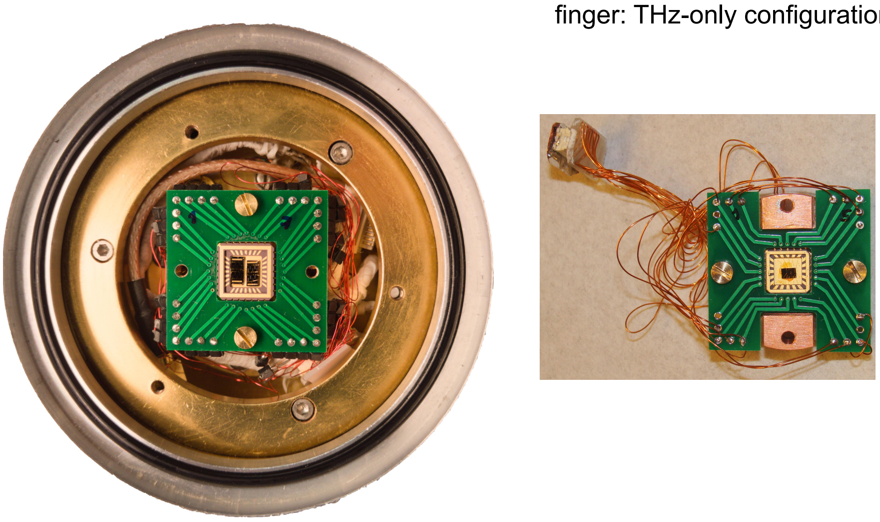

Figure 2.11: **Sample holders.** (a) The THz+Optics configuration with a LCC28 sample facing upwards. (b) The second part of the coldfinger, with a LCC20 sample mounted and grounded contact termination.

carrier. This way, it is possible to illuminate it from the top using the existing capabilities of the microphotoluminescence setup. For terahertz access, a hole (4.6 mm – 5 mm diameter) has to be drilled through the chip carrier, such that the terahertz radiation from the waveguide can illuminate the sample from the back. On the sides around the 4.6 mm hole, the sample has thermal contact to the coldfinger, which is cooled to liquid helium temperatures.

Optionally, a permanent ring magnet can be installed on top of the sample. With a distance of 1.2 mm from the sample away, neodymium magnets can achieve magnetic fields of about 80 mT at the sample surface [192]. Although it is not a tunable magnetic field and it is not very high as compared to fields of several Tesla employed in magnetotransport measurements of two-dimensional electron system [193–195], it can be essential for some experiments. For example, in InGaAs quantum dots, the magnetic field generated by spins of nuclei in the quantum dot, the Overhauser field, is around 20 mT [196]. When studying spin dynamics in quantum dots, the spin of a stored charge carrier in a quantum dot can be randomized by coupling to the Overhauser field. An external magnetic field creates a preferred direction for the spin precession and thus prevents this dephasing mechanism. This means that a ring magnet on top of the sample can be used to eliminate dephasing due to the Overhauser field for optical measurements with self-assembled quantum dots.

The second configuration, for THz-only measurements without optical access, is shown in Fig. 2.10 on the right. Here, the sample is mounted in either a LCC20 or a LCC28 chip carrier and inserted into a socket on a PCB. This PCB is screwed onto a second copper part of the coldfinger, Fig. 2.11, and subsequently this second copper part is mounted on the main coldfinger.

This operation mode is especially suited for experiments that do not need optical access, such as measurements on two-dimensional electron gases. The advantage is that all surfaces that the sample faces (except the HDPE window that it faces through the coldfinger) are at liquid helium temperatures. In contrast, in the face-upwards geometry the sample faces the upper cryostat plate that is at 300 K. Comparing measurements on the same sample in face-upwards and face-downwards geometries is also a possibility to get an estimate of the effects that incident thermal radiation has on the performance of the sample.

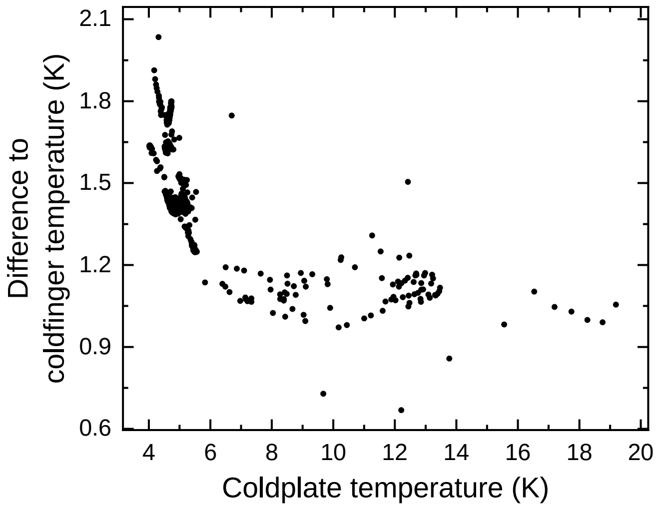

Figure 2.12: **Temperature difference** between the readings of a sensor mounted on top of the second part of the coldfinger and the values of a sensor mounted directly on the coldplate of the cryostat.

The fact that in this operation mode the coldfinger is separated in two parts raises questions about cooling performance of this setup. To evaluate this, one temperature sensor was mounted on the coldplate in the cryostat, through which the helium flows, and another one on top of the second coldfinger part. In initial tests, the main coldfinger did not cool down below 11 K. However, upon use of “Apiezon N” grease on the coldfinger threads, polishing and greasing the copper areas where the first and second coldfinger parts touch, thermal performance improved substantially. This is shown in Fig. 2.12: during a cooldown, the temperature readings were recorded, and their difference (by how much the second coldfinger part is warmer than the coldplate) is plotted against the coldplate temperature in Fig. 2.12. At most temperatures above 6 K, the difference is only about 1 K, and in the range of 4.2 K–6 K it rises to 1.5–2 K.

2.3 Development of a universal measurement software

In order to efficiently carry out experiments described throughout this thesis, computer-aided acquisition of measurement values is highly desireable. Communication with scientific devices is usually carried out through interfaces such as GPIB, RS232, USB and Ethernet, and some companies provide device drivers in the NI LabView programming language, therefore this was chosen as the language for computer automation.

While research programs are often designed to fit a very specific purpose (for example: scan x and y motors and measure signal, or set voltage and measure current), I aimed to design and develop a universal measurement software that is easily reconfigurable and modularised while balancing the need of fitting a specific measurement task. Under the codename *APMAS* ("*All-purpose measurement & acquisition system*"), I created a measurement software that allows acquisition of arbitrarily user-chosen values from instruments in dependence on one or two user-chosen measurement parameters. For a modularised architecture of the program, a datastructure-based approach was chosen. All measurements are based on two arrays shown in Fig. 2.13: the "Measurement Header Cluster", and the "Measurement Data Array". The first contains information about position and lengths of measurement and parameter values as well as the respective titles and units, while the second is a 2D array of the data values. These two data structures can be created by reading them from a file or by acquiring the data from the instruments. They can then be used to save the data to a file (after a measurement) or to display it as a plot. In particular, there is e. g. no arrow from "measurement" to "plot": the plotting program does not know what has been measured, or whether the data originates from a file, and reconstructs the data solely from these two data structures. The clear separation of the four actions allows modularisation and independent design of the individual program components, with the two main ones being the measurement and the plotting component.

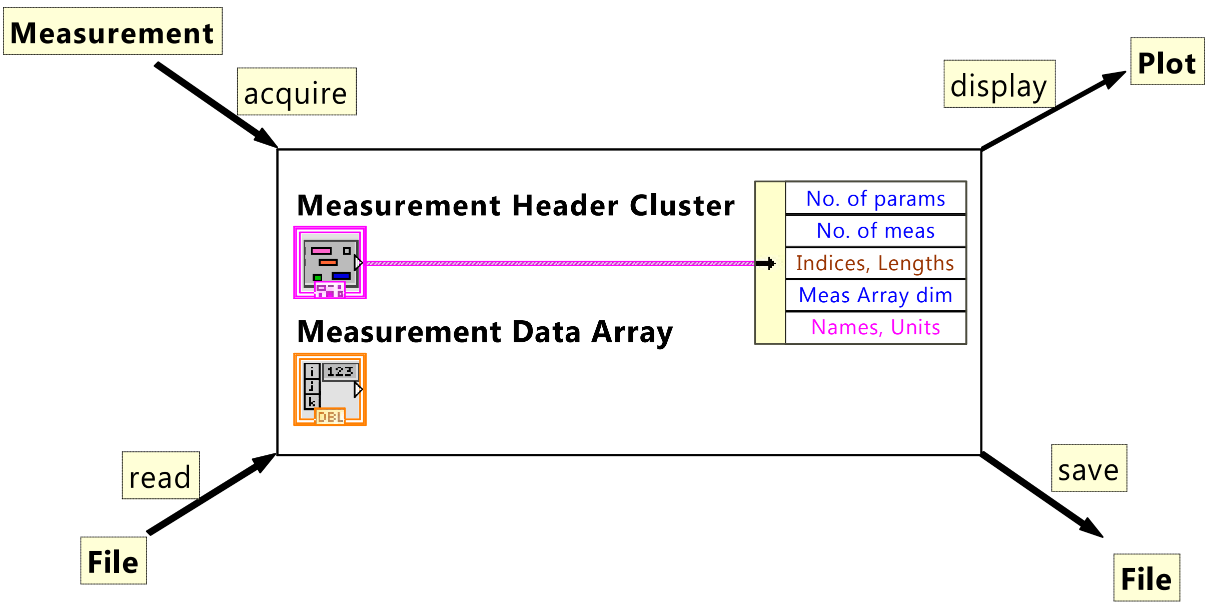

Figure 2.13: **Data structures underlying the APMAS measurement program.**

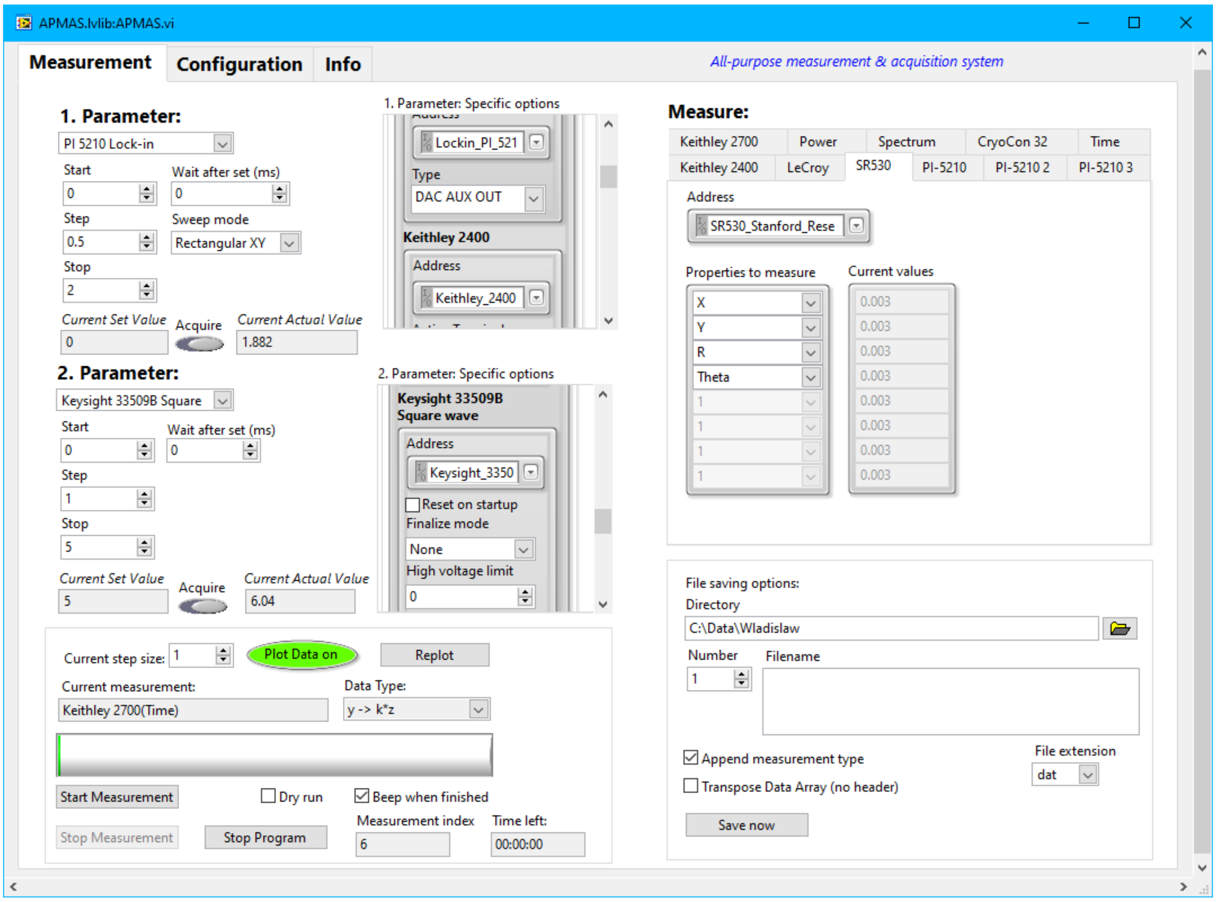

Figure 2.14: **Graphical user interface of APMAS.**

The graphical user interface is illustrated in Fig. 2.14. Available parameters are: time; a user-input value; the wavelength of the grating position of a Triax monochromator; parameters on the Arduino function generator; the set-point temperature of a CryoCon32 temperature controller; output parameters of a Keithley 2400 source-measurement unit; a Keysight 33509B square wave arbitrary function generator; Stanford Research 530 and Princeton Instruments 5210 lock-in amplifiers; as well as motor positions of the Thorlabs Kinesis Motioncontrol, KCube DCServo, KCube Stepper, and TCube DCServo motor drivers. Possible measurement values are: time; power measurement of an optical powermeter; current, voltage and resistance on Keithley 2400 and 2700 devices; X, Y, amplitude, phase and analog inputs of the SR530 and PI-5210 lock-in amplifiers; spectrum of an Andor spectrometer; waveform statistics (amplitude, frequency, root-mean-square value etc.) for each channel of a LeCroy 424 Wavesurfer oscilloscope; and finally the temperature inputs of a CryoCon32 temperature controller. Some of the device drivers were written from scratch while others are wrappers around existing drivers or low-level manufacturer libraries. Thanks to the modularised application design, extensions with subsequent device drivers can be completed very quickly, once the core application framework was developed. Due to the dynamic

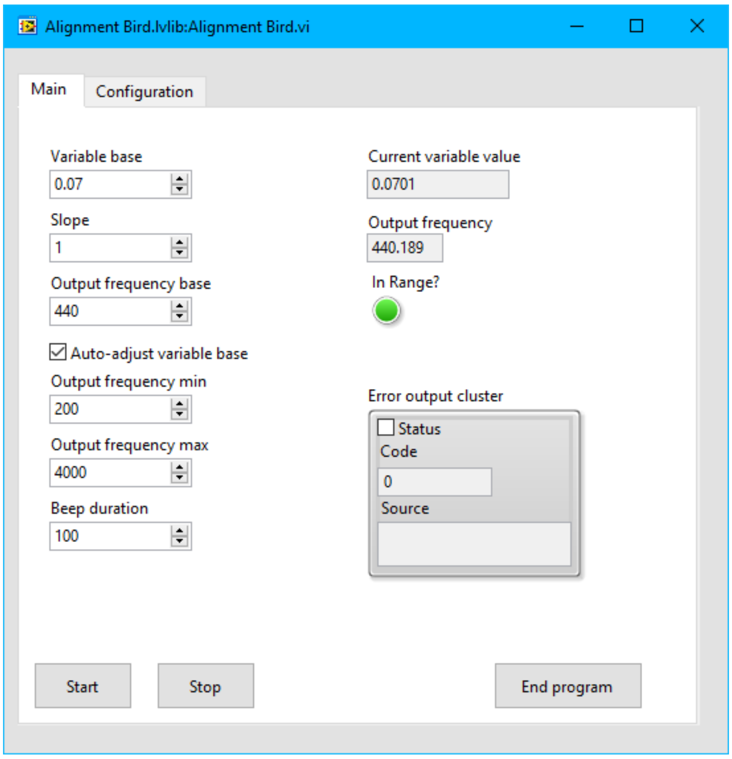

Figure 2.15: **The alignment bird.** Graphical user interface of the program.

choice of measurement settings, any of these values can be measured as a function of any one or two parameters, which has greatly improved productivity of measurements and also paved the way to remote measurements.

For alignment of THz and optical setups, another useful tool was developed: the "*alignment bird*". This program, shown in Fig. 2.15, transforms a value from an instrument into an audible sine wave. The value is scaled exponentially in order to match the approximately logarithmic pitch perception by the human ear. This made it possible to align the THz waveguided system to the Golay cell response signal, or an optical setup to the power meter at the end, by listening to the pitch of a tone, rather than having to physically look at the displayed value which may be far away depending on the position of the setup. Any instrument can be used with this program if the paths of suitable initialize, read-out and finalize functions of its LabView-library are provided, without the need to recompile the program.

2.4 Measurements of power, intensity and electric field distribution

After alignment of the waveguided THz system, its performance is evaluated by measurements of the transmitted power and intensity. A Golay cell is used to measure the relative transmission of the system. As a reference, the incident power at the waveguide input is used, which is measured using a Golay cell placed at the position of the waveguide input with a 4.6mm limiting copper aperture in front of it. The transmission from the waveguide input until after the aluminium mirror is 81 %. The transmission from the point after the mirror to the sample space is 77 %. This includes the HDPE window, and partially cut off side lobes that do not enter the second waveguide. Thus the total power transmission at 1.9 THz from the waveguide input to the sample space is as high as (60±5) %, which corresponds to about 2.1 dB of losses.

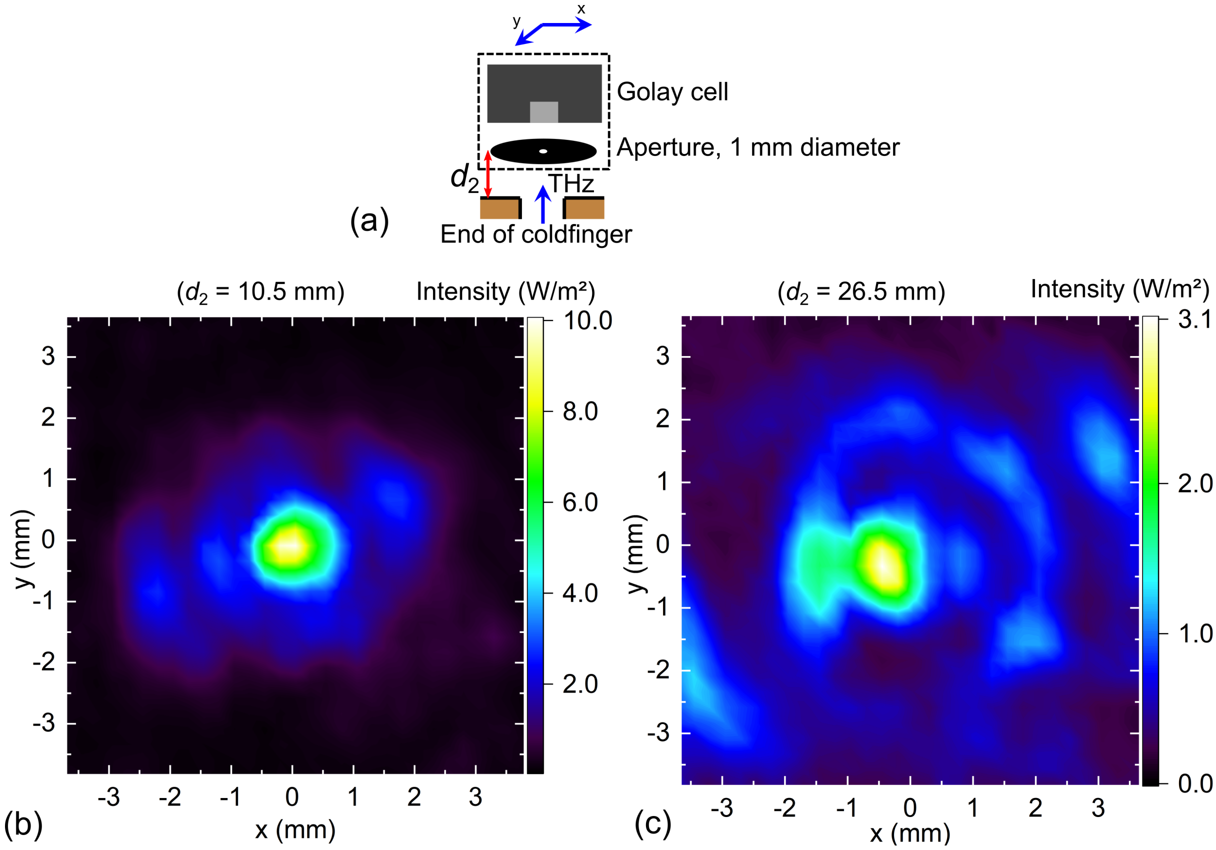

Figure 2.16: **Mode profiles: spatial intensity distribution** (a) Setup to measure the mode profiles at the end of the coldfinger waveguide, i.e. at the sample space, by lateral scanning of the Golay cell with a 1 mm aperture. (b), (c) Resulting mode profiles at d_2 = 10.5 mm (b) and d_2 = 26.5 mm (c).

The intensity distribution is obtained by mounting a 1 mm aperture in front of the Golay cell, which is then scanned in lateral directions in front of the coldfinger, see Fig. 2.16 (a). The intensity profile obtained at distances d_2 = 10.5 mm and 26.5 mm between the end of the coldfinger waveguide and the aperture is shown in Fig. 2.16 (b) and (c), respectively. A Thomas Keating absolute power metering system is used to measure the THz power delivered into the sample space. It captures the total power emitted from the coldfinger waveguide, which equals 48 µW. This allows the intensity scale in Fig. 2.16 (b) and (c) to be displayed in absolute values.

A clear and symmetric central spot can be seen. Remarkably, although the diameter of the waveguide is 4.6 mm, the strongest intensity is achieved in a much narrower central region, around 1 mm in size. Some lateral intensity peaks are present. They move away from the center as the distance between coldfinger and Golay cell increases. In chapter 3, the nature of the mode profiles will be explained.

Apart from the intensity distibution, knowledge of the electric field polarisation direction is equally important. It is extracted at each position (x,y) from several polarisation-resolved measurements. The electric field amplitude can be described by a vector

$$A\begin{pmatrix}\cos\delta\\ \sin\delta\end{pmatrix} + \vec{U}\,. \tag{2.1}$$

Here, the term with A represents arbitrary linearly polarised light, and $\vec{U}$ unpolarised light with vanishing time-averaged amplitudes $\langle U_x\rangle = \langle U_y\rangle = 0$, but non-zero power $\langle U_x^2\rangle = \langle U_y^2\rangle = \langle \vec{U}^2\rangle/2$. A predominantly linear polarisation is expected since the QCL as THz source is intrinsically linearly polarised in the heterostructure growth direction. Circular polarisation is not considered: for a linearly polarised input electric field, the waveguide will not create any circular polarisation, since there is no difference in propagation speeds for different polarisation directions.

At least four polarised measurements of transmitted power are required to unambiguously determine A^2, U^2, and δ. I use a set consisting of a co-polarised (0°) measurement P_1, a cross-polarised (90°) one, P_2, and two measurements, P_3 and P_4, at the polariser rotation angles 45° and −45°. They can be evaluated using the corresponding Jones matrices of a rotated polariser as

$$P_1 = \left\langle\left|\begin{pmatrix}1 & 0\\ 0 & 0\end{pmatrix}\left[A\begin{pmatrix}\cos\delta\\ \sin\delta\end{pmatrix}+\vec{U}\right]\right|^2\right\rangle = A^2\cos^2\delta + U^2/2\,; \tag{2.2}$$

$$P_2 = \left\langle\left|\begin{pmatrix}0 & 0\\ 0 & 1\end{pmatrix}\left[A\begin{pmatrix}\cos\delta\\ \sin\delta\end{pmatrix}+\vec{U}\right]\right|^2\right\rangle = A^2\sin^2\delta + U^2/2\,; \tag{2.3}$$

$$P_3 = \left\langle\left|\begin{pmatrix}1/2 & 1/2\\ 1/2 & 1/2\end{pmatrix}\left[A\begin{pmatrix}\cos\delta\\ \sin\delta\end{pmatrix}+\vec{U}\right]\right|^2\right\rangle = \frac{A^2}{2}(1+\sin(2\delta)) + U^2/2\,. \tag{2.4}$$

$$P_4 = \left\langle\left|\begin{pmatrix}1/2 & -1/2\\ -1/2 & 1/2\end{pmatrix}\left[A\begin{pmatrix}\cos\delta\\ \sin\delta\end{pmatrix}+\vec{U}\right]\right|^2\right\rangle = \frac{A^2}{2}(1-\sin(2\delta)) + U^2/2\,. \tag{2.5}$$

P_1 is obtained from:

$$P_1 = \langle(A\cos\delta+U_x)(A\cos\delta+U_x)\rangle = \langle A^2\cos^2\delta+U_x^2+2A\cos\delta U_x\rangle = A^2\cos^2\delta+U^2/2\,, \tag{2.6}$$

and similarly, for the other values. Their linear combinations give A^2 and U^2:

$$P_1 + P_2 = P_3 + P_4 = A^2 + U^2 \tag{2.7}$$
$$P_1 - P_2 = A^2 \cos(2\delta) \tag{2.8}$$
$$P_3 - P_4 = A^2 \sin(2\delta) \tag{2.9}$$

These identities give A^2 and U^2:

$$\Rightarrow \quad A^2 = \sqrt{(P_1 - P_2)^2 + (P_3 - P_4)^2}\,; \tag{2.10}$$
$$U^2 = P_1 + P_2 - A^2 = P_3 + P_4 - A^2\,. \tag{2.11}$$

Now the angle δ has to be found. As for U^2, this is possible in two ways. The first way is from Eq. (2.8):

$$\cos(2\delta) = \frac{P_1 - P_2}{A^2} \tag{2.12}$$
$$\Rightarrow \quad \delta = \pm\frac{1}{2}\arccos\left(\frac{P_1 - P_2}{A^2}\right) \tag{2.13}$$

This gives two solutions for δ. The correct sign has to be determined by checking with Eq. (2.9):

$$\frac{(P_1 - P_2) - (P_3 - P_4)}{A^2} = \cos(2\delta) - \sin(2\delta) = \frac{P_1 - P_2}{A^2} \mp \sin\left(\arccos\left(\frac{P_1 - P_2}{A^2}\right)\right) \tag{2.14}$$
$$\Rightarrow \quad \frac{P_3 - P_4}{A^2} = \pm\sin\left(\arccos\left(\frac{P_1 - P_2}{A^2}\right)\right) = \pm\sqrt{1 - \left(\frac{P_1 - P_2}{A^2}\right)^2} \tag{2.15}$$
$$\Rightarrow \quad \frac{P_3 - P_4}{A^2} = \pm\sqrt{1 - \frac{(P_1 - P_2)^2}{(P_1 - P_2)^2 + (P_3 - P_4)^2}} = \pm\sqrt{\frac{(P_3 - P_4)^2}{A^4}} \tag{2.16}$$

The upper sign is correct for $P_3 > P_4$:

$$\frac{P_3 - P_4}{A^2} = +\frac{|P_3 - P_4|}{A^2} \quad \Rightarrow \quad \delta = +\frac{1}{2}\arccos\left(\frac{P_1 - P_2}{A^2}\right) \tag{2.17}$$

The lower sign is for $P_3 < P_4$:

$$\frac{P_3 - P_4}{A^2} = -\frac{|P_3 - P_4|}{A^2} \quad \Rightarrow \quad \delta = -\frac{1}{2}\arccos\left(\frac{P_1 - P_2}{A^2}\right) \tag{2.18}$$

The second way to obtain δ is using Eq. (2.9):

$$\sin(2\delta) = \frac{P_3 - P_4}{A^2} \tag{2.19}$$

$$\Rightarrow \quad \delta_1 = \frac{1}{2}\arcsin\left(\frac{P_3 - P_4}{A^2}\right) \;\; ; \;\; \delta_2 = \frac{\pi}{2} - \frac{1}{2}\arcsin\left(\frac{P_3 - P_4}{A^2}\right) \tag{2.20}$$

The equation gives two solutions, δ_1 and δ_2. Which one is correct in which case is determined by Eq. (2.8):

$$\frac{(P_1 - P_2) - (P_3 - P_4)}{A^2} = \cos(2\delta_{1,2}) - \frac{P_3 - P_4}{A^2} = \pm\cos\left(\arcsin\left(\frac{P_3 - P_4}{A^2}\right)\right) - \frac{P_3 - P_4}{A^2} \tag{2.21}$$

$$\Rightarrow \quad \frac{P_1 - P_2}{A^2} = \pm\cos\left(\arcsin\left(\frac{P_3 - P_4}{A^2}\right)\right) = \pm\sqrt{\frac{(P_1 - P_2)^2}{A^4}} \tag{2.22}$$

The upper sign corresponds to the solution δ_1, and is valid for $P_1 > P_2$:

$$\frac{P_1 - P_2}{A^2} = +\frac{|P_1 - P_2|}{A^2} \quad \Rightarrow \quad \delta = \delta_1 = \frac{1}{2}\arcsin\left(\frac{P_3 - P_4}{A^2}\right) \tag{2.23}$$

The lower sign corresponds to the solution δ_2, and is valid for $P_1 < P_2$:

$$\frac{P_1 - P_2}{A^2} = -\frac{|P_1 - P_2|}{A^2} \quad \Rightarrow \quad \delta = \delta_2 = \frac{\pi}{2} - \frac{1}{2}\arcsin\left(\frac{P_3 - P_4}{A^2}\right) \tag{2.24}$$

As a result, this yields the following solution for A^2, U^2 and δ (which is defined up to πn):

$$A^2 = \sqrt{(P_1 - P_2)^2 + (P_3 - P_4)^2} \tag{2.25}$$

$$U^2 = P_1 + P_2 - A^2 = P_3 + P_4 - A^2 \tag{2.26}$$

$$\begin{aligned} \delta &= \frac{1}{2}\mathrm{sign}(P_3 - P_4)\arccos\left(\frac{P_1 - P_2}{A^2}\right) = \\ &= \frac{1}{2}\mathrm{sign}(P_1 - P_2)\arcsin\left(\frac{P_3 - P_4}{A^2}\right) + \frac{\pi}{2}\Theta(P_2 - P_1) \end{aligned} \tag{2.27}$$

Here $\Theta()$ is Heaviside's Theta function. The Stokes parameters $S_0 = P_1 + P_2 = P_3 + P_4$, $S_1 = P_1 - P_2$, and $S_2 = P_3 - P_4$ can be identified, with $S_4 \equiv 0$ as no circular polarisation is considered. The fact that there are two different ways to calculate U^2 and δ from the experimental values provides a route to estimate the error of the analysis.

To measure P_1, P_2, P_3, and P_4, a wire-grid polariser is mounted on top of the 1 mm aperture of the Golay cell, as shown in Fig. 2.17 (b), and the Golay cell is scanned with 0.1 mm step size in lateral directions. The transmitted power, $A^2+U^2 = (P_1+P_2+P_3+P_4)/2$, is shown as a colormap in Fig. 2.17 (a). Using the analysis described above, the total power is decomposed into the linearly polarised part, Fig. 2.17 (c), and the unpolarised part, Fig. 2.17 (d). On top of the colormap in Fig. 2.17 (c), the electric field is shown as a plot of lines whose direction is determined by the angle δ and indicates the polarisation of the electric

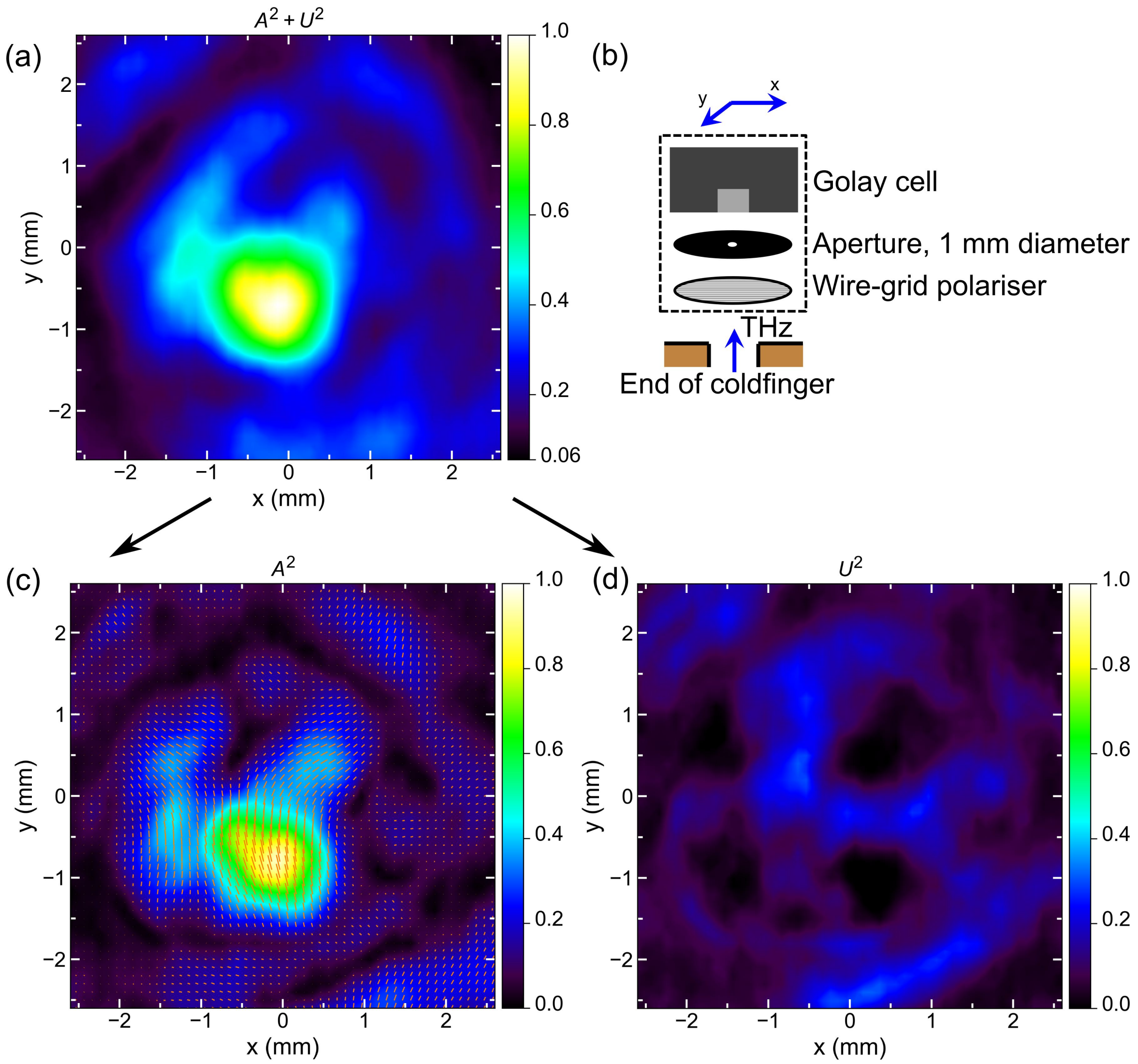

Figure 2.17: **Polarisation-resolved measurement.** The total mode intensity (a) is decomposed into the linearly polarised part (c), where the direction of the electric field known up to a period of π is shown by a superimposed line plot, and a rest (d), which could not be interpreted as linearly polarised light. The setup for this measurement is shown in (b).

field at each point. The magnitude of the electric field corresponds to the length of the line markers.

The main mode peak exhibits an almost vertical polarisation direction, slightly tilted anti-clockwise. The magnitude of U^2 is less than $\sim (1/3)A^2$ at any point, and where the linear part reaches its maximum, the unpolarised part vanishes, confirming the linearly polarised nature of the output light.

Experimentally, there are three situations which would give rise to a non-zero value of $\vec{U}$, which are shown in Fig. 2.18. Firstly, truly randomly polarised light. This has a small

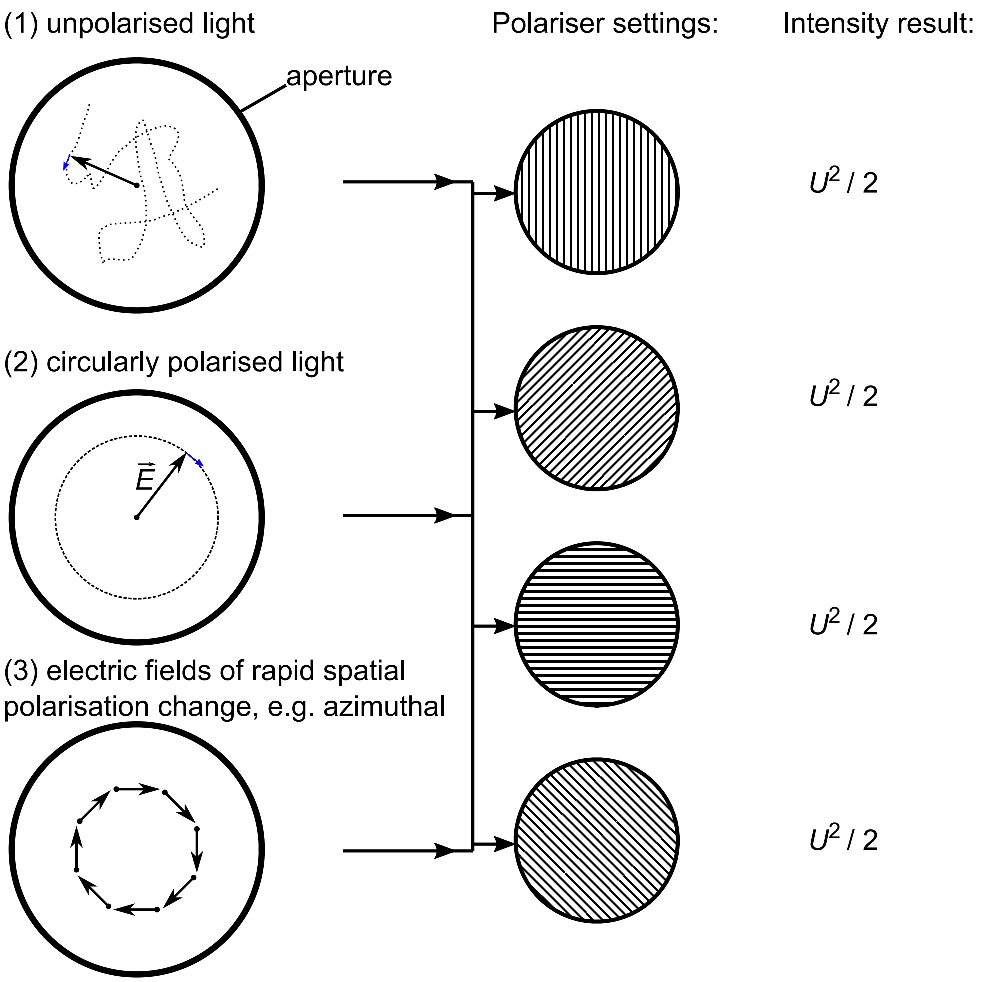

Figure 2.18: **Three cases giving rise to non-zero U^2 in the analysis.** (1) unpolarised light, (2) circular polarisation, (3) a rapid change of polarisation direction on the length scale of the aperture, shown for azimuthal polarisation as an example. All three cases would result in a constant, time-averaged intensity measurement value for any polariser rotation angle, and hence contribute to the U^2 term in the analysis.

contribution to U^2 given that the QCL has a well-defined polarisation direction with a degree of polarisation of at least 92.2 %. Secondly, circular polarisation, if present but neglected in the model, would give rise to a non-zero U^2 while simultaneously distorting the result for the linear polarisation. However this possibility is excluded above. And finally, U^2 will be non-zero when the light is perfectly linearly polarised, but its direction of polarisation changes significantly over the length scale of the aperture used to spatially probe the intensity. This is what happens here. In some regions, see Fig. 2.17 (c), the polarisation changes its direction over a length scale comparable with 1 mm, the size of the aperture. It is in these regions that the value for U^2 is maximal. The measurement yields averaged values of the four P-values over the aperture size, and spatial curls of the electric field will look like unpolarised light in the above analysis.

The origin of such rapid spatial changes in polarisation in the measurement can be understood considering the eigenmodes of cylindrical waveguides. For example, the TE_{01}-mode has an azimuthal electric field direction; the TE_{21}-mode has electric field lines move towards and away from the center (see a more detailed discussion in the introduction to chapter 3, Fig. 3.2). The observed mode profiles originate from superpositions of many cylindrical eigenmodes within the waveguide, that propagate into free space after the end of the waveguide, and therefore the mode profiles inherit the complicated polarisation characteristics of the waveguide eigenmodes.

Interestingly, the presented system is also capable of determining the frequency of the QCL used. The 1 mm aperture on the Golay cell is reflective, and the reflected wave interferes with the incident beam, giving rise to oscillations on the length scale of $\lambda/2$, when d_2, the distance between the coldfinger waveguide end and the Golay detector, is varied. The resulting interferogram is shown in Fig. 2.19 (a). A similar interferogram is seen when the QCL rather than the Golay cell is moved along the waveguide axis. The QCL–waveguide–detector system can be understood as an external cavity system (see section 1.2.8 or Ref. [197]): the QCL radiation is back-reflected from the partially reflective Golay cell aperture into the QCL through the partially reflective QCL facet. This creates an external cavity in addition to the internal cavity of the QCL, which leads to the observed interference effects.

A Fourier transform of the oscillations gives the red line in Fig. 2.19 (b). It is compared to the QCL spectrum measured by a Fourier-transform infrared spectrometer (FTIR, blue dotted line). The peak frequency determined from the FTIR is 1.881 THz; from the interferogram measured using the Golay cell, the determined frequency is 1.875 THz ($\sim$ 0.3 %

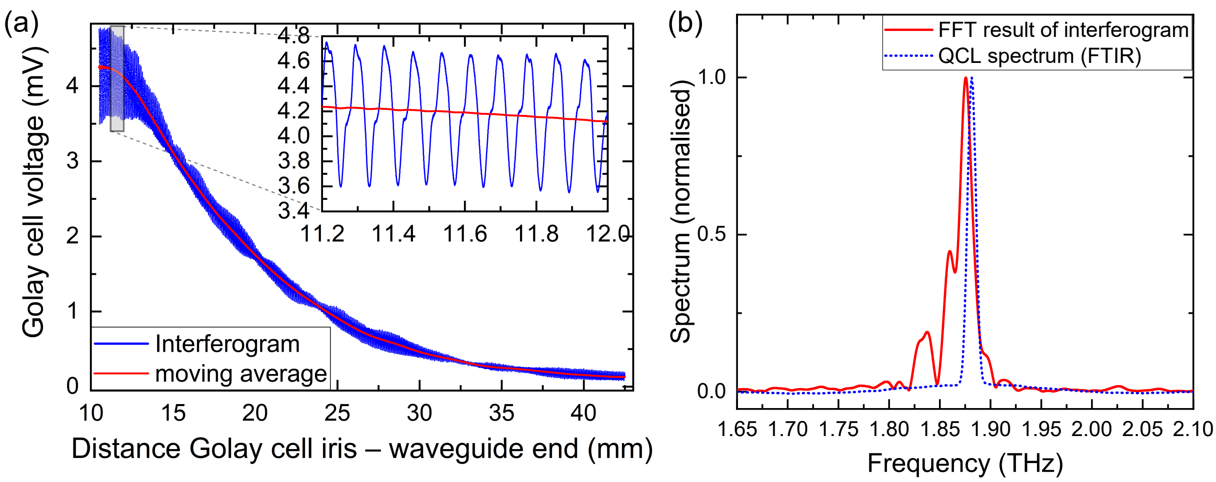

Figure 2.19: **Determination of the QCL frequency.** (a) Interferogram obtained by scanning the distance between the Golay cell with 1 mm aperture and the coldfinger waveguide end. (b) Spectra obtained as Fourier transform of the interferogram in (a) in comparison with a separate spectral measurement from a Fourier-transform infrared spectrometer. The difference in peak maxima is $\sim$ 0.3 %.

difference). Thus the presented system is capable of determing the frequency of the QCL with high accuracy.

2.5 Advantages of the system compared to a free-space setup

The presented system has several key advantages compared to a free-space setup with parabolic mirrors or lenses. When a new sample needs to be studied, it is typically not known whether it exhibits any response to THz radiation. Therefore it is crucial to ensure before a measurement that the alignment is ideal. With the constructed bench-top setup, the system can be first aligned to maximal transmission, and when a sample is inserted, it is known that it is exposed to maximal achievable THz radiation intensity.

This is complemented by the ability of accurate quantification of the intensity at the position of the sample. This is a challenging task in the area of THz research [135, 198]. Not only the intensity, but also the electric field polarisation can be mapped across the sample space.

Furthermore, the setup can efficiently be purged with nitrogen, if atmospheric absorption lines are an issue. The baseplate holding the waveguide in Fig. 2.7 on the left has an additional bore on the right, where a tube connected to a nitrogen gas supply can be mounted. The gas then flushes the cavity with the 45° mirror, the inner volume of the copper waveguide, and escapes through the left waveguide. The purging process is very efficient since the gas volume required is very low, substantially lower than volumes of whole free space setups containing parabolic mirrors and lenses.

2.6 Summary

In this chapter, the design, construction and characterisation of a THz waveguide-coupled system was described, which allows measurements of electrically contacted samples at liquid helium temperatures with simulaneous THz excitation and optical access. The driving electronics for a THz quantum cascade laser was designed and the QCL emission characteristics were characterised using a Golay cell and Fourier-transform infrared spectroscopy. Supporting software, an "all-purpose measurement and acquistion system" and an acoustic alignement helper, the "alignment bird", were programmed in LabView to provide the basis for subsequent experiments. The waveguide-coupled THz system was assembled and its total power transmission was found to be (60±5) % at 1.9 THz. The mode profile at the sample space was characterised: the two-dimensional distribution of THz intensity, electric field, and polarisation were measured and analysed. This revealed an interesting pattern with a sharply focused central spot and rings/cones moving away from the waveguide axis, which will be explained in the next chapter.

3 Multimode terahertz waveguides as focusing interferometric systems

In chapter 2, the mode profiles at the output of the waveguide system were shown in Fig. 2.16 (b) and (c). Interestingly, the radiation is strongly focused in the center of the waveguide, and the divergence is low: even when the detector is placed as far as 26.5 mm away from the waveguide end, $\sim$ 12-times the radius, the beam does not widen up noticably, within the resolution of the 1 mm aperture used for measurements. The beam profile is not Gaussian: instead of a widening of the central peak, the power seems to redistribute from the central mode to the side lobes that move away from the center, with the central spot remaining sharp.

As will be shown, the observed effect has its origin in multimode interference, also referred to as self-imaging in waveguides. The first observation of self-imaging was done by Talbot in 1836 [200]: if a transmission grating with holes is placed after an object, the image of the object is reproduced after the grating at multiple positions, a phenomenon called the Talbot effect. Thus a grating can be regarded as a "lens" with multiple "focal positions", where the image is reproduced, see Fig. 3.1 [199, 201]. In multimode waveguides, the Talbot effect [202] is referred to as self-imaging [203]: each point within a multimode

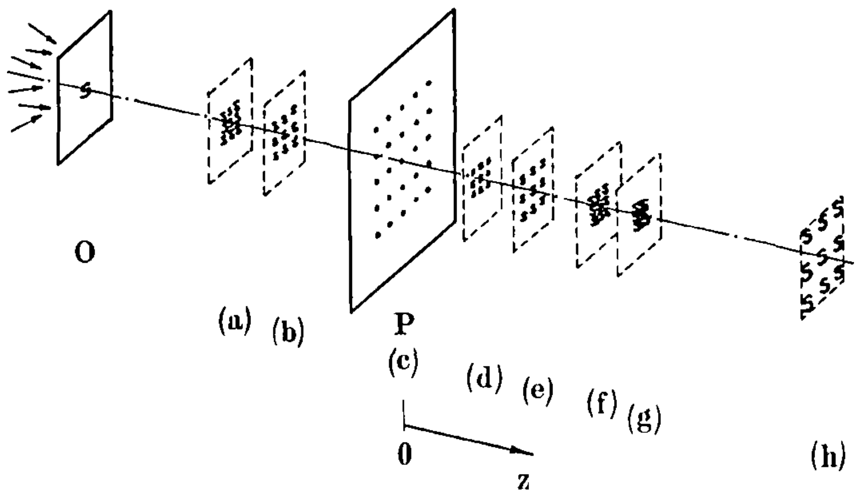

Figure 3.1: **The Talbot effect in free space:** an object imaged by a grating is reproduced in arrays in multiple planes before and after the grating. Reprinted with permission from Ref. [199] © The Optical Society.

waveguide has a corresponding set of points where the wavefield is reproduced. Initial demonstrations were done on planar, or rectangular, waveguides [204]. It has been shown that the resolution of the self-imaging effect in planar waveguides is about $\sqrt{W\lambda}/4$, which is much smaller than the waveguide width W [205]. This enables multimode waveguides to be used as focusing systems [206]. In 2006, self-imaging in cylindrical waveguides was theoretically analysed [207]. Multimode interference can form the basis of various devices, e.g. to split [208] and to combine beams [209], and photonic crystal waveguides enable integrated versions of such systems to be realised [210, 211]. In the area of terahertz research, most of the work is based on theoretical treatments or numerical simulations, while practical realisations of multimode interference in waveguides at THz frequencies have not been reported so far.

Using wave optics, the wave propagation within a cylindrical waveguide can be calculated. This gives two sets of solutions, with Bessel functions in the radial direction: transverse electric (TE) and transverse magnetic (TM) modes, which are shown in Fig. 3.2. The lowest eigenmodes are the TE_{11} and TM_{01} modes [212]. While this approach describes well the wave propagation within the waveguide, it does not provide information about the field after the end of waveguide, which is of particular interest to the experiment.

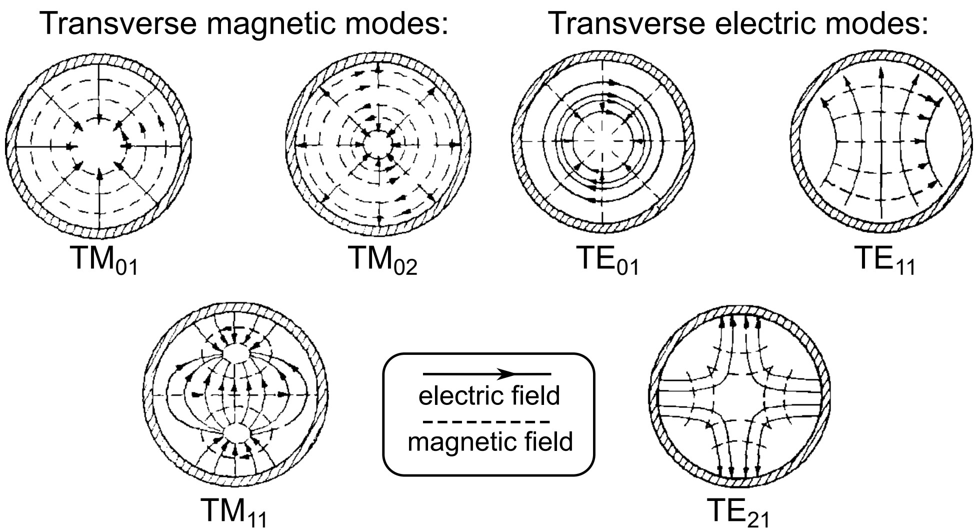

Figure 3.2: **Cylindrical waveguide eigenmodes.** The three lowest transverse magnetic (TM) and transverse electric (TE) eigenmodes are shown on the left and right hand sides, respectively. Adapted pictures from Ref. [212], reused as work in public domain.

How can the evolution of the mode profiles at the end of a waveguide be understood? Within a wave-optical approach, reflected and transmitted waves before, within, and after the waveguide would need to be calculated, with the input electric field being decomposed into the eigenmodes [207]. Due to the complexity of this approach, hardly analytically solvable, the treatment of such problems is often limited to finite-difference time-domain simulations [208, 210, 211], which unfortunately do not provide an opportunity for easy analysis and interpretation of the result as an analytical solution would do. To answer the question about propagation after the end of a waveguide, I have developed a fully analytic, ray-optical description of wave propagation within a cylindrical multimode waveguide. It allows calculation not only of the wave propagation within the multimode waveguide, but also of the diverging beam profile after the waveguide. It is shown that a multimode cylindrical waveguide itself can be used as a focusing element, and the positions of maxima along the waveguide axis can be calculated. Furthermore, one can infer information about the distribution of the incident beam from measurements at the end of the waveguide, thus utilizing the waveguide as a sensitive interferometric device.

3.1 Theory of multimode cylindrical waveguides

3.1.1 Analytical ray-optical model

Consider a coherent THz source (such as a quantum cascade laser) located at the point Q, which emits radiation into the waveguide until it hits the observer at point P, where a screen to measure the electric field is located (see Fig. 3.3). The distance from the source Q to the waveguide input is d_1; the separation between the waveguide output and the screen equals d_2. The waveguide is assumed to be lossless and straight, has a length L and a radius R, and its axis is in z-direction. A large multimode waveguide with $R \gg \lambda$ is considered, which justifies the use of the ray-optical treatment.

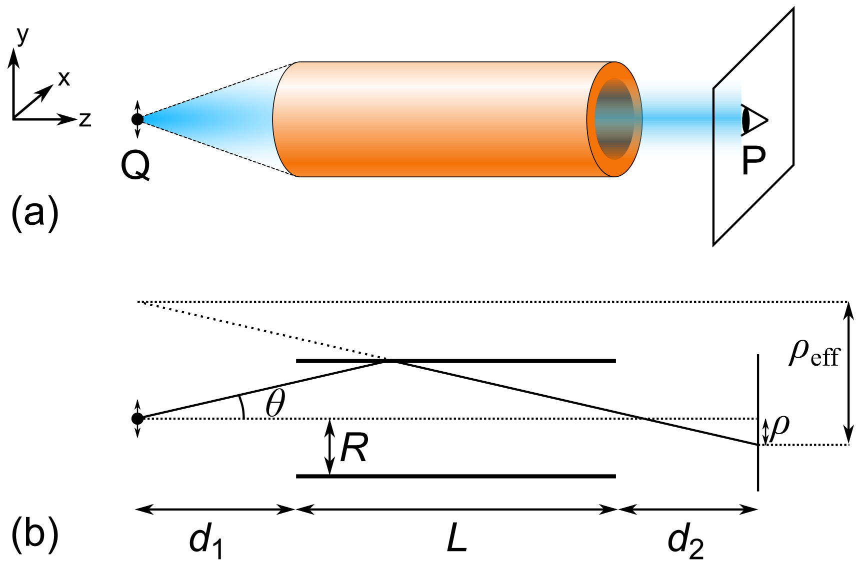

Figure 3.3: **Ray-optical model.** (a) Source Q emits radiation predominantly in z-direction along the axis of the hollow metal cylindrical waveguide and hits a screen at point P. (b) Distance and variable definitions for the ray paths shown in the radial cross section of the waveguide. ϱ is the actual radius on the screen, ϱ_{eff} is the total distance travelled perpendicular to the z-axis.

Rays emitted by the source at Q may go straight through the waveguide, without reflections, or be reflected at the waveguide walls once, twice, or more. To calculate the resulting electric field at the screen, the electric fields of all rays incident at a point (x,y) at the screen are summed up.

The radial coordinate on the screen is $\varrho = \sqrt{x^2+y^2}$. The total travelled distance of a ray in lateral directions (x and y) is ϱ_{eff}; it is also the radial coordinate where a ray would end up on the screen if it was not reflected, i. e. if there was no waveguide. For the ray that goes straight through, which we will label with an index $m = 0$, ϱ_{eff} equals ϱ, see Fig. 3.4 (a). For any rays that have been reflected at the walls of the cylindrical waveguide, ϱ_{eff} is larger than ϱ, and their relationship depends on the number of reflections experienced and can be derived geometrically as shown in Fig. 3.4 (a). When a ray experiences at least one reflection, there are two cases: it will either end up above or below the z-axis as shown in Fig. 3.4 (a), which will be considered separately. For a ray that experiences one reflection, but still ends up above the z-axis on the screen, which will be labelled by $m = 1$, $\varrho_{\text{eff}} = 2R - \varrho$. The case $m = 2$ corresponds to one reflection that ends up below the z-axis; since $\varrho > 0$ always, this corresponds to a flip of $\varphi \to \varphi + \pi$ in the wavevector $\vec{k}$, with $\varrho_{\text{eff}} = 2R + \varrho$. In general,

$$\varrho_{\text{eff},m} = \begin{cases} mR + \varrho & , \quad m \text{ even} \\ (m+1)R - \varrho & , \quad m \text{ odd} \end{cases} \tag{3.1}$$

For an observer at P, rays with indices $m > 0$ seem to originate from an imaginary annulus

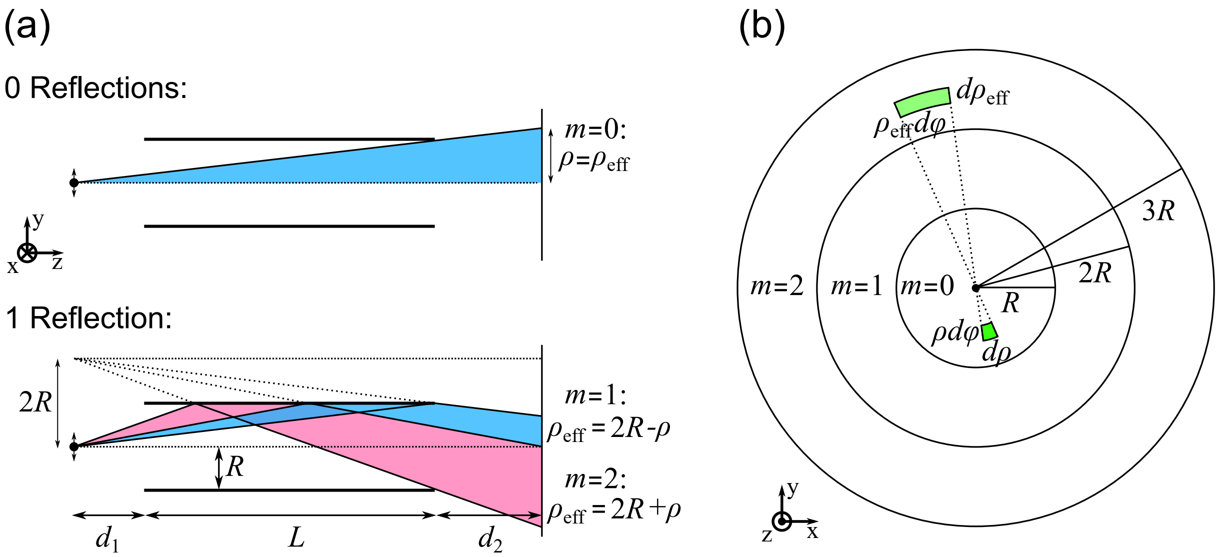

Figure 3.4: **Ansatz to calculate the individual rays.** (a) Ray paths and beam orders m for rays experiencing zero and one reflections. (b) Image seen by an observer in P looking into the waveguide along its axis. The rays seem to come from imaginary annuli around the central circle of radius R. Energy conservation leads to the intensity amplification factor $\varrho_{\text{eff}}/\varrho$ for reflected rays.

around the ring of radius R at the position $z = d_1$ of the waveguide start, see Fig. 3.4 (b). Each ray of index m effectively originates from an annulus bound by circles of radii mR and $(m+1)R$, and experiences $N_{\text{refl}} = \lfloor (m+1)/2 \rfloor$ reflections, where $\lfloor \cdot \rfloor$ indicates the floor function.

The total travelled distance $r_{\text{eff},m}$ of ray m is

$$r_{\text{eff},m} = \sqrt{\varrho_{\text{eff},m}^2 + z_{\text{tot}}^2}\,, \tag{3.2}$$

where the total distance travelled in z-direction is $z_{\text{tot}} = d_1 + L + d_2$. The angle ϑ_m with respect to the z-axis is given by

$$\tan\vartheta_m = \frac{\varrho_{\text{eff},m}}{z_{\text{tot}}}\,. \tag{3.3}$$

The source Q is modelled as a Hertzian dipole $\vec{p} = \vec{e}_y$ parallel to the y-axis, which emits an electric field $\vec{u}$ in the far field. Its angular intensity distribution is described by a function $f(\vartheta,\varphi)$:

$$\begin{aligned}\vec{u}(\vec{r},t) &= u_0(\vec{e}_r \times \vec{p}) \times \vec{e}_r \frac{\cos(\omega t - kr)}{kr} f(\vartheta,\varphi) = \\ &= u_0 \begin{pmatrix} -\sin^2\vartheta\sin(2\varphi)/2 \\ 1 - \sin^2\vartheta\sin^2\varphi \\ -\sin\varphi\sin(2\vartheta)/2 \end{pmatrix} \frac{\cos(\omega t - kr)}{kr} \exp\left(-\frac{\vartheta^2}{\alpha^2}\right)\,.\end{aligned} \tag{3.4}$$

While the emission pattern of a Hertzian dipole is cylindrically symmetric around the dipole axis, the QCL emits predominantly in a cone from its facet, in a solid angle around the z-axis with angles $0 \le \vartheta \lesssim \alpha$. To take this into account, a factor of $f(\vartheta,\varphi) = \exp(-\vartheta^2/\alpha^2)$ is used in the formula.

Summing up contributions from all rays, the resulting electric and magnetic fields at the point (x,y) are:

$$\begin{aligned}\vec{E}(\varrho,\varphi,t) = \sum_{m=0}^{m_{\max}} \vec{\varepsilon}_m = \sum_{m=0}^{m_{\max}} \sqrt{\frac{\varrho_{\text{eff},m}}{\varrho}} \cdot F(m,\varrho,\vartheta_m) \cdot \\ \cdot\big[(\vec{u}(r_{\text{eff},m},\vartheta_m,\varphi,t) \cdot \vec{e}_\varphi)\vec{e}_\varphi(-1)^{N_{\text{refl}}} + \\ + (\vec{u}(r_{\text{eff},m},\vartheta_m,\varphi,t) \cdot \vec{e}_\varrho)\vec{e}_\varrho + \\ + (\vec{u}(r_{\text{eff},m},\vartheta_m,\varphi,t) \cdot \vec{e}_z)\vec{e}_z(-1)^{N_{\text{refl}}}\big]\,;\end{aligned} \tag{3.5}$$

$$\vec{H}(\vec{r},t) = \sum_{m=0}^{m_{\max}} \frac{\vec{k}_m \times \vec{\varepsilon}_m}{\mu_0\omega} = \sum_{m=0}^{m_{\max}} \frac{1}{\mu_0 c}\vec{e}_r(\vartheta_m,\varphi + \pi \cdot N_{\text{refl}}) \times \vec{\varepsilon}_m\,. \tag{3.6}$$

In Eq. (3.5), the sum of the electric fields in the brackets is multiplied by a conditional function $F(m,\varrho_m,\vartheta_m)$, that is either 1 or 0, and a "density of states"-type factor $\sqrt{\varrho_{\text{eff},m}/\varrho}$.

The sum of the electric fields is understood as follows. When a ray is reflected at the cylindrical hollow metal waveguide, conservation of the parallel components of the electric field requires the reflected wave to have a phase flip of π, or a sign flip. Thus the electric field is decomposed in the cylindrical coordinate system, and the parallel φ- and z-components gain a sign flip of $(-1)^{N_{\text{refl}}}$. Similarly in the $\vec{H}$-field, reflections flip the vector $\vec{k}$ of each ray antisymmetrically with respect to the z-axis, which adds π to φ whenever the number of reflections is odd.

The conditional function $F(m,\varrho,\vartheta_m)$ tells when a ray has to be considered in the sum:

$$
\begin{aligned}
&F(m,\varrho,\vartheta) = 1, \text{ when:}\\
&\qquad (i)\ \tan\vartheta < R/d_1\\
&\qquad\quad \text{(only rays that entered the waveguide input are considered)}\\
&\qquad \text{and } (ii) \begin{cases} m \text{ even:} & \frac{(m-1)Rd_2}{d_1+L} - R < \varrho < R + \frac{(m+1)Rd_2}{d_1+L},\\ m \text{ odd:} & \varrho < R - \frac{mRd_2}{d_1+L} \end{cases} \qquad (3.7)\\
&\qquad\quad \text{(condition when an } m\text{-th order beam ends up on the screen)}\\
&F(m,\varrho,\vartheta) = 0, \text{ in any other case.}
\end{aligned}
$$

Using the first condition (3.7) as well as Eqs. (3.1) and (3.3), the number $m_{\max}$ of terms in the sum to be considered can be derived to be $m_{\max} = \lceil L/d_1 \rceil$, where $\lceil\cdot\rceil$ denotes the ceiling function.

The factor $\sqrt{\varrho_{\text{eff},m}/\varrho}$ in Eq. (3.5) can be understood as follows, see Fig. 3.4 (b): All rays that would have illuminated the annular segment $\varrho_{\text{eff}}\mathrm{d}\varphi\mathrm{d}\varrho_{\text{eff}}$ on the screen if they were not reflected (i. e. if there was no waveguide), actually end up on the screen in the annular segment $\varrho\mathrm{d}\varphi\mathrm{d}\varrho$. Since the power contained within the segments must be the same, $I_0|\varrho_{\text{eff}}\mathrm{d}\varphi\mathrm{d}\varrho_{\text{eff}}| = I_1|\varrho\mathrm{d}\varphi\mathrm{d}\varrho|$, it follows that $I_1/I_0 = \varrho_{\text{eff}}/\varrho$, and its square root accounts for this in the sum of the electric fields, Eq. (3.5).

This leads to a $\sim 1/\varrho$-divergence of the intensity at the center of the waveguide. It demonstrates the focusing ability the waveguide: a 1D circle circumference is focused onto the 0D spot at $\varrho = 0$. A remarkable property is that even in the case of incoherent light, cylindrical waveguides exhibit focusing of an incident beam onto the axis due to the $\sqrt{\varrho_{\text{eff},m}/\varrho}$ factor derived from power conservation – an effect that is not expected for rectangular or planar waveguides.

Within the ray-optical model it is impossible to get information on the achievable resolution. In reality, the electric field will not have any singularities, since diffraction restricts the resolution to a value which can only be derived from wave optics, on a length scale determined by λ and R. Experimentally, how tight the focus will be, is limited by the dimensions of the source and the aperture of the detector measuring the transmitted power through the waveguide. Therefore, the resulting intensity distribution $P(x,y)$ will be convolved with a power-conserving Gaussian function

$$f(x,y) = e^{-(x^2+y^2)/a^2}/(\pi a^2) \tag{3.8}$$

with an averaging constant a,

$$\tilde{P}(x,y) = \int \mathrm{d}x \int \mathrm{d}y P(x',y') f(x-x',y-y')\,, \tag{3.9}$$

in order to obtain physically sensible mode profiles $\tilde{P}(x,y)$.

3.1.2 Theoretical mode profiles

Fig. 3.5 shows the calculated mode profiles for $L = 46$ mm length, $R = 2.3$ mm radius, and $d_1 = 12$ mm distance to the source with total transmitted power of 48 µW at a wavelength of $\lambda = 160$ µm ($\hat{=}$ 1.87 THz) and an exemplary divergence angle $\alpha = 15°$. These values correspond to the experimental situation in Fig. 2.7. The input mode profile at the entrance of the waveguide can be seen in Fig. 3.5 (a). The color map indicates the intensity values, and an arrow plot shows the distribution of the electric field for a phase where the y-component of the electric field is maximal in the center. As expected, a Gaussian-type input mode profile that is cut off at the radius of the waveguide can be seen.

Now this electric field distribution propagates through the waveguide, and for these values given above, we plot the expected output mode profile measured at a distance of $d_2 = 10.5$ mm and $d_2 = 26.5$ mm from the waveguide end in Fig. 3.5 (b) and (c). Common to the graphs is the central spot of maximal intensity, illustrating the focusing ability of the cylindrical waveguide. With increasing distance from the waveguide end, some rings/cones or sidelobes originating from the center move further out. In the center, the electric field is maximal and is pointing in the y-direction. The x-component of the electric field is comparable in magnitude with the y-component in all four quadrants, except for the x- and y-axes themselves, where it vanishes due to symmetry reasons. This is remarkable given that the input electric field was predominantly y-polarised, as seen in Fig. 3.5 (a), with a negligible x-component. This phenomenon represents a mixing of x and y polarisation states and has its origin in the sign flip of the $\vec{e}_\varphi$-component of the electric field upon reflection at the cylinder walls, see Eq. (3.5). This leads to a rapidly changing direction of the electric field in the center, i.e. some spatial “curls”.

An important question is the amount of error introduced by the neglection of wave optics, since the ray-optical treatment is only valid in the limit $R \gg \lambda$. This can be illustrated by considering the total transmitted power. As the waveguide is considered lossless, the transmitted power through the waveguide should be equal to the incident power at the waveguide input. In Fig. 3.5 (d), the total input power is displayed as a function of the radius of the waveguide (black curve). The integrated power at the output in the case of an incoherent power sum (dashed line), when the intensity is calculated for each individual ray of order m and then the intensities are summed up, is equal to the input power. When the rays are coherently interfering, a deviation from the input power can be seen (blue curve),

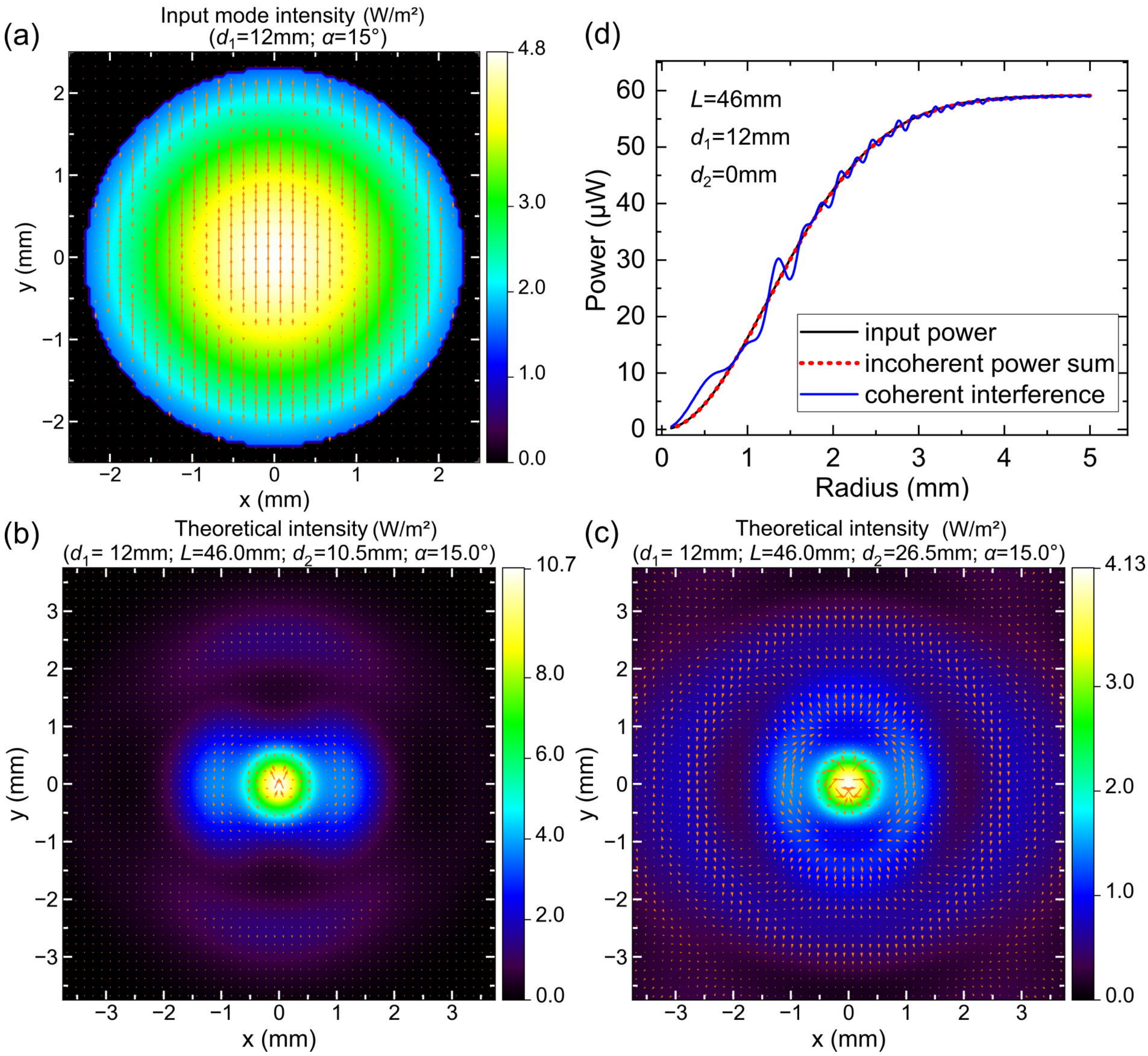

Figure 3.5: **Theoretically predicted input and output mode profiles,** at a wavelength of λ = 160 µm. (a)-(c): Mode profiles, the intensity is shown as color map, and the electric field is indicated by an arrow plot (orange arrows). (a) Input mode profile, (b) Output mode profile at a distance of 10.5 mm, (c) Output mode profile at a distance of 26.5 mm. In (b) and (c), the intensity was averaged with a Gaussian with a = 0.47 mm, which optimally describes the experimental measurement resolution, and the electric field was averaged with $a = \lambda/2$. (d) Comparison of the input power with the output power in the case of an incoherent superposition of the rays (intensities of each ray are summed up), and in the case of coherent interference of rays at the screen (electric and magnetic fields are summed up), as a function of the waveguide radius: the ray-optical theory is applicable for $R \gg \lambda$.

which becomes prominent at small radii. For large radii $R \gg \lambda$, the deviation becomes negligible and the total power in the coherent case is equal to the incident power. For the waveguide radius $R = 2.3$ mm considered here, the relative error in output power is less than 3 %.

Let us now consider the evolution of the mode profiles within the waveguide in cross section along the x- or y-axes. This leads to the question of how to handle averaging, Eqs. (3.8)–(3.9), in the x-z- and y-z-planes.

In the case of cylindrical symmetry of the mode profile, $P(x,y) = P(r)$, the 2D-convolution in Eqs. (3.8)–(3.9) can be transformed into a 1D-convolution only along the radial coordinate. Using

$$\begin{pmatrix} x \\ y \end{pmatrix} = \begin{pmatrix} r\cos\varphi \\ r\sin\varphi \end{pmatrix} \quad ; \quad \begin{pmatrix} x' \\ y' \end{pmatrix} = \begin{pmatrix} r'\cos\varphi' \\ r\sin\varphi' \end{pmatrix} , \tag{3.10}$$

Eq. (3.9) becomes:

$$\tilde{P}(r) = \int_0^\infty r'\mathrm{d}r' \int_0^{2\pi} \mathrm{d}\varphi' P(r') \cdot \frac{1}{\pi a^2} \exp\left(-\frac{r^2 + r'^2 - 2rr'\cos(\varphi - \varphi')}{a^2}\right) . \tag{3.11}$$

By substituting $\varphi' - \varphi = \chi$, using the 2π-periodicity in χ and symmetry around $\chi = 0$, this equation transforms to

$$\begin{aligned} \tilde{P}(r) &= \frac{2}{\pi a^2} \int_0^\infty r'\mathrm{d}r' P(r') \int_0^\pi \mathrm{d}\chi \exp\left(-\frac{r^2 + r'^2 - 2rr'\cos\chi}{a^2}\right) \\ &= \frac{2}{a^2} \int_0^\infty r'\mathrm{d}r' P(r') \exp\left(-\frac{r^2 + r'^2}{a^2}\right) \cdot \frac{1}{\pi} \int_0^\pi \mathrm{d}\chi \exp\left(\frac{2rr'\cos\chi}{a^2}\right) \\ &= \frac{2}{a^2} \int_0^\infty r'\mathrm{d}r' P(r') \exp\left(-\frac{r^2 + r'^2}{a^2}\right) \cdot I_0\left(\frac{2rr'}{a^2}\right) . \end{aligned} \tag{3.12}$$

Here, I_0 is the modified Bessel function of the first kind. Eq. (3.12) allows calculation of the convolved mode profile $\tilde{P}(r)$ in the case of cylindrical symmetry of the mode profile.

To plot the mode evolution in a cross section parallel to the x- or y-axes, Eq. (3.12) is used to average the calculated data of $P(x,y)$ along the x- or y-axes. It should be noted that this represents an approximation, since the mode profile is not perfectly cylindrically symmetric. This is in contrast to the accurate 2D-convolution used in the plots as a function of x and y, perpendicular to the waveguide axis, that are shown in Fig. 3.5 and allow evaluation of the total transmitted power. However, this approximation is used in this analysis to visualise the relative evolution along the waveguide axis and establish periodicities, without claim of absolute numerical accuracy.

Thus obtained mode evolution over a large length $L = 1$ m is shown in cross section along the x-axis, see Fig. 3.6. In Fig. 3.6 (a), the total power $P_\mathrm{x} + P_\mathrm{y}$ originating from the x- and y- components of the electric field is shown in the x-z-plane, with $y = 0$. Since this

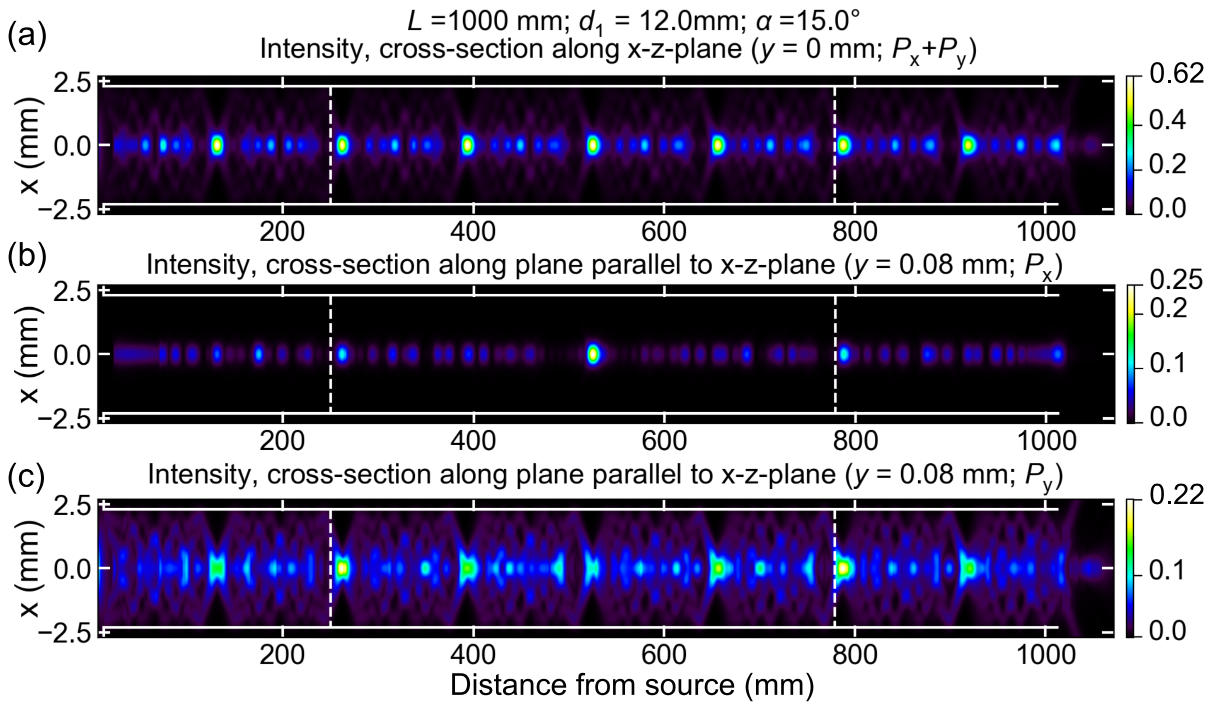

Figure 3.6: **Wave propagation within the waveguide.** Cross-sectional cuts showing the intensity, radially averaged over $a = 2\lambda$. Power generated by x- and y-components of the incident electric field in the x-z-plane (a); Power generated by the x- component (b) and y-component (c) of the incident electric field in a plane parallel to the x-z-plane shifted by $\lambda/2$. A periodicity is observed which is well described by the Talbot-distance $16R^2/\lambda$ = 529 mm derived from wave optics [207]. The colour bar is scaled such that a value of 1.0 corresponds to the peak intensity of a Gaussian function with sharpness a containing the full input power (ideal focusing).

is a symmetry plane, P_x vanishes there, and $P_x + P_y = P_y$ in this plane. To illustrate the evolution of the x-polarised electric field, in Fig. 3.6 (b) and (c) the P_x and P_y powers are shown in a plane parallel to the x-z-plane, shifted by $y = \lambda/2 = 0.08$ mm.

The mode profile repeats itself periodically. While at symmetry planes shorter periods are observed, the longest period can be seen in the P_x-diagram, and corresponds to ca. 53 cm, indicated by the dashed white lines. In Ref. [207], the Talbot distance (the waveguide length, after which an electric field profile within a cylindrical waveguide is reproduced), has been calculated theoretically within a wave-optical approach. It yields a value of $16R^2/\lambda$ = 529 mm [207]. This is in excellent agreement with the period value obtained from the ray-optical model employed in this work, and demonstrates its validity.

Within a distance $d_2 \lesssim d_1$ after the waveguide, the axial beam pattern follows the mode profile within the waveguide. To obtain a focused central spot at a distance $d_2 \lesssim d_1$ after the end of the waveguide, the waveguide has to be cut off at a length $L = z_{max} - d_2$, where z_{max} is the z-position of a maximum along the waveguide axis.

For example, we consider the second clearly visible maximum position in Fig. 3.6 (a) for

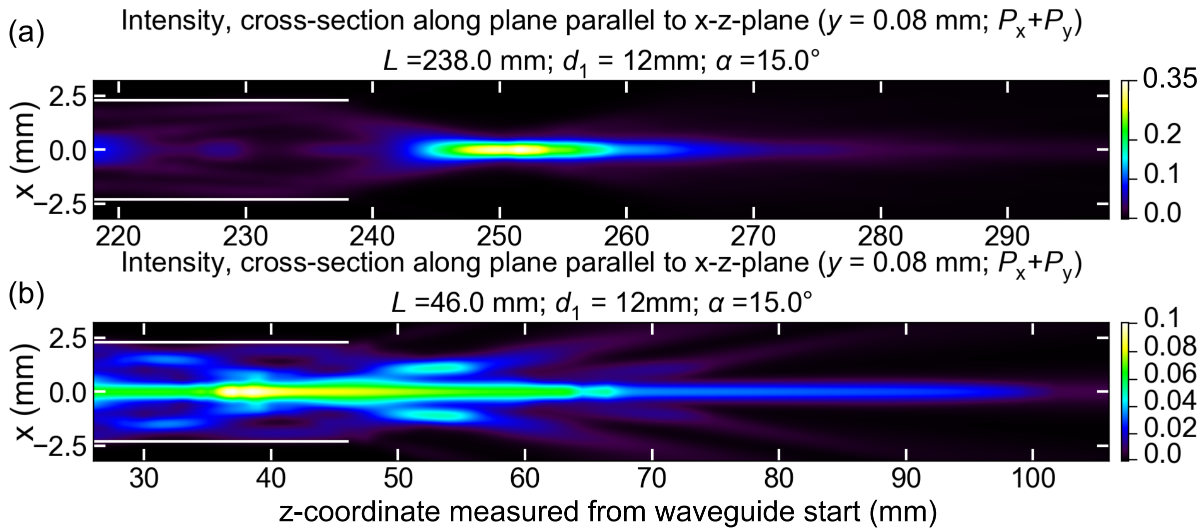

Figure 3.7: **Focusing effect of the multimode waveguide.** (a) Mode pattern propagation after the waveguide end if the waveguide is cut off at $L = 238$ mm, 12 mm before the second maximum, at the first dashed line in Fig. 3.6. Optimal focusing is achieved after the waveguide, corresponding to an effective "focal distance" of 12 mm. (b) Mode propagation for a waveguide length $L = 46$ mm. The focusing is less optimal but the maximum intensity is still achieved along the waveguide axis.

focusing at the end of the waveguide. The waveguide is "cut" at $L = 238$ mm, indicated by the first white dashed line in Fig. 3.6, and the behaviour at the output of the waveguide is shown in cross section in Fig. 3.7 (a). A clear focal spot is obtained at 1.2 cm after the end of the waveguide, demonstrating the focusing ability of the waveguide. For comparison, the output mode profile is also shown for a length $L = 46$ mm in Fig. 3.7 (b). Here, the output intensity distribution is less well focused. Nevertheless a common feature is that the central peak remains sharp over a wide range, while side-lobes or cones separate themselves and move outwards, away from the axis. The central peak does not widen up following a Gaussian beam profile; instead its power is redistributed to the side lobes. The output beam has a complicated structure originating from the multiple beam interferences. The divergence is low: over a distance of 2 cm after the waveguide end, most of the power is still contained within a radius of 3 mm.

Similarly, if a length L of a waveguide is given, the above calculation can be used to answer the question, how far away from the waveguide input the source should be positioned, in order to obtain maximal central intensity at a given distance d_2 from the waveguide end.

To some extent, misalignment effects can be incorporated in the theoretical treatment – in particular, an angular misalignment of the source. This can be included by considering a dipole moment $\vec{p} = (\sin\delta, \cos\delta, 0)$ that is rotated by an angle δ from the y-axis around the z-axis, and an angular distribution function

$$f_{\vartheta_0,\varphi_0}(\vartheta,\varphi) = \exp\left(-\frac{(\vec{r}-\vec{r}_0)^2}{\alpha^2}\right)\bigg|_{r=1,r_0=1} \tag{3.13}$$

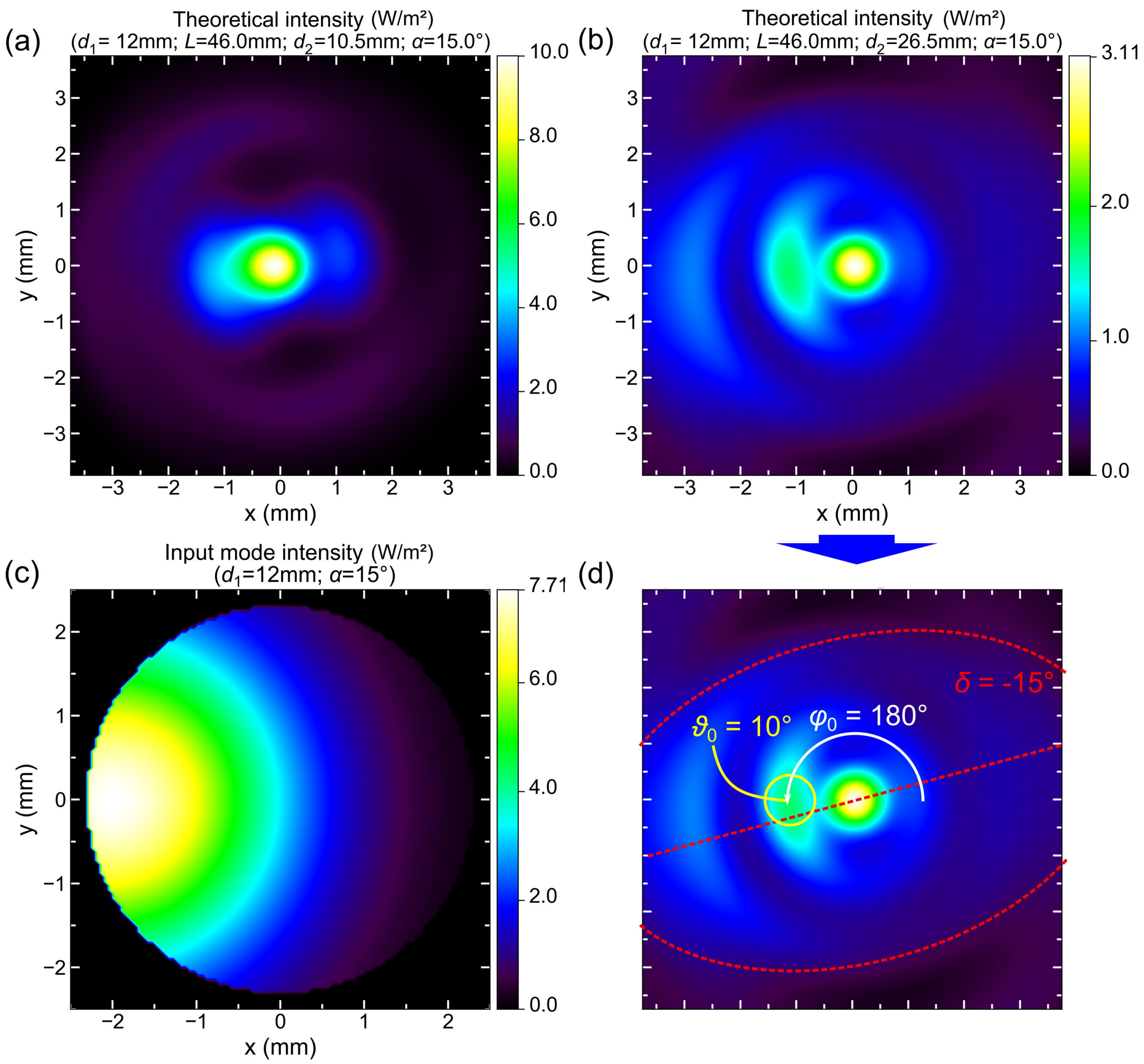

Figure 3.8: **Theoretically expected mode profiles for an angular misalignment** given by $\vartheta_0 = 10°$, $\varphi_0 = 180°$, and a rotation of the Hertzian electrical dipole of $\delta = -15°$. (a) $d_2 = 10.5$ mm, (b) $d_2 = 26.5$ mm. The power distribution into the sidelobes, the side mode rotation and the peak intensity are in excellent agreement with the experiment (Fig. 2.16 (b) and (c)). (c) The corresponding mode pattern at the waveguide input. (d) The features in the output mode profile (b) relating to the misalignment parameters ϑ_0, φ_0, and δ.

$$= \exp\left[-\frac{2}{\alpha^2}\left(1 - \sin\vartheta \sin\vartheta_0 \cos(\varphi - \varphi_0) - \cos\vartheta \cos\vartheta_0\right)\right] . \tag{3.14}$$

This function describes maximal emission probability under polar angles ϑ_0, φ_0, i.e. angular misalignment. For $\vartheta_0 = 0$ and small angles ϑ it reduces to the previously considered angular distribution in Eq. (3.4).

For examplary values of $\vartheta_0 = 10°$, $\varphi_0 = 180°$, and $\delta = -15°$ the calculated mode pattern is shown in Fig. 3.8 (a) and (b). The corresponding misaligned input mode is shown in Fig. 3.8 (c).

Fig. 3.8 (d) shows what effect the parameters have on the output mode profile: ϑ_0 relates to the intensity, and φ_0 to the polar angle of the prominent side lobe, which is seen left from the central peak (along the negative x-direction). δ tunes the input polarisation direction and results in the rotation of the outer sidelobes. Thus, taking into account the misalignment effects, the intensity distribution at the output is no longer symmetric. Fig. 3.8 (d) makes it clear how characteristics of the input beam are encoded in the output beam profile.

The ratio of the theoretical peak intensities for the two values of d_2 is 10.7/4.13 $\approx$ 2.59 without misaligment effects (Fig. 3.5 (b) and (c)), and 10.0/3.11 $\approx$ 3.22 when considering angular misalignment (Fig. 3.8 (a), (b)). This shows that angular misalignment leads to a faster decay of the central peak intensity with distance from the waveguide end.

3.1.3 Multimode waveguide as an interferometric system

The presented equations (3.5), (3.6) transform an input electric field to the electric field within or after the waveguide. The formulas take electric fields of arbitrary angular distribution, as long as the source is on the axis of the waveguide. As a result, the output mode profile of the multimode waveguide can be understood as a "fingerprint" or, more precisely, a *two-dimensional interferogram* of the input electric field distribution, that is described by the above calculations.

The direct consequence is that the output mode profile can be used as a sensitive probe of the input field, a remarkable property that I would like to highlight. The mode profiles have a pronounced dependence on the angle φ. In Fig. 3.5 (b) for example, pronounced side lobes are seen along the x-direction, but less noticable along the y-direction. This is because of the input polarisation being y-polarised; the pattern rotates with the dipole moment $\vec{p}$ around the z-axis, and is a consequence of the sign flip of the $\vec{e}_\varphi$-component upon reflections. Notably, the intensity profile of the input field is axially symmetric (see Fig. 3.5 (a); a slight deviation due to the Hertzian dipole is negligible at the small angles considered). This means that there is no way to determine the input polarisation merely from a measurement of the input intensity distribution, if there is no polariser available. In contrast, the intensity profile at the output of the waveguide allows determination of the input polarisation from the direction where distinct side lobes can be seen. This means that *the cylindrical waveguide maps the input polarisation information onto the intensity distribution at its output*, and thus can serve as a polarimeter.

In addition, asymmetric features in a mode profile contain valuable information about the characteristics of the input electric field. The consideration of misalignment in the model demonstrates the effect of off-axis deviation (angles ϑ_0, φ_0) on the intensity distribution at the waveguide end. The polar angle (calculated anticlockwise from the positive x-axis) φ_0

determines the prominent side lobe in Fig. 3.8, its magnitude relative to the central peak intensity is related to ϑ_0, and the tilt of the outer lobes is related to the polarisation direction δ. A single two-dimensional map of the intensity distribution at a known distance, which can be understood as a two-dimensional interferogram, contains all this information.

3.1.4 Comparison with experimental mode profiles

The ray-optical model presented in the previous sections provides a theoretical description of the mode profiles. In Fig. 3.9, the obtained theoretical and experimental mode profiles from the Figs. 3.5, 2.16, and 3.8 are combined for easy comparison. Fig. 3.9 (a) and (b) shows the theoretical mode profiles calculated for the experimental parameters. As the length L, the coldfinger waveguide length 46 mm is used, since the free-space optical path between horizontal and vertical waveguide is much larger than the waveguide radius. Moreover, at the end of the first, 302 mm long horizontal waveguide, the ray-optical treatment predicts an axial maximum, which can be seen as a source for the subsequent vertical waveguide. Thus the distance to the source d_1 can be taken as the free-space optical path between the horizontal and vertical waveguides, 12 mm. The experimentally determined power of 48 µW is used, as well as a value of $\alpha = 15°$, which results in similar mode profiles, and a Gaussian averaging value a corresponding to a full width at half maximum of 0.78 mm, that optimally describes the experimentally obtained resolution of the mode profiles.

This way, the theoretical mode profiles Fig. 3.9, (a) and (b), can be compared to the experimentally measured mode profiles in Fig. 3.9, (c) and (d). Apart from a slight asymmetry of the experimental pattern, good agreement is obtained. In particular, the extension of side lobes is reproduced in Fig. 3.9 (a), and the radial circles of modal cones moving outwards from the axis are reproduced in Fig. 3.9 (b). The theoretical plot displays a central intensity of 10.7 W/m^2, similar but slighty higher than the 10.0 W/m^2 experimental value for d_2 = 10.5 mm. The ratio of peak intensities for the two values of d_2 considered is 10.7/4.13 $\approx$ 2.59 theoretically, and 10.0/3.1 $\approx$ 3.22 experimentally.

The theoretical result is point-symmetric around $(x,y) = (0,0)$, due to the symmetry of the model for the input electric field. In the experiment, some residual misalignment will distort the mode profile and break the point-symmetry.

Misalignment in the experiment may have several origins, such as angular misalignment of the QCL source, angular misalignment of the waveguide, and a lateral shift of the QCL source causing it to be off-axis with respect to the waveguide. If the misalignment is assumed to originate only from the angular off-axis emission of the source, then Fig. 3.9 (e) and (f) can be considered as a theoretical fit to the experimentally measured mode profiles, Fig. 3.9 (c) and (d), in which the key features of the mode profile are very well reproduced.

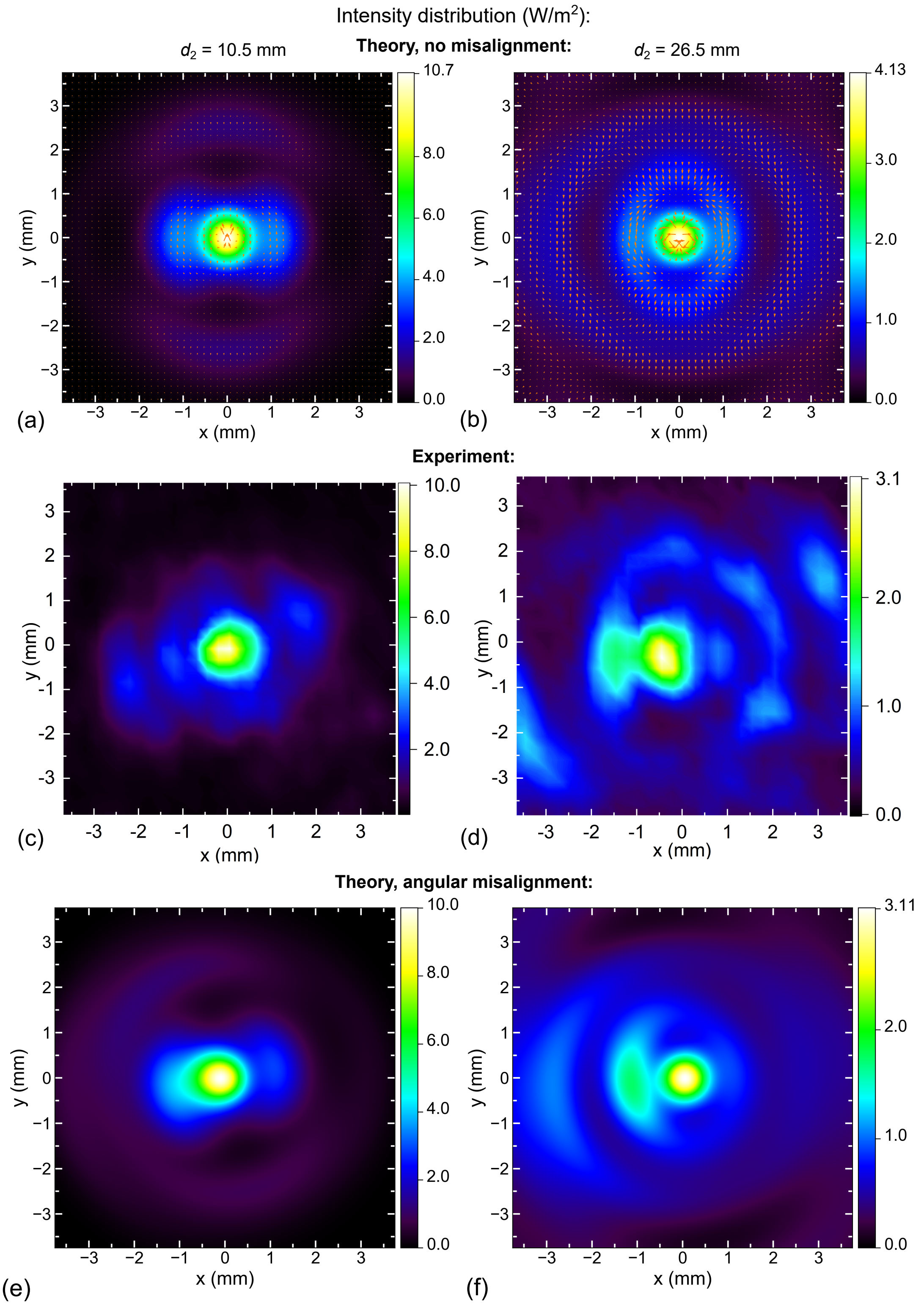

Figure 3.9: **Comparison of experimental and theoretical mode profiles.** (a), (b): Theoretical mode profiles. (c), (d): Measured mode profiles. (e), (f): Theoretical mode profiles assuming angular misalignment of $\vartheta_0 = 10°$, $\varphi_0 = 180°$, and $\delta = -15°$. All figures are plotted for an integrated output mode power of 48 μW at the waveguide end. The figure reproduces the data in Fig. 3.5, (b) and (c), Fig. 2.16, (b) and (c), and Fig. 3.8, (a) and (b).

Interestingly, the circles of increasing radius shown in Fig. 3.4 (b) are not a purely theoretical construct, but can be visualised. This is shown in Fig. 3.10 (a). A red laser spot is incident on an HDPE sheet at the start of a waveguide, which acts as a diffusor. The spot hits the HDPE sheet at the center of the waveguide, i. e. can be seen as a radial source on the waveguide axis. For its wavelength of 632.8 nm (helium-neon laser), the waveguide of radius 2.3 mm is a multimode waveguide. The image seen at the end of the waveguide is captured by a camera, yielding Fig. 3.10 (b) and (c) for two different lengths of the waveguide. Indeed, circular rings of increasing radius can be observed. More rings are seen for the longer length, as in this case rays undergo more reflections. The number of reflections, $N_{\mathrm{refl}} = \lfloor (m+1)/2 \rfloor$, increases with L since $m_{\mathrm{max}} = \lceil L/d_1 \rceil$, and those rays within the solid angle of the camera lens aperture are captured. Not all rings are concentric, and some are slightly ellipsoidal, which highlights the imperfections of the real waveguide.

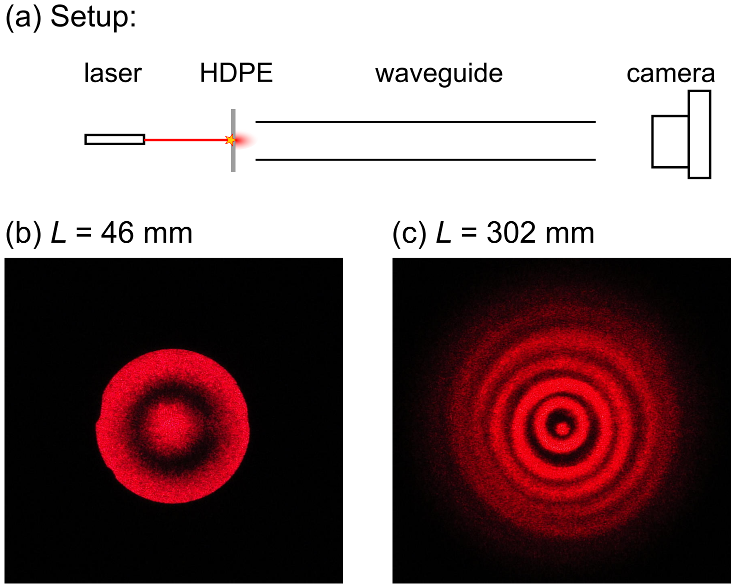

Figure 3.10: **Circular rings in the visible range.** (a) Setup to capture the output of a multimode waveguide with a camera using laser light in the visible. (b), (c) Photos at the waveguide output for different waveguide lengths L.

3.2 Experimental demonstration of the waveguide focusing effect

The ray-optical theory of multimode cylindrical waveguides in section 3.1.2 was initially developed to explain the mode profiles observed at the sample space of the waveguided THz delivery system. As part of this analysis, the developed theory has predicted an exciting phenomenon: at certain waveguide lengths, multimode waveguides should focus the input radiation, Fig. 3.7 (a). In order to check this prediction, THz propagation through a single waveguide of 238 mm length, which is expected to be one of the optimal lengths for focusing, is studied in this section.

3.2.1 Characterisation of the QCL far field

For subsequent analysis, knowledge of the quantum cascade laser properties will be required. What is the exact position, the divergence angle, and the misalignment angles of the QCL? These questions can be answered by studying its far field emission pattern.

The far field emission is measured using a Golay cell mounted on x, y, z motorised scanning stages with an iris of 1 mm diameter in front of it. Multiple x-y-scans are carried out at different distances d_1 from the QCL in the z-direction, which result in the plots in Fig. 3.11.

In the waveguide theory section, d_1 has denoted the distance between the QCL as a point source and the waveguide input. More generally, d_1 can be understood as the distance between the QCL point source and the next optical element, which is in this case the input aperture of the Golay cell.

As expected, a spot can be seen that widens up as the distance grows. Its intensity also falls down by an order of magnitude as the distance d_1 is increased from 7.3 mm to 23.3 mm. At short distances, the spot looks almost Gaussian. Deviations can be seen at values of $x > 0$, which might be related to imperfections of the QCL facet that occured during the cleaving process.

To quantify the QCL emission pattern, the mode profiles are fitted with a two-dimensional Gaussian function:

$$I(x,y) = A\exp\left(-\left(\frac{x-x_{\mathrm{c}}}{w_{\mathrm{x}}}\right)^2 - \left(\frac{y-y_{\mathrm{c}}}{w_{\mathrm{y}}}\right)^2\right) \tag{3.15}$$

This allows to extract the center positions x_{c}, y_{c} and beam widths w_{x}, w_{y} along the x- and y-directions. These are plotted in Fig. 3.12.

First of all, the data is used to find the z-position where the QCL source is located. In the experiment, it is easily possible to measure the distance d_{HDPE} between the Golay cell aperture (or later, waveguide input) and the HDPE window enclosing the QCL cryostat using a caliper, see Fig. 3.13 (a). However, the distance of interest is d_1, which is larger than the HDPE window–waveguide distance by an offset Δz, $d_1 = d_{\mathrm{HDPE}} + \Delta z$. In principle, one could try to measure it by warming up and opening the cryostat and removing the HDPE window. But even in this case, this could hardly be achieved with reasonable accuracy without damaging the QCL facet. What matters for the analysis is, however, d_1 as the position of the QCL as the point source of emitted radiation. Therefore, I define d_1 such that $d_1 = 0$ when the width as a function of the z-coordinate vanishes, as seen in Fig. 3.12. This gives the offset Δz that needs to be added to the d_{HDPE}-values known from the z-position of the stepper motor to calculate d_1. This analysis yields $\Delta z = (3.3 \pm 0.2)$ mm, determined from the x-axis cross-section of the extrapolated linear fits of w_x and w_y in Fig. 3.12 (b). The transformation from d_{HDPE} to d_1 has already been done for all data plots presented here.

The obtained offset Δz is reasonable, as can be confirmed from the following estimations. Given the width of the coldfinger of 6.1 mm in QCL lasing direction, and the outer diameter of the HDPE window of 14.7 mm, it can be calculated that the QCL facet is (14.7 – 6.1)/2 – Δz = 1.0 mm closer to the waveguide input than the coldfinger edge, assuming that the coldfinger is located centrally in the HDPE window. This “overhang” value agrees well with

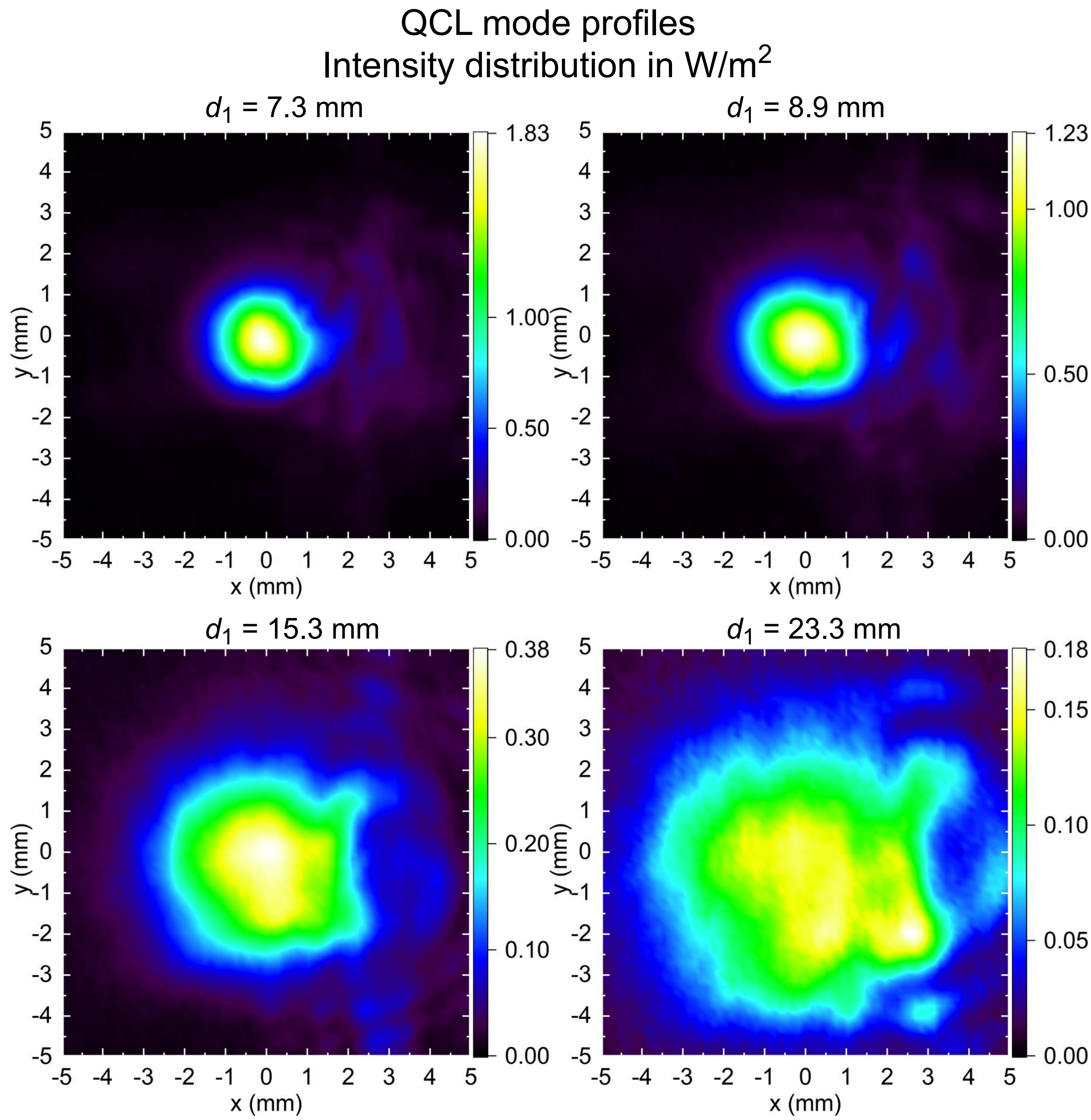

Figure 3.11: **Far field measurement of the QCL emission.** Intensity distributions in W/m^2 at different distances d_1 between 1 mm iris at the Golay cell and QCL facet. An almost Gaussian beam spot at small distances from the QCL widens up and loses intensity as d_1 increases.

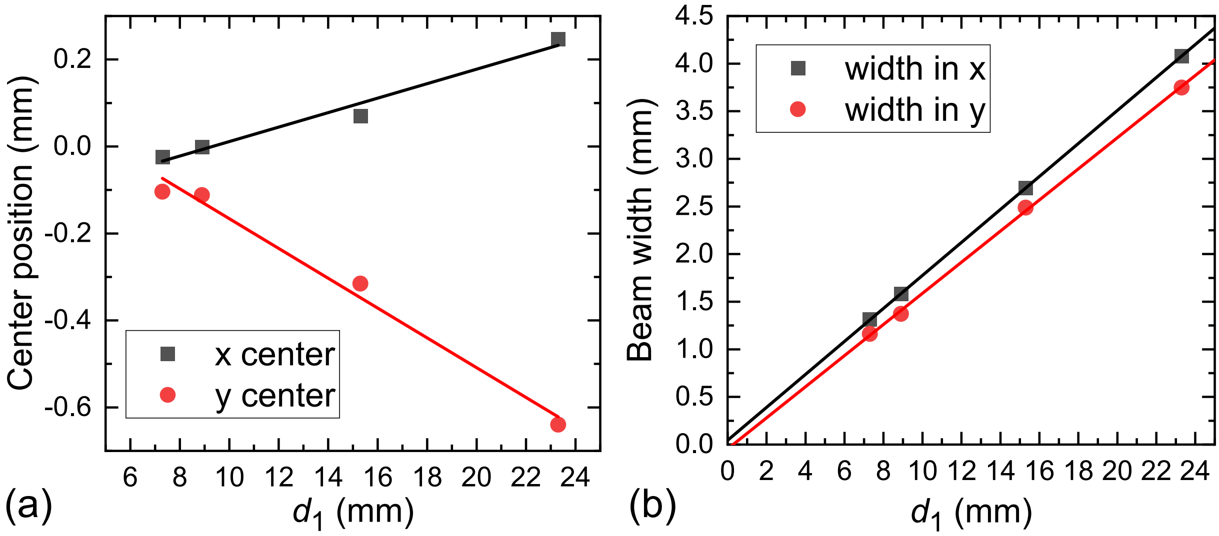

Figure 3.12: **Characterisation of the QCL: position, divergence and misalignment.** Analysis of two-dimensional Gaussian fits to the mode profiles in Fig. 3.11. (a) The center position and (b) the width of the spot along the x- and y-directions as a function of the distance d_1 between the QCL and the Golay cell aperture are shown. The width data was used to define the zero position of d_1 and to find the offset $\Delta z = d_1 - d_{\mathrm{HDPE}}$, such that $d_1 = 0$ when the width vanishes. The slopes of the linear fits to the width data are 0.1731 in x- and 0.1634 in y-directions, and allow to find the divergence half-angle of the QCL beam as 9.8° and 9.3°, respectively. The slope of the linear fits to the center positions are 0.0171 in x- and –0.0351 in y-direction. This defines the misalignment of $\vartheta_0 = 2.18°$ at a polar angle of $\varphi_0 = -64°$.

the coldfinger photo, Fig. 3.13 (b). Using the inner diameter of the HDPE window of 12 mm, the distance between QCL facet and inner wall of the HDPE window can then be calculated to be about (12 – 6.1)/2 – 1.0 = 1.95 mm.

The linear slopes of w_x and w_y are a measure for the divergence of the QCL radiation. By setting the slope equal to $\tan\alpha$, this allows to find the divergence half-angles $\alpha_\mathrm{x} = 9.8°$ and $\alpha_\mathrm{y} = 9.3°$. Notably, $\alpha_\mathrm{x} > \alpha_\mathrm{y}$, which is reasonable: since the QCL is mounted vertically, the x-direction corresponds to the growth direction of the QCL in this case. In y-direction, the ridge is 0.25 mm wide, which is larger than the height of the QCL chip in growth direction, where the chips are thinned down to 0.1–0.2 mm to increase thermal conductivity. Thus in x-direction, where the mode has been restricted stronger in space, the divergence is higher.

The center positions of the beam spots can be used to find its misalignment angles. The slopes of the corresponding linear fits indicate how much the propagating beam moves away from the z-axis. They allow to find the misalignment of $\vartheta_0 = 2.18°$ at a polar angle of $\varphi_0 = -64°$ (measured with respect to the positive x-axis).

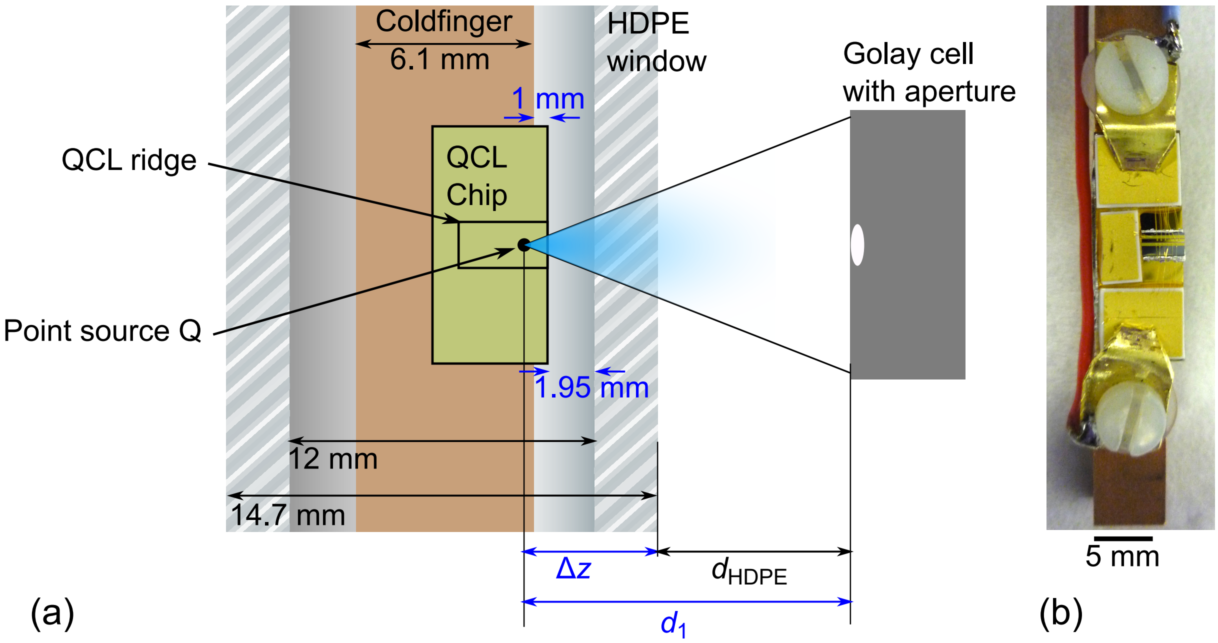

Figure 3.13: **Sketch of the QCL cryostat geometry.** (a) The dimensions shown in black are known from caliper measurements, while the dimensions shown in blue are deduced from the QCL far field measurement. The distance d_{HDPE} is known, and the offset Δz is found from a linear extrapolation of the measured beam spot width to zero. This allows finding the distance of interest d_1 between the QCL modelled as a point source and the Golay cell. The estimation of the QCL overhang of 1 mm and the distance between QCL and the HDPE inner wall yields reasonable results, in good agreement with the photo of the coldfinger shown in (b).

3.2.2 Experimental setup

In the previous section, Fig. 3.7, one can see that at certain values of the waveguide length L the focusing is optimal, and a highly focused spot is achieved along the axis of the cylin-

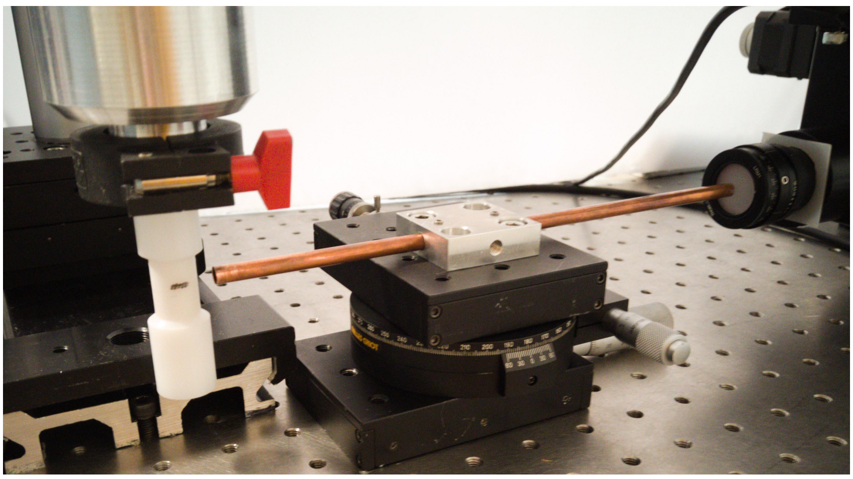

Figure 3.14: **Setup for waveguide measurements.** The QCL on the left emits radiation into the copper waveguide, and the output of the waveguide is measured by a Golay cell on the right.

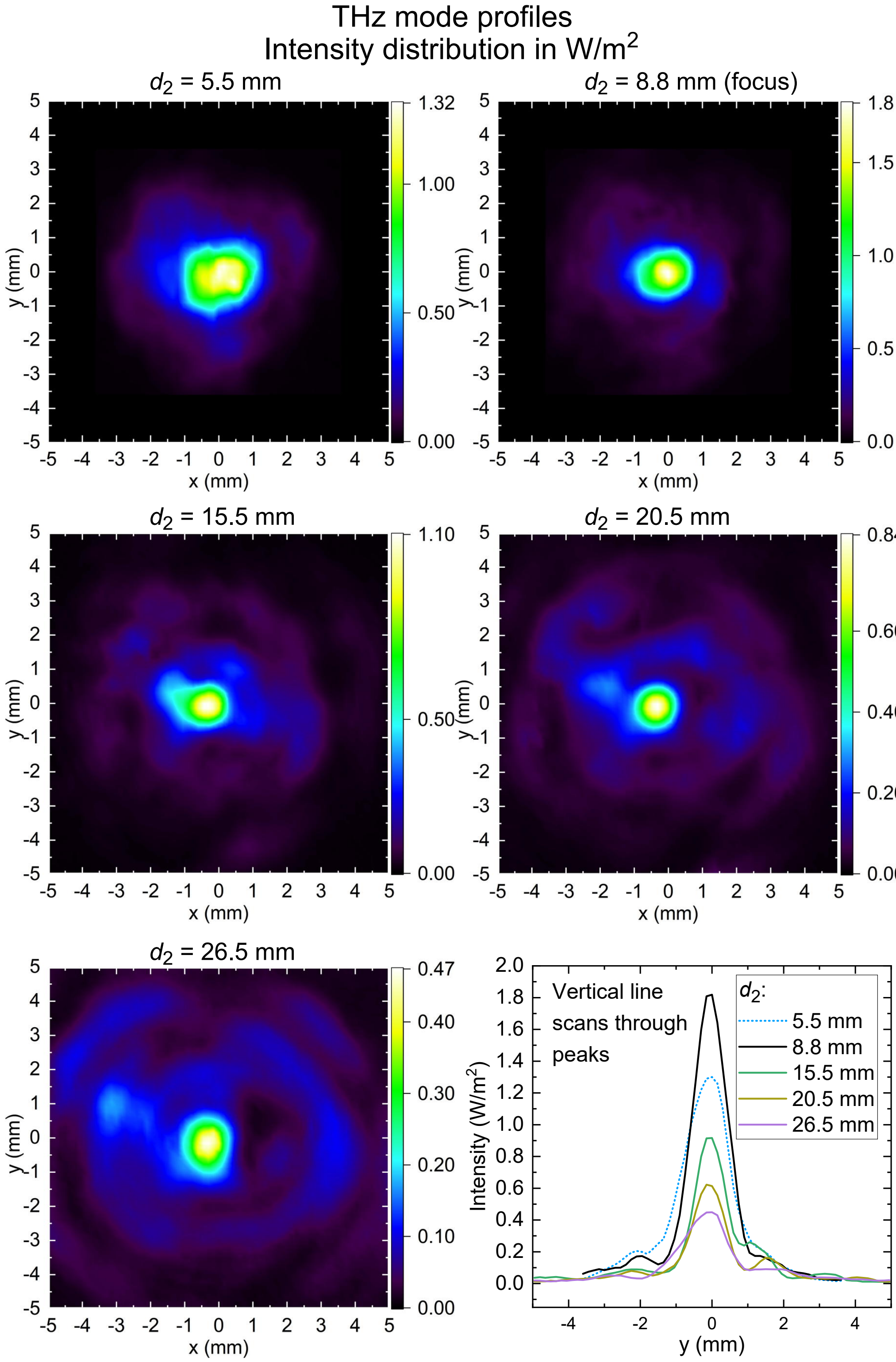

Figure 3.15: **Measurements of the mode profiles at the waveguide output at different distances d_2 from the waveguide end.** The intensity distributions are acquired by scanning the Golay cell in x- and y-directions with a 1.0 mm iris in front of it. d_2 = 8.8 mm corresponds to the maximum achievable central intensity, i. e. the "focal spot" of the waveguide. Closer to the waveguide end, the intensity is smaller since the power is less focused, and further away from this position, the power is redistributed into cones moving away from the waveguide axis, while the central spot becomes sharper but dimmer. At the bottom-right, vertical line scans through the peaks are shown to illustrate the peak amplitudes.

drical waveguide. In order to demonstrate this experimentally, a 238 mm long waveguide is cut. A setup is built that allows to align the waveguide, the quantum cascade laser, and the Golay cell with all necessary degrees of freedom, Fig. 3.14.

A holder is designed specifically to mount a waveguide of 6.4 mm outer diameter, and is fabricated by the Mechanical Workshop. It has a through-hole that allows for the waveguide to slide in. The waveguide is fixed by two grub screws with rubber ends at the top. The QCL as well as the Golay cell are each mounted on three micrometer stages that allow movement in x, y, and z directions. As in the previous section, z is the direction of the waveguide axis, x the horizonal and y the vertical direction. The Golay cell stages are motorised. The waveguide stage allows movement in x and z directions. It also allows fine tuning of the waveguide angle with respect to the z-axis. In the horizontal direction, this is realised by the rotation stage, and in the vertical direction, this is realised by fine-tuning of the two grub screws holding the waveguide.

3.2.3 Mode profiles after the waveguide

After alignment of the system, the intensity distributions are measured using the Golay cell at different z-positions, see Fig. 3.15. The maximum intensity is achieved in the center, at a distance of $d_2 = 8.8$ mm from the waveguide end. This will be called the focus / the focal spot of the waveguide.

Closer to the waveguide, i. e. at lower d_2, the power is less focused, i. e. the central spot is broader. This results in a lower peak intensity. For $d_2 > 8.8$ mm, it can be seen that cones diverge away from the waveguide axis. In contrast to a Gaussian propagation profile, the width of the central spot does not change within measurement accuracy, although its intensity decays. The power is redistributed into the side cones moving away from the axis.

3.2.4 Sensitivity to misalignment

It should be noted that the alignment of the waveguide is critical for achieving optimal focusing with the maximum possible peak intensity. The behaviour of the measured power in

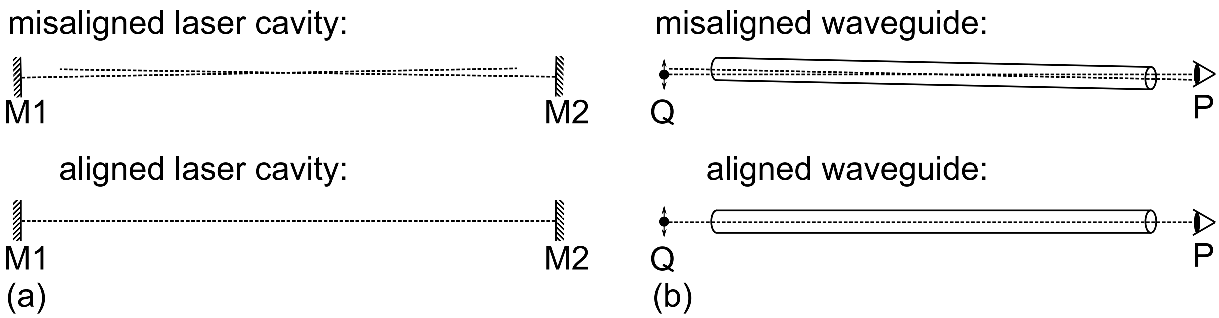

Figure 3.16: **A misaligned and an aligned (a) laser cavity, (b) multimode waveguide system.**

the focal spot during alignment resembles the alignment of a laser cavity: away from the optimal alignment parameters, the dependence of the measured power on the alignment parameters is rather weak, but becomes substantially stronger closer to the optimal parameters. Most critical is the waveguide angle: for the 238 mm long waveguide, the FWHM of the measured power as a function of the waveguide angle in the horizontal plane is 0.33°. That means, by rotating the waveguide by a small angle $\vartheta_x = 0.165°$, the measured power is halved. Over the experimental total path length $T = d_1 + L + d_2 = 255.7$ mm, this angle corresponds to 0.74 mm of lateral deviation.

An analogy with a laser cavity can be drawn by considering Fig. 3.16. A laser cavity is aligned when the normals to the two mirrors are collinear. In the multimode waveguide system, optimal alignment means that the connecting line between source Q and detector P is identical to the waveguide axis.

3.2.5 Focusing in a z-scan

The focusing effect can also be studied as a one-dimensional scan in the z-direction. This is shown in Fig. 3.17. The Golay cell detector is positioned at the center, and scanned in the z-direction with different diameters of the graduated iris (1.0 mm and 4.6 mm). The power is recorded as a function of d_2, which is the distance between the end of the waveguide and the blades of the graduated iris. 4.6 mm is the inner diameter of the copper waveguide used.

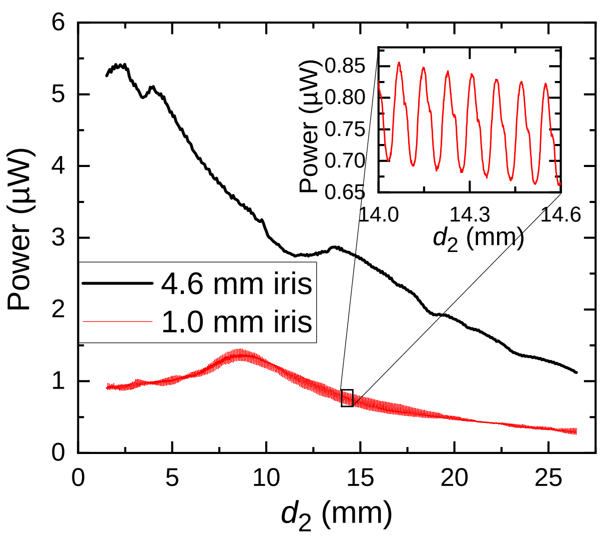

Figure 3.17: **z-scan of the Golay cell.** A scan along the z-axis through the mode profile peak with different diameters of the iris entrance, illustrating the focusing effect. The power measured with a 4.6 mm iris decays with distance from the waveguide end d_2. In contrast, the measurement with the 1.0 mm iris reveals that the maximum central intensity is achieved at $d_2 = 8.8$ mm. Inset: for the 1.0 mm iris measurement, reflections at the iris blades give rise to interference at a length scale of $\lambda/2 \approx 80$ µm.

The power contained within an area around the z-axis corresponding to the cross-section of the waveguide, measured with the 4.6 mm iris diameter, generally decays with distance from the waveguide end. This is related to the sidelobes that widen up after the waveguide end. However, the maximum intensity is located in the center, and is achieved only at a distance of 8.8 mm after the end of the waveguide, as the measurement with a 1.0 mm iris diameter demonstrates. This demonstrates the focusing effect of the waveguide.

For the 1.0 mm iris measurement, rapid oscillations of the power are observed. These occur with a period of half a wavelength, $\lambda/2 \approx 80\,\mu$m. They can be explained as an interference pattern. The metallic blades of the graduated iris are reflective, and thus are able to send radiation back into the waveguide. Reflections at one interface alone would however not give rise to interference. The observed pattern can be understood by considering that the QCL facet at the other end of the waveguide is another reflective surface, that forms a cavity with the iris at the entrance of the Golay cell. The resulting standing waves give rise to the observed interference pattern, provided that the iris diameter is low enough (1 mm) to have sufficient reflectance. This is the reason why the frequency of the THz source can be extracted from such a z-scan measurement, as was done in section 2.4, Fig. 2.19.

3.2.6 Cross-sectional profile of the waveguide output

Can we observe the focusing in a cross-sectional plot, such as in Fig. 3.7? This would require an x-z-scan, or a y-z-scan. Because of the interference pattern observed in Fig. 3.17, care has to be taken as to how the discrete points of such a scan will be placed. If a random number, unrelated to the wavelength, is chosen for the z-data points, the result will be a noisy graph showing the wave propagation overlaid with a Moiré-pattern generated by the z-spacing and $\lambda/2$. For best results, it is sensible to choose the z-spacing as $\lambda/4 + n\lambda/2$, $n \in \mathbb{N}$, and start with a z-coordinate known to have an extremum in Fig. 3.17. Neighboring values will then correspond to the maxima and minima of the interference fringes, and the average of neighboring values spaced by this distance would correspond to the power value without any interference.

In this case, 8.8 mm is chosen as the start coordinate in the z-direction, which is known to be the position of a constructive interference fringe. The QCL–waveguide distance is $d_1 = 8.9$ mm. The result of such a cross-sectional measurement is shown in Fig. 3.18 (a). It shows the measured intensity in the y-z-plane, normalised to a total power of 1.0, therefore the unit is 1/mm^2. The total power was determined by integrating the intensity over x and y at the focal position in Fig. 3.15. Some fringing (vertical lines) can be seen particularly for $d_2 > 11$ mm, where the z-step size was larger. This data is now deinterlaced along the waveguide axis, i. e. it is split into “even” and “odd” lines. These make up the two graphs Fig. 3.18 (b), (c). Compared to Fig. 3.18 (a), they both look smoother, but they differ from each other.

Now, the odd and even lines can be averaged, which gives rise to Fig. 3.19 (a). This is the result of the discussed analysis, and represents the experimental wave propagation with interference effects eliminated as far as possible. Fig. 3.19 (a) clearly shows that around $d_2 = 8.8$ mm, a focused spot can be seen. It is remarkable that the intensity remains high within a 1 mm radius in the center, even within 2 cm after the waveguide end.

For comparison, in Fig. 3.19 (b) the theoretically expected mode is shown. This is a plot similar to Fig. 3.7 (a). It is plotted for the parameters used in the experiment: a waveguide length $L = 238$ mm, a QCL–waveguide distance $d_1 = 8.9$ mm, and a wavelength of 159.38 µm wavelength. This is the wavelength corresponding to 1.881 THz frequency of the QCL lasing mode as measured according to the FTIR. For the Gaussian averaging value, 0.78 mm FWHM was used. This best describes the amount of smoothness introduced by the use of the 1 mm iris. For R, a value of 2.257 mm was chosen in the plot.

Fig. 3.19 (c) shows the case if the incident rays were incoherent, i. e. their intensities rather the electric fields were summed. Although the intensity is maximal in the center due to the theoretical $\varrho_{\text{eff}}/\varrho$-factor, the enhancement is rather weak (0.22 vs. 0.68 in the coherent case), and no clear focal spot can be seen.

As mentioned in section 3.1.2, the Talbot distance, after which an electric field profile

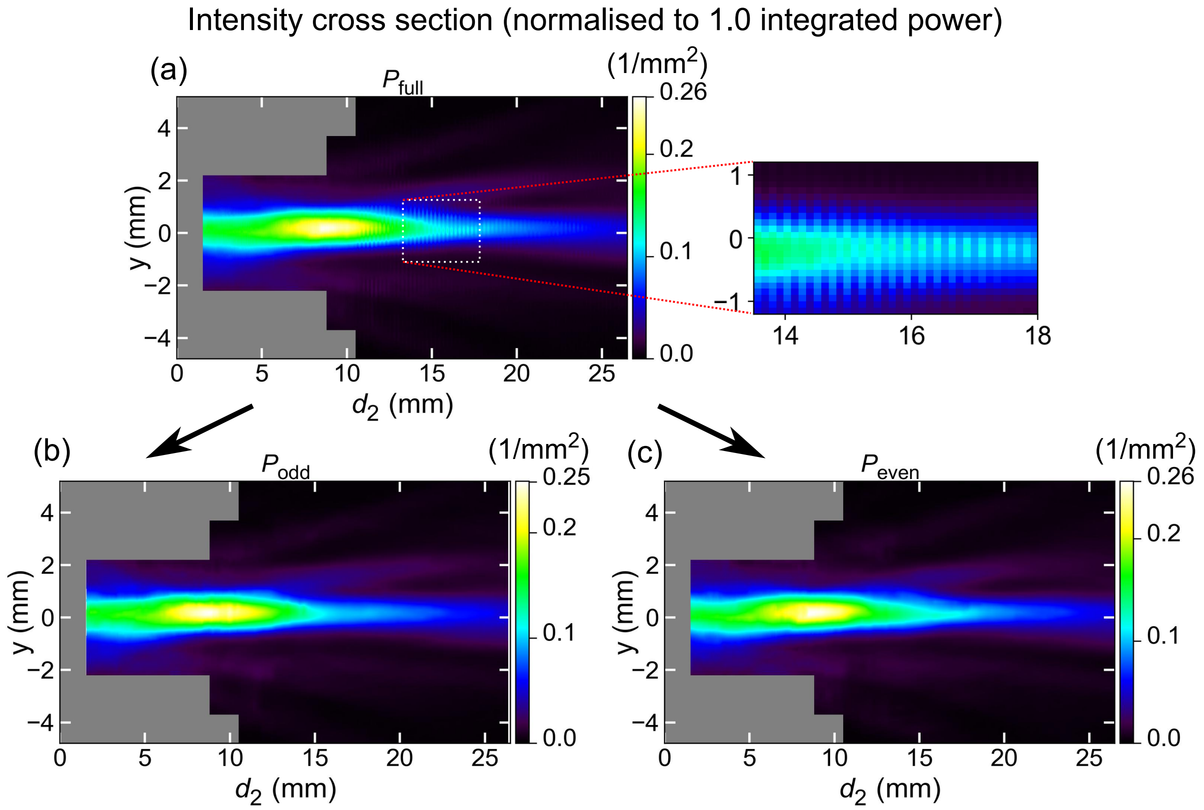

Figure 3.18: **Cross-sectional measurement of the intensity in the y-z-plane.** (a) Original data. (b), (c) deinterlaced measurement data split across alternating lines into “even” and “odd” lines.

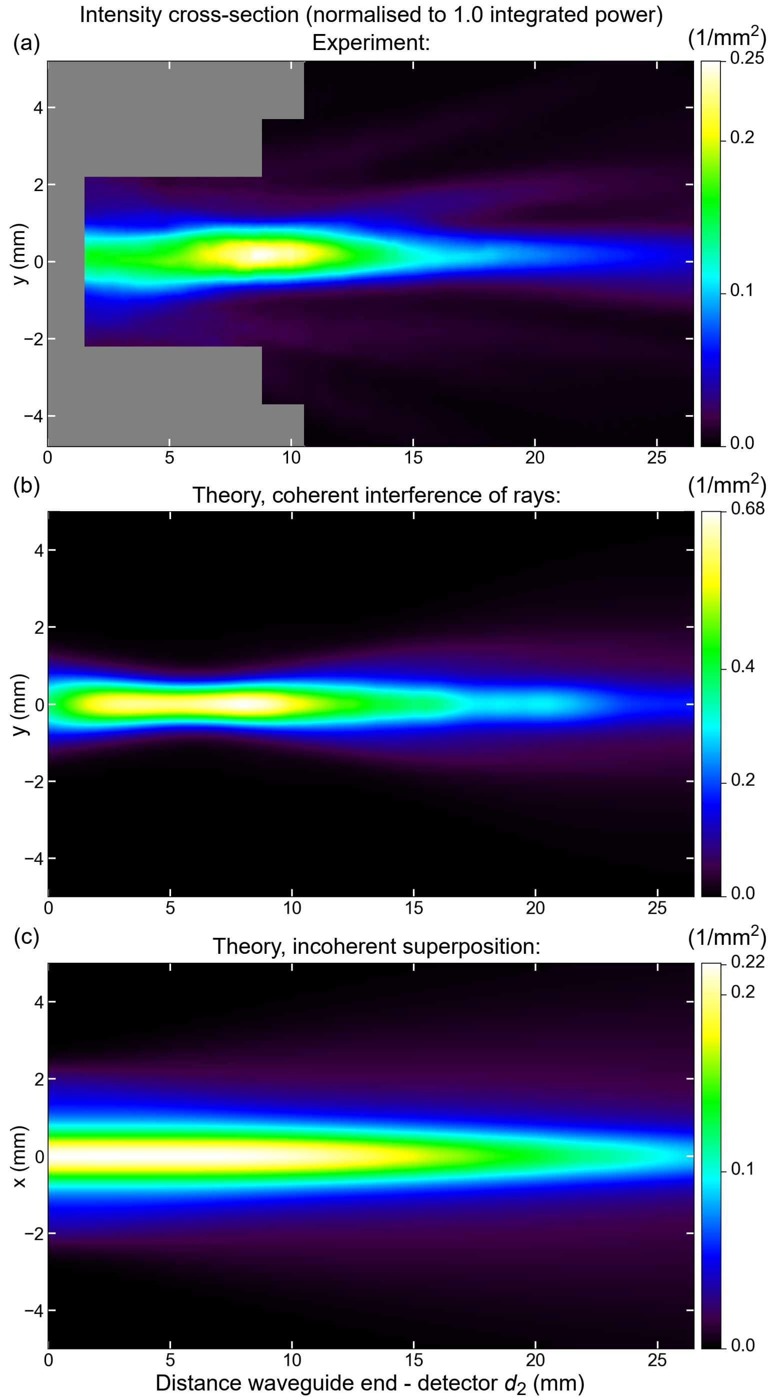

Figure 3.19: **Cross-sectional plot of the wave propagation after the waveguide end.** Both experimentally and theoretically, a clearly focused spot is seen around d_2 = 8.8 mm. (a) Measurement of the intensity distribution in the y-z-plane, i. e. a cross-section through the maximal intensity peak located at d_2 = 8.8 mm, which will be called the focal spot. The grey area is not accessible for measurements in the experiment. d_1 = 8.9 mm in the experiment. (b), (c) Theoretically expected propagation in a plane parallel to the y-z-plane, shifted by 0.08 mm. (b) is the case of coherent interference of the rays; (c) corresponds to an incoherent intensity sum of each ray. The experimental parameters of 159.38 µm wavelength (1.881 THz), d_1 = 8.9 mm QCL–waveguide distance, L = 238 mm waveguide length, and α = 6.5° divergence half-angle of the QCL were used. A radius R = 2.257 mm and 0.78 mm FWHM of the Gaussian averaging were used in the plot. Note the different colourbar limits.

within a cylindrical waveguide is reproduced, is $16R^2/\lambda$ [207]. As seen from the ray-optical model, Fig. 3.6, in the case of a symmetrical axial excitation as considered here, maxima along the waveguide axis occur at multiples of a smaller distance,

$$T = 4nR^2/\lambda \;\; ; \;\; n \in \mathbb{N} \, . \tag{3.16}$$

In this case, the waveguide length of L = 238 mm was chosen such that the focal spot is at the second ($n = 2$) maximum along the waveguide axis, $T = 8R^2/\lambda$, as shown in Fig. 3.7. Experimentally, we have

$$T = d_1 + L + d_2 \, , \tag{3.17}$$

and in this case, $d_1 + L + d_2$ = 255.7 mm. Theoretically, for R = 2.257 mm and wavelength 159.38 µm, T = 256.4 mm – a very similar value. Taking the values d_1 and L as given, the "focal length" d_2 after the waveguide can be calculated as

$$d_2 = (4nR^2/\lambda) - (d_1 + L) \, . \tag{3.18}$$

For R = 2.257 mm and wavelength 159.38 µm, this gives 9.5 mm, close to the experimental value of 8.8 mm.

It should be noted that d_2 is very sensitive to small changes of the wavelength λ, and particularly, of the waveguide radius R, that T has a quadratic dependence on. Experimentally, the inner waveguide radius is known to be (2.3±0.1) mm. For example, for a radius of 2.3 mm, $d_2 = 8R^2/\lambda - d_1 - L$ = 18.6 mm. This means, a change in radius of 43 µm, about a quarter wavelength, is amplified by (18.6 mm–9.5 mm)/43 µm $\approx$ 212, and doubles the focal length d_2 after the waveguide.

The Talbot distance is scale-invariant: if $T \to sT$ and $\lambda \to s\lambda$ change by a scaling factor s, $R \to sR$ will have to change by the same scaling factor. The sensitivity towards R comes from the fact that d_2 is measured from the end of the waveguide, after a long length L of the waveguide, and therefore the experimental determination of d_2 is a differential measurement according to Eq. (3.18). Furthermore, resolving Eq. (3.18) towards R gives

$$R = \sqrt{\frac{\lambda(d_1 + L + d_2)}{4n}} \, , \tag{3.19}$$

which due to the square-root dependence of R on all other parameters is a well defined problem.

Such a sensitive dependence on R demonstrates that a measurement of the focusing position can be used as a very sensitive probe of the radius of cylindrical tubes. At macroscopic sizes of the waveguides as used here, this may not be of particular interest, however due to the scale-invariancy it can be used in any types of multimode cylindrical waveguides, including studies of micrometer-sized cylindrical tubes with optical or UV light.

Comparing Fig. 3.19 (a) and (b) shows that experimentally, optimal focusing is achieved over a smaller range of d_2 and the maximum intensity achieved is smaller. Furthermore, experimentally some side rays (cones diverging from the waveguide axis) can be seen, that are absent in the theoretical prediction. However, such rays are predicted theoretically, if the waveguide length is not optimal for focusing. They are clearly seen in Fig. 3.7 (b), where the expected output profile was plotted in cross-section for a 46 mm waveguide length. Given the strong dependence of the focal position on the waveguide radius, any deviations of the waveguide geometry from an ideal cylindrical tube will disturb the required phase coherence and reduce the quality and the depth (extension along the z-axis) of the focus. This may be due to a variation of the radius along the length of the metallic tube, or of the geometry (ellipsoidal rather than circular cross-section, for example). Indeed, such imperfections could be visualised in Fig. 3.10. This is the most likely reason for the side rays observed in the experiment.

3.2.7 Standing wave ratio

An interesting result can be obtained when the odd lines are subtracted from the even lines, Fig. 3.18 (b), (c). This gives the difference plot $P_{\text{diff}} = P_{\text{odd}} - P_{\text{even}}$ shown in Fig. 3.20 (a). It shows where the difference between constructive and destructive interference is largest. Unsurprisingly, the difference values are large where the measured power is large, too. If the difference plot Fig. 3.20 (a) is normalised to the sum of the intensities, i. e. divided by twice the values in Fig. 3.19 (a), the result is shown Fig. 3.20 (b). This is an indication of the power standing wave ratio $(P_{\text{odd}} - P_{\text{even}})/(P_{\text{odd}} + P_{\text{even}})$.

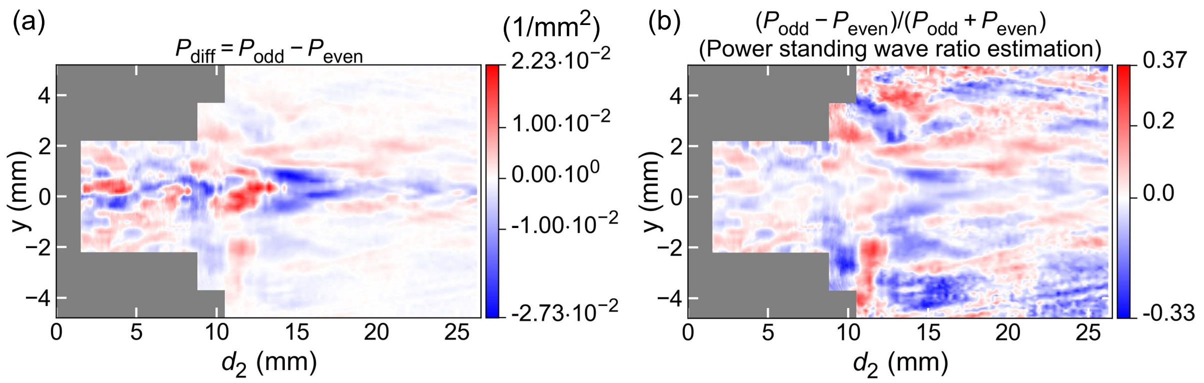

Figure 3.20: **Difference plots: estimation of the standing wave ratio.** (a) Plot of the point-by-point difference $P_{\text{diff}} = P_{\text{odd}} - P_{\text{even}}$ of the values in Fig. 3.18 (b) and (c). This indicates the amount of interference effects present in the measurement Fig. 3.18 (a) of the mode profile with a 1 mm aperture of the Golay cell. (b) Normalised difference $(P_{\text{odd}} - P_{\text{even}})/(P_{\text{odd}} + P_{\text{even}})$. This can be used to estimate the power standing wave ratio.

In both Fig. 3.20 (a) and (b), the values change sign, indicating a complex pattern of the phase $\delta = \delta(y,z)$. Although the wavelength-aware positioning of the z-data points minimised the interference effects in measurements of the averaged intensity $(P_{\text{odd}} + P_{\text{even}})/2$ in Fig. 3.19 (b), it does not remove the Moiré-effect occuring in Fig. 3.20 based on the difference $(P_{\text{odd}} - P_{\text{even}})$. Constructive and destructive interference cannot be assigned to the even or odd lines only; it depends on both z and y. In areas where the values are zero and change sign, this is not due to the value itself being zero; it is because the y-z-measurement grid points happened to be at interference nodes. More generally, if the power standing wave ratio is A, then Fig. 3.20 (b) is a plot of $A \cos \delta(y,z)$, where $\delta(y,z)$ is the (unknown) respective phase resulting from the multi-beam interference. Therefore Fig. 3.20 (b) can be used as a large-area estimation of the power standing wave ratio, but is not its point-by-point evaluation.

Interestingly, the standing wave ratio is largest off-axis, where the power is low. This is reasonable considering the explanation that the interference is observed due to reflections at the iris blades at the entrance of the Golay cell: during a measurement close to the waveguide axis, around $y = 0$, the reflectance from the Golay cell is lowest, since most of the power enters the iris. But off-axis, the central spot is incident on the metallic iris blades and is reflected back into the waveguide, effectively increasing the reflectance of the Golay cell and thus the standing wave ratio.

3.2.8 Proof of the focusing effect

To prove that a multimode cylindrical waveguide has a focusing effect, the mode profile at the output of the waveguide has to be compared with that at the input of the waveguide. This is done in Fig. 3.21.

In Fig. 3.21 (a), the QCL beam profile is shown in the plane of the waveguide input, at $d_1 = 8.9\,\text{mm}$. The white circle indicates the diameter of the waveguide of 4.6 mm, i.e. its input aperture. In Fig. 3.21 (b), the mode profile after the waveguide from Fig. 3.15 is shown at the z-position where the central peak reaches maximum intensity. Both data sets were measured with a 1 mm aperture in front of the Golay cell and were normalised to a total integrated power of 1.0.

For an accurate normalisation and quantitative analysis of the transmission, care has to be taken about the noise present in the lock-in output. The mode profiles that have been presented so far were measured as the amplitude (R) output of the dual-phase lock-in amplifier which captures the signal from the Golay detector. However, the lock-in amplifier output has noise, which at the 10 mV sensitivity setting used in the measurement yields a root-mean-square value of around 25 µV. When the lock-in amplifier is configured to read the signal amplitude, its output gives only positive values, and this noise floor would lead in a simple integration over x and y to an overestimation of the total power emitted by the waveguide. This issue can be solved during a measurement by setting the reference phase

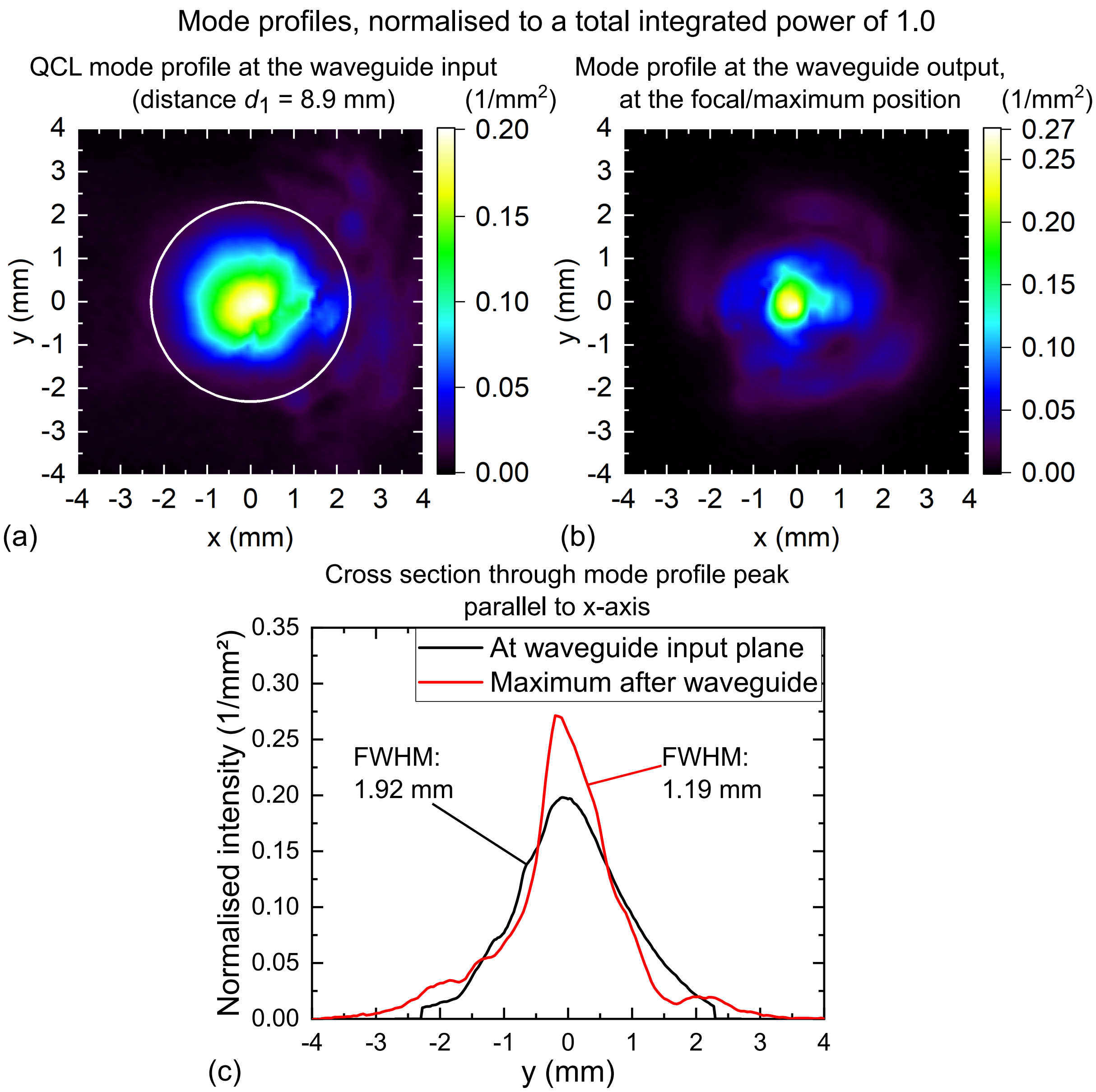

Figure 3.21: **Experimental proof of the focusing ability of cylindrical multimode waveguides.** (a) Mode profile of the QCL before the waveguide, measured in the plane of the waveguide input at $d_1 = 8.9$ mm. The mode profile is cropped to the circular area of the waveguide of 4.6 mm diameter. (b) Mode profile after the waveguide output. The intensities are normalised to a value of 1.0 of the total integrated power. The comparison of (a) with (b) demonstrates that the central peak is focused tighter after the waveguide and has a higher intensity (0.27 vs. 0.20/mm^2). (c) A one-dimensional plot in a slice through the peaks in (a) and (b) parallel to the y-axis. A Gaussian fit to the central peaks shows a FWHM of 1.92 mm before the waveguide, and 1.19 mm after the waveguide.

of the lock-in amplifier so that the signal is in-phase with the X-demodulator, and measuring the X-component of the signal. In this analysis, the phase tuning is done as part of the post-processing. In addition to the R amplitude setting, the X and Y signals were captured for each measurement. From them, the phase of the signal from the Golay cell was determined as

$$\varphi = \arctan(Y/X) + \pi\Theta(-X)\,. \tag{3.20}$$

The phases from all measurement points yielding more than 80% of the maximum signal value were averaged. The sign-sensitive signal G is extracted from a rotation by the angle φ as

$$G = \cos(\varphi)X + \sin(\varphi)Y\,. \tag{3.21}$$

This value corresponds to the amplitude R-value in areas with a strong QCL signal, but in contrast to R, the noise of G is evenly distributed around zero and cancels out when integrated over the spatial coordinates. The systematic error introduced by using R instead of G depends on the signal strength, lock-in sensitivity and noise, as well as integration area. In practice, the overestimation of the integrated total power can exceed 10 % for some measurements.

The normalisation in Fig. 3.21 was carried out using the phase-alignment method as described above. In Fig. 3.21 (a), the intensity within the white circle was integrated over x and y to yield the total input power available to the waveguide, while in Fig. 3.21 (b), the integral was carried out over the large ±5 mm measured area, to also take into account the power contained in cones diverging away. In addition, this data allows measurement of the power transmission of the waveguide: from the ratio of the 2D integrals, the total transmission of the waveguide is determined to be 81.3 %.

It is evident from the 2D plot that after traveling through the waveguide, the THz beam spot is much tighter. In Fig. 3.21 (c), a one-dimensional cross-section along the x-axis is shown. The fit with a Gaussian function shows that the FWHM is reduced by a factor of more than 1.6, from 1.92 to 1.19 mm. The peak intensity has increased from 0.20/mm^2 to 0.274/mm^2. Even considering the loss along the waveguide, the output intensity of 0.274/mm$^2 \cdot$ 81.3 % = 0.222/mm^2 is larger than the input intensity. This proves that the waveguide acts indeed as a focusing element, redirecting most of the input power towards its axis.

3.2.9 Polarisation mapping

At a distance $d_2 =$ 26.5 mm from the waveguide end to the Golay cell iris, the polarisation of the transmitted light from the waveguide is characterised. A wire-grid polariser on a rotation mount is attached to the Golay cell, and the transmitted power at each point (x,y) is measured under angles 0°, 45°, 90°, and 135°. Following the polarisation analysis in section 2.4, Eqs. (2.25)–(2.27) are used to find the amount of purely linearly polarised light A^2 and the unpolarised part U^2. These values are shown in Fig. 3.22, together with the polarisation direction of the linearly polarised light as an arrow plot. From A^2 and U^2, the degree of linear polarisation (DOLP) can be calculated as $A^2/(A^2+U^2)$.

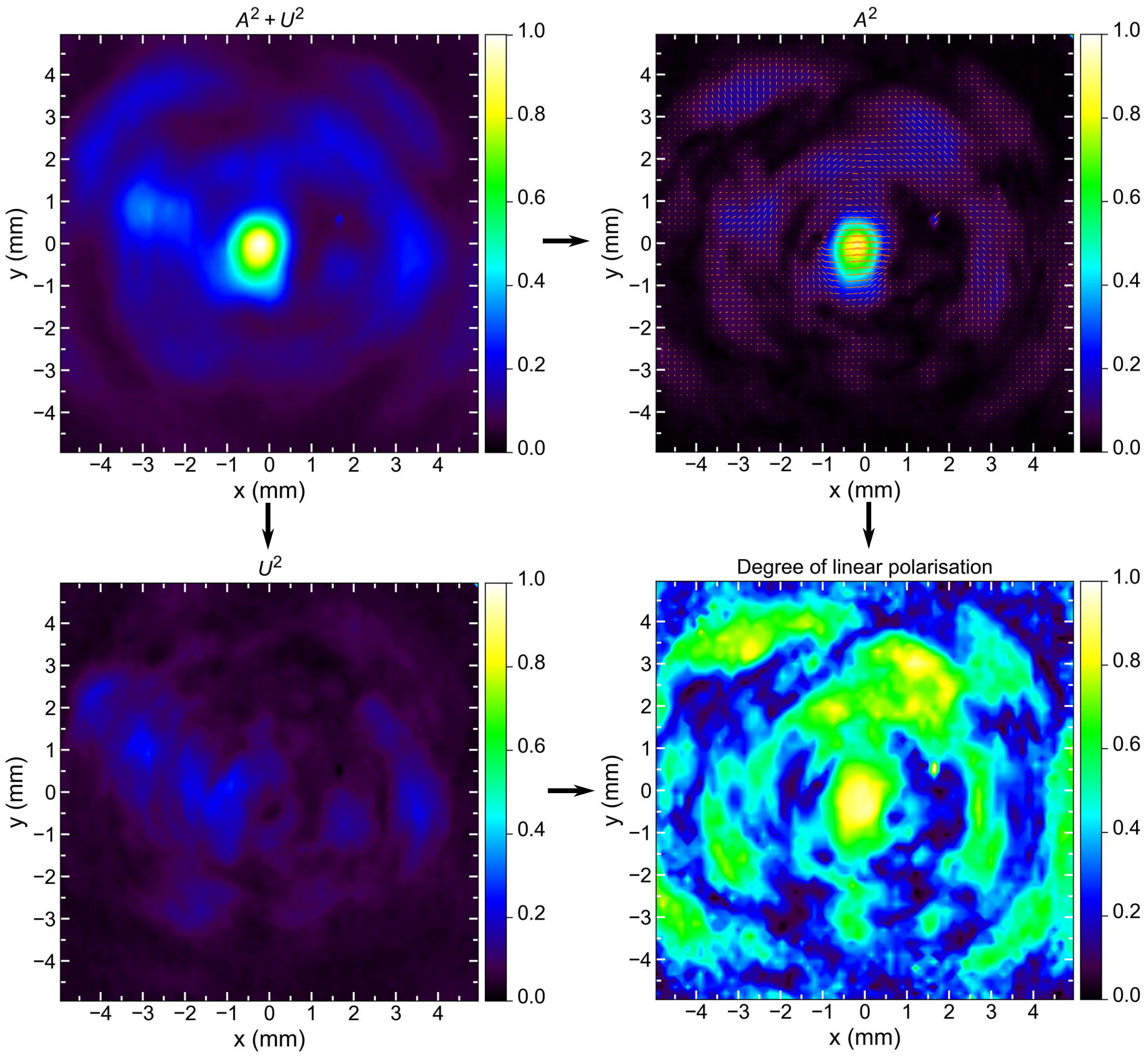

Figure 3.22: **Polarisation mapping of the output mode profile.** For each coordinate (x,y), the total transmitted power $A^2 + U^2 = (P_1 + P_2 + P_3 + P_4)/2$ is separated into the purely linearly polarised part A^2 and the unpolarised part U^2. From them, the degree of linear polarisation $A^2/(A^2 + U^2)$ is calculated.

The maximum DOLP is obtained in the central spot, where the polarisation direction is almost horizontal. This is the expected direction since in this setup the QCL growth direction corresponds to the horizontal direction. The maximum DOLP in the center achieved is 93.5 %. At first, this may seem surprising, since the DOLP of the source was measured to be lower, only 92.2 %. However, taking into account that coherent light is focused much stronger than incoherent light, as seen in Fig. 3.19 (b) and (c), we can see that this makes sense. The coherent part of the QCL emission is strongly focused along the waveguide axis. U^2 is seen at the position of the sidelobes, where the polarisation direction may change laterally over a small length scale. The diffuse light/background noise is seen only in U^2, and likely originates from the unpolarised light of the QCL. Thus, not only does a multimode cylindrical waveguide focus the input light onto its axis, but it also reduces the relative amount of incoherent light along the axis when a partially linearly polarised source is used at the waveguide input.

3.3 Summary

In this chapter, a ray-optical model of cylindrical multimode waveguides was presented. The radiation of a point source positioned centrally in front of a cylindrical waveguide will be focused onto the waveguide axis after the waveguide end under certain geometrical conditions. The effect has its origin in multimode interference within the waveguide. The electric fields within the waveguide reproduce themselves after at a given distance, which was found to be the Talbot distance. In contrast to wave optics, in this ray optical approach the expected mode profiles of a cylindrical multimode waveguide can be calculated fully analytically, both within and after the end of a waveguide, provided that the radius of the waveguide is much larger than the wavelength. The effect of angular and polarisation misalignment was studied, too. Multimode waveguides can be understood as an interferometric system, whose output mode profile is a two-dimensional interferogram of the input beam, which contains information about the input electric field distribution.

To confirm the theoretical predictions, a waveguide of the expected length for optimal focusing was cut. The mode profiles were studied both in x-y and x-z planes. Interference between the QCL source and the Golay cell aperture gave rise to interference fringes, which allowed estimation of the power standing wave ratio. Thanks to wavelength-aware positioning of the measurement grid points, interference effects could be eliminated in the analysis. A comparison of the mode profile at the waveguide output with that at the waveguide input plane proved the predicted focusing effect. This shows that cylindrical multimode waveguides can be used as a focusing optical element, without the need for additional lenses or parabolic mirrors, but rather instead of them. Polarisation sensitive measurements of the output mode profile showed linearly polarised radiation at the waveguide output, with the same polarisation direction as that of the source. The experimentally observed phenomenon constitutes the first realisation of the Talbot self-imaging effect in multimode cylindrical waveguides at THz frequencies.

4 Antenna-coupled dual-gated two-dimensional electron gas for terahertz detection

A crucial element in the development of terahertz technology is the availability of suitable detectors. Of particular interest are solid-state semiconductor detectors, due to their compact size and fast response [98].

Physical mechanisms operating at lower than THz frequencies (radio, microwaves) no longer work when the frequency increases and approaches the THz range from below, and the mechanisms operating at higher than THz frequencies (mid-IR through visible)

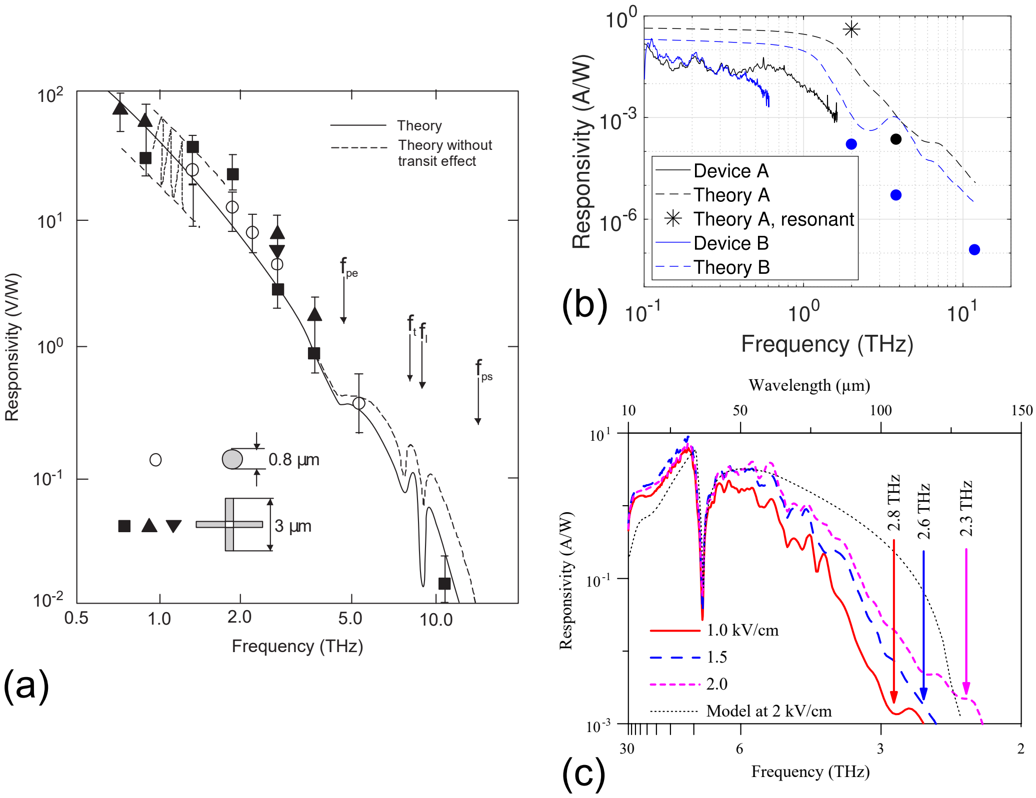

Figure 4.1: **Rapid fall-off of detector sensitivities towards the THz range.** (a) Schottky barrier diodes, (b) field-effect transistors based on plasmonic mixing, (c) heterojunction internal photoemission detectors. *Reuse permissions:* (a) Reprinted from Ref. [64], copyright 2010, with permission from Elsevier, and adapted by permission from Springer Nature: Ref. [213], Copyright 2003. (b) Copyright © 2018 IEEE, from Ref. [214]. (c) Reprinted from Ref. [149], Copyright 2008, with permission from Elsevier.

fail when the frequency decreases and approaches the THz range from above. This is illustrated in Fig. 4.1: Schottky diodes and field-effect transistors are detectors that work at lower frequencies, and internal photoemission detectors represent devices that approach the THz range from above.

A promising system for THz detection is a two-dimensional electron gas (2DEG), whose response to far-infrared radiation has been studied over the last few decades [215] and has been utilized for detection using a variety of mechanisms, which were reviewed in section 1.2.4. The response of field effect transistors incorporating 2DEGs is commonly interpreted by classical plasmonic mixing [119] or distributed resistive mixing [80]. Over the course of the past quarter century, many researchers have been building devices specifically intended to work on this mechanism, and optimising them step-by-step [71, 72, 78, 80, 120, 121, 123, 216, 217]. In such devices, the THz electric field is often applied simultaneously to the gate and the drain, in order to induce resistive self-mixing. Although the sensitivity of devices has improved, shrinking the THz gap with time, THz detection is still an active area of research. Further improvements are needed, in order to develop highly efficient, cheap, fast, compact, reliable, and tunable THz detectors.

In this work, I choose an operation frequency of 1.9 THz, right in the middle of the THz gap, and create a highly sensitive direct detector based on a two-dimensional electron gas. In contrast to previous works, I follow a different approach. For optimal performance, an antenna is coupled to the channel, however, both wings are used as gates. Source and drain contacts are placed far away to eliminate their influence on the channel. The resulting device can be seen as a dual-gated, antenna-coupled field-effect transistor. The presence of two gates allows *independent* tuning of responsivity and output impedance – a feature not available in conventional single-gate field-effect transistors. This facilitates impedance matching to external circuits.

This chapter starts with the design idea of the detector, describes the fabrication procedure including the required preparation, and then guides the reader through the journey of searching for a THz photoresponse. After experimental challenges were solved, the direct detection is demonstrated. Following that, the electron transport in the 2DEG and the operation of the device are analysed, and the mechanisms of THz photoresponse generation in 2D electron gases are considered, as to whether they can explain the observed photoresponse. This analysis leads to an unexpected conclusion: the observed THz photoresponse is at least an order of magnitude higher than expected from classical plasmonic mixing, and cannot be explained by known mechanisms of THz photoresponse generation in field-effect transistors. The puzzle is resolved in the next chapter.

4.1 Device design

The device consists of a narrow 2DEG channel, which has two gates that are shaped as an antenna, see Fig. 4.2. The antenna, in this case in the form of a bow-tie for a broadband frequency response, is used to increase the coupling of incident THz radiation to the 2DEG. In contrast to a conventional field-effect transistor geometry [71, 77, 78, 84, 87, 119–121, 123, 218], both wings of the antenna are used as gates. This gives an additional tunable "knob" in the form of a second gate voltage, which, as will be seen later, is a crucial element to the function of the detector.

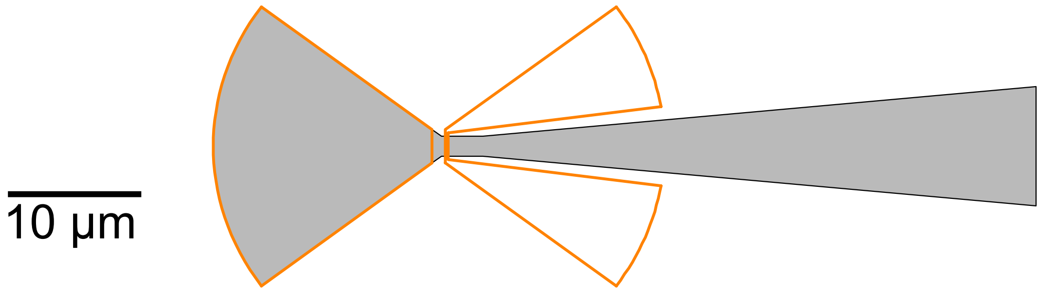

Figure 4.2: **Design of the bow-tie antenna based terahertz detector.** Orange shape: metallised gates. Grey areas: etched mesa of the two-dimensional electron gas. The two-dimensional electron gas has Ohmic contacts for source on the left part and for drain on the right part (not shown).

Under incident THz radiation, the THz electric field will be amplified between the antenna wings, and will give rise to a component both in x-direction, within the 2DEG plane, as well as to an out-of-plane z-component. For optimal coupling to the 2DEG, the axis of the antenna is aligned with the channel. The right wing of the antenna has a cut-out, such that the gate on top of the channel is made narrow, in the form of a bridge. This amplifies the out-of-plane component of the THz electric field, and will enable the dependence on the gate width to be studied. As material system forming the 2DEG, a standard modulation doped GaAs/AlGaAs heterostructure [219] was chosen. In these heterostructures, a conducting layer is created by doping of the semiconductor, but the layer containing the dopants is spatially separated from the region where the 2DEG is. As a result, very high mobilities exceeding 10^7cm^2/(Vs) can be achieved [220], which at low temperatures are limited by impurity scattering [221]. The mobility and charge carrier density of the 2DEG in such structures can be changed by illumination: a cooldown in dark will yield lower mobility and density values, that can be increased by illumination with infrared or visible light [220], a phenomenon called persistent photoconductivity, which will be discussed in more detail in section 4.6. The heterostructure used in this chapter was deposited on a GaAs semi-insulating substrate by molecular beam epitaxy. The growth by molecular beam epitaxy was carried out by Harvey E. Beere at the Cavendish Laboratory. The sequence was, after a 1 µm undoped GaAs buffer layer, 40 nm undoped $Al_{0.33}Ga_{0.67}As$; 40 nm n-doped $Al_{0.33}Ga_{0.67}As$ with $10^{18}/cm^3$ doping density of Si donors; 10 nm GaAs cap. Thus the distance from wafer surface to the AlGaAs/GaAs heterojunction is located about d = 90 nm below the surface; the distance to the 2DEG is slightly larger due to the finite extension of the wave function in growth (z-)direction.

Simulations using the commercial finite element analysis software “Comsol Multiphysics” were performed to optimize the antenna geometry for a center frequency of around 2 THz. The substrate is modelled as insulating GaAs with permittivity ε_r = 12.6 [222]. Gold is used as the antenna material, with a dielectric function according to the Drude theory with parameters from Ref. [223]. The software solves the wave equation in a periodic structure of bow-tie antennas with a quadratic unit cell of 130 µm×130 µm. In the vertical direction, perfectly matched layers as a highly absorbing material replicate an infinite space. The incident electric field polarisation is parallel to the main axis of the antenna (i. e. in x-direction).

Maxwell’s equation for a medium are ($\mathrm{div} \equiv \vec{\nabla}\cdot$; $\mathrm{rot} \equiv \vec{\nabla}\times$):

$$\mathrm{div}\vec{D} = \varrho \;\; ; \;\; \mathrm{div}\vec{B} = 0 \tag{4.1}$$

$$\mathrm{rot}\,\vec{E} = -\frac{\partial \vec{B}}{\partial t} \;\; ; \;\; \mathrm{rot}\,\vec{H} = \vec{j} + \frac{\partial \vec{D}}{\partial t} \tag{4.2}$$

Here, $\vec{E}$ is the electric field, $\vec{D} = \varepsilon_0\varepsilon_\mathrm{r}\vec{E}$ the displacement electric field, $\vec{H}$ the magnetic field, $\vec{B} = \mu_0\mu_\mathrm{r}\vec{H}$ the magnetic induction, ϱ the charge carrier density, and $\vec{j}$ the current density. Applying rot to $\frac{1}{\mu_\mathrm{r}}\mathrm{rot}\,\vec{E}$, we get with $\vec{j} = \sigma\vec{E}$ and $E \sim e^{i\omega t}$:

$$\mathrm{rot}\left(\frac{1}{\mu_\mathrm{r}}\mathrm{rot}\,\vec{E}\right) = -\mu_0\frac{\partial}{\partial t}\left(\sigma\vec{E} + \varepsilon_0\varepsilon_r\frac{\partial \vec{E}}{\partial t}\right) = -\mu_0\frac{\partial}{\partial t}\left(\sigma\vec{E} + i\omega\varepsilon_0\varepsilon_r\vec{E}\right) = \tag{4.3}$$

$$= -i\mu_0\omega\left(\sigma + i\omega\varepsilon_0\varepsilon_r\right)\vec{E} = \boxed{\frac{\omega^2}{c^2}\left(\varepsilon_\mathrm{r} - \frac{i\sigma}{\omega\varepsilon_0}\right)\vec{E} = \mathrm{rot}\left(\frac{1}{\mu_\mathrm{r}}\mathrm{rot}\,\vec{E}\right)} \tag{4.4}$$

This is the equation that Comsol solves in the simulation [224]. With $\mu_\mathrm{r} = 1$ in a medium without static charges ($\varrho = 0$), it yields using $\mathrm{rot}\,\mathrm{rot}\,\vec{E} = \mathrm{grad}\,\mathrm{div}\,\vec{E} - \Delta\vec{E}$ the well-known wave equation

$$\Delta\vec{E} = \frac{\omega^2}{c^2}\left(\varepsilon_\mathrm{r} - \frac{i\sigma}{\omega\varepsilon_0}\right)\vec{E}\,. \tag{4.5}$$

From the simulations, an optimal opening angle of around 74° and a radius of 17 µm was determined. For fabrication, different combinations of channel width, width of the narrow gate bridge, and distance between the antenna wings were designed. In Fig. 4.3 on the left the absolute values of the electric field vector and its x and z components are shown.

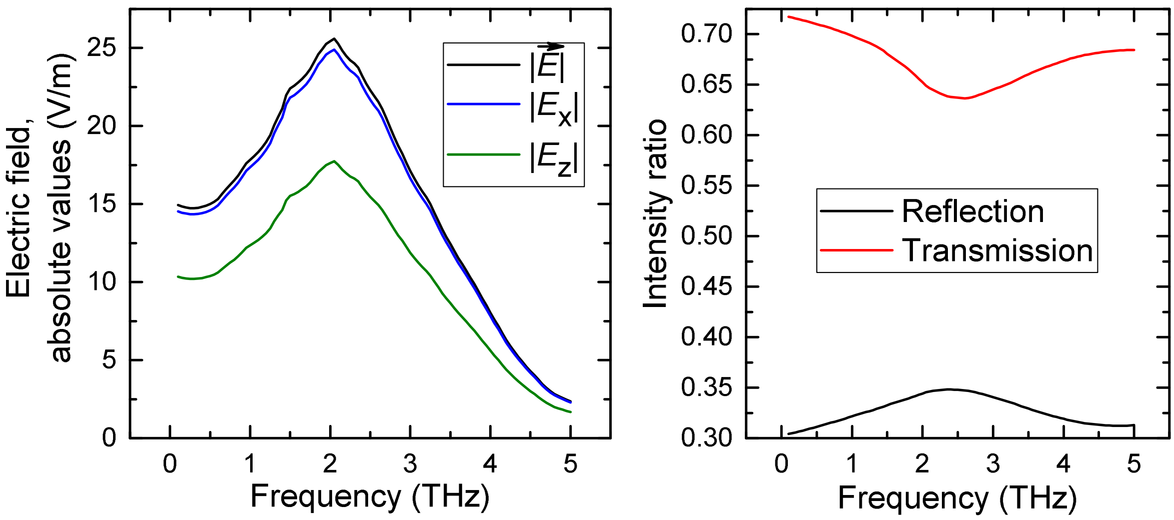

Figure 4.3: **Results of the simulations of a bow-tie antenna optimized for 2 THz.** *Left:* Maximum electric field amplification achieved along the symmetry line of the antenna, 90 nm below the surface, for E_{x}, E_{z}, and $\vec{E}$. The maxima for E_{x} and E_{z} are achieved at different coordinates along the antenna axis (therefore in the plot, $\vec{E}^2$ is not equal to the sum of the squares of the x- and z-maximum values). *Right:* Intensity reflection and transmission coefficients of a periodic array of bow-tie antennas with a period of 130×130 µm.

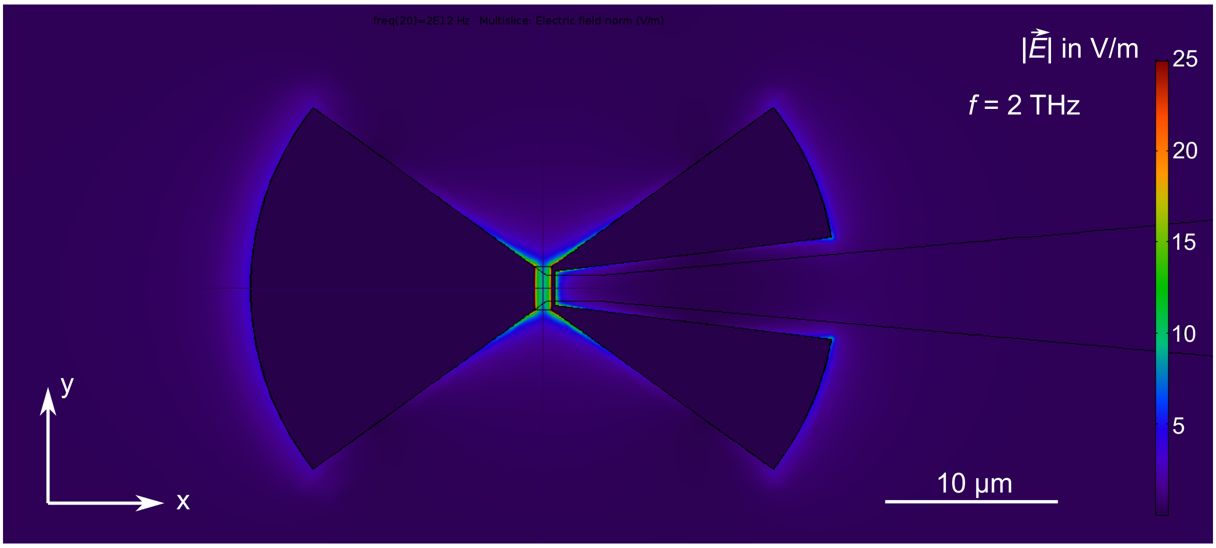

Figure 4.4: **Spatial dependence of the absolute value of the electric field at a frequency of 2 THz.** The indicent electric field without antenna structure is normalised to 1 V/m, thus the plotted values display the electric field amplification factor.

These are the maximum values along the symmetry line of the antenna, 90 nm below the surface, where the 2DEG is expected to be. The incident electric field was normalized to 1 V/m without metallic antenna; therefore the values show the relative amplification with respect to the incident electric field. On the right of Fig. 4.3, the transmission and reflection of the structure are shown. In Fig. 4.4, the distribution of the absolute value of the electric field at the resonance frequency of the antenna, 2 THz, is illustrated in a colour-coded plot. The amplification of the electric field in the gap as well as nodes of the electric field along the sides of the antenna are clearly seen.

Fig. 4.5 shows a finished and processed sample. The idea behind the design, and the pathway to successful fabrication, will be explained in the following.

Both antenna wings need to be connected to bond pads for application of gate voltages. It makes sense to place the connection leads along equi-potential lines in order to cause minimal disturbance to the antenna function. Since the device is primarily intended for excitation with THz waves polarised along the antenna axis, the connection leads were made perpendicular to the antenna axis.

The connection point along the side of the antenna wing was chosen to be where the field distribution, Fig. 4.4, has a node: this way, the connection to the antenna has minimal influence on the THz field distribution. In a separate Comsol simulation it was confirmed that a vertical metallic line going through the antenna has a negligible influence on its resonance characteristics, Fig. 4.3, at the frequencies of interest. Similarly, the leads to the 2DEG below the antenna are designed orthogonally to the antenna axis.

To exclude contact resistances in measurements, the sample is designed in such a way that there are at least two Ohmic contacts to either end of the thin channel. By sharing the source contact, pairs of dual-gated detectors can be fabricated on one chip. The distance between an antenna and the closest features (Ohmic contacts or the other bow-tie antenna on the chip) is designed to be at least 100 µm ($> \lambda/2$), so as to avoid influence on the antenna characteristics.

In the lower one of the solid bow-tie wings, circular holes of different diameters (4, 2, 1, 0.6 µm) are placed. The idea is to cover them with a thin, semi-transparent layer of titanium, which would be electrostatically connected to the antenna gold, but would allow microphotoluminescence studies on the gated 2DEG as an optional feature.

The distance between the bow-tie antenna halves was chosen to match plasmonic resonances. If a negative potential is applied to both gates, a “resonator” may form in the gap between the two gates: when the 2DEG is depleted under both gates, a rectangular 2DEG region would form with extension W in the y-direction and b_{gap} in the x-direction (corresponding to the gap between the antenna gates). If a THz photoresponse will be observed, it is likely that the response could be increased if the gap matches the wavelength of plasma waves. Therefore the antenna gap b_{gap} is chosen to match expected plasmonic resonances.

In a 2D electron gas, the plasma frequency is given by [101]

$$\omega_{\mathrm{P}}^2(q) = \frac{n_{\mathrm{s}} e^2 q}{2 m_{\mathrm{eff}} \varepsilon_0 \varepsilon_{\mathrm{r}}} \,. \tag{4.6}$$

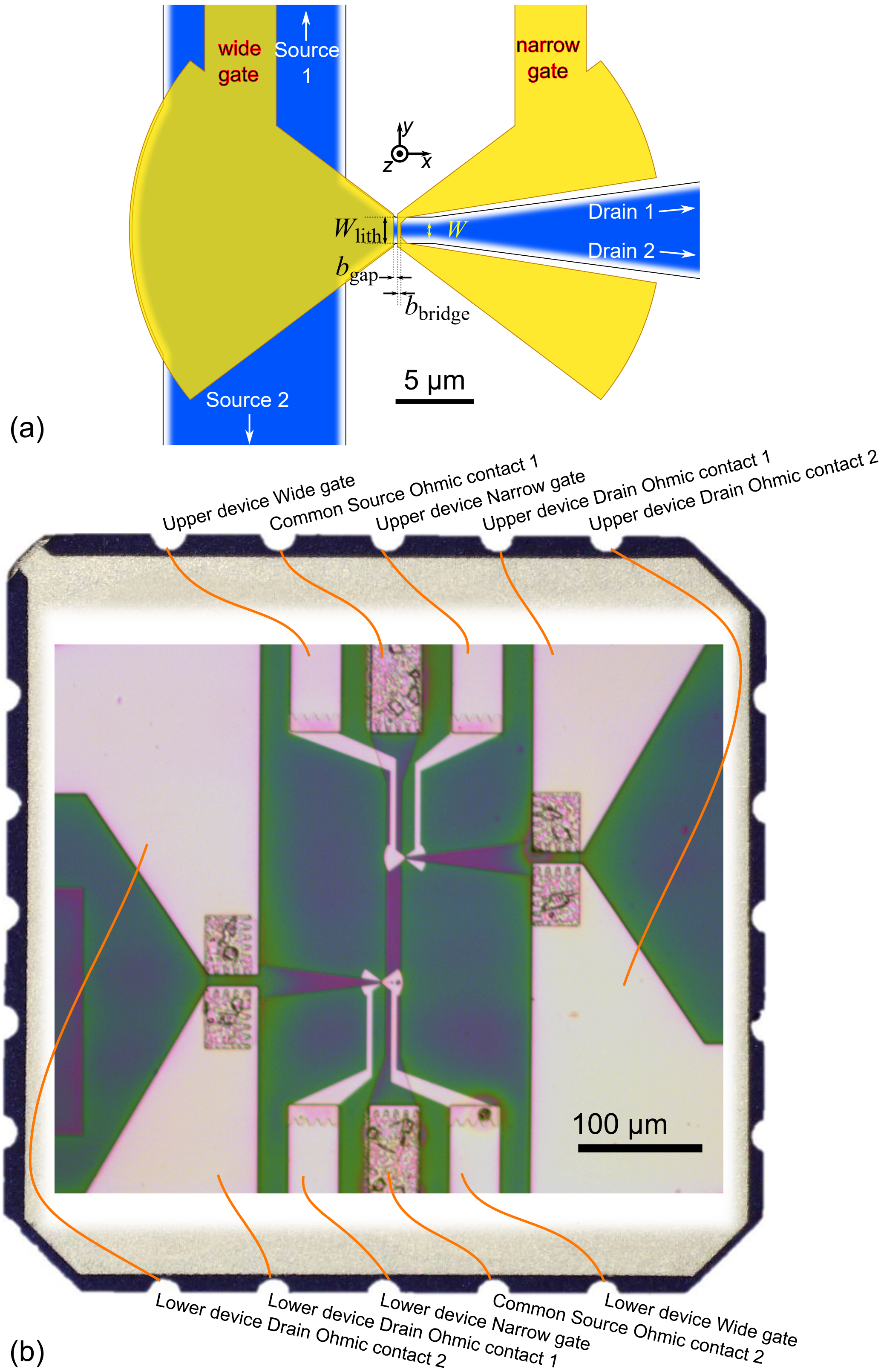

Figure 4.5: **Layout of a THz detector sample.** (a) Schematic diagram with definitions of the antenna gap b_{gap}, antenna bridge width b_{bridge}, lithographically defined mesa width W_{lith} and the smaller width W of the 2DEG, shown in blue. (b) Large scale view of a processed device, including pin-out of the bonded-up devices and corresponding contacts in LCC20 packages (LCC20 chip carrier not to scale).

For a finite size of b_{gap}, the lowest plasmonic eigenmode would correspond to a wave vector $q \approx \pi/b_{\text{gap}}$. Because the channel width W is much larger than the distance between the two gates b_{gap}, the 2DEG between the two antenna halves can be modelled as a stripe extended in the y-direction with width b_{gap}. The plasmonic resonance of a stripe with a given width is, however, not exactly at the frequency given by Eq. (4.6), but at an about 0.85 times lower frequency [225].

In Eq. (4.6), ε_r is the relative permittivity. For GaAs it is around 12.6 at low temperatures [222]. But the 2DEG is very close to the surface of the GaAs wafer, and its interface with vacuum, that has a permittivity of 1. In Ref. [226], the effective relative permittivity for a 2DEG enclosed in two layers of materials has been calculated. In this case, the depth $d = 90$ nm is small compared to plasma wavelengths, but the substrate thickness of 0.5 mm is macroscopically large. Therefore, a model can be considered with a semi-infinite volume of GaAs under the 2DEG with permittivity $\varepsilon_{\text{GaAs}}$, a $d = 90$ nm thin layer with the same permittivity above the 2DEG, and after that the semi-infinite vacuum with permittivity of 1. In this case, the effective dielectric constant can be calculated to be [226]:

$$\varepsilon_{\text{r,eff}}(qd) = \frac{\varepsilon_{\text{GaAs}}}{2}\left(1 + \frac{\varepsilon_{\text{GaAs}}\tanh(qd) + 1}{\varepsilon_{\text{GaAs}} + \tanh(qd)}\right) \tag{4.7}$$

Combining the above, the dependence of the expected resonance frequency $\omega(q)$ is

$$\omega(q) = 0.85\sqrt{\frac{n_s e^2 q}{2m_{\text{eff}}\varepsilon_0\varepsilon_{\text{r,eff}}(qd)}}\,. \tag{4.8}$$

In Fig. 4.6, the frequency $\omega(q)/(2\pi)$ is plotted as a function of the gap between the antenna halves b_{gap}, which corresponds to the width of the 2DEG stripe created when a negative potential is applied to the gates. The curves are plotted for a 2D electron density of $3.28 \cdot 10^{11}/\text{cm}^2$, corresponding to the illuminated nominal electron density of the wafer used for device fabrication. Resonances can only be expected for the odd multiples of π/b_{gap}, indicated by the solid lines: when the antenna is excited with its resonance frequency, the electric field is maximal in the gap, and thus the charge density is of opposite sign on the left and right antenna edges in the gap. This excitation can only couple to plasmonic modes corresponding to the odd multiples of π/b_{gap}, which also have charge densities of opposite sign on each side of the stripe. The dashed lines are the modes lying in-between and corresponding to the even multiples of π/b_{gap}, which are not expected to exhibit plasmonic resonance. The intersection with the solid line at 2 THz gives the 2DEG stripe width required for a plasmonic resonance.

The values b_{gap} chosen for the sample fabrication are those indicated in bold. Since the amplified electric field in the antenna gap has spatial extensions of around the antenna gap, it is not sensible to choose an antenna gap commensurate with or smaller than the

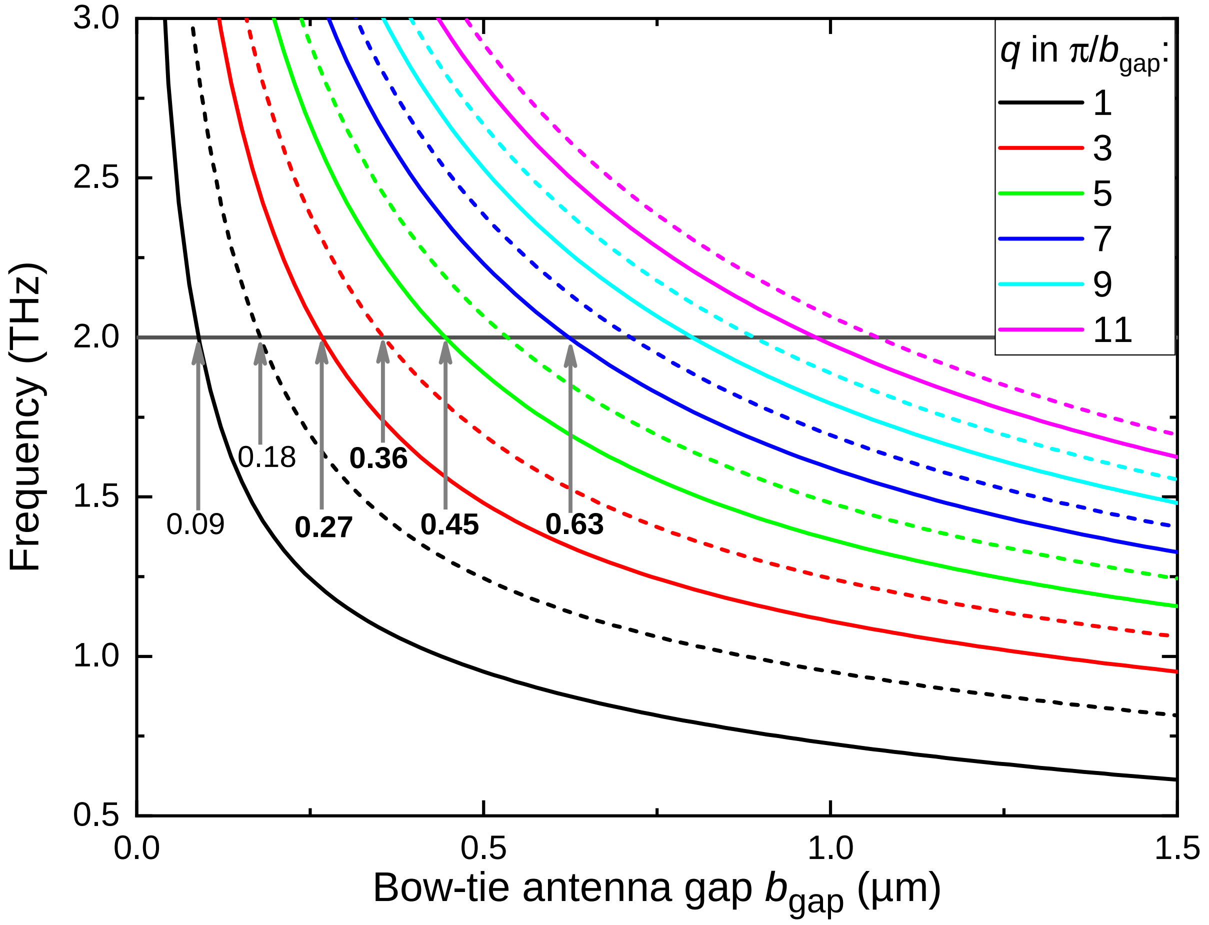

Figure 4.6: **Theoretically expected plasmonic resonances.** The resonance frequency is plotted as a function of the 2DEG stripe width for a 2D electron density of $3.28 \cdot 10^{11}/\text{cm}^2$, corresponding to the gap between the antenna halves b_{gap}, assuming different relationships between b_{gap} and wave vector q as indicated in the legend. The solid lines are the odd multiples of π/b_{gap}, the dashed lines in-between are the even multiples of π/b_{gap}. The horizontal line indicates the frequency of interest of 2 THz, and the arrows indicate the b_{gap}-values of the intersection of the curves with the horizontal line.

distance to the 2DEG, which would result in a weak coupling to the 2DEG. Therefore, the first possible resonance position located at 0.09 µm is not chosen for fabrication. The values of 0.27 µm, 0.45 µm and 0.63 µm are the approximate values where resonances may be observed. 0.36 µm is deliberately placed on a dark mode, and 1 µm is a rather large size for non-resonant coupling.

4.2 Fabrication

The fabrication of this type of sample requires mesa etching, to create the desired shape of the 2DEG, and evaporation of the gate antenna to cover the active area of the device. Both of these processes require sub-micron precision, therefore electron beam (e-beam) lithography is the method of choice for these steps. Apart from that, Ohmic contacts will need to be processed in order to contact the 2DEG, and bond pads, fractions of a millimeter in size for bonding, are required for sample mounting. The Ohmic contacts and bond pads are large-area features where an accuracy of several micron is acceptable. Thus, optical lithography is the best method for these, as a quicker and cheaper processing step as compared to e-beam lithography.

The critical part is the narrow bridge of the gate with the cut-out. The gate metal has to climb up on the side of the mesa, form the thin sub-micron sized bridge, and climb down again on the other side of the mesa. The gate metal may break at the edges of the mesa. This would leave one part of the antenna ungated, and disturb the antenna function. Furthermore, the thin bridge itself may get unstuck during lift-off.

These concerns put constraints on the fabrication process. The mesa height has to be as small as possible. Given that the GaAs/AlGaAs interface, where the 2DEG is formed, is 90 nm under the surface, a value of 100 nm desired etch depth is chosen, so as to definitely remove all AlGaAs layers and account for inhomogeneities in the etching process. The gate metal needs to be thick enough to not break at the mesa edges. At the same time, if it is too thick, the lift-off may fail, e. g. the thin gold bridge may be ripped off by the other gold areas to be removed, or closed shapes of metal that need to be removed may remain if the solvent cannot get underneath the metal due to its thickness.

4.2.1 Test sample fabrication

In order to check the fabrication process, test samples were fabricated. The aim is to optimise the e-beam steps: the mesa etching and the gate fabrication. The electron beam exposure/writing process for the samples described in this thesis was carried out by the Cavendish Electron Beam Lithography Suite. The basis for the development of the tailored fabrication recipes used in this thesis were the photoresist and electron beam resist manufacturers' datasheets, known common processes in the cleanroom of the Semiconductor Physics group, and fabrication recipes of Joanna Waldie and Stephen Kindness. The wafer used for the test samples (W1313) is based on the same GaAs-AlGaAs heterostructure intended for the device fabrication. It has the same chemical layer structure but does not support a native 2DEG due to low doping.

Two 12 mm×12 mm samples, each containing 5×5 device units were fabricated. Five different widths W of the narrow channels were designed, ranging from 1.0 µm to 3.0 µm in 0.5 µm step size. Thus, 10 test chips of each geometry were made.

4.2.1.1 Mesa etching

Since the area of the mesa is much smaller than the chip area, a negative e-beam resist was chosen: ma-N 2410. With the negative resist, only the areas of resist to remain have to be exposed, which reduces the e-beam writing time. Within the mesa etching as the first processing step, alignment marks are deposited at the corners of the sample, as the positional reference for future processing steps.

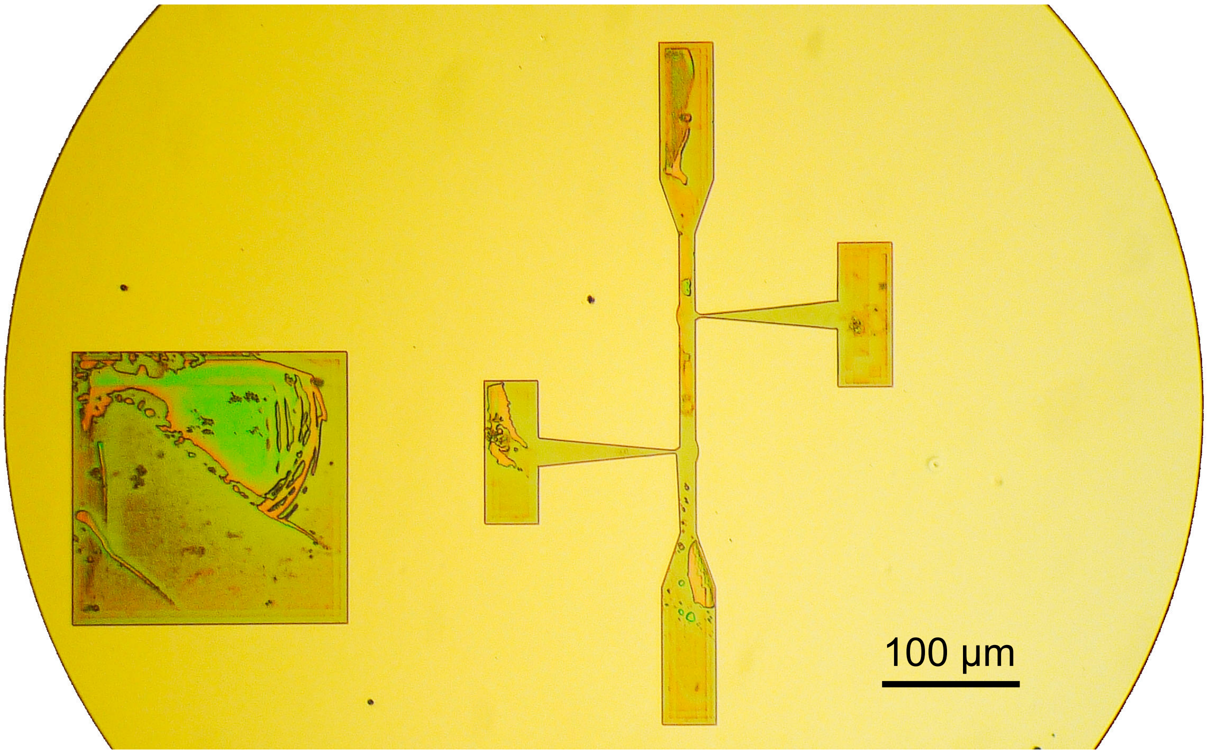

Figure 4.7: **Resist mask used for etching,** after development of the ma-N 2410 resist. The square on the left-hand side serves the purpose of measuring the etching depth.

A recipe for working with the negative resist was developed using the manufacturer's datasheet. The sequence of steps needed for the etching process and the process parameters are shown in Fig. 4.8. After surface cleaning with acetone and isopropanol, the ma-N 2410 resist is deposited and baked. Following e-beam exposure, the sample is developed in ma-D 525. The development is checked with a microscope and repeated if necessary. After development, a sample unit looks as shown in Fig. 4.7. The resist mask for fabrication of the device 2DEG mesa is shown on the right-hand side. On the left-hand side, a square of 0.2 mm×0.2 mm size is placed. This macroscopically sized feature is for measurements of the etching depth using a Dektak surface profilometer.

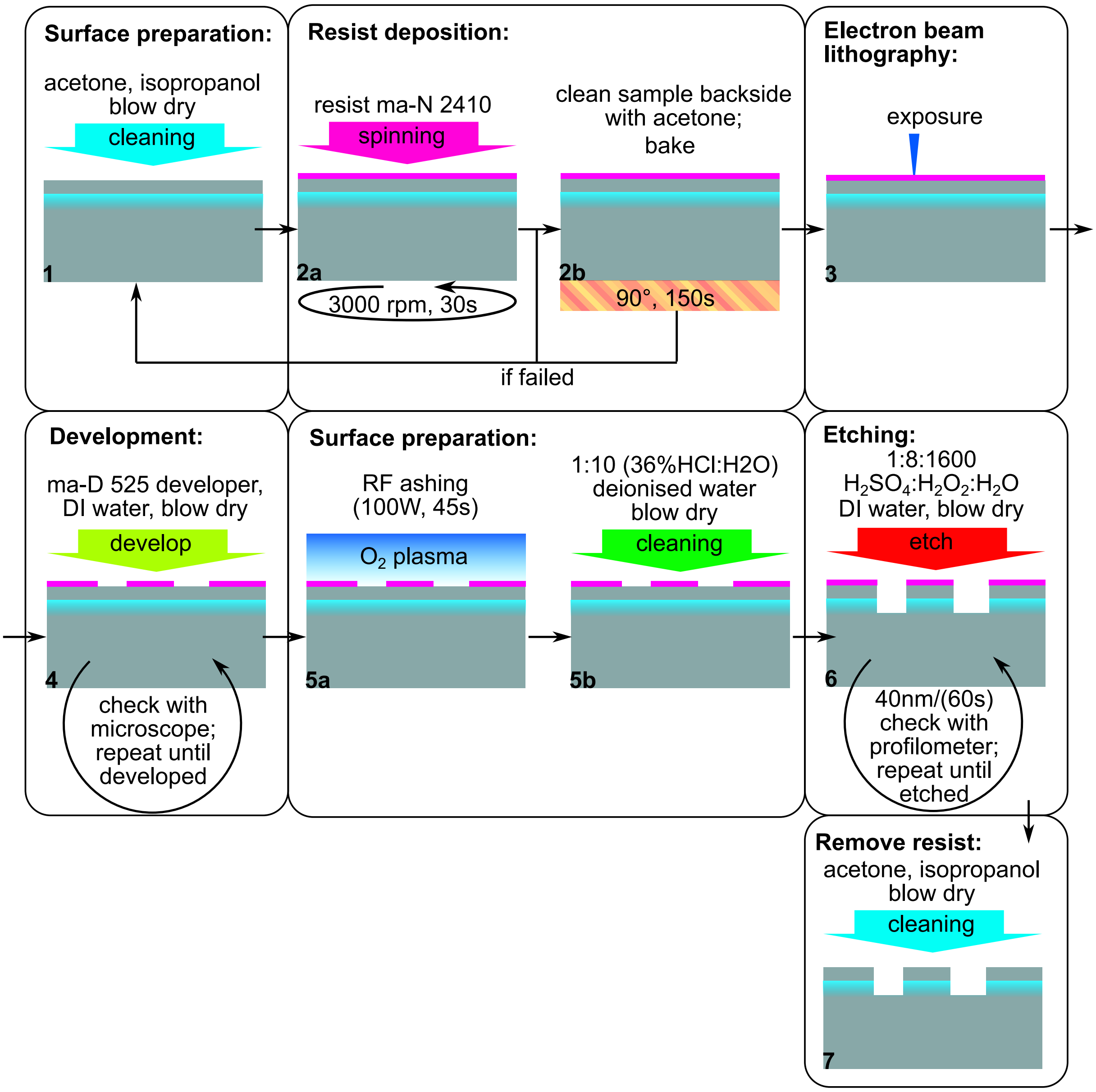

Figure 4.8: **The etching process.**

Two different speeds were used during spinning of the resist: 3000 rpm and 7100 rpm. The resulting resist height was consistent with manufacturer's specifications (for example, 0.94–1.07 µm of resist height were obtained for the 3000 rpm sample, in agreement with the expected 1 µm), although for the etching, the resist height did not play any apparent role.

After that, oxygen plasma ashing is used to remove organic residues, and a short (30 s) HCl etching step strips surface oxides. This makes the sample ready for etching in a weak Piranha etching solution, 1:8:1600 H_2SO_4:H_2O_2:H_2O. The etching is done in small steps. After each step, the change in resist height is monitored using the Dektak profilometer on the large square.

Finally, acetone and isopropanol are used to remove the resist after the etching process. It was found that an etch depth of 100 nm on the studied heterostructure is achieved after 150 s of etching time.

However, the mesa height in the narrow channel may not be the same as the one measured at the macroscopically large square using the Dektak measurement. Etching rates may be different in small channels or at resist edges than on a large area. To measure any deviations, the dimensions of the mesa in the area of the thin channel are also studied with an atomic force microscope (AFM).

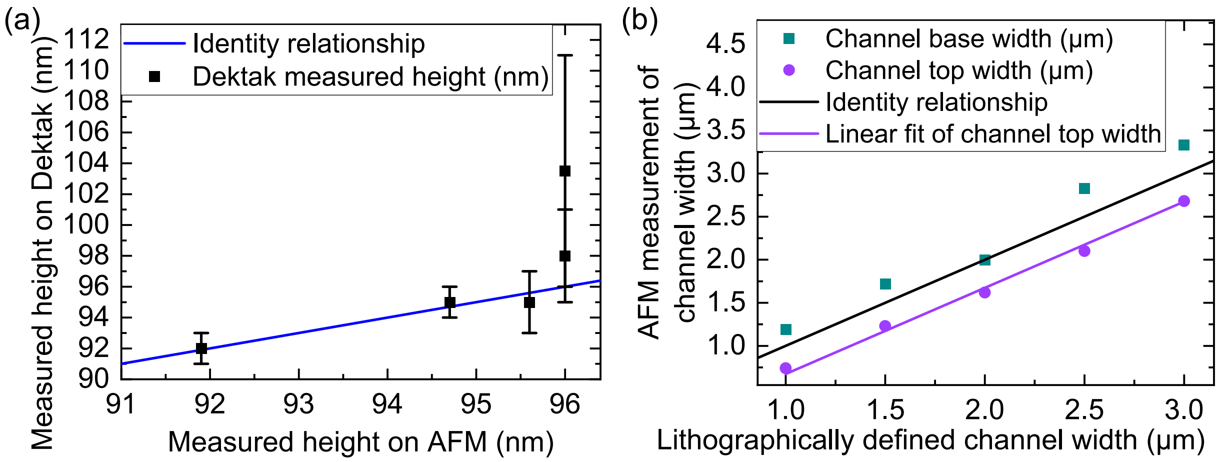

Figure 4.9: **Calibration of etching parameters.** (a) Height of the 0.2 mm×0.2 mm mesa square measured on the Dektak surface profilometer as a function of the mesa height measured using an atomic force microscope. (b) For the five lithographically defined channel widths shown on the horizontal axis, the real channel width obtained after mesa etching is shown on the vertical axis, for the top and the bottom of the mesa as measured using the atomic force microscope. The channel top widths is offset by 0.33 µm from the identity relationship.

First, the AFM height accuracy is checked using a calibration target[1] of (107 ± 2) nm height and (3.00 ± 0.01) µm period. No deviation of the measured height within the specified error was found. Then, the geometries of the narrow channels were characterised.

In Fig. 4.9 (a), for each channel width W_{lith} the mesa height determined from the Dektak on the square is plotted against the AFM measurement of the etching depth of the narrow channel. The profilometer measurement is less accurate, but within the measurement error, both heights are the same. The five measurements are done on a row of a sample, so the etching depth may vary across the sample by about 5 nm.

Fig. 4.9 (b) shows a measurement of the width of the narrow channels with the AFM, measured at the top and the bottom of the mesa. The mesa widths at the top follow a consistent linear trend as a function of the lithographically defined mesa width. Compared to the identity relationship, the linear fit shows a vertical offset of –0.33 µm. This yields a

[1] TGZ2 from NT-MDT, www.ntmdt-tips.com

value of about 165 nm for the amount of sideways etching occuring along the perimeter of the mesa.

4.2.1.2 Gates evaporation

The other crucial part is the fabrication of the antenna-shaped gates. To check whether the gate metal is continuous over the narrow mesa channel, both parts of the antenna wing with the cut-out are connected to 0.3 mm×0.3 mm large pads, see Fig. 4.10. Thus, the three gold pads will make it possible to check the conductivity of the metal across the narrow bridge.

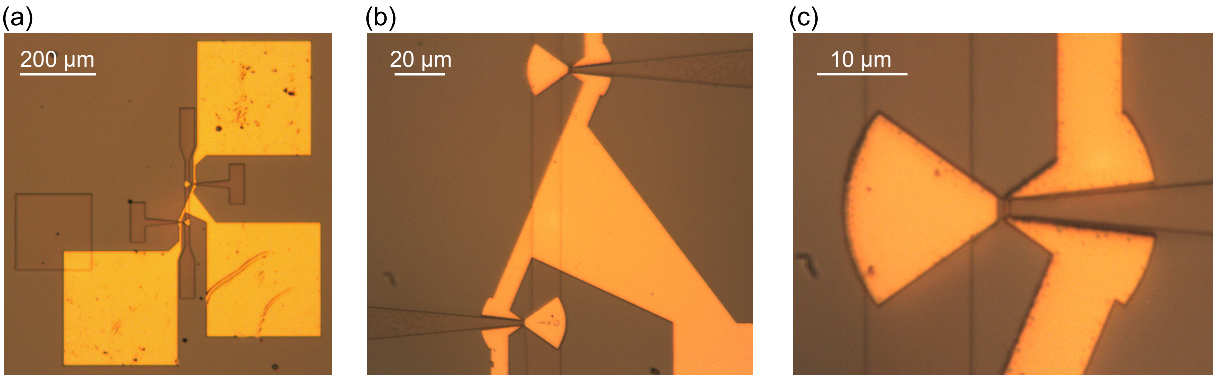

Figure 4.10: **Photo of the test sample after deposition of the gates using electron beam lithography,** at different magnifications in (a), (b), and (c).

Schematically, the fabrication process is shown in Fig. 4.11. The steps 1, 3, and 5 are the same, but now poly(methyl methacrylate) positive electron beam resist is used, and the development is carried out in a mixture of methyl ethyl ketone (MEK) and methyl isobutyl ketone (MIBK) in isopropanol (IPA). The metal evaporation is done in a thermal evaporator where heated tungsten boats boil off the materials titanium (Ti) and gold (Au). During evaporation the deposited thickness is measured using a built-in crystal thickness monitor, however the real thicknesses on the samples are larger by about 20 %–35 % than the “nominal” thicknesses displayed by the crystal monitor.

The first test on a row of 5 devices was a thin vertical evaporation, giving a total height of (77±3) nm as measured by the Dektak profilometer. The nominal thicknesses according to the crystal thickness monitor in the evaporator were 8 nm Ti and 40 nm Au. This resulted in four out of five top devices showing metallic conduction in the range of 35–80 Ω, while the bottom devices had broken metal bridges, as the >0.5 MΩ resistance indicated. Apparently, this metal thickness was slightly less than enough, and the variation in the top and bottom devices can be explained by the fact that the devices are not positioned exactly normal above the metal source in the evaporator. A slightly tilted incidence of the metal particles may result in unequal coverage of the mesa edges depending on their orientation.

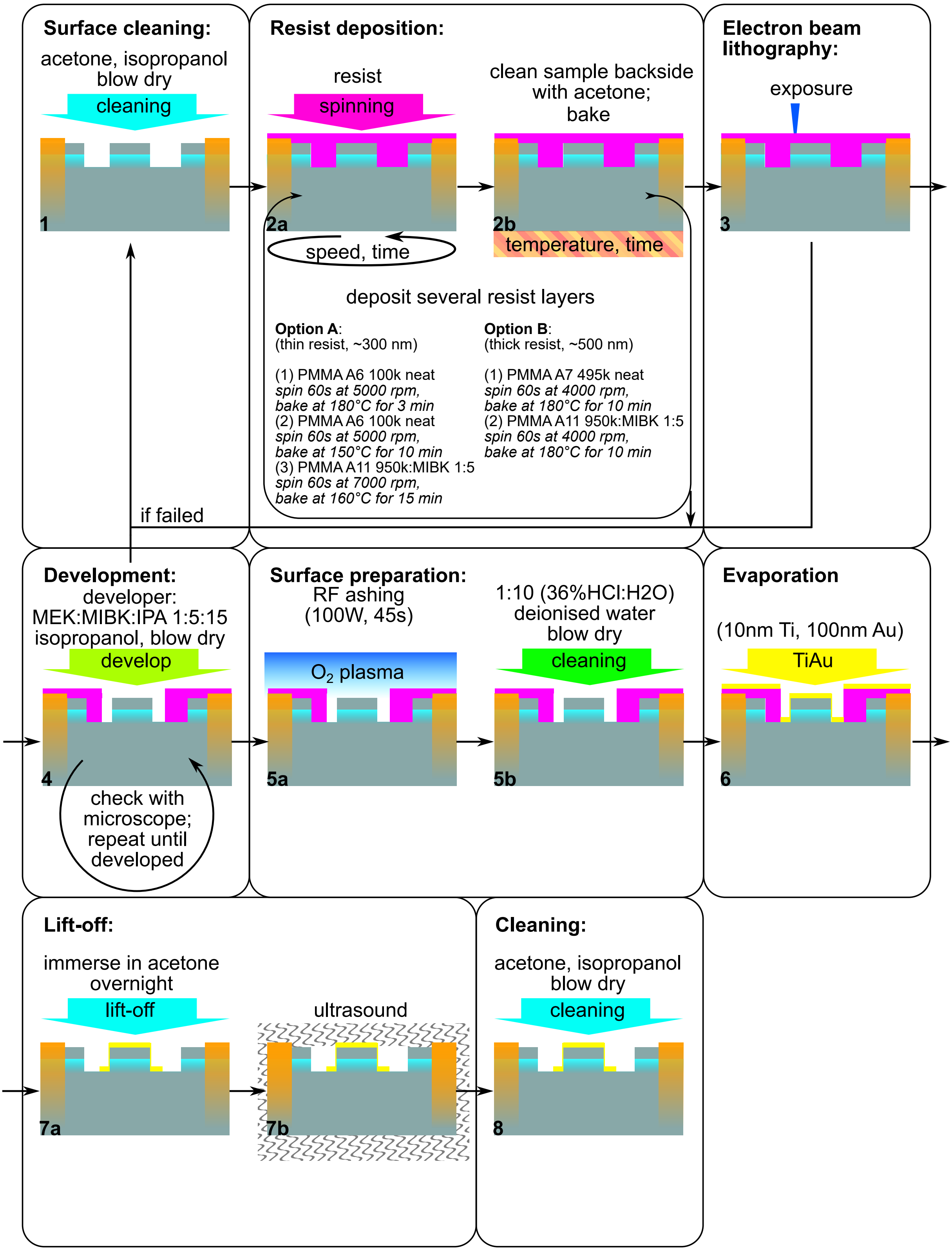

Figure 4.11: **Gates fabrication.** The process of depositing TiAu gates using electron-beam lithography.

To achieve better coverage of the edges, evaporation using a “rotatilt”-stage was attempted. Here, the sample stage is tilted at 45° and rotates during the evaporation. To evaporate the same total thickness, the targeted crystal monitor metal thickness values were multiplied by $\sqrt{2}$ compared to the previous evaporation. The evaporation of 11.3 nm Ti and 56.6 nm Au according to the crystal monitor gave a total real thickness of (60±3) nm measured by an AFM, less than before, due to the larger distance of the sample to the heated tungsten boats because of the use of the rotatilt stage. This time, all eight test devices exhibited metallic conduction of 45–70 Ω across the thin gate bridges. However, the tilted evaporation also resulted in a poorer lift-off: the resist patches that should create the small circles within the gate antennas remained enclosed by the metal.

The two evaporations suggest that a normal vertical evaporation with a thicker layer thickness will yield success for this type of samples. Therefore, a nominal amount of 8 nm Ti and 65.8 nm Au measured on the crystal monitor was evaporated, yielding a total metal thickness of (133±3) nm. This time, all ten gate bridges in the batch exhibited metallic conduction between 16 and 36 Ω.

The lift-off went well in most areas of the sample, however at some places along the border of features thin metal strips/flakes can be seen (the darker edges in Fig. 4.10 (c)). Apparently, the metal seems to break at the top edge of the resist during lift-off, rather than at the bottom, and the thin metal area that had covered the resist edges may stay connected to the gold features on the sample. During the test sample fabrication, samples were not exposed to ultrasound (7b in Fig. 4.11), but for the actual samples, an ultrasonic bath of the sample, still immersed in acetone after lift-off, solved this issue. No issues with unintentional removal of metal (by ripping off) were encountered during any lift-off or ultrasonic bath, indicating a properly prepared sample surface before the evaporation.

4.2.2 Real sample fabrication

Successful testing of the fabrication process as described in the last section paves the way towards fabrication of the actual samples. The samples are fabricated on the wafer V837. From previous MBE assessment data, the 2DEG in this wafer is known to exhibit an electron density of $3.28 \cdot 10^{11}/\mathrm{cm}^2$ and a mobility of $2.1 \cdot 10^6\ \mathrm{cm}^2/(\mathrm{Vs})$ at 1.5 K after illumination with red light. This corresponds to a scattering time of $\tau = 80\,\mathrm{ps}$ and a mean free path of $\lambda_\mathrm{e} = 18\,\mu\mathrm{m}$. (The dark density and mobility values are $1.5 \cdot 10^{11}/\mathrm{cm}^2$ and $7.4 \cdot 10^5 \mathrm{cm}^2/(\mathrm{Vs})$, respectively.)

A set of masks was designed in order to carry out the processing. The required optical mask sets were sent to JD Photo Data for fabrication of a chrome optical mask on soda lime glass.

First, electron beam lithography is used to define an etch mask using negative ma-N 2410 resist onto the as-grown wafer, and to form a mesa of the 2DEG by wet-chemical etching

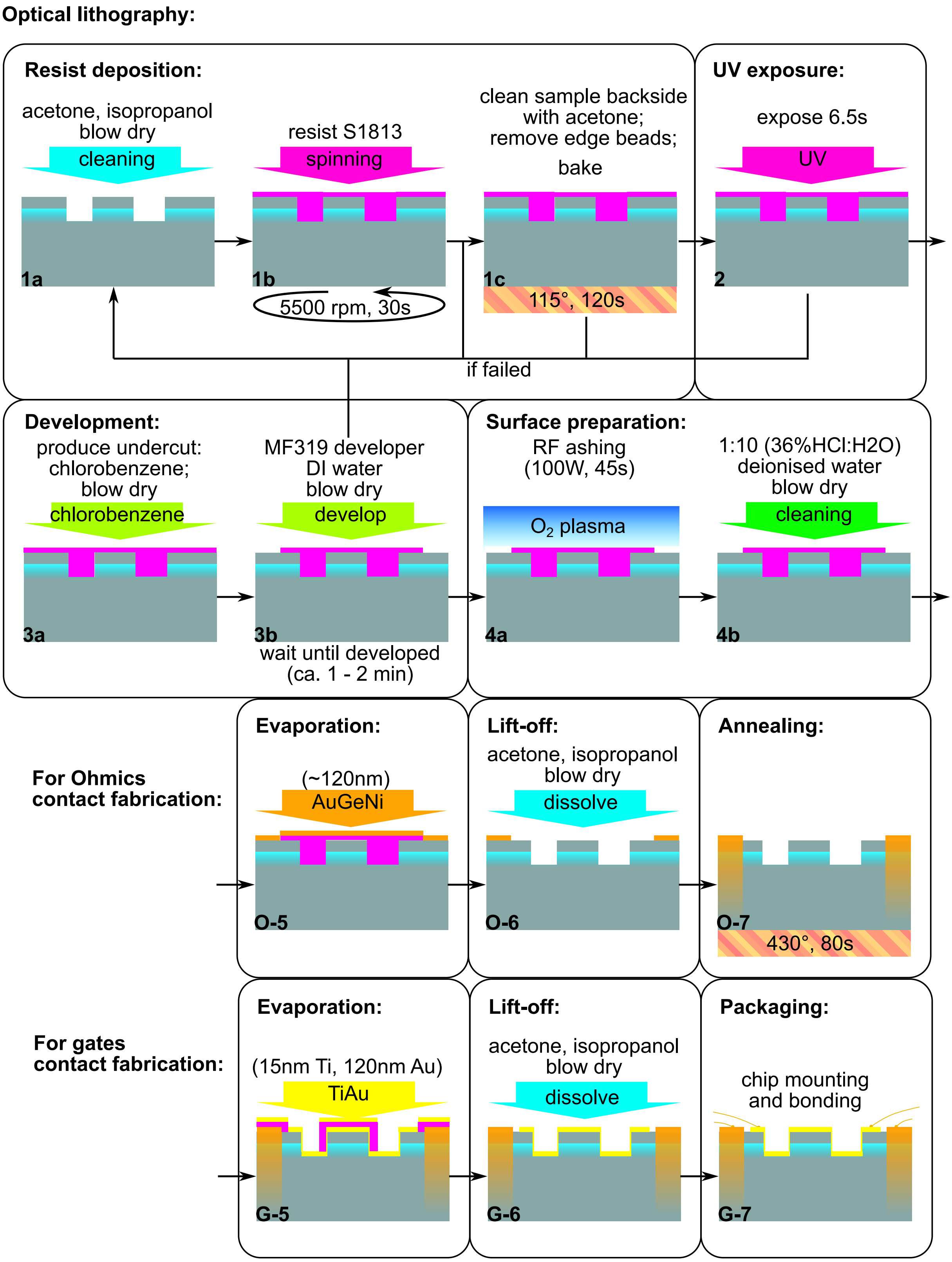

Figure 4.12: **Optical lithography process.** The processing steps required to create Ohmic contacts, made out of an AuGeNi (gold-germanium-nickel) eutectic alloy, and TiAu gates, are shown. Both are done using optical lithography; thus the first steps are the same.

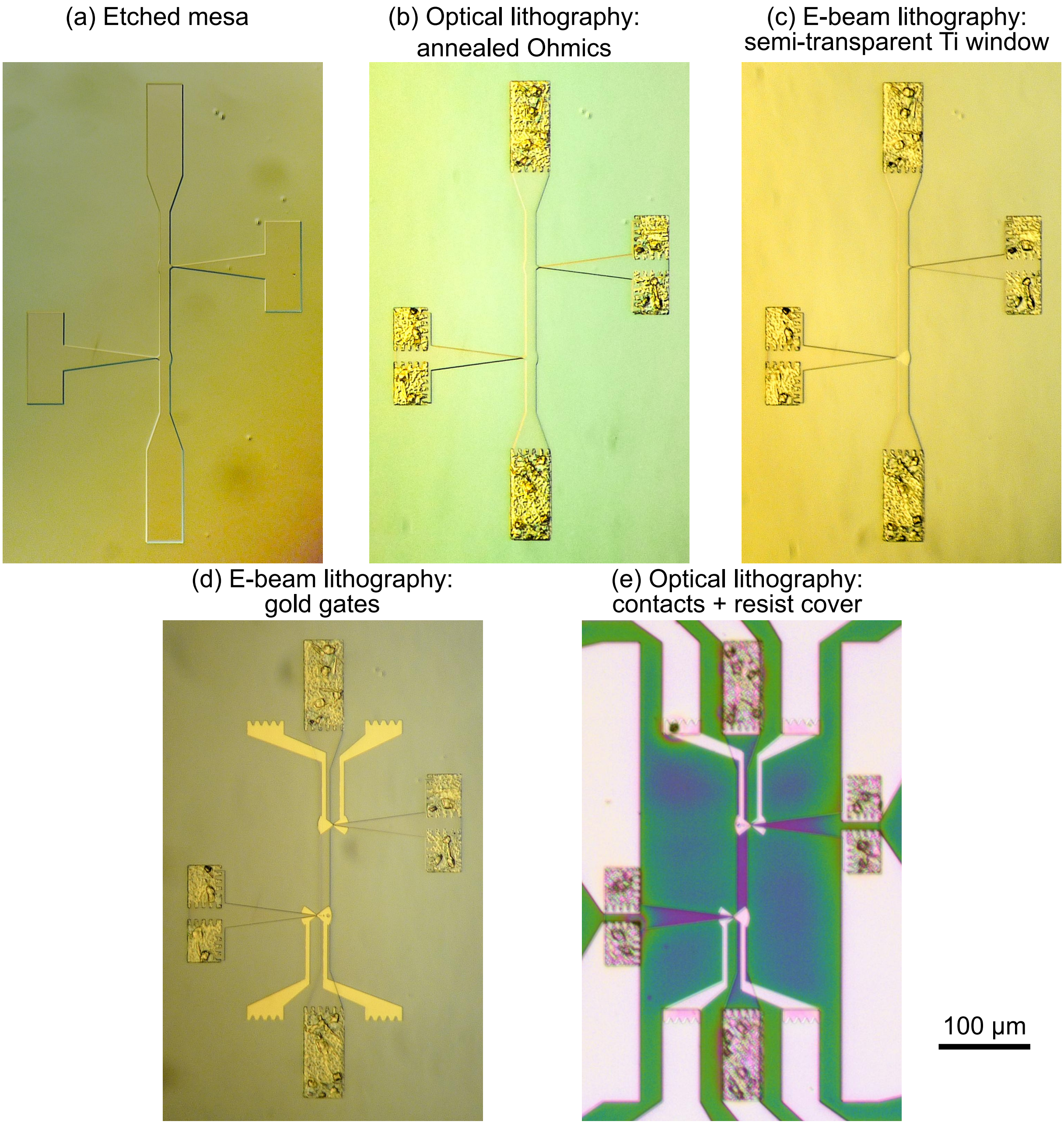

Figure 4.13: **Fabrication of actual samples.** Evolution of a device unit over the course of the processing.

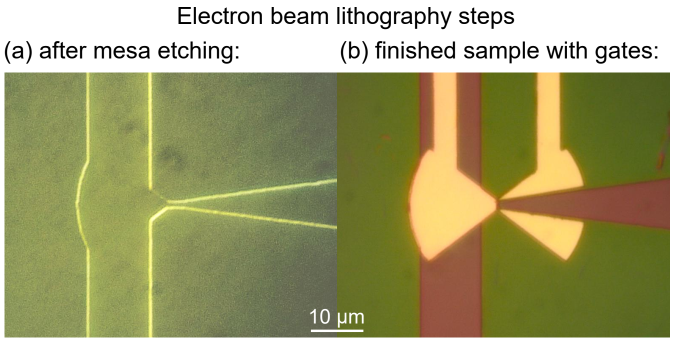

Figure 4.14: **Microscope photos of the active part of the device,** after the steps utilizing electron beam lithography: (a) the mesa definition of the 2DEG region, (b) the antenna gates.

(see test sample fabrication, Fig. 4.8 in section 4.2.1). During this stage, markers are also etched into the sample at the four corners of each device unit, which are used for mask alignment during the subsequent optical and electron beam lithographic processes. After that, a device unit looks as shown in Fig. 4.13 (a) and Fig. 4.14 (a).

In the second step, Ohmic source and drain contacts to the channel are processed using optical lithography with a Karl Suss MJB-3 mask aligner. This process, employing UV exposure with a mercury lamp, is shown in Fig. 4.12. Shipley S1813 resist and MF319 developer are used, and after that a AuGeNi eutectic alloy is thermally evaporated on the sample. After lift-off the sample is annealed at 430°C for 80 s, which creates Ohmic contacts to the 2DEG, Fig. 4.13 (b). At this stage, it becomes possible to check whether there is a 2DEG using a needle probe station, i. e. whether the sample passes current. Between the top and bottom Ohmic contacts of an exemplary mesa, a resistance of 2.5 – 2.9 kΩ (with and without illumination on the microscope used) is found, confirming the presence of a conducting layer as well as successful annealing of the Ohmic contacts.

In the third step, electron beam lithography with poly(methyl methacrylate) resist is used to cover the lower bow-tie wing, the area that will be under the circular holes, with semi-transparent Ti. The same process as shown in Fig. 4.11 is used, except that instead of the thick TiAu-layer only a thin layer of titanium is deposited, see Fig. 4.13 (c). The nominal evaporated titanium thickness of 4.7 nm on the crystal monitor resulted in an actually 8.8 nm – 9.5 nm thick Ti layer, as measured by an AFM.

E-beam lithography of the gates follows as the fourth step, as described in the test sample fabrication, Fig. 4.11 in section 4.2.1. This time, titanium and gold (TiAu) are deposited, and this results in Fig. 4.13 (d) and Fig. 4.14 (b).

As a fifth step, optical lithography is employed for the creation of large-area TiAu bond pads, as shown in Fig. 4.12. The resist deposition and lithographic processes are the same as for the Ohmic contacts, and after that, Ti (nominally $\sim$ 15 nm on crystal monitor) and Au (nominally $\sim$ 120 nm) is evaporated, and the unnecessary metal areas are removed during lift-off. This procedure covers most of the sample with metal, which connects the small patches of Ohmic and gate regions to large pads for bonding.

Before bonding, the sample is encapsulated in Shipley S1805 resist for surface protection. This serves the purpose of preventing progressive oxidation of exposed AlGaAs at the mesa edges, and thus degrading sample quality over time. For the encapsulation, the steps 1–3 (except 3a) in Fig. 4.12 are repeated, this time with the thinner S1805 resist, with the same mask as used for the bond pads. This way, the bond pads are opened up and are accessible for bonding, but all other areas of the device, including the active area with the channel, remain covered in the resist and are thus protected from ambient environment. As a result, Fig. 4.13 (e) (and Fig. 4.5) shows an example of a processed sample.

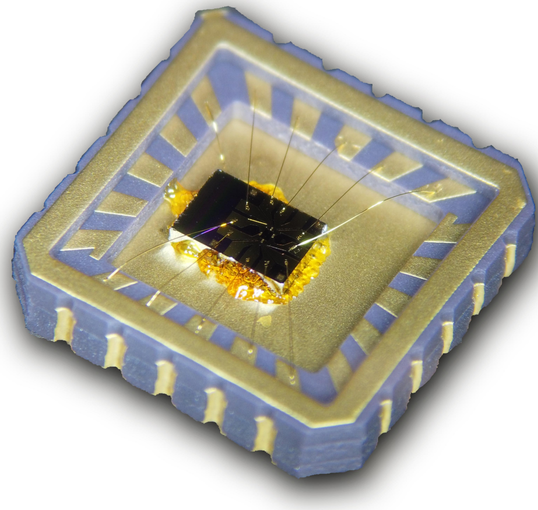

Figure 4.15: **Sample chip** in an LCC20 chip carrier after finished packaging and bonding.

As a last step, the sample is mounted into an LCC20 chip carrier with GE varnish and bonded up on a wedge bonder with gold wires. The final chip is shown in Fig. 4.15.

Each device unit is 2 mm×2 mm large. The processing was carried out on four 12 mm×14 mm chips containing 5×6 device units with 1 mm free edge on all sides. Each of the 30 devices on a chip has a slightly different geometry, in order to be able to systematically study and optimise the device architecture. The width W_{lith} of the narrow channel, the width b_{bridge} of the bridge, and the distance b_{gap} between the two bow-tie antennas were tuned as shown in Table 4.1. As a result, for each of the 30 unique geometries, four devices were fabricated, yielding a total of 120 devices available.

For the width b_{bridge} of the narrow gate, values of 120 nm, 200 nm, and 500 nm were selected. This range of values was selected as lower values are not sensible, since the induced potential from the gate in the 2DEG will be blurred on a length scale of around the distance to the 2DEG of 90 nm, and higher values would represent a macroscopically large gate-induced potential barrier. Lithographically defined widths W_{lith} of the 2DEG channel of 1.0, 1.5, 2.0, and 3.0 µm were chosen: for lower values, conduction may freeze out due to surface states at the mesa edges, and for higher values, the strength of the THz focusing of the antenna will diminish. The bow-tie gaps b_{gap} in Table 4.1 were chosen from the expected plasmonic resonance values described in the device design section 4.1.

A number of the fabricated samples were bonded up and tested. Table 4.2 lists the studied samples with comments. Highlighted in yellow are the samples that have demonstrated a THz response. Some other samples had shorted gates or gates with a high leakage current or a high resistance of Ohmic contacts, that had frozen out conduction at low temperatures or exhibited diode-like characteristics. In samples with a 1 µm wide lithographically defined channel width, conduction of the 2DEG through the narrow channel freezes out at

ID	Row	Column	Width W_{lith} (µm)	Bridge thickness b_{bridge} (µm)	Bowtie gap B b_{gap} (µm)
V837-⟨N⟩-1.1	1	1	1.00	0.20	0.27
V837-⟨N⟩-1.2	1	2	1.00	0.20	0.36
V837-⟨N⟩-1.3	1	3	1.00	0.20	0.45
V837-⟨N⟩-1.4	1	4	1.00	0.20	0.63
V837-⟨N⟩-1.5	1	5	1.00	0.20	1.00
V837-⟨N⟩-2.1	2	1	1.50	0.20	0.27
V837-⟨N⟩-2.2	2	2	1.50	0.20	0.36
V837-⟨N⟩-2.3	2	3	1.50	0.20	0.45
V837-⟨N⟩-2.4	2	4	1.50	0.20	0.63
V837-⟨N⟩-2.5	2	5	1.50	0.20	1.00
V837-⟨N⟩-3.1	3	1	2.00	0.20	0.27
V837-⟨N⟩-3.2	3	2	2.00	0.20	0.36
V837-⟨N⟩-3.3	3	3	2.00	0.20	0.45
V837-⟨N⟩-3.4	3	4	2.00	0.20	0.63
V837-⟨N⟩-3.5	3	5	2.00	0.20	1.00
V837-⟨N⟩-4.1	4	1	3.00	0.20	0.27
V837-⟨N⟩-4.2	4	2	3.00	0.20	0.36
V837-⟨N⟩-4.3	4	3	3.00	0.20	0.45
V837-⟨N⟩-4.4	4	4	3.00	0.20	0.63
V837-⟨N⟩-4.5	4	5	3.00	0.20	1.00
V837-⟨N⟩-5.1	5	1	1.50	0.12	0.27
V837-⟨N⟩-5.2	5	2	1.50	0.12	0.36
V837-⟨N⟩-5.3	5	3	1.50	0.12	0.45
V837-⟨N⟩-5.4	5	4	1.50	0.12	0.63
V837-⟨N⟩-5.5	5	5	1.50	0.12	1.00
V837-⟨N⟩-6.1	6	1	1.50	0.50	0.27
V837-⟨N⟩-6.2	6	2	1.50	0.50	0.36
V837-⟨N⟩-6.3	6	3	1.50	0.50	0.45
V837-⟨N⟩-6.4	6	4	1.50	0.50	0.63
V837-⟨N⟩-6.5	6	5	1.50	0.50	1.00

Table 4.1: **Table of samples.** Each of the four fabricated samples contains 6 rows and 5 columns of device units. ⟨N⟩ is the sample number from 1 to 4. All 30 device pairs on one sample have slightly different geometries, which vary in the width W_{lith} of the narrow channel, the width b_{bridge} of the bridge, and the distance b_{gap} between the two bow-tie antennas.

low temperatures, as will be discussed in section 4.7.1. Thus these samples were used as test samples for elimination of electrostatic discharge issues, discussed in section 4.4.4. This chapter describes in detail the representative measurements and results obtained on samples V837-2-4.1 (section 4.3) and V837-2-3.1 (section 4.5).

Sample ID	W_{lith}	b_{bridge}	b_{gap}	Comment
V837-2-4.1	**3.00**	**0.20**	**0.27**	**First demonstration of a THz response, section 4.3**
V837-2-1.5	1.00	0.20	1.00	1µm lithographic channel: No 2DEG at low temperatures, conduction through channel frozen out Samples used for testing of electrostatic issues
V837-2-1.1	1.00	0.20	0.27	
V837-2-1.2	1.00	0.20	0.36	
V837-2-1.3	1.00	0.20	0.45	
V837-2-1.4	1.00	0.20	0.63	
V837-2-5.1	1.50	0.12	0.27	THz response not observed
V837-2-4.2	3.00	0.20	0.36	High gate leakage
V837-2-4.5	3.00	0.20	1.00	High gate leakage
V837-2-4.3	3.00	0.20	0.45	High gate leakage
V837-2-3.1	**2.00**	**0.20**	**0.27**	**Demonstration of direct THz detection, section 4.5**
V837-3-1.1	1.00	0.20	0.27	1µm lithographic channel for testing of electrostatic issues
V837-3-1.2	1.00	0.20	0.36	
V837-3-1.3	1.00	0.20	0.45	
V837-1-3.1	2.00	0.20	0.27	Ohmic contacts behave as diodes, THz response not observed
V837-3-2.1	1.50	0.20	0.27	Ohmic contacts behave as diodes, THz response not observed
V837-3-3.1	2.00	0.20	0.27	THz response, similar to V837-2-3.1
V837-4-3.1	2.00	0.20	0.27	THz response, but high Ohmic contact resistance
V837-3-4.1	3.00	0.20	0.27	THz response, but high gate leakage
V837-3-3.2	2.00	0.20	0.36	THz response, gates and Ohmics work well

Table 4.2: **Table of tested samples.** Highlighted in yellow are the samples that have demonstrated a THz response. The ones highlighted in bold are described in detail in the subsequent sections. The values for W_{lith}, b_{bridge}, and b_{gap} are in µm.

4.3 Searching for initial indications of a THz photoresponse

Here, after a test of the electrical conduction of the samples, the journey of searching for a THz response is described. This section shows how systematic optimisations, starting from a non-existing THz response, lead to the demonstration of a THz photocurrent of substantial magnitude.

The first sample to be studied has a 3 µm wide channel with 0.27 µm distance between the antenna halves and a 0.2 µm narrow gate bridge (V837-2-4.1).

4.3.1 Testing sample conductance

After cooling the sample down to a temperature around 7–9 K, the conductance of the 2DEG and the gate leakage are tested. Initially, the wide gate is shorted externally to the source contact, and only the narrow gate is used. In this case, the sample can be seen as a field-effect transistor, with pin assignments as shown in Fig. 4.16 (a).

The current flowing through the narrow gate, the leakage current, is shown in Fig. 4.17 (a). The measurement is carried out using a Keithley 2400 source-measurement unit. It is capable of setting the desired current and a compliance, i. e. the maximum voltage to be applied. Over the whole measurement interval, the gate leakage stays below 1 nA, and in the region from –1 V to 0.5 V, even below 10 pA.

Fig. 4.17 (b) shows the change in source-drain conductance when the narrow gate voltage is tuned, the transfer characteristic. The circuit for this measurement is shown in Fig. 4.16 (b). At gate voltages around 0 V, when the load resistance is low, the applied source-drain voltage is lower than the compliance limit, and the current is regulated by the device to be held constant at the given set-point. When the resistance becomes too high, the desired current flow of 1 µA cannot be sustained without exceeding the compliance voltage. In this

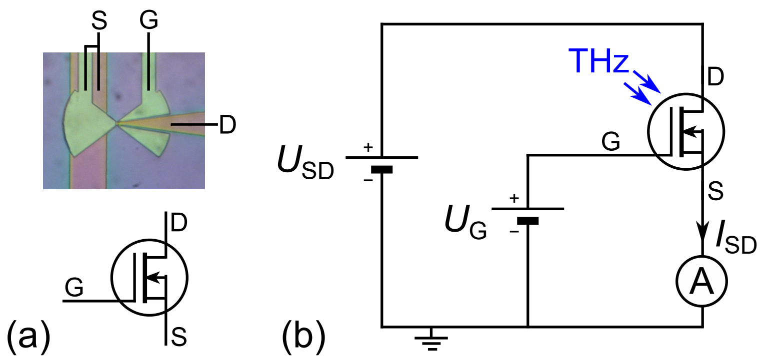

Figure 4.16: **The sample as a field-effect transistor.** (a) Pin assignments on the sample. Electrically, it is used as a field effect transistor. (b) Lock-in measurement circuit. A gate voltage is applied to the narrow gate, and a source drain voltage to the channel. The wide gate is not used and grounded to the source contact. The DC source-drain current is measured.

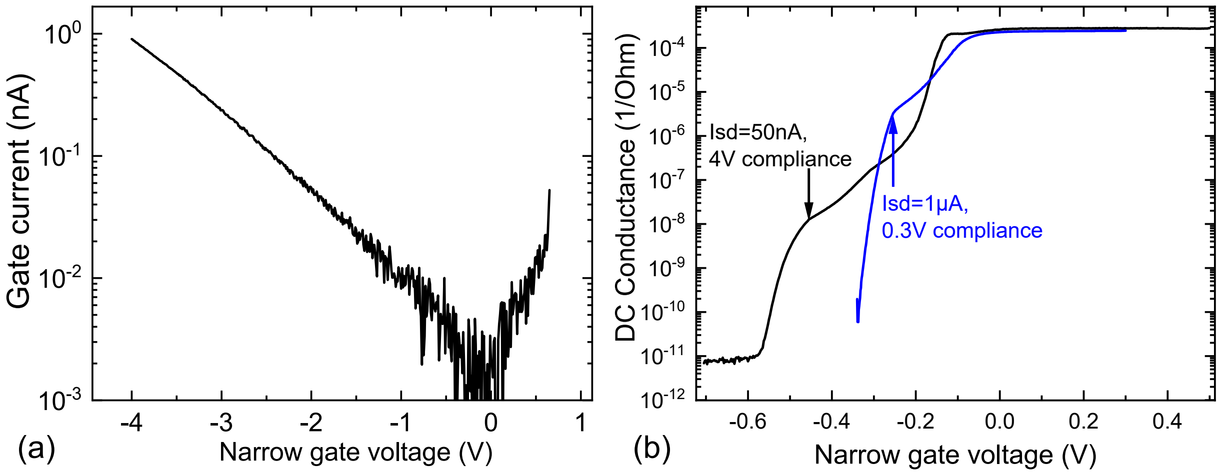

Figure 4.17: **DC characterisation of the device.** (a) Absolute value of the narrow gate leakage current as a function of the gate voltage. No source-drain bias is applied. (b) Source-drain current as a function of narrow gate voltage. Negative gate voltages pinch off the conducting channel. The measurement is done for two settings of maximum source-drain current and voltage as indicated on the plot. Right from the arrow, at higher conductances, the current is limited by the current set point, with the voltage being lower. Left from the arrow, at lower conductances, the voltage is equal to the compliance voltage, and the current is lower than the set point.

case, the voltage becomes equal to the compliance voltage, and the current is lower than the set point.

The measurements in Fig. 4.17 (b) were performed in a 2-wire configuration with two different settings of the current set-point and voltage compliance limit: 1 μA current with 0.3 V compliance, and 50 nA current with 4 V compliance. When the narrow gate voltage is negative and grows in magnitude, the negative gate voltage depletes the carriers in the conducting channel, which increases the resistance. At the point indicated by the arrow on each respective curve, the transition from constant current mode on the right and constant voltage mode on the left takes place. As can be seen, the resulting curves are different, since the source-drain voltage also influences the transfer characteristic: at source-drain voltages strong compared to the gate voltages, the local gate-to-channel voltage becomes strongly dependent on the coordinate along the channel, and the source-gate and drain-gate voltages become substantially different. The gate voltage shown on the horizontal axis of the graph is the source-gate voltage. Positive gate voltages influence the conductance only weakly: in this case, the conductance of the 2DEG under the gate may well increase, but the total conductance is limited by the ungated 2DEG regions whose resistance adds in series. The two measurements in Fig. 4.17 show that the gates are working (not leaking), the 2DEG is conducting, and can successfully be controlled by the gates – i. e. the device fabrication was successful.

As seen in a sample photograph, e. g. Fig. 4.5, there are two Ohmic contacts for each end of the channel: both for the source and for the drain there is an upper and a lower

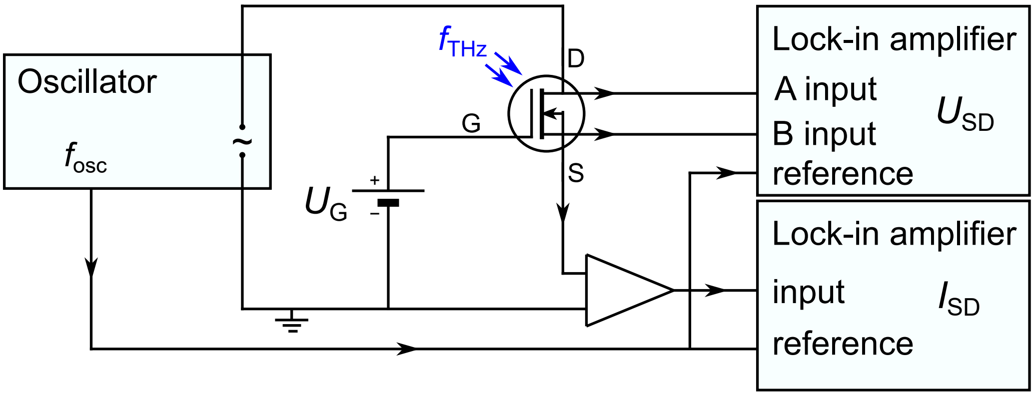

Figure 4.18: **Circuit for an AC conductance measurement.** Source and drain are excited by a small AC voltage, and the resulting AC current and voltage are detected with the lock-in amplifier.

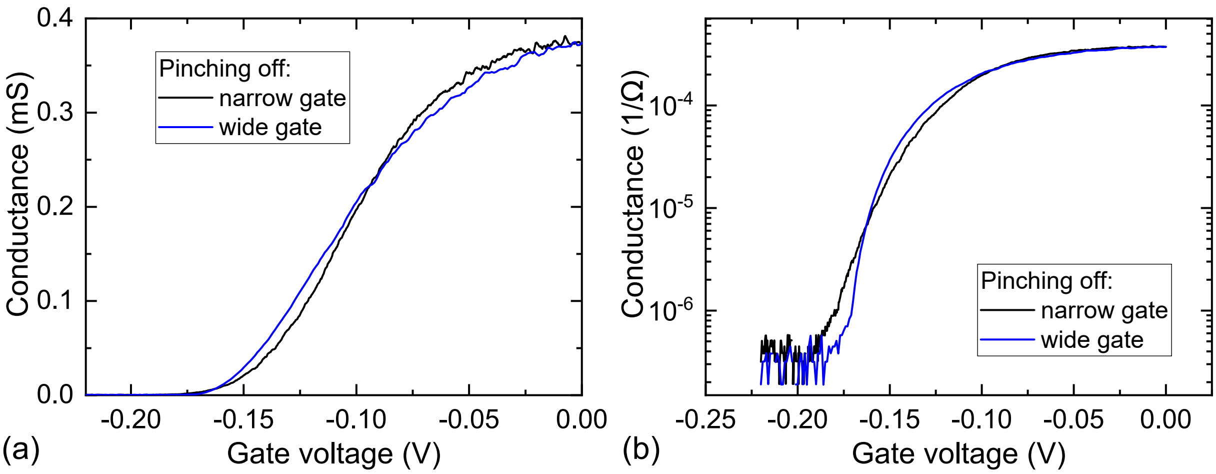

Figure 4.19: **Transfer characteristics of the sample** measured in a four-terminal AC measurement. Black: the narrow gate voltage is tuned with the wide gate voltage grounded at 0 V (connected to the source contact). Blue: the wide gate voltage is tuned with the narrow gate voltage at 0 V. (a) linear, (b) logarithmic scaling of the conductance axis.

Ohmic contact which probe the 2DEG independently of each other. In order to eliminate the DC source-drain artefacts and the contact resistances, an AC measurement of the conductance is carried out in a four-terminal configuration as shown in Fig. 4.18. Here, a small sinusoidal AC voltage of 100 µV at 86.5 Hz is generated by the function generator integrated in a lock-in amplifier. The current flowing through from source contact 1 to drain contact 1 is measured by a current amplifier and a lock-in amplifier at the same frequency. The voltage is measured at the other two Ohmic contacts to the channel (source contact 2 to drain contact 2 in Fig. 4.5, upper device unit), and the ratio yields the channel conductance, which is shown in Fig. 4.19. This measurement is free from source-drain effects shifting the gate voltage, and the sinusoidal source-drain AC voltage has been chosen small enough to minimize “smoothing” of the curve. Both the narrow and the wide gate have a similar pinch-off behaviour and threshold voltage.

4.3.2 Measurements with THz excitation

So far, measurements without THz excitation have been presented. Given that the sample works electrically, the goal is now to illuminate it with THz radiation and see whether a response can be observed. Using the developed THz waveguide system described in chapter 2, section 2.2, the sample is exposed to ~ 1.9 THz radiation from the single-plasmon quantum cascade laser described in section 2.1 (see Figs. 2.5, 2.6).

The first attempts were to measure the DC current through the sample, as discussed in Fig. 4.16 and 4.17 (b), with and without THz irradiation, and to look for any differences between the resulting curves as a function of the narrow gate voltage. No THz-related signal could be established this way, and the minor deviations observed were due to long-term drifts of charge carrier concentration or temperature. The same is valid for attempts of photoconductance measurements by comparing the AC conductance, as measured in Figs. 4.18 and 4.19, with and without THz radiation incident.

As no direct response could be established, a lock-in measurement referenced to the QCL modulation frequency f_{mod} is used for subsequent measurements. The DC current I_{SD} in Fig. 4.16 is now measured using a current preamplifier connected to a lock-in amplifier with a time constant of 1 second. The QCL was first driven as in Fig. 2.3, with the same pulse train as a Golay cell, but no THz signal was observed, neither at the slow (~ 12.4 Hz) nor at the fast (~ 8.95 kHz) modulation frequencies, nor at their second harmonics. Finally, the QCL was driven with a simple square wave form with frequency f_{mod} set to 781 Hz with 2.19 % duty cycle – but again, no THz signal at f_{mod} or $2f_{\mathrm{mod}}$. Integrating with longer time constants (3 seconds and more) on the lock-in amplifier, applying moving

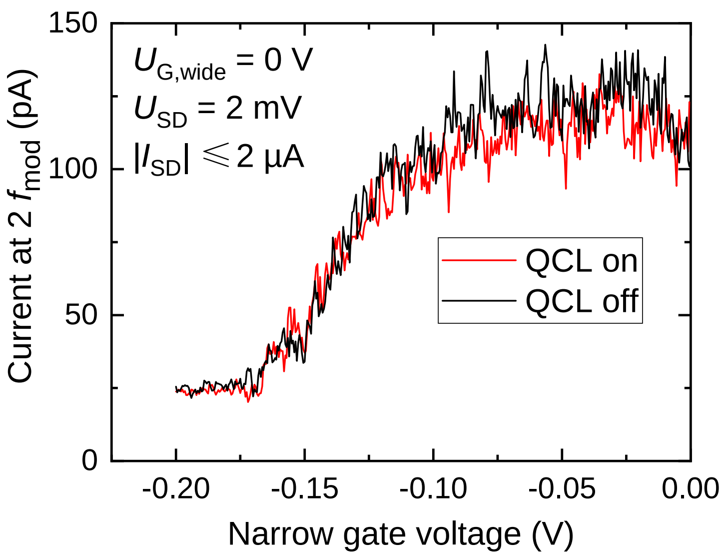

Figure 4.20: **No THz signal observed.** The initial measurements only showed noise, independent of THz irradiation, as the example shown here.

average filters to the data and calculating derivatives of the data during post-processing was equally attempted. A typical measurement looks as shown in Fig. 4.20: whatever the lock-in amplifier detects is only noise of unstable phase that does not depend on whether the QCL is operating or not. At any random frequency around $2f_{\mathrm{mod}}$ (or f_{mod}), the noise is similar. In general, it seems that the noise follows the same trend as the current and likely originates in the regulating/stabilising operation of the Keithley 2400 source-measurement unit that is used to apply the source-drain voltage.

A challenge in searching for a THz response on a new type of device is the lack of any previous experience of its operation. More formally, the tunable measurement parameters span a four-dimensional space with the following independent variables: the source-drain voltage U_{SD}, the narrow gate voltage $U_{\mathrm{G,narrow}}$, the wide gate voltage $U_{\mathrm{G,wide}}$ and the equilibrium surface charge carrier concentration n_0. Where in this space a THz response may be located is unknown, and the space needs to be systematically probed to find or prove the non-existence of a THz response. Fortunately, what is known is that THz radiation is incident on the device: the waveguided setup presented in chapter 2 was aligned before any THz measurements, and the sample is placed to face the center of the waveguide bore in the coldfinger, so the possibility of THz radiation not hitting the sample can be ruled out.

So far, only one gate (the narrow gate) has been tuned during the experiments with THz excitation, with the other gate being grounded. Let us now also tune the wide gate, and study the sample behaviour as a function of both gate voltages. Electrically, the sample is now a dual-gate field effect transistor, with pin assignments as shown in Fig. 4.21 (a).

Such a two-dimensional measurement is carried out using the circuit shown in Fig. 4.21 (b). Both the DC current measured by the preamplifier and the AC current at frequency

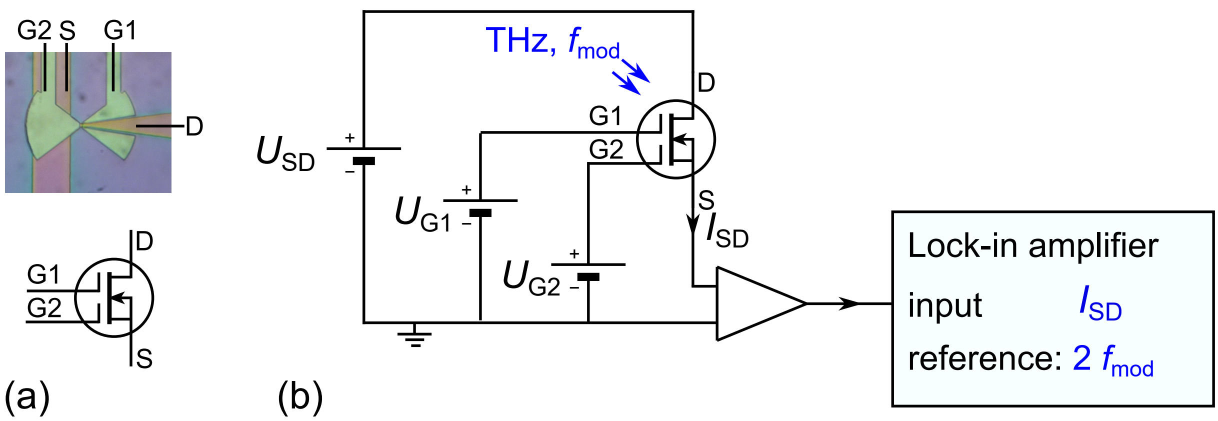

Figure 4.21: **Lock-in measurement of the THz photoresponse.** (a) Pin assignments on the sample. Electrically, it can be seen as a dual-gate field effect transistor. (b) Lock-in measurement circuit. Two gate voltages are applied to the FET gates, and a source drain voltage to the channel. The DC current and the current at $2f_{\mathrm{mod}}$ is measured, where f_{mod} it the modulation frequency of the lock-in amplifier.

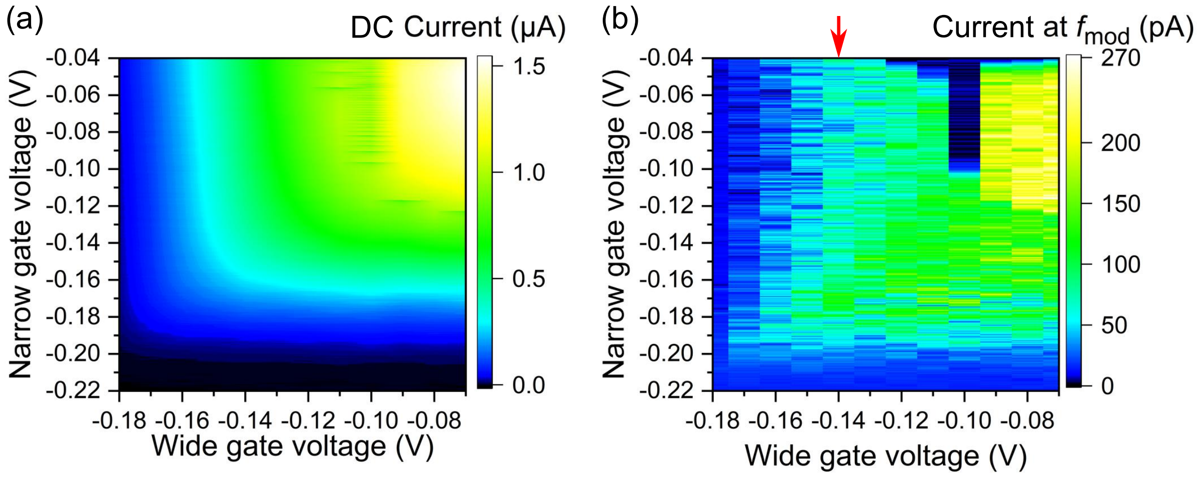

Figure 4.22: **Two-dimensional map of (a) the DC current and (b) the current at f_{mod}, i. e. the THz signal.** The data was measured simultaneously, with THz radiation incident on the device. The values are shown as colour-coded plots as a function of the wide and narrow gate voltages. The measurement is conducted with a source-drain voltage of 8 mV; the THz signal is measured as the current at f_{mod} = 781 Hz. The dark lines around –0.1 V in (b) are artefacts where input overload protection of the preamplifier was triggered. In the left-bottom corner a higher signal is observed than a noise artefact of the DC current, and the red arrow shows the gate voltage of –0.14 V which is used for the detailed line scan in Fig. 4.23.

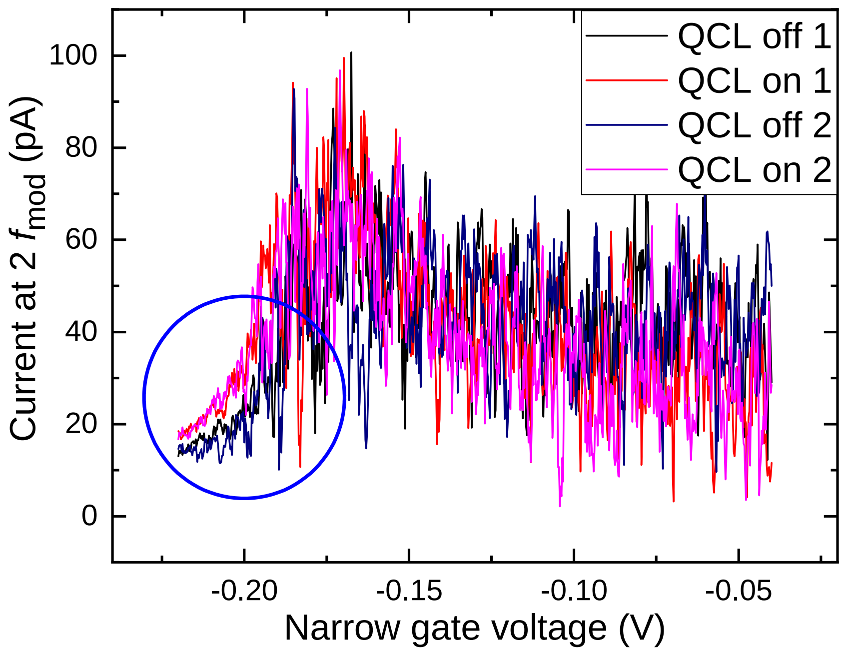

Figure 4.23: **First observation of a THz photoresponse.** At a source-drain voltage of 8 mV and a wide gate voltage of –0.14 V, the source-drain current at frequency $2f_{\mathrm{mod}}$ is measured with (red) and without (black) THz irradiation. Two measurements were done for each, and the deviation marked with the blue circle was reproduced.

$2f_{\mathrm{mod}}$ are recorded at the same time, yielding Fig. 4.22 (a) and (b). When either one of the gate voltages becomes strongly negative (i. e. approaching pinch-off), the current decays. This leads to a square-like/corner-shaped current form in Fig. 4.22 (a).

Interestingly, the signal at the QCL modulation frequency f_{mod} follows the same trend, but in the pinch-off corner around ($U_{\mathrm{G,wide}}$,$U_{\mathrm{G,narrow}}$) = (−0.16 V, −0.19 V) a signal at f_{mod} is observed in spite of the current diminishing towards this corner.

Let us now consider this corner in more detail, and tune the narrow gate voltage while the wide gate voltage is held at –0.14 V. This yields Fig. 4.23. While merely noise is observed over most of the narrow gate voltage range, there is indeed a slightly higher current signal for narrow gate voltages below –0.20 V. The curves were measured twice, and the deviation was reproduced. The difference is observed not only when the QCL is switched on and off, but also when the THz waveguide is blocked and un-blocked, proving that it is a true THz response and not electromagnetic interference from the QCL driver. This constitutes the first observation of a THz photoresponse on the studied sample.

Now that a point ($U_{\mathrm{G,wide}}$,$U_{\mathrm{G,narrow}}$) is known where a THz signal is established, the next step is to tune the source-drain voltage. Fig. 4.24 shows the outcome. As the source-drain

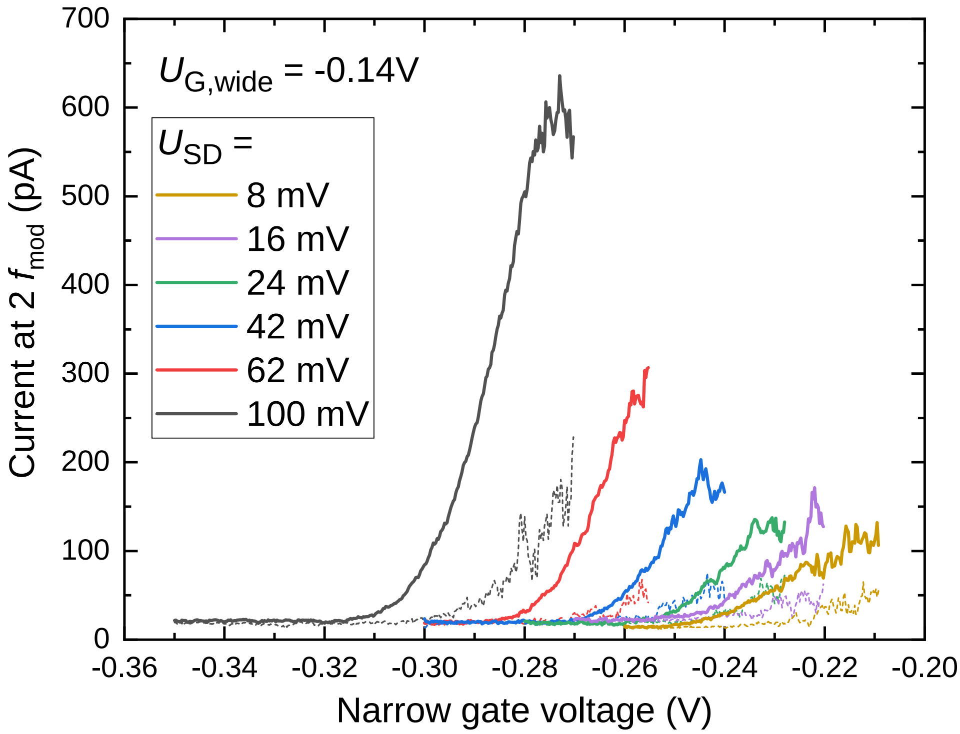

Figure 4.24: **THz photoresponse with increasing source-drain bias.** At –0.14 V of wide gate voltage, the pinch-off region of the narrow gate is studied under different source-drain voltages as indicated. The solid lines represent the current at the second harmonic of the QCL modulation frequency with incident THz waves; the dashed lines are the corresponding noise without THz irradiation.

voltage grows, so does the THz photoresponse, and reaches a value of almost 0.5 nA for U_{SD} = 0.1 V. The current with THz illumination is always higher than without THz illumination.

Why are the measurements carried out at $2f_{mod}$, rather than just f_{mod}? Due to the square-wave QCL operation, a rectified signal corresponding to the THz power will be observed at f_{mod} and multiples of f_{mod}, with the Fourier harmonics decaying weakly because of the low duty cycle (2.19 %). Experimentally, the noise generated from the DC current falls down with frequency and is lower at $2f_{mod}$ than at f_{mod}. One reason is that during the same time constant setting on the lock-in amplifier, twice as many cycles will be averaged at $2f_{mod}$ as compared to f_{mod}.

For comparison, a 2D map is measured again at U_{SD} = 0.1 V, see Fig. 4.25. Two lock-in amplifiers were used to simultaneously record Fourier components of the current at $2f_{mod}$ = 1.562 kHz in (a) and at a "random" frequency of 1.404 kHz in (b). The latter one was chosen close to $2f_{mod}$, and this measurement gives an estimate for the broadband noise present in the circuit which is independent of the THz excitation. The THz signal moving into the pinch-off corner, first seen in Fig. 4.22, is even more pronounced at the higher source drain voltage.

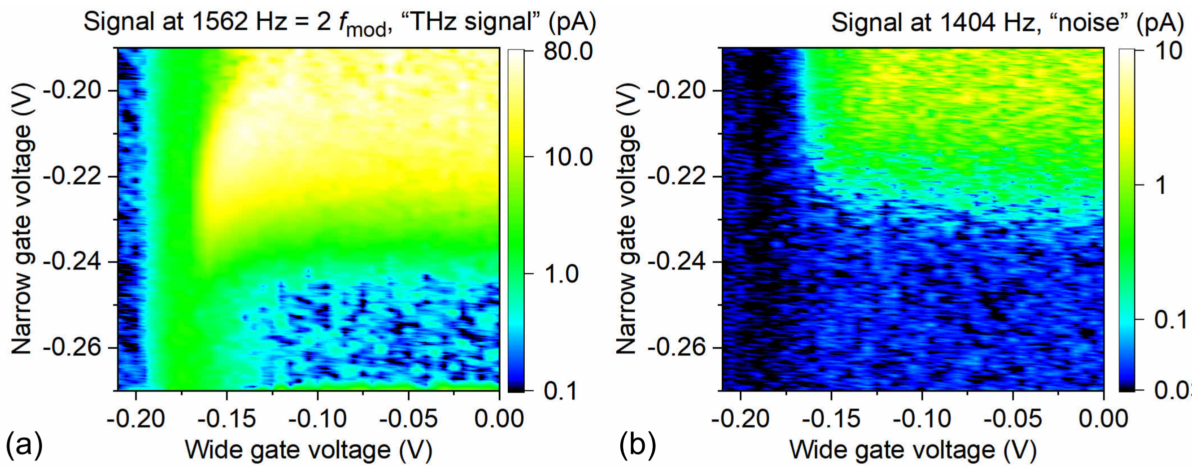

Figure 4.25: **Two-dimensional map of (a) the current at $2f_{mod}$ = 1.562 kHz and (b) the current at 1.404 kHz.** Both (a) and (b) were recorded simultaneously with a source-drain voltage of 100 mV, while the sample was exposed to THz radiation. The plot (a) is expected to show the THz signal, as it is the current at the second harmonic of f_{mod} = 781 Hz. The plot (b) provides an estimate for the noise present, which exhibits a broadband character, by a measurement of the current at an unrelated nearby frequency of 1.404 kHz. The colour scale is logarithmic to highlight all featured despite their rapid change in magnitude. The substantial amount of THz signal present in the pinch-off corner around ($U_{G,wide}$,$U_{G,narrow}$) ≈ (–0.16 V,–0.22 V) is clearly visible.

The optimum in Fig. 4.25 of $U_{G,wide}$ = –0.157 V is now chosen to study the effect of a further increase of the source-drain voltage from 0.1 V to 1.0 V, shown in Fig. 4.26. At U_{SD} = 0.3 V, the maximal photoresponse is achieved, then the amount of photocurrent saturates and slightly decays. As U_{SD} grows, the peak position shifts towards the more negative gate voltages.

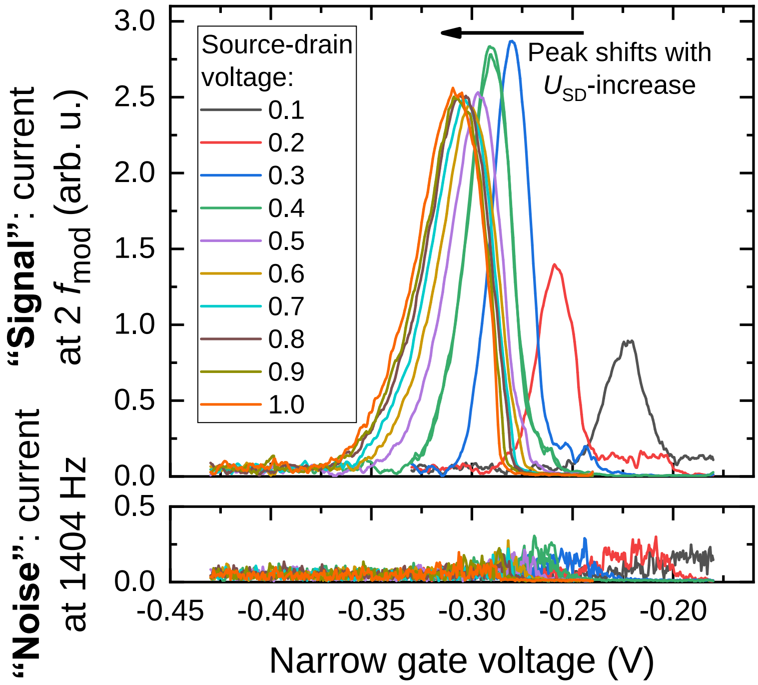

Figure 4.26: **Photoresponse dependence on the source-drain voltage.** The THz photocurrent for different source-drain voltages as indicated is measured as a function of the narrow gate voltage, with the wide gate being held at a voltage of –0.157 V, the optimum from Fig. 4.25. As in the previous figure, "noise" refers here to a simultaneous measurement of the current at 1.404 kHz which is used to estimate the broadband noise present in the measurement.

To summarise the results above, this first proof-of-principle experiment on an exemplary device proved its successful operation. The observed THz response disappears when the waveguide is blocked and can be used as an alignment signal, which proves that it is indeed originating from THz radiation and is not due to interference or inductive pick-up of the QCL current from the pulsed driver.

4.4 Optimisations and improvements of the setup

Over the course of the previous work, several issues with the setup have become apparent. Technical details of the work on eliminating them is documented in this section, whereas exciting physics awaits the reader in the next section.

4.4.1 Drift of charge carrier density

It was found that over the course of a cooldown, the charge carrier density creeps up. This is seen from repeated measurements of the threshold voltage in Fig. 4.19, which keeps shifting towards more negative values over the course of a measurement day. This can happen if ambient light is falling on the sample, releasing electrons from the doped layer and increasing the surface electron density [227]. Blocking the obvious point of entrance, the waveguide input, did not stop the process, even when room lights were switched off. As it turned out, once the cryostat was evacuated, the few millimeter thick bottom baseplate of the cryostat bends inwards, creating an approximately 1 mm thin slit, through which incident ambient light could reach the sample after being scattered on the HDPE window.

This issue was solved by glueing a black velvet piece along the perimeter of the HDPE window, see Fig. 4.27. This soft textile piece effectively blocked any ambient light: once glued in, no drifts of the conduction could be found within measurement noise, even with room lights on, provided that all waveguide inputs are blocked.

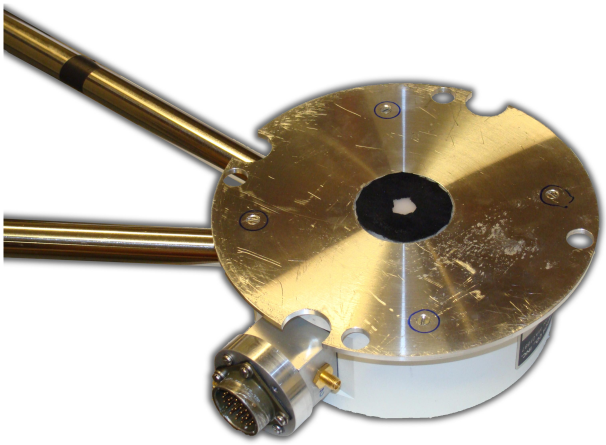

Figure 4.27: **Bottom view of the sample cryostat.** The circular black velvet piece is an effective remedy for light ingress.

4.4.2 Electrical noise

The previous measurements highlighted the need for improvements of the electrical sensitivity. Two issues had to be addressed: static noise present during the measurements, and interference of other signals at the detection frequency.

The sample breakout box present at the setup has a separate output that allows the shielding of the cable to the cryostat to be disconnected from or connected to a different potential than the breakout box itself. This option was not needed, thus the two ground planes can be connected together. The BNC terminator with 50 Ω resistance at this connection was replaced by a 0 Ω-terminator, which drastically reduced the broadband noise amplitude measured with a current preamplifier from about 10 µA to ca. 5 nA.

All BNC RG58 coaxial wires used were checked for proper contact of both shielding and inner wire as well as noise performance. Several cables that appeared visibly flawless induced a considerably higher noise in the measurement circuit and were replaced.

Apart from random noise, another issue is interference and pick-up of coherent signals at the detection frequency – the QCL modulation frequency and its harmonics. It is worth noting that the QCL driving electronics pushes pulses of around 1.5 A (Fig. 2.5) into the QCL. At the same time, the goal is to detect signals as low as a few pA (Fig. 2.5) – 12 orders of magnitude less. Any pick-up, e. g. from ground loops or improper shielding, is detrimental for the experiment. In particular, this is why it is crucial to demonstrate a difference between measurements with the waveguide input physically blocked and opened to ensure that a "true" THz signal is measured (as done in the previous section); it is not enough to see a difference with the QCL switched on or off as this may merely be a interference from the pulse electronics.

As an example, sometimes a strong signal at the modulation frequency of the QCL was detected by the lock-in amplifier when moving the sample cryostat. This artefact resulted not from a change in alignment, but from an unreliable shielding connection of the cable between cryostat and sample breakout box. Copper clamps were fabricated and soldered in place, ensuring a proper shielding of the complete system cryostat–cable–breakout box.

Some of the lock-in amplifiers used were connected to a different mains socket because of their physical position. This induced interference from the QCL pulse driver, in particular, when the outer shield of the BNC cable with the reference input was connected to a lock-in amplifier. This is one reason why a constant signal is superimposed on all THz signal measurements (Fig. 4.20, 4.23, 4.24). The setup was re-arranged so that all sensitive equipment (in particular: source-measurement unit, current pre-amplifier, and lock-in amplifiers) were all connected to the same socket following the principle of "star grounding" as far as possible.

Subsequent noise analysis and improvements showed that even better noise performance can be achieved by switching from the "single-ended" configuration, used so far, to a "true differential" measurements setup. In the "single-ended" configuration, the source contact is grounded to the BNC shield, and all other gate and drain voltages are applied via coaxial cables with respect to the common ground, i. e. the source. However, using coaxial cables as unbalanced lines leads to electromagnetic interference being introduced in the measurement through the coaxial outer wiring. In the "true differential" configuration, none of the sample contacts connect to the common ground of the measurements instruments and/or the cryostat; instead, the outer wire of the coaxial cable is used as a shield for the inner wire. This arrangement is more complicated as most of the lab instruments have single-ended outputs, therefore this required the use of a differential amplifier, and the gate voltage sources had to be decoupled from the common ground as well. But this configuration yields significantly lower noise; in particular, it was the only arrangement that allowed the noise level including electromagnetic interference to drop below the input noise of the amplifier used and was therefore used in studies of the noise-equivalent power described in section 4.5.5.

4.4.3 Liquid helium cooling

There are two main methods of cooling a cryostat to liquid helium temperatures. The first one, used so far, consists in pressurising the dewar. In this case, the return valve is closed and an overpressure of about 150–200 mbar is induced in the helium vessel. This pushes liquid helium through the transfer line into the cryostat, whose outlet is connected to the helium return system.

In the second method, the dewar is left unpressurised, and instead the cryostat is pumped on its helium gas outlet connection. The reduced pressure at the cryostat outlet draws liquid helium through the transfer line into the cryostat.

The first method has several drawbacks. The pressure in a pressurised helium vessel with a closed return valve will keep slowly rising with time. Firstly, this is a safety risk and means that the vessel cannot be left unattended for long periods of time. Secondly, this results in the helium flow steadily rising with time, making it impossible to keep the cryostat temperature stable at higher values than the boiling point of liquid helium only by limiting the flow using the needle valve on the transfer line. The second point also means that experiments with reasonable temperature stability can only be achieved at the liquid helium boiling temperature (if not using a temperature controller), in which case the helium usage will keep increasing with time from the minimal flow required to achieve base temperature. Any more helium flow than necessary is a waste of this valuable resource, reduces the amount of measurement time available given a finite amount of helium, and increases ice build-up at the helium outlet, which in turn causes undesireable dripping water after warming up.

Because of these reasons, the second method will be used for subsequent experiments. The outlets of the two cryostats (QCL and sample cryostat) were connected to a membrane pump. At each outlet, a valve restricts the helium flow to the desired amount. The output of the membrane pump is connected to the lab helium return system through a valve, with an overpressure relief valve protecting against pressure build-up due to accidental pumping against a closed valve.

This arrangement substantially reduced the amount of helium required to carry out the experiments. Previously, about 30 liters of liquid helium per 24 hours were required to cool down one cryostat. Since the QCL lases over a wide range of temperatures, it can be operated at temperatures about 16 K–20 K. The sample temperature is set to around 7.5 K–10 K. By pumping on the return, 30 L/(24 h) is enough for cooling of both cryostats. Temperature drifts were reduced to below 40 mK due to the steady flow ensured by the pump. Furthermore, the setup became intrinsically safe: there is no longer a closed vessel with rising pressure; both helium dewars are always connected to the helium return system and are thus held at almost ambient pressure. This substantially extended the available measurement time and, together with the installation of a remote power switch for the He pump, paved the way to remote operation required for subsequent long measurements.

4.4.4 Electrostatic discharge

After all previously described improvements, THz measurements were attempted again. However, upon reinsertion of the sample, several gates exhibited strong leakage currents or even Ohmic behaviour, i. e. the sample was damaged beyond recovery.

This showcased electrostatic discharge (ESD) as an unresolved issue. At any point when handling the sample, the gates may break if suddenly static charge is deposited on a contact of the chip. As a remedy, a protocol was developed to ensure all contacts of the sample are the same, known potential at any point in time when handling a sample, see Table 4.3. A similar protocol is used in reverse for removing the sample from the cryostat.

State of chip:	**Grounding is ensured by:**
(1) Chip is in ESD-safe box	ESD-safe box
↓ *take chip with earthed tweezers*	
(2) Chip is in tweezers	tweezers, operator, metallic bench grounded to earth point
↓ *push chip into LCC-socket on PCB*	
(3) Chip is in PCB holder	shorting plug connected to PCB
↓ *mount PCB on coldfinger (2nd part)*	
(4) PCB holder is glued on 2nd coldfinger part	shorting plug connected to PCB, coldfinger is on earthed metallic bench
↓ *Operator detaches earthing strap, transfers sample in holder*	
(5) 2nd coldfinger part is transferred to the cryostat	Operator connects earthing strap to cryostat ground,
↓ *sample shorting plug is removed, sample connected to internal cryostat pins*	PCB shorting plug touches cryostat ground
(6) Sample connector is connected to breakout box	All breakout box connectors are terminated with BNC50 terminators

Table 4.3: **ESD-safe protocol for sample mounting.**

4.5 Demonstration of direct THz detection

In this section, measurements on the sample V837-2-3.1 will be discussed. It has a geometry as shown in Fig. 4.5 and Fig. 4.28, which is the same as the geometry studied in section 4.3 except for a reduction of the lithographic width from 3 µm to 2 µm.

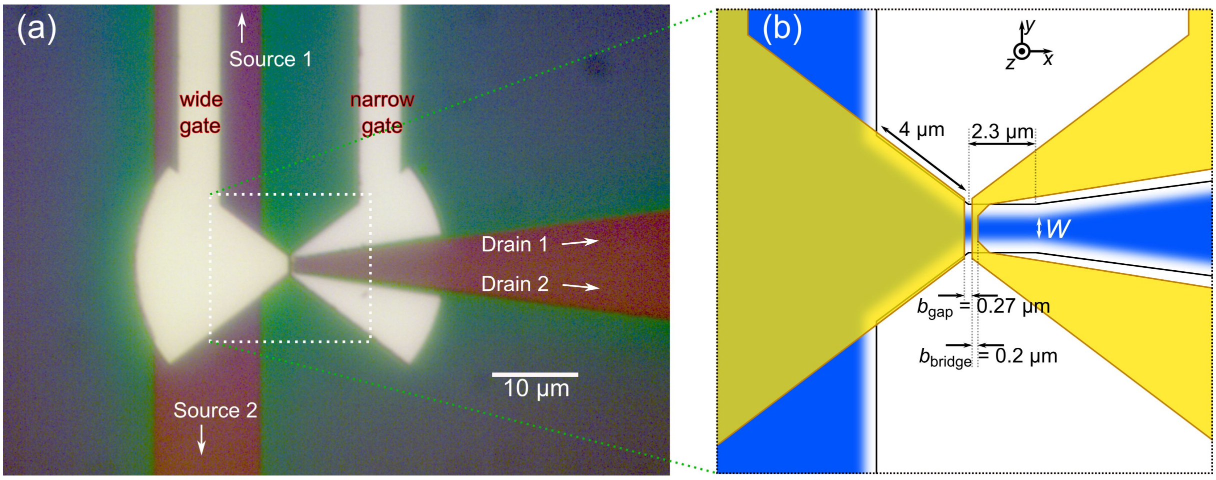

Figure 4.28: **Sample view.** (a) Optical microscope image of the sample: the wide and narrow gates are made in the form of a bow-tie antenna; the 2DEG is contacted by two source and two drain Ohmic contacts; (b) schematic illustration of the device: the black shape shows the contour of the mesa, while the blue area shows the 2DEG. Its blurred edges account for uncertainty in the amount of edge depletion; $W \sim 0.5 - 1$ µm (see section 4.7.1). The metallised gates are shown semitransparent in yellow.

4.5.1 Initial zero-bias photocurrent measurements

The sample is cooled to approximately 9 K ($k_B T \approx 0.78$ meV) in a liquid helium continuous flow cryostat (the horizontal cryostat in Fig. 2.7) while being illuminated with a yellow LED at a current of approximately 20 mA. Then the LED is switched off and the sample is exposed to 1.9 THz radiation from the single-plasmon quantum cascade laser using the THz waveguide system. The QCL is electrically modulated with a modulation frequency of f_{mod} = 764 Hz and a duty cycle of 4.11 %.

The first demonstration of a THz response presented in section 4.3 was carried out under an applied source drain bias. However, this has the disadvantage of introducing current noise into the measurements, which obscures the THz response except in the threshold region where the current is very low: only around the pinch-off region, where the current noise decays, a very clear photoresponse as shown in Figs. 4.25 and 4.26 could be observed.

Therefore, now the measurement of a photoresponse is attempted without any source-drain bias, to remove the current noise, using the circuit shown in Fig. 4.29. At zero wide gate voltage, the narrow gate voltage is tuned and the photocurrent measured with a

20 nA/V amplification setting on a SR570 current preamplifier connected to the source and drain contacts of the sample. The resulting photocurrent amplitude, measured by a lock-in amplifier at the second harmonic of the QCL modulation frequency f_{mod}, is shown in Fig. 4.30 (a).

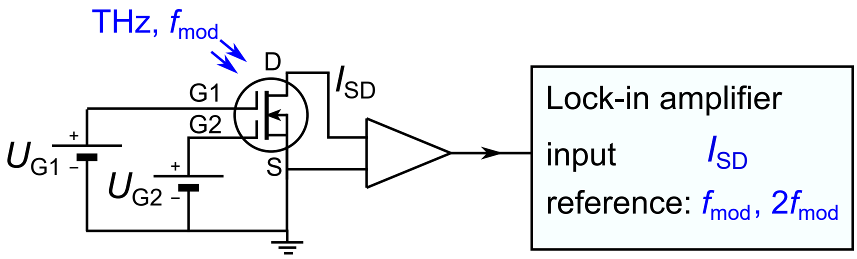

Figure 4.29: **Lock-in measurement of the THz zero-bias photocurrent.** The wide and narrow gate voltages are applied to the gates, and the source and drain contacts are directly wired to a current preamplifier connected to a lock-in amplifier, without any applied source-drain bias. The DC current and the current at the first or second harmonic of the QCL modulation frequency is measured.

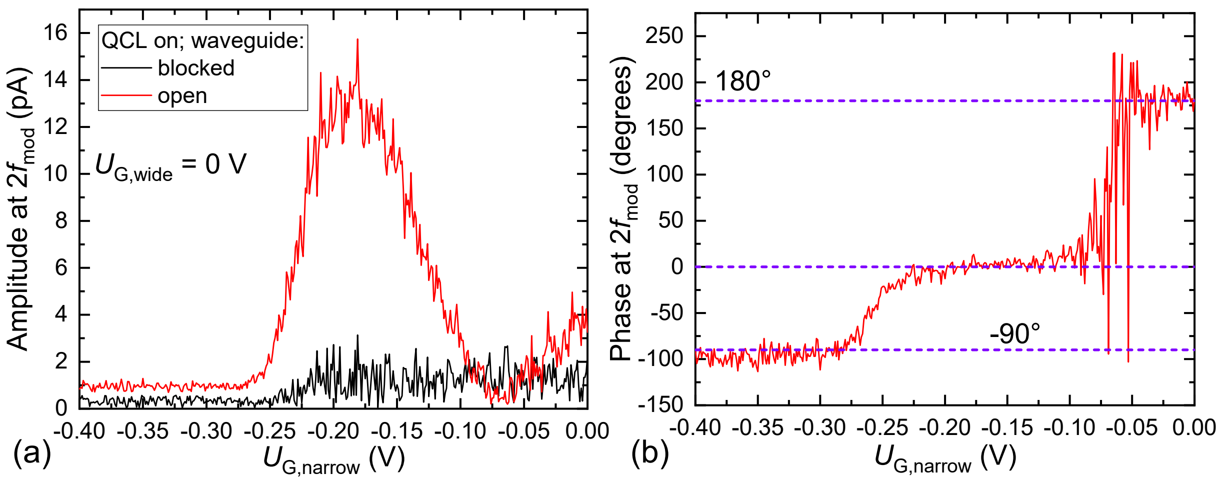

Figure 4.30: **Initial THz photocurrent measurement on the sample V837-2-3.1.** (a) Current amplitude at $2f_{\mathrm{mod}}$, measured with a lock-in amplifier at zero wide gate voltage. The black trace is with the THz waveguide input blocked, the red trace is with THz radiation incident. (b) Phase of the red signal shown in (a). The reference phase of the lock-in amplifier has been adjusted to zero degrees at the maximum response shown in (a).

A clear increase in current at $2f_{\mathrm{mod}}$ is observed when compared to the signal with the waveguide input blocked. Notably, around –0.07 V narrow gate voltage, the signal with incident THz radiation falls below the noise amplitude and then rises again. This behaviour may originate from a sign change of the photocurrent. To check this, the simultaneously acquired phase of the lock-in signal is studied in Fig. 4.30 (b). Indeed, at –0.07 V, the phase changes by 180°. For voltages below –0.3 V, the phase changes by a further 90°,

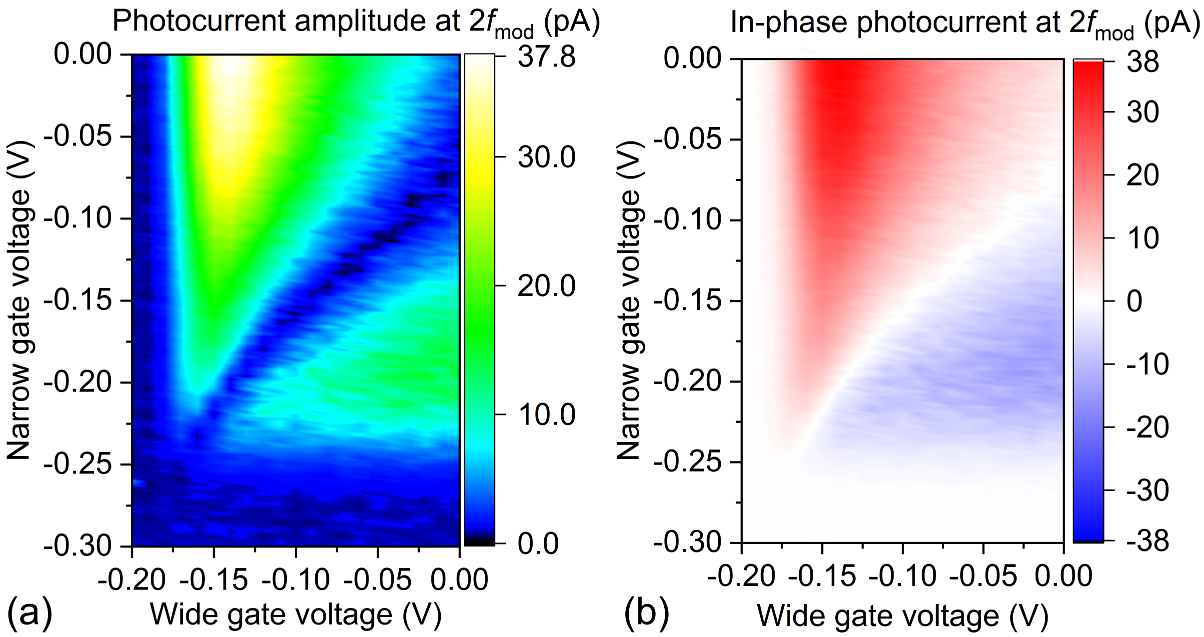

Figure 4.31: **Two-parameter map of the photocurrent at zero source-drain bias.** (a) Amplitude, (b) in-phase "X" component of the photocurrent measured using a current preamplifier at 20 nA/V amplification and a lock-in amplifier as a function of the wide and narrow gate voltages. The reference phase of the lock-in amplifier has been adjusted to yield an in-phase response at the maximum signal.

indicating a capacitive response when the conducting channel is depleted by the narrow gate.

Thanks to the zero-bias photocurrent measurement, there is now minimal noise across the whole studied gate voltage range, which reveals new features including a sign change of the photoresponse. The photocurrent is now studied as a function of both wide and narrow gate voltages, see Fig. 4.31.

These results show that there are two regions with a different sign of the photoresponse, separated by approximately a diagonal line. Additionally, it becomes clear that the response grows at the top-left area, suggesting that applying positive gate voltages may further increase the photoresponse.

To study this, a full gate voltage map is measured on the next cooldown. This time, during the cooldown the sample was illuminated with a 3 W red LED at the waveguide input. Fig. 4.32 shows the measured photoresponse, from negative voltages below threshold to positive gate voltages of 0.9 V. This demonstrates that the photoresponse can be further increased by applying positive gate voltages.

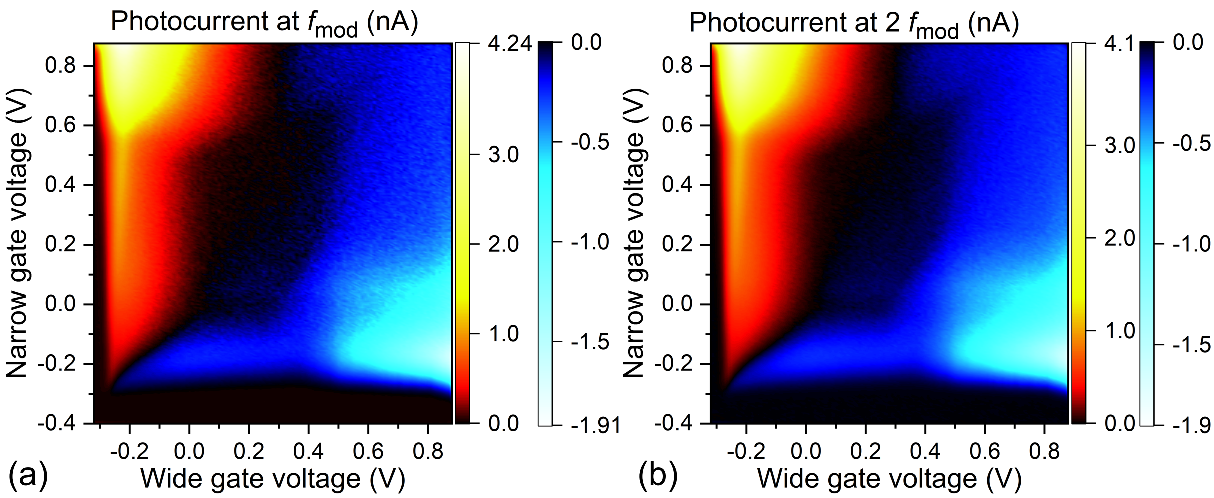

Figure 4.32: **Full gate voltage map of the photocurrent.** (a) at the modulation frequency, (b) at the second harmonic of the modulation frequency. The demodulated photoresponse is the same at $2f_{\mathrm{mod}}$ as at f_{mod} except for a marginally smaller amplitude and lower noise.

4.5.2 Conductance characterisation

The photocurrent has shown interesting features in dependence on the wide and narrow gate voltages. In order to understand them better, these results should be compared with measurements of the conductance and of the photovoltage of the sample, both of which will also depend on both gate voltages. This will be carried out in this and the next sections.

During the next cooldown, the sample is illuminated with a green 3 W LED for more than an hour, to increase electron density and mobility until saturation. Then the illumination is switched off, and the sample is left to equilibrate in the dark for another hour. It should be noted that the measurements that will be presented in Figs. 4.33–4.37 were obtained during one cooldown under stable sample conditions, which makes it possible to compare them quantitatively.

The conductance of the sample is measured in a 4-terminal configuration (as in Fig. 4.18, as a function of both gate voltages). The conductance is calculated as the ratio of current to voltage when the sample is driven with a 1.6 mV sinusoidal signal at 86.5 Hz. The current is passed through Source 1 and Drain 1, the voltage is measured from Source 2 to Drain 2 in Fig. 4.28 (a). The result is illustrated in Fig. 4.33 (a) as a function of the two gate voltages in a 2D colourmap.

At zero gate voltages, the 4-wire channel conductance is 0.92 mS, corresponding to a resistance of $R_0 \approx 1.1\,\mathrm{k\Omega}$. The conductance vanishes at the left and at the bottom in Fig. 4.33 (a), at strongly negative voltages on one or the other gate, which corresponds to the pinch-off of the channel using the wide or narrow gate, respectively.

There are many ways of determining the threshold voltage, the gate voltage corresponding to the onset of conduction. At least 11 different methods to extract the threshold voltage

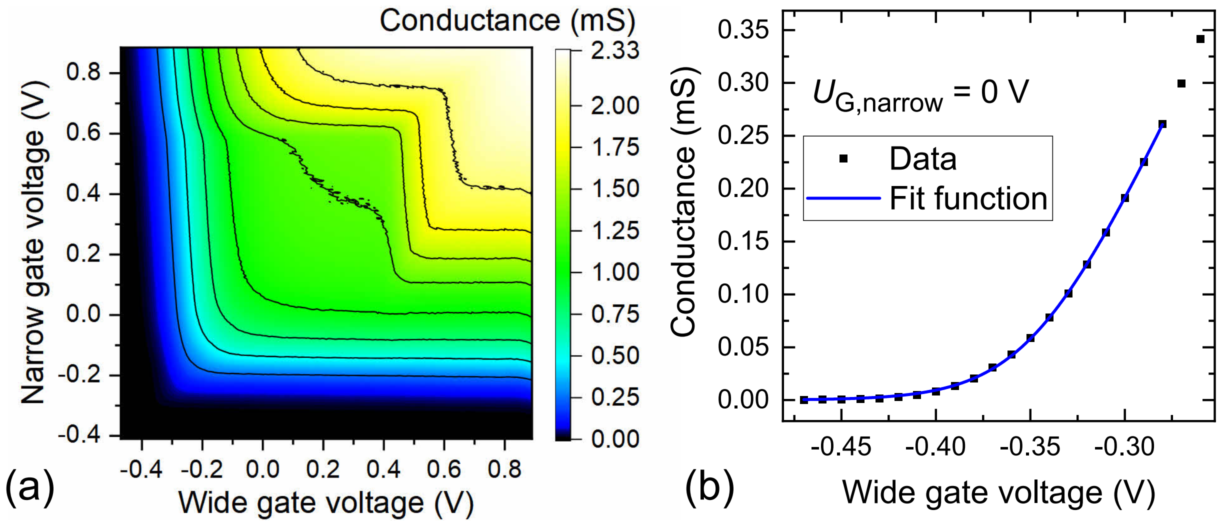

Figure 4.33: **4-terminal conductance measurement** (a) 2D map as a function of the wide gate voltage (horizontal axis) and the narrow gate voltage (vertical axis). Contour line values are indicated on the colourbar. (b) Threshold region when the wide gate is used to pinch off the channel, with 0 V narrow gate voltage.

are reviewed in Ref. [228]. A very common method relies on studying the transfer characteristic curve of a field effect transistor, and extracting the threshold voltage from the extrapolation of a linear fit to the data points above threshold.

In Fig. 4.33 (b), the conductance is plotted as a function of the wide gate. Here, a fit to the datapoints with the following function is used:

$$f(U_\mathrm{G}) = A \ln\left(1 + \exp\left(\frac{U_\mathrm{G} - U_{\mathrm{th},\sigma}}{\eta k_\mathrm{B} T}\right)\right) . \tag{4.9}$$

A function of this form describes the dependence of the charge carrier density on the chemical potential [121]; here it is used as a reasonable fit function to determine the position of the "kink" more accurately than from a linear extrapolation. This yields a threshold voltage from the conductance of $U_{\mathrm{th},\sigma} \approx -0.35$ V. At this point, the 4-wire channel resistance is 17 kΩ, 16 times higher than R_0. For $U_{\mathrm{G,wide}} < -0.44$ V, the resistance exceeds 1 MΩ, and the channel is completely switched off. The value for the ideality factor η from the fit is approximately $\eta \approx 31$.

4.5.3 Terahertz photoresponse

Now, the sample is exposed to incident THz radiation. The 1.9 THz QCL ($\hbar\omega \approx 7.9$ meV) is electrically modulated with a frequency of $f_\mathrm{mod} = 772$ Hz and a duty cycle of 2.14 %.

With incident THz radiation, the sample generates a photoresponse under zero source-drain bias. The measurement is carried out in a circuit as shown in Fig. 4.29. (A small source-drain voltage of around 1.2 mV is still applied in order to zero out the DC input offset current of the current preamplifier.)

The photocurrent is shown in Fig. 4.35. The photoresponse is mostly anti-symmetric with respect to the diagonal line $U_{\mathrm{G,narrow}} = U_{\mathrm{G,wide}}$. Compared to Fig. 4.32, the photoresponse amplitude is now more symmetric, since the sample has been illuminated until saturation, which has ionised all DX centers including those under both metallic gates. On this sample, the highest THz photoresponse is obtained when the sample is illuminated until saturation, which yields the highest electron density and mobility.

Two regimes can be identified: (i) $U_{\mathrm{G,wide}}$ and $U_{\mathrm{G,narrow}} \lesssim 0.6\,\mathrm{V}$, shown in detail at the bottom of Fig. 4.35, and (ii) $U_{\mathrm{G,wide}}$ or $U_{\mathrm{G,narrow}} \gtrsim 0.6\,\mathrm{V}$, where the photoresponse increases strongly in the top-left and bottom-right corners under strong asymmetry of the gate-induced left and right chemical potentials.

A further increase of the gate voltage, beyond $U_{\mathrm{G,narrow}} > 0.885\,\mathrm{V}$ and $U_{\mathrm{G,wide}} > 0.75\,\mathrm{V}$, leads to the onset of a rapidly growing gate leakage. This can be seen from Fig. 4.34. In this regime, undesirable for detector operation, the sample becomes unstable and noisy.

Physically blocking and unblocking the incident THz radiation did not result in any measureable change of the gate currents, see Fig. 4.34. In Fig. 4.34 (b), it can be observed that any potential difference in narrow gate leakage is less than the measurement accuracy of 10 pA, which is orders of magnitude less than the measured THz photoresponse of 2.4 nA under positive narrow gate bias in Fig. 4.35. This excludes gate currents, which could be observed as artefacts in the source-drain current measurement, as a possible origin of the photoresponse, e. g. due to Schottky barrier rectification.

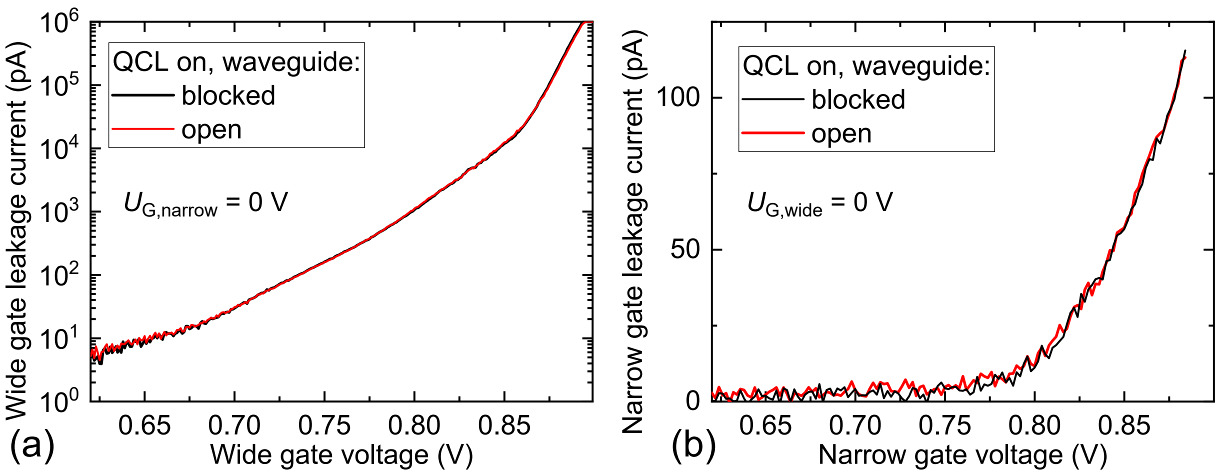

Figure 4.34: **Gate leakage currents.** (a) Wide gate leakage, with a logarithmically scaled vertical axis. (b) Narrow gate leakage, with linear scaling of the vertical axis. The comparison between red and black curves, with and without exposure to THz radiation, shows no measureable change in gate currents. In (b), it can be seen that any potential difference is less than the measurement accuracy of 10 pA.

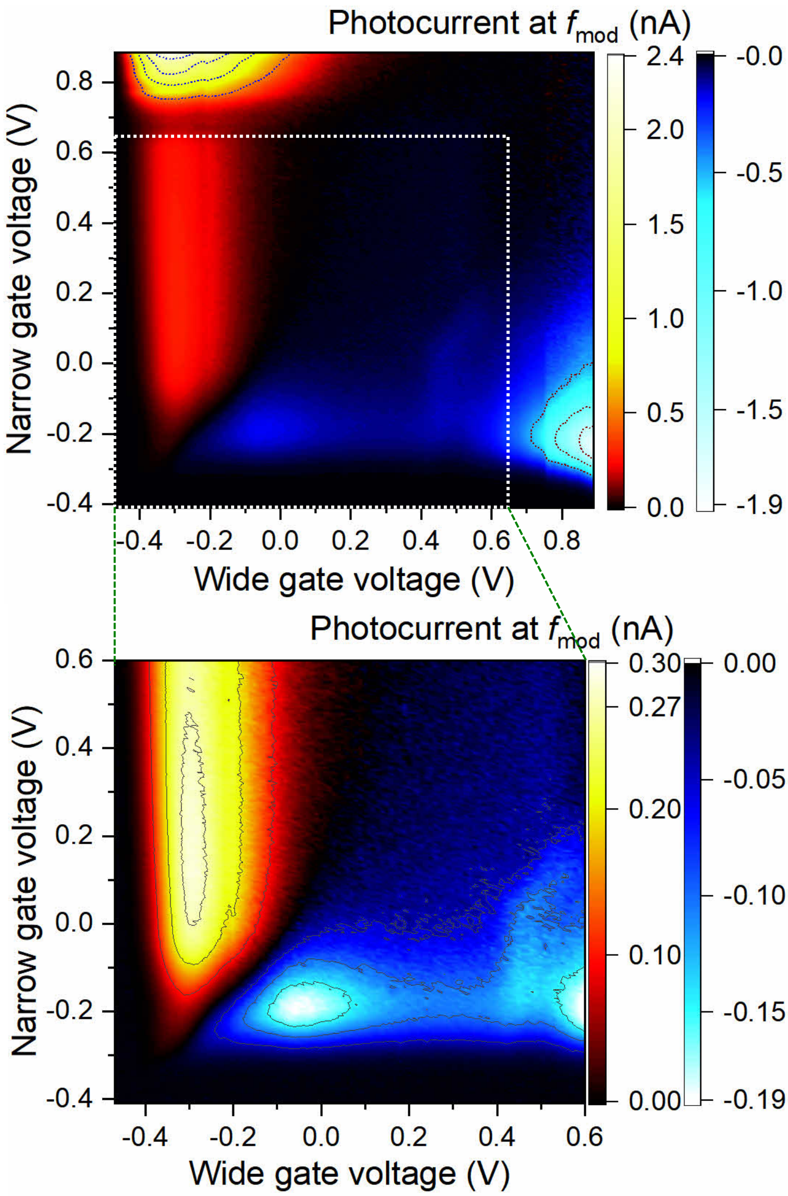

Figure 4.35: **THz photoresponse.** Photocurrent as a function of the wide gate voltage (horizontal axis) and the narrow gate voltage (vertical axis). The photoresponse changes sign; for each sign, a separate colourbar is shown. At the bottom, the region for gate voltages smaller than 0.6 V is shown.

Similarly, the photovoltage acquired in an open-circuit measurement is depicted in Fig. 4.36 (b). In this case, instead of using a current preamplifier, the source and drain contacts are directly connected to a lock-in amplifier. The measurements are done using a lock-in amplifier with the QCL modulation frequency f_{mod} as reference.

Pinching off a gate creates a potential barrier for the electrons under the gate. A negative voltage on the narrow gate creates a barrier of 0.2 µm width, whereas on the wide gate it creates a $\gtrsim$ 4 µm wide barrier, see Fig. 4.28 (b). A remarkable result is that the photoresponse changes by less than 30 %: the photocurrent amplitude in Fig. 4.35 is 2.4 nA in the top-left vs. |–1.9 nA| in the bottom-right corner; the photovoltage amplitude in Fig. 4.36 is 48 µV vs. |–42 µV| with the gate voltage polarity reversed. This is in spite of a more than 20-fold difference in barrier width. This fact rules out a tunneling origin of the effect, in which case a strong, exponential dependence on the barrier width would be expected.

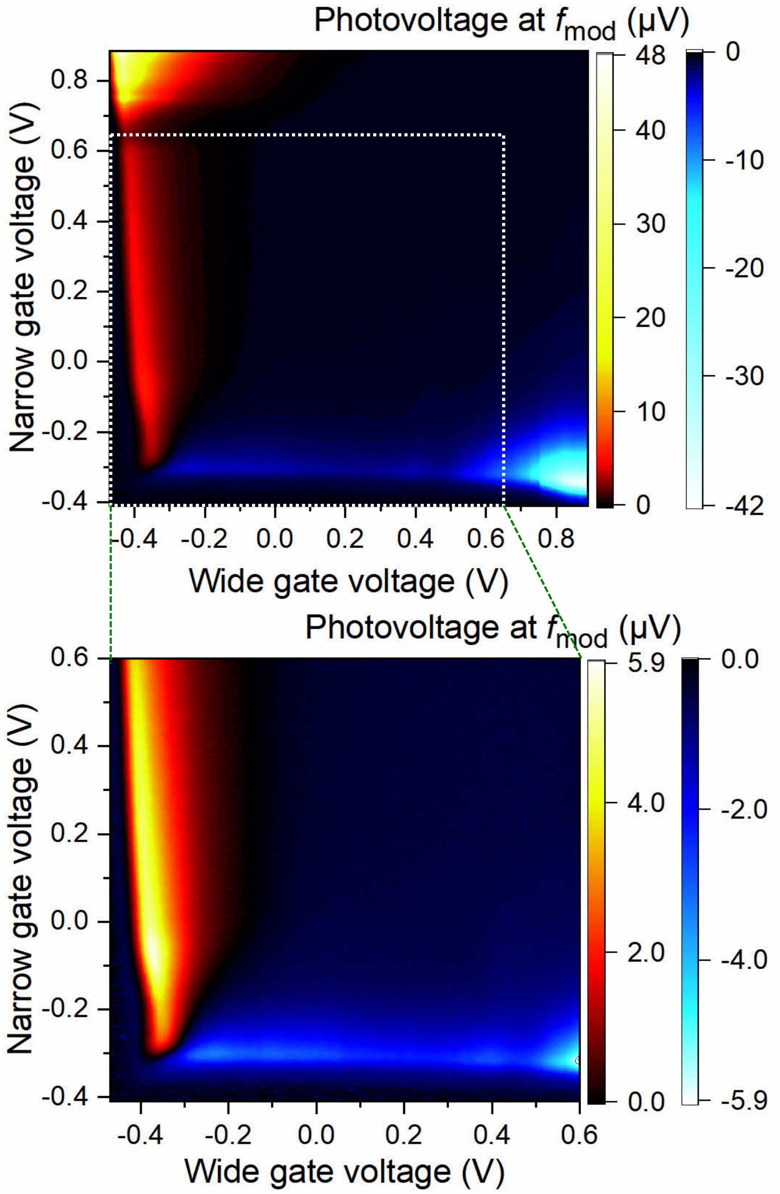

Figure 4.36: **THz photoresponse.** Photovoltage as a function of the wide gate voltage (horizontal axis) and the narrow gate voltage (vertical axis). The photoresponse changes sign; for each sign, a separate colourbar is shown. At the bottom, the region for gate voltages smaller than 0.6 V is shown.

4.5.4 Direct current measurements, responsivity, and direction of the photocurrent

The ability of the setup described in chapter 2 to measure the intensity distribution is very useful for a responsivity estimation. The total power at the sample space, where the device is placed, is determined using a Thomas Keating absolute power meter, and the intensity distribution is found by scanning a Golay cell. The time-averaged intensity is $\langle I \rangle = I_0 \cdot 2.14\% = 6.25\,\mu\mathrm{W/mm}^2$. Within a pulse, the intensity is $I_0 = 0.29\,\mathrm{mW/mm}^2$.

The best photovoltage performance is achieved at the point $(U_{\mathrm{G,wide}}, U_{\mathrm{G,narrow}}) = (-0.45\,\mathrm{V}, 0.885\,\mathrm{V})$, Fig. 4.36. At this point, the 4-wire channel resistance is $\sim 70\,\mathrm{k\Omega}$. Fig. 4.37 (a) shows the source-drain voltage measured at this gate voltage point using a DC voltmeter, while the THz radiation is mechanically blocked and unblocked. The clear DC response demonstrates that the device can operate as a direct THz detector. The DC photovoltage response is 56 µV. From the numerical finite element simulations in Comsol Multiphysics, the absorption cross section of the antenna at the THz radiation frequency is found to be $(22.5\,\mu\mathrm{m})^2$. Together with the incident intensity $\langle I \rangle$ this gives an estimate for the photovoltage responsivity of 17.6 kV/W.

The DC response makes it possible to determine the sign of the photoresponse and thus the direction of the THz-induced current flow. The photoresponse in Figs. 4.35 and 4.36 arises predominantly in the left or bottom areas in the 2D map, where either of the narrow or wide gate voltages are negative. Here, one of the gates depletes the 2DEG, creating

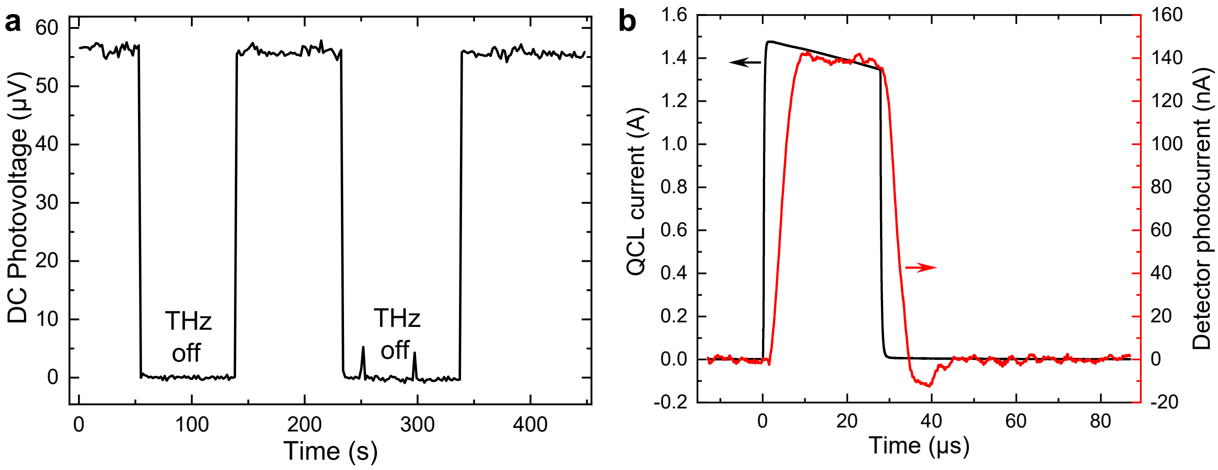

Figure 4.37: **THz detection with the presented device.** (a) DC source-drain voltage response in photovoltage readout mode $(U_{\mathrm{G,wide}}, U_{\mathrm{G,narrow}}) = (-0.45\,\mathrm{V}, 0.885\,\mathrm{V})$, when the THz waveguide is repeatedly mechanically blocked and unblocked. When the THz waveguide is open, QCL emission with 2.14 % duty cycle is incident on the sample. A maximum time-averaged DC photovoltage of 56 µV is induced by the electrically modulated QCL emission. (b) Sample response to incident THz pulses. Left axis: QCL current, right axis: measured detector current. A photocurrent of ~ 142 nA is observed during a THz pulse emitted by the QCL at the optimal photocurrent readout point $(U_{\mathrm{G,wide}}, U_{\mathrm{G,narrow}}) = (-0.32\,\mathrm{V}, 0.885\,\mathrm{V})$.

a region with a lower electron density under the gate. This gives rise to a potential step in the channel between the gates. The sign of the photoresponse is always such that the THz-induced electron flow moves from the higher density region to the lower density region, i. e. onto the potential step.

Optimal photocurrent readout is achieved at the point $(U_{\mathrm{G,wide}}, U_{\mathrm{G,narrow}})$ = (−0.32 V, 0.885 V) in Fig. 4.35, where the low output impedance of the device, $\sim$ 2.6 kΩ, allows for fast detection of the photocurrent. Notably, the best photocurrent is thus achieved when the device is far from pinch-off: the channel resistance is merely 2.4 times higher than at zero gate voltages. Fig. 4.37 (b) shows the response to incident THz pulses from the QCL on a microsecond time scale under these conditions. The rise and fall times of the detector are limited by the bandwidth of 200 kHz of the current preamplifier used, a Stanford Research model SR570. During a pulse, the THz intensity $I_0 \approx$ 0.29 mW/mm^2 yields a photocurrent of ∼142 nA. This is higher than the 2.4 nA photocurrent observed in Fig. 4.35 since the response corresponds to the THz intensity during a pulse, I_0, rather than the time-averaged intensity $\langle I \rangle$ that corresponds to the lock-in measurement. With the same absorption cross section of (22.5µm)^2, the photocurrent responsivity can thus be estimated as 0.96 A/W.

4.5.5 Noise-equivalent power

The noise of the THz detector is characterised by amplifying the voltage between the source and drain contacts with a differential amplifier and capturing a voltage time trace of 1 s length and 1 µs step size with an oscilloscope. The sample is put in the photocurrent operating point, where the 2-wire source-drain resistance is 3.24 kΩ. The THz input to the sample is blocked. As reference, the amplifier output voltage is captured with its input shorted. In the measurement data, hum from the 50 Hz mains voltage is present. To remove this, the oscilloscope trigger is set to the mains frequency, and for each noise measurement, a set of many voltage traces is averaged (corresponding to ca. 1500 mains voltage periods in total). This reveals the interfering mains voltage signal that is subtracted from the voltage traces.

After this, a fast fourier transform (FFT) is performed on the voltage time traces, which gives the spectral voltage noise density, see Fig. 4.38. Two measurements are presented: a measurement of the sample noise between the source-drain contacts, which includes the noise of the sample as well as the noise of the amplifier, and a measurement without sample, with the input of the amplifier shorted. The latter is a reference measurement that characterises the noise of the amplifier only.

The difference between the two spectra corresponding to the THz detector noise, “amplifier + sample” minus “amplifier only”, is substantially lower than the internal voltage noise of the amplifier. The five sharp peaks above 1 kHz do not originate from the sample; they

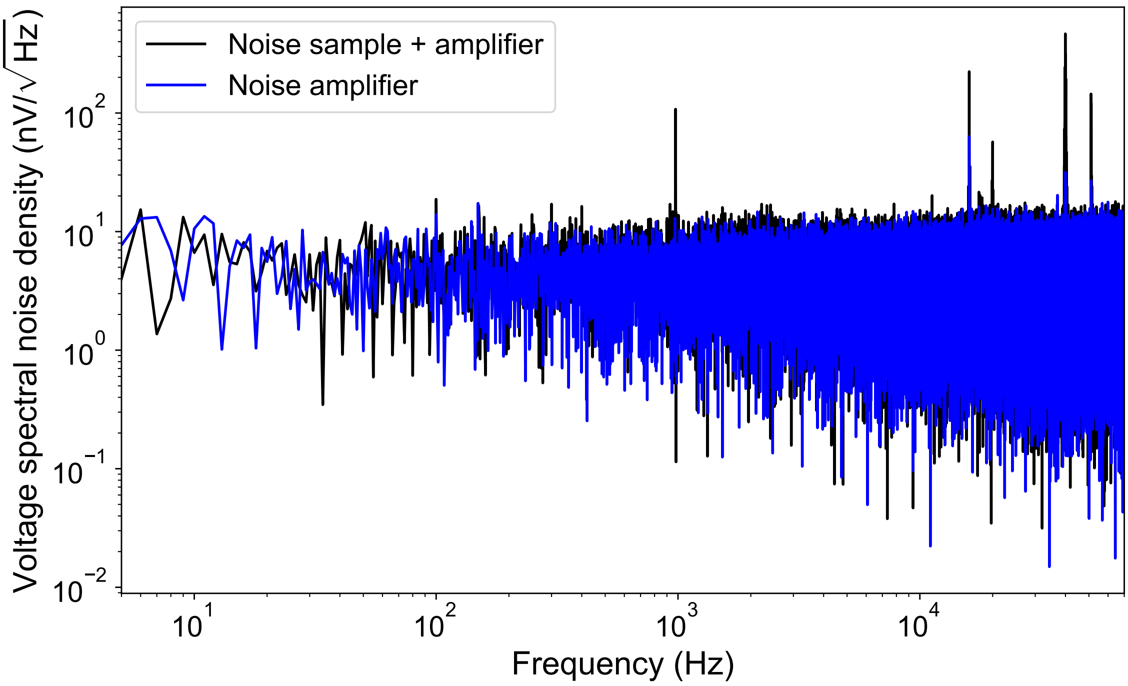

Figure 4.38: **Spectral voltage noise density as a function of frequency in a double-logarithmic plot.** The measured noise in the frequency domain is shown for the amplifier connected to the source-drain contacts of the sample (black, "Noise sample + amplifier") and, as reference, for the amplifier input shorted (blue, "Noise amplifier").

arise from electromagnetic pick-up of interfering signals in the lab that are also present with a floating amplifier input, without the THz detector sample.

To visualise this small difference in Fig. 4.39, it is convolved with a normalised, power-conserving Gaussian function $e^{-(f/\sigma)^2}/(\sqrt{\pi}\sigma)$ in the frequency domain with $\sigma = 400$ Hz. Although this decreases the frequency resolution, it reveals the low spectral voltage noise density of the detector sample.

The theoretical, lowest physically possible noise level corresponds to the Johnson-Nyquist noise of the source-drain sample resistance at the temperature 9.6 K. It is shown for comparison in blue, for the resistance of the sample and the temperature during the noise measurement. It represents the minimum possible noise for a sample of this resistance.

From the voltage noise density, the noise equivalent power (NEP) is calculated. The current responsivity of 0.96 A/W at the point of optimal photocurrent read-out is transformed into a voltage responsivity over the 3.24 kΩ 2-wire source-drain resistance. The NEP as a function of measurement bandwidth is shown in Fig. 4.40. In-between 100 and 900 Hz, the NEP is about 1.1 pW/√Hz. If the only noise source of the sample were Johnson noise of the source-drain resistance, the given responsivity would correspond to a noise-equivalent power of 0.42 pW/√Hz. The difference to the experimentally measured value is related to remaining noise pick-up and electromagnetic interference.

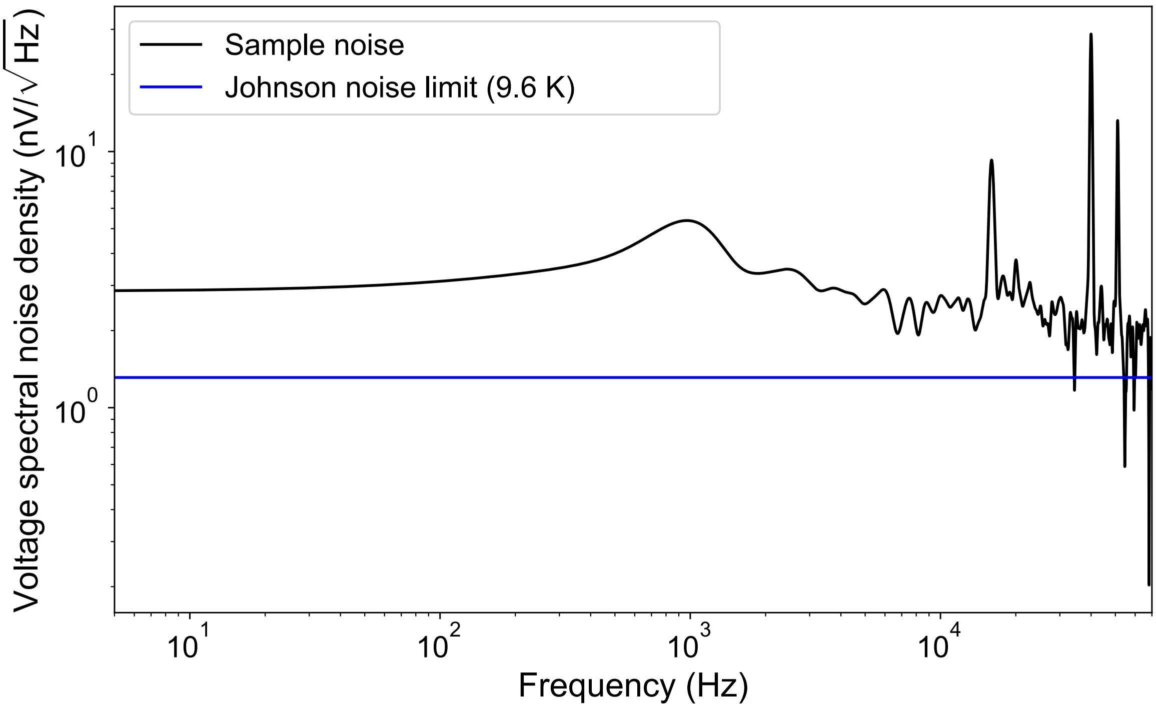

Figure 4.39: **Noise of the THz detector sample.** Difference between "sample + amplifier" and "amplifier only" signal from Fig. 4.38, averaged with a Gaussian in the frequency space.

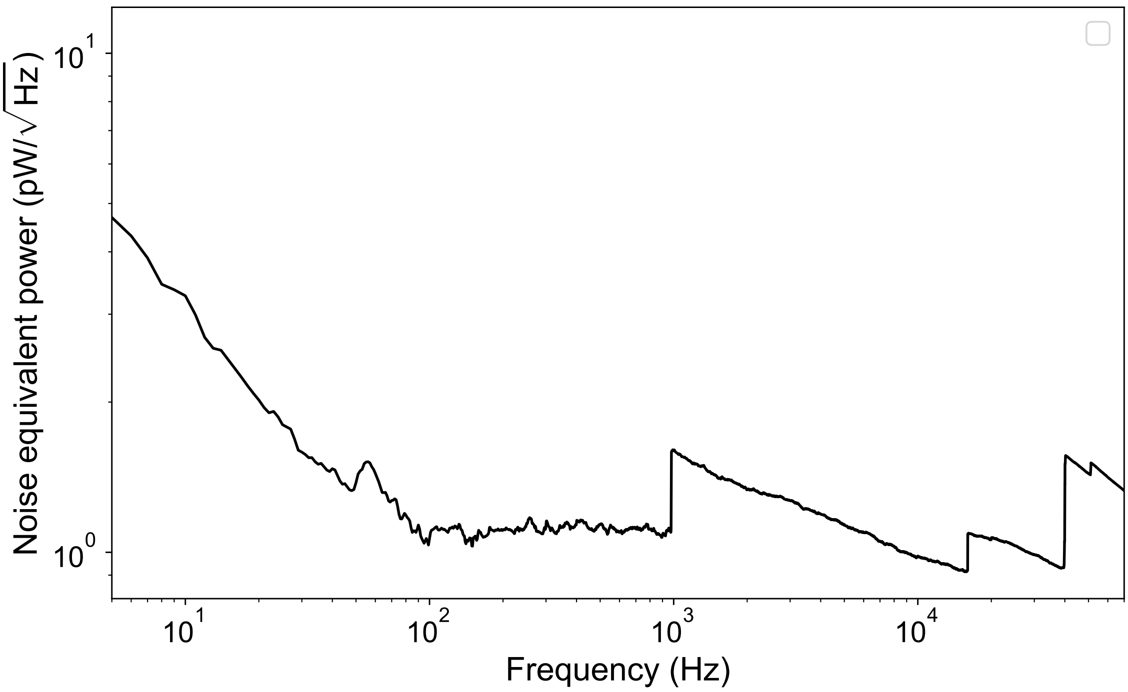

Figure 4.40: **Noise-equivalent power** of the sample in the photocurrent readout mode in a double-logarithmic plot as a function of frequency.

4.5.6 Tunable output impedance

A key advantage of the dual-gate design is the independent tuning of output impedance and responsivity. By following an equi-photocurrent line in Fig. 4.35, the responsivity stays constant, while the output impedance can be tuned over a wide range, see Fig. 4.33 (a). This facilitates impedance matching of the device to external circuitry – a capability which is inherently built-in within the device design. Alternatively, detection sensitivity can be switched on or off with the gate voltages, while maintaining the device's impedance by following an equi-conductance line in Fig. 4.33 (a), thus making it appear the same in the external circuit. The target working point for a desired photocurrent response and output impedance, i.e. the two gate voltages, is to be determined from the intersection of equi-photocurrent contours in Fig. 4.35 with equi-conductance contours in Fig. 4.33 (a).

The available range, in which a user can freely choose the desired responsivity and output impedance, is shown in Fig. 4.41, where the photoresponse is plotted as a function of the device conductance. Each point in the 2D scatter plot corresponds to a given wide and narrow gate voltage. As an example, the range for a photocurrent amplitude of 1.5 nA (63 % of the maximum value) is shown: by tuning the gate voltages, the THz detector's output resistance can be adjusted from 7.7 kΩ (0.13 mS) to 0.79 kΩ (1.27 mS) while the device yields a given photocurrent value of 1.5 nA in response to the incident THz radiation. For a negative photocurrent of –1.5 nA, the output impedance range is 17 kΩ–2.4 kΩ (0.06 mS–0.41 mS).

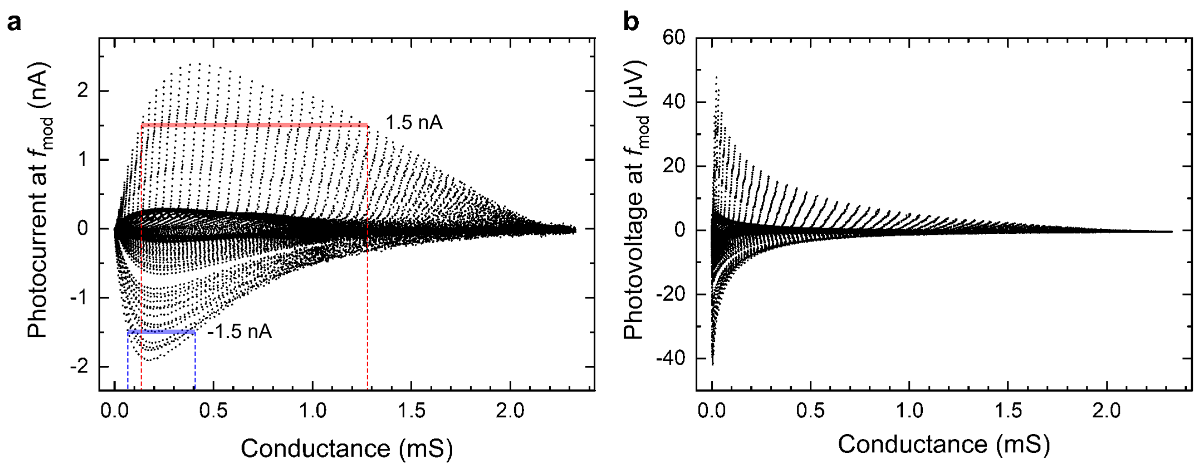

Figure 4.41: **Available photoresponse–output impedance ranges.** (a) Photocurrent and (b) photovoltage as a function of 4-wire sample conductance. Each data point corresponds to a certain value of the wide and narrow gate voltages. The area enclosed by the data points indicates the available range of responsivity and resistance. For impedance matching to external circuits, the wide and narrow gate voltages should be chosen at the intersection of the desired photoresponse and output impedance. As an example, the available conductance range available for a photocurrent amplitude of 1.5 nA is shown.

4.5.7 Use as a power detector

The sample can readily be used as a direct THz detector. Two examples are shown in Fig. 4.42.

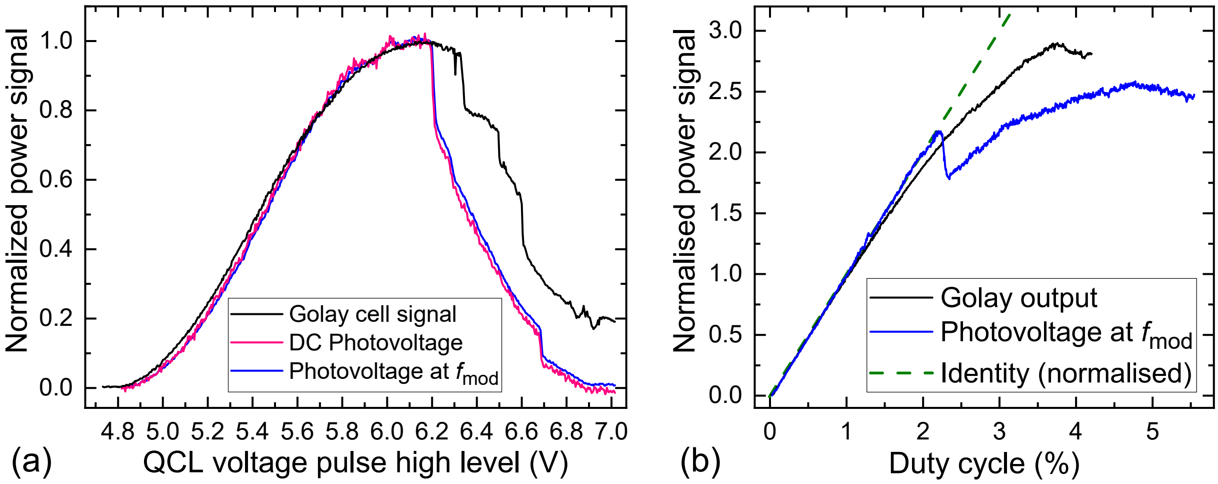

Figure 4.42: **The sample used as a THz detector:** (a) QCL characterisation using both Golay cell and detector sample. All curves are normalised to a maximum of 1.0 for comparison. The QCL high level pulse is tuned while the duty cycle is held at 2.14 %. (b) Dependence of the Golay cell and the detector sample response on the duty cycle of the QCL driving pulses, while the QCL high voltage level is set to 6.184 V. Both curves are normalised to a derivative of 1.0/% at low duty cycles. The identity relationship as a guide to the eye is shown as a dashed line. The measurements were carried out at 772 Hz QCL driving frequency and photovoltage detection mode of the sample.

In Fig. 4.42 (a), the voltage of the QCL is tuned, and its output power is measured. For the detector sample, the response is shown as both DC photovoltage measured using a Keithley 2700 multimeter, and as the response at f_{mod}. They are compared with the corresponding Golay cell response to the QCL power obtained in a separate measurement. Up to the maximum power point (~ 6.2 V QCL voltage), the measurements agree very well. The sample accurately reproduces the dependence of the power on the QCL voltage, even in a direct DC measurement, in spite of having a significantly smaller aperture than the Golay cell.

Fig. 4.42 (b) shows a dependence on the QCL power, which is tuned by changing the duty cycle of the incident PWM (pulse width modulation) signal. The dashed line is the identity line in this plot, having a slope of 1.0/% (i. e. 1.0 per percent or 100). All curves have been normalised to this derivative value at low duty cycles to make them comparable. The detector has a linear response on the power and exhibits a better linearity than the Golay cell.

At high powers in Fig. 4.42 (b), and at high voltages in Fig. 4.42 (a), the detector sample response deviates from the Golay cell response. The origin is seen from the QCL spectrum,

Fig. 2.6: approximately at that point, the QCL switches to a different frequency. The sudden power drop does not result from a different response of the antenna, which is very broadband (Fig. 4.3); in fact it is the waveguided THz delivery system that is responsible for this. The waveguided system was aligned at the maximum power in Fig. 4.42 (a) (6.184 V QCL high level voltage, 2.14 % duty cycle). As discussed in section 3.2, the waveguide focus position, and the output mode profile in general, is very sensitive to small changes in the radiation wavelength. On top of that, the sample surface is reflective, which induces standing waves in the waveguided system. Therefore, a small change in frequency of the QCL from 1.881 THz to 1.904 THz can result in constructive interference at the sample changing to destructive. The precise voltages where a sudden drop in power occurs in Fig. 4.42 (a) can be different in the Golay cell measurement and in the sample response since QCL operation becomes unstable after the maximum power point.

The Golay cell does not pick up the slight change in frequency due to its large input aperture. This highlights how the THz waveguided system in combination with the sensitive detector has the potential to be used as a frequency-sensitive measurement setup, that is capable of distinguishing between single QCL modes.

4.5.8 Reproducability of results

The THz photoresponse of sample V837-2-3.1, that was previously studied in this section, is also reproduced on other samples. For example, Fig. 4.43 shows a photocurrent

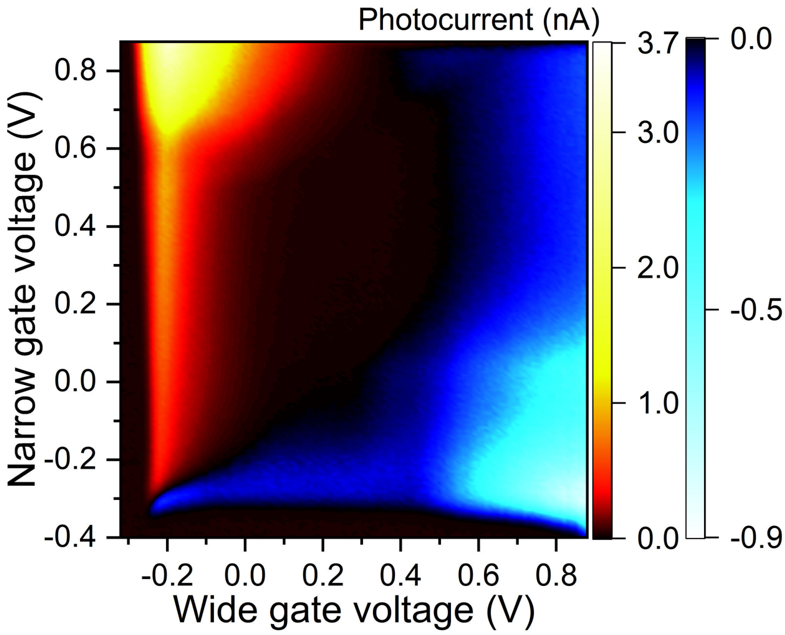

Figure 4.43: **THz photoresponse of sample V837-3-3.1.** Photocurrent observed under illumination with a 1.9 THz QCL modulated at 772 Hz with a duty cycle of 2.14 %, i. e. under the same electrical configuration as in Fig. 4.35.

measurement on sample V837-3-3.1, which has the same lithographical geometry. Both quantatively and qualitatively, a similar response is obtained. The qualitative form is in particular very similar to the one seen in Fig. 4.31.

Fig. 4.43 shows a measurement of the upper device on the sample. An analogous response is seen on the lower device with a photocurrent ranging from 2.09 to –0.74 nA; the main reason for the discrepancy is likely a slightly different alignment condition for the lower antenna. This shows that the THz photoresponse demonstrated in this section is a reproducible effect that is observed across multiple devices.

In addition, it is worth noting that a similar response although lower in magnitude was observed on the samples V837-4-3.1 and V837-3-4.1, which had high Ohmic contact resistances or high gate leakage, respectively, and V837-3-3.2 (see Table 4.2).

4.6 Electron density and mobility measurements on a reference Hall bar

Subsequent analysis will require a good understanding of the density and mobility of the used 2DEG, including their dependencies on the gate voltage. To characterise these magnetotransport characteristics of the bulk 2DEG in the wafer, measurements were done on reference Hall bars in a magnetic field. After a brief overview of electron transport physics in a magnetic field, the fabrication procedure of the Hall bars as well as the corresponding measurements and analysis are described. Following that, the results are explained and interpreted.

4.6.1 Electron transport in a magnetic field: an overview

The Hall effect describes the generation of a voltage perpendicular to the motion of charge carriers. It has its origin in the Lorentz force. A charge q moving in transverse electric and magnetic fields, $\vec{E} = E\vec{e}_\mathrm{x}$ and $\vec{B} = B\vec{e}_\mathrm{z}$, experiences the force $\vec{F} = q\vec{E} + q\vec{v} \times \vec{B}$. Without magnetic field, $\vec{F} \parallel \vec{E}$, but with $B \neq 0$, the Lorentz force leads to an electron flow in the direction perpendicular to the externally applied E-field in x-direction. In the case of a finite 2DEG in the x-y-plane, the electron flow will stop once it hits the boundaries in y-direction, and will lead to the build-up of an electric field E_y. In steady state, the y-component of the force will thus cancel:

$$F_\mathrm{y} = 0 = q(E_\mathrm{y} - v_\mathrm{x}B_\mathrm{z}) \quad \Rightarrow \quad E_\mathrm{y} = v_\mathrm{x}B_\mathrm{z}\,. \tag{4.10}$$

If the width of the 2DEG in y-direction is W, the voltage in y-direction will be $U_\mathrm{y} = E_\mathrm{y}W$. The current in x-direction is $I_\mathrm{x} = n_\mathrm{s}qv_\mathrm{x}W$. This way, the Hall resistance can be derived:

$$\frac{U_\mathrm{y}}{I_\mathrm{x}} = \frac{B_\mathrm{z}}{n_\mathrm{s}q} = \frac{E_\mathrm{y}}{j_\mathrm{x}} \equiv \varrho_\mathrm{yx} \,. \tag{4.11}$$

The transverse, "Hall" voltage U_y is proportional to the magnetic field, and the slope of the transverse resistance plotted as a function of the magnetic field,

$$\frac{\varrho_\mathrm{yx}}{B_\mathrm{z}} = \frac{1}{n_\mathrm{s}q} \,, \tag{4.12}$$

allows to find the sign of the charge carriers (hole vs. electron gas, $q = \pm e$) as well as the 2D charge carrier density n_s.

More generally, magnetotransport is described by a conductivity tensor $\overleftrightarrow{\sigma}$ or a resistivity tensor $\overleftrightarrow{\varrho}$, which is derived as follows. The force acting on electrons is described using the equation

$$m\dot{\vec{v}} = q\vec{E} + q\vec{v} \times \vec{B} - m\frac{\vec{v}}{\tau} \,. \tag{4.13}$$

If $\vec{B} = 0$, the equation yields the Drude conductivity formula. If $\vec{B} \neq 0$, the formula yields the conductivity in a magnetic field. Here, we are interested in low-frequency/DC measurements of the conductivity in a magnetic field and will consider the steady state solution with $m\dot{\vec{v}} = 0$. As the current density $\vec{j}$ equals $\vec{j} = nq\vec{v}$, the solution of the linear system of the two coupled equations for v_x and v_y yields

$$\vec{j} = \overleftrightarrow{\sigma}\vec{E} \quad \Leftrightarrow \quad \begin{pmatrix} j_\mathrm{x} \\ j_\mathrm{y} \end{pmatrix} = \begin{pmatrix} \sigma_\mathrm{xx} & \sigma_\mathrm{xy} \\ \sigma_\mathrm{yx} & \sigma_\mathrm{yy} \end{pmatrix} \cdot \begin{pmatrix} E_\mathrm{x} \\ E_\mathrm{y} \end{pmatrix} \;\text{ with }\; \overleftrightarrow{\sigma} = \frac{\sigma_0}{1 + \omega_\mathrm{c}^2\tau^2} \begin{pmatrix} 1 & \omega_\mathrm{c}\tau \\ -\omega_\mathrm{c}\tau & 1 \end{pmatrix} \tag{4.14}$$

The relationships $\sigma_\mathrm{xx} = \sigma_\mathrm{yy}$ and $\sigma_\mathrm{xy} = -\sigma_\mathrm{yx}$ hold for an isotropic two-dimensional electron gas. $\sigma_0 = nq\mu$ is the Drude conductivity of the material without a magnetic field. The inverse of the conductivity tensor $\overleftrightarrow{\sigma}$ is the resistivity tensor $\overleftrightarrow{\varrho}$:

$$\vec{E} = \overleftrightarrow{\varrho}\vec{j} \;\;;\;\; \overleftrightarrow{\varrho} = \overleftrightarrow{\sigma}^{-1} = \begin{pmatrix} \varrho_\mathrm{xx} & \varrho_\mathrm{xy} \\ \varrho_\mathrm{yx} & \varrho_\mathrm{yy} \end{pmatrix} = \frac{1}{\sigma_\mathrm{xx}^2 + \sigma_\mathrm{xy}^2} \begin{pmatrix} \sigma_\mathrm{xx} & -\sigma_\mathrm{xy} \\ \sigma_\mathrm{xy} & \sigma_\mathrm{yy} \end{pmatrix} = \begin{pmatrix} \frac{1}{\sigma_0} & -\frac{B}{nq} \\ \frac{B}{nq} & \frac{1}{\sigma_0} \end{pmatrix} \tag{4.15}$$

The components of the resistivity tensor can be measured using a four-contact geometry on a rectangular stripe of 2DEG, a "Hall bar", of width W and length L. A current is passed through the stripe, and side contacts measure the voltage along ($\varrho_\mathrm{xx}j_\mathrm{x}L = \varrho_\mathrm{xx}IL/W = R_\mathrm{xx}I$) or across ($\varrho_\mathrm{yx}j_\mathrm{x}W = \varrho_\mathrm{yx}I = R_\mathrm{yx}I$) the stripe, since this measurement geometry corresponds to the $j_\mathrm{y} = 0$ boundary condition at the edges of the stripe.

The above is the classical picture of electron transport in a magnetic field. In reality, quantum effects starts to determine the transport behaviour at low temperatures and high magnetic fields. In quantum mechanics, the electron motion in a magnetic field $B\vec{e}_z$ is described by the Schrödinger equation [194, 195, 229–231]

$$\hat{H}\Psi|S\rangle = \left[\frac{(\hat{\vec{p}}+e\hat{\vec{A}})^2}{2m} + g\mu_B B\frac{\hat{\sigma}_z}{2}\right]\Psi|S\rangle = E\Psi|S\rangle \text{ , with } \vec{A} = Bx\vec{e}_y \tag{4.16}$$

being a possible choice of the vector potential $\vec{A}$ with $\vec{B} = \vec{\nabla} \times \vec{A}$, that fulfils the Coulomb gauge $\vec{\nabla} \cdot \vec{A} = 0$. In the 3D case, the equation can be solved using the ansatz $\Psi = e^{ik_y y}e^{ik_z z}\varphi(x)$ for the wave function in position space, with plane waves in the y- and z-direction. In the z-direction parallel to the magnetic field, the electrons behave as usual free electrons with dispersion $E_z = \hbar^2 k_z^2/(2m_{\mathrm{eff}})$. In the case of a 2DEG confined in z-direction, discrete energy levels in z-direction, the subbands, will be seen. In the perpendicular plane, the Schrödinger equation is transformed to the equation of the harmonic oscillator:

$$\left(\frac{\hat{p}_x^2}{2m} + \frac{m\omega_c^2}{2}\left(x + \frac{\hbar k_y}{m\omega_c}\right)^2\right)\varphi(x) = \left(E - E_z - E_{\mathrm{Spin}}\right)\varphi(x) \tag{4.17}$$

Here, $\omega_c = eB/m$ is the cyclotron frequency, and $\lambda_m^2 = \hbar/(m\omega_c) = \hbar/(eB)$ can be introduced as the magnetic length. The oscillator center position is $-\lambda_m^2 k_y$. The resulting electron energy is

$$E = E_z + \hbar\omega_c\left(n + \frac{1}{2}\right) + g\mu_B B S_z \text{ with } S_z = \pm\frac{1}{2}\,, \tag{4.18}$$

i.e. the electron motion in the x-y-plane becomes quantised. The quantised energy levels are called Landau levels. Each of them has a certain density of states, or maximum occupation number, which in Landau's approach [229] (not considering edge states [232]) is determined by restricting the oscillator position to the dimensions of the sample, which shall have the sizes L_x and L_y:

$$0 < \lambda_m^2 k_y < L_x \;\;;\;\; k_y = \frac{2\pi}{L_y}N \;\;\Rightarrow\;\; \frac{N}{L_x L_y} < \frac{eB}{2\pi\hbar}\,. \tag{4.19}$$

Here, N is the number of states, and the formula gives the maximum electron density that a Landau level can support. In a sample with a given electron density n_s, this allows the definition of the *filling factor*

$$\nu = \frac{n_s}{N/(L_x L_y)} = 2\pi n_s \lambda_m^2 = \frac{h n_s}{eB}\,. \tag{4.20}$$

The quantised energy levels lead to a quantisation of the transverse resistance ϱ_{xy} – the *quantum Hall effect* [193, 195]. ϱ_{xy} takes the values corresponding to integer filling factors

$\nu \in \mathbb{N}$:

$$\varrho_{xy} = \frac{B_z}{n_s e} = \frac{h}{e^2 \nu} \,. \tag{4.21}$$

From the argumentation above alone it is not yet clear why ϱ_{xy} would stabilise at integer filling factors. To explain this, localisation of electron states is considered [195]. According to Eq. (4.18), the density of states consists of a set of delta functions corresponding to the spin-split Landau levels. In a real sample, these energy levels will be broadened as shown in Fig. 4.44 (a). At the center positions of the Landau levels, there are extended states shown in blue – these states contribute to the electron transport through the sample. At the tails of the Landau level peaks, there are localised states, which do not contribute to the electron transport, but provide energy levels that can take up electrons [233]. When the Landau level spacing is tuned by changing the magnetic field, the transport properties do not change while the chemical potential goes through the localised states. Therefore, around integer filling factors, the Hall resistance exhibits plateaus.

At the same time, the quantisation gives rise to oscillations of the longitudinal resistance – the *Shubnikov-de Haas effect* [194, 234]. Electron transport is possible when the chemical potential lies within the extended states of a Landau level, but at integer filling factors, the chemical potential lies between Landau levels, suppressing the longitudinal conduction of the 2DEG, σ_{xx}. At low temperatures and high magnetic fields (i. e. large spacing between the Landau levels), this results in the longitudinal conductance dropping to zero around integer filling factors, when the chemical potential lies in the localised states. At lower magnetic fields, the longitudinal resistance displays oscillations that behave as (Eqs. (6.66)-

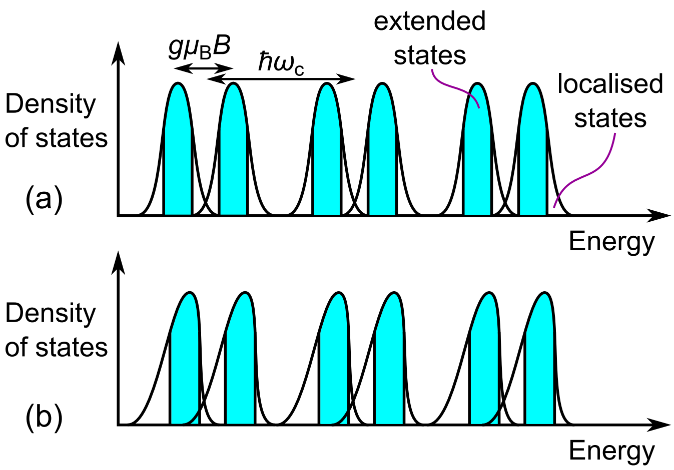

Figure 4.44: **Density of states of the spin-split Landau levels.** (a) symmetric broadening, (b) asymmetric broadening with low-energy tail expected for attracting impurities.

(6.67) in Ref. [194])

$$\sigma_{\mathrm{xx}} \sim \cos\left(\frac{2\pi\mu}{\hbar\omega_{\mathrm{c}}}\right) \underset{\mu = \pi\hbar^2 n_{\mathrm{s}}/m}{\overset{\uparrow}{=}} \cos\left(2\pi \cdot \underbrace{\frac{h n_{\mathrm{s}}}{2e}}_{\text{frequency}} \cdot \frac{1}{B}\right). \tag{4.22}$$

When σ_{xx} or ϱ_{xx} is plotted as a function of $1/B$ for low magnetic fields, it exhibits harmonic oscillations, whose frequency allows determination of the electron density n_{s}. Compared to determining the electron density from the transverse Hall voltage, this comprises an alternative method to find n_{s} based on the longitudinal magnetoresistance oscillations.

Since the conductance is proportional to the density of states at the Fermi level, the shape of the Shubnikov-de Haas oscillations can be understood as a probe of the density of states at larger magnetic fields, where individual spin-split Landau levels can be recognised. From symmetrical tails of the Landau levels, symmetrical Shubnikov-de Haas oscillations would be expected. In the case of attractive impurities, the Landau levels are expected to exhibit more localised states on the low-energy side, which would lead to an asymmetric broadening as shown in Fig. 4.44 (b). The lower-energy spin-split Landau level peak corresponds to the higher magnetic field peak in the Shubnikov-de Haas oscillations. Thus in the case of attractive scattering centers, the spin-split peak at higher magnetic fields would be weaker and broadened towards the higher magnetic fields. The opposite effect would be seen in the case of repulsive impurities. [233, 235, 236]

4.6.2 Hall bar fabrication

For the magnetotransport measurements, reference Hall bars are fabricated from the same wafer as the detector samples. The fabrication process is based on optical lithography and is very similar to the detector fabrication. After etching of a laterally contacted 80 µm wide 2DEG mesa stripe, the “Hall bar”, AuGeNi Ohmic contacts are annealed to the samples. An example of a bonded-up Hall bar is shown in Fig. 4.45 (a).

On some samples, the Hall bar is then covered with a thin, semi-transparent TiAu gate on top of the Hall bar mesa as a gate. The nominal thicknesses read by the evaporator crystal monitor were 3 nm Ti and 1.5 nm Au (the real evaporated thickness is higher). The semitransparent gate enables characterisation of the 2DEG not only in the dark, but also after illumination. Finally, another thick (>120 nm) layer of TiAu is deposited with finger gates that climb up on the mesa and contact the thin semitransparent top gate. A gated Hall bar is shown in Fig. 4.45 (b).

4.6.3 Magnetotransport measurements on ungated Hall bars

Once fabricated, the samples are mounted in a 1.5 K cryostat capable of applying magnetic fields up to 8 T. From measurements of the longitudinal and transverse voltages across the

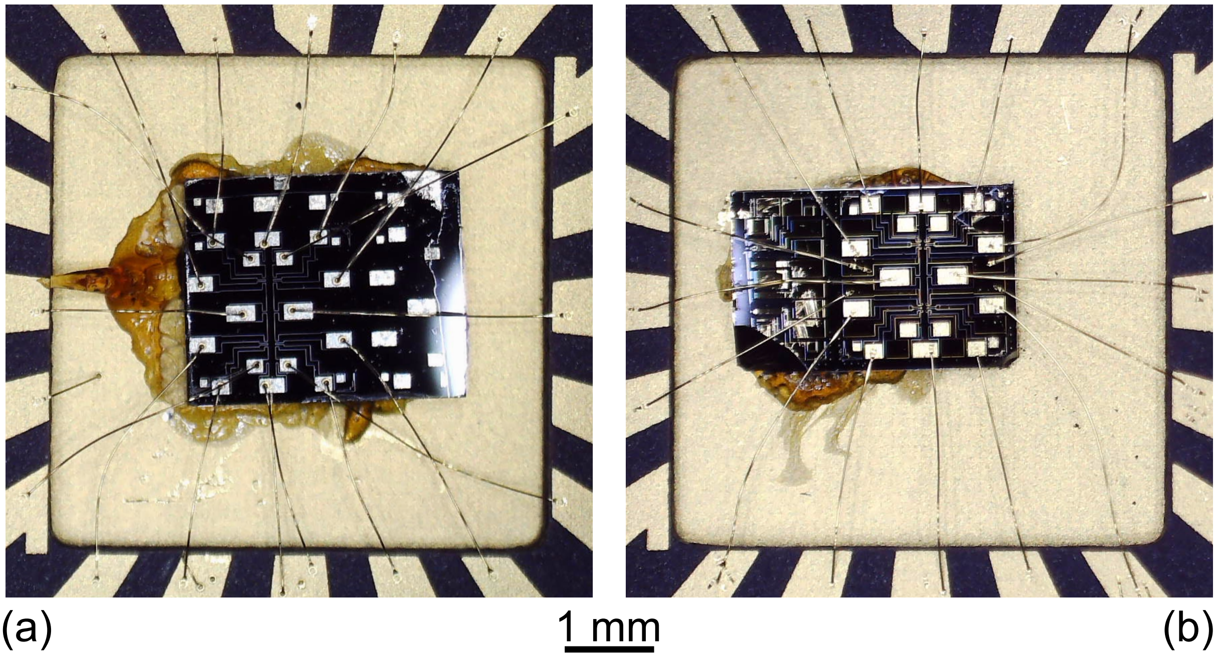

Figure 4.45: **Photos of bonded-up Hall bar chips.** (a) Ungated Hall bar, (b) gated Hall bar. In both cases, the 2DEG stripe is vertical. Two Ohmic contacts are at the top and bottom, and multiple Ohmic contacts are at the side of the 2DEG stripe. In the case of the gated Hall bar (b), additional gate contacts are present that contact the thin semitransparent top gate.

Hall bar contacts, the electron density is extracted from Hall data and Shubnikov-de Haas oscillations. An example of such measurements is shown in Fig. 4.46, which shows the longitudinal and transverse resistivities ϱ_{xx} and ϱ_{xy} for an ungated, unilluminated Hall bar.

Fig. 4.46 (b) shows the transverse resistance, which at low fields follows a linear trend proportional to B. The electron density is extracted from a linear fit to the data below 0.4 T. At higher fields, the quantum Hall effect with the step-like behaviour becomes visible. $R_{\mathrm{xy}} = \varrho_{\mathrm{xy}}$ becomes pinned at the values corresponding to integer filling factors. The theoretically expected ϱ_{xy} values at these integer filling factors, calculated from the low-field electron density, are indicated by the dots. The steps at even numbers are clearer than those at odd filling factors due to the effect of the spin splitting: each Landau level becomes split in spin-up and spin-down levels as seen from Eq. (4.18), but the spin-splitting $g\mu_{\mathrm{B}}B$ is lower than the $\hbar\omega_{\mathrm{c}}$-splitting of the Landau levels, since the Landé g-factor is smaller than 2, $|g| < 2$.

Similarly, ϱ_{xx} in Fig. 4.46 (a) exhibits oscillations of the longitudinal resistance, which reach down to zero at even integer filling factors. At odd filling factors, a dip becomes visible at high magnetic fields. Using Fourier transformation of the measured data as a function of $1/B$, the electron density can also be extracted. The analysis is done in the range between 0.15 T and 1 T, where harmonic oscillations are seen, and with a Blackman-Harris windowing function to eliminate discontinuity at the interval edges.

2DEGs in GaAs/AlGaAs heterostructures have anisotropic transport properties due to

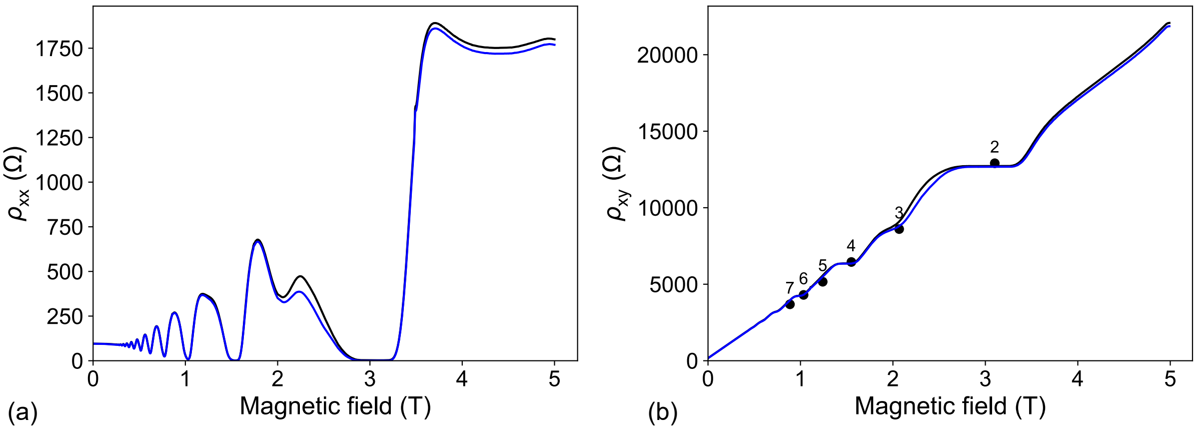

Figure 4.46: **Magnetic field measurements.** (a) Shubnikov-de Haas oscillations in the longitudinal resistance, (b) Transverse resistance: Hall data. The dots indicate the magnetic field and transverse resistance expected for the respective integer filling factors corresponding to the electron density extracted from a linear fit to the low-field data. Two traces are shown, in black and blue, which corresponds to voltage measurements using two probes on either side along or across the sample.

direction-dependent interface scattering [227]. The mobility is anisotropic, with the [$\bar{1}$10] crystal direction being the “fast” and [110] the “slow” mobility direction [227]. Therefore, different ungated Hall bars were fabricated, with the channel parallel to either of both mobility directions. The transport parameters were measured for Hall bars cooled down in the dark, and then after the sample has been flood illuminated with a red light source for three minutes. The results are presented in Table 4.4.

		Conductivity	**Electron density**	**Mobility**
		mS	**1/cm²**	**cm²/(Vs)**
GaAs slow	**dark**	10.5	$1.52\cdot10^{11}$	$4.30\cdot10^{5}$
direction	**light**	65.0	$3.72\cdot10^{11}$	$1.09\cdot10^{6}$
GaAs fast	**dark**	16.1	$1.52\cdot10^{11}$	$6.62\cdot10^{5}$
direction	**light**	105.0	$3.65\cdot10^{11}$	$1.79\cdot10^{6}$

Table 4.4: **Conductivity, electron density, and mobility** for an ungated structure.

It is evident that illumination increases both electron density and mobility. The electron density does not depend on the crystal direction within experimental error, as expected, but the mobility and conductivity are higher along the fast direction, in agreement with the typical behaviour of GaAs/AlGaAs 2DEGs [227].

4.6.4 Magnetotransport measurements on a gated Hall bar

To study the dependence of electron density on the gate voltage, a gated Hall bar with channel parallel to the fast mobility direction and covered with a semi-transparent TiAu gate

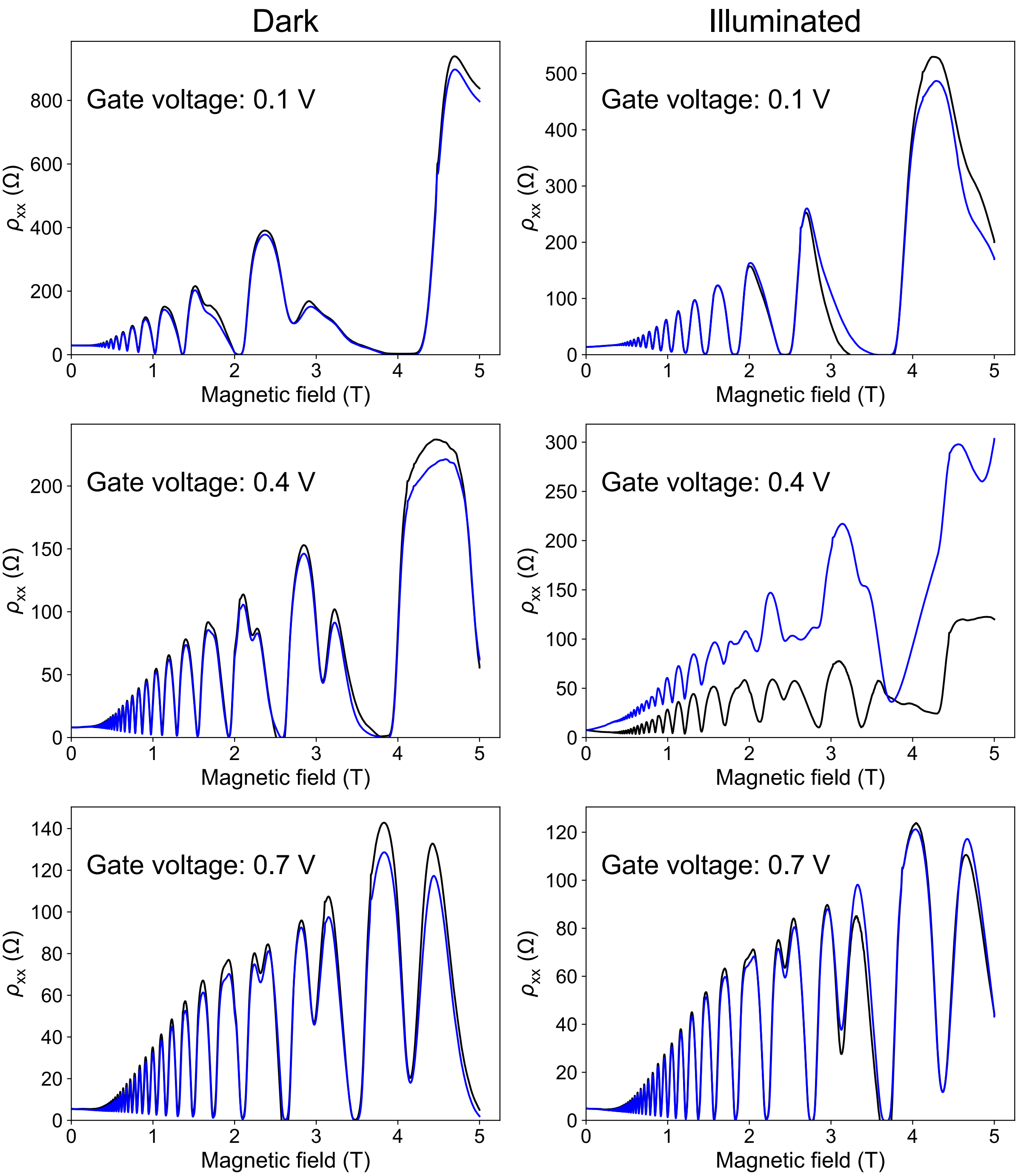

Figure 4.47: **Longitudinal resistance: Shubnikov-de Haas oscillations** for a set of gate voltages measured in the dark (left column) and after above-band gap illumination (right column).

is studied. At a set of gate voltages, the magnetic field was tuned and the magnetotransport data was acquired.

Fig. 4.47 shows the longitudinal resistivity for three exemplary gate voltages. In the left column is the data before illumination, and in the right column the data after the cooled-down sample was illuminated with red light until saturation of the transport parameters. The respective Hall data (transverse resistivity, not shown) looks qualitatively similar to Fig. 4.46 (b).

In the THz detection experiments described in the sections 4.5.2 and 4.5.3, the sample was measured after illumination with above-band gap light until saturation. Therefore, we will first consider the transport properties after illumination.

Fig. 4.48 (a) shows the longitudinal conductivity at zero magnetic fields, and Fig. 4.48 (b) shows the electron density extracted using two different methods: from the Hall data, and from the FFT of the Shubnikov-de Haas oscillations, as described in section 4.6.1.

At the lowest gate voltage of −0.35 V, the FFT method cannot be used, since the oscillation frequency is too low to reliably extract a peak frequency. In the interval between 0.2 V–0.4 V, the magnetotransport data exhibits hysteresis effects, and the transverse voltages acquired between two different probes along the same channel significantly differ between each other: the Hall slope is different and the plateaus occur at different magnetic fields, which gives different densities for the two probes across the channel. At the same time, the Shubnikov-de Haas oscillations in this gate voltage range, e. g. at 0.4 V, look irregular, see Fig. 4.47. This can be understood by an inhomogenous electron density across the sample. The width of the Hall bar is 80 µm, while the distance between the side contacts along the length of the Hall bar is 0.7 mm. The Hall values probe the electron density around the respective side contacts to the 2DEG locally, and the difference between the two extracted values suggests an inhomogenous electron density across the sample, which varies on a length scale of 0.7 mm. At the same time, the longitudinal resistance probes the conduction along the whole 0.7 mm long length between the side contacts to the 2DEG. If the electron density and mobility values are spatially varying, this can give rise to the observed irregularities in the longitudinal resistance. However, the FFT of the longitudinal resistance measured using the left or right probes along the Hall bar still gives the same consistent result from a clearly visible single peak in the frequency domain. The FFT method appears to be a more reliable extraction of the electron density in this gate voltage range, as it probes the entire length of the Hall bar. To get the most accurate results, the average electron density shown in Fig. 4.49 (a) was determined from the FFT method at positive gate voltages but from the Hall method at $U_\mathrm{G} \leq 0$ V. Using the relation $\mu_\mathrm{e} = \sigma_\mathrm{xx}/(n_\mathrm{s}e)$, the corresponding mobility was extracted in Fig. 4.49 (b).

Thanks to the electron density–gate voltage dependence provided by the magnetotransport, it now becomes possible to determine the threshold voltage U_th in a more accurate way. For the treatment in the subsequent chapter, I will use a physically sensible definition of U_th as the gate voltage where the chemical potential coincides with the lowest energy level of the 2DEG. At this point, the electron density would vanish assuming zero temperature and no disorder. This corresponds to the electron density vs. chemical potential

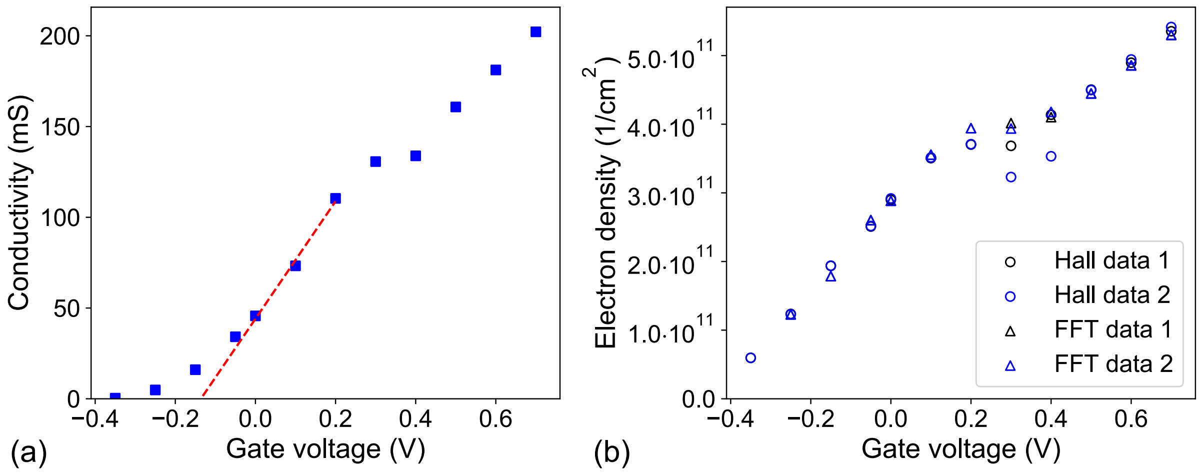

Figure 4.48: **Measurements on a gated Hall bar after illumination.** (a) Longitudinal conductivity, (b) electron density as a function of gate voltage. In (b), "1" and "2" refer to the two values extracted from the two longitudinal or transverse voltage probes. Circles represent the electron density extracted from the transverse Hall voltage, triangles show the one from the FFT of the Shubnikov-de Haas oscillations of the longitudinal resistivity.

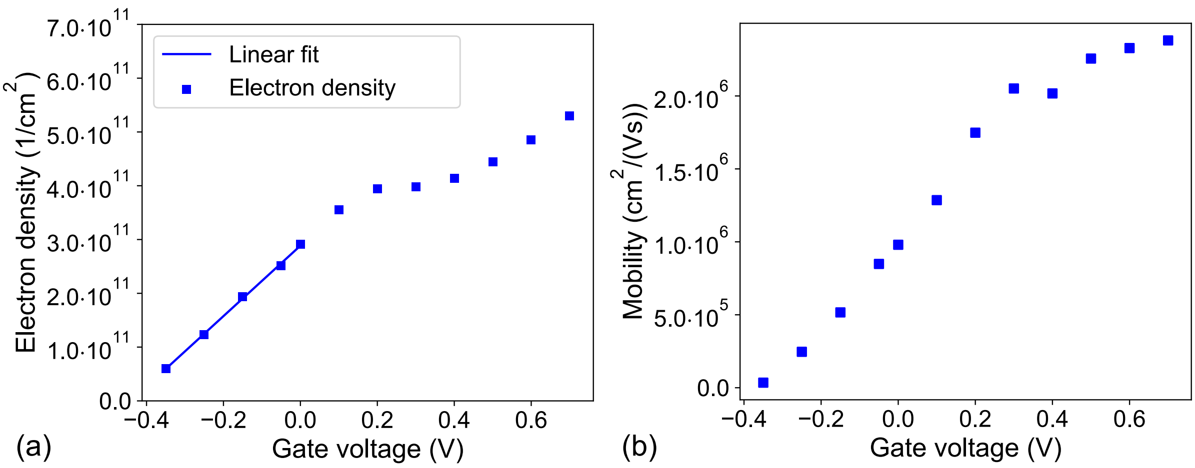

Figure 4.49: **(a) Average electron density and (b) mobility** as a function of the gate voltage. In (a), the line represents a linear fit to the data points for $U_G \leq 0$ V. At 0 V gate voltage, the electron density is $2.91 \cdot 10^{11}/\text{cm}^2$ and the mobility is $9.8 \cdot 10^5 \text{cm}^2/(\text{Vs})$.

dependence in a 2DEG of

$$n_s = \frac{m_{\text{eff}} k_B T}{\pi \hbar^2} \ln \left[1 + \exp \left(\frac{\mu - (-e\varphi_{\text{tot}})}{k_B T} \right) \right] , \tag{4.23}$$

obtained from integration of the Fermi function in two dimensions [237], where the electron potential energy is $V = -e\varphi_{\text{tot}}$ (also discussed in section 5.3.1).

This point U_{th} is extracted from a linear fit to the electron density in the depletion region, see Fig. 4.49 (a). By extrapolating the linear fit, the intersection with the horizontal axis of $U_{\mathrm{th}} = -0.44$ V is extracted.

It should be noted that the definition of the threshold voltage, as well as the methods for its extraction, are a matter of considerable debate. For example, in Ref. [228], more than 11 different methods of threshold voltage extraction are reviewed, each of which yields different results. In section 4.5.2, the conventional way of determining the threshold voltage from the conductance gave $U_{\mathrm{th},\sigma} = -0.35$ V. If the linear region of the transfer characteristic is extrapolated to the horizontal axis on the gated Hall bar, as shown in Fig. 4.48 (a), it gives an intersection of −0.14 V – a considerably different value. The reason for the difference is not different electron density, as both samples are from the same wafer and have been exposed to above-band gap illumination until saturation, but is likely due to the mobility and disorder. The less negative value for $U_{\mathrm{th},\sigma}$ on the gated Hall bar is due to a very gradual onset of the conductance, which is due to the macroscopically large gate, in contrast to the microscopically small gate as in the THz detector samples. Obviously, methods such as these relying on the transfer characteristic are more appropriate with three-terminal field effect transistors, where the device geometry does not allow to conduct Hall bar measurements in a more accurate way [194]. The measurements in a magnetic field provide a more reliable and device-independent way of extracting the electron density; therefore the value of $U_{\mathrm{th}} = -0.44$ V will be used for the subsequent analysis.

Using the parallel-plate capacitor model, the distance d between the "plates", i. e. the top gate–2DEG separation, can be deduced from the slope of the $n_{\mathrm{s}}(U_{\mathrm{G}})$-data. This yields $d \approx 106$ nm, a reasonable value given that 90 nm is the distance between wafer surface and GaAs-AlGaAs heterojunction. Since the wave function of the 2DEG in z-direction has a certain spatial extension, the extracted value is slightly larger than the geometrical layer thickness of 90 nm.

Before discussing the effects taking place at the 0.2 V–0.4 V gate voltages, it makes sense to compare the data presented above with the analysis results from the same Hall bar measured in the dark, prior to any illumination. These are shown in Fig. 4.50.

In the dark, the Hall data measured on the two probes across the Hall bar is stable and yields the same results, which are in good agreement with the FFT data. The linear fit extrapolated to the horizontal axis gives a threshold voltage of −0.19 V for the dark data.

4.6.5 Interpretation of the data

In the dark, no plateau is observed at the 0.2 V–0.4 V gate voltages; instead, the electron density keeps steadily increasing. The monotonous growth of dark density and mobility values in Fig. 4.50 corresponds well to a parallel-plate capacitor model in the range where the linear fits are shown: as the gate voltage increases, the positive top gate potential induces

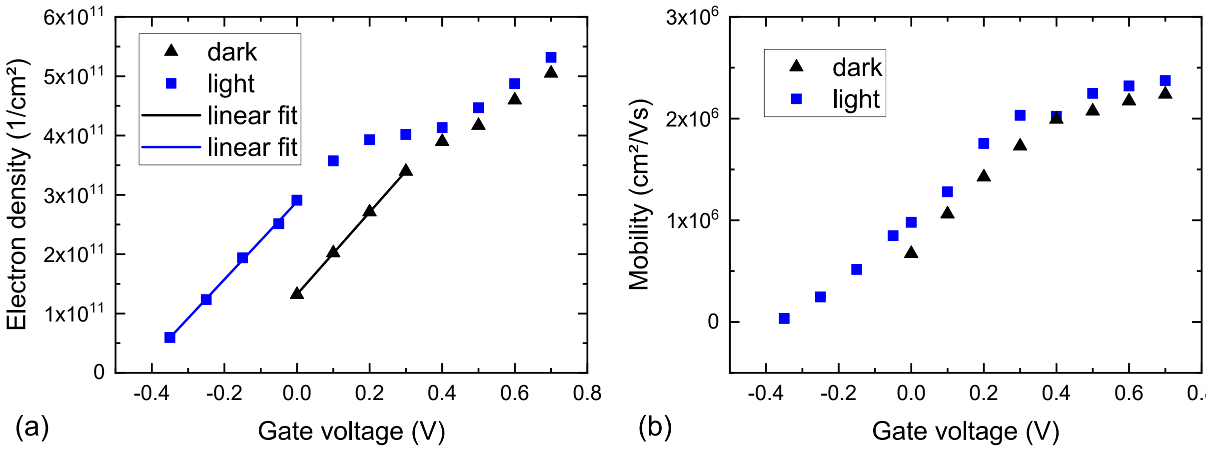

Figure 4.50: **Comparison of dark and illuminated transport data.** (a) Electron density, (b) mobility as a function of the gate voltage. Black: measurement in dark; blue: measurement after illumination for comparison (same data as in previous figure, Fig. 4.49).

more electrons in the triangular quantum well of the GaAs-AlGaAs heterojunction, leading to an increase in electron density, and concomitant with it, an increase in the mobility.

Once the sample has been exposed to red light for long enough time to reach a steady state, both density and mobility show higher values. The density values appear shifted to the left, i. e. to the more negative gate voltage values. Consequently, the threshold voltage shifts to more negative values, and the zero gate voltage electron density is increased.

This phenomenon is called **persistent photoconductivity**, and arises from two phenomena: due to electron-hole generation in bulk GaAs with subsequent charge separation with electrons moving into the heterojunction quantum well and holes into the bulk, but most importantly, due to photo-ionisation of DX centers in the AlGaAs doped region [238–240].

DX centers are deep donor levels in III-V semiconductors [241, 242]. When $Al_xGa_{1-x}As$ as a III-V semiconductor is doped with silicon, the arising impurity has a bistable behaviour between two configurations [243]: a substitutional configuration that gives rise to shallow, hydrogenic bound states, and a lattice distorted configuration which results in a deep donor level with thermally activated electron capture – the DX state [244].

The energy levels of the ternary semiconductor compound $Al_xGa_{1-x}As$ with aluminium mole fraction x are shown in Fig. 4.51. For $x < 0.22$, the DX state is not seen in transport characteristics since it lies above the Γ-conduction band, and thus in GaAs a Si impurity appears as a shallow donor. However, in $Al_xGa_{1-x}As$ with $x > 0.22$ (or under sufficient hydrostatic pressure in GaAs), the DX state becomes the lowest state in the band gap and thus controls the transport properties. [241, 244]

This is in particular the case with the Si-doped $Al_{0.33}Ga_{0.67}As$ barrier material in the studied samples. The $x = 0.33$ aluminium mole fraction is pointed out in Fig. 4.51. Physically, the above-band gap illumination leads to the DX centers in AlGaAs being ionised and elec-

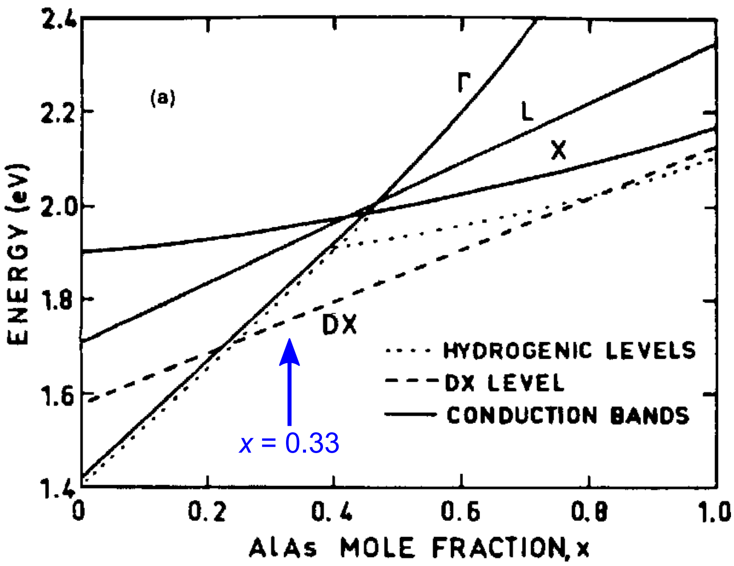

Figure 4.51: **Bands and donor levels in Si-doped Al$_x$Ga$_{1-x}$As as a function of aluminium mole fraction x.** Reprinted from Ref. [241], with permission from Taylor & Francis. The overlaid blue arrow indicates $x = 0.33$, the relevant point for the $Al_{0.33}Ga_{0.67}As$ barrier.

trons from them being transferred to the conduction band, where they increase the electron density.

But why do the electrons not rapidly fall down into the deep DX states as soon as illumination is switched off? This is due to the remarkable properties of these states, which can be well described by a configuration coordinate diagram:

In Fig. 4.52, the lower parabola indicates the DX center, while the upper parabola indicates a delocalised electron state. The difference in energies of the minima of the parabolas is the binding energy of the DX center shown in Fig. 4.51. However, the capture process is thermally activated, and an energy barrier of the capture energy has to be overcome. Equally, the sum of the capture and binding energy is the emission energy that needs to be overcome for thermal ionisation of the DX center. For optical ionisation of the defect a considerably larger energy is required shown by the vertical photonic transition.

As a result, once DX centers are ionised at low temperatures (liquid helium temperatures and up to ~100 K), electrons cannot be captured again (within reasonable time scales) by the deep DX states due to the large capture barrier energy and thermally activated capture rate, which results in an extremely small capture cross section. The state can be reset by thermal cycling: warming the sample up to room temperature and back down, which enables thermal capture of electrons by the DX states.

This also means that in the persistent photoconductivity state, the sample is not in thermal equilibrium [242]. After a thermalised cooldown in the dark, the electron occupancy in the semiconductor heterostructure (including free electrons in the conduction band and the deep and shallow donor states) can be characterised by the Fermi function with a single

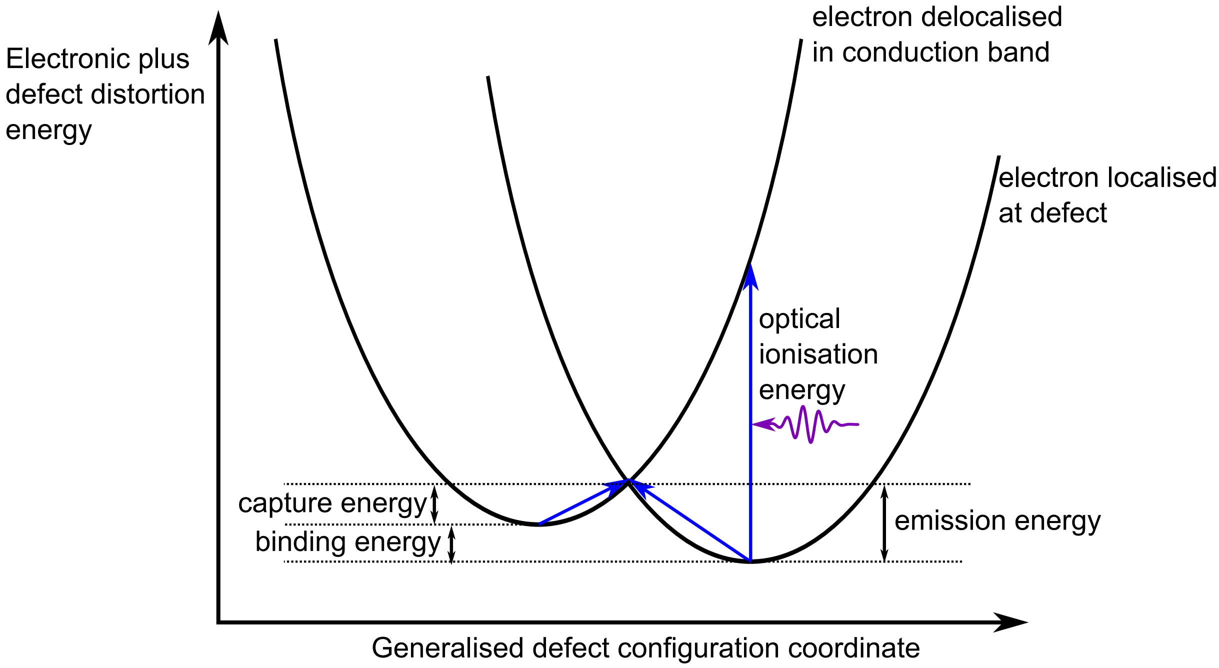

Figure 4.52: **Configuration coordinate diagram for the DX center**, drawn with information from Refs. [238, 239].

chemical potential. In contrast, this is no longer possible after illumination. Instead, separate quasi-Fermi levels have to be introduced for the deep DX donor states on the one hand, μ_{d}, and the conduction band electrons and shallow donors on the other hand, μ_{c}, to describe the system [245]. This is illustrated in Fig. 4.53.

Since illumination ionises the DX centers, less of the DX centers are occupied by electrons, and the μ_{d} quasi-Fermi level for the deep DX states is pushed down. The generated electrons push μ_{c} upwards, resulting in a larger electron occupation in the triangular quantum well, and may lead to a higher occupation of the shallow donor states and potentially free electrons in the doped AlGaAs region.

DX centers are most effectively ionised by above-band gap illumination. This is due to the hole capture rate of DX centers being several orders of magnitude larger than the electron capture rate. The efficient increase in electron density by illumination of the sample with above-band gap radiation, which was used in the course of this work, is thus explained by holes generated in the valence band being captured by the DX centers, while the electrons excited in the conduction band fall down into the conduction band minima as the triangular heterojunction quantum well. [227]

Let us now return to the dark and illuminated transport data measured on the reference Hall bar made from the same wafer as the detector samples. In the gate voltage region of 0.2 V–0.4 V, the following observations can be seen:

1. The electron density has a plateau.

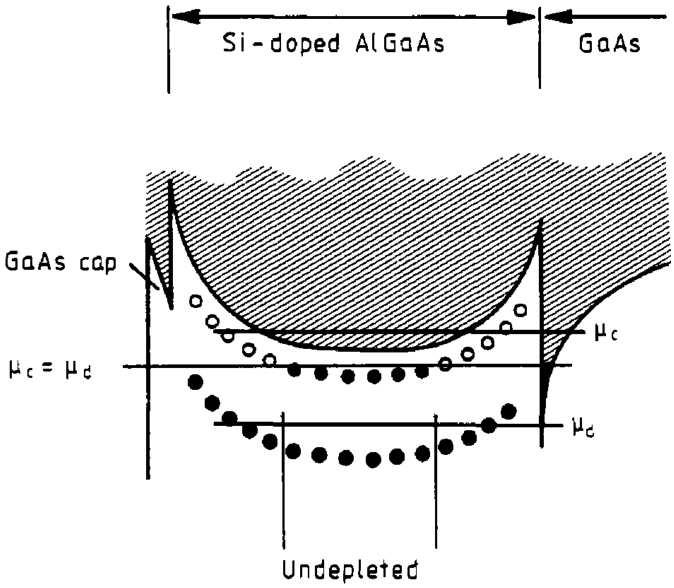

Figure 4.53: **Fermi levels before and after photoionisation of DX centers**, from Ref. [245]. Before illumination, a single chemical potential $\mu_c = \mu_d$ described the semiconductor heterostructure. After illumination, different quasi-Fermi levels are introduced for the conducting electrons and shallow donors (μ_c) and the DX centers (μ_d). Figure copyright: © IOP Publishing. Reproduced with permission. All rights reserved.

2. Shubnikov-de Haas data shows irregularities at high magnetic fields instead of well-defined oscillations.

3. The minima of the ϱ_{xx} Shubnikov-de Haas oscillations do not reach zero at high magnetic fields.

4. Data from the two (longitudinal or transverse) probes across the Hall bar do not agree with each other.

A possible explanation of these observations is parallel conduction with a second conductive layer. This could be, for example, a second subband forming in the heterojunction quantum well. However, this assumption can be ruled out for the following reasons:

1. In similar structures, a second subband starts to be filled only at electron concentrations in excess of 7–8·10^{11}/cm^2 [246, 247], much higher than the maximum achieved electron densities in this range.

2. Parallel conduction through a second subband is characterised by a drop in mobility of the first subband due to the onset of inter-subband scattering [246, 247], which is not observed in this wafer.

3. If a second subband were the reason for parallel conduction between 0.2 V and 0.4 V, it should also be seen at even higher gate voltages corresponding to higher concen-

trations. But as the gate voltage is increased to 0.5 V and above, no indications of parallel conduction can be seen.

Another possibility is parallel conduction with the doped AlGaAs region, if the conduction band edge is pulled below the Fermi level at the doped layer, which would lead to a second conducting channel. This hypothesis is unlikely for the following reasons:

1. In samples where a second 2DEG layer is seen, there are two electron density values extracted from the Fourier transform of the $\varrho_{\mathrm{xx}}(1/B)$-data, both of which are significantly lower than the Hall density value, and the difference increases with gate voltage [227, 246]. In contrast, the wafer in this work shows the same density value from both the ϱ_{xx}-Fourier transform and the Hall data above 0.5 V.

2. The interaction between the two 2DEGs has been shown to give rise to a strong non-monotonous mobility-gate voltage dependence as well as negative differential transconductance in Ref. [227], neither of which are observed in the wafer studies here.

3. A conducting electron gas in the doped layer with a low mobility has been shown to give rise to a strong photomagnetoresistance [248]. In this case, the longitudinal resistance is replaced by a $\sim B^2$ dependence with superimposed oscillations, and the longitudinal resistance grows with the Hall electron density. However, the effect in Ref. [248] has been observed with a sharp onset at Hall electron densities in the range of 4–4.9·10^{11}/cm^2, and on samples with a highly doped, 50 nm-thick AlGaAs layer with 2·10^{18}/cm^3 doping density. Although the Shubnikov-de Haas oscillations in the Hall bar studied in this thesis do not reach zero in the 0.2 V–0.4 V gate voltage range, the effect is much weaker than in Ref. [248], and limited to this narrow gate voltage range.

Given the above arguments, the most likely explanation for the observed behaviour are empty donor states in the doped AlGaAs layer, which become filled back with electrons at positive gate voltages. The observed plateau in n_{s} in the 0.2 V–0.4 V gate voltage region indicates that the chemical potential becomes resonant with a sharp peak in the density of states as a function of energy. The electrons cannot be captured by the deep DX states due to their extremely low capture cross section at low temperatures. However, they could be captured by the shallow hydrogenic states created by Si donors in $Al_{0.33}Ga_{0.67}As$, which do not have a barrier energy for electron capture and equilibrate quickly with the conduction band [244]. Such a δ-peak in the density of states could well originate from bound shallow donor levels in the conduction band. As a result, the electron density in the 2DEG will remain constant as the gate voltage is increased, while increasingly more electrons fill unoccupied donor states, until they are filled. After that, n_{s} starts rising again.

The δ-peak in the density of states will give rise to Fermi level pinning. Such phenomena are known in literature, as indicated in Fig. 4.54: the Fermi level becomes pinned at donor states in AlGaAs as the top gate bias is increased [243, 249, 250]. Fermi level pinning at donor levels was also shown to be responsible for the decrease in transconductance in AlGaAs/GaAs high electron mobility transistors [250]. A decrease in transconductance (as compared to a linear transfer characteristic) is also observed in the wafer studied here, Fig. 4.48 (a), and also occurs in the region 0.2 V–0.4 V.

To summarise, the density and mobility densities can be understood as follows. In the dark, the density follows a linear trend up to ca. 0.3 V gate voltage as expected from a similar parallel plate capacitor model. Above this range, the slope becomes lower, since the chemical potential becomes high enough that ionised donors that have created the equilibrium electron density at zero gate voltage become filled back with electrons.
After illumination, DX centers become ionised and give rise to a significant increase in electron density at zero gate voltage, but a lower increase in mobility, since not only the electron density and thus screening of scattering centers has increased (which increases the mobility), but also the number of attractive scattering centers has increased (which lowers the mobility). As positive gate bias is applied, the chemical potential touches donor levels in the doped AlGaAs already at a lower gate voltage of around 0.1 V, where the electron density corresponds to roughly the same value as where the density in the dark experiences a decrease in slope. Over the range of ca. 0.1 V–0.4 V, donor levels in the doped AlGaAs become filled back. Because of the persistent photoconductivity, there are much more ionised donor states in the doped AlGaAs region. As a result, the Fermi level becomes pinned at them, and the electron density shows a plateau. While the density stays constant, the mobility keeps increasing, since the backfilling of ionised impurities reduces the number of charged remote impurities that lead to scattering in the 2DEG due to their Coulomb potential. Finally, above about 0.4 V, the density approaches similar values as in the dark measurement, and follows the same trend as the dark values with a lower slope

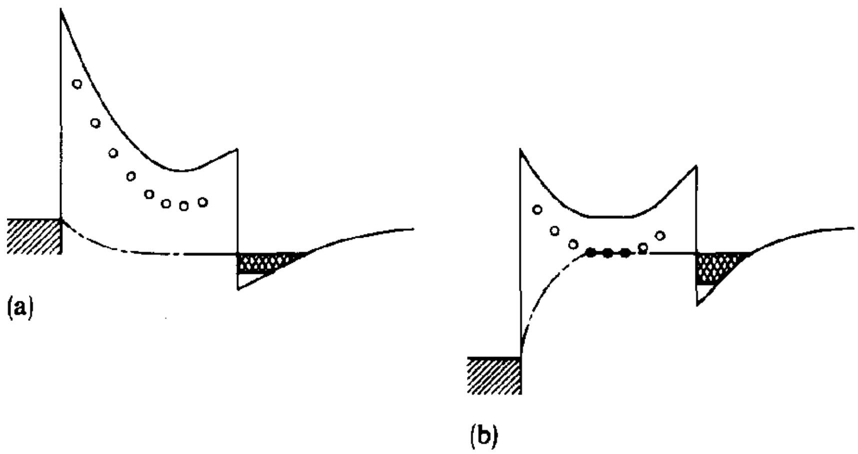

Figure 4.54: **Fermi level pinning in AlGaAs-GaAs heterostructures.** Reprinted from Ref. [249], with the permission of AIP Publishing.

than in the negative gate voltage range. This is due to the same effect, that donors that have created the equilibrium electron density in the dark at zero gate voltage become filled back with electrons. In this region, the mobility grows only weakly, since the majority of attractive scattering centers has already been neutralised.

This interpretation is also supported by the shape of the Shubnikov-de Haas oscillations in Fig. 4.47. In the dark (left column) at 0.1 V gate voltage, the spin-split peak at lower magnetic field, i.e. corresponding to higher energy, is the dominating one, and the tails are extended towards higher magnetic fields i.e. lower energy, which is consistent with electrons experiencing scattering at attractive impurities. As the gate voltage is increased, the lower energy spin-split Landau level peak becomes gradually better resolved, reaching nearly symmetric peaks at 0.7 V gate voltage, where electrons fill back the unoccupied donor states and thus neutralise the attractive scattering centers. For the illuminated data (right column in Fig. 4.47), the effect is even more pronounced: at 0.1 V gate voltage, the ionisation of DX centers led to so many attractive scattering centers that the lower-energy spin-split peak is almost suppressed, resulting in very asymmetric Shubnikov-de Haas oscillations. At 0.4 V, donor states are being filled back. The amount of empty defect states can vary spatially, since it also relates to the amount of surface states present, which depends on processing quality of the semiconductor surface. Electrons moving between the two reservoirs, the triangular heterojunction quantum well and the donor states in the doped AlGaAs, is a process which can amplify any existing minuscule inhomogeneities across the sample. Along the 0.7 mm length of the probed 2DEG Hall bar, this can give rise to spatial variations in electron density. Therefore, the process of backfilling of donor states taking place at this gate voltage can indeed lead to a hysteresis in the measured density and mobility data and substantial irregularities in the Shubnikov-de Haas oscillations. As in the case of the dark data, at 0.7 V gate voltage the oscillations are symmetric, showing that attractive scattering centers have been neutralised. Since at this gate voltage empty donor levels have been filled, the density and mobility data displays very similar data for the dark and illuminated case.

For the understanding of the THz detector operation in the following, the unstable region of 0.2 V–0.4 V is of little significance. The important conclusion of this section is that in the area where the THz detector is operated, with one gate being negatively biased and the other gate being positively biased at 0.7 V (or higher), the 2DEG is a single conducting layer with known electron density, no parallel conduction, and well defined Shubnikov-de Haas oscillations reaching zero ϱ_{xx} at high magnetic fields.

4.6.6 Temperature dependence of transport parameters

The above measurements on the Hall bar were conducted at 1.5 K, but the measurements with the THz detectors were done around 9 K temperature. For a better comparison of the data, the temperature dependence of the electron density and the mobility is measured in the cryostat with the magnetic field on the gated Hall bar at zero gate voltage, using the sample space heater to increase the temperature.

The resulting data is shown in Fig. 4.55. The electron density was extracted from the slope of the transverse resistance, since the Shubnikov-de Haas oscillations decay very quickly in amplitude as the temperature is increased. After changing the temperature set-point, the conductance change was monitored, and the system was given about 30–40 minutes to reach a steady state. The temperature was measured using a thermometer in the sample space and on the probe, which show different steady-state values when heating using the sample space heater. The mean and deviation is shown as the large horizontal error bars.

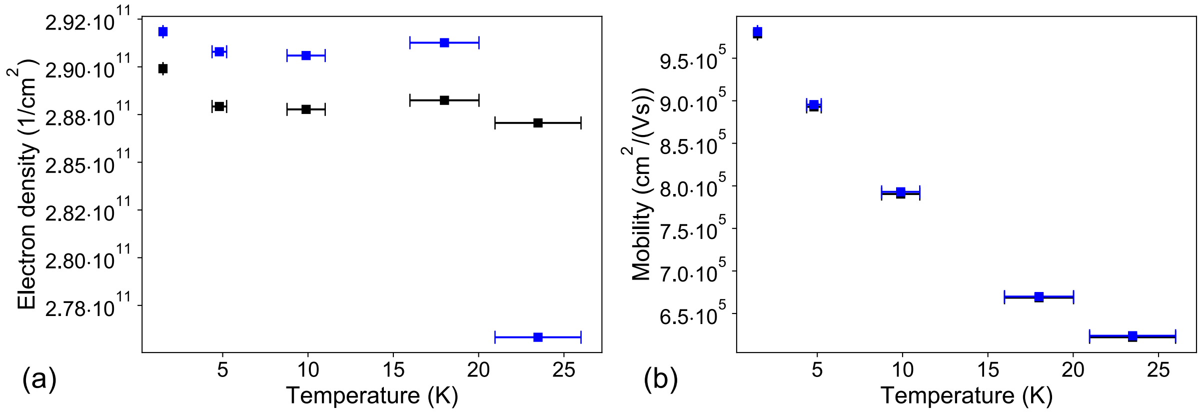

Figure 4.55: **Temperature dependence** of electron density (a) and mobility (b). The blue and black colours are the measurements data corresponding to the the two probes on the Hall bar.

The density does not change significantly as the temperature is increased up to about 25 K, but the mobility drops with temperature. Compared to the 1.5 K-data, the decrease in mobility is about 19 % upon heating to 10 K, and about 36 % upon heating to 24 K.

4.7 Analysis of the transport in the channel

4.7.1 Edge depletion

To get an estimate for the amount of edge depletion, other samples with thinner channel widths were studied. Their conductance was measured and is shown in Fig. 4.56.

A channel of 1.5 µm lithographically defined width still exhibits conduction at zero gate voltages, Fig. 4.56 (a). Taking into account sideways etching, the etched channel width is about 1.5 µm–0.33 µm = 1.17 µm. However, for the thinnest channel in the batch, 1.0 µm corresponding to 0.67 µm of etched channel width, no conduction is observed at zero gate voltages. Even illuminating the sample with white light for 1 minute does induce a conduct-

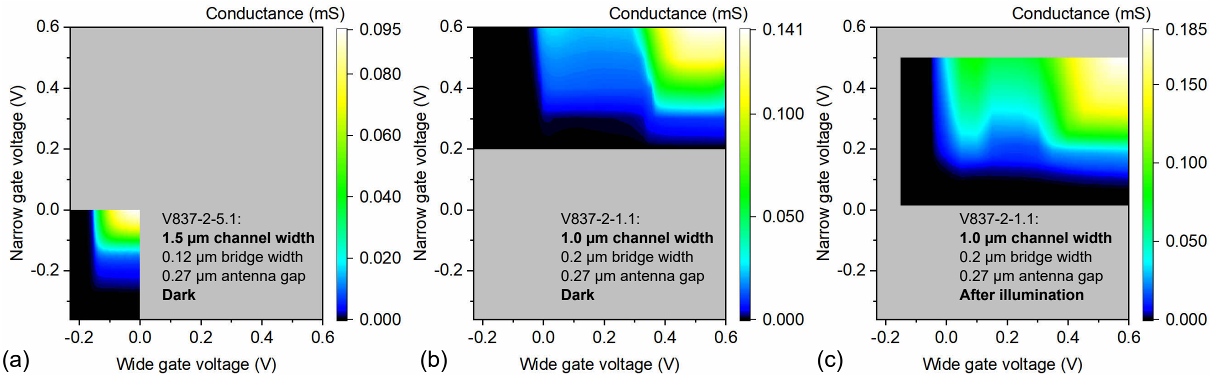

Figure 4.56: **2-wire conductance measurement for samples with different channel widths.** (a) A sample with a lithographically defined channel width of 1.5 µm exhibits conduction at zero gate voltages. (b), (c) For 1.0 µm channel width, no conductance is observed at zero gate voltages, even after illumination of the sample with white light for 1 minute in (c), unless positive gate voltages are used to induce a 2DEG in the channel.

ing channel. Conduction is only observed at strongly positive gate voltages. In this case, the positive gate potential induces a 2DEG in the material, and conduction is found to be unstable and drift with time. This observation allows us to make a statement on the amount of edge depletion: edge depletion reduces the channel width by more than 0.67 µm, but less than 1.17 µm.

For the sample V837-2-3.1 studied in the previous section 4.5, the lithographically defined channel width is 2.0 µm. Due to edge depletion, the actual width W of the 2DEG in the channel is shorter. From the characterisation above, the actual channel width can be inferred to be between 0.5 and 1 µm, and will be assumed to be $W \approx 0.7$ µm in the following.

4.7.2 Ballistic transport

Is the electron transport in the channel of the sample V837-2-3.1 considered in section 4.5 ballistic or not? In the ballistic transport regime, electrons move without scattering over long distances, which is only possible if the mean free path of electrons is large compared to the channel dimensions. In contrast, if the channel dimensions are large compared to the mean free path, conduction is described by the Drude model.

The 2D electron surface density n is given by

$$n = \frac{k_F^2}{2\pi}, \tag{4.24}$$

where k_F is the radius of the Fermi circle in reciprocal space. From this, the Fermi electron velocity v_F corresponding to the Fermi momentum p_F or the Fermi wave vector k_F can be calculated:

$$v_\mathrm{F} = \frac{p_\mathrm{F}}{m_\mathrm{eff}} = \frac{\hbar k_\mathrm{F}}{m_\mathrm{eff}} = \frac{\hbar\sqrt{2\pi n}}{m_\mathrm{eff}}\,. \tag{4.25}$$

m_eff is the effective electron mass. The mean free path λ_e in the Drude model equals

$$\lambda_\mathrm{e} = v_\mathrm{F}\tau = v_\mathrm{F}\frac{m_\mathrm{eff}\mu_\mathrm{e}}{e} = \frac{\hbar\sqrt{2\pi n}\mu_\mathrm{e}}{e}\,. \tag{4.26}$$

Let us estimate the mean free path using the analysis in section 4.6, taking the ungated, illuminated transport parameters in the worst case of the slow GaAs direction. This corresponds to an electron density of $3.7\cdot10^{11}$/cm^2 and a mobility of $1.09\cdot10^6$cm^2/(Vs). At around 10 K measurements temperature, the mobility will be lower by around 19 %, i. e. $0.88\cdot10^6$cm^2/(Vs). This corresponds to a mean free path of 8.9 µm. This is orders of magnitude larger than the dimensions of the active part of the device, $b_\mathrm{gap} = 0.27$ µm, the distance between the gates. This corresponds to very low scattering and ballistic transport.

However, in the thin etched channel, the mobility will likely decrease due to edge roughness and the narrow constriction. Is the transport ballistic even in the narrow channel?

A narrow constriction in form of a quantum point contact exhibits quantised conductance $1/R_\mathrm{quantum}$, that equals [251, 252]

$$\frac{1}{R_\mathrm{quantum}} = \frac{2e^2}{h}\cdot N = \left(\frac{2e^2}{h}\right)\cdot\left\lfloor\frac{k_\mathrm{F}W}{\pi}\right\rfloor\,, \tag{4.27}$$

where $N = \lfloor k_\mathrm{F}W/\pi\rfloor$ is the number of filled one-dimensional subbands. Notably, this is the value of the conductance, not the conductivity, and it does not depend on l, the length of the channel. In the sample V837-2-3.1 studied in section 4.5, the value of N is about 34, i. e. much larger than one, for a width W of 0.7 µm and $n_0 = 3.7\cdot10^{11}$/cm^2.

But what happens if the length L grows and becomes larger than the electron mean free path? The transition from the quantised one-dimensional conductance to the Drude model applicable for collisive transport can be understood by rearranging the Drude conductivity $\sigma_\mathrm{classical}$ as a function of k_F and the mean free path:

$$\sigma_\mathrm{classical} = ne\mu_\mathrm{e} = \frac{ne^2\tau}{m} = \frac{k_\mathrm{F}^2e^2\tau}{2\pi m} = \frac{e^2k_\mathrm{F}p_\mathrm{F}\tau}{2\pi\hbar m} = \left(\frac{e^2}{h}\right)\frac{k_\mathrm{F}p_\mathrm{F}\tau}{m} = \left(\frac{e^2}{h}\right)k_\mathrm{F}v_\mathrm{F}\tau = \left(\frac{e^2}{h}\right)k_\mathrm{F}\lambda_\mathrm{e} \tag{4.28}$$

Thus the classical conductance for a channel of width W and length L is

$$\frac{1}{R_\mathrm{classical}} = \left(\frac{2e^2}{h}\right)\frac{k_\mathrm{F}W}{\pi}\frac{\pi\lambda_\mathrm{e}}{2L}\,. \tag{4.29}$$

By comparing Eqs. (4.27) and (4.29) one can see that the classical and quantum conductances become comparable when $L \approx \pi\lambda_e/2$. For $L \gg \pi\lambda_\mathrm{e}/2$, scattering dominates

Region	Length (µm)	Width (µm)	α_{geom}
1. Trapezoid under wide gate after vertical contact	2.87	2×([3.2..1.0]-0.65)	1.3
2. Ungated gap between antenna wings	0.27	2×([1.0]-0.65)	0.39
3. 2DEG under narrow gate	0.2	2×([1.0]-0.65)	0.29
4. Ungated narrow channel	2.04	2×([1.0]-0.65)	2.9
5. Ungated trapezoid to the right Ohmic contacts	98.6	2×([1.0..14.0]-0.65)	13.8

Table 4.5: **Geometrical parameters of the conducting channel,** whose resistance is measured in the four-terminal conductance measurement. Starting from the vertical 2DEG contacting the left wing of the channel, the channel is split into trapezoidal and rectangular sections. Their lengths and widths are given. For the trapezoids, the varying width W_{lith} is indicated by $[w_1..w_2]$. When the x-axis is placed along the symmetry axis of the channel, the values in square brackets are the y-coordinates of the lithographically defined geometry. The edge depletion, assumed to be 0.65 µm, is subtracted, and the value is doubled to take into account the same width below the x-axis. The geometrical weights α_{geom}, or number of "squares" contained in the region, are calculated in the rightmost column.

the nature of the transport, and the Drude model applies, which predicts a resistance proportional to L. In the limit $L \lesssim \pi\lambda_{\mathrm{e}}/2$, the resistance becomes limited by the quantum constriction, and thus saturates at a value of $h/(2e^2N)$. The quantum-mechanical result sets a lower limit below which the resistance cannot fall.

In the following, the expected channel resistance is calculated within the classical Drude model. Even though for ballistic transport in a narrow channel it is not applicable, it can be used to find a lower limit to the mobility, since considering quantum effects will only increase the resistance.

To calculate the resistance of the channel within the Drude model, I consider a simple model, where the 2DEG channel is regarded as a series resistance of five regions, shown in Table 4.5:

$$R_{\mathrm{total}} = \varrho \sum_{i=1}^{5} \alpha_{\mathrm{geom},i} \tag{4.30}$$

α_{geom} is a factor taking into account the geometrical dimensions of a 2DEG region. For a rectangular piece, α_{geom} is simply the length-to-width ratio. For the trapezoidal sections with a width $w(x) = w_1 + (w_2 - w_1)x/L$, α_{geom} is estimated by calculating

$$\begin{aligned} R = \int_0^L \varrho \frac{\mathrm{d}x}{w(x)} &= \int_0^L \varrho \frac{\mathrm{d}x}{w_1 + (w_2 - w_1)x/L} = \varrho \frac{L}{w_2 - w_1} \int_0^L \frac{\mathrm{d}(w_1 + x(w_2 - w_1)/L)}{w_1 + (w_2 - w_1)x/L} = \\ &= \varrho \frac{L}{w_2 - w_1} \left[\ln(w_1 + (w_2 - w_1)) - \ln(w_1)\right] = \varrho \frac{L}{w_1} \frac{w_1}{w_2 - w_1} \ln\left(1 + \frac{w_2 - w_1}{w_1}\right) . \end{aligned} \tag{4.31}$$

$$\Rightarrow R = \varrho\alpha_{\mathrm{geom}} = \varrho \frac{L}{w_1} F\left(\frac{w_2 - w_1}{w_1}\right) \;;\ \text{with}\ \ F(w) = \frac{1}{w}\ln(1 + w) . \tag{4.32}$$

It should be noted that this is an approximation, since the integration along x assumes that equipotential lines are parallel to the cartesian axes, an assumption that becomes less accurate the larger the opening angle of the trapezoid is.

The resulting geometrical weights α_{geom} are calculated in Table 4.5. The total resistance R is the sum of all resistances, Eq. (4.30), and the conductance is its inverse value $1/R$.

With $n_0 = 3.7 \cdot 10^{11}/\mathrm{cm}^2$ and $\mu_\mathrm{e} = 8.8 \cdot 10^5\,\mathrm{cm}^2/(\mathrm{Vs})$, the equilibrium conductivity value is 52 mS. Dividing this by the sum of the geometrical factors $\sum \alpha_{\mathrm{geom}} \approx 18.7$ yields a conductance of 2.7 mS at zero gate voltages. Experimentally, the value is lower and equals $\sigma_{\mathrm{exp}}(0{,}0) \approx 0.91$ mS. If the mobility within the narrow channel is assumed to be reduced by a factor γ because of increased edge scattering, this can be taken into account by increasing the weight factors α_{geom} within the narrow channel (regions 2, 3, 4) by γ. A γ=12-times higher resistivity within the narrow channel yields a conductance of 0.90 mS, very close to the experimental value of $\sigma_{\mathrm{exp}}(0{,}0)$. This corresponds to a reduced mobility of $\mu_\mathrm{e}/\gamma \approx 7.3 \cdot 10^4\,\mathrm{cm}^2/(\mathrm{Vs})$ and a mean free path of 0.74 µm. This is on the order of the channel width, which would mean that the electrons lose their phase at every scattering on the edges. This is highly unlikely, but represents a lower limit, a conservative estimate of the mean free path.

The actual mobility within the narrow channel cannot be smaller than ca. $7.3 \cdot 10^4\,\mathrm{cm}^2/(\mathrm{Vs})$. The mobility may be higher, if quantum effects of the narrow constriction are limiting the conductance of the narrow channel rather than the Drude mobility, but it cannot be lower than this value. If it were lower, it would be impossible to experimentally measure a conductivity as high as 0.91 mS. This way, a lower limit for the mean free path of 0.74 µm is found. This is substantially larger than the gap between the antenna wings of 0.27 µm size. Thus electrical transport is ballistic in the active area of the device.

4.7.3 Conductance enhancement

An unclear phenomenon in the conductance measurement of sample V837-2-3.1 (Fig. 4.33) is its enhancement at strongly positive gate voltages. The pinch-off regime at negative gate voltages is clear, since there the electron channel is depleted, but what happens at positive gate voltages? The phenomenon is illustrated in one-dimensional line scans of the 4-terminal conductance in Fig. 4.57. Clearly, there is some other mechanism that has an onset around 0.6 V narrow gate voltage and 0.45 V wide gate voltage.

One hypothesis is that it may be related to the Schottky barrier at the TiAu/GaAs interface. The Schottky barrier between n-type GaAs and titanium is about 0.83 eV [253]. However, the gate conductance is orders of magnitude below the source-drain conductance for $U_{\mathrm{G,narrow}} < 0.885$ V and $U_{\mathrm{G,wide}} < 0.75$ V, but the onset is at lower gate voltages. The Schottky barrier hypothesis can be ruled out by considering conductance measurements at different equilibrium electron densities, shown in Fig. 4.58.

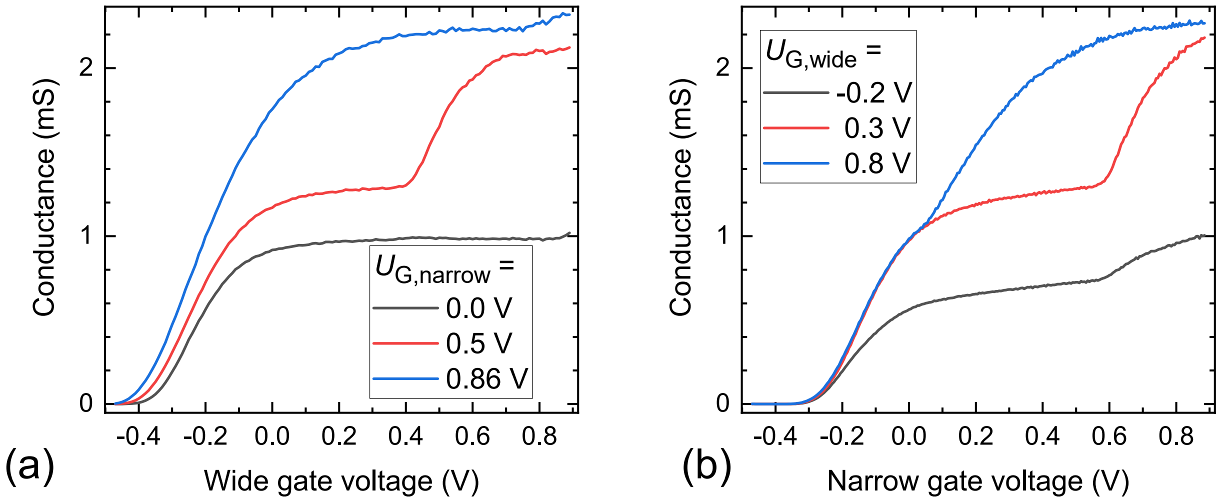

Figure 4.57: **Line scans of the 4-terminal conductance,** with one of the gate voltages held constant. The data corresponds to horizontal and vertical lines from the 2D map in Fig. 4.33. (a) Narrow gate voltage held constant, (b) wide gate voltage held constant at the given values.

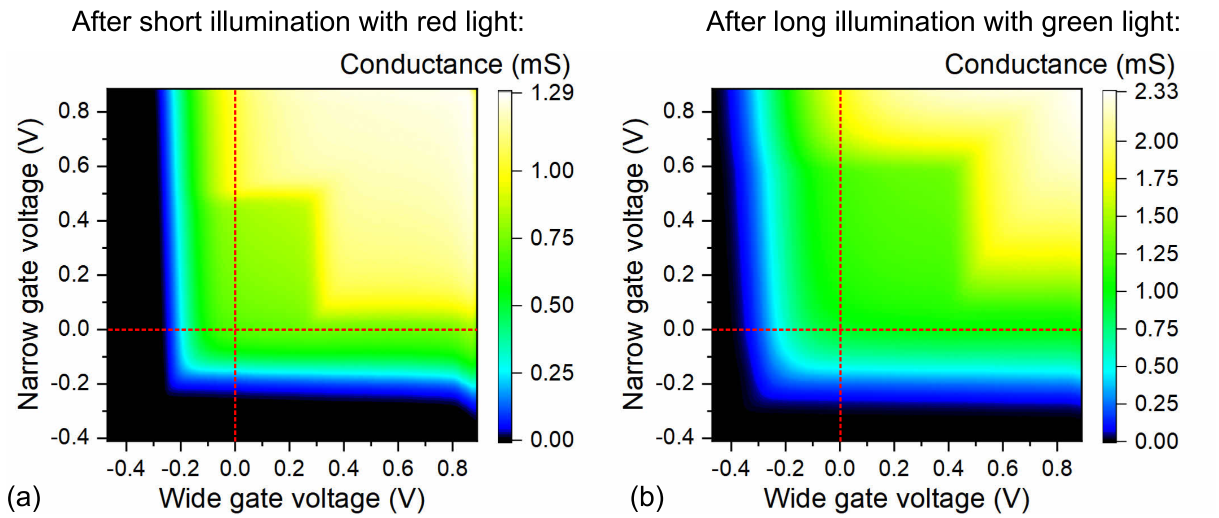

Figure 4.58: **4-wire conductance at different electron densities.** (a) After a short (~1 minute) illumination with a red 3 W LED. (b) After a long (~1 hour) illumination with a green 3 W LED, from Fig. 4.33 (a). The conductance was measured some time after the illumination, when the illumination has been switched off and the conductance has stabilised.

In Fig. 4.58 (a), the sample conduction was measured after a short, ca. 1 minute long illumination with red light after a cooldown in a dark environment. In (b), the sample was illuminated for ca. 1 hour with a green LED. This very long illumination leads to the maximum possible electron density in this wafer. The onset of conduction for the narrow gate is similar for both (a) and (b), suggesting that the impurities were ionised under the narrow gate already during the short red illumination, but not yet under the wide gate, where the metallic gate shadows the wafer underneath of it. Importantly, the onset of the conductance enhancement is different for both measurements, ruling out an effect related to the built-in Schottky barrier at the gates.

Another reason for the conductance enhancement could be the plateau in the electron density–gate voltage dependence, Fig. 4.49 (a): the plateau around 0.2 V–0.4 V might lead to the step/square in the two-dimensional plot of the conductance. However, there are several arguments that make this hypothesis unlikely. Firstly, although there is a plateau in $n_\mathrm{s}(U_\mathrm{G})$, it is hardly noticable in the bulk conductivity of the 2DEG, Fig. 4.48 (a). Secondly, the end of the plateau (i. e. the right end at higher gate voltages) is consistently around 0.4 V, above which $n_\mathrm{s}(U_\mathrm{G})$ follows almost the same trend irrespectively of whether the sample has been illuminated or not. But the data in Fig. 4.58 shows a clear shift in the onset depending on the illumination dose.

The clear onset behaviour indicates that there must be some series resistance which is the bottleneck at zero gate voltages, but is eliminated at high positive gate voltages. Considering the analysis in the previous section 4.7.2, Table 4.5, this series resistance is likely region 4, the ungated 2.04 µm long channel right from the narrow gate, whose resistance contribution is additionally enhanced due to the narrow size of channel. This hypothesis is supported by the fact that it is enough to apply a positive voltage on the narrow gate with zero wide gate voltage to induce the enhancement effect (Fig. 4.58, vertical dashed line). In contrast, a positive wide gate voltage alone is not sufficient with zero narrow gate voltage (Fig. 4.58, horizontal dashed line). This shows that the narrow gate voltage has a stronger influence on the series bottleneck resistance than the wide gate voltage. The additional increase in conductance when a positive gate voltage is also applied to the wide gate may be related to the ungated region in-between the two gates. Most likely, at high positive gate voltages, the narrow gate or the wings of the cutout in the bow-tie half widen up the conducting channel and reduce the amount of edge depletion. This conclusion is consistent with the findings on other samples: Fig. 4.56 shows that at approximately the same gate voltage regions the gates are able to induce conduction even in samples where conduction is frozen out in equilibrium.

4.7.4 Antenna amplification

Subsequent analysis will require knowledge about the electric field that electrons experience, and thus the field amplification in the gap. This is obtained from finite element simulations (done in Comsol Multiphysics) for the given geometry of the antenna gap of 0.27 µm, narrow gate width of 0.2 µm, and antenna tip width of 2 µm. The results are shown in Fig. 4.59.

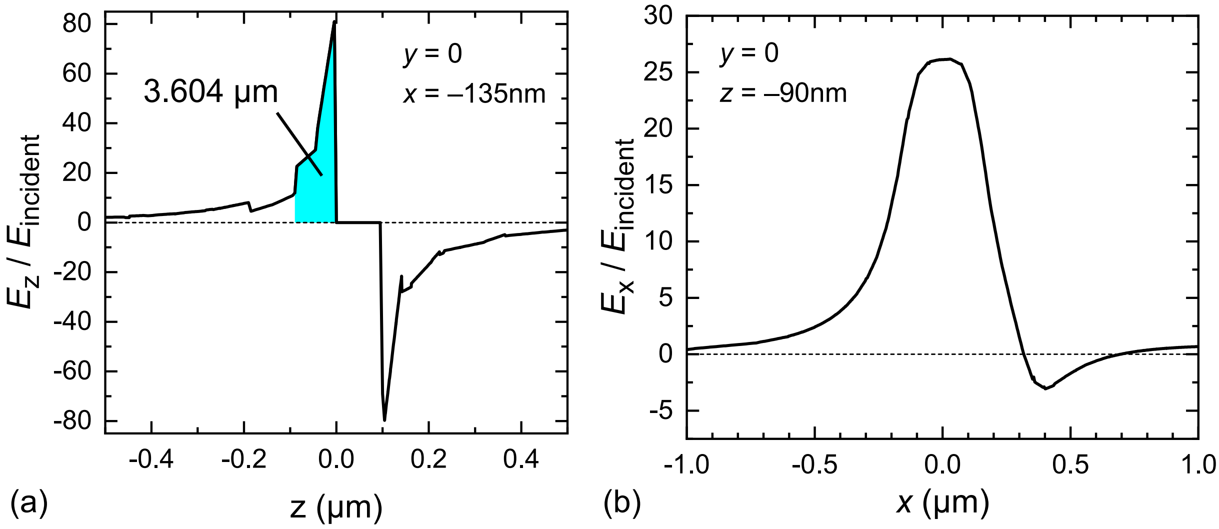

Figure 4.59: **Electric field amplification by the bow-tie antenna.** Amplification of the electric field in (a) z-direction, (b) x-direction. In (a), the electric field is evaluated below the tip of the wide gate, located at x = −0.27 µm/2. In (b), the electric field is evaluated along the axis of the antenna, 90 nm under the surface, approximately where the 2DEG is. $x = y = 0$ is the center of the bow-tie antenna; $z = 0$ is the GaAs-vacuum interface.

From Fig. 4.59 (a), the THz gate-to-channel voltage can be calculated:

$$u_{\mathrm{ac,z}} = E_{\mathrm{incident}} \int_{-d}^{0} \mathrm{d}z \left(\frac{E_{\mathrm{z}}}{E_{\mathrm{incident}}} \right) . \tag{4.33}$$

Here, E_{incident} is the amplitude of the incident electric field which is polarised in x-direction. The value of the integral, evaluated numerically, is shown in Fig. 4.59.

From the definition of the Poynting vector, the electric field can be calculated from the intensity I in W/m^2 as

$$E = \sqrt{c\mu_0 I} . \tag{4.34}$$

In the experiment, there are two intensities: I_0 during a THz pulse, and the time-averaged value $\langle I \rangle = I_0 \cdot 2.14\%$. It will be assumed that the time-average of the photoresponse corresponding to an intensity value is equal to the photoresponse corresponding to the time-average of the intensity value:

$$\langle U_{\mathrm{ph}}(I(t)) \rangle = U_{\mathrm{ph}}(\langle I(t) \rangle) , \tag{4.35}$$

and equally, for the photocurrent. This assumption is justified given the low powers used, and considering the linearity of the detector response as a function of the duty cycle, Fig. 4.42.

The incident average intensity is $\langle I \rangle = I_0 \cdot 2.14\% = 6.25\,\mu\text{W/mm}^2$, which corresponds to 49 V/m of electric field. This yields $u_{\text{ac,z}} = 0.18\,\text{mV}$.

The x-component of the electric field is amplified by a factor of about 26 in the gap. This gives a peak electric field of 87 V/cm during a pulse (corresponding to the intensity $I_0 \approx 0.29\,\mu\text{W/mm}^2$).

4.8 Comparison with known photodetection mechanisms

Let us now discuss detection mechanisms known in literature, and consider whether they could explain the observed THz response.

4.8.1 Bolometric, thermal or heating mechanisms

Thermal mechanisms have been reviewed in section 1.2.4.3. One of them is the bolometric mechanism, which commonly gives rise to photoconductance [81, 141, 142], and dominates in the pinch-off regime, where conduction is sensitive to small temperature changes [141]. In contrast, in our case, we measure a zero-bias photocurrent, which is maximal in the open regime, when the 2DEG is well conducting. Another thermal mechanism is the photo-thermoelectric effect [143, 144]. This effect occurs in the case of a broken symmetry (which is the case when the gate voltages are different) and could give rise to a zero-bias photocurrent. However, both bolometric and photo-thermoelectric mechanisms can be ruled out: they rely on a local increase of the electron temperature, which is not relevant in our case, as will be shown in the following.

Electron gas heating is relevant when the electron-electron scattering time is much smaller than the momentum relaxation time due to scattering of electrons with impurities, i.e., when electrons scatter with each other more often than with the lattice imperfections [254, 255]. Such a situation is typically the case in narrow-band or gapless semiconductors (e.g. in graphene [144]), where the number of mobile charge carriers (electrons and holes) can be much larger than the number of impurities. In modulation doped heterostructures such as the 2DEG samples studied here, electrons originate from donors, electron concentrations are orders of magnitude lower, and the low-temperature mobility is limited by impurity scattering [221]. Therefore, electron-impurity scattering is more important than electron-electron scattering. This can also be seen from an estimation: for the electron density $3.7 \cdot 10^{11}/\text{cm}^2$ and mobility $8.8 \cdot 10^5\,\text{cm}^2/(\text{Vs})$, the electron momentum relaxation time estimated from the Drude model is $\tau_\text{p} \approx 34\,\text{ps}$. The electron-electron scattering time for a degenerate Fermi gas can be estimated from [255]

$$\tau_{\text{ee}} = \frac{\hbar}{E_{\text{Rydberg}}} \left(\frac{E_\text{F}}{k_\text{B} T} \right)^2 , \text{ with } E_{\text{Rydberg}} = \frac{m_{\text{eff}} e^4}{2(4\pi\varepsilon_0\varepsilon_\text{r}\hbar)^2} \tag{4.36}$$

being the hydrogen atom confinement energy from Bohr's atomic model in a material environment. For 9 K temperature and 13.2 meV Fermi energy corresponding to the given electron density of $3.7 \cdot 10^{11}/\text{cm}^2$, this gives $\tau_\text{ee} \approx 33$ ps – i. e. both scattering times are of the same order of magnitude. In fact, as discussed in section 4.7.2, the mobility in the narrow channel could likely be lower, down to about $7.3 \cdot 10^4$ cm^2/(Vs), which corresponds to $\tau_\text{p} \approx 2.8$ ps, an order of magnitude higher scattering rate than electron-electron scattering. So the condition $\tau_\text{ee} \ll \tau_\text{p}$ required for electron heating to dominate is not fulfilled, and hence electron heating does not play an important role in this experiment. Since the mean free path is much larger than the gap between the antenna wings, the observed THz photoresponse does not rely on a scattering-based mechanism.

A collisionless mechanism (when scattering with the lattice is negligible), as discussed in section 1.2.4.3, is possible. However, the increase in the mean energy of the electrons can be estimated according to Eq. (1.14) as $e^2E_\text{ac}^2/(4m_\text{eff}\omega^2) \approx 0.46$ µeV. This is a negligible amount, which is orders of magnitude smaller than $k_\text{B}T$. The estimation is done for the maximum electric field of $E_\text{ac} \sim 10^2$ V/cm obtained during a THz pulse, with intensity I_0.

4.8.2 Photon-assisted tunneling

Another mechanism to consider is photon-assisted tunneling [138–140]. This can be ruled out in the present experiment. Firstly, the photocurrent dominates in the open regime, when the sample is well conducting, i. e. it is not in the tunneling regime. Secondly, the size of the barriers created by the gates is macroscopic ($\sim$ 4 µm in the case of the wide gate), which excludes tunneling-related phenomena.

4.8.3 Plasmonic or distributed resistive mixing

Many THz detection experiments [71, 77, 78, 84, 87, 120, 121, 123, 218] were interpreted in terms of the plasma-wave mixing theory in 2DEGs [119] or distributed or quasistatic resistive mixing [77, 120].

Let us estimate the absolute value predicted by the plasmonic mixing mechanism. The sample can be modelled as a back-to-back series connection of two 2DEGs with different densities. The source-drain distance is much longer than the plasmon decay length, and $\omega\tau \gg 1$. Under these conditions, the plasmonic mixing theory [119] predicts a photovoltage of

$$U_\text{ph} = \frac{3}{4}\frac{u_\text{ac}^2}{U_\text{G} - U_\text{th}}\,. \tag{4.37}$$

This is derived from Eq. (1.10), when the function $f(\omega\tau, s\tau/l)$ equals 3.

In the sample V837-2-3.1 studied here, the THz gate-to-channel voltage amplitude u_ac equals 0.18 mV for the average incident power (section 4.7.4). At the point of maximum experimental photocurrent in the $U_G < 0.6$ V area, ($U_{G,wide}$,$U_{G,narrow}$) = (–0.29 V,0.15 V), this predicts a photovoltage of 0.2 µV. The measured photovoltage is 1.8 µV, i. e. considerably higher.

Another estimation can be done by considering the maximum possible photovoltage for non-resonant detection, which is $\approx eu_{ac}^2/(4\eta k_B T)$ according to Ref. [121]. Taking a value of $\eta \gtrsim 10$ for GaAs based FETs at low temperatures [121] and $T \approx 9$ K, this gives ~1 µV. This is smaller than the experimental photovoltage of 5.6 µV in the area $U_G < 0.6$ V, and more than an order of magnitude smaller than the maximal DC photovoltage of 56 µV at strong gate asymmetry as seen in Fig. 4.37 (a).

In addition, the qualitative form of the photoresponse is also not explained. The expected plasmonic mixing response can be estimated by

$$U_{\mathrm{Ph,\,1\,gate}}(U_0) = \frac{eu_{\mathrm{ac,z}}^2}{4\eta k_B T} \frac{1}{\left[1+\exp\left(-\frac{eU_0}{\eta k_B T}\right)\right]\left[1+\exp\left(\frac{eU_0}{\eta k_B T}\right)\right]}, \quad (4.38)$$

for a negligible gate leakage current according to Ref. [121]. Here, U_0 is the gate voltage at the threshold, $U_0 = U_G - U_{th}$. The expected response for a junction of two differently gated regions would be

$$U_{\mathrm{Ph,\,2\,gates}}(U_{G,L},U_{G,R}) = U_{\mathrm{Ph,\,1\,gate}}(U_{G,L} - U_{th}) - U_{\mathrm{Ph,\,1\,gate}}(U_{G,R} - U_{th})\,. \quad (4.39)$$

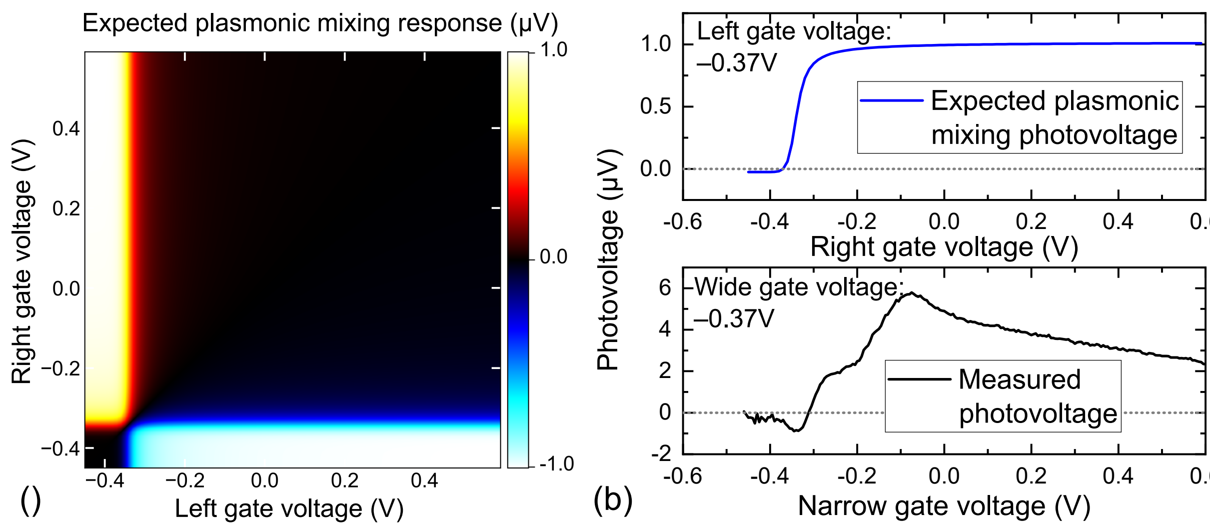

Figure 4.60: **Theoretically expected photoresponse in the case of plasmonic mixing.** (a) Two-dimensional plot of the expected plasmonic mixing photovoltage. (b) One-dimensional plots comparing the photovoltage at –0.37 V wide (left) gate voltage, at the top: expected plasmonic mixing response; at the bottom: measured photovoltage from Fig. 4.36.

This is plotted in Fig. 4.60 (a). As can be seen, plasmonic mixing would result in a monotonous increase of the photovoltage the further apart the gate voltages are. The broad maximum of the photovoltage (or -current) observed experimentally in Figs. 4.36 (or 4.35) is not reproduced. This maximum is highlighted in Fig. 4.60 (b) at the bottom in a one-dimensional plot of the photovoltage through the experimental photovoltage maximum in the $U_{\mathrm{G,narrow}} \gtrsim 0.6\,\mathrm{V}$ region at –0.37 V wide gate voltage, i.e. a vertical line in the 2D plot. The top graph of Fig. 4.60 (b) shows the corresponding line plot of the theoretically expected plasmonic mixing photoresponse at –0.37 V left gate voltage for comparison. By contrast, it does not exhibit a maximum as a function of the right gate voltage.

Furthermore, in the device studied here, the ideality factor can be estimated to be ≈ 31 from the conductance characteristic Fig. 4.33 (b). In this case, the expected photovoltage amplitude will be even lower.

4.9 Summary

In this chapter, an antenna-coupled, dual-gated THz detector based on a 2DEG was presented. First, the antenna structure was designed using numerical simulations in Comsol. After fabrication of test samples to establish optimal processing parameters for the mesa etching and the evaporation of a continuous gate bridge, actual THz detector samples were fabricated. Then the journey of searching for a THz response started, which finally revealed a THz photocurrent at a finite source-drain bias. After solving multiple set-up related issues concerning electrostatic discharge, electric noise, electromagnetic interference, and light ingress, the THz photoresponse was confirmed on a different device. The measurements showed that both a THz photovoltage and photocurrent can be observed even at zero source-drain bias. The photoresponse and sample conductance were studied as a function of the full accessible voltage range on the wide and narrow gates. Direct detection was demonstrated, and the responsivity and noise-equivalent power were estimated. The dual-gated device architecture was shown to allow independent tuning of output impedance and responsivity of the detectors. Measurements on other samples confirmed the reproducability of results. Gated and ungated Hall bars, made from the same wafer material as the detector samples, were measured both in the dark and after illumination to quantify electron density and mobility in the 2DEG. The device operation was analysed and the photoresponse was compared to theories of THz photoresponse generation in 2DEGs, which showed that the observed effect cannot be explained by known mechanisms. In the next chapter, I will show that the response is due to a new effect – an “in-plane photoelectric effect”.

5 Discovery of the in-plane photoelectric effect

A key milestone in the history of quantum mechanics was the discovery of the photoelectric effect. In 1902, Lenard found that the energy of electrons emitted from a metal under irradiation by X-rays depends only on the frequency, but not the intensity, of the incident light [256]. This puzzling observation stimulated Einstein in 1905 to put forward the idea that formed the foundation to the development of quantum mechanics: Light is absorbed in the form of discrete quanta (photons), and a photon can excite an electron from the surface of a metal, if its quantized energy $\hbar\omega$ is larger than the potential step height formed at the material interface – the work function [257]. This had fundamental consequences for the understanding of wave propagation. It introduced the concept of wave-particle dualism, the idea that light propagates as waves, but is absorbed in the form of single quanta of energy. This process, the external photoelectric effect, takes place in the UV–Xray region of the electromagnetic spectrum, since workfunctions of metals are in the range of several electronvolt.

At lower frequencies, in the visible–near infrared ranges, a related process, where photoexcitation leads to a photocurrent, is the photovoltaic effect that takes place within a material. The most prominent example is a solar cell: electron-hole pairs are generated within an interband photoexcitation process, and give rise to a photovoltaic response as electrons and holes are dragged in opposite directions due to the built-in electric field at the p-n-junction of the solar cell. Here, the photoresponse originates at the interface of two semiconducting materials, which differ due to their doping.

Moving towards even lower frequencies, mid infrared–far infrared, the photon energy becomes smaller than band gaps of semiconductors, which excludes interband photoexcitation. Instead, intraband transitions form the basis of the internal photoelectric effect at such frequencies. They are utilised in homojunction and heterojunction internal photoemission detectors [147, 148, 258, 259]. As mentioned in section 1.2.5, in these devices a potential step is formed at the interface of two semiconducting materials, created during epitaxial growth. They either differ in their bulk chemical composition (heterojunction), or in their doping concentration (homojunction). In both cases, the potential step formed at the interface of the materials creates an energy barrier, the work function, for electrons in the conduction band. These detectors work well in the mid and far infrared, but as the frequencies approach the THz region, their sensitivity quickly decays [149, 260, 261]. As discussed in the introduction to chapter 4, Fig. 4.1 (c), below 5 THz, the responsivity rapidly

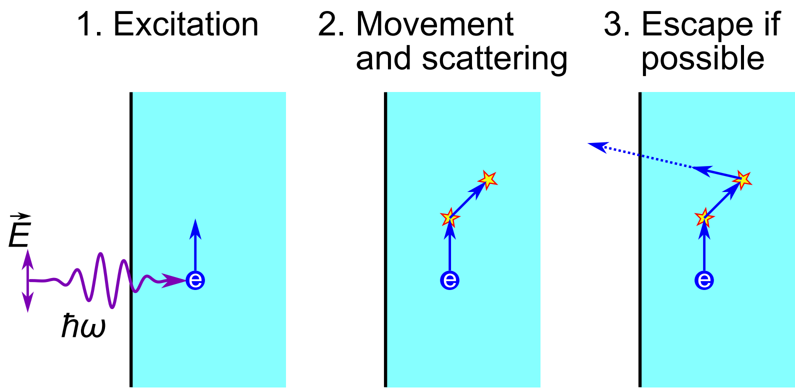

Figure 5.1: **The three stages of the photoelectric effect.**

falls off by orders of magnitude towards ~ 2.5 THz. Furthermore, these three-dimensional, bulk photoemissive detectors are photoconductive and thus require an applied external bias in order to extract the photoexcited electrons [261–264].

But this is only half of the story. Apart from the energy, the momentum of photoexcited electrons needs to be considered as well: it has to have a sufficiently large component perpendicular to the interface in order to produce a current. In general, the photoemission from a material in three dimensions is a complicated process consisting of several steps [265, 266], see Fig. 5.1: first photons excite electrons, these then move and, potentially, scatter within the solid, and finally leave into the collecting medium, provided they have sufficient energy and momentum *perpendicular* to the interface.

This can be visualised by an escape cone model [98, 267, 268], Fig. 5.2. Before exci-

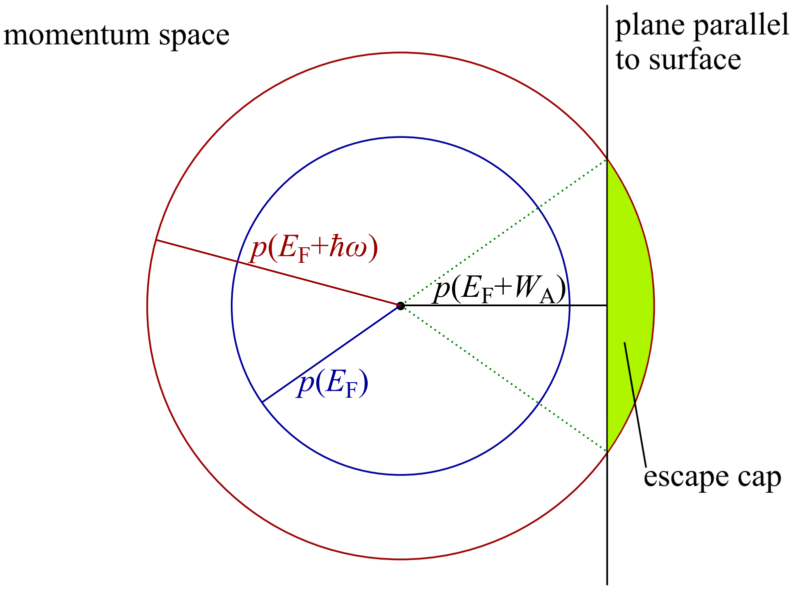

Figure 5.2: **The escape cone model.** Only electrons with momenta in the green region can escape from the material.

tation, the electrons form a Fermi sphere with maximal energy E_F, the Fermi energy (blue sphere). They are contained within a material that has a work function W_A. Upon excitation with photons with an energy $\hbar\omega$, electrons gain a larger energy and corresponding momenta up to $p(E_\mathrm{F} + \hbar\omega)$. This is shown as a larger, red sphere in Fig. 5.2. In order to leave the material, electrons have to exceed a threshold momentum corresponding to the energy $E_\mathrm{F} + W_\mathrm{A}$ in the direction normal to the interface. The electrons contained in the green region are those capable of fulfilling this criterion and leaving the material. This gives rise to an escape cone defined by the energy values between $E_\mathrm{F} + W_\mathrm{A}$ and $E_\mathrm{F} + \hbar\omega$.

Whether the electrons will absorb a photon, how many of them will be able to leave the material, and under which angle, depends on the likelihood of scattering and the angular distribution of photoexcited electrons. This non-trivial question [266] has been studied during the past century.

An electron can only absorb an incident photon if both energy and momentum are conserved at the same time. For this reason, a free electron cannot absorb a photon. In the photoelectric effect, there are two possibilities how photons can be absorbed. The first option constitutes vertical transitions to a higher lying band – interband transitions. This is called the *volume photoelectric effect*. The second possibility is excitation of electrons close to the interface, where the work function creates a potential discontinuity that breaks translation symmetry and thus no conservation law applies to the perpendicular momentum component. This is the *surface photoelectric effect* [269, 270].

In the volume photoelectric effect, electrons are absorbed in the bulk of a crystal. This takes place by photonic, almost vertical interband transitions in the bandstructure [266, 271]. The angular distribution of photoelectron momenta was shown to be related to momentum-conserving transitions in the momentum space, with a large fraction of photoelectrons not undergoing scattering processes [272]. For nearly-free electrons, this results in photoexcited electrons being predominantly emitted parallel to the electric field vector [271].

However, in the case of low-energy photons, such as in the THz range, the volume photoelectric effect is not relevant, since in typical materials there are no interband transitions with low enough transition energies to be excited by THz photons. The threshold energy for the volume photoelectric effect is much higher than for the surface photoelectric effect [269].

In the case of the surface photoelectric effect [270, 273], electrons absorb a photon at the interface. In this model, only the electric field component perpendicular to the surface causes photoemission [266, 274].

These peculiarities lead to an inherent inefficiency when exploiting the photoelectric effect for detection of radiation: under normal incidence of radiation, the photoexcited electrons gain predominantly a momentum $\vec{p}$ parallel to the electric field [271] and thus *parallel* to

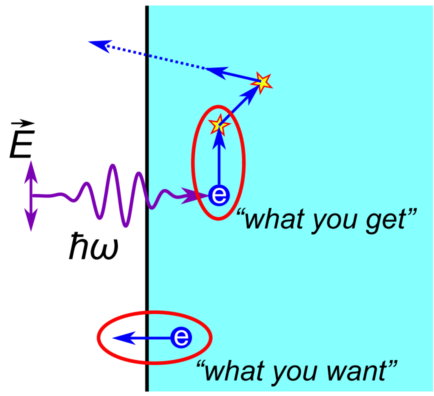

Figure 5.3: **The issue with the three-dimensional photoelectric effect:** The normally incident electric field generates electrons with momenta mostly parallel to the interface. But to leave the material, momenta perpendicular are necessary.

the surface. But to leave the material, the momentum needs to be *perpendicular* to the interface. This issue is highlighted in Fig. 5.3.

To increase the yield, electrons need to be redirected towards the material interface in order to leave the material. One option is to use p-polarised light under oblique or grazing incidence. This increases the electric field component perpendicular to the interface, and thus the photoelectric yield [266, 275], but reduces the effective input aperture of the detector given a certain detector area by the cosine of the incidence angle. Another mechanism is scattering, which is always present in reality. This randomises the direction of motion of photoexcited electrons, and thus also creates a momentum component perpendicular to the interface. Both cases are not optimal; in addition, scattering is a non-deterministic, random process that reduces the energy of photoexcited electrons and thus diminishes the efficiency. Moreover, it limits the intrinsic response time of the effect to scattering times.

In an ideal world, we would want to take the benefits of the photoelectric effect, but without its drawbacks. The momentum of photoexcited electrons should be perfectly aligned with the desired direction of motion, i. e. perpendicular to the potential step. Such a process would not require any scattering, and with scattering eliminated, the intrinsic response time will not be limited by scattering times. Furthermore, we want the workfunction to be easily tunable *in-situ*, and for best noise performance, we wish to see a photoresponse without any external bias applied. As we will see in this chapter, this is exactly what is realised in two dimensions in the demonstrated THz detector.

5.1 Physics of the phenomenon

How can the detection mechanism of the device demonstrated in chapter 4 be understood? To answer this question, let us consider a uniform 2DEG covered by two gates, see Fig. 5.4

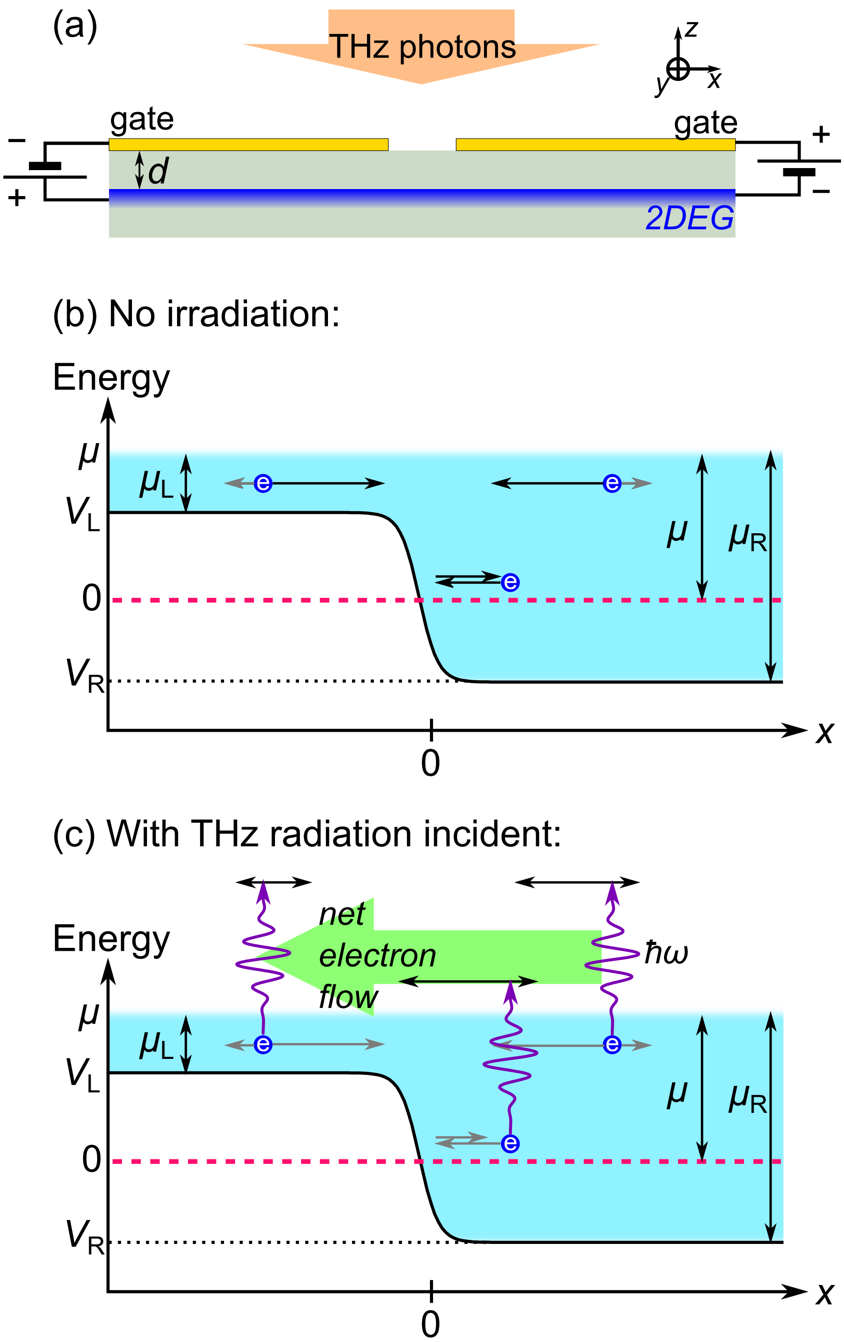

Figure 5.4: **Physical principle of the photoelectric tunable-step detection mechanism.** (a) Side view of the device: a semiconductor heterostructure with a 2D electron gas is covered by two gates and irradiated by electromagnetic radiation. (b) Energy diagram of the device. μ is the equilibrium chemical potential, $V_L > 0$ and $V_R < 0$ are the conduction band edges in the left and right parts of the device. A potential step of value $V_L - V_R$ is artificially created by applying different voltages to the gates. This gives rise to different electron densities and different chemical potentials, $\mu_L = \mu - V_L$ and $\mu_R = \mu - V_R$, in the left and right areas of the 2D electron gas. (c) Incident electromagnetic radiation on a potential step excites electrons on both sides of the barrier, resulting in a net electron flow onto the step.

(a). In equilibrium, the bottom of the conduction band (dashed purple line) and the chemical potential μ are position-independent. By applying two different voltages on the gates, $U_{\mathrm{G,L}}$ and $U_{\mathrm{G,R}}$, we create an *artificial, gate voltage tunable potential step* for electrons moving in the 2DEG in the horizontal (x-) direction. This shifts the bottom of the equilibrium conduction band under the left and right gates by V_{L} and V_{R}, respectively, resulting in the local chemical potentials μ_{L} and μ_{R}, see Fig. 5.4 (b). Without any incident radiation, the net particle flow vanishes: electrons with energies $E < V_{\mathrm{L}}$ do not contribute to the current since they are reflected backwards at the step, while for $E > V_{\mathrm{L}}$ the current flow cancels out due to equal reflection and transmission probabilities regardless of the direction of electron motion.

Once the potential step in the gap between the gates is exposed to incident electromagnetic radiation of frequency $f = \omega/(2\pi)$, electrons can absorb a photon of energy $\hbar\omega$, Fig. 5.4 (c). Those with energies $E < V_{\mathrm{L}}$ on the right side, that previously could not overcome the step, are now able to do so by absorbing incident photons. For electrons with energies $V_{\mathrm{L}} < E < \mu$, photon absorption will lead to a higher probability to move to the left (onto the step) than to the right (as will be seen from the theoretical treatment in the following, Fig. 5.7 (c)). As a result, the radiation induces a net particle flow from the higher-density region to the lower-density region.

As seen from this qualitative picture, the considered structure with a two-dimensional electron gas has multiple advantages as compared to the standard, three dimensional realisations of the photoelectric effect: the THz wave is normally incident on the working material, the electric field of the wave is parallel to the device surface and *parallel* to the desired direction of the electron motion. The potential step for electrons is artificially created by the gate voltages and can be electrically tuned to any desirable value. In addition, the gates varying the 2D electron gas densities can simultaneously serve as THz antennas, resulting in a substantial enhancement of the AC electric field acting on electrons under the gates. This can be understood as an *"in-plane photoelectric effect"*, that occurs within the plane of the 2DEG.

5.2 Theoretical description

5.2.1 Without THz irradiation (zeroth order)

For a quantitative description of the phenomenon, let us consider a 2DEG stripe which is infinite in the x-direction. In the y-direction it has a width W, and it is covered by two semi-infinite gates at negative and positive x-values lying on the surface of the semiconductor. The DC gate voltages $U_{\mathrm{G,L}}$ and $U_{\mathrm{G,R}}$ induce a potential step in the 2DEG, see Fig. 5.5 (a), which is modelled as a step-like function $V_0(x) = V_{\mathrm{L}} - (V_{\mathrm{L}} - V_{\mathrm{R}})\Theta(x)$, Fig. 5.5 (b). Without loss of generality, $V_{\mathrm{L}} > V_{\mathrm{R}}$ is assumed. In the transverse, y-direction, the potential $\tilde{V}_0(y)$

is modelled by two infinite potential walls at $y = 0$ and $y = W$. Without THz irradiation, the motion of electrons in the 2DEG stripe is described by the Schrödinger equation:

$$i\hbar\frac{\partial\Psi^{(0)}}{\partial t} = \hat{H}_0\Psi^{(0)} = -\frac{\hbar^2}{2m}\frac{\partial^2\Psi^{(0)}}{\partial x^2} - \frac{\hbar^2}{2m}\frac{\partial^2\Psi^{(0)}}{\partial y^2} + V_0(x)\Psi^{(0)} + \tilde{V}_0(y)\Psi^{(0)} . \tag{5.1}$$

As for the y-dependence of the wavefunction, the infinite potential well gives rise to wavefunctions of the form $\sin(\pi n y/W)$ with quantisation energies $E_W n^2$, where

$$E_W = \pi^2\hbar^2/(2mW^2) , \tag{5.2}$$

and n is the subband index. For a width W of 0.7 µm, as estimated for the THz detector sample in section 4.7.1, $E_W \approx$ 12 µeV.

Then the zeroth-order wavefunction $\Psi^{(0)}(x,y,t)$ can be searched for in the form

$$\Psi^{(0)}(x,y,t) = e^{-iEt/\hbar}\sin\frac{\pi n y}{W}\psi^{(0)}_{E,n}(x) , \tag{5.3}$$

where the function $\psi^{(0)}_{E,n}(x)$ satisfies the one-dimensional Schrödinger equation

$$E\psi^{(0)}_{E,n}(x) = -\frac{\hbar^2}{2m}\frac{\partial^2\psi^{(0)}_{E,n}(x)}{\partial x^2} + E_W n^2\psi^{(0)}_{E,n}(x) + V_0(x)\psi^{(0)}_{E,n}(x) , \tag{5.4}$$

which can be solved as usual in quantum mechanics [276]. With the function $Q(E)$, corresponding to the wavevector of particles with the energy E,

$$Q(E) = \begin{cases} \sqrt{2mE}/\hbar \; ; & E \geq 0 \\ i\sqrt{2m(-E)}/\hbar \; ; & E < 0 \end{cases} , \tag{5.5}$$

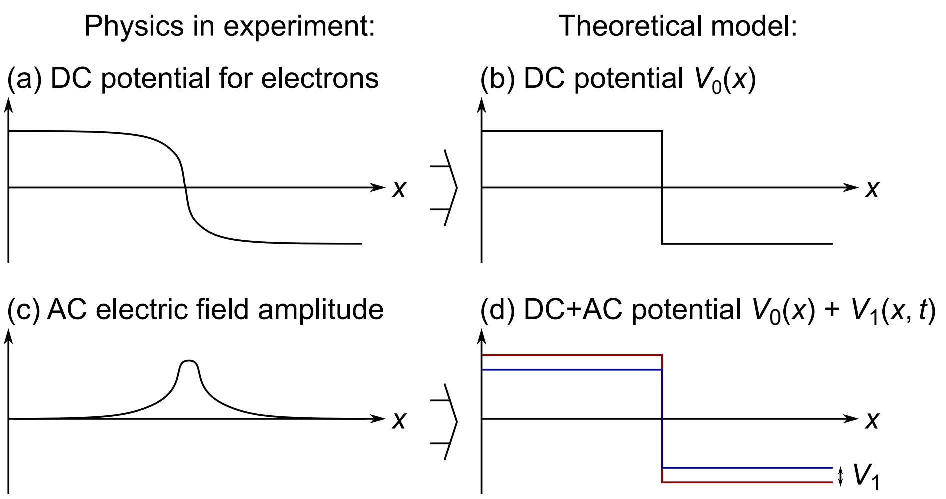

Figure 5.5: **Physical model.** (a), (c) Situation in the experiment; (b), (d) the theoretical model considered. The AC electric field results in the potential step height "wiggling" around its DC value.

the resulting wave function for the particles running to the left is:

$$\psi_{E,n}^{(0)\Leftarrow}(x) = \begin{cases} e^{-iQ(E-E_W n^2-V_\mathrm{R})x} + r_{E,n}^{(0)\rightleftarrows} e^{iQ(E-E_W n^2-V_\mathrm{R})x}, & \text{if } x > 0, \\ t_{E,n}^{(0)\leftleftarrows} e^{-iQ(E-E_W n^2-V_\mathrm{L})x}, & \text{if } x < 0\,. \end{cases} \tag{5.6}$$

For the particles running to the right it is:

$$\psi_{E,n}^{(0)\Rightarrow}(x) = \begin{cases} t_{E,n}^{(0)\rightrightarrows} e^{iQ(E-E_W n^2-V_\mathrm{R})x}, & \text{if } x > 0, \\ e^{iQ(E-E_W n^2-V_\mathrm{L})x} + r_{E,n}^{(0)\leftrightarrows} e^{-iQ(E-E_W n^2-V_\mathrm{L})x}, & \text{if } x < 0. \end{cases} \tag{5.7}$$

Here, the direction of particle motion is indicated in the superscripts. The lower arrow is the direction of the incident wave; the upper arrow is the direction of the outgoing wave after interaction with the potential step, see Fig. 5.6.

The transmission and reflection amplitudes $t_{E,n}^{(0)\rightrightarrows}$, $r_{E,n}^{(0)\leftrightarrows}$, $t_{E,n}^{(0)\leftleftarrows}$, and $r_{E,n}^{(0)\rightleftarrows}$ are calculated by applying boundary conditions

$$\psi_{E,n}^{(0)}(+0) = \psi_{E,n}^{(0)}(-0) \;\; ; \;\; \frac{d\psi_{E,n}^{(0)}(+0)}{dx} = \frac{d\psi_{E,n}^{(0)}(-0)}{dx}. \tag{5.8}$$

Using

$$E_\mathrm{x,L} = E - E_W n^2 - V_\mathrm{L} \;\text{ and }\; E_\mathrm{x,R} = E - E_W n^2 - V_\mathrm{R}\,, \tag{5.9}$$

they can be expressed as

$$t_{E,n}^{(0)\leftleftarrows} = \frac{2}{1+\frac{Q(E_\mathrm{x,L})}{Q(E_\mathrm{x,R})}},\quad r_{E,n}^{(0)\rightleftarrows} = \frac{1-\frac{Q(E_\mathrm{x,L})}{Q(E_\mathrm{x,R})}}{1+\frac{Q(E_\mathrm{x,L})}{Q(E_\mathrm{x,R})}},\quad t_{E,n}^{(0)\rightrightarrows} = \frac{2}{1+\frac{Q(E_\mathrm{x,R})}{Q(E_\mathrm{x,L})}},\quad r_{E,n}^{(0)\leftrightarrows} = \frac{1-\frac{Q(E_\mathrm{x,R})}{Q(E_\mathrm{x,L})}}{1+\frac{Q(E_\mathrm{x,R})}{Q(E_\mathrm{x,L})}}. \tag{5.10}$$

For energies below the potential step height, $V_\mathrm{R} < E - E_W n^2 < V_\mathrm{L}$, the results remain valid, considering that Q becomes imaginary according to Eq. (5.5).

The zeroth-order transmission/reflection coefficients are then calculated as the ratios of

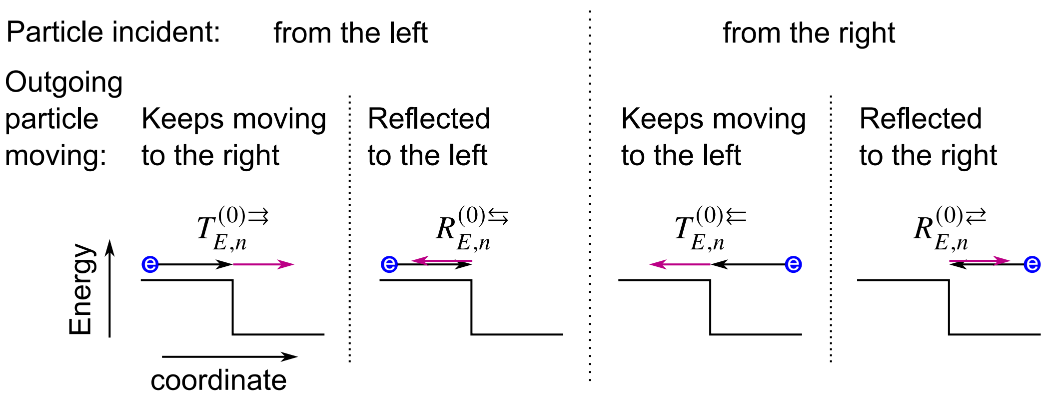

Figure 5.6: **Definition of the double-arrow notation.**

the particle flows of the transmitted/reflected waves to the particle flow of the incident wave,

$$T_{E,n}^{(0)\leftleftarrows} = \frac{Q(E_{\mathrm{x,L}})}{Q(E_{\mathrm{x,R}})} \left| t_{E,n}^{(0)\leftleftarrows} \right|^2 , \quad R_{E,n}^{(0)\rightleftarrows} = \left| r_{E,n}^{(0)\rightleftarrows} \right|^2 , \tag{5.11}$$

$$T_{E,n}^{(0)\rightrightarrows} = \frac{Q(E_{\mathrm{x,R}})}{Q(E_{\mathrm{x,L}})} \left| t_{E,n}^{(0)\rightrightarrows} \right|^2 , \quad R_{E,n}^{(0)\leftrightarrows} = \left| r_{E,n}^{(0)\leftrightarrows} \right|^2 . \tag{5.12}$$

Introducing the height of the potential step

$$V_{\mathrm{B}} = V_{\mathrm{L}} - V_{\mathrm{R}}\, , \text{ and } \mathcal{E} = \frac{E - E_W n^2 - V_{\mathrm{R}}}{V_{\mathrm{B}}} \tag{5.13}$$

as the energy available for x-motion measured from the bottom of the potential, the result can be written as a function of the dimensionless energy parameter $\mathcal{E}$:

$$T_{E,n}^{(0)\rightrightarrows} = T_{E,n}^{(0)\leftleftarrows} = \Theta(\mathcal{E}-1)\frac{4\sqrt{\mathcal{E}(\mathcal{E}-1)}}{\left|\sqrt{\mathcal{E}}+\sqrt{\mathcal{E}-1}\right|^2} = \Theta(E_{\mathrm{x,L}})\frac{4\sqrt{E_{\mathrm{x,R}}E_{\mathrm{x,L}}}}{\left|\sqrt{E_{\mathrm{x,R}}}+\sqrt{E_{\mathrm{x,L}}}\right|^2} \equiv \mathcal{T}_0(E_{\mathrm{x,R}},E_{\mathrm{x,L}})\, , \tag{5.14}$$

$$R_{E,n}^{(0)\leftrightarrows} = R_{E,n}^{(0)\rightleftarrows} = 1 - \mathcal{T}_0(E_{\mathrm{x,R}},E_{\mathrm{x,L}})\, . \tag{5.15}$$

The zero-order transmission and reflection coefficients for the right- and left-going electrons are equal: the transmission and reflection of the studied potential step does not depend on from what direction the electrons are incident.

5.2.2 Conductance in zeroth order

From the results in the previous section, the conductance of the potential step can be calculated. At the left ($x < 0$) of the quantum region containing the potential step, it shall be connected to a classical electron reservoir with chemical potential μ_{S}. At the right, the chemical potential shall be μ_{D}. The channel width in the y-direction is W, and the extension in the x-direction is L. The current can be written as:

$$\vec{I} = (-e)g_{\mathrm{s}}\frac{1}{LW}W\sum_{\vec{k}}\vec{v}T_{E,n}^{(0)}f(\vec{k}) = (I_{\rightarrow} + I_{\leftarrow})\vec{e}_{\mathrm{x}}\, . \tag{5.16}$$

Here, $f(\vec{k})$ is the Fermi function, and g_{s} is the spin degeneracy factor which equals 2. The current going to the right in the x-direction is

$$I_{\rightarrow} = -\frac{e g_{\mathrm{s}}}{L}\sum_{n=1}^{\infty}\sum_{k_{\mathrm{x,L}}>0} v_{\mathrm{x}} f(E,\mu_{\mathrm{S}},T)\mathcal{T}_0(E_{\mathrm{x,R}},E_{\mathrm{x,L}})\, , \tag{5.17}$$

where the energy-wavevector expression for electrons coming from the left is given by

$$E = E_W n^2 + V_\mathrm{L} + \frac{\hbar^2 k_{\mathrm{x,L}}^2}{2m} \,. \tag{5.18}$$

The expression for the current considers the fact that in the channel, where electron transport is ballistic, the velocity distribution of electrons moving to the right ($v_\mathrm{x} > 0$) is determined by the chemical potential in the source contact at the left, μ_S. Similarly, the current going to the left in the x-direction is

$$I_\leftarrow = -\frac{e g_\mathrm{s}}{L} \sum_{n=1}^{\infty} \sum_{k_{\mathrm{x,R}}<0} v_\mathrm{x} f(E,\mu_\mathrm{D},T)\mathcal{T}_0(E_{\mathrm{x,R}},E_{\mathrm{x,L}}) \,, \tag{5.19}$$

and the energy-wavevector expression for electrons going from the right is

$$E = E_W n^2 + V_\mathrm{R} + \frac{\hbar^2 k_{\mathrm{x,R}}^2}{2m} \,. \tag{5.20}$$

Using $v_\mathrm{x} = \hbar k_\mathrm{x}/m$ and transforming the sum to an integral, $\sum \ldots \to \int \mathrm{d}k_\mathrm{x} L/(2\pi) \ldots$, the formulas yield

$$\begin{aligned}
I = &-\frac{e g_\mathrm{s}\hbar}{2\pi m} \sum_{n=1}^{\infty} \left(\int_0^\infty \mathrm{d}k_{\mathrm{x,L}} \cdot k_{\mathrm{x,L}} f(E,\mu_\mathrm{S},T)\mathcal{T}_0(E_{\mathrm{x,R}},E_{\mathrm{x,L}}) + \right.\\
&\left. + \int_{-\infty}^0 \mathrm{d}k_{\mathrm{x,R}} \cdot k_{\mathrm{x,R}} f(E,\mu_\mathrm{D},T)\mathcal{T}_0(E_{\mathrm{x,R}},E_{\mathrm{x,L}}) \right) = \\
= &-\frac{e\hbar}{\pi m} \sum_{n=1}^{\infty} \left(\int_0^\infty \frac{k_{\mathrm{x,L}}\mathcal{T}_0(E_{\mathrm{x,R}},E_{\mathrm{x,L}})\mathrm{d}k_{\mathrm{x,L}}}{1+\exp\left(\frac{E-\mu_\mathrm{S}}{k_\mathrm{B}T}\right)} - \int_0^\infty \frac{k_{\mathrm{x,R}}\mathcal{T}_0(E_{\mathrm{x,R}},E_{\mathrm{x,L}})\mathrm{d}k_{\mathrm{x,R}}}{1+\exp\left(\frac{E-\mu_\mathrm{D}}{k_\mathrm{B}T}\right)} \right) = \\
= &-\frac{e}{\pi\hbar} \sum_{n=1}^{\infty} \int_{-\infty}^{\infty} \mathcal{T}_0(E_{\mathrm{x,R}},E_{\mathrm{x,L}})\mathrm{d}E \left(\frac{1}{1+\exp\left(\frac{E-\mu_\mathrm{S}}{k_\mathrm{B}T}\right)} - \frac{1}{1+\exp\left(\frac{E-\mu_\mathrm{D}}{k_\mathrm{B}T}\right)} \right) .
\end{aligned} \tag{5.21}$$

Here, the integral over k_x was transformed to an integral over the energy E, using Eqs. (5.18) and (5.20). The Heaviside Theta-function in $\mathcal{T}_0(E_{\mathrm{x,R}},E_{\mathrm{x,L}})$ takes care of the correct integration limits, therefore in both integrals they can be extended to $\pm\infty$.

The voltage V applied between the Ohmic contacts is given by $-eV = \mu_\mathrm{D} - \mu_\mathrm{S}$. This way it becomes possible to express the chemical potentials as $\mu_\mathrm{D} = \bar{\mu} + eV/2$ and $\mu_\mathrm{S} = \bar{\mu} - eV/2$

using the mean chemical potential $\bar{\mu} = (\mu_\mathrm{D} + \mu_\mathrm{S})/2$:

$$I = -\frac{e}{\pi\hbar}\sum_{n=1}^{\infty}\int_{-\infty}^{\infty}\mathcal{T}_0(E_\mathrm{x,R},E_\mathrm{x,L})\mathrm{d}E\left(\frac{1}{1+\exp\left(\frac{E-(\bar{\mu}-eV/2)}{k_\mathrm{B}T}\right)} - \frac{1}{1+\exp\left(\frac{E-(\bar{\mu}+eV/2)}{k_\mathrm{B}T}\right)}\right). \quad (5.22)$$

By bringing this to a common denominator, one gets

$$I = \frac{e}{\pi\hbar}\sum_{n=1}^{\infty}\int_{-\infty}^{\infty}\mathcal{T}_0(E_\mathrm{x,R},E_\mathrm{x,L})\mathrm{d}E\frac{\exp\left(\frac{E-\bar{\mu}}{k_\mathrm{B}T}\right)2\sinh\left(\frac{eV}{2k_\mathrm{B}T}\right)}{\left(1+\exp\left(\frac{E-(\bar{\mu}-eV/2)}{k_\mathrm{B}T}\right)\right)\left(1+\exp\left(\frac{E-(\bar{\mu}+eV/2)}{k_\mathrm{B}T}\right)\right)}. \quad (5.23)$$

In the Ohmic conduction regime, the voltage V is assumed to be small. Therefore the integrand can be Taylor-expanded keeping only the first-order term in V:

$$\begin{aligned} I &\approx \frac{e^2V}{\pi\hbar k_\mathrm{B}T}\sum_{n=1}^{\infty}\int_{-\infty}^{\infty}\mathcal{T}_0(E_\mathrm{x,R},E_\mathrm{x,L})\mathrm{d}E\frac{\exp\left(\frac{E-\bar{\mu}}{k_\mathrm{B}T}\right)}{\left(1+\exp\left(\frac{E-\bar{\mu}}{k_\mathrm{B}T}\right)\right)^2} = \\ &= \frac{e^2V}{\pi\hbar k_\mathrm{B}T}\sum_{n=1}^{\infty}\int_{-\infty}^{\infty}\frac{\mathcal{T}_0(E_\mathrm{x,R},E_\mathrm{x,L})\mathrm{d}E}{4\cosh^2\left(\frac{E-\bar{\mu}}{2k_\mathrm{B}T}\right)}. \end{aligned} \quad (5.24)$$

From here, the Ohmic conductance $\sigma = \mathrm{d}I/\mathrm{d}V$ of the potential step is found to be

$$\sigma = \frac{2e^2}{h}\cdot\frac{1}{k_\mathrm{B}T}\sum_{n=1}^{\infty}\int_{-\infty}^{\infty}\frac{\mathcal{T}_0(E-E_W n^2-V_\mathrm{R},E-E_W n^2-V_\mathrm{L})\mathrm{d}E}{4\cosh^2\left(\frac{E-\bar{\mu}}{2k_\mathrm{B}T}\right)}. \quad (5.25)$$

It can be evaluated by numerical integration and summation using the above formula and $\mathcal{T}_0(E_\mathrm{x,R},E_\mathrm{x,L})$ from Eq. (5.14).

5.2.3 With THz irradiation (first order)

Let us now calculate the photoresponse of the potential step when it is exposed to electromagnetic radiation. Incident THz radiation is amplified by the antenna and creates a locally focused AC electric field $\sim \sin(\omega t)$, Fig. 5.5 (c). The corresponding potential will have a similar form as Fig. 5.5 (a), but will be oscillating in time. For a simple model, the AC electric field is assumed to be present in an infinitesimally small region around the step. In this case, the potential $V_0(x)$ is replaced with the potential $V_0(x) + V_1(x,t)$, where V_1 is the time-dependent potential $V_1(x,t) = (u_\mathrm{ac,x}/2)\mathrm{sign}(x)\cos(\omega t)$. $u_\mathrm{ac,x}$ is the amplitude of the potential difference induced by the AC electric field. It can be estimated as $u_\mathrm{ac,x} \approx eE_\mathrm{ac}b_\mathrm{gap}$, where E_ac is the average amplitude of the THz electric field in x-direction acting on the 2DEG at the step, and b_gap is the gap between the antenna wings. Under THz irradiation, this results in a potential step "wiggling" as shown in Fig. 5.5 (d). Electrons are assumed to pass the gap b_{gap} between the antenna wings ballistically, i.e. to have a mean free path exceeding $b_{\mathrm{gap}} = 0.27\,\mu\mathrm{m}$ – this was shown to be fulfilled in the experiment in section 4.7.2.

The dynamics of photoexcited electrons under incident THz radiation is determined by the time-dependent Schrödinger equation:

$$i\hbar\frac{\partial\Psi}{\partial t} = (\hat{H}_0 + \hat{H}_1)\Psi = \hat{H}_0\Psi + V_1(x,t)\Psi\,. \tag{5.26}$$

For a small amplitude of the AC electric field, this equation can be solved treating V_1 as a perturbation.

The theoretical calculations in the first-order perturbation theory described in this section 5.2.3 were carried out by collaborator Sergey A. Mikhailov from the University of Augsburg [277]. The substitution $\Psi = \Psi^{(0)} + \Psi^{(1)}$ yields

$$i\hbar\frac{\partial\Psi^{(0)}}{\partial t} + i\hbar\frac{\partial\Psi^{(1)}}{\partial t} = \hat{H}_0\Psi^{(0)} + \hat{H}_1\Psi^{(0)} + \hat{H}_0\Psi^{(1)} + \hat{H}_1\Psi^{(1)} \tag{5.27}$$

$$\Rightarrow \quad i\hbar\frac{\partial\Psi^{(1)}}{\partial t} = \hat{H}_1\Psi^{(0)} + \hat{H}_0\Psi^{(1)}\,, \tag{5.28}$$

where the second-order term $\hat{H}_1\Psi^{(1)}$ is omitted. This leads to the inhomogeneous first-order Schrödinger equation

$$i\hbar\frac{\partial\Psi^{(1)}}{\partial t} + \frac{\hbar^2}{2m}\frac{\partial^2\Psi^{(1)}}{\partial x^2} + \frac{\hbar^2}{2m}\frac{\partial^2\Psi^{(1)}}{\partial y^2} - V_0(x)\Psi^{(1)} - \tilde{V}_0(y)\Psi^{(1)} =$$

$$= \frac{u_{\mathrm{ac,x}}}{4}\left(e^{-i(E+\hbar\omega)t/\hbar} + e^{-i(E-\hbar\omega)t/\hbar}\right)\mathrm{sign}(x)\sin\frac{\pi n y}{W}\psi^{(0)}_{E,n}(x). \tag{5.29}$$

On the right hand side, the first term in the brackets corresponds to the absorption of a photon, and the second one to photon emission. Only the absorption term with $E + \hbar\omega$ will be considered in the following. Then, the solution is searched for in the form

$$\Psi^{(1)}(x,y,t) = e^{-i(E+\hbar\omega)t/\hbar}\sin\frac{\pi n y}{W}\psi^{(1)}_{E,n}(x)\,, \tag{5.30}$$

which, with the t and y-dependent factors cancelled, results in the following differential equation for $\psi^{(1)}_{E,n}(x)$:

$$\frac{\hbar^2}{2m}\frac{\partial^2\psi^{(1)}_{E,n}(x)}{\partial x^2} + \left[E + \hbar\omega - E_W n^2 - V_L - (V_R - V_L)\Theta(x)\right]\psi^{(1)}_{E,n}(x) = \frac{1}{4}u_{\mathrm{ac,x}}\mathrm{sign}(x)\psi^{(0)}_{E,n}(x). \tag{5.31}$$

This equation should be solved for waves incident from both directions, and for all energies $E - E_W n^2 > V_{\mathrm{R}}$. For example, for the case of electrons with energies $\tilde{E} \equiv E - E_W n^2 > V_{\mathrm{L}}$

(over-barrier) running to the left, equation (5.31) transforms into:

$$\frac{\hbar^2}{2m}\frac{\partial^2\psi_{E,n}^{(1)}(x)}{\partial x^2} + \left(\tilde{E} + \hbar\omega - V_{\mathrm{R}}\right)\psi_{E,n}^{(1)}(x) = \frac{1}{4}u_{\mathrm{ac,x}}\left(e^{-iQ(\tilde{E}-V_{\mathrm{R}})x} + r_{E,n}^{(0)\rightleftarrows}e^{iQ(\tilde{E}-V_{\mathrm{R}})x}\right) \tag{5.32}$$

for $x > 0$, and

$$\frac{\hbar^2}{2m}\frac{\partial^2\psi_{E,n}^{(1)}(x)}{\partial x^2} + \left(\tilde{E} + \hbar\omega - V_{\mathrm{L}}\right)\psi_{E,n}^{(1)}(x) = -\frac{1}{4}u_{\mathrm{ac,x}}t_{E,n}^{(0)\leftleftarrows}e^{-iQ(\tilde{E}-V_{\mathrm{L}})x} \tag{5.33}$$

for $x < 0$, with the coefficients $t_{E,n}^{(0)\leftleftarrows}$ and $r_{E,n}^{(0)\rightleftarrows}$ given by Eq. (5.10). The solution of this inhomogeneous differential equation is the sum of the general solution of the corresponding homogeneous differential equation and a particular solution of the inhomogeneous differential equation, i. e.:

$$\psi_{E,n}^{(1)}(x) = A_{E,n}e^{iQ(\tilde{E}+\hbar\omega-V_{\mathrm{R}})x} + \frac{u_{\mathrm{ac,x}}}{4\hbar\omega}\left(e^{-iQ(\tilde{E}-V_{\mathrm{R}})x} + r_{E,n}^{(0)\rightleftarrows}e^{+iQ(\tilde{E}-V_{\mathrm{R}})x}\right), \quad x > 0\,, \tag{5.34}$$

$$\psi_{E,n}^{(1)}(x) = B_{E,n}e^{-iQ(\tilde{E}+\hbar\omega-V_{\mathrm{L}})x} - \frac{u_{\mathrm{ac,x}}}{4\hbar\omega}t_{E,n}^{(0)\leftleftarrows}e^{-iQ(\tilde{E}-V_{\mathrm{L}})x}, \ x < 0\,. \tag{5.35}$$

The boundary conditions at $x \to \pm\infty$, corresponding to the absence of the waves with the energy $E + \hbar\omega$ coming from infinity, have been already taken into account. The coefficients $A_{E,n}$ and $B_{E,n}$ are determined from the boundary conditions at $x = 0$, analogous to Eq. (5.8):

$$A_{E,n} = \frac{u_{\mathrm{ac,x}}}{\hbar\omega}\frac{Q(\tilde{E}-V_{\mathrm{R}})\Big(Q(\tilde{E}-V_{\mathrm{L}}) - Q(\tilde{E}+\hbar\omega-V_{\mathrm{L}})\Big)}{\Big(Q(\tilde{E}-V_{\mathrm{L}}) + Q(\tilde{E}-V_{\mathrm{R}})\Big)\Big(Q(\tilde{E}+\hbar\omega-V_{\mathrm{L}}) + Q(\tilde{E}+\hbar\omega-V_{\mathrm{R}})\Big)}, \tag{5.36}$$

$$B_{E,n} = \frac{u_{\mathrm{ac,x}}}{\hbar\omega}\frac{Q(\tilde{E}-V_{\mathrm{R}})\Big(Q(\tilde{E}-V_{\mathrm{L}}) + Q(\tilde{E}+\hbar\omega-V_{\mathrm{R}})\Big)}{\Big(Q(\tilde{E}-V_{\mathrm{L}}) + Q(\tilde{E}-V_{\mathrm{R}})\Big)\Big(Q(\tilde{E}+\hbar\omega-V_{\mathrm{L}}) + Q(\tilde{E}+\hbar\omega-V_{\mathrm{R}})\Big)}. \tag{5.37}$$

They allow calculation of the probability of an electron wave, incident on the potential step from the right, to absorb a photon and to continue to move in the same direction. The particle flow of the incident wave, $j_{E,n}^{0\leftarrow}$, is proportional to $Q(E - E_W n^2 - V_{\mathrm{R}})$. The particle flow of the transmitted wave after absorption of a photon, $j_{E,n}^{+\leftarrow}$, is proportional to

$$\Theta(E + \hbar\omega - E_W n^2 - V_{\mathrm{L}})Q(E + \hbar\omega - E_W n^2 - V_{\mathrm{L}})|B_{E,n}|^2. \tag{5.38}$$

The particle flows are illustrated in Fig. 5.7 (b). As shown in Fig. 5.7, $j_{E,n}^{0\leftarrow}$ is the flow of particles with energy E incident onto the step from the right. $j_{E,n}^{+\leftarrow}$ is the flow of particles

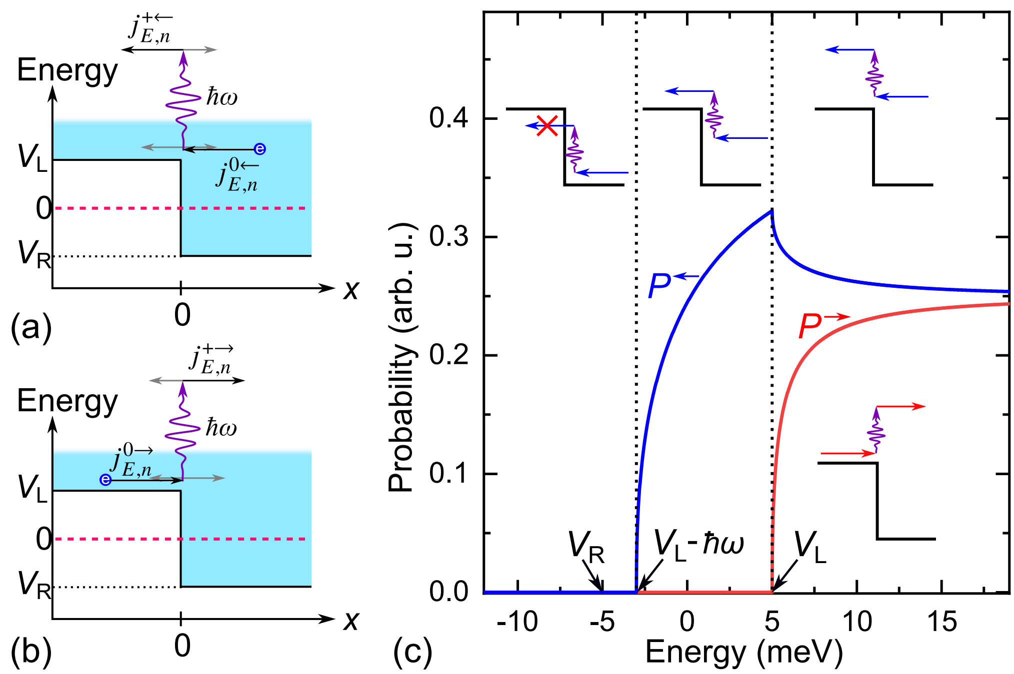

Figure 5.7: **Particle flows.** (a), (b) Definition of the particle flows: Zero-order particle flows $j^{0\leftarrow}_{E,n}$, $j^{0\rightarrow}_{E,n}$ incident on the potential step, and first-order particle flows $j^{+\leftarrow}_{E,n}$, $j^{+\rightarrow}_{E,n}$ of electrons that absorb a photon and continue to move in the same direction. (c) Probability of electrons, as a function of their energy, moving to the left in the right part (blue) and moving to the right in the left part (red) to absorb a photon and pass the step. The curves are plotted for $\hbar\omega = 8\,\text{meV}$, $V_L = 5\,\text{meV}$, and $V_R = -5\,\text{meV}$.

which absorbed a photon, thus now having the energy $E + \hbar\omega$, and continue to move in the same direction (to the left).

The ratio $T^{+\leftleftarrows}_{E,n} = j^{+\leftarrow}_{E,n}/j^{0\leftarrow}_{E,n}$ yields the first-order "transmission coefficient" of particles which have absorbed a THz quantum $\hbar\omega$ and continue to move in the same direction:

$$T^{+\leftleftarrows}_{E,n} = \Theta(E + \hbar\omega - E_W n^2 - V_L)\frac{Q(E + \hbar\omega - E_W n^2 - V_L)}{Q(E - E_W n^2 - V_R)}|B_{E,n}|^2. \tag{5.39}$$

This formula can be written as:

$$T^{+\leftleftarrows}_{E,n} = \left(\frac{u_{\mathrm{ac,x}}}{\hbar\omega}\right)^2 \mathcal{P}^{\leftarrow}_{+}\left(\frac{E - E_W n^2 - V_R}{V_B}, \frac{\hbar\omega}{V_B}\right), \tag{5.40}$$

where

$$\mathcal{P}^{\leftarrow}_{+}(\mathcal{E}, \Omega) = \Theta(\mathcal{E})\Theta(\mathcal{E} + \Omega - 1)\frac{\sqrt{\mathcal{E}}\sqrt{\mathcal{E} + \Omega - 1}\left|\sqrt{\mathcal{E} - 1} + \sqrt{\mathcal{E} + \Omega}\right|^2}{\left|\sqrt{\mathcal{E}} + \sqrt{\mathcal{E} - 1}\right|^2\left|\sqrt{\mathcal{E} + \Omega} + \sqrt{\mathcal{E} + \Omega - 1}\right|^2}. \tag{5.41}$$

Here, $\Omega = \hbar\omega/V_B$.

A similar calculation yields the first-order transmission coefficient of photoexcited particles moving to the right, $T^{+\rightrightarrows}_{E,n} = j^{+\rightarrow}_{E,n}/j^{0\rightarrow}_{E,n}$:

$$T^{+\rightrightarrows}_{E,n} = \left(\frac{u_{\mathrm{ac,x}}}{\hbar\omega}\right)^2 \mathcal{P}^{\rightarrow}_{+} \left(\frac{E - E_W n^2 - V_{\mathrm{R}}}{V_{\mathrm{B}}}, \frac{\hbar\omega}{V_{\mathrm{B}}}\right) , \tag{5.42}$$

where

$$\mathcal{P}^{\rightarrow}_{+} (\mathcal{E},\Omega) = \Theta(\mathcal{E} - 1)\Theta(\mathcal{E} + \Omega) \frac{\sqrt{\mathcal{E} - 1}\sqrt{\mathcal{E} + \Omega}\left|\sqrt{\mathcal{E}} + \sqrt{\mathcal{E} + \Omega - 1}\right|^2}{\left|\sqrt{\mathcal{E}} + \sqrt{\mathcal{E} - 1}\right|^2 \left|\sqrt{\mathcal{E} + \Omega} + \sqrt{\mathcal{E} + \Omega - 1}\right|^2} . \tag{5.43}$$

These formulas, Eqs. (5.40) – (5.43), are valid for all values of the particle energy.

The first-order transmission coefficients give the portion of electrons that thanks to the THz excitation were able to reach the other end of the device. It is worth stressing that in contrast to the zero-order transmission coefficients, which do not depend on the direction of electron flow ($T^{(0)\rightrightarrows}_{E,n} = T^{(0)\leftleftarrows}_{E,n}$), this is not the case for the first order transmission coefficients. For all energies, $T^{+\leftleftarrows}_{E,n} > T^{+\rightrightarrows}_{E,n}$, provided that $V_{\mathrm{L}} > V_{\mathrm{R}}$. This is illustrated in Fig. 5.7 (c), where the functions $P^{\rightarrow}$, $P^{\leftarrow}$ are plotted for $\hbar\omega = 8\,\mathrm{meV}$, $V_{\mathrm{L}} = 5\,\mathrm{meV}$, and $V_{\mathrm{R}} = -5\,\mathrm{meV}$. That means, the particles flow onto the step, in agreement with the experimental data.

The photocurrent I_{ph} is then calculated as:

$$\boxed{I_{\mathrm{ph}} = -\frac{e}{\pi\hbar}\sum_{n=1}^{\infty}\int_{-\infty}^{\infty} \mathrm{d}E \left(T^{+\rightrightarrows}_{E,n} - T^{+\leftleftarrows}_{E,n}\right) f(E,\mu,T)\,(1 - f(E + \hbar\omega,\mu,T))} \tag{5.44}$$

Here, $f(E,\mu,T) = 1/\{1 + \exp[(E - \mu)/(k_{\mathrm{B}}T)]\}$ is the Fermi distribution function, and μ is the chemical potential of the unbiased system. The Fermi factors take into account the occupation of electron states: the initial state with energy E must be occupied, and the final state with energy $E + \hbar\omega$ must be empty.

In the limit $T \to 0$, the Fermi function can be approximated as a Theta-function:

$$\begin{aligned} f(E,\mu,T)\,(1 - f(E + \hbar\omega,\mu,T)) &= \Theta(\mu - E)[1 - \Theta(\mu - (E + \hbar\omega))] = \\ &= \Theta(\mu - E)\Theta(E + \hbar\omega - \mu) . \end{aligned} \tag{5.45}$$

This implies the condition $\mu - \hbar\omega < E < \mu$ which can then be embedded into the integration limits:

$$I_{\mathrm{ph}} = -\frac{e}{\pi\hbar}\sum_{n=1}^{\infty}\int_{\mu-\hbar\omega}^{\mu} \mathrm{d}E \left(T^{+\rightrightarrows}_{E,n} - T^{+\leftleftarrows}_{E,n}\right) . \tag{5.46}$$

Using the relationships Eqs. (5.40) – (5.43), this transforms to

$$I_{\mathrm{ph}}=-\frac{e}{\pi\hbar}\left(\frac{u_{\mathrm{ac,x}}}{\hbar\omega}\right)^2\sum_{n=1}^{\infty}\int_{\mu-\hbar\omega}^{\mu}\mathrm{d}E\left(\mathcal{P}_+^{\rightarrow}\left(\frac{E-E_W n^2-V_{\mathrm{R}}}{V_{\mathrm{B}}},\frac{\hbar\omega}{V_{\mathrm{B}}}\right)-\mathcal{P}_+^{\leftarrow}\left(\frac{E-E_W n^2-V_{\mathrm{R}}}{V_{\mathrm{B}}},\frac{\hbar\omega}{V_{\mathrm{B}}}\right)\right)=$$
$$=-\frac{e}{\pi\hbar}\left(\frac{u_{\mathrm{ac,x}}}{\hbar\omega}\right)^2\sum_{n=1}^{\infty}\int_{-\hbar\omega}^{0}\mathrm{d}\varepsilon\left(\mathcal{P}_+^{\rightarrow}\left(\frac{\mu_{\mathrm{R}}+\varepsilon-E_W n^2}{V_{\mathrm{B}}},\frac{\hbar\omega}{V_{\mathrm{B}}}\right)-\mathcal{P}_+^{\leftarrow}\left(\frac{\mu_{\mathrm{R}}+\varepsilon-E_W n^2}{V_{\mathrm{B}}},\frac{\hbar\omega}{V_{\mathrm{B}}}\right)\right). \quad (5.47)$$

Here, $E=\mu+\varepsilon$ was substituted for ε, and the variable $\mu_{\mathrm{R}}=\mu-V_{\mathrm{R}}$ was defined.

The integrand of this formula depends on V_{R}, V_{B}, $\hbar\omega$, and E_W. In the following, we aim to express the main functional dependence as a function of two dimensionless variables, $\mu_{\mathrm{L}}/(\hbar\omega)$ and $\mu_{\mathrm{R}}/(\hbar\omega)$.

To this end, the sum over n is replaced by an integral over $k_{\mathrm{y}}=\hbar\pi n/W$ (and subsequently E_{y}) using

$$E_{\mathrm{y}}=E_W n^2=\pi^2\hbar^2 n^2/(2mW^2)=\hbar^2 k_{\mathrm{y}}^2/2m \quad (5.48)$$

and the transformation $\sum\ldots\rightarrow\int\mathrm{d}k_{\mathrm{y}}W/\pi\ldots$:

$$I_{\mathrm{ph}}\Bigg/\left[-\frac{e}{\pi\hbar}\left(\frac{u_{\mathrm{ac,x}}}{\hbar\omega}\right)^2\right]\approx \quad (5.49)$$
$$\approx\frac{W}{\pi}\int_0^{\infty}\mathrm{d}k_{\mathrm{y}}\int_{-\hbar\omega}^{0}\mathrm{d}\varepsilon\left(\mathcal{P}_+^{\rightarrow}\left(\frac{\varepsilon+\mu_{\mathrm{R}}-\frac{\hbar^2k_{\mathrm{y}}^2}{2m}}{V_{\mathrm{B}}},\frac{\hbar\omega}{V_{\mathrm{B}}}\right)-\mathcal{P}_+^{\leftarrow}\left(\frac{\varepsilon+\mu_{\mathrm{R}}-\frac{\hbar^2k_{\mathrm{y}}^2}{2m}}{V_{\mathrm{B}}},\frac{\hbar\omega}{V_{\mathrm{B}}}\right)\right)=$$
$$=\frac{W}{\pi\hbar}\sqrt{\frac{m}{2}}\int_0^{\infty}\frac{\mathrm{d}E_{\mathrm{y}}}{\sqrt{E_{\mathrm{y}}}}\int_{-\hbar\omega}^{0}\mathrm{d}\varepsilon\left(\mathcal{P}_+^{\rightarrow}\left(\frac{\varepsilon+\mu_{\mathrm{R}}-E_{\mathrm{y}}}{V_{\mathrm{B}}},\frac{\hbar\omega}{V_{\mathrm{B}}}\right)-\mathcal{P}_+^{\leftarrow}\left(\frac{\varepsilon+\mu_{\mathrm{R}}-E_{\mathrm{y}}}{V_{\mathrm{B}}},\frac{\hbar\omega}{V_{\mathrm{B}}}\right)\right)=\ldots$$

The substitution $\varepsilon=E_{\mathrm{x}}+E_{\mathrm{y}}$ yields:

$$\cdots=\frac{W}{\pi\hbar}\sqrt{\frac{m}{2}}\int_0^{\infty}\frac{\mathrm{d}E_{\mathrm{y}}}{\sqrt{E_{\mathrm{y}}}}\int_{-\hbar\omega-E_{\mathrm{y}}}^{-E_{\mathrm{y}}}\mathrm{d}E_{\mathrm{x}}\left(\mathcal{P}_+^{\rightarrow}\left(\frac{\mu_{\mathrm{R}}+E_{\mathrm{x}}}{V_{\mathrm{B}}},\frac{\hbar\omega}{V_{\mathrm{B}}}\right)-\mathcal{P}_+^{\leftarrow}\left(\frac{\mu_{\mathrm{R}}+E_{\mathrm{x}}}{V_{\mathrm{B}}},\frac{\hbar\omega}{V_{\mathrm{B}}}\right)\right)=$$
$$=\frac{W}{\pi\hbar}\sqrt{\frac{m}{2}}\int_0^{\infty}\frac{\mathrm{d}E_{\mathrm{y}}}{\sqrt{E_{\mathrm{y}}}}\int_{-\infty}^{\infty}\mathrm{d}E_{\mathrm{x}}\left(\mathcal{P}_+^{\rightarrow}\left(\frac{\mu_{\mathrm{R}}+E_{\mathrm{x}}}{V_{\mathrm{B}}},\frac{\hbar\omega}{V_{\mathrm{B}}}\right)-\mathcal{P}_+^{\leftarrow}\left(\frac{\mu_{\mathrm{R}}+E_{\mathrm{x}}}{V_{\mathrm{B}}},\frac{\hbar\omega}{V_{\mathrm{B}}}\right)\right)\cdot$$
$$\cdot\Theta(-E_{\mathrm{x}}-E_{\mathrm{y}})\Theta(E_{\mathrm{x}}-(-\hbar\omega-E_{\mathrm{y}}))\ldots$$

The E_{x}-integration limits are now transferred to the E_{y}-integral using Heaviside Theta-functions as an intermediate step, in order to evaluate the integral over E_{y}:

$$\cdots=\frac{W}{\pi\hbar}\sqrt{\frac{m}{2}}\int_{-\infty}^{\infty}\mathrm{d}E_{\mathrm{x}}\left(\mathcal{P}_+^{\rightarrow}\left(\frac{\mu_{\mathrm{R}}+E_{\mathrm{x}}}{V_{\mathrm{B}}},\frac{\hbar\omega}{V_{\mathrm{B}}}\right)-\mathcal{P}_+^{\leftarrow}\left(\frac{\mu_{\mathrm{R}}+E_{\mathrm{x}}}{V_{\mathrm{B}}},\frac{\hbar\omega}{V_{\mathrm{B}}}\right)\right)\cdot$$
$$\cdot\int_{-\infty}^{\infty}\frac{\mathrm{d}E_{\mathrm{y}}}{\sqrt{E_{\mathrm{y}}}}\Theta(-E_{\mathrm{x}}-E_{\mathrm{y}})\Theta(E_{\mathrm{x}}+\hbar\omega+E_{\mathrm{y}})\Theta(E_{\mathrm{y}})$$

$$=\frac{W}{\pi\hbar}\sqrt{\frac{m}{2}}\int_{-\infty}^{\infty}\mathrm{d}E_{\mathrm{x}}\left(\mathcal{P}_{+}^{\rightarrow}\left(\frac{\mu_{\mathrm{R}}+E_{\mathrm{x}}}{V_{\mathrm{B}}},\frac{\hbar\omega}{V_{\mathrm{B}}}\right)-\mathcal{P}_{+}^{\leftarrow}\left(\frac{\mu_{\mathrm{R}}+E_{\mathrm{x}}}{V_{\mathrm{B}}},\frac{\hbar\omega}{V_{\mathrm{B}}}\right)\right)\cdot\Theta(-E_{\mathrm{x}})\int_{\max(-E_{\mathrm{x}}-\hbar\omega,0)}^{-E_{\mathrm{x}}}\frac{\mathrm{d}E_{\mathrm{y}}}{\sqrt{E_{\mathrm{y}}}}$$
$$=\frac{W}{\pi\hbar}\sqrt{\frac{m}{2}}\int_{-\infty}^{0}\mathrm{d}E_{\mathrm{x}}\left(\mathcal{P}_{+}^{\rightarrow}\left(\frac{\mu_{\mathrm{R}}+E_{\mathrm{x}}}{V_{\mathrm{B}}},\frac{\hbar\omega}{V_{\mathrm{B}}}\right)-\mathcal{P}_{+}^{\leftarrow}\left(\frac{\mu_{\mathrm{R}}+E_{\mathrm{x}}}{V_{\mathrm{B}}},\frac{\hbar\omega}{V_{\mathrm{B}}}\right)\right)\cdot 2\left[\sqrt{-E_{\mathrm{x}}}-\sqrt{\max(-E_{\mathrm{x}}-\hbar\omega,0)}\right]$$
$$=\frac{W}{\pi\hbar}\sqrt{\frac{m}{2}}\int_{0}^{\infty}\mathrm{d}E_{\mathrm{x}}\left(\mathcal{P}_{+}^{\rightarrow}\left(\frac{\mu_{\mathrm{R}}-E_{\mathrm{x}}}{V_{\mathrm{B}}},\frac{\hbar\omega}{V_{\mathrm{B}}}\right)-\mathcal{P}_{+}^{\leftarrow}\left(\frac{\mu_{\mathrm{R}}-E_{\mathrm{x}}}{V_{\mathrm{B}}},\frac{\hbar\omega}{V_{\mathrm{B}}}\right)\right)\cdot 2\left[\sqrt{E_{\mathrm{x}}}-\sqrt{\max(E_{\mathrm{x}}-\hbar\omega,0)}\right].$$

Using the following expressions for the terms containing $\mathcal{E}$ and Ω together with the definition $\mu_{\mathrm{L}} = \mu - V_{\mathrm{L}}$,

$$\begin{aligned}\mathcal{E} &= \frac{\mu_{\mathrm{R}}-E_{\mathrm{x}}}{V_{\mathrm{B}}} \quad ; & \mathcal{E}-1 &= \frac{\mu_{\mathrm{L}}-E_{\mathrm{x}}}{V_{\mathrm{B}}}\\ \mathcal{E}+\Omega &= \frac{\mu_{\mathrm{R}}-E_{\mathrm{x}}+\hbar\omega}{V_{\mathrm{B}}} \quad ; & \mathcal{E}+\Omega-1 &= \frac{\mu_{\mathrm{L}}-E_{\mathrm{x}}+\hbar\omega}{V_{\mathrm{B}}},\end{aligned} \tag{5.50}$$

the brackets with $\mathcal{P}_{+}^{\rightarrow}$ and $\mathcal{P}_{+}^{\leftarrow}$ can be evaluated according to the definitions in Eqs. 5.41, 5.43:

$$\left(\mathcal{P}_{+}^{\rightarrow}\left(\mathcal{E}=\frac{\mu_{\mathrm{R}}-E_{\mathrm{x}}}{V_{\mathrm{B}}},\Omega=\frac{\hbar\omega}{V_{\mathrm{B}}}\right)-\mathcal{P}_{+}^{\leftarrow}\left(\mathcal{E}=\frac{\mu_{\mathrm{R}}-E_{\mathrm{x}}}{V_{\mathrm{B}}},\Omega=\frac{\hbar\omega}{V_{\mathrm{B}}}\right)\right)= \tag{5.51}$$
$$=\Theta\left(\frac{\mu_{\mathrm{L}}-E_{\mathrm{x}}}{V_{\mathrm{B}}}\right)\Theta\left(\frac{\mu_{\mathrm{R}}-E_{\mathrm{x}}+\hbar\omega}{V_{\mathrm{B}}}\right)\frac{\sqrt{\frac{\mu_{\mathrm{L}}-E_{\mathrm{x}}}{V_{\mathrm{B}}}}\sqrt{\frac{\mu_{\mathrm{R}}-E_{\mathrm{x}}+\hbar\omega}{V_{\mathrm{B}}}}\left|\sqrt{\frac{\mu_{\mathrm{R}}-E_{\mathrm{x}}}{V_{\mathrm{B}}}}+\sqrt{\frac{\mu_{\mathrm{L}}-E_{\mathrm{x}}+\hbar\omega}{V_{\mathrm{B}}}}\right|^2}{\left|\sqrt{\frac{\mu_{\mathrm{R}}-E_{\mathrm{x}}}{V_{\mathrm{B}}}}+\sqrt{\frac{\mu_{\mathrm{L}}-E_{\mathrm{x}}}{V_{\mathrm{B}}}}\right|^2\left|\sqrt{\frac{\mu_{\mathrm{R}}-E_{\mathrm{x}}+\hbar\omega}{V_{\mathrm{B}}}}+\sqrt{\frac{\mu_{\mathrm{L}}-E_{\mathrm{x}}+\hbar\omega}{V_{\mathrm{B}}}}\right|^2}-$$
$$-\Theta\left(\frac{\mu_{\mathrm{R}}-E_{\mathrm{x}}}{V_{\mathrm{B}}}\right)\Theta\left(\frac{\mu_{\mathrm{L}}-E_{\mathrm{x}}+\hbar\omega}{V_{\mathrm{B}}}\right)\frac{\sqrt{\frac{\mu_{\mathrm{R}}-E_{\mathrm{x}}}{V_{\mathrm{B}}}}\sqrt{\frac{\mu_{\mathrm{L}}-E_{\mathrm{x}}+\hbar\omega}{V_{\mathrm{B}}}}\left|\sqrt{\frac{\mu_{\mathrm{L}}-E_{\mathrm{x}}}{V_{\mathrm{B}}}}+\sqrt{\frac{\mu_{\mathrm{R}}-E_{\mathrm{x}}+\hbar\omega}{V_{\mathrm{B}}}}\right|^2}{\left|\sqrt{\frac{\mu_{\mathrm{R}}-E_{\mathrm{x}}}{V_{\mathrm{B}}}}+\sqrt{\frac{\mu_{\mathrm{L}}-E_{\mathrm{x}}}{V_{\mathrm{B}}}}\right|^2\left|\sqrt{\frac{\mu_{\mathrm{R}}-E_{\mathrm{x}}+\hbar\omega}{V_{\mathrm{B}}}}+\sqrt{\frac{\mu_{\mathrm{L}}-E_{\mathrm{x}}+\hbar\omega}{V_{\mathrm{B}}}}\right|^2}=\ldots$$

Now, the nominator and denominator are divided by $\hbar\omega/V_{\mathrm{B}}$:

$$\ldots=\Theta\left(\frac{\mu_{\mathrm{L}}-E_{\mathrm{x}}}{\hbar\omega}\right)\Theta\left(\frac{\mu_{\mathrm{R}}-E_{\mathrm{x}}}{\hbar\omega}+1\right)\frac{\sqrt{\frac{\mu_{\mathrm{L}}-E_{\mathrm{x}}}{\hbar\omega}}\sqrt{\frac{\mu_{\mathrm{R}}-E_{\mathrm{x}}}{\hbar\omega}+1}\left|\sqrt{\frac{\mu_{\mathrm{R}}-E_{\mathrm{x}}}{\hbar\omega}}+\sqrt{\frac{\mu_{\mathrm{L}}-E_{\mathrm{x}}}{\hbar\omega}+1}\right|^2}{\left|\sqrt{\frac{\mu_{\mathrm{R}}-E_{\mathrm{x}}}{\hbar\omega}}+\sqrt{\frac{\mu_{\mathrm{L}}-E_{\mathrm{x}}}{\hbar\omega}}\right|^2\left|\sqrt{\frac{\mu_{\mathrm{R}}-E_{\mathrm{x}}}{\hbar\omega}+1}+\sqrt{\frac{\mu_{\mathrm{L}}-E_{\mathrm{x}}}{\hbar\omega}+1}\right|^2}-$$
$$-\Theta\left(\frac{\mu_{\mathrm{R}}-E_{\mathrm{x}}}{\hbar\omega}\right)\Theta\left(\frac{\mu_{\mathrm{L}}-E_{\mathrm{x}}}{\hbar\omega}+1\right)\frac{\sqrt{\frac{\mu_{\mathrm{R}}-E_{\mathrm{x}}}{\hbar\omega}}\sqrt{\frac{\mu_{\mathrm{L}}-E_{\mathrm{x}}}{\hbar\omega}+1}\left|\sqrt{\frac{\mu_{\mathrm{L}}-E_{\mathrm{x}}}{\hbar\omega}}+\sqrt{\frac{\mu_{\mathrm{R}}-E_{\mathrm{x}}}{\hbar\omega}+1}\right|^2}{\left|\sqrt{\frac{\mu_{\mathrm{R}}-E_{\mathrm{x}}}{\hbar\omega}}+\sqrt{\frac{\mu_{\mathrm{L}}-E_{\mathrm{x}}}{\hbar\omega}}\right|^2\left|\sqrt{\frac{\mu_{\mathrm{R}}-E_{\mathrm{x}}}{\hbar\omega}+1}+\sqrt{\frac{\mu_{\mathrm{L}}-E_{\mathrm{x}}}{\hbar\omega}+1}\right|^2}\equiv$$
$$\equiv f\left(\frac{\mu_{\mathrm{L}}}{\hbar\omega},\frac{\mu_{\mathrm{R}}}{\hbar\omega},\frac{E_{\mathrm{x}}}{\hbar\omega}\right). \tag{5.52}$$

The resulting expression depends on the three energies μ_L, μ_R, and E_x normalised to $\hbar\omega$. This allows the functional form of the photocurrent to be captured in a dimensionless function J:

$$I_{ph} \Bigg/ \left[-\frac{e}{\pi\hbar}\left(\frac{u_{ac,x}}{\hbar\omega}\right)^2 \frac{W}{\pi\hbar}\sqrt{2m}\right] = I_{ph} \Bigg/ \left[-\frac{e}{\pi\hbar}\left(\frac{u_{ac,x}}{\hbar\omega}\right)^2 \frac{1}{\sqrt{E_W}}\right] \approx \tag{5.53}$$

$$\approx \int_0^\infty dE_x \left(\mathcal{P}_+^{\rightarrow}\left(\frac{\mu_R - E_x}{V_B},\frac{\hbar\omega}{V_B}\right) - \mathcal{P}_+^{\leftarrow}\left(\frac{\mu_R - E_x}{V_B},\frac{\hbar\omega}{V_B}\right)\right) \cdot \left[\sqrt{E_x} - \sqrt{\max\left(E_x - \hbar\omega,0\right)}\right] =$$

$$=(\hbar\omega)^{(3/2)} \int_0^\infty d\left(\frac{E_x}{\hbar\omega}\right)\left[\sqrt{\frac{E_x}{\hbar\omega}} - \sqrt{\max\left(\frac{E_x}{\hbar\omega} - 1,0\right)}\right] f\left(\frac{\mu_L}{\hbar\omega},\frac{\mu_R}{\hbar\omega},\frac{E_x}{\hbar\omega}\right)$$

The substitution $\xi = E_x/(\hbar\omega)$ yields

$$\Rightarrow\ I_{ph} = ef\left(\frac{u_{ac,x}}{\hbar\omega}\right)^2 \cdot 2\frac{\sqrt{\hbar\omega}}{\sqrt{E_W}} \cdot \underbrace{\int_0^\infty d\xi \left[\sqrt{\max\left(\xi - 1,0\right)} - \sqrt{\xi}\right] f\left(\frac{\mu_L}{\hbar\omega},\frac{\mu_R}{\hbar\omega},\xi\right)}_{\text{Function } J(\mu_L/(\hbar\omega),\mu_R/(\hbar\omega))} \tag{5.54}$$

Thus, at the temperature $T \rightarrow 0$ and $E_W \ll \hbar\omega$, the photocurrent obtained from Eq. (5.44) is

$$\boxed{I_{ph} = ef\left(\frac{u_{ac,x}}{\hbar\omega}\right)^2 \left[2\sqrt{\frac{\hbar\omega}{E_W}} J\left(\frac{\mu_L}{\hbar\omega},\frac{\mu_R}{\hbar\omega}\right)\right]}, \tag{5.55}$$

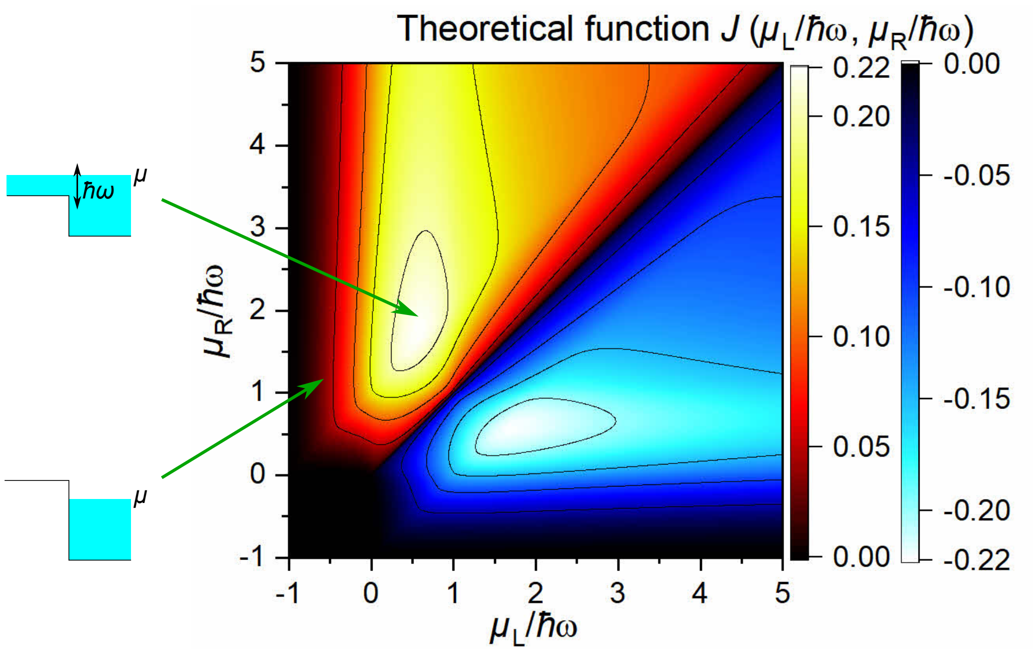

Figure 5.8: **Theoretical function** J as a function of its parameters $\mu_L/(\hbar\omega)$ and $\mu_R/(\hbar\omega)$.

where $\mu_L = \mu - V_L$ and $\mu_R = \mu - V_R$. The photocurrent's dependence on the chemical potentials is described by a universal dimensionless function J that depends on the two dimensionless parameters $\mu_L/(\hbar\omega)$ and $\mu_R/(\hbar\omega)$ and is antisymmetric, see Fig. 5.8. The gates are pinched off at $\mu_{L/R} = 0$. In the area with $\mu_L < 0$ and $\mu_R < 0$, where there are no electrons in both parts of the sample, the photocurrent vanishes. When only one of the chemical potentials, e. g. μ_L, is negative, down to $-\hbar\omega$, the function J is non-zero: photoexcited electrons are still able to jump onto the step when $\mu < V_{L/R} < \mu + \hbar\omega$. This is similar to the "conventional" photoelectric effect, with a "work function" corresponding to $-\mu_{L/R} = V_{L/R} - \mu$, see lower inset in Fig. 5.8 (d). However, this region is of little significance for the experimentally observed photoresponse: in practice, the very large channel resistance beyond the pinch-off would strongly suppress the photocurrent.

The main features of the in-plane photoelectric effect are located at positive chemical potentials. The maximum of the function $J(\mu_L/\hbar\omega; \mu_R/\hbar\omega)$ equals 0.221 and is located at $\mu_L = 0.57\hbar\omega$; $\mu_R = 1.73\hbar\omega$. Notably, this corresponds to the open regime far away from the pinch-off, where in both parts of the system, $x > 0$ and $x < 0$, electrons form a degenerate Fermi gas with chemical potentials well above the conduction band edges, as illustrated in Fig. 5.4 (b) and the pictograms in Fig. 5.8. This is in contrast to the conventional photoelectric effect, where the chemical potential always lies below the barrier height.

The relationship between the radiation frequency and the chemical potentials allows determination of the optimal frequency range for detection. Since typical electron concentrations $n = m_{\text{eff}}\mu/(\pi\hbar^2)$ in 2DEGs range from $\lesssim 10^{10}/\text{cm}^2$ [278] to $\gtrsim 4 \cdot 10^{12}/\text{cm}^2$ [279], optimal photodetection can be achieved between 0.15 – 20 THz. Apart from the function J, the photocurrent Eq. (5.55) contains a prefactor $\sim \omega^{-1/2}$. Thus, the amplitude of the response scales weakly with frequency, which makes the in-plane photoelectric effect ideally suited for detection of radiation in the entire THz range.

The quantity $\beta \equiv \left(u_{\text{ac,x}}/\hbar\omega\right)^2$ in the formulas (5.40), (5.42) and (5.55) is the perturbation theory parameter. For the applicability of the theory, $\beta \ll 1$ must be valid. With the incident intensity of I_0 during a THz pulse, the electric field in x-direction acting on the 2DEG between the gates is $E_{\text{ac,x}} \approx 1$ V/m according to the numerical antenna simulations in Comsol Multiphysics. This gives $u_{\text{ac,x}} \sim eE_{\text{ac,x}}b_{\text{gap}} \approx 2.7$ meV and $\beta \approx 0.12 \ll 1$, which justifies the perturbative approach and neglection of higher-order contributions to the photocurrent.

5.3 Comparison with experiment

In order to compare the theoretically predicted photocurrent with the experimentally measured values, two additional steps are necessary. Firstly, the dependencies on chemical potentials in Eq. (5.55) and Fig. 5.8 need to be transformed into gate voltage dependencies. This is possible using either a theoretical calculation (corresponding to a parallel-plate capacitor model with screening taken into account) or using the experimentally measured data for the electron density. Secondly, the effect of resistive loading of the quantum mechanical current source has to be considered.

5.3.1 Theoretical electron density–gate voltage dependence

In this section, the connection between external gate potentials $U_{\mathrm{G,L}}$, $U_{\mathrm{G,R}}$ and chemical potentials μ_{L}, μ_{R} is calculated from a parallel-plate capacitor model. The relationship is obtained from the Poisson equation, taking into account the screening of the external potential created by the gates [194].

The voltage U_{G} on a gate creates the external potential

$$\varphi_{\mathrm{ext}} = U_{\mathrm{G}} \,. \tag{5.56}$$

The total potential that electrons experience is given by the sum of the external and the induced potentials:

$$\varphi_{\mathrm{tot}} = \varphi_{\mathrm{ext}} + \varphi_{\mathrm{ind}} \,. \tag{5.57}$$

Assuming a parallel-plate capacitor model, φ_{ind} is given by

$$\varphi_{\mathrm{ind}} = -e\frac{d(n_{\mathrm{s}} - n_0)}{\varepsilon_0\varepsilon_{\mathrm{r}}} \,, \tag{5.58}$$

where n_0 is the equilibrium charge carrier density (here “equilibrium” means at zero gate voltage), and n_{s} is the gate voltage tunable electron density. Thus the total potential is

$$\varphi_{\mathrm{tot}} = U_{\mathrm{G}} - e\frac{d(n_{\mathrm{s}} - n_0)}{\varepsilon_0\varepsilon_{\mathrm{r}}} \,, \tag{5.59}$$

and the electron potential energy is $V = -e\varphi_{\mathrm{tot}}$. The total potential is, in turn, related to the electron sheet density obtained from integration of the Fermi function in two dimensions [237]:

$$n_{\mathrm{s}} = \frac{m_{\mathrm{eff}} k_{\mathrm{B}} T}{\pi\hbar^2} \ln\left[1 + \exp\left(\frac{\mu - (-e\varphi_{\mathrm{tot}})}{k_{\mathrm{B}} T}\right)\right] \tag{5.60}$$

μ is the equilibrium chemical potential. The two equations (5.59) and (5.60) define a self-consistent problem on the unknowns n_{s} and φ_{tot}.

In equilibrium, $\varphi_{\mathrm{tot}} = \varphi_{\mathrm{ext}} = 0$ and Eq. (5.60) yields

$$n_0 = \frac{m_{\mathrm{eff}} k_{\mathrm{B}} T}{\pi\hbar^2} \ln\left[1 + \exp\left(\frac{\mu}{k_{\mathrm{B}} T}\right)\right] \tag{5.61}$$

Then the term $(n_s - n_0)$ in Eq. (5.59) can be evaluated:

$$n_s - n_0 = \frac{m_{\text{eff}} k_B T}{\pi \hbar^2} \ln \left[\frac{1 + \exp\left(\frac{\mu - V}{k_B T}\right)}{1 + \exp\left(\frac{\mu}{k_B T}\right)} \right] \tag{5.62}$$

Eq. (5.61) defines the equilibrium chemical potential μ as a function of the equilibrium concentration n_0, and in the limit $\mu \gg k_B T$, this yields $\mu = \pi\hbar^2 n_0 / m_{\text{eff}}$.

Inserting Eq. (5.62) into Eq. (5.59) and multiplying by $(-e)$ yields:

$$V = -eU_G + \frac{4d}{a_B^*} k_B T \ln \left[\frac{1 + \exp\left(\frac{\mu - V}{k_B T}\right)}{1 + \exp\left(\frac{\mu}{k_B T}\right)} \right] \tag{5.63}$$

Here, the effective Bohr radius in GaAs has been introduced:

$$a_B^* = \frac{4\pi\varepsilon_0\varepsilon_r\hbar^2}{m_{\text{eff}} e^2} . \tag{5.64}$$

For the left gate, the gate voltage $U_{G,L}$ creates a screened potential V_L, which changed the chemical potential under the left gate to $\mu_L = \mu - V_L$. Then Eq. (5.63) can be expressed in terms of the chemical potentials:

$$\boxed{eU_{G,L} = (\mu_L - \mu) + \frac{4d}{a_B^*} k_B T \ln \left(\frac{1 + e^{\mu_L/(k_B T)}}{1 + e^{\mu/(k_B T)}} \right)} . \tag{5.65}$$

An analogous expression relates $U_{G,R}$ and μ_R. This constitutes an implicit expression for $\mu_L(U_{G,L})$, but provides a direct analytical expression for $U_{G,L}(\mu_L)$.

The Bohr radius in GaAs is ca. 10 nm. With $d \approx$ 90 nm, $4d/a_B^* \approx$ 36. In a degenerate electron gas with $\mu_L \gg k_B T$, in order to change the chemical potential by an energy $\Delta\mu_L$, the gate potential has to be tuned by an approximately 37-times larger value: $e\Delta U_{G,L} = (1 + 4d/a_B^*)\Delta\mu_L$. A non-degenerate electron gas ($\mu_L \ll -k_B T$) is incapable of screening the applied potential, therefore beyond pinch-off $e\Delta U_{G,L} = \Delta\mu_L$.

Using the relationship Eq. (5.65), the (time-averaged) theoretical photocurrent can be plotted as a function of the gate voltages, see Fig. 5.9. The amplitude of the AC THz potential $u_{\text{ac,x}}$ determines the absolute value of the photocurrent, and is found from the finite element simulations in Fig. 4.59 (b). It can be estimated as ca. 0.4 meV for the time-averaged intensity $\langle I \rangle$. Here, the time-averaged intensity is used, since the lock-in measurement of the photocurrent in the experiment corresponds to the time-averaged value of the photoresponse.

The theoretical plot of Fig. 5.9 looks similar to the function J shown in Fig. 5.8. Plotting

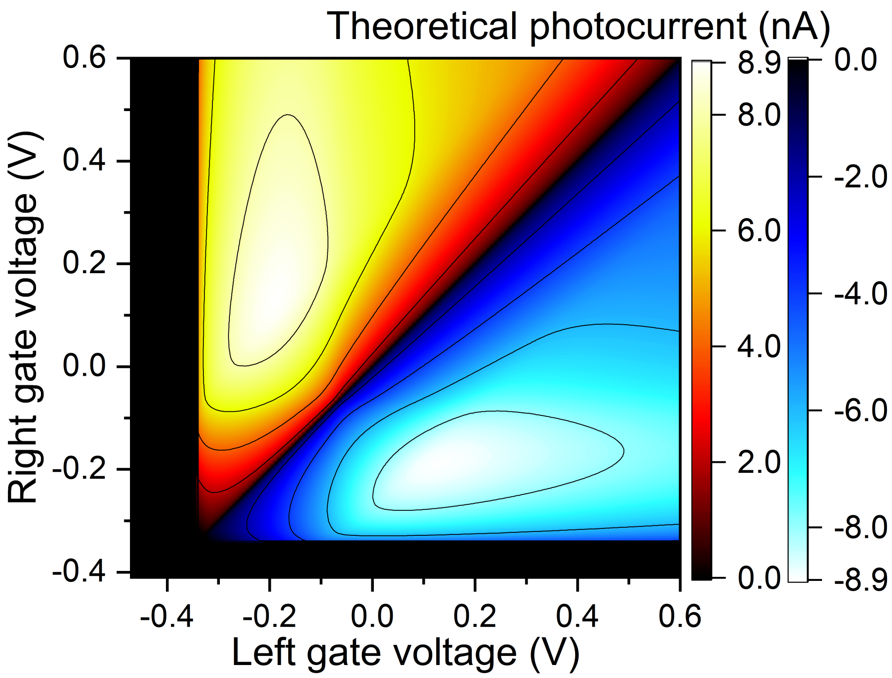

Figure 5.9: **Theoretically expected photocurrent as a function of the two (right and left) gate voltages.** The relationship between electron density and chemical potentials from Eq. (5.65) is used.

the photocurrent as a function of the gate voltages instead of the chemical potentials has the effect of quenching the area in the pinch-off regime towards the threshold voltage. This is because Eq. (5.65) corresponds to $e\Delta U_{\mathrm{G,L}} \approx 37\Delta\mu_L$ in a well conducting 2DEG and $e\Delta U_{\mathrm{G,L}} = \Delta\mu_L$ beyond threshold. Quantitatively, the theoretically calculated photocurrent shows a large value of 8.9 nA – higher than the measured value of 0.3 nA. This shows the theoretical potential of the in-plane photoelectric effect. However, to compare it with the experiment, resistive loading needs to be considered, see section 5.3.3.

5.3.2 Experimental electron density–gate voltage dependence

In the actual samples, the $n_{\mathrm{s}}(U_{\mathrm{G}})$-dependence does not follow a simple linear model as expected from the parallel-plate capacitor model described in the previous section. Instead, there is a plateau in the $n_{\mathrm{s}}(U_{\mathrm{G}})$-function, which has been extensively studied during the magnetotransport analysis in section 4.6. The Hall bars measured there were fabricated from the same wafer as the actual THz detector samples. The THz detector samples were measured after illumination with above-band gap light and show similar conductivity characteristics. Therefore, in the following, the experimental data for the illuminated $n_{\mathrm{s}}(U_{\mathrm{G}})$-dependence measured on the reference Hall bar will be used as a more accurate model, with

$$\mu = \frac{\pi \hbar^2 n_s}{m} \tag{5.66}$$

as $\mu(n_s)$-dependence.

5.3.3 Resistive loading

The photocurrent given by Eq. (5.55) is the internal current generated by the potential step. In order to compare it with the measured photocurrent, the loading of the quantum mechanical current source with the external classical resistances has to be considered.

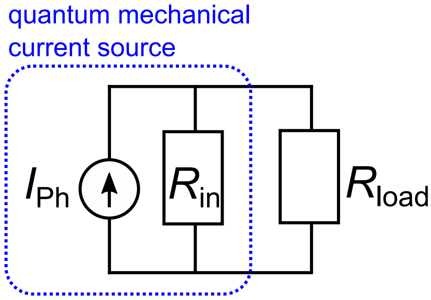

Figure 5.10: **Effect of resistive loading:** The quantum mechanical current source with internal resistance R_{in} is loaded by an external resistance R_{load}.

The expected photocurrent with external loading is given by $I_{ph,loaded} = R_{in}I_{ph}/R_{total}$. Here, $R_{total} = R_{in} + R_{load}$ is the total circuit resistance. R_{total} consists of the 4-wire sample resistance, which includes R_{in}, and is shown in Fig. 4.33 (a), the resistance of the connecting leads and Ohmics contacts, measured to be approx. 1.82 kΩ, as well as the input impedance of the current amplifier of 100 Ω. The bare internal resistance R_{in} of the quantum mechanical current source cannot be accessed in the experiment, but can be estimated theoretically as the inverse of the conductance of the potential step calculated in zeroth order, without THz irradiation, from Eq. (5.25).

5.3.4 Comparison of the theoretically predicted with the experimentally measured photocurrent

Using the experimental electron density–gate voltage dependence from section 5.3.2 and the resistive loading model from section 5.3.3, it becomes now possible to plot the theoretically expected photocurrent of the in-plane photoelectric effect under the experimental conditions. This is shown in Fig. 5.11 (a). For comparison, the experimentally measured photocurrent in the region $U_{G,wide}$, $U_{G,narrow} < 0.6$ V is shown in Fig. 5.11 (b).

There is a good qualitative agreement with the experimental photocurrent for $U_{G,wide}$, $U_{G,narrow} < 0.6$ V in Fig. 5.11. The theory predicts a photocurrent in the same regions where it is observed experimentally, with the same sign and of the same order of magnitude.

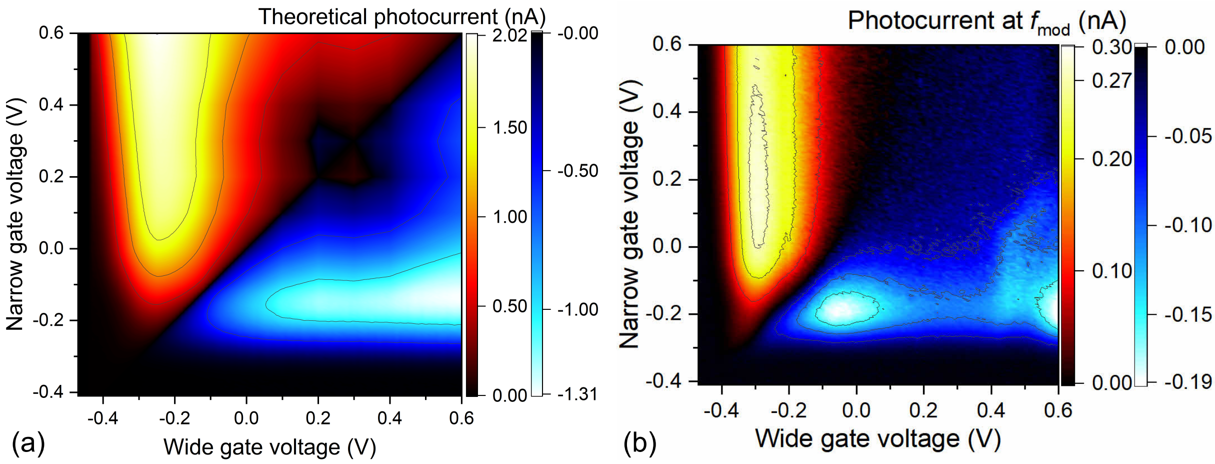

Figure 5.11: **Comparison of theory with experiment.** (a) Theoretically expected photocurrent as a function of the two (right and left) gate voltages, with resistive loading considered and using the experimentally determined $n_s(U_G)$-dependence. (b) 2D map of the experimentally measured photocurrent in the region $U_{G,wide}$, $U_{G,narrow} < 0.6$ V as a function of the wide gate voltage (horizontal axis) and the narrow gate voltage (vertical axis), same data as in Fig. 4.35. The experimental features are well reproduced.

The match between theory and experiment is best when considering the red regions with $I_{ph} > 0$. This is reasonable since it corresponds to a barrier under the wide gate, which is a better approximation of a semi-infinite potential step as considered in the theory, than the 200 nm narrow gate. The darker area at positive gate voltages originates from the plateau in the $n_s(U_G)$-dependence in the region of about 0.2 – 0.4 V seen in Fig. 4.49 (a). In spite of the simplicity of the model, all key features are thus reproduced.

The strong increase in photocurrent under maximum asymmetry in the top-left and bottom-right regions, seen in Fig. 4.35 is not covered in the theoretical framework. As discussed in section 4.7.3, this is likely related to an effect of the device geometry, such as a widening of the conducting channel, as edge depletion effects start to diminish at strongly positive gate voltages, combined with a reduction of the series resistance of the narrow channel. An increase in channel width, which is $\sim 0.5 - 1$ µm in equilibrium, would not only increase the conductance, but also lead to an enhanced photocurrent $I_{ph} \sim W$, which increases with the channel width.

Quantitatively, the theoretical photocurrent is expected to be up to 1.5 – 2 nA, Fig. 5.11 (a). The experimentally measured maximum value in the region $U_{G,wide}$, $U_{G,narrow} < 0.6$ V is 0.3 nA, Fig. 5.11 (b). The difference may be due to the smoothness of the potential step neglected in the theory as well as device-related effects such as mobility reduction in the pinch-off area. This indicates that the experimentally observed signal could be further increased by optimizing the wafer structure and device geometry.

It is remarkable that, while the in-plane photoelectric effect gives a value *higher* than the measured one, other possible interpretations, such as plasmonic mixing [119–121], bolometric [141], electron heating [81], photo-thermoelectric effects [143, 144], or photon-assisted tunneling [139, 140], cannot explain the effect or predict a *lower* value than measured, as was described in section 4.8.

To achieve a better agreement between theory and experiment, one could use a more accurate model of the device. In the theoretical plot, the boundary at the threshold voltage is very sharp. The smoother boundary observed experimentally can be reproduced by introducing an empirical ideality factor/subthreshold swing into Eq. (5.65). A more detailed model of the potential, which takes into account the ungated region between the wide and narrow gates, may improve the theoretical description. In reality, instead of a $\Theta(x)$-like potential, the potential step in the 2DEG will be smoothed by a combination of two characteristic length scales. The first is d, the distance between the 2DEG and the gate. As long as the 2DEG is degenerate and able to screen the external potential, one can understand the induced potential in the 2DEG as the result of an image charge of the gate mirrored by the 2DEG. As the 2DEG-gate distance is increased, the potential within the 2DEG becomes smoother on a length scale of $d \approx 90$ nm. The other length scale is the Bohr radius of 10 nm in GaAs, which is the characteristic length scale of charge screening in a 2DEG [101]. Therefore, the potential step will be smoothed on a length scale of 0.1 µm$<$0.27 µm $= b$, the distance between the gates. In a more detailed view of the potential, two potential steps will be induced by the narrow and the wide gate. When one of the gates is in the pinch-off regime, this can be neglected. But when both gates have positive voltages, lowering the potential both left and right from the gap between the antenna halves, a thin barrier is formed in the ungated region between the gates, which is (more or less symmetrically) excited with THz radiation. This could be a reason why experimentally, no photocurrent is observed in the region of positive gate voltages, but the theoretical model, that considers one potential step, predicts a photocurrent in this region.

5.4 Comparison with the physics of other photonic radiation detection mechanisms

In this section, we compare the physics of the in-plane photoelectric effect with other photonic detection mechanisms, i.e. phenomena where a photoresponse is obtained when charge carriers absorb photons due to quantum transitions.

5.4.1 Photovoltaic effect in p-n-junctions

In p-n-junctions, the photovoltaic effect is expoited for photodetection. The prerequisite for this mechanism is an internal electric field, which separates photoexcited electron-hole pairs. This electric field is created by band bending in the bipolar p-n-junction, which can be generated in different ways. In 3D diodes, it is created chemically by doping regions with different impurity types. In 2D materials, it can also be generated electrostatically by applying different gate voltages in a dual-gated device architecture. [280]

However, this mechanism relies on interband photoexcitation to create electron-hole pairs, which requires the band gap to be less than the photon energy. Hence this mechanism works in the visible or infrared range for semiconductors [280]. In the THz range, this effect can only be observed in gapless materials such as graphene [85].

The application of different gate biases in the device presented in this thesis creates bending, but since the device is based on a GaAs/AlGaAs heterostructure with a large bandgap of $> 1.42\,\mathrm{eV}$ [222], interband transitions due to THz radiation are impossible. In addition, in the presented device geometry, the photovoltaic effect is expected to lead to a photocurrent of opposite sign. This is shown in Fig. 5.12.

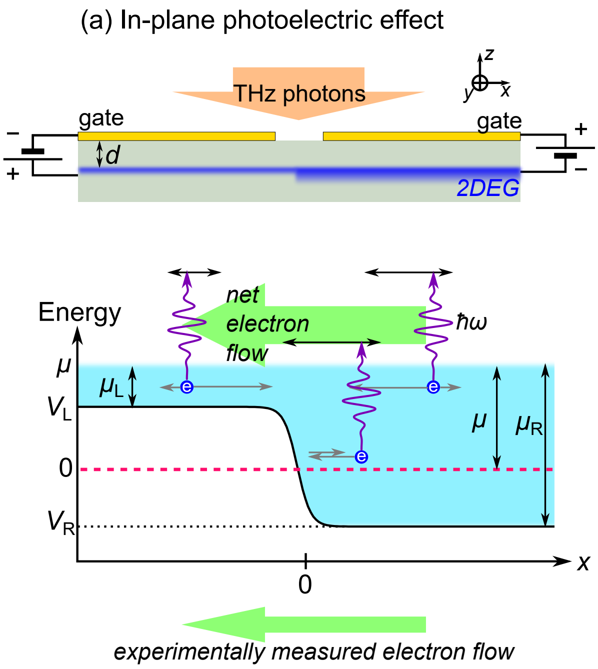

Figure 5.12: **Expected current flows for (a) the in-plane photoelectric effect and (b) the photovoltaic effect.** In both (a) and (b), two gates are placed on top of a two-dimensional conducting layer. In (a), the expected current flow is shown in a unipolar device as the one studied in this work. In (b), the expected current flow is shown in the case of a dual-gated geometry with interband photoexcitation.

Fig. 5.12 (a) shows the in-plane photoelectric effect, which predicts an electron flow from the region with a positively biased gate to the region with a negatively biased gate. Fig. 5.12 (b) shows the expected electron flow in the case of the photovoltaic effect for comparison, if photoexcitation were due to interband transitions. This could be the case with 2D semiconducting layers with photon energies in the visible range [280], or alternatively, if the energy gap is zero, in graphene [85]. The diagrams show that while the gate voltages are applied with the same polarity in Fig. 5.12 (a) and (b), the expected electron flow is in opposite directions.

The THz detector presented in this work is a unipolar device that utilises only electrons as majority carriers, which is also beneficial for high-speed operation, and its response is explained by the in-plane photoelectric effect occuring due to intraband transitions. The theoretically expected direction of electron flow in the in-plane photoelectric effect agrees with the experimental observation.

5.4.2 Photon-assisted tunneling

When the in-plane photoelectric effect is compared with photon-assisted tunneling across a thin barrier in the tunneling regime [138–140], one can think of the latter as being the difference of two photocurrents generated at the two edges of the barrier, which is considered as two mirrored potential steps with the chemical potential lying below the step height. The total photocurrent will vanish at zero bias due to the inherent symmetry of the barrier, and a photoresponse will only be observed if the symmetry is intentionally broken by an applied voltage across the barrier. This explains why the photoresponse of thin tunneling systems such as quantum point contacts presents itself predominantly as photoconductance [81, 140, 141], rather than zero-bias photocurrent or photovoltage [142]. In the device studied here, the translational symmetry is broken by the gate-induced potential step without any external source-drain bias, which is advantageous for noise performance. The potential step is implemented using a macroscopically wide barrier that is irradiated on one edge only. Thus the giant photocurrent signal, that tends to remain hidden in quantum point contacts, is recovered.

5.4.3 3D photoelectric effect

It should be noted that the in-plane photoelectric effect is substantially different from the "conventional" photoelectric effect in three dimensions. These key differences are illustrated in Fig. 5.13. As discussed in the introduction to this section, in the 3D case, photoexcited electrons gain a momentum predominantly parallel, rather than perpendicular, to the material interface [271]. The photoexcited electrons can get a perpendicular momentum component, needed to escape from the material, under oblique incidence of p-polarised light (the surface photoelectric effect is proportional to the squared sinus of the angle of incidence [269, 270, 274]), or by scattering processes that randomise their direction of motion [265]. Both cases are not optimal; in addition, scattering reduces the electron energy, diminishes the efficiency, and limits the intrinsic response time of the effect to scattering times. Furthermore, three-dimensional, bulk internal photoemissive detectors are photo-

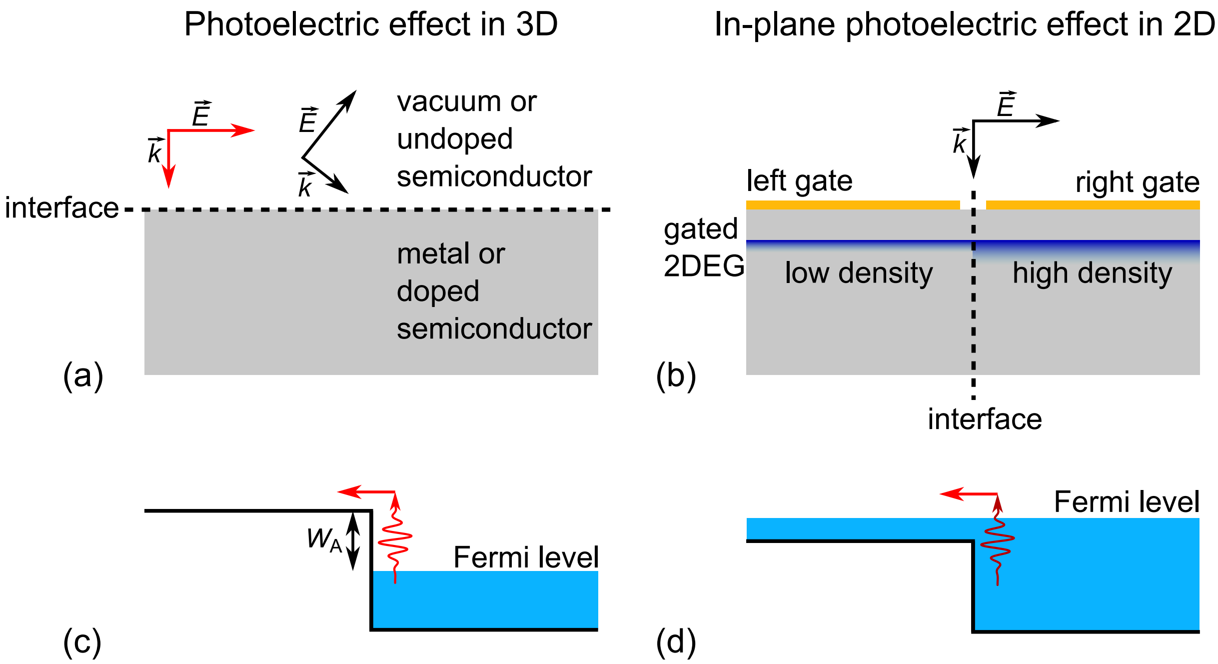

Figure 5.13: **Fundamental differences between the conventional 3D photoelectric effect (a), (c) and the in-plane photoelectric effect (b), (d) in two dimensions.** (a) The material interface is between two three-dimensional regions. Normally incident radiation is ineffective at generating photoexcited electrons (red arrows) due to the absence of an electric field component normal to the interface. Oblique incidence of p-polarised light (black arrows) is required for optimal efficiency. (b) The material interface is artificially created by the gate voltages and is perpendicular to the 2DEG plane. Normal incidence is by design the most efficient excitation method. (c) In the 3D photoelectric effect the Fermi level is below the conduction band in one of the materials, with an energy distance equal to the work function W_A. (d) In the whole system, the Fermi level is above the conduction band edge, with the 2DEG being a degenerate, well-conducting electron gas in the case of the in-plane photoelectric effect.

conductive and thus require an applied external bias to achieve high responsivities [261–264], and towards the THz range, their responsivity rapidly decays.

The in-plane photoelectric effect in 2D electron systems is free from these drawbacks: the effect is observed under normal incidence of radiation. The electric field of the wave and the desired direction of the electron flow, i. e. in the plane of the 2DEG perpendicular to the potential step, are perfectly aligned in the same direction by design. Thus no scattering is required to redirect electrons, and as a result, the mechanism has no *intrinsic* response time limit. The photocurrent arises at zero source-drain bias, and the potential step height V_B is artificially created and *in situ* tunable by gate voltages. Remarkably, the maximum photocurrent is obtained when the chemical potential lies above the potential step in both parts of the 2DEG, i.e., the 2DEG is well conducting. This is a striking difference to the 3D photoelectric effect: such a situation has not been implemented so far, and would not work in a 3D case (as it would require a junction of two highly doped materials, that would screen and reflect incoming radiation before it reaches the material interface). The effect is substantially stronger than THz photoresponse mechanisms previously considered in 2D electron systems, and the theory shows that the effect is ideally suited for utilization across the entire THz range.

5.5 Summary

In this chapter, a new fundamental physical phenomenon was described – the in-plane photoelectric effect. It is a purely quantum-mechanical, scattering-free phenomenon which leads to a strong THz photoresponse in a 2DEG with an uneven in-plane potential. This potential can be artificially created by two differently biased gates, which gives rise to a potential step in the 2DEG plane. Following a general explanation of the physical principle, the quantum mechanical solution of the corresponding Schrödinger equation in zeroth and first order was described. The theoretical results were compared with the experiment taking into account resistive loading of the quantum mechanical current source and both theoretical and measured electron density–gate voltage dependencies. It was shown that the maximum photocurrent is obtained when the chemical potential lies above the potential step in both parts of the 2DEG, i.e., the 2DEG is degenerate and well conducting. Such a situation has not been implemented so far and would not work in the case of the "conventional", 3D photoelectric effect. The effect is substantially stronger than THz photoresponse mechanisms previously considered in 2D electron systems. The potential step is tunable by gate voltages, and no DC source-drain bias is required to observe the photoresponse. The theory shows that the effect is ideally suited for utilization across the whole THz range. As an inherent effect of 2D systems, it should also be possible to observe and utilize it in 2DEGs on the basis of III-V materials other then GaAs, silicon, as well as the novel 2D layered, graphene-related materials.

The results on the THz detector and the in-plane photoelectric effect (chapters 4 and 5) are available as a preprint on arXiv [277] and have been submitted for publication.

6 Towards an all-optical THz-to-Optics interface based on quantum dot molecules

The term “quantum dot” refers to an object that is confined in all three spatial directions to length scales where quantum effects become important. This gives rise to confined quantum states with discrete energy levels. Therefore, their energy level structure resembles atoms, which is why they are often called “artificial atoms”. This makes it possible to study a solid-state, tunable analogue of atoms. [281]

The interband transitions in quantum dots lie predominantly in the infrared–visible region, and have been studied by many researchers. The spins of confined electron and hole can be used as qubits [282], which can be initialised, manipulated, and read-out optically. The energy differences between levels within a band lie in the far infrared spectral area. Research on intraband transitions in quantum dots was dedicated to measurements of their electrical response [135, 136], but not to optical read-out of intraband transitions.

The constructed experimental setup combining THz and optics (chapter 2) opens up the exciting opportunity of realising all-optical read-out with manipulation in the THz domain: by initialising and reading out states in quantum dots optically, but manipulating them using THz photons. The information carried by THz photons would be mapped onto the charge and/or the spin of charge carriers trapped in quantum dots. This would constitute a breakthrough in the area of THz technology, as it would bring quantum computation to the THz spectral region.

Careful preparation is necessary to realise this ambitious goal. In this chapter, I will describe the preparatory work carried out to get closer to this goal. After a brief review of state-of-the-art research on quantum dots, I will present measurements on InAs self-assembled quantum dots. Compared to InAs quantum dots, a novel material system – GaAs droplet-epitaxial quantum dots – has multiple advantages, such as a better control over the density and transition energies. Therefore, GaAs quantum dots grown by droplet epitaxy were also measured and were chosen as the basis for future measurements of THz interactions. All quantum dot wafers studied in this chapter were grown by molecular beam epitaxy by Peter Spencer at the Cavendish Laboratory.

However, THz irradiation of quantum dots alone is unlikely to yield success in the search for a THz response. Although the quantum dot intersublevel transition energies lie in the THz range [283], each individual dot has its own, unique energy levels. When being illuminated with the monochromatic radiation emitted by QCL, the chances that the THz photon energy matches a transition in the quantum dot are relatively low. Consequently a tuning element is required. It is possible to tune the energy levels by applying an electric field through the heterostructure using a gate voltage, but the tuning range available by electrostatic gating is too small ($\lesssim$ 1 meV), and strong electric fields will also influence other parameters besides the transition energy, such as electron and hole tunneling times [284]. Therefore, looking for a resonant THz response on single quantum dots will likely be a "hit-and-miss" experiment with poor reproducability and low chances of success.

These issues can be mitigated by using quantum dot *molecules* instead of single quantum dots. These objects consist of two coupled quantum dots interacting with each other, and feature a richer set of states. In particular, the electrical tuning range of indirect excitons in quantum dot molecules is much larger than in quantum dots. This makes quantum dot molecules the ideal system for the desired study. The fabrication of a tunable device structure incorporating these quantum dot molecules is described in section 6.3, and photoluminescence measurements revealed features proving the presence of quantum dot molecules. Finally, design criteria necessary for the realisation of a THz-to-Optics interface are discussed, and a novel semiconductor heterostructure is proposed and simulated, which features bipolar tuning of the bandstructure to facilitate all-optical readout over a wide range of electric fields with negligible parasitic leakage currents.

6.1 Quantum dots – an overview

6.1.1 Growth of quantum dots

There are many different types of quantum dots, such as interface fluctuation quantum dots [285, 286], colloidal nanocrystal quantum dots [287, 288], electrostatically defined quantum dots [289] or twofold cleaved-edge overgrowth quantum dots [290]. Among the more commonly used types are self-assembled quantum dots [291, 292], which will be studied in this chapter. These dots are fabricated by epitaxial growth of a material of slightly larger lattice constant and smaller bandgap (such as InAs) on top of the substrate semiconducting material (such as GaAs). The first monolayers are deposited as layers, but later 3D islands start to build up, because the layer-by-layer growth is no longer energetically favorable, see Fig. 6.1. This *Stranski-Krastanow* growth mode gives rise to small semiconductor islands embedded in the semiconductor heterostructure [293].

6.1.2 Energy level structure of self-assembled quantum dots

The in-plane confinement potential of self-assembled quantum dots can be well approximated as parabolic. The energy levels for charge carriers arising from lateral confinement

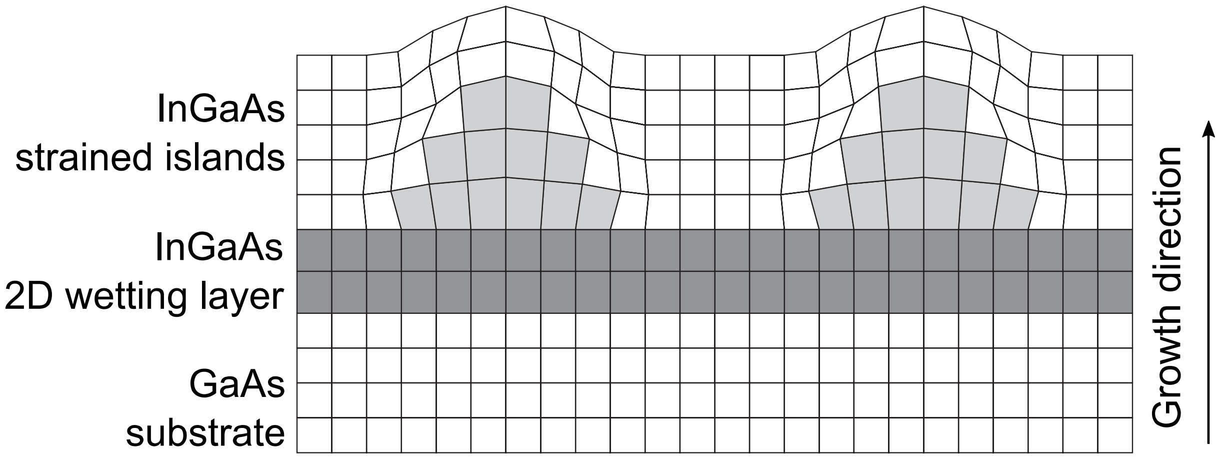

Figure 6.1: **Stranski-Krastanow growth of quantum dots.** Republished with permission of John Wiley & Sons, from Ref. [281]; permission conveyed through Copyright Clearance Center, Inc.

are then, assuming cylindrical symmetry of the quantum dot [281]:

$$E_{m,n} = \hbar\omega(m + n + 1)\,, \tag{6.1}$$

where m and n are the quantum numbers characterising motion in the lateral parabolic potential. The extent of self-assembled quantum dots in the transverse, growth direction ($\sim$ 5 nm) is much smaller than in the lateral direction ($\sim$ 20 nm). Therefore, the confinement energy in the lateral direction is much smaller than in the growth direction. The shell structure seen in optical experiments has its origin in excited states of the lateral quantization, while in the growth direction, only the lowest energy level can be considered. [281]

In Fig. 6.2, the energy levels arising from Eq. (6.1) are shown. The shells can be filled with charge carriers, i. e. electrons in the conduction band or holes in the valence band. If the semiconductor with the quantum dots is excited by photons with an energy above the bandgap of the bulk semiconductor, the photo-generated holes and electrons can relax into the lowest energetic states. The discrete states in the quantum dot cause both the photoluminescence and absorption spectra of quantum dots to consist of discrete lines.

At low temperatures ($\sim$ 5 K) the quantum dot states are empty, if the chemical potential lies between conduction and valence band states. This is the crystal ground state. If charge carriers of opposite signs exist in a quantum dot simultaneously, radiative recombination of electron-hole pairs under emission of a photon is possible. The simplest excitation consists of one electron and one hole, each in the lowest intraband state. This constitutes a neutral exciton that can recombine to the crystal ground state. If two electrons and two holes are present in a quantum dot, a biexciton is in the dot [294]. Quantum dots can also contain confined charge carriers, such as a single electron or a single hole.

These systems exhibit many interesting quantum optical phenomena, especially when coherently interacting with light [295]. Apart from studies of fundamental physics, such as

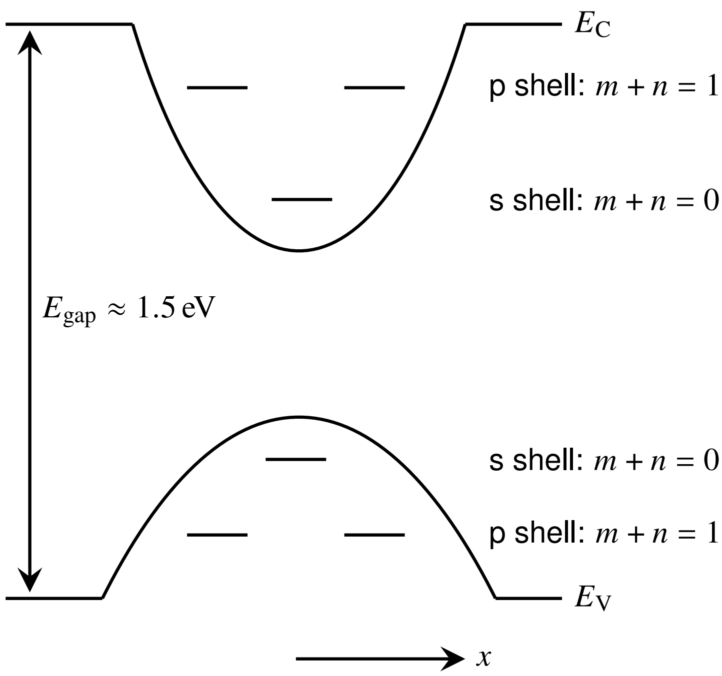

Figure 6.2: **Structure of the discrete energy levels of a quantum dot,** in the model of a parabolic in-plane confinement potential. The band-gap energy is not to scale. From [284].

the interaction between electron spins and nuclear spins, quantum dots are of vivid interest for the area of quantum computing [282, 296]: quantum dots can be used as a "box" to store single charge carriers with a certain spin. For example, an exciton is created in the dot, but then one of the carriers (e. g. the hole) tunnels out, leaving only the electron behind. This can be achieved by engineering the electron and hole tunneling times using barriers in the semiconductor heterostructure [297, 298]. In classical computers, the smallest unit of information is the bit, which may have only two values: 0 or 1. Quantum bits, or "qubits", can exist in an arbitrary superposition of the two states, $\alpha|0\rangle+\beta|1\rangle$, even though a measurement would always yield only one of the two states. The spin of a charge carrier in a quantum dot is a physical impementation of a qubit. In a mathematical sense, a qubit is a vector of two complex numbers [299, 300]. This allows computation with quantum operators rather than classical operators, which leads to quantum algorithms of lower complexity classes than their classical analogues [299, 301–303].

6.1.3 Interaction with terahertz radiation

Quantum dots have been shown to respond to infrared radiation, which was detected by a change in conductivity [305]. This photoconductivity signal under the presence of an applied bias and incident infrared radiation ($\sim 5-20\,\mu$m) has given rise to the *Quantum Dot Infrared Photodetectors (QDIP)*. The principle of operation relies on the photoexcitation of electrons from confined conduction band states into the continuum, see Fig. 6.3. Under the presence of an applied bias, the excited electrons drift in the electric field and cause an increase in current. [304]

Interactions of single, self-assembled quantum dots with THz radiation have recently

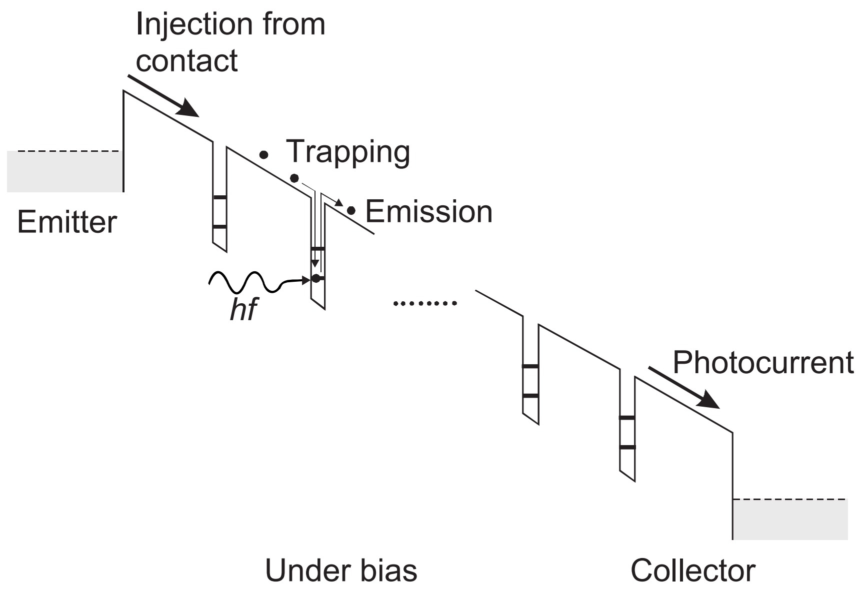

Figure 6.3: **Quantum dot infrared photodetector:** Principle of operation. Reprinted from Ref. [304], Copyright 2008, with permission from Elsevier, adapted.

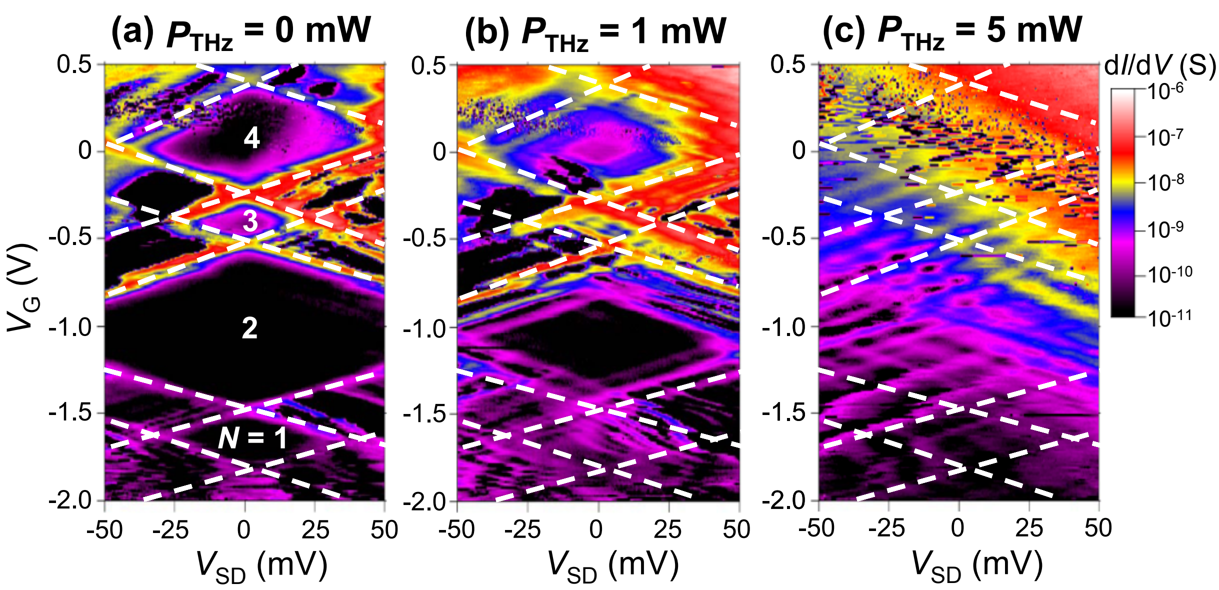

Figure 6.4: **Photon-assisted tunneling in InAs quantum dots.** Coulomb stability diagram: colour-coded plot of differential conductance dI/dV as function of source-drain voltage V_{SD} and gate voltage V_G of an InAs quantum dot in single-electron transistor geometry. Lines parallel to the Coulomb diamonds appear under illumination with 2.5 THz radiation and can be explained by photon-assisted tunneling. Reprinted figure with permission from Ref. [135]. Copyright 2012 by the American Physical Society.

been demonstrated in InAs quantum dots by electrical measurements [135, 136]: Under illumination with monochromatic terahertz radiation, a change in the electrical transport characteristics was observed which was explained by photon-assisted tunneling, see Fig. 6.4 [135, 136, 306–308]. Lifetimes of intersublevel transitions in the THz range have also been studied using a free electron laser [283].

6.1.4 Semiconductor heterostructures with tunable electric fields

A crucial advantage of quantum dots over atoms is that their transitions can be tuned. This can be accomplished if the quantum dots are embedded in a semiconductor heterostructure such as a *p-i-n* diode [309] or an *n-i* Schottky diode [297], Fig. 6.5. This results in an intrinsic electric field that bends the bandstructure. The top gate contact is made semi-transparent by evaporation of a very thin (~4.5 nm) metal layer of e. g. titanium. This allows the application of a DC potential while still being enough optically transparent for microphotoluminescence studies.

The voltage applied to such a heterostructure with an Ohmic back contact and top gate contact also represents a "knob" to tune the transition energies. The reason is the DC quantum-confined Stark effect [281, 310–312]: electron and hole wavefunctions are drawn apart from each other, which results in an energy change of the exciton. The exciton energy in the presence of an electric field $\vec{F}$ is changed by the energy of an electric dipole in an external field,

$$\Delta E = -\vec{p} \cdot \vec{F} \, .$$

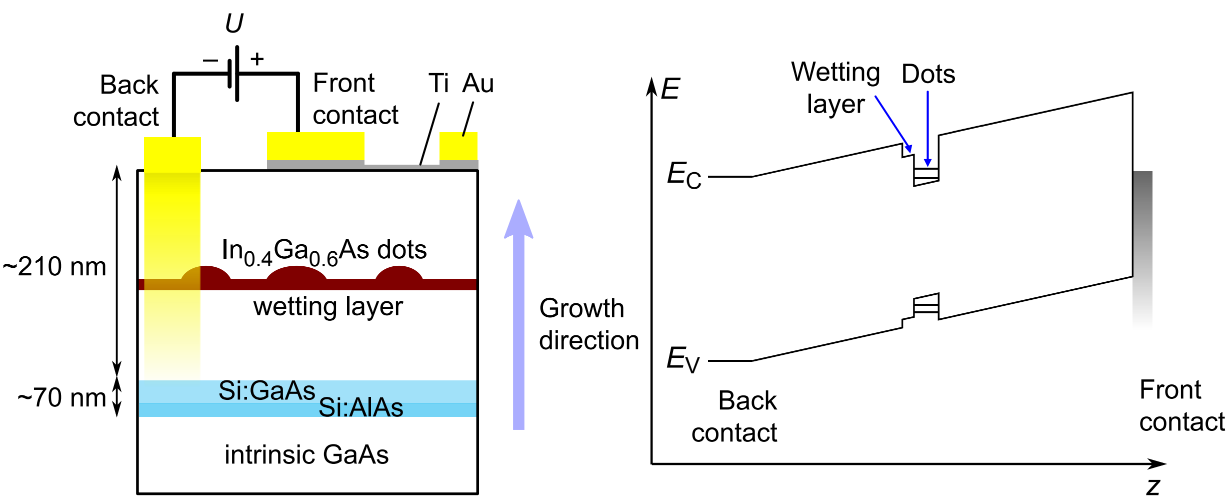

Figure 6.5: **Tunable semiconductor heterostructures with quantum dots.** *Left:* An exemplary cross-section of an *n-i* diode with quantum dots. InGaAs dots and wetting layer are in the middle of an intrinsic region between *n*-doped region with an Ohmic contact and the surface with a Schottky contact. *Right:* Resulting band structure without external voltage. Adapted from Ref. [284].

Here, $\vec{p}$ is the dipole moment of the exciton, which can be written as

$$\vec{p} = \vec{p}_0 + \beta \cdot \vec{F} \,.$$

$\vec{p}_0$ accounts for the fact that even without an applied external field the electron and hole wavefunction centers can be separated from each other. β is the polarizability of the exciton. $\beta \cdot \vec{F}$ is the change of the dipole moment in the field $\vec{F}$ (in a linear approximation). [281]

Thus, the field-dependent transition energy $E(F)$ is

$$E = E_0 - \vec{p}_0 \cdot \vec{F} - \beta F^2 \,,$$

with E_0 being the transition energy without external field. [281, 311, 312]

A typical voltage dependence of the photoluminescence of InGaAs quantum dots in a *n-i* Schottky diode is shown in Fig. 6.6. Around 0.7 V, the electric field in the structure is minimal; here the neutral exciton X^0 is observed, which partly overlaps with the X^+ exciton. As the electric field is increased, the energy of transitions is decreased, and more positively charged excitons appear. At very high fields $>$ 30 kV/cm, the photoluminescence lines become invisible as the tunneling rates of charge carriers in the dots have become faster than the radiative recombination rate – photoexcited charge carriers in the dots will instead lead to a photocurrent response. For voltages above 0.7 V, electrons from the n-doped

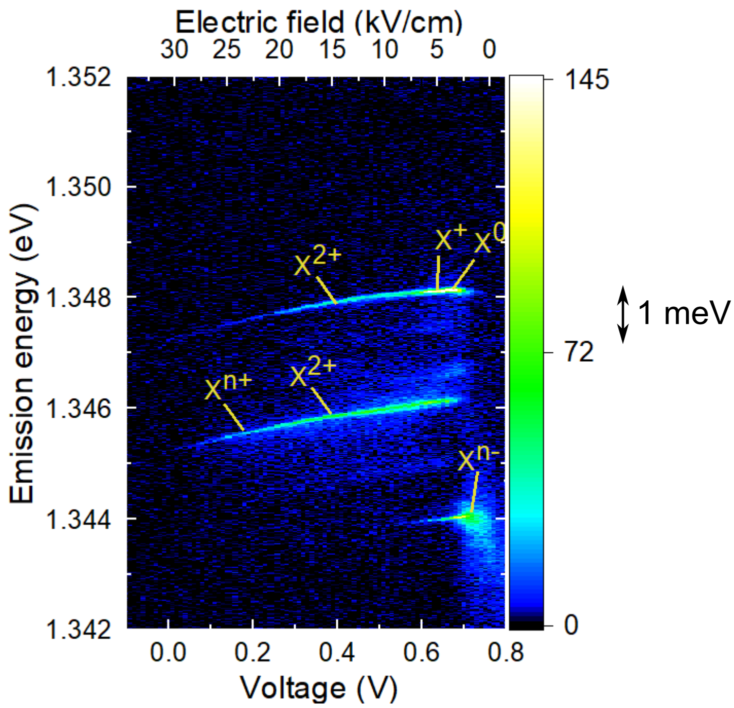

Figure 6.6: **Voltage-dependent photoluminescence of InGaAs quantum dots.** Adapted from Ref. [284].

contact flood quantum dot states, leading to smeared out photoluminescence of multiply negatively charged excitons.

If the quantum dot layer is placed close to the heavily n-doped contact, the external voltage can tune the quantum dot levels with respect to the chemical potential. In this case, the charge state of the quantum dot can be controlled: states below the chemical potential are filled, those above are empty (charge-tunable structure) [313].

6.2 InAs and GaAs quantum dots

6.2.1 Optical setup

I carried out the microphotoluminescence measurements described in this chapter on the optical setup shown in Fig. 6.7. A helium-neon (HeNe) laser capable of emitting 3 mW of power, filtered with a laser line filter for 632.8 nm, is used for above-bandgap excitation of the quantum dots. Continuous tuning of the excitation power is achieved by a combination of

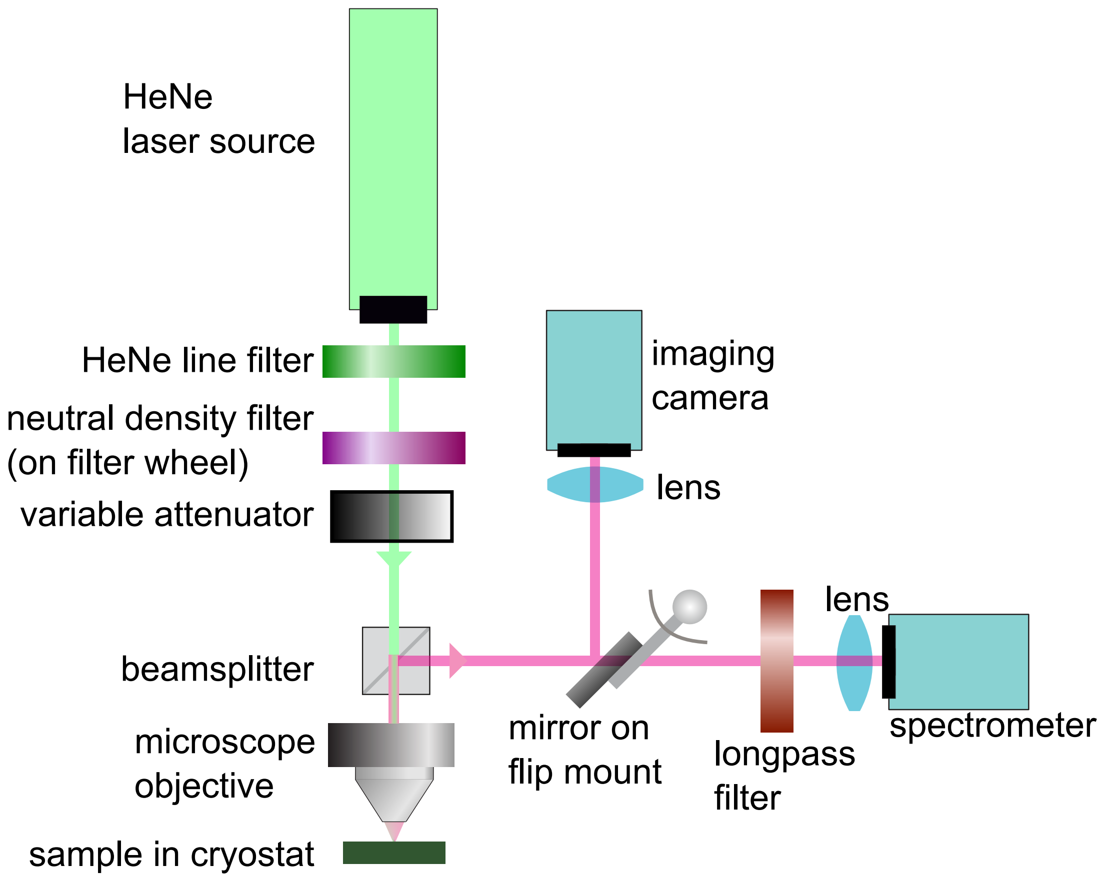

Figure 6.7: **Simplified schematic of the experimental microphotoluminescence setup** used for studies of semiconductor quantum dots. The excitation path is shown in green and the detection path in purple.

neutral density filters and a continuously variable filter wheel. The excitation and detection paths are combined and split using a beam splitter. For cryogenic cooling to temperatures around 5 K, the horizontal optical Janis ST-500 sample cryostat is used, which has been modified to allow simultaneous THz excitation as described in chapter 2. It is mounted on x and y micrometer stages (initially manual, later motorised micrometer stages). The photoluminescence signal at lower photon energies, spectrally separated from the excitation by a longpass filter, is collected by an Andor spectrometer with a thermoelectrically cooled silicon charge-coupled device array (Andor Newton) as a detector.

6.2.2 Power-dependent spectroscopy on InAs self-assembled quantum dots

Initially, the photoluminescence of InAs quantum dots is studied on as-grown wafers (wafer numbers W1378 – W1383). The wafer studied here, W1378, contains InAs quantum dots created by growing a 450 nm GaAs buffer layer on the GaAs (100) semi-insulating substrate at 580°C substrate temperature, depositing 0.7 nm of InAs at 475°C, and capping with 100 nm of GaAs at 580°C. A typical emission spectrum of the quantum dots under low excitation power in a sample from the wafer is shown in Fig. 6.8: it shows sharp, separated lines that are typical for transitions between the quantised energy levels of the zero-dimensional system.

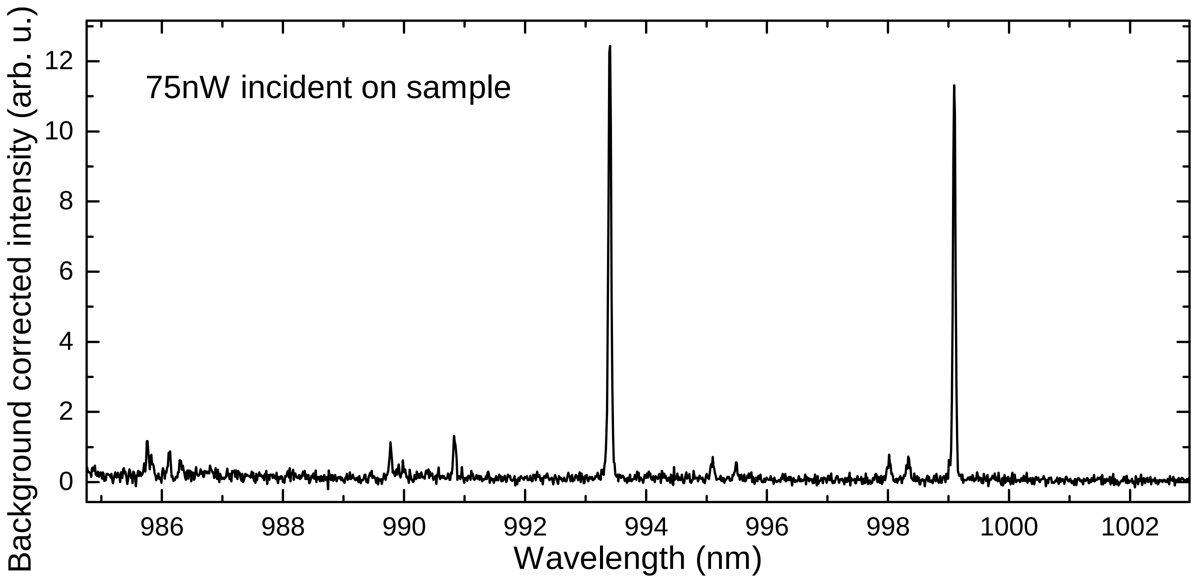

Figure 6.8: **Exemplary photoluminescence spectrum of a quantum dot sample** at a temperature of ca. 5 K, measured on wafer W1378. Characteristic sharp emission lines are visible.

To distinguish lines arising from different numbers of charge carriers, excitation power dependent spectroscopy was carried out. The results are shown in Fig. 6.9 (a).

For each power, the photoluminescence peak intensity was integrated over the narrow (∼ 0.3 nm) wavelength window containing the peak, and the background signal was sub-

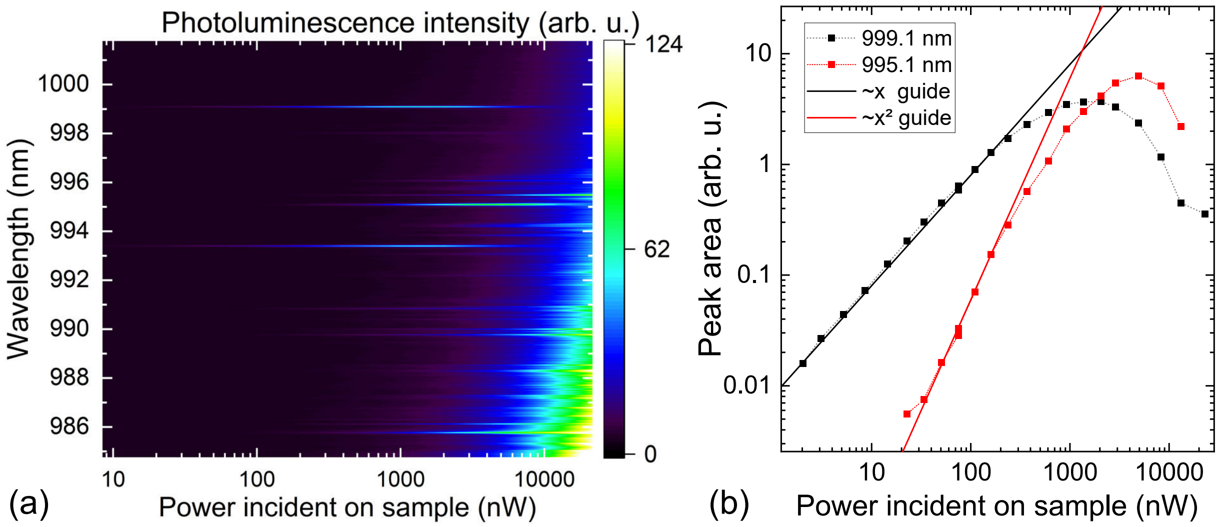

Figure 6.9: **Power dependence of the quantum dot photoluminescence.** (a) Spectrum of a spot on wafer W1378 shown as colour-coded intensity map. Vertical axis: wavelength in nm; horizontal axis: power incident on sample in nW (logarithmically scaled). (b) Integrated and background corrected photoluminescence intensity of two quantum dot PL lines as function of excitation power in a double-logarithmic plot. Linear and quadratic power dependencies indicate exciton and biexciton transitions.

tracted. The background was determined by integrating a wavelength interval of comparable width without a signal close to the PL transition, and subtracted from the PL peak intensity. The resulting corrected PL line intensity is plotted against excitation power in Fig. 6.9 (b) on a double-logarithmic scale.

The peak at 999.1 nm has a linear power dependence, while the other peak at 995.1 nm has a quadratic power dependence. A linear power dependence is characteristic for neutral or charged excitons, while a quadratic power dependence indicates biexcitons [314]. This way, the peak at 999.1 nm arises from an exciton – presumably a neutral exciton, since no electric fields were applied to the sample and it is the first peak visible at low excitation powers. The transition at 995.1 nm originates from a biexciton. These signatures demonstrate presence of quantum dots in the wafer, and confirm successful growth of the quantum dots.

6.2.3 GaAs droplet-epitaxial quantum dots

One issue with InAs quantum dots is the difficulty in controlling the growth process [315]. In particular, once the nucleation of dots has started in the Stranski-Krastanow growth mode, the time window between the onset of nucleation and completed growth of highly dense dot structures is measured in seconds. The growth is highly temperature dependent and requires a well calibrated and stable MBE effusion cell flux. Fractions of a second in the timing of the movement of an effusion cell shutter, together with its speed of motion, can strongly influence the quality, density, and transition energies in quantum dots. It can easily happen that the growth process yields either too many dots, or no dots at all [315]. In addition, the spatial density of dots and their transition energies are interdependent. To mitigate this problem, researchers sometimes stop rotation of the wafer during quantum dot growth, in order to find a local place on the wafer where the density and wavelength of dots just happened to have the desired values [316]. This way it is possible to find dots with the correct parameters, at the expense of a low yield of useful wafer material.

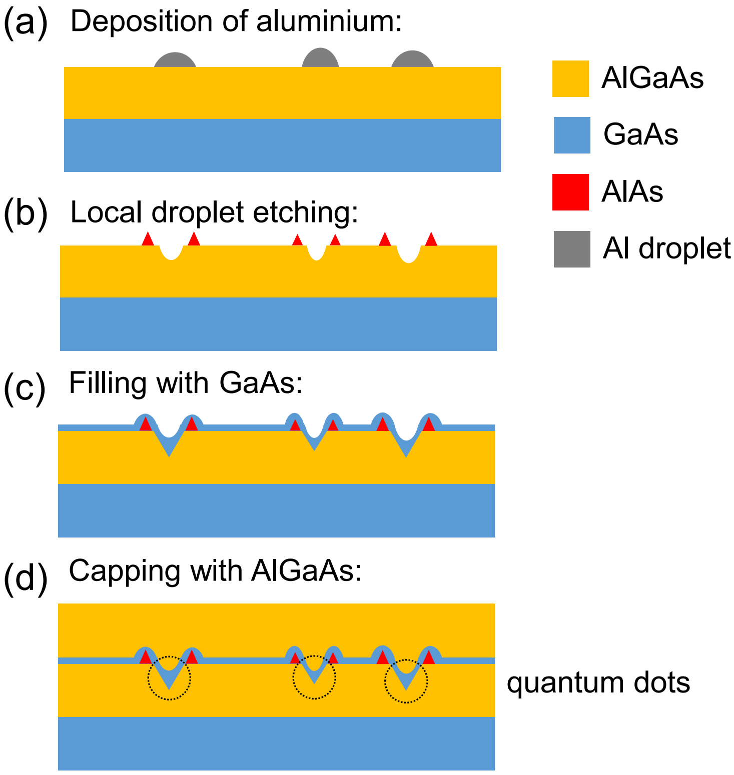

Figure 6.10: **Local droplet etching of quantum dots,** showing the four growth steps in a molecular beam epitaxy machine.

As a way of eliminating such issues, a different, novel material system was chosen for future experiments: GaAs quantum dots [317–319], which are grown by droplet epitaxy with subsequent local droplet etching, in a process described in Refs. [317–319] and illustrated in Fig. 6.10. The Stranski-Krastanow growth mode employed in growth of InAs quantum dots is strain-driven and requires a mismatch in lattice constant for the dots to form. In contrast, the droplet epitaxial growth enables quantum dot formation on lattice matched materials which results in strain-free dots [320]. This growth method is thus also more flexible towards the choice of quantum dot material: GaAs, InAs, InGaAs, and InSb quantum dots have been grown using droplet epitaxy [318].

The growth procedure is as follows [317–319]: after growth of a GaAs buffer layer, AlGaAs is deposited as a higher-bandgap material. Following that, the As shutter is closed, which results in a >100-fold reduction in As flux. Then, aluminium is deposited for a time frame corresponding to a few monolayers. Due to the lack of arsenic, the aluminium does not form an AlAs layer. Instead, it forms droplets distributed over the surface of the wafer. Subsequently, the droplets are thermally annealed by interrupting the growth process for several minutes with closed effusion cell shutters. During this step, the metal droplets on the surface etch pits (nanoholes) into the wafer surface. The substrate underneath the metal droplets becomes dissolved, and the material moves to the edges of the droplet, which results in an Al-rich AlGaAs ring around the nanoholes. After this droplet etching step, growth is resumed and the pits are filled with GaAs as a lower-bandgap material, which accumulates in the nanoholes. Finally, the wafer is capped with AlGaAs. This encapsulates the GaAs material trapped in the pits in a higher-bandgap AlGaAs material and creates a local confinement potential in all three dimensions – i. e., a quantum dot [317–319].

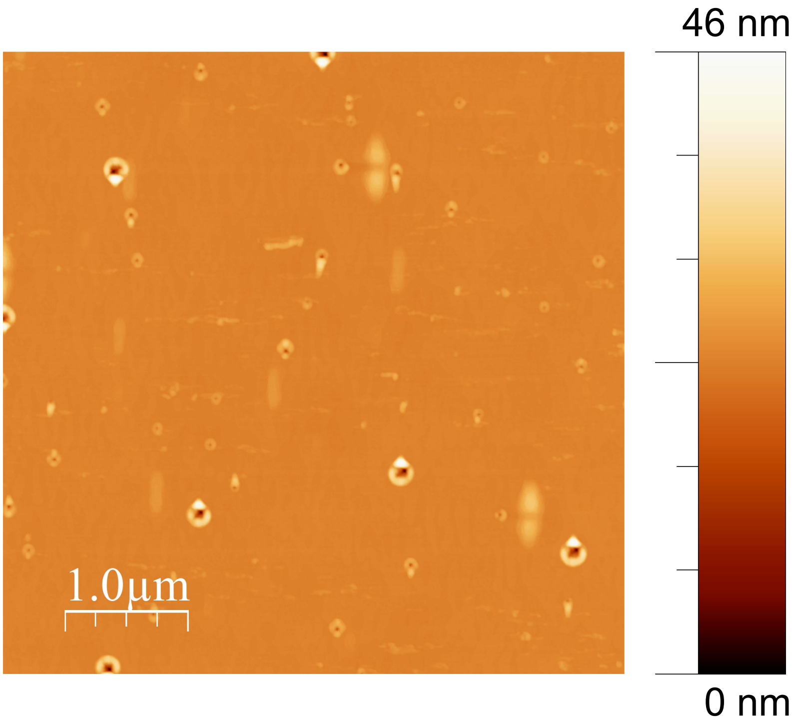

Figure 6.11: **AFM image of nanoholes formed by local droplet etching.** The AFM data was measured by Dr Peter Spencer on the wafer V888.

The growth process enables easier control. Notably, in this process, the nucleation and the filling of the dots are decoupled: the nanohole density and depth are controlled by the droplet etching phase, whereas the emission wavelength is independently set by the thickness of GaAs deposited in the filling phase [321]. With GaAs being used as dot material, the emission wavelengths lie in the range of 690–810 nm, compared to 900–1300 nm for InAs quantum dots. Due to the higher energy of the transitions, they also have a better overlap with the emission spectrum of a tunable Ti:Sapphire laser and the optimal responsivity of silicon charge-coupled device cameras, making them easier to excite and detect with common laboratory instruments.

As a first test, the wafer V888 was grown according to the procedure described in Ref. [319]. After depositing a 300 nm thick GaAs buffer layer at 580°C temperature on the (100) semi-insulating GaAs substrate, the substrate temperature is ramped up to 620°C and a 200 nm thick $Al_{0.33}Ga_{0.67}As$ layer is grown. Then the As shutter is closed and arsenic is pumped out during 8 minutes of growth interruption. The subsequent droplet epitaxy was carried out by depositing a thin Al layer, by opening the Al shutter for 4 s, the amount of time that would result in a 0.5 nm thin AlAs layer if arsenic were present. Then the droplet etching is carried out during 180 s of growth interruption. The quantum dots are then created by filling the pits with a 0.57 nm GaAs layer. To this end, the Ga shutter was opened for 2 s, followed immediately by re-introducing arsenic into the growth chamber and waiting for 30 s. Finally, another 200 nm thick $Al_{0.33}Ga_{0.67}As$ layer is grown, and the droplet etching step (without filling) is repeated on the surface to enable evaluation of the nanoholes by an AFM.

A characterisation of the wafer surface by AFM showed the characteristic pits created by the local droplet etching, see Fig. 6.11. The deeper holes surrounded by a ring are clearly seen. The faint oval shapes likely indicate quantum dots embedded under the surface, where the lattice distortion propagates to the top of the surface through the top 200 nm $Al_{0.33}Ga_{0.67}As$ layer.

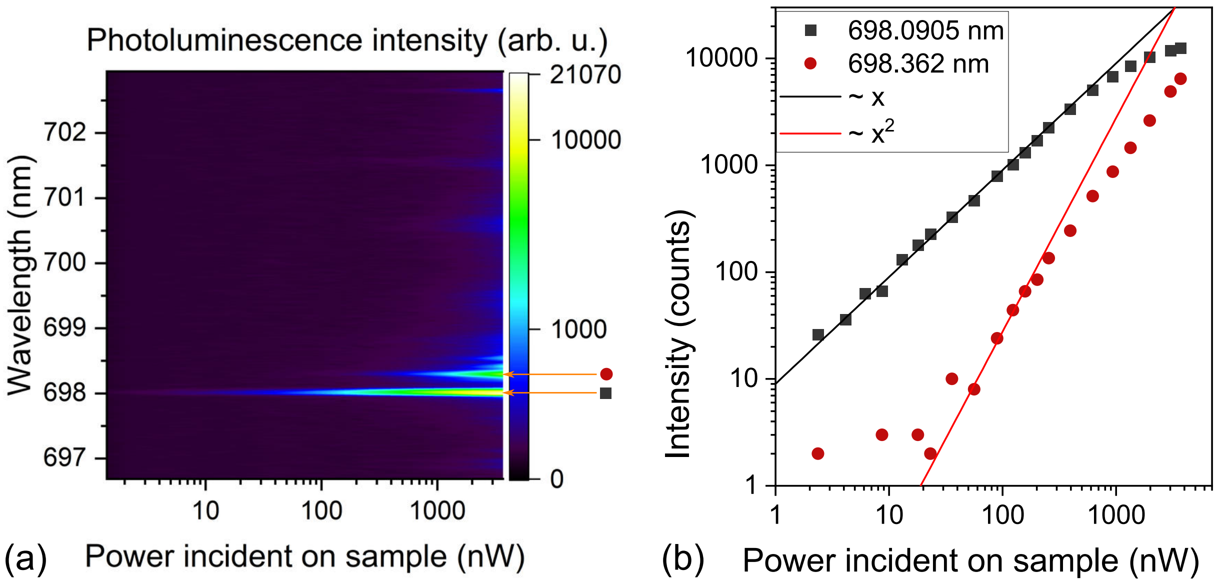

Figure 6.12: **Photoluminescence of GaAs droplet-epitaxial quantum dots.**(a) Spectrum shown as colour-coded intensity map, (b) integrated and background corrected photoluminescence intensity of the two visible quantum dot PL lines as function of excitation power in a double-logarithmic plot.

Following successful demonstration of the droplet-epitaxial growth process in the AFM scan, a sample of the wafer V888 is measured in the photoluminescence setup. The measured PL spectrum is shown in Fig. 6.12 (a) and the corresponding analysis is shown in Fig. 6.12 (b). Distinct sharp lines can be seen in the spectrum, and power-dependent spectroscopy shows again excitonic and bi-excitonic features, demonstrating successful growth of quantum dots. The other lines at higher wavelengths are likely charged excitons or multi-excitonic complexes with a steeper power dependence that appear at the stronger excitation powers.

6.3 GaAs droplet-epitaxial quantum dot molecules in a tunable structure

6.3.1 Quantum dot molecules

So far we discussed semiconductor heterostructures containing a single layer of quantum dots. But what happens, if another layer of quantum dots is deposited close to the first one?

In the case of Stranski-Krastanow self-assembled quantum dots, the dots in the second layer can "feel" the strain from the buried dots in the first layer, which act as nucleation sites. Therefore, subsequent layers of quantum dots grow in vertically aligned stacks, while the lateral positions of the dots are determined by the positions of quantum dots in the first layer. This can be seen in Fig. 6.13: A total of five layers of InAs quantum dots were deposited in a stack on a GaAs substrate. If the thickness of the spacer layer between the dots is $\lesssim 70$ monolayers, the quantum dots self-organise vertically [322].

Two layers of quantum dots on top of each other yield vertically coupled pairs – "quantum dot molecules" [323]. Photoluminescence spectra of such objects, acquired under different electric fields in the structure, yield a complex set of curves. An example is shown in Fig. 6.14. It can be seen that there are photoluminescence lines with both strong and weak dependencies of transition energies on the electric field, i. e. Stark shifts. The lines with weak Stark shifts originate from radiative recombination of *direct excitons*. These are excitons where both the electron and the hole are in one quantum dot. In contrast, *indirect*

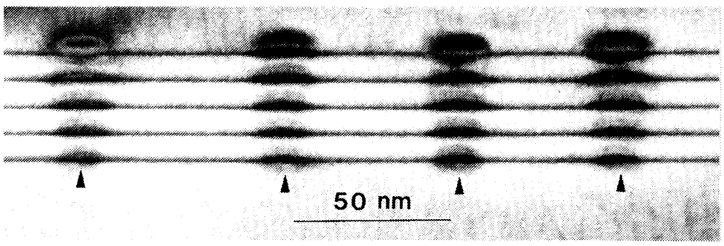

Figure 6.13: **A stack of five quantum dots.** Transmission electron microscope image, reprinted figure with permission from Ref. [322]. Copyright 1995 by the American Physical Society.

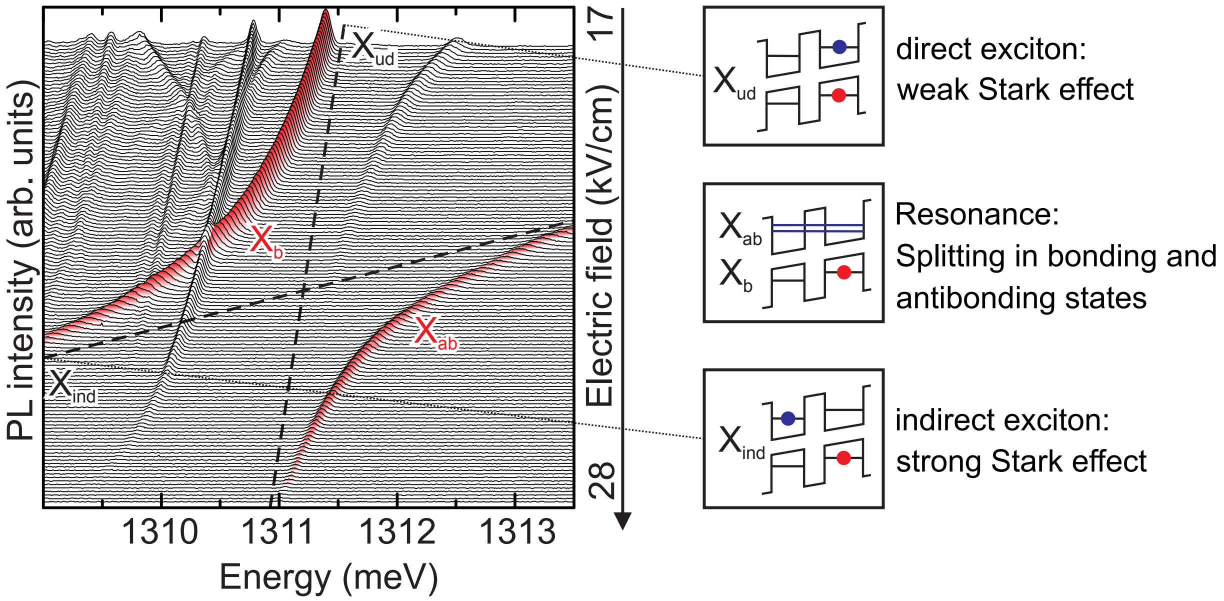

Figure 6.14: **Photoluminescence signatures of a quantum dot molecule.** The studied excitonic transitions are highlighted in red: indirect and direct excitons are tuned in resonance, form bonding and anti-bonding states when in resonance, and are detuned out of resonance as the electric field is increased. Adapted from Ref. [316].

excitons have electrons and holes in different quantum dots of the quantum dot molecule, and exhibit a strong Stark effect. The two excitonic lines are shown in Fig. 6.14 by dashed lines [316, 323].

When the electric field is tuned, an anticrossing of the PL lines of the direct and indirect excitons can be observed. Similar to the H_2 molecule, the two coupled states are split in bonding and anti-bonding states. This property has allowed demonstration of conditional switching of quantum dot molecules by optical means: The generation of an exciton in one dot of the molecule changes the excited states of the other dot and can therefore block absorption in the other dot [324].

The coupling strength of the two quantum dots can be varied by tailoring the growth process. In reference [325], two asymmetrically thick InAs quantum dot layers were deposited, and the PL signatures of the resulting wafers were studied. When the first dot layer is the thinner one, the quantum dot molecules exhibit PL as in Fig. 6.15 (a). Fig. 6.15 (b) shows the PL of the wafer where the first dot layer is thicker. The energy scale of the anticrossing in Fig. 6.15 (a) and the amount of achievable Stark shift tuning are commensurate with the photon energies in the terahertz range. In Fig. 6.15, the red arrow indicates a transition energy corresponding to a frequency of 2 THz (8.28 meV). Even though the photoluminescence spectrum does not show the energy levels themselves, but only the transitions, i. e. the energy differences between them, this indicates a much larger tuning range of the energy levels as compared to single quantum dots, Fig. 6.6.

Less research has been done on droplet-epitaxial quantum dot molecules, but they exhibit similar properties as well [321]. The upper and lower dot energy levels are tuned by the amount of GaAs and AlAs deposited into the nanoholes during the molecular beam epitaxial growth.

6.3.2 A quantum dot molecule as an interface between terahertz and optics

To observe a strong interaction between a semiconductor nanostructure and incident photons, the energy has to be in resonance with a transition. As seen from Fig. 6.15, the electric field parallel to the growth direction, which can be adjusted by applied gates, can act as a “knob” to bring transitions in a quantum dot molecule in resonance with incident terahertz photons. It is reasonable that in this case, the terahertz photon could e. g. transform a direct exciton into an indirect exciton, or vice versa, by moving charge carriers between

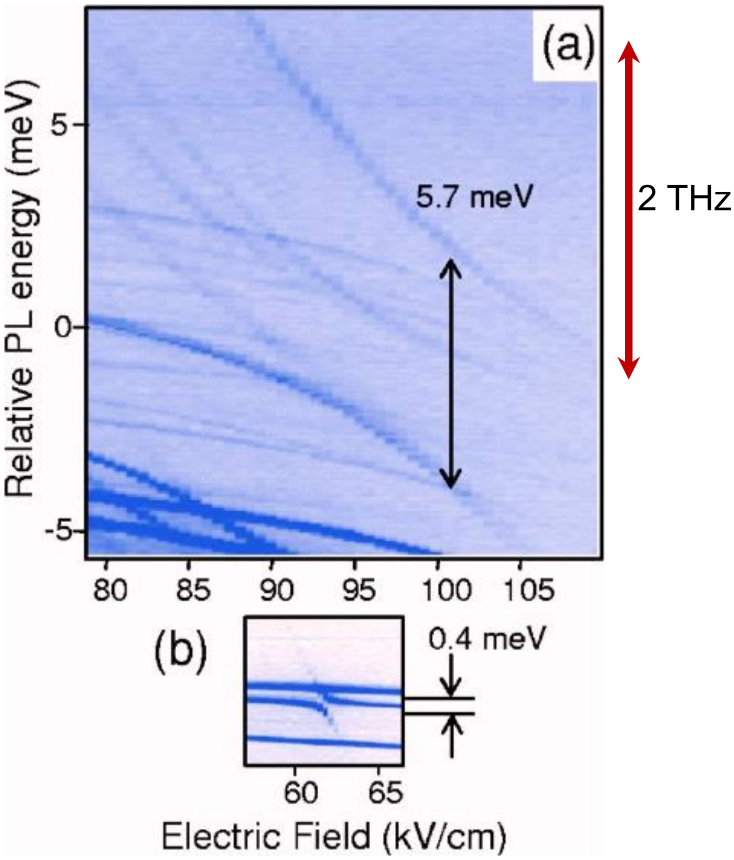

Figure 6.15: **Tailoring the anticrossing magnitude by controlling growth parameters of quantum dot molecules.** (a): 2.5 nm height of lower dot, 4 nm interdot barrier, 4 nm height of upper dot; (b): height values reversed for top and bottom dot. Reprinted from Ref. [325], with the permission of AIP Publishing. The red arrow on the right-hand side illustrates an energy splitting of 2 THz, commensurate with photon energies available from QCL sources.

the dots. This could be seen as a change in oscillator strength in the photoluminescence spectrum (Fig. 6.15), especially in the case of resonant excitation.

A demonstration of this effect will have paramount impact on the area of quantum computing and communication, as this would constitute coherent manipulation of quantum states by single terahertz photons with the possibility of optical readout.

In order to combine the advantages of the GaAs droplet-epitaxial dots with the tunability of quantum dot molecules, GaAs quantum dot molecules were investigated. The quantum dot molecules were formed by depositions of nominally 0.57 nm GaAs for the bottom quantum dot, 3 nm AlAs for the barrier between the dots, and 0.88 nm GaAs for the top quantum dot.

To study the pholuminescence as a function of the applied electric field, a wafer with a Si n-doped layer below the molecules was grown. The wafer, V890, has first a 300 nm GaAs buffer grown followed by a 50 nm Si-doped GaAs bottom contact layer (doping density $10^{18}/\mathrm{cm}^3$). After growth of the n-doped layer, the substrate temperature is increased from 580°C to 620°C. The quantum dot molecules are sandwiched in an AlGaAs matrix (120 nm below the dot layer, 80 nm above). This is so that the quantum dots, formed at the bottoms of the nanoholes, will be placed approximately centrally in the AlGaAs barrier. The droplet etching for the dot molecules and the first dot layer was grown in the same way as in the previous wafer V889, described in section 6.2.3, but after this, 3 nm AlAs for the tunnel barrier and 0.88 nm GaAs for the top quantum dot were deposited additionally before proceeding with growth of the AlGaAs matrix and capping the wafer with 5 nm GaAs for surface protection against oxidation.

6.3.3 Fabrication of test devices

It is impossible to distinguish single quantum dots from quantum dot molecules based on power-dependent spectroscopy alone. Therefore, the wafer needs to be processed into a tunable device structure, as shown in Fig. 6.5, in order to identify signatures of quantum dot molecules by tuning of the transitions.

The fabrication procedure is shown in Fig. 6.16. It consists of three evaporations to deposit three types of features: the Ohmic contacts, the semi-transparent Ti layer for electrostatic gating of the dots, and TiAu bond pads. Finally, the sample is covered with photoresist in some areas to prevent oxidation and degradation of the Ti layer with time.

When tailoring recipes for quantum dot molecule growth, parameters such as the thicknesses (or growth times) of deposited GaAs and AlAs layers may need to be adjusted from wafer to wafer to find the optimal values. Therefore, the key priority for this fabrication procedure is a quick processing time, in order to enable rapid feedback to the growth process.

To meet this criterion, I chose a shadow-mask process, as this eliminates time-consuming steps of resist deposition and lift-off, leaving only the alignment of the shadow mask and the evaporation itself. To press the shadow mask onto the sample, I fabricated custom copper

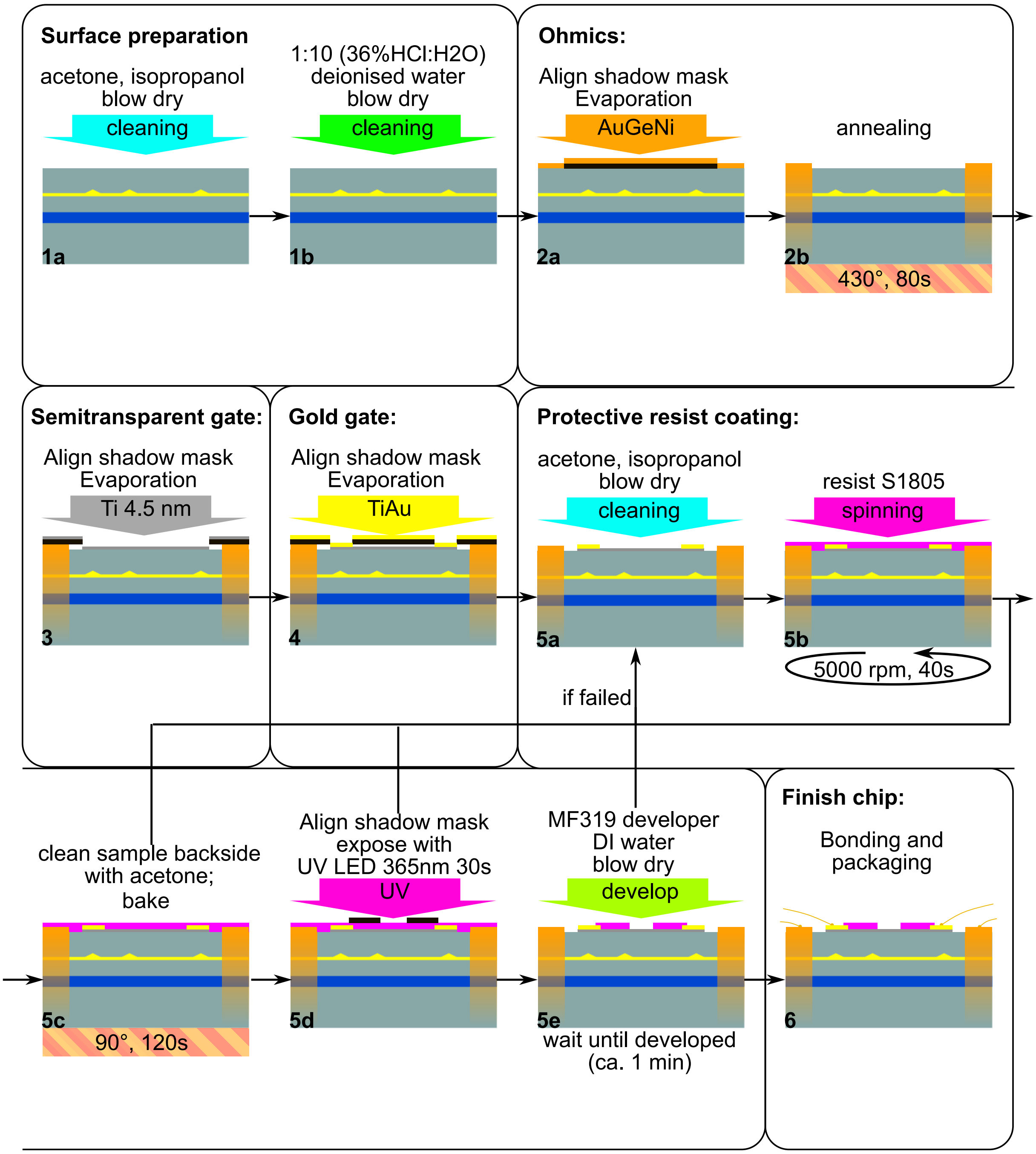

Figure 6.16: **Shadow-mask fabrication procedure** of the quantum dot test wafers, consisting of Ohmic contact deposition, semitransparent gate cover, gold bond pad fabrication, and resist encapsulation.

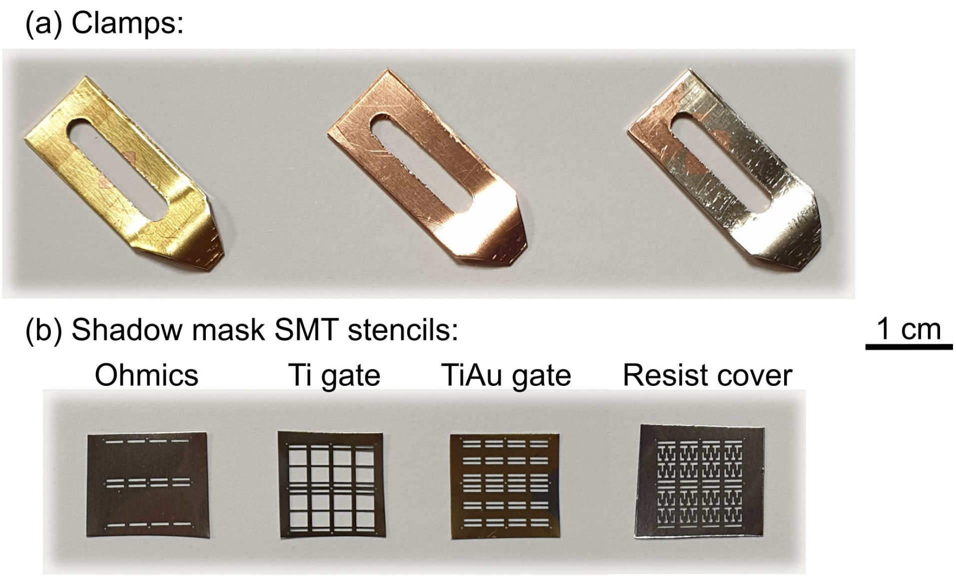

Figure 6.17: **Shadow mask fabrication elements.** (a) Custom-made copper clamps for shadow mask mounting in the evaporator. (b) Shadow masks made from SMT stencils for the four process steps of quantum dot sample fabrication.

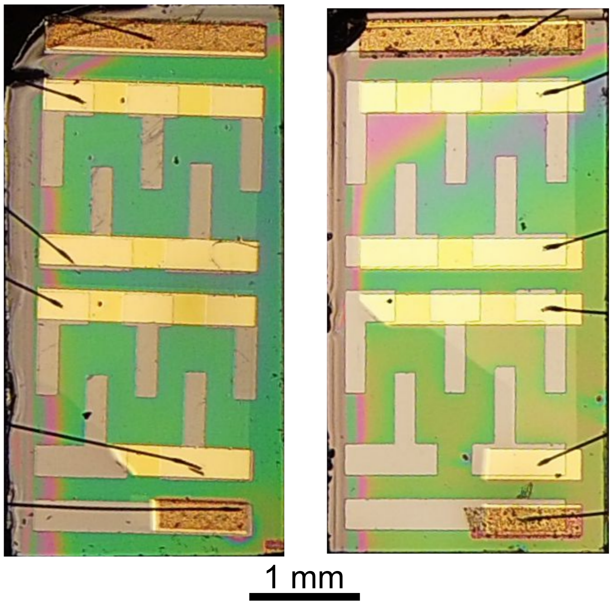

Figure 6.18: **Tunable *n-i* Schottky diode chip with quantum dots.** The Ohmic contacts are at the top and bottom; the gate bond pads are the light-yellow bars. In-between the two top and bottom pairs of light-yellow bars, lighter areas of the GaAs surface can be seen: this is the semi-transparent titanium layer. The sample is covered in a thin layer of Shipley S1805 photoresist which is removed in the L- and T-shaped areas.

clamps to fit in the sample holders in the thermal evaporators, Fig 6.17 (a). Since this fabrication procedure does not require precise alignment accuracy ($\sim$ 0.1 mm accuracy is enough), an SMT stencil (solder paste stencil) as a cheaper alternative was ordered. SMT stencils are used to deposit solder paste on printed circuit boards for reflow soldering of surface-mounted devices (SMD), and are usually thin ($\sim$ 0.1 mm) laser-cut stainless steel sheets. The individual shadow masks were designed on the SMT stencil by arranging SMD bond pads of a certain shape to form the desired cut-outs, Fig. 6.17 (b). The last step, the photoresist cover, was also done with a shadow mask, and a 365 nm ultraviolet LED torch.

Thanks to this lithography-less procedure, the time to fabricate a sample starting from the as-grown wafer to the bonded chip could be reduced down to a day and a half in the cleanroom. The resulting chips are shown in Fig. 6.18.

6.3.4 Photoluminescence signatures of quantum dot molecules

Once the chips are successfully processed, they are mounted in the optical cryostat (using the holder shown in Fig. 2.11 (a)) and cooled to liquid helium temperatures. At a point of the sample where a photoluminescence signal is obtained, its dependence on the applied gate voltage is recorded and shown in Fig. 6.19.

The photoluminescence scan exhibits some striking differences compared to that of single-dot samples, Fig. 6.6. It shows a richer set of features, including closely spaced sets of photoluminescence lines that look as “feathers”. Instead of single transitions, multiple lines are seen, with different directions of the Stark shift. Another exemplary spectrum acquired at an about 10-times lower excitation power is shown in Fig. 6.20. A close look shows that a set of sharp lines is tuned through a weaker, broader line, so that several sharp transitions are only seen within a certain broader range.

The observed features are indicative of successful growth of quantum dot molecules; they are not expected when considering the energy levels of a single dot alone. The spectrum may be explained by strongly asymmetric quantum dot molecules, with energy levels as shown in Fig. 6.21. When the gate voltage is tuned, a set of closely spaced energy levels in one dot is shifted with respect to a few energy levels in the other dot, which modulates the oscillator strength of the transitions.

Characteristic anticrossing features typical for quantum dot molecules are not observed in this experiment. It should be noted, however, that the experiment is conducted with red HeNe light of 632.8 nm wavelength, but the barrier material $Al_{0.33}Ga_{0.67}As$ has a photoluminescence peak at around 620 nm [326]. That means that the laser light does not generate excitons within the barrier material. This way, indirect excitons are unlikely to be excited and may remain as dark states. In contrast, the experiments in Ref. [321] were conducted with 532 nm above-bandgap excitation. Further measurements with above-bandgap excitation are necessary to study indirect exciton transitions.

At positive gate voltages, the Schottky diode is forward-biased. For gate voltages above ca. 0.9 V, the photoluminescence signal grows significantly and is smeared out. This correlates with a significant increase in gate leakage current. At this voltage, the bandstructure

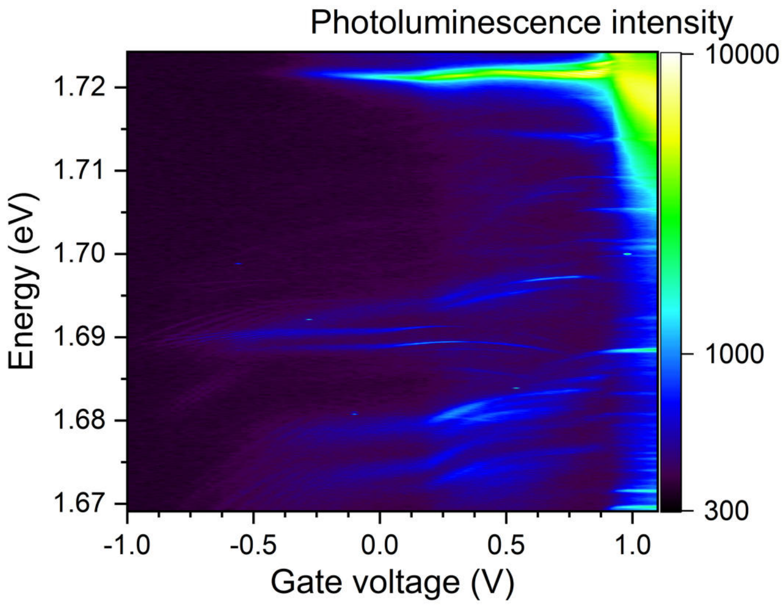

Figure 6.19: **Photoluminescence of quantum dot molecules,** with 47.8 µW HeNe power at the sample space. The spectrum is recorded as a function of the gate voltage on the Schottky diode, which tunes the transitions.

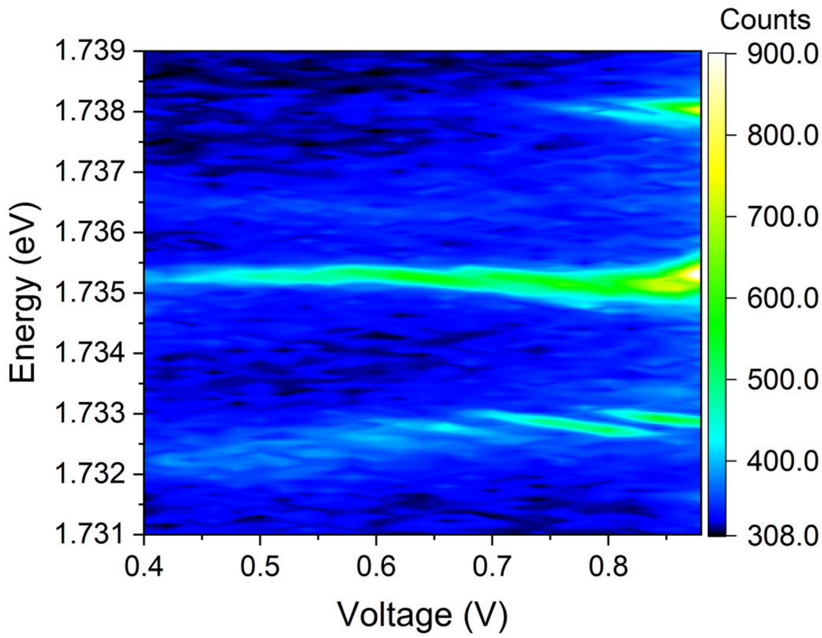

Figure 6.20: **Photoluminescence of quantum dot molecules.** The GaAs quantum dot molecules are excited with the HeNe laser at a power of 4.4 µW at the sample. (This spectrum was acquired at a different position than Fig. 6.19.)

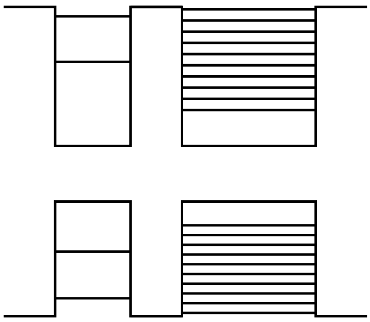

Figure 6.21: **Potential explanation for the observed spectral features.** If one quantum dot is substantially larger than the other, a DC electric field will result in a dense set of states in one dot shifting across a few single energy levels in the other dot, giving rise to stripes in the spectrum.

is biased close to flat-band conditions (the low-temperature bandgap of $Al_{0.33}Ga_{0.67}As$ is 1.954 eV [326]). This leads to electrons from the n-doped bottom contact "flooding" the quantum dot conduction band states with electrons. As a result, a range of negatively charged excitons can be seen, and the transitions become smeared out above this point.

6.4 Tunable heterostructures for simultaneous THz and optical excitation

In order to study the interaction of quantum dots and molecules with THz radiation, devices need to be fabricated where the THz field is coupled to the quantum dot, and simultaneously, optical microphotoluminescence with excitation and detection can be performed on thes same quantum dot. This results in a number of design criteria. In this section, I propose a wafer heterostructure suitable for this task.

The THz coupling requires an antenna structure, e. g. as used in chapter 4. Quantum dots in the gap between the antenna wings can then be studied.

In order to optically access the dots, the gap between the antenna wings should not be smaller than the wavelength of the optical/near-infrared transitions. Otherwise the antenna gap would constitute a sub-wavelength aperture that will reduce the amount of light emitted into the microscope objective. At the same time, the larger the gap is, the smaller the THz amplification will be. Therefore, a gap size on the order of 1 µm is reasonable. The antenna does not have to be a bow-tie, it may be e. g. a split-ring resonator or another antenna geometry depending on the required amplification and frequency response.

Another point is the direction of the THz electric field. To induce transitions between indirect and direct excitons, e. g. by causing an electron to tunnel from the top to the bottom quantum dot, the electric field polarisation should ideally be parallel to the growth (z-)direction, i. e. out-of-plane. But in the center of the gap between the antenna wings, the electric field will be in-plane. One way to mitigate this is to study quantum dots that are not placed centrally between the antenna wings, but shifted to the edge of one antenna wing, where the z-component of the electric field is larger. In more sophisticated device geometries, mesa etching can be considered as an option to enhance the out-of-plane electric field by placing one antenna wing lower, at the bottom of a mesa containing the quantum dot molecules with the other antenna wing on top of the mesa.

For best coupling of the E_z-electric field, the vertical position of the quantum dots in the heterostructure is important as well. If the antenna gap is ~1 µm, the electric field lines will widen up on a commensurate distance. Therefore, the quantum dots should be placed ca. 0.5 µm below the surface.

Furthermore, it is desirable to tune transitions over as wide a range of gate voltages as possible. *n-i* or *n-i-p* structures have the issue that once the diode is forward biased towards flat-band condition, the quantum dot states are flooded with charge carriers from the current through the diode, making it impossible to study single exciton behaviour beyond flat-band conditions. On the other hand, once the field within the structure becomes too strong, tunneling rates of charge carriers through the barrier exceed the radiative recombination rates. Beyond a certain field, transitions can no longer be observed optically, but have to be traced using photocurrent absorption spectroscopy. [324, 327–329]

The proposed *nipipini* structure (*n-i-p-i-p-i-n-i*) aims to solve this issue and enable all-optical access to quantum dot transitions over a wide range of electric fields without leakage currents, both for positive and negative directions of the electric field within the heterostructure. It is shown in Fig. 6.22.

The structure has been simulated in one dimension (the growth direction) using the Poisson electrostatic solver in the "nextnano" modelling software. In the simulation, quantum dots are modelled as a thin quantum well. The idea is based on a *n-i-n-i* structure, which would enable tuning with a negligible equilibrium built-in electric field, but has the drawback that the chemical potential would be very close to the quantum dot states. The n-doped regions are shown in orange in Fig. 6.22, and constitute the top and bottom Ohmic contacts. p-doped "pull-up" layers are placed in-between the quantum dots and the n-doped contacts. Electrons from the n-doped contact are captured by the donors, and thus pull up the bandstructure by introducing a built-in electric field on either side of the quantum dots. This way, the Fermi level can be set to be in the middle of the bandgap at the position of the quantum dots, without exposing the dots (or dot molecules) to a built-in electric field. The ca. 0.3 – 0.4 µm thick barriers on either side of the quantum dots should effectively block tunneling currents. The bottom pull-up layer is placed before the AlGaAs barrier to reduce floating of dopants. The "etching tolerances" are there to aid with processing. The purpose of the top intrinsic layer is to avoid shorting the THz antennas (or damping their resonance) by placing it directly on a conducting n-doped layer, but instead have an insulating GaAs Schottky barrier for the gate antenna structure. In addition, it allows the application of lateral

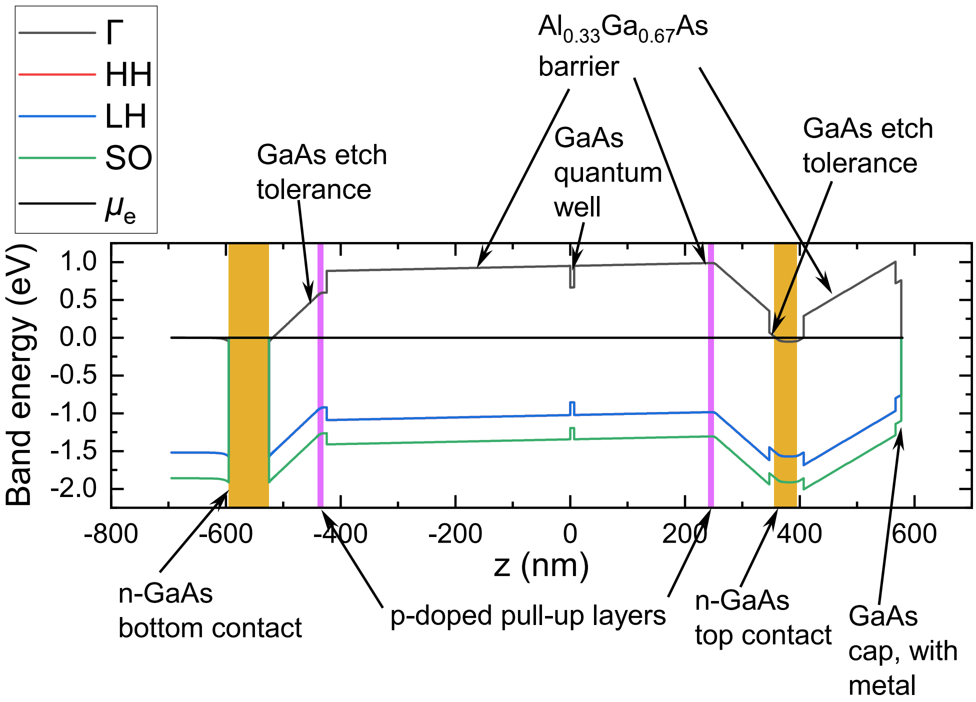

Figure 6.22: **The proposed nipipini device structure** at zero electric field. The plots show: the chemical potential μ_e, the Γ conduction band, the heavy-hole (HH), light-hole (LH), and split-off (SO) valence bands.

surface		
10nm	GaAs	cap
160nm	$Al_{0.33}Ga_{0.67}As$	gates isolation layer
5nm	GaAs	top etching tolerance (a) / spacer
40nm	n-GaAs, Si: 2e18 cm^{-3}	top contact
15nm	GaAs	top etching tolerance (b)
90nm	$Al_{0.33}Ga_{0.67}As$	top barrier (a)
10nm	p-$Al_{0.33}Ga_{0.67}As$, C: 5e17 cm^{-3}	top pull-up layer
240nm	$Al_{0.33}Ga_{0.67}As$	top barrier (b)
	quantum dots / molecules	
425nm	$Al_{0.33}Ga_{0.67}As$	bottom barrier
5nm	GaAs	small spacer before barrier
10nm	p-GaAs, C: 5e17 cm^{-3}	bottom pull-up layer
85nm	GaAs	bottom etching tolerance
70nm	n-GaAs, Si: 1e18 cm^{-3}	bottom contact
	GaAs buffer	

Table 6.1: **The layer sequence in the nipipini heterostructure.**

electric fields in the case of an antenna consisting of two parts, such as the bow-tie, and potentially inducing a lateral Stark shift.

The simulations in nextnano show that under zero bias, the quantum dots experience a weak electric field of around 2.7 kV/cm. A self-consistent simulation of the Poisson and current (continuity) equations in nextnano predicts that under an applied bias, the structure is field-tunable in both directions with negligible leakage current, from around –6.8 V (77 kV/cm) to 7 V (–75 kV/cm). Here, the voltages given are the electric potential values of the top n-doped contact if the bottom n-doped contact potential is defined at 0 V.

The pull-up effect is determined by the amount of charge introduced by the p-doped layers, i. e. by the sheet density $N_V d_{\text{p-doped}}$, where N_V is the acceptor concentration and $d_{\text{p-doped}}$ the thickness of the p-doped layer. N_V and $d_{\text{p-doped}}$ can be tuned as desired as long as their product remains the same. Within an error of 30%–40% of $N_V d_{\text{p-doped}}$, the Fermi level is still well within the bandgap at the position of the dots.

The n-doped regions are made thin enough in order to minimise transmission losses of THz radiation, which will be illuminating the sample from the bottom (from the side of the substrate), through a hole in the chip carrier. An estimation of the transmission losses using the Drude model shows that the expected loss in THz transmission due to the n-doped layers in Table 6.1 is expected to stay below 5% at 2 THz.

Full fabrication of a sample from a wafer of this sort would consist of the following steps:

1. local etching to the bottom etching tolerance;
2. depositing and annealing AuGeNi Ohmic contacts to the bottom n-doped layer in the etched area;
3. local etching to the top etching tolerance (a);
4. depositing and annealing shallow PdGe Ohmic contacts to the top n-doped layer in the etched area;
5. depositing TiAu gates including the THz antennas on the mesa.

Notably, the structure is designed to be backwards-compatible with simpler fabrication techniques, e. g. if the goal is to merely test quantum dot photoluminescence by optical means without the THz capability. There are two options to achieve this. The first is to reduce the structure back to a Schottky design as follows:

1. etch away the whole wafer surface down to the top etching tolerance (b), which will remove the top n-doped layer;
2. proceed with standard Schottky diode fabrication as in section 6.3.3.

The second option is to etch local areas to access the bottom n-doped contact, leaving the rest of the wafer surface unetched:

1. local etching to the bottom etching tolerance;
2. depositing and annealing AuGeNi Ohmic contacts to the bottom n-doped layer in the etched area;
3. depositing Schottky gates at the unetched wafer surface as top contacts.

With the latter option, the top n-doped layer remains uncontacted, but a change in potential on the Schottky top gate will “drag along” the n-doped top contact as well.

6.5 Summary

In this chapter, I discussed preparatory work carried out with the goal of realising a THz-to-optics switch based on quantum dots. In the beginning, InAs quantum dots grown by the conventional Stranski-Krastanow growth mode were studied in photoluminescence. Power-dependent spectroscopy revealed excitons and biexcitons, proved the presence of quantum dots in the grown wafer, and confirmed the microphotoluminescence capability of the optical setup. With the aim for superior growth control and improved tailorability of the quantum dots, the more recently described droplet-epitaxial growth of strain-free GaAs quantum dots was studied. The growth recipe described in literature was reproduced in the MBE machine at the Cavendish Laboratory and yielded both successful nanohole local droplet etching as well as optically active quantum dots, as was confirmed by microphotoluminescence measurements. To achieve more tunable structures, needed to tune the quantum objects in resonance with THz radiation, MBE-grown droplet-epitaxial GaAs quantum dot molecules were processed in a Schottky device with a semi-transparent gate using a highly efficient shadow mask cleanroom fabrication recipe. The resulting samples showed a set of features which confirmed the presence of quantum dot molecules in the wafer material and indicated a highly asymmetric energy level structure in the top vs. bottom dot.

Further experimental work on this research area has been suspended due to a shut-down of the laboratory in March 2020. To achieve optimal coupling of quantum objects to both THz and optical radiation, a tailored semiconductor heterostructure was simulated. The proposed tunable *nipipini* device structure is predicted to allow all-optical read-out of quantum states over a large range of electric fields. Its fabrication with embedded GaAs quantum dots and molecules would be the next logical step, and pave the way to quantum computing with THz-manipulated quantum states.

7 Conclusion and outlook

7.1 Summary

In conclusion, I designed and constructed an experimental setup that combines the areas of terahertz research, optical spectroscopy, and electrical transport at cryogenic temperatures. It enables measurements of electrically contacted samples at liquid helium temperature with simultaneous terahertz and optical access. The system combines the advantage of multimode waveguides of low propagation losses with the capability of tight focusing at the sample space. It provides accurate quantification of the THz power, as well as of the intensity and electric field distribution at the sample space. It can be optimally aligned without sample, allows determination of the source laser frequency, and can efficiently be purged with a gas. Integrated plug-and-play systems based on multimode waveguides, as the one presented here, will be a valuable toolkit in the rapidly developing area of terahertz research and technology.

To describe the propagation of waves within and after a multimode waveguide, I developed a fully analytical, ray-optical theory of multimode cylindrical waveguides. The theory shows how a waveguide can be used as a focusing element, without any external lenses or parabolic mirrors. It demonstrates that a multimode waveguide represents an interferometric device, and the output mode profile is a two-dimensional interferogram of the input beam. The theory also shows what influence parameters of the input beam have on the output mode profile. In particular, it makes it clear how the polarisation direction and the source misalignment angles are encoded in the output mode profile. The theoretical model will allow deterministic design of waveguided systems. To check the predicted focusing effect, I fabricated waveguides of the expected focal length. Measurements of the beam propagation at the waveguide end showed the expected pattern, confirming the theory and proving the focusing effect of multimode cylindrical waveguides. The focusing effect is based on multimode interference, and the waveguided terahertz delivery system represents the first practical realisation of the Talbot effect at terahertz frequencies in a cylindrical multimode waveguide.

I designed, simulated, fabricated, and measured a device for THz detection based on a 2D electron gas. The antenna-coupled, dual-gated detector demonstrates a giant photocurrent, which cannot be explained by known mechanisms of photoresponse generation in 2D electron gases. The presence of two gates allows independent tuning of output impedance and responsivity of the device, which facilitates integration into external circuits. The dual-gated, antenna-coupled device architecture will advance the development of fast and large-scale integrated THz detectors and focal plane arrays.

In the search for an interpretation of the observed effect, I discovered a new phenomenon of light-matter interaction in gated 2D electron systems: the in-plane photoelectric effect. Compared to the conventional photoelectric effect, it is a purely quantum-mechanical, scattering-free phenomenon which has no intrinsic response time limit. The effect is more than ten times stronger than those previously considered in 2D electron systems. In contrast to three-dimensional photoemissive detectors, no DC source-drain bias is required, and the analogue of the workfunction, the potential step height, is artificially created and tunable by gate voltages. Most strikingly, the maximum photocurrent is obtained when the 2DEG is degenerate and well conducting. The utilisation of the in-plane photoelectric effect paves the way to a new class of highly efficient THz detectors operating across the entire THz range.

Preparation work with the goal of realising a THz-to-optics interface based on quantum dot molecules was carried out. Different material systems were measured: conventional InAs self-assembled quantum dots, as well as GaAs droplet-epitaxial quantum dots and quantum dot molecules, with the latter being found to be the most promising candidates for the realisation of this task. Finally, I proposed a semiconductor heterostructure for all-optical tuning of quantum states over a wide range of electric fields with minimal leakage currents, and suggested the required fabrication procedure. This brings quantum computing in the THz range a step closer.

7.2 Outlook and future research directions

The work done so far opens a myriad of opportunities for further research in various directions. These will be overviewed in the following.

7.2.1 Waveguide theory and technological applications

The mode profile analysis conducted in chapters 2 and 3 was carried out using a 1 mm diameter iris. The aperture diameter sets a lower limit to the resolvable features in the waveguide mode profile. Very recent measurements of waveguide mode profiles using a smaller, 0.5 mm diameter iris indicate that the focusing effect can be even stronger than shown in these chapters. As an example, Fig. 7.1 shows the focusing after the 238 mm long waveguide.

The intensity amplification ratio is 0.52/0.20 = 2.6. From the inverse of the peak value of 0.52/mm^2, the effective area containing the whole power can be estimated to be 1.9 mm^2.

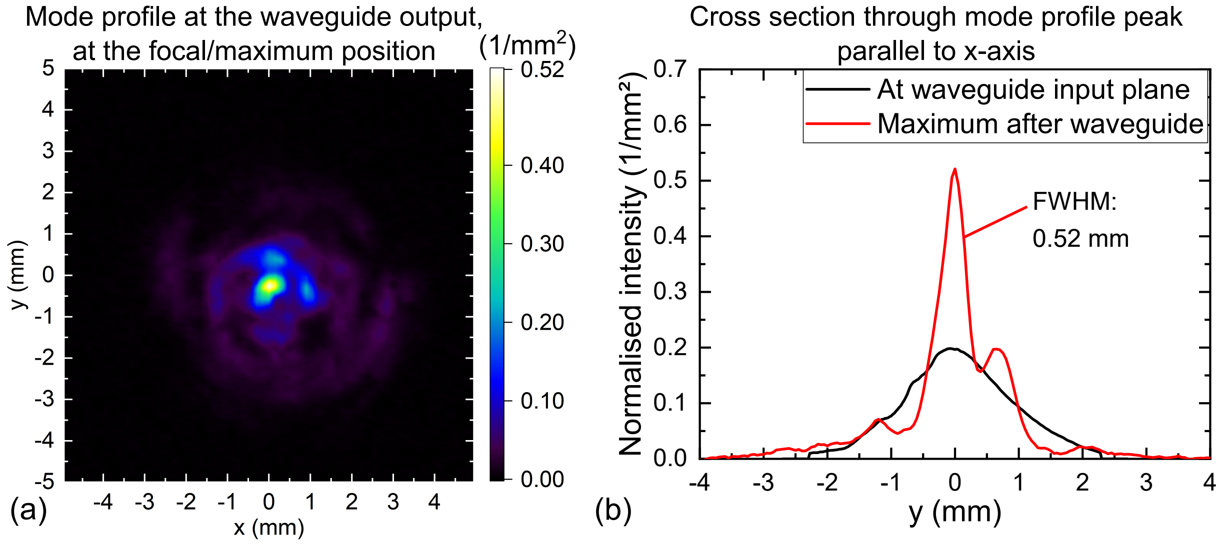

Figure 7.1: **Mode profile after 238 mm long waveguide, measured with a 0.5 mm-diameter aperture,** at $d_2 = 5.6$ mm after the end of the waveguide. (a) 2D map, (b) one-dimensional slice through the peak, in red. For comparison, the black curve in (b) shows the cross-section of the QCL mode at the plane of the waveguide input, from Fig. 3.21 (c).

This corresponds to the area that would contain the whole power from the waveguide if a top-hat intensity distribution with the peak intensity value is assumed. Relating this to the waveguide cross-sectional area of $\pi(4.6\,\text{mm})^2/4$ shows that the whole THz power is concentrated in only ca. 12 % of the waveguide circular area. If the waveguide transmission of 81.3 % is taken into account, the intensity amplification ratio of the waveguide is still 2.1.

On the other hand, apart from focusing maxima, the waveguide theory in chapter 3 predicts also distinctive minima along the waveguide axis (Fig. 3.6). To study them, a waveguide of 215 mm length was cut and the mode profile analysis was carried out in the same way as described previously, but with a 0.5 mm aperture.

The corresponding x-y-scans at various distances d_2 from the waveguide are shown in Fig. 7.2 (a). They reveal an exciting feature, which has not been observed so far in other waveguides. Normally, the waveguide focuses the radiation onto its center, resulting in a beam pattern after the end of the waveguide that has always a maximum along the waveguide axis. But in this case, at some distance after the waveguide around $d_2 = 14.1$ mm, the central peak vanishes, and results in a clear node at the waveguide axis. All the THz power is contained in side modes, and the maximum overall intensity strongly drops off. Interestingly, further away from the waveguide end, the central peak recovers again, and its intensity grows again.

The phenomenon, which can equally well be seen in the cross-sectional measurement Fig. 7.2 (b), indicates that at this particular geometry of d_1, L, d_2, R and λ, the rays travelling through the waveguide happen to interfere destructively and cancel each other out. This

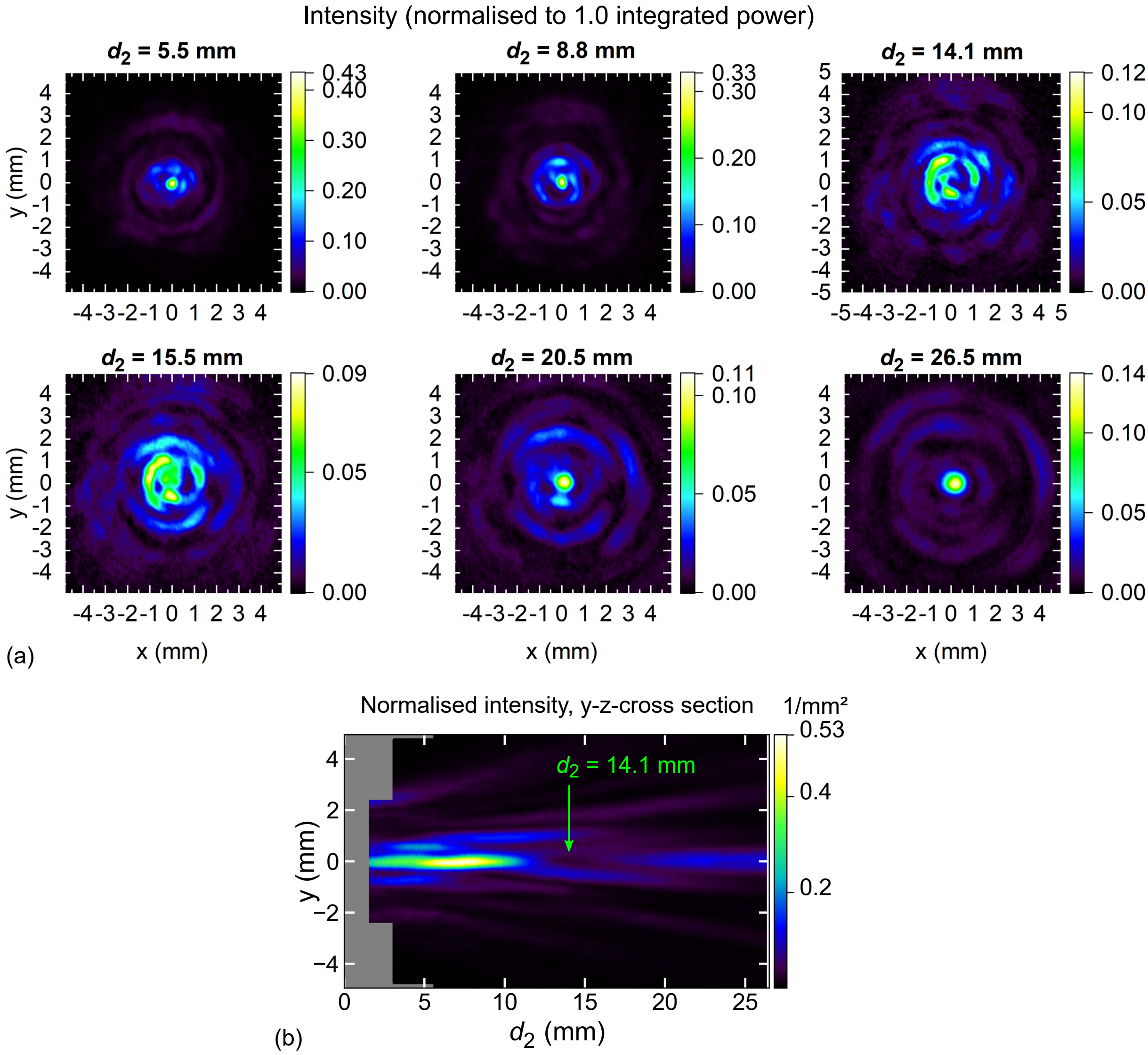

Figure 7.2: **Mode profiles after 215 mm long waveguide, measured with a 0.5 mm-diameter aperture.** (a) x-y-scans at a set of distances d_2 after the end of the waveguide. (b) y-z-scans showing the mode pattern in cross section. The output pattern of this waveguide reveals a node at an interval $d_2 \approx 14.1$ mm after the waveguide.

gives rise to a node right at the waveguide axis, where usually the maximum intensity would have been expected.

Awareness of such effects is crucial for the design of waveguide-coupled THz systems. The simple assumption of a maximum occuring along the waveguide axis can break down under specific geometries. If this is ignored, a sample placed centrally on the waveguide axis can happen to receive a minuscule amount of THz power.

At the same time, it is possible to take advantage of this phenomenon. The THz mode pattern with the node at the center corresponds essentially to a “doughnut” shape. Such fields are used e. g. as a means of breaking the diffraction limit in the stimulated emission depletion microscopy [330] in the visible range, where an optical vortex is used to achive the desired doughnut shape. Cylindrical waveguides can be a means of generating doughnut-shaped THz fields, which is their *intrinsic* capability. Notably, using free-space optics with mirrors, this would require additional complex components such as spatial light modulators.

Fig. 7.2 (b) also shows that the width of the central peak increases with distance from the waveguide end. Qualitatively, this can be understood by drawing an analogue with Fourier series: to represent a sharp feature, many harmonics have to be summed up. In the ray-optical picture, as the distance from the waveguide end increases, there are fewer rays that end up on the waveguide axis, as higher-order rays with larger angles ϑ (side lobes) diverge away. As a result, while a large number of interfering rays leads to a sharp peak close the waveguide end, the few remaining rays at larger distances can only produce a broad central peak.

These observations highlight the range of phenomena that future research on waveguides can be dedicated to. The theoretical model of the waveguide propagation can be further extended. One aspect would be the consideration of finite spatial extensions of the radiation source. The current approach assumes a point source, which results in a divergence along the waveguide axis. A more realistic, finite-sized model of the source is desirable to accurately describe the wave field along the waveguide axis, including the observed interference nodes. Another aspect to consider are wave-optical phenomena that arise when a finite wavelength is considered. If the diameter of the aperture used to scan the THz field is further reduced, approaching values on the order of the wavelength, the resolution of the wave field will be limited by physical effects rather than by the detector aperture, as was the case with the experiments in the waveguide chapters 2 and 3 carried out using a macroscopically large, classical aperture. As a result, a more sophisticated treatment is necessary to explain wavefields captured using detectors with smaller apertures. From the experimental side, comparison of the predicted mode profiles with the measurement is currently hindered by the deviation of the real annealed copper hollow metal waveguide from a perfect cylinder form. The theoretical treatment has shown how sub-wavelength changes of the radius can lead to significant changes of the output mode pattern. Any deviations from the cylinder form lead to decoherence of the rays, distort the output beam pattern, lead to side lobes in cases when perfect focusing is expected, and thus reduce the focusing strength. Therefore, waveguides with tighter manufacturing tolerances are needed, that would keep the same radius and a straight axis along their entire length. Potentially, silver-coated dielectric waveguides could be a viable alternative.

7.2.2 In-plane photoelectric effect and detector physics

The fundamental physics of the in-plane photoelectric effect needs to be further studied. This includes measurements at different frequencies and at different temperatures. In addition, further physics could be revealed by studying the dependence of the THz response on the equilibrium charge carrier concentration and illumination dose. As was mentioned in chapter 4, the observed photoresponse and its strength has a dependence on the illumination dose. The effect of above-bandgap illumination is complicated, but can be qualitatively explained as follows: upon illumination, the first DX centers to be ionised are those in the 2DEG areas not covered by gates, in particular, between the antenna gate halves. As the illumination dose is increased, the donors under the narrow gate are ionised, and the narrow gate threshold voltage shifts to more negative values. Further illumination leads also to full donor ionisation under the wide gate, which correspondingly shifts the wide gate threshold to more negative values. The main analysis in section 4.5 focused on this fully ionised, saturated case, where the ionisation state of donors is expected to be spatially independent thus leading to a stable sample state. Systematic measurements of the photoresponse in dependence on the illumination dose, leading to a spatially non-uniform built-in potential, could provide further insights into the device operation. To this end, new THz detector samples are now mounted together with small LEDs in a surface mounted device package. The fixed placement of the LEDs will lead to a reproducible illumination dose across multiple measurements and in different setups and will enable the THz detector to be used even in setups that do not provide a native way of sample illumination.

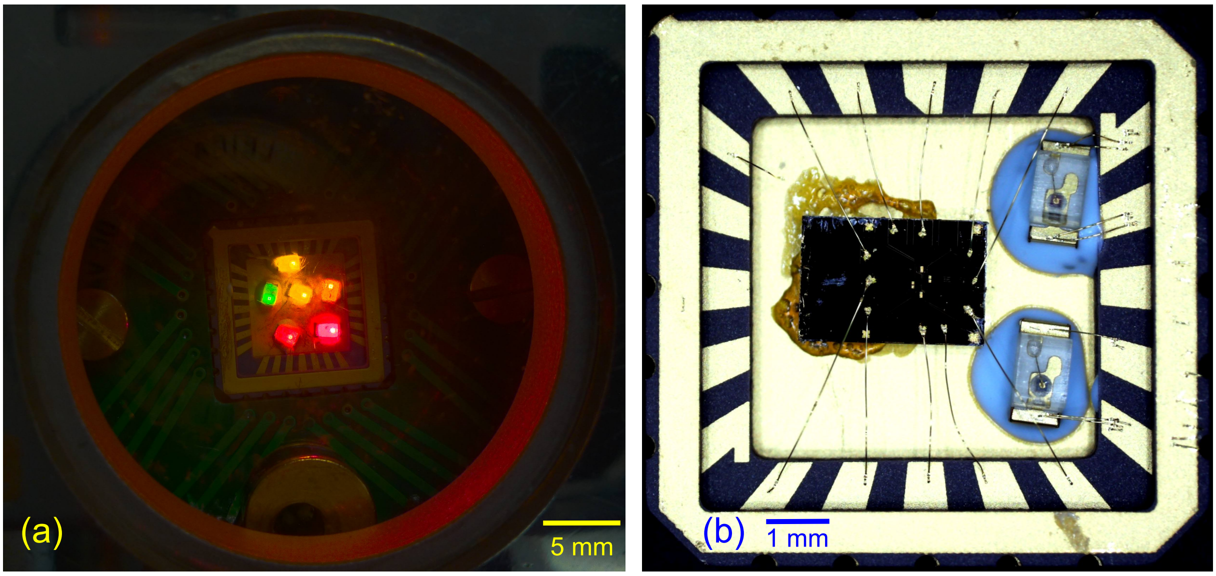

Figure 7.3: **Chip carriers with integrated LED illumination.** (a) Test sample for evaluation of the low-temperature performance of commercial surface mounted LEDs in 0603 form factor. (b) Mounted THz detector device with integrated red and green LEDs for on-chip above-band gap sample illumination.

The behaviour of the in-plane photoelectric effect in a magnetic field is another open question to be answered. Another research direction is the study of the in-plane photoelectric effect in a one-dimensional channel: by introducing additional gate electrodes, the channel width can be further reduced, which will allow measurements on a channel exhibiting quantised conductance.

Special antenna designs, as well as geometries exploiting plasmonic resonances amplifying the in-plane photo-electric effect, have the prospect of making the detectors frequency- and polarisation-sensitive. For example, a more detailed study of the photovoltage of the THz detector demonstrated in chapter 4 shows that under a strong positive gate voltage on the narrow gate and pinch-off of the wide gate, oscillations as a function of the gate voltage can be observed, see Fig. 7.4. Further investigations are required to understand the physics of these oscillations, which may be due to electronic or plasmonic resonances.

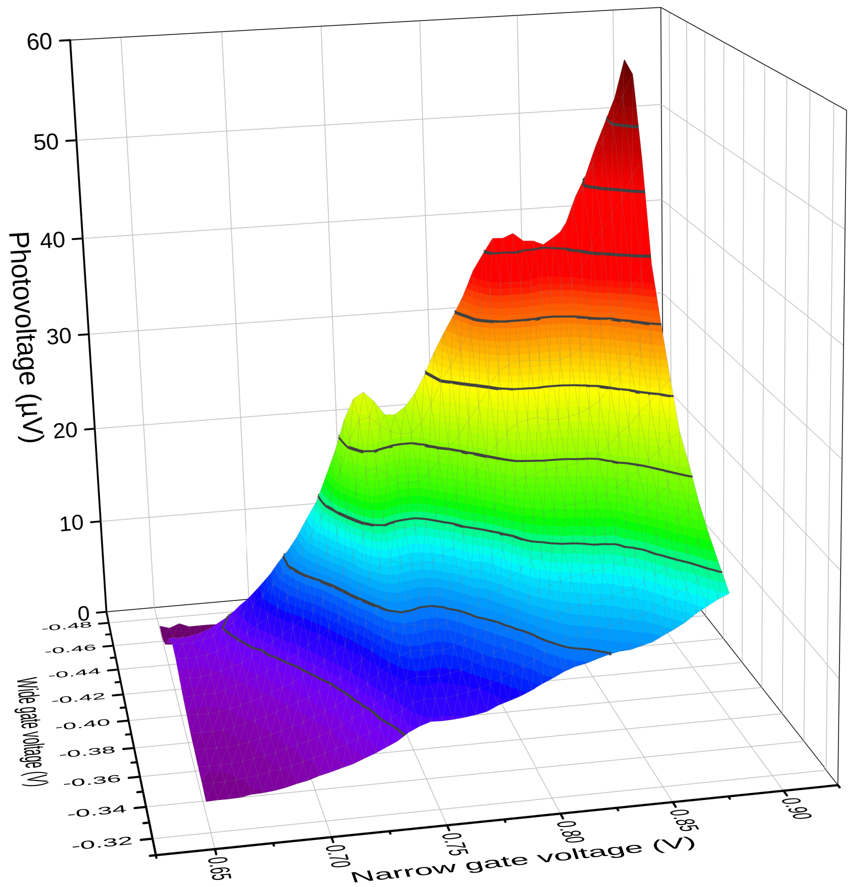

Figure 7.4: **Photovoltage oscillations under strong gate asymmetry.** Zoom-in to the 2D map of the THz photovoltage measured on sample V837-2-3.1 under strong asymmetry of the wide and narrow gates.

The in-plane photoelectric effect makes it possible to create a new class of highly sensitive THz detectors. Integrating such detectors with quantum cascade lasers, as is routinely done with state-of-the-art laser diodes in the visible and near-infrared ranges, will be a valuable advancement towards market-ready QCL-based THz sources. They can be used not only as power monitors, but also as a feedback element for stabilisation of the QCL. Embedding detectors into multiplexing circuits will give rise to fast focal plane arrays and low-noise THz cameras. For practical useability, it is desirable to further increase responsivity and operating temperature. To achieve this goal, the wafer structure should be optimised, e. g. attempting to realise smaller gate-surface distances d and corresponding smaller antenna gap sizes with larger channel widths. By placing a dielectric material such as Al_2O_3 between the gate and the semiconductor, gate leakage could potentially be further reduced.

The demonstration of room-temperature operation would make the detector a useful tool in biophysical applications. For example, organic materials or biomolecules could be placed on the active area of the detector, which will make it possible to study their THz interaction using very small quantities of materials. The particles could be delivered to the active area using microfluidic channels, a technique becoming increasingly widely used with the idea of a biochemical "lab on a chip".

An emerging research direction is low temperature THz scanning near-field optical microscopy (SNOM). Based on the in-plane photoelectric effect, detectors with sub-wavelength apertures can be designed and fabricated. On one hand, SNOM can be used to study the discovered effect in the near field, by scanning the THz focusing tip across the edges of gates. On the other hand, such THz detectors can be used to align and to calibrate a SNOM itself, and thus be a crucial tool for in-situ calibration and for measurements of the THz power at the sample and the amplification of the tip.

7.2.3 Terahertz quantum computing using quantum dots

So far, the THz and optics measurement capabilities of the constructed experimental setup have only been used separately, and this has already given a plethora of scientific findings. The system can be used to study self-assembled, optically active quantum dots using protocols involving both optical control and THz manipulation. To date, quantum dots have been studied by means of optical spectroscopy in the visible and near-infrared, while the few experiments on their interaction with THz radiation were dedicated to their electrical response, rather than a change in the optical properties. A device where optically controlled qubits in a quantum dot are switched using THz photons will represent an interface between THz and Optics, and be a breakthrough in the area of quantum computing and THz technology.

Acknowledgements

I would like to thank my supervisor Prof David Ritchie for the opportunity to do my PhD project in his group, for his invaluable support, helpful advice, and motivating discussions.

I would like to thank Dr Harvey Beere, for moral support, useful feedback, fruitful advice, sharing his great experience, and proofreading this thesis.

I am grateful to Dr Robert Wallis, for introducing me to the THz lab and the cleanroom, and our long conversations about terahertz science. I am grateful to Dr Peter Spencer for all the time and effort invested in me, showing me the optical setup and molecular beam epitaxy machine, sharing experience on working with scientific equipment, for our extensive scientific discussions and our joint work on the quantum dot project. Many thanks are due to Dr Joanna Waldie for sharing her great experience with me and her helpful advice on fabrication recipes and mask design rules. I would like to thank Dr Sergey Mikhailov for discussions about the theory of two-dimensional electron systems and calculations of the Schrödinger equation in the first-order perturbation theory, which are presented in section 5.2.3 of this thesis. I am grateful to Dr Chong Chen, Dr Benjamin Ramsay and Yuqing Wu for teaching me on using the cryostat in the assessment lab with the superconducting magnet. I thank Dr Ateeq Nasir and Dr Riccardo Degl'Innocenti for many helpful scientific conversations.

Many thanks are due to the members of our terahertz group, namely Nikita Almond, Stephen Kindness, Binbin Wei, Yuqing Wu, Dr Huifang Zhang and Dr Varun Kamboj. I am grateful to Nikita for being always supportive and happy to help, and Stephen for introducing me to the Comsol simulation process. I thank Binbin and Yuqing for advice on QCLs and waveguides, and the great time together in Cambridge. I would also like to thank Antonio Rubino for helpful advice and Shak Fernandes for friendly chats.

I thank Dr Harvey Beere for the growth of the wafer with the two-dimensional electron gas by molecular beam epitaxy and Dr Peter Spencer for the growth of all quantum dot wafers studied within this thesis. I am grateful to the team of the Cavendish Electron Beam Lithography Suite, namely Thomas Mitchell, Jonathan Griffiths, and Abbie Lowe, for help with the electron beam exposure of samples. I would also like to thank Gavin Ross, Oliver Norris, Gary Large, Scott Dell, and Nigel Palfrey from the Mechanical Workshop for fabrication of mechanical parts required for the experiments, and Huw Prytherch, Barry Shores, and David Gladding from the Cavendish Electronics Workshop for advice on and fabrication of some electronic components. I thank Kevin Mott for training me how to use the equipment in the Students' Mechanical Workshop and Matthew Pluck for advice on mechanical questions and help with technical issues. Thanks are also due to Melanie Tribble, for always ensuring that the cleanroom is a great place to work.

I am grateful to the members of Trinity College, especially my Tutors Dr John Rudge and Dr Richard Serjeantson, for their helpful support.

I want to thank my family, especially my parents, for their love and continuous support throughout my whole life.

I would like to thank the George and Lilian Schiff Studentship of the University of Cambridge and the Semiconductor Physics Group for financial support. I am grateful to the Cambridge Trust for being an Honorary Scholar of the Vice-Chancellor's Award. I would like to acknowledge funding for equipment from EPSRC via the grant Hyperterahertz, number EP/P021859/1.

Publications during the PhD work

Papers and preprints

- S. A. Mikhailov, **W. Michailow**, H. E. Beere, and D. A. Ritchie, "Theory of the in-plane photoelectric effect in a two-dimensional electron system". *arXiv preprint arXiv:2110.15932* (2021).
- **W. Michailow**, P. Spencer, N. W. Almond, S. J. Kindness, R. Wallis, T. A. Mitchell, R. Degl'Innocenti, S. A. Mikhailov, H. E. Beere, and D. A. Ritchie, "An in-plane photoelectric effect in two-dimensional electron systems for terahertz detection". *arXiv preprint arXiv:2011.04177* (2020, submitted).
- S. J. Kindness, N. W. Almond, **W. Michailow**, B. Wei, K. Delfanazari, P. Braeuninger-Weimer, S. Hofmann, H. E. Beere, D. A. Ritchie, and R. Degl'Innocenti, "A Terahertz Chiral Metamaterial Modulator". *Advanced Optical Materials* **8**, 2000581 (2020).
- N. W. Almond, X. Qi, R. Degl'Innocenti, S. J. Kindness, **W. Michailow**, B. Wei, P. Braeuninger-Weimer, S. Hofmann, P. Dean, D. Indjin, E. H. Linfield, A. G. Davies, A. D. Rakić, H. E. Beere, and D. A. Ritchie, "External cavity terahertz quantum cascade laser with a metamaterial/graphene optoelectronic mirror". *Applied Physics Letters* **117**, 041105 (2020).
- S. J. Kindness, N. W. Almond, **W. Michailow**, B. Wei, L. A. Jakob, K. Delfanazari, P. Braeuninger-Weimer, S. Hofmann, H. E. Beere, D. A. Ritchie, and R. Degl'Innocenti, "Graphene-Integrated Metamaterial Device for All-Electrical Polarization Control of Terahertz Quantum Cascade Lasers". *ACS Photonics* **6**, 1547–1555 (2019).
- P. Spencer, C. Chen, **W. Michailow**, H. Beere, and D. Ritchie, "Triggering InAs/GaAs Quantum Dot nucleation and growth rate determination by in-situ modulation of surface energy". *arXiv preprint arXiv:1906.05842* (2019).
- S. J. Kindness, N. W. Almond, B. Wei, R. Wallis, **W. Michailow**, V. S. Kamboj, P. Braeuninger-Weimer, S. Hofmann, H. E. Beere, D. A. Ritchie, and R. Degl'Innocenti, "Active control of electromagnetically induced transparency in a terahertz metamaterial array with graphene for continuous resonance frequency tuning". *Advanced Optical Materials* **6**, 1800570 (2018).

Conference proceedings and presentations

- **W. Michailow**, P. Spencer, N. W. Almond, S. J. Kindness, R. Wallis, T. A. Mitchell, R. Degl'Innocenti, S. A. Mikhailov, H. E. Beere, and D. A. Ritchie, "The in-plane photoelectric effect – Experiment". *9th Russia-Japan-USA-Europe Symposium on Fundamental & Applied Problems of Terahertz Devices & Technologies, RJUSE-TeraTech 2021, Tohoku University, Sendai, Japan*. 2021.
- S. A. Mikhailov, **W. Michailow**, H. E. Beere, and D. A. Ritchie, "The in-plane photoelectric effect – Theory". *9th Russia-Japan-USA-Europe Symposium on Fundamental & Applied Problems of Terahertz Devices & Technologies, RJUSE-TeraTech 2021, Tohoku University, Sendai, Japan*. 2021.
- **W. Michailow**, P. Spencer, N. Almond, S. Kindness, R. Wallis, T. Mitchell, R. Degl'Innocenti, S. Mikhailov, H. Beere, and D. Ritchie, "A new quantum mechanism of detecting terahertz radiation in 2D electron systems". *24th International Conference on Electronic Properties of Two-Dimensional Systems, EP2DS-24/MSS-20 Joint Conference, Toyama, Japan*. 2021.
- **W. Michailow**, J. Waldie, P. Spencer, N. Almond, S. Kindness, Y. Wu, B. Wei, R. Wallis, T. Mitchell, R. Degl'Innocenti, H. Beere, and D. Ritchie, "Direct terahertz detection in a dual-gated GaAs-AlGaAs two-dimensional electron gas". *SPb Photonic, Optoelectronic & Electronic Materials Conference*. 2021.
- **W. Michailow**, J. Waldie, P. Spencer, N. Almond, S. Kindness, Y. Wu, B. Wei, R. Wallis, T. Mitchell, R. Degl'Innocenti, H. Beere, and D. Ritchie, "An Antenna-Coupled Dual-Gated Electron Channel as Direct Detector of 2 THz Radiation". *2020 45th International Conference on Infrared, Millimeter, and Terahertz Waves (IRMMW-THz)*. 2020, 1–2.
- **W. Michailow**, J. Waldie, P. Spencer, N. Almond, S. Kindness, Y. Wu, B. Wei, R. Wallis, T. Mitchell, R. Degl'Innocenti, H. Beere, and D. Ritchie, "Direct Detection of Terahertz Radiation in a Dual-Gated GaAs-AlGaAs Two-Dimensional Electron Gas". *2nd European Conference on SPb Photonic, Optoelectronic & Electronic Materials*. 2020, Invited talk.
- S. J. Kindness, N. W. Almond, **W. Michailow**, B. Wei, P. Braeuninger-Weimer, S. Hofmann, H. E. Beere, D. A. Ritchie, and R. Degl'Innocenti, "Active metamaterial polarization modulators for the Terahertz frequency range". *Journal of Physics: Conference Series*. Vol. 1571. 2020, 012003.
- N. W. Almond, S. J. Kindness, **W. Michailow**, B. Wei, P. Braeuninger-Weimer, S. Hofmann, H. E. Beere, D. A. Ritchie, and R. Degl'Innocenti, "Double Layer Active Terahertz Chiral Metamaterial/graphene Modulators". *CLEO: Science and Innovations*. 2020, SM3F–4.
- N. W. Almond, R. Hermans, L. L. Hale, S. J. Kindness, **W. Michailow**, B. Wei, X. Romain, S. Ye, R. Young, R. Degl'Innocenti, H. E. Beere, D. A. Ritchie, and O. Mitrofanov, "Terahertz aperture SNOM mapping of metamaterial coupled resonators". *Metamaterials, Metadevices, and Metasystems 2020: SPIE Optics + Photonics 2020*. Vol. 11460. 2020, 114601R.

- N. W. Almond, S. J. Kindness, **W. Michailow**, B. Wei, L. Jakob, P. Braeuninger-Weimer, S. Hofmann, H. E. Beere, D. A. Ritchie, and R. Degl'Innocenti, "Terahertz polarisation modulator by electronic control of graphene loaded chiral metamaterial device". *2019 Conference on Lasers and Electro-Optics Europe & European Quantum Electronics Conference (CLEO/Europe-EQEC)*. 2019, 1–1.
- R. Degl'Innocenti, S. J. Kindness, N. W. Almond, **W. Michailow**, P. Braeuninger-Weimer, S. Hofmann, H. E. Beere, and D. A. Ritchie, "Metamaterial/graphene active terahertz modulators". *2019 IEEE MTT-S International Wireless Symposium (IWS)*. 2019, 1–3.

Bibliography

[1] A. Rogalski and F. Sizov, "Terahertz detectors and focal plane arrays". *Opto-electronics Review* **19**, 346–404 (2011).

[2] B. Ferguson and X.-C. Zhang, "Materials for terahertz science and technology". *Nature Materials* **1**, 26 (2002).

[3] S. S. Dhillon, M. S. Vitiello, E. H. Linfield, A. G. Davies, M. C. Hoffmann, J. Booske, C. Paoloni, M. Gensch, P. Weightman, G. P. Williams, E. Castro-Camus, D. R. S. Cumming, F. Simoens, I. Escorcia-Carranza, J. Grant, S. Lucyszyn, M. Kuwata-Gonokami, K. Konishi, M. Koch, C. A. Schmuttenmaer, T. L. Cocker, R. Huber, A. G. Markelz, Z. D. Taylor, V. P. Wallace, J. A. Zeitler, J. Sibik, T. M. Korter, B. Ellison, S. Rea, P. Goldsmith, K. B. Cooper, R. Appleby, D. Pardo, P. G. Huggard, V. Krozer, H. Shams, M. Fice, C. Renaud, A. Seeds, A. Stöhr, M. Naftaly, N. Ridler, R. Clarke, J. E. Cunningham, and M. B. Johnston, "The 2017 terahertz science and technology roadmap". *Journal of Physics D: Applied Physics* **50**, 043001 (2017).

[4] Y.-S. Lee, *Principles of terahertz science and technology*. Vol. 170. Springer Science & Business Media, 2009. ISBN: 0387095403.

[5] R. M. Woodward, V. P. Wallace, R. J. Pye, B. E. Cole, D. D. Arnone, E. H. Linfield, and M. Pepper, "Terahertz pulse imaging of ex vivo basal cell carcinoma". *Journal of Investigative Dermatology* **120**, 72–78 (2003).

[6] D. M. Mittleman, "Twenty years of terahertz imaging". *Optics Express* **26**, 9417–9431 (2018).

[7] A. Dobroiu, C. Otani, and K. Kawase, "Terahertz-wave sources and imaging applications". *Measurement Science and Technology* **17**, R161 (2006).

[8] Y. Watanabe, K. Kawase, T. Ikari, H. Ito, Y. Ishikawa, and H. Minamide, "Component spatial pattern analysis of chemicals using terahertz spectroscopic imaging". *Applied Physics Letters* **83**, 800–802 (2003).

[9] Y. C. Shen, T. Lo, P. F. Taday, B. E. Cole, W. R. Tribe, and M. C. Kemp, "Detection and identification of explosives using terahertz pulsed spectroscopic imaging". *Applied Physics Letters* **86**, 241116 (2005).

[10] H.-J. Song and T. Nagatsuma, "Present and future of terahertz communications". *IEEE Transactions on Terahertz Science and Technology* **1**, 256–263 (2011).

[11] M. Planck, "Über das Gesetz der Energieverteilung im Normalspectrum". *Annalen der Physik* **309**, 553–563 (1901).

[12] H. K. Onnes, "Further experiments with Liquid Helium G. On the electrical resistance of Pure Metals etc. VI. On the Sudden Change in the Rate at which the Resistance of Mercury Disappears". *KNAW, Proceedings*. Vol. 14. 1911, 1911–1912.

[13] G. Schmidt and W. H. Keesom, "New measurements of liquid helium temperatures: I. The boiling point of helium". *Physica* **4**, 963–970 (1937).

[14] D. P. Blair and P. H. Sydenham, "Phase sensitive detection as a means to recover signals buried in noise". *Journal of Physics E: Scientific Instruments* **8**, 621 (1975).

[15] M. L. Meade, "Advances in lock-in amplifiers". *Journal of Physics E: Scientific Instruments* **15**, 395 (1982).

[16] M. Asada and S. Suzuki, "Terahertz emitter using resonant-tunneling diode and applications". *Sensors* **21**, 1384 (2021).

[17] J. B. Gunn, "Microwave oscillations of current in III–V semiconductors". *Solid State Communications* **1**, 88–91 (1963).

[18] A. Khalid, N. J. Pilgrim, G. M. Dunn, M. C. Holland, C. R. Stanley, I. G. Thayne, and D. R. S. Cumming, "A planar Gunn diode operating above 100 GHz". *IEEE Electron Device Letters* **28**, 849–851 (2007).

[19] A. Khalid, G. M. Dunn, R. F. Macpherson, S. Thoms, D. Macintyre, C. Li, M. J. Steer, V. Papageorgiou, I. G. Thayne, M. Kuball, C. H. Oxley, M. Montes Bajo, A. Stephen, J. Glover, and D. R. S. Cumming, "Terahertz oscillations in an In0.53Ga0.47As submicron planar Gunn diode". *Journal of Applied Physics* **115**, 114502 (2014).

[20] K. K. Ng, *Complete guide to semiconductor devices*. John Wiley & Sons, Inc., New York, 2002.

[21] A. Acharyya and J. P. Banerjee, "Potentiality of IMPATT devices as terahertz source: an Avalanche response time-based approach to determine the upper cut-off frequency limits". *IETE Journal of Research* **59**, 118–127 (2013).

[22] J. Strong, "Investigations in the far infrared". *Physical Review* **38**, 1818 (1931).

[23] S. Silverman, "The emissivity of globar". *JOSA (Journal of the Optical Society of America)* **38**, 989–989 (1948).

[24] Commercial reference, Silicon carbide globar source from Thorlabs Inc., `https://www.thorlabs.com/newgrouppage9.cfm?objectgroup_id=7269&pn=SLS203L/M`, visited on 10/06/2018.

[25] Historical information about the "Globar" trademark, `http://www.chemie.de/lexikon/Globar.html`, visited on 25/06/2018.

[26] L. G. Bonner, "A new type globar support for infrared spectrometry". *Review of Scientific Instruments* **8**, 264–265 (1937).

[27] J. H. Booske, R. J. Dobbs, C. D. Joye, C. L. Kory, G. R. Neil, G.-S. Park, J. Park, and R. J. Temkin, "Vacuum electronic high power terahertz sources". *IEEE Transactions on Terahertz Science and Technology* **1**, 54–75 (2011).

[28] Commercial reference, NPP Istok, 2A, Vokzalnaya Str., Fryazino, Moscow Region 141190, Russia; `http://www.istokmw.ru/vakuumnie-generatori-maloy-moshnosti/`; visited on 14/06/2018.

[29] Commercial reference, Terahertz Components and Imaging Systems, 858 West Park Street, Eugene, OR 97401, USA; `http://mtinstruments.com/2017/08/01/thz-generators/`; visited on 14/06/2018.

[30] A. A. Andronov, I. V. Zverev, V. A. Kozlov, Y. N. Nozdrin, S. A. Pavlov, and V. N. Shastin, "Stimulated emission in the long-wavelength IR region from hot holes in Ge in crossed electric and magnetic fields". *JETP Letters* **40**, 804–807 (1984).

[31] A. A. Andronov, V. A. Kozlov, L. S. Mazov, and V. N. Shastin, "Amplifications of far infrared radiation in germanium during the population inversion of 'hot' holes". *JETP Letters* **30**, 551–555 (1979).

[32] S. Komiyama, N. Iizuka, and Y. Akasaka, "Evidence for induced far-infrared emission from p-Ge in crossed electric and magnetic fields". *Applied Physics Letters* **47**, 958–960 (1985).

[33] K. Unterrainer, M. Helm, E. Gornik, E. E. Haller, and J. Leotin, "Mode structure of the p-germanium far-infrared laser with and without external mirrors: Single line operation". *Applied Physics Letters* **52**, 564–566 (1988).

[34] J. Faist, *Quantum Cascade Lasers*. Series on Semiconductor Science and Technology. Oxford University Press, 2013. ISBN: 9780191663833.

[35] R. F. Kazarinov and R. A. Suris, "Possibility of amplification of electromagnetic waves in a semiconductor with superlattice". *Soviet Physics – Semiconductors* **5**, 707–709 (1971).

[36] F. Capasso, K. Mohammed, and A. Y. Cho, "Resonant tunneling through double barriers, perpendicular quantum transport phenomena in superlattices, and their device applications". *IEEE Journal of Quantum Electronics* **22**, 1853–1869 (1986).

[37] H. C. Liu, "A novel superlattice infrared source". *Journal of Applied Physics* **63**, 2856–2858 (1988).

[38] J. Faist, F. Capasso, D. L. Sivco, C. Sirtori, A. L. Hutchinson, and A. Y. Cho, "Quantum cascade laser". *Science* **264**, 553–556 (1994).

[39] C. Sirtori, P. Kruck, S. Barbieri, P. Collot, J. Nagle, M. Beck, J. Faist, and U. Oesterle, "GaAs/Al$_x$Ga$_{1-x}$As quantum cascade lasers". *Applied Physics Letters* **73**, 3486–3488 (1998).

[40] R. Köhler, A. Tredicucci, F. Beltram, H. E. Beere, E. H. Linfield, A. G. Davies, D. A. Ritchie, R. C. Iotti, and F. Rossi, "Terahertz semiconductor-heterostructure laser." *Nature* **417**, 156–159 (May 2002). ISSN: 0028-0836.

[41] B. S. Williams, "Terahertz quantum-cascade lasers". *Nature Photonics* **1**, 517 (2007).

[42] W. T. Silfvast, *Laser Fundamentals*, 2nd ed. Cambridge University Press, 2004.

[43] L. Esaki and R. Tsu, "Superlattice and negative differential conductivity in semiconductors". *IBM Journal of Research and Development* **14**, 61–65 (1970).

[44] R. Köhler, R. C. Iotti, A. Tredicucci, and F. Rossi, "Design and simulation of terahertz quantum cascade lasers". *Applied Physics Letters* **79**, 3920–3922 (2001).

[45] B. S. Williams, "Terahertz quantum cascade lasers". PhD thesis. Massachusetts Institute of Technology, 2003.

[46] R. Wallis, "Novel THz technologies: waveguiding, imaging and near-field microscopy". PhD thesis. Cavendish Laboratory, University of Cambridge, 2017.

[47] L. Li, L. Chen, J. Zhu, J. Freeman, P. Dean, A. Valavanis, A. G. Davies, and E. H. Linfield, "Terahertz quantum cascade lasers with> 1 W output powers". *Electronics Letters* **50**, 309–311 (2014).

[48] A. Khalatpour, A. K. Paulsen, C. Deimert, Z. R. Wasilewski, and Q. Hu, "High-power portable terahertz laser systems". *Nature Photonics* **15**, 16–20 (2021).

[49] N. Kim, J. Shin, E. Sim, C. W. Lee, D.-S. Yee, M. Y. Jeon, Y. Jang, and K. H. Park, "Monolithic dual-mode distributed feedback semiconductor laser for tunable continuous-wave terahertz generation". *Optics Express* **17**, 13851–13859 (Aug. 2009).

[50] K. Vijayraghavan, Y. Jiang, M. Jang, A. Jiang, K. Choutagunta, A. Vizbaras, F. Demmerle, G. Boehm, M. C. Amann, and M. A. Belkin, "Broadly tunable terahertz generation in mid-infrared quantum cascade lasers". *Nature Communications* **4**, 2021 (2013).

[51] D. H. Auston, "Picosecond optoelectronic switching and gating in silicon". *Applied Physics Letters* **26**, 101–103 (1975).

[52] G. Mourou, C. V. Stancampiano, A. Antonetti, and A. Orszag, "Picosecond microwave pulses generated with a subpicosecond laser-driven semiconductor switch". *Applied Physics Letters* **39**, 295–296 (1981).

[53] N. M. Burford and M. O. El-Shenawee, "Review of terahertz photoconductive antenna technology". *Optical Engineering* **56**, 010901 (2017).

[54] Y. C. Shen, P. C. Upadhya, E. H. Linfield, H. E. Beere, and A. G. Davies, "Ultrabroadband terahertz radiation from low-temperature-grown GaAs photoconductive emitters". *Applied Physics Letters* **83**, 3117–3119 (2003).

[55] M. Mittendorff, M. Xu, R. J. Dietz, H. Künzel, B. Sartorius, H. Schneider, M. Helm, and S. Winnerl, "Large area photoconductive terahertz emitter for 1.55 µm excitation based on an InGaAs heterostructure". *Nanotechnology* **24**, 214007 (2013).

[56] G. J. Nissiyah and M. G. Madhan, "A narrow spectrum terahertz emitter based on graphene photoconductive antenna". *Plasmonics* **14**, 2003–2011 (2019).

[57] D. R. Bacon, A. D. Burnett, M. Swithenbank, C. Russell, L. Li, C. D. Wood, J. Cunningham, E. H. Linfield, A. G. Davies, P. Dean, et al., "Free-space terahertz radiation from a LT-GaAs-on-quartz large-area photoconductive emitter". *Optics express* **24**, 26986–26997 (2016).

[58] S. Winnerl, F. Peter, S. Nitsche, A. Dreyhaupt, B. Zimmermann, M. Wagner, H. Schneider, M. Helm, and K. Kohler, "Generation and detection of THz radiation with scalable antennas based on GaAs substrates with different carrier lifetimes". *IEEE Journal of Selected Topics in Quantum Electronics* **14**, 449–457 (2008).

[59] N. T. Yardimci, S.-H. Yang, C. W. Berry, and M. Jarrahi, "High-power terahertz generation using large-area plasmonic photoconductive emitters". *IEEE Transactions on Terahertz Science and Technology* **5**, 223–229 (2015).

[60] J. Lloyd-Hughes, E. Castro-Camus, M. Fraser, C. Jagadish, and M. B. Johnston, "Carrier dynamics in ion-implanted GaAs studied by simulation and observation of terahertz emission". *Physical Review B* **70**, 235330 (2004).

[61] J. Lloyd-Hughes, E. Castro-Camus, and M. Johnston, "Simulation and optimisation of terahertz emission from InGaAs and InP photoconductive switches". *Solid state communications* **136**, 595–600 (2005).

[62] A. Rostami, H. Rasooli, and H. Baghban, *Terahertz Technology – Fundamentals and Applications*. Springer-Verlag Berlin Heidelberg, 2011. ISBN: 978-3-642-15793-6.

[63] A. Rogalski, *Infrared detectors*. CRC Press, 2000.

[64] F. Sizov and A. Rogalski, "THz detectors". *Progress in Quantum Electronics* **34**, 278–347 (2010).

[65] V. Mackowiak, J. Peupelmann, Y. Ma, and A. Gorges, *NEP - Noise Equivalent Power,* URL: https://www.thorlabs.com/images/TabImages/Noise_Equivalent_Power_White_Paper.pdf. Thorlabs Inc., visited on 10/06/2018.

[66] Cryogenic Composite Bolometer System Operating Manual, Model QSIB/2 (2005). QMC Instruments Ltd., School of Physics and Astronomy, Cardiff University, Queens Buildings, The Parade, Cardiff, CF24 3AA, United Kingdom.

[67] Commercial reference, http://www.tydexoptics.com/pdf/Golay_Detectors.pdf.

[68] Commercial reference, Gentec Electro-optics Inc., 445, rue St-Jean-Baptiste, bureau 160, Québec G2E 5N7. Pyroelectric detector datasheet THZ-I-BNC, https://www.gentec-eo.com/Content/downloads/specifications-sheet/THZ-I-BNC_2018_V1.0.pdf; visited on 29/06/2018.

[69] Commercial reference, TPS 334 Thermopile detector datasheet; PerkinElmer Optoelectronics, Wenzel-Jaksch-Str. 31 D-65199 Wiesbaden, Germany; http://www.farnell.com/datasheets/1332115.pdf, visited on 29/06/2018.

[70] F. Voltolina, A. Tredicucci, and P. H. Bolivar, "Low cost thermopile detectors for THz imaging and sensing". *33rd International Conference on Infrared, Millimeter and Terahertz Waves (IRMMW-THz).* 2008, 1–2.

[71] S. Nadar, H. Videlier, D. Coquillat, F. Teppe, M. Sakowicz, N. Dyakonova, W. Knap, D. Seliuta, I. Kašalynas, and G. Valušis, "Room temperature imaging at 1.63 and 2.54 THz with field effect transistor detectors". *Journal of Applied Physics* **108**, 054508 (2010).

[72] A. Lisauskas, W. Von Spiegel, S. Boubanga-Tombet, A. El Fatimy, D. Coquillat, F. Teppe, N. Dyakonova, W. Knap, and H. G. Roskos, "Terahertz imaging with GaAs field-effect transistors". *Electronics Letters* **44**, 408–409 (2008).

[73] I. Kašalynas, D. Seliuta, R. Simniškis, V. Tamošiūnas, K. Köhler, and G. Valušis, "Terahertz imaging with bow-tie InGaAs-based diode with broken symmetry". *Electronics Letters* **45**, 833–835 (2009).

[74] D. Seliuta, I. Kasalynas, V. Tamosiunas, S. Balakauskas, Z. Martunas, S. Asmontas, G. Valusis, A. Lisauskas, H. G. Roskos, and K. Kohler, "Silicon lens-coupled bow-tie InGaAs-based broadband terahertz sensor operating at room temperature". *Electronics Letters* **42**, 825–827 (2006).

[75] L. Minkevičius, V. Tamošiūnas, I. Kašalynas, D. Seliuta, G. Valušis, A. Lisauskas, S. Boppel, H. G. Roskos, and K. Köhler, "Terahertz heterodyne imaging with InGaAs-based bow-tie diodes". *Applied Physics Letters* **99**, 131101 (2011).

[76] H. Liu, J. Yu, P. Huggard, and B. Alderman, "A multichannel THz detector using integrated bow-tie antennas". *International Journal of Antennas and Propagation* **2013**, 417108 (2013).

[77] S. Boppel, A. Lisauskas, M. Mundt, D. Seliuta, L. Minkevicius, I. Kasalynas, G. Valusis, M. Mittendorff, S. Winnerl, V. Krozer, and H. G. Roskos, "CMOS integrated antenna-coupled field-effect transistors for the detection of radiation from 0.2 to 4.3 THz". *IEEE Transactions on Microwave Theory and Techniques* **60**, 3834–3843 (2012).

[78] R. Al Hadi, H. Sherry, J. Grzyb, Y. Zhao, W. Forster, H. M. Keller, A. Cathelin, A. Kaiser, and U. R. Pfeiffer, "A 1 k-pixel video camera for 0.7–1.1 terahertz imaging applications in 65-nm CMOS". *IEEE Journal of Solid-State Circuits* **47**, 2999–3012 (2012).

[79] R. Al Hadi, H. Sherry, J. Grzyb, N. Baktash, Y. Zhao, E. Öjefors, A. Kaiser, A. Cathelin, and U. Pfeiffer, "A broadband 0.6 to 1 THz CMOS imaging detector with an integrated lens". *Microwave Symposium Digest (MTT), 2011 IEEE MTT-S International*. 2011, 1–4.

[80] U. R. Pfeiffer, E. Ojefors, A. Lisauskas, D. Glaab, F. Voltolina, V. M. F. Nzogang, P. H. Bolivar, and H. G. Roskos, "A CMOS focal-plane array for terahertz imaging". *33rd International Conference on Infrared, Millimeter and Terahertz Waves (IRMMW-THz).* 2008, 1–3.

[81] A. D. Levin, G. M. Gusev, Z. D. Kvon, A. K. Bakarov, N. A. Savostianova, S. A. Mikhailov, E. E. Rodyakina, and A. V. Latyshev, "Giant microwave photo-conductance of a tunnel point contact with a bridged gate". *Applied Physics Letters* **107**, 072112 (2015).

[82] S. Komiyama, "Single-photon detectors in the terahertz range". *IEEE Journal of selected topics in quantum electronics* **17**, 54–66 (2011).

[83] T. Ueda and S. Komiyama, "Novel ultra-sensitive detectors in the 10–50 µm wavelength range". *Sensors* **10**, 8411–8423 (2010).

[84] L. Viti, J. Hu, D. Coquillat, A. Politano, C. Consejo, W. Knap, and M. S. Vitiello, "Heterostructured hBN-BP-hBN Nanodetectors at Terahertz Frequencies". *Advanced Materials* **28**, 7390–7396 (2016).

[85] R. Degl'Innocenti, L. Xiao, D. S. Jessop, S. J. Kindness, Y. Ren, H. Lin, J. A. Zeitler, J. A. Alexander-Webber, H. J. Joyce, P. Braeuninger-Weimer, S. Hofmann, H. E. Beere, and D. A. Ritchie, "Fast Room-Temperature Detection of Terahertz Quantum Cascade Lasers with Graphene-Loaded Bow-Tie Plasmonic Antenna Arrays". *ACS Photonics* **3**, 1747–1753 (2016).

[86] M. S. Vitiello, D. Coquillat, L. Viti, D. Ercolani, F. Teppe, A. Pitanti, F. Beltram, L. Sorba, W. Knap, and A. Tredicucci, "Room-temperature terahertz detectors based on semiconductor nanowire field-effect transistors". *Nano Letters* **12**, 96–101 (2011).

[87] A. Zak, M. A. Andersson, M. Bauer, J. Matukas, A. Lisauskas, H. G. Roskos, and J. Stake, "Antenna-integrated 0.6 THz FET direct detectors based on CVD graphene". *Nano Letters* **14**, 5834–5838 (2014).

[88] P. L. Richards, "Bolometers for infrared and millimeter waves". *Journal of Applied Physics* **76**, 1–24 (1994).

[89] M. M. Nobili and M. Melloni, "Recherches sur plusieurs Phénomènes calorifiques entreprises au moyen du thermo-multiplicateur". *Annales de chimie et de physique* **48**, 198 (1831).

[90] F. Watkins, "XXXVII. On thermo-electricity". *The London, Edinburgh, and Dublin Philosophical Magazine and Journal of Science* **11**, 304 (1837).

[91] J. Locke, "ART. XXI.–On a large and very sensible Thermoscopic Galvanometer". *American Journal of Science and Arts (1820-1879)* **33**, 365 (1838).

[92] E. S. Cornell, "The radiant heat spectrum from Herschel to Melloni.—II. The work of Melloni and his contemporaries". *Annals of Science* **3**, 402–416 (1938).

[93] J. Cooper, "Minimum detectable power of a pyroelectric thermal receiver". *Review of Scientific Instruments* **33**, 92–95 (1962).

[94] A. Hadni, "Possibilités actuelles de détection du rayonnement infrarouge". *Journal de Physique* **24**, 694–702 (1963).

[95] H. A. Zahl and M. J. E. Golay, "Pneumatic heat detector". *Review of Scientific Instruments* **17**, 511–515 (1946).

[96] M. J. E. Golay, "A Pneumatic Infra-Red Detector". *Review of Scientific Instruments* **18**, 357–362 (1947).

[97] M. J. E. Golay, "The Theoretical and Practical Sensitivity of the Pneumatic Infra-Red Detector". *Review of Scientific Instruments* **20**, 816–820 (1949).

[98] A. Rogalski, *Infrared and Terahertz Detectors*. CRC Press, 2019.

[99] W. Wang, Q. Li, N. An, X. Tong, and J. Zeng, "Fabrication and characterization of 8.87 THz schottky barrier mixer diodes for mixer". *AIP Conference Proceedings*. Vol. 1955. 2018, 040177.

[100] R. A. Barrett, "Broadband RF power detector using FET". *US Patent 4,647,848* (1987).

[101] F. Stern, "Polarizability of a two-dimensional electron gas". *Physical Review Letters* **18**, 546 (1967).

[102] A. L. Fetter, "Electrodynamics of a layered electron gas. I. Single layer". *Annals of Physics* **81**, 367–393 (1973).

[103] A. V. Chaplik, "Possible Crystallization of Charge Carriers in Low-Density Inversion Layers". *Soviet Physics JETP* **35**, 395 (1972).

[104] M. Bauer, R. Venckevičius, I. Kašalynas, S. Boppel, M. Mundt, L. Minkevičius, A. Lisauskas, G. Valušis, V. Krozer, and H. Roskos, "Antenna-coupled field-effect transistors for multi-spectral terahertz imaging up to 4.25 THz". *Optics express* **22**, 19235–19241 (2014).

[105] K. Ikamas, A. Lisauskas, S. Boppel, Q. Hu, and H. G. Roskos, "Efficient detection of 3 THz radiation from quantum cascade laser using silicon CMOS detectors". *Journal of Infrared, Millimeter, and Terahertz Waves* **38**, 1183–1188 (2017).

[106] J. Zdanevičius, K. Ikamas, J. Matukas, A. Lisauskas, H. Richter, H.-W. Hübers, M. Bauer, and H. G. Roskos, "TeraFET detector for measuring power fluctuations of 4.75-THz QCL-generated radiation". *2017 International Conference on Noise and Fluctuations (ICNF)*. 2017, 1–4.

[107] J. Zdanevičius, D. Čibiraitė, K. Ikamas, M. Bauer, J. Matukas, A. Lisauskas, H. Richter, T. Hagelschuer, V. Krozer, H.-W. Hübers, et al., "Field-effect transistor based detectors for power monitoring of THz quantum cascade lasers". *IEEE Transactions on Terahertz Science and Technology* **8**, 613–621 (2018).

[108] K. Ikamas, A. Lisauskas, S. Massabeau, M. Bauer, M. Burakevič, J. Vyšniauskas, D. Čibiraitė, V. Krozer, A. Rämer, S. Shevchenko, et al., "Sub-picosecond pulsed THz FET detector characterization in plasmonic detection regime based on autocorrelation technique". *Semiconductor Science and Technology* **33**, 124013 (2018).

[109] S. Preu, M. Mittendorff, S. Winnerl, H. Lu, A. Gossard, and H. B. Weber, "Ultra-fast transistor-based detectors for precise timing of near infrared and THz signals". *Optics express* **21**, 17941–17950 (2013).

[110] T. Watanabe, S. B. Tombet, Y. Tanimoto, Y. Wang, H. Minamide, H. Ito, D. Fateev, V. Popov, D. Coquillat, W. Knap, et al., "Ultrahigh sensitive plasmonic terahertz detector based on an asymmetric dual-grating gate HEMT structure". *Solid-State Electronics* **78**, 109–114 (2012).

[111] L. Viti, A. R. Cadore, X. Yang, A. Vorobiev, J. E. Muench, K. Watanabe, T. Taniguchi, J. Stake, A. C. Ferrari, and M. S. Vitiello, "Thermoelectric graphene photodetectors with sub-nanosecond response times at terahertz frequencies". *Nanophotonics* **10**, 89–98 (2021).

[112] Y. Miyajima, T. Nukariya, and S. Suzuki, "Terahertz detector using 70-nm T-gate InAlAs/InGaAs HEMT integrated with bow-tie antenna". *39th International Conference on Infrared, Millimeter, and Terahertz Waves (IRMMW-THz)*. 2014, 1–2.

[113] Y. Kurita, G. Ducournau, D. Coquillat, A. Satou, K. Kobayashi, S. Boubanga Tombet, Y. Meziani, V. Popov, W. Knap, T. Suemitsu, et al., "Ultrahigh sensitive sub-terahertz detection by InP-based asymmetric dual-grating-gate high-electron-mobility transistors and their broadband characteristics". *Applied Physics Letters* **104**, 251114 (2014).

[114] D. Coquillat, V. Nodjiadjim, S. Blin, A. Konczykowska, N. Dyakonova, C. Consejo, P. Nouvel, A. Pènarier, J. Torres, D. But, et al., "High-speed room temperature terahertz detectors based on InP double heterojunction bipolar transistors". *FUNDAMENTAL AND APPLIED PROBLEMS OF TERAHERTZ DEVICES AND TECHNOLOGIES: Selected papers from the Russia-Japan-USA-Europe Symposium (RJUSE-TeraTech 2016)*. 2017, 1–9.

[115] S. Blin, L. Tohme, D. Coquillat, S. Horiguchi, Y. Minamikata, S. Hisatake, P. Nouvel, T. Cohen, A. Pénarier, F. Cano, et al., "Wireless communication at 310 GHz using GaAs high-electron-mobility transistors for detection". *Journal of Communications and Networks* **15**, 559–568 (2013).

[116] L. Tohmé, S. Blin, G. Ducournau, P. Nouvel, D. Coquillat, S. Hisatake, T. Nagatsuma, A. Pénarier, L. Varani, W. Knap, et al., "Terahertz wireless communication using GaAs transistors as detectors". *Electronics letters* **50**, 323–325 (2014).

[117] H. Qin, X. Li, J. Sun, Z. Zhang, Y. Sun, Y. Yu, X. Li, and M. Luo, "Detection of incoherent terahertz light using antenna-coupled high-electron-mobility field-effect transistors". *Applied Physics Letters* **110**, 171109 (2017).

[118] J. Sun, W. Feng, Q. Ding, Y. Zhu, Z. Zhang, X. Li, H. Qin, J. Zhang, X. Li, Y. Shangguan, et al., "Smaller antenna-gate gap for higher sensitivity of GaN/AlGaN HEMT terahertz detectors". *Applied Physics Letters* **116**, 161109 (2020).

[119] M. Dyakonov and M. Shur, "Detection, mixing, and frequency multiplication of terahertz radiation by two-dimensional electronic fluid". *IEEE Transactions on Electron Devices* **43**, 380–387 (1996).

[120] A. Lisauskas, U. Pfeiffer, E. Öjefors, P. H. Bolìvar, D. Glaab, and H. G. Roskos, "Rational design of high-responsivity detectors of terahertz radiation based on distributed self-mixing in silicon field-effect transistors". *Journal of Applied Physics* **105**, 114511 (2009).

[121] W. Knap, V. Kachorovskii, Y. Deng, S. Rumyantsev, J.-Q. Lü, R. Gaska, M. S. Shur, G. Simin, X. Hu, M. A. Khan, C. A. Saylor, and L. C. Brunel, "Nonresonant detection of terahertz radiation in field effect transistors". *Journal of Applied Physics* **91**, 9346–9353 (2002).

[122] V. M. Muravev, I. V. Kukushkin, J. Smet, and K. Von Klitzing, "Millimeter/submillimeter mixing based on the nonlinear plasmon response of two-dimensional electron systems". *JETP Letters* **90**, 197–201 (2009).

[123] J.-Q. Lü, M. S. Shur, J. L. Hesler, L. Sun, and R. Weikle, "Terahertz detector utilizing two-dimensional electronic fluid". *IEEE Electron Device Letters* **19**, 373–375 (1998).

[124] U. R. Pfeiffer, E. Ojefors, A. Lisauskas, and H. G. Roskos, "Opportunities for silicon at mmwave and terahertz frequencies". *Bipolar/BiCMOS Circuits and Technology Meeting, 2008. BCTM 2008. IEEE*. 2008, 149–156.

[125] L. Viti, J. Hu, D. Coquillat, W. Knap, A. Tredicucci, A. Politano, and M. S. Vitiello, "Black phosphorus terahertz photodetectors". *Advanced Materials* **27**, 5567–5572 (2015).

[126] L. Viti, J. Hu, D. Coquillat, A. Politano, W. Knap, and M. S. Vitiello, "Efficient Terahertz detection in black-phosphorus nano-transistors with selective and controllable plasma-wave, bolometric and thermoelectric response". *Scientific Reports* **6**, 20474 (2016).

[127] X. G. Peralta, S. J. Allen, M. C. Wanke, N. E. Harff, J. A. Simmons, M. P. Lilly, J. L. Reno, P. J. Burke, and J. P. Eisenstein, "Terahertz photoconductivity and plasmon modes in double-quantum-well field-effect transistors". *Applied Physics Letters* **81**, 1627–1629 (2002).

[128] E. A. Shaner, M. Lee, M. C. Wanke, A. D. Grine, J. L. Reno, and S. J. Allen, "Single-quantum-well grating-gated terahertz plasmon detectors". *Applied Physics Letters* **87**, 193507 (2005).

[129] G. R. Aizin, V. V. Popov, and O. V. Polischuk, "Plasmon enhanced electron drag and terahertz photoconductance in a grating-gated field-effect transistor with two-dimensional electron channel". *Applied Physics Letters* **89**, 143512 (2006).

[130] A. Dayem and R. Martin, "Quantum interaction of microwave radiation with tunneling between superconductors". *Physical Review Letters* **8**, 246 (1962).

[131] B. Josephson, "Possible new effects in superconductive tunneling". *Physics Letters* **1**, 251 (1962).

[132] L. Kouwenhoven, S. Jauhar, K. McCormick, D. Dixon, P. McEuen, Y. V. Nazarov, N. Van Der Vaart, and C. Foxon, "Photon-assisted tunneling through a quantum dot". *Physical Review B* **50**, 2019 (1994).

[133] L. Kouwenhoven, S. Jauhar, J. Orenstein, P. McEuen, Y. Nagamune, J. Motohisa, and H. Sakaki, "Observation of photon-assisted tunneling through a quantum dot". *Physical Review Letters* **73**, 3443 (1994).

[134] R. Blick, R. Haug, K. Von Klitzing, and K. Eberl, "Photon-assisted tunneling through a double quantum dot". *Surface Science* **361**, 595–599 (1996).

[135] K. Shibata, A. Umeno, K. M. Cha, and K. Hirakawa, "Photon-Assisted Tunneling through Self-Assembled InAs Quantum Dots in the Terahertz Frequency Range". *Physical Review Letters* **109**, 077401 (Aug. 2012).

[136] Y. Zhang, K. Shibata, N. Nagai, C. Ndebeka-Bandou, G. Bastard, and K. Hirakawa, "Terahertz Intersublevel Transitions in Single Self-Assembled InAs Quantum Dots with Variable Electron Numbers". *Nano Letters* **15**, 1166–1170 (Jan. 2015).

[137] H. Drexler, J. Scott, S. Allen, K. Campman, and A. Gossard, "Photon-assisted tunneling in a resonant tunneling diode: Stimulated emission and absorption in the THz range". *Applied Physics Letters* **67**, 2816–2818 (1995).

[138] S. Verghese, R. Wyss, T. Schäpers, A. Förster, M. Rooks, and Q. Hu, "Photon-assisted transport through quantized energy states in a lateral dual-gate device". *Physical Review B* **52**, 14834 (1995).

[139] O. A. Tkachenko, V. A. Tkachenko, and Z. D. Kvon, "Photon-assisted electron transport through a quantum point contact in a microwave field". *JETP Letters* **102**, 378–382 (2015).

[140] M. Otteneder, Z. Kvon, O. Tkachenko, V. Tkachenko, A. Jaroshevich, E. Rodyakina, A. Latyshev, and S. Ganichev, "Giant Terahertz Photoconductance of Quantum Point Contacts in the Tunneling Regime". *Physical Review Applied* **10**, 014015 (2018).

[141] J. Song, G. Aizin, J. Mikalopas, Y. Kawano, K. Ishibashi, N. Aoki, J. Reno, Y. Ochiai, and J. Bird, "Bolometric terahertz detection in pinched-off quantum point contacts". *Applied Physics Letters* **97**, 083109 (2010).

[142] T. Janssen, J. Maan, J. Singleton, N. Patel, M. Pepper, J. Frost, D. Ritchie, and G. Jones, "A new mechanism for high-frequency rectification in a ballistic quantum point contact". *Journal of Physics: Condensed Matter* **6**, L163 (1994).

[143] L. Molenkamp, H. Van Houten, C. Beenakker, R. Eppenga, and C. Foxon, "Quantum oscillations in the transverse voltage of a channel in the nonlinear transport regime". *Physical Review Letters* **65**, 1052 (1990).

[144] N. M. Gabor, J. C. Song, Q. Ma, N. L. Nair, T. Taychatanapat, K. Watanabe, T. Taniguchi, L. S. Levitov, and P. Jarillo-Herrero, "Hot carrier–assisted intrinsic photoresponse in graphene". *Science* **334**, 648–652 (2011).

[145] M. Buscema, M. Barkelid, V. Zwiller, H. S. van der Zant, G. A. Steele, and A. Castellanos-Gomez, "Large and tunable photothermoelectric effect in single-layer MoS2". *Nano Letters* **13**, 358–363 (2013).

[146] D. J. Groenendijk, M. Buscema, G. A. Steele, S. Michaelis de Vasconcellos, R. Bratschitsch, H. S. van der Zant, and A. Castellanos-Gomez, "Photovoltaic and photothermoelectric effect in a double-gated WSe2 device". *Nano Letters* **14**, 5846–5852 (2014).

[147] A. Perera, H. Yuan, and M. Francombe, "Homojunction internal photoemission far-infrared detectors: photoresponse performance analysis". *Journal of Applied Physics* **77**, 915–924 (1995).

[148] W. Shen, "Recent Progress in Mid-and Far-Infrared Semiconductor Detectors". *International Journal of Infrared and Millimeter Waves* **21**, 1739–1746 (2000).

[149] A. Perera, G. Ariyawansa, P. Jayaweera, S. Matsik, M. Buchanan, and H. Liu, "Semiconductor terahertz detectors and absorption enhancement using plasmons". *Microelectronics Journal* **39**, 601–606 (2008).

[150] A. Juozapavičius, L. Ardaravičius, A. Sužiedelis, A. Kozič, J. Gradauskas, J. Kundrotas, D. Seliuta, E. Širmulis, S. Ašmontas, G. Valušis, H. G. Roskos, and K. Köhler, "Microwave sensor based on modulation-doped GaAs/AlGaAs structure". *Semiconductor Science and Technology* **19**, S436 (2004).

[151] D. Seliuta, E. Širmulis, V. Tamošiūnas, S. Balakauskas, S. Ašmontas, A. Sužiedėlis, J. Gradauskas, G. Valušis, A. Lisauskas, H. G. Roskos, and K. Köhler, "Detection of terahertz/sub-terahertz radiation by asymmetrically-shaped 2DEG layers". *Electronics Letters* **40**, 631–632 (2004).

[152] O. Astafiev, S. Komiyama, T. Kutsuwa, V. Antonov, Y. Kawaguchi, and K. Hirakawa, "Single-photon detector in the microwave range". *Applied Physics Letters* **80**, 4250–4252 (2002).

[153] G. Giuliani, M. Norgia, S. Donati, and T. Bosch, "Laser diode self-mixing technique for sensing applications". *Journal of Optics A: Pure and Applied Optics* **4**, S283 (2002).

[154] P. Dean, Y. L. Lim, A. Valavanis, R. Kliese, M. Nikolić, S. P. Khanna, M. Lachab, D. Indjin, Z. Ikonić, P. Harrison, A. D. Rakić, E. H. Linfield, and A. G. Davies, "Terahertz imaging through self-mixing in a quantum cascade laser". *Optics Letters* **36**, 2587–2589 (2011).

[155] M. J. Rudd, "A laser Doppler velocimeter employing the laser as a mixer-oscillator". *Journal of Physics E: Scientific Instruments* **1**, 723 (1968).

[156] A. Seko, Y. Mitsuhashi, T. Morikawa, J. Shimada, and K. Sakurai, "Self-quenching in semiconductor lasers and its applications in optical memory readout". *Applied Physics Letters* **27**, 140–141 (1975).

[157] Y. Mitsuhashi, T. Morikawa, K. Sakurai, A. Seko, and J. Shimada, "Self-coupled optical pickup". *Optics Communications* **17**, 95–97 (1976).

[158] R. Lang and K. Kobayashi, "External optical feedback effects on semiconductor injection laser properties". *IEEE Journal of Quantum Electronics* **16**, 347–355 (1980).

[159] J. Von Staden, T. Gensty, W. Elsäßer, G. Giuliani, and C. Mann, "Measurements of the α factor of a distributed-feedback quantum cascade laser by an optical feedback self-mixing technique". *Optics Letters* **31**, 2574–2576 (2006).

[160] Y. Ren, R. Wallis, D. S. Jessop, R. Degl'Innocenti, A. Klimont, H. E. Beere, and D. A. Ritchie, "Fast terahertz imaging using a quantum cascade amplifier". *Applied Physics Letters* **107**, 011107 (2015).

[161] M. Tani, Y. Hirota, C. T. Que, S. Tanaka, R. Hattori, M. Yamaguchi, S. Nishizawa, and M. Hangyo, "Novel terahertz photoconductive antennas". *International Journal of Infrared and Millimeter Waves* **27**, 531–546 (2006).

[162] Y. C. Shen, P. C. Upadhya, H. E. Beere, E. H. Linfield, A. G. Davies, I. S. Gregory, C. Baker, W. R. Tribe, and M. J. Evans, "Generation and detection of ultrabroadband terahertz radiation using photoconductive emitters and receivers". *Applied Physics Letters* **85**, 164–166 (2004).

[163] P. R. Griffiths and J. A. de Haseth, *Fourier transform infrared spectrometry*, 2nd edition. Hoboken, N.J.: Wiley-Interscience, 2007. ISBN: 9780470106297.

[164] Fourier transform infrared spectrometer manual, IFS 66v/S spectrometer from Bruker Optik GmbH, Rudolf-Plank-Str. 27, 76275 Ettlingen. (1998).

[165] M. Van Exter, C. Fattinger, and D. Grischkowsky, "High-brightness terahertz beams characterized with an ultrafast detector". *Applied Physics Letters* **55**, 337–339 (1989).

[166] M. Van Exter, C. Fattinger, and D. Grischkowsky, "Terahertz time-domain spectroscopy of water vapor". *Optics Letters* **14**, 1128–1130 (1989).

[167] M. Van Exter and D. Grischkowsky, "Optical and electronic properties of doped silicon from 0.1 to 2 THz". *Applied Physics Letters* **56**, 1694–1696 (1990).

[168] P. Y. Han and X. C. Zhang, "Free-space coherent broadband terahertz time-domain spectroscopy". *Measurement Science and Technology* **12**, 1747 (2001).

[169] L. Rayleigh, "XV. On the theory of optical images, with special reference to the microscope". *The London, Edinburgh, and Dublin Philosophical Magazine and Journal of Science* **42**, 167–195 (1896).

[170] R. Degl'Innocenti, R. Wallis, B. Wei, L. Xiao, S. J. Kindness, O. Mitrofanov, P. Braeuninger-Weimer, S. Hofmann, H. E. Beere, and D. A. Ritchie, "Terahertz Nanoscopy of Plasmonic Resonances with a Quantum Cascade Laser". *ACS Photonics* **4**, 2150–2157 (2017).

[171] H.-T. Chen, R. Kersting, and G. C. Cho, "Terahertz imaging with nanometer resolution". *Applied Physics Letters* **83**, 3009–3011 (2003).

[172] R. Kersting, H.-T. Chen, N. Karpowicz, and G. C. Cho, "Terahertz microscopy with submicrometre resolution". *Journal of Optics A: Pure and Applied Optics* **7**, S184 (2005).

[173] G. C. Cho, H.-T. Chen, S. Kraatz, N. Karpowicz, and R. Kersting, "Apertureless terahertz near-field microscopy". *Semiconductor Science and Technology* **20**, S286 (2005).

[174] H. Von Ribbeck, M. Brehm, D. W. Van der Weide, S. Winnerl, O. Drachenko, M. Helm, and F. Keilmann, "Spectroscopic THz near-field microscope". *Optics Express* **16**, 3430–3438 (2008).

[175] A. J. Huber, F. Keilmann, J. Wittborn, J. Aizpurua, and R. Hillenbrand, "Terahertz near-field nanoscopy of mobile carriers in single semiconductor nanodevices". *Nano Letters* **8**, 3766–3770 (2008).

[176] M. Wächter, M. Nagel, and H. Kurz, "Tapered photoconductive terahertz field probe tip with subwavelength spatial resolution". *Applied Physics Letters* **95**, 041112 (2009).

[177] A. J. L. Adam, "Review of near-field terahertz measurement methods and their applications". *Journal of Infrared, Millimeter, and Terahertz Waves* **32**, 976 (2011).

[178] V. P. Barsukov, A. G. Verhoglad, V. V. Gerasimov, I. S. Glebus, M. A. Zavyalova, B. A. Knyazev, S. N. Makarov, M. F. Stupak, V. K. Ovchar, D. G. Rodionov, Y. Y. Choporova, and V. Y. Shtatnov, "A terahertz scanning near-field optical microscope with an attenuated total internal reflection module". *Instruments and Experimental Techniques* **57**, 579–586 (2014).

[179] B. Wei, R. Wallis, S. Kindness, O. Mitrofanov, H. E. Beere, D. A. Ritchie, and R. Degl'Innocenti, "Terahertz s-SNOM with> λ/1000 resolution based on self-mixing in quantum cascade lasers". *The European Conference on Lasers and Electro-Optics*. 2017, CC_4_2.

[180] M. C. Giordano, L. Viti, O. Mitrofanov, G. Scamarcio, S. Mastel, R. Hillenbrand, D. Ercolani, L. Sorba, and M. S. Vitiello, "Sub-wavelength near field imaging techniques at terahertz frequencies". *Quantum Sensing and Nano Electronics and Photonics XV*. Vol. 10540. 2018, 105400N.

[181] V. Rogalin, I. Kaplunov, and G. Kropotov, "Optical materials for the THz range". *Optics and Spectroscopy* **125**, 1053–1064 (2018).

[182] E. Abbe, "Beiträge zur Theorie des Mikroskops und der mikroskopischen Wahrnehmung". *Archiv für mikroskopische Anatomie* **9**, 413–418 (1873).

[183] M. Born and E. Wolf, *Principles of Optics*, 6th Edition. Pergamon Press, 1980.

[184] M. Navarro-Cía, J. E. Melzer, J. A. Harrington, and O. Mitrofanov, "Silver-coated Teflon tubes for waveguiding at 1–2 THz". *Journal of Infrared, Millimeter, and Terahertz Waves* **36**, 542–555 (2015).

[185] O. Mitrofanov, R. James, F. A. Fernández, T. K. Mavrogordatos, and J. A. Harrington, "Reducing transmission losses in hollow THz waveguides". *IEEE Transactions on Terahertz Science and Technology* **1**, 124–132 (2011).

[186] "IEEE Standard for Rectangular Metallic Waveguides and Their Interfaces for Frequencies of 110 GHz and Above – Part 1: Frequency Bands and Waveguide Dimensions". *IEEE Std 1785.1-2012*, 1–22 (2013).

[187] S. Atakaramians, S. Afshar, T. M. Monro, and D. Abbott, "Terahertz dielectric waveguides". *Advances in Optics and Photonics* **5**, 169–215 (2013).

[188] J. A. Harrington, R. George, P. Pedersen, and E. Mueller, "Hollow polycarbonate waveguides with inner Cu coatings for delivery of terahertz radiation". *Optics Express* **12**, 5263–5268 (2004).

[189] Y.-S. Jin, G.-J. Kim, and S.-G. Jeon, "Terahertz dielectric properties of polymers". *Journal of the Korean Physical Society* **49**, 513–517 (2006).

[190] C. H. Worrall, "Long wavelength terahertz quantum cascade lasers". PhD thesis. Cavendish Laboratory, University of Cambridge, 2006.

[191] R. Wallis, R. Degl'Innocenti, D. S. Jessop, O. Mitrofanov, C. M. Bledt, J. E. Melzer, J. A. Harrington, H. E. Beere, and D. A. Ritchie, "Investigation of hollow cylindrical metal terahertz waveguides suitable for cryogenic environments". *Optics Express* **24**, 30002–30014 (2016).

[192] Online magnetic field calculator, `https://www.kjmagnetics.com/calculator.asp?calcType=ring`.

[193] K. von Klitzing, G. Dorda, and M. Pepper, "New method for high-accuracy determination of the fine-structure constant based on quantized Hall resistance". *Physical Review Letters* **45**, 494 (1980).

[194] T. Ando, A. B. Fowler, and F. Stern, "Electronic properties of two-dimensional systems". *Reviews of Modern Physics* **54**, 437 (1982).

[195] K. Von Klitzing, "The quantized Hall effect". *Reviews of Modern Physics* **58**, 519 (1986).

[196] R. J. Warburton, "Single spins in self-assembled quantum dots". *Nature Materials* **12**, 483 (2013).

[197] N. W. Almond, X. Qi, R. Degl'Innocenti, S. J. Kindness, W. Michailow, B. Wei, P. Braeuninger-Weimer, S. Hofmann, P. Dean, D. Indjin, E. H. Linfield, A. G. Davies, A. D. Rakić, H. E. Beere, and D. A. Ritchie, "External cavity terahertz quantum cascade laser with a metamaterial/graphene optoelectronic mirror". *Applied Physics Letters* **117**, 041105 (2020).

[198] E. Bründermann, H.-W. Hübers, and M. F. Kimmitt, *Terahertz techniques*. Vol. 151. Springer, 2012.

[199] O. Bryngdahl, "Image formation using self-imaging techniques". *Journal of the Optical Society of America* **63**, 416–419 (1973).

[200] W. H. F. Talbot Esq. FRS, "LXXVI. Facts relating to optical science. No. IV". *Philos. Mag. Series* **9**, 401–407 (1836).

[201] B. A. Knyazev, V. S. Cherkassky, Y. Y. Choporova, V. V. Gerasimov, and M. G. Vlasenko, "The Talbot effect in the terahertz spectral range". *35th International Conference on Infrared, Millimeter, and Terahertz Waves*. 2010, 1–2.

[202] J. Wen, Y. Zhang, and M. Xiao, "The Talbot effect: recent advances in classical optics, nonlinear optics, and quantum optics". *Advances in Optics and Photonics* **5**, 83–130 (2013).

[203] L. B. Soldano and E. C. Pennings, "Optical multi-mode interference devices based on self-imaging: principles and applications". *Journal of Lightwave Technology* **13**, 615–627 (1995).

[204] R. Ulrich and G. Ankele, "Self-imaging in homogeneous planar optical waveguides". *Applied Physics Letters* **27**, 337–339 (1975).

[205] R. Ulrich and T. Kamiya, "Resolution of self-images in planar optical waveguides". *Journal of the Optical Society of America* **68**, 583–592 (1978).

[206] H. Wang, F. Groen, S. Pereira, and J. Braat, "Integrated optical waveguide as a focussing system". *Proceedings Symposium IEEE/LEOS Benelux Chapter, 2003, Enschede* (2003).

[207] L. Praxmeyer and K. Wódkiewicz, "Talbot effect in cylindrical waveguides". *Optics Communications* **268**, 215–225 (2006).

[208] C. Markides, C. Themistos, H. Tanvir, B. Rahman, and K. Grattan, "Multimode interference 3 dB splitters in hollow core metallic waveguides for low-loss THz wave transmission". *IEEE Journal of Selected Topics in Quantum Electronics* **19**, 8500606 (2012).

[209] S. E. Christensen, I. T. McKinnie, and J. R. Unternahrer, "Method and apparatus to coherently combine high-power beams in self-imaging waveguides". *US Patent 7,239,777* (2007).

[210] Y. Zhang, Z. Li, and B. Li, "Multimode interference effect and self-imaging principle in two-dimensional silicon photonic crystal waveguides for terahertz waves". *Optics Express* **14**, 2679–2689 (2006).

[211] Z. Li, Y. Zhang, and B. Li, "Terahertz photonic crystal switch in silicon based on self-imaging principle". *Optics Express* **14**, 3887–3892 (2006).

[212] S. Silver, *Microwave antenna theory and design*, 1st edition. McGraw-Hill, 1949.

[213] V. Bozhkov, "Semiconductor detectors, mixers, and frequency multipliers for the terahertz band". *Radiophysics and Quantum Electronics* **46**, 631–656 (2003).

[214] S. Regensburger, A. k. Mukherjee, S. Schönhuber, M. A. Kainz, S. Winnerl, J. M. Klopf, H. Lu, A. C. Gossard, K. Unterrainer, and S. Preu, "Broadband Terahertz Detection With Zero-Bias Field-Effect Transistors Between 100 GHz and 11.8 THz With a Noise Equivalent Power of 250 pW/$\sqrt{\mathrm{Hz}}$ at 0.6 THz". *IEEE Transactions on Terahertz Science and Technology* **8**, 465–471 (2018).

[215] T. Otsuji, "Trends in the research of modern terahertz detectors: plasmon detectors". *IEEE Transactions on Terahertz Science and Technology* **5**, 1110–1120 (2015).

[216] Y. Sun, J. Sun, Y. Zhou, R. Tan, C. Zeng, W. Xue, H. Qin, B. Zhang, and D. Wu, "Room temperature GaN/AlGaN self-mixing terahertz detector enhanced by resonant antennas". *Applied Physics Letters* **98**, 252103 (2011).

[217] J. Sun, Y. Sun, D. Wu, Y. Cai, H. Qin, and B. Zhang, "High-responsivity, low-noise, room-temperature, self-mixing terahertz detector realized using floating antennas on a GaN-based field-effect transistor". *Applied Physics Letters* **100**, 013506 (2012).

[218] W. Knap, S. Nadar, H. Videlier, S. Boubanga-Tombet, D. Coquillat, N. Dyakonova, F. Teppe, K. Karpierz, J. Łusakowski, M. Sakowicz, I. Kasalynas, D. Seliuta, G. Valusis, T. Otsuji, Y. Meziani, A. El Fatimy, S. Vandenbrouk, K. Madjour, D. Théron, and C. Gaquière, "Field effect transistors for terahertz detection and emission". *Journal of Infrared, Millimeter, and Terahertz Waves* **32**, 618–628 (2011).

[219] R. Dingle, H. Störmer, A. Gossard, and W. Wiegmann, "Electron mobilities in modulation-doped semiconductor heterojunction superlattices". *Applied Physics Letters* **33**, 665–667 (1978).

[220] L. Pfeiffer, K. West, H. Stormer, and K. Baldwin, "Electron mobilities exceeding 10^7 cm^2/Vs in modulation-doped GaAs". *Applied Physics Letters* **55**, 1888–1890 (1989).

[221] W. Walukiewicz, H. Ruda, J. Lagowski, and H. Gatos, "Electron mobility in modulation-doped heterostructures". *Physical Review B* **30**, 4571 (1984).

[222] J. Blakemore, "Semiconducting and other major properties of gallium arsenide". *Journal of Applied Physics* **53**, R123–R181 (1982).

[223] R. L. Olmon, B. Slovick, T. W. Johnson, D. Shelton, S.-H. Oh, G. D. Boreman, and M. B. Raschke, "Optical dielectric function of gold". *Physical Review B* **86**, 235147 (2012).

[224] Comsol Multiphysics website, information about used equation; `https://www.comsol.com/blogs/computational-electromagnetics-modeling-which-module-to-use/`, visited on 15/06/2018.

[225] S. A. Mikhailov and N. A. Savostianova, "Microwave response of a two-dimensional electron stripe". *Physical Review B* **71**, 035320 (2005).

[226] V. Volkov and S. A. Mikhailov, "Edge magnetoplasmons: low frequency weakly damped excitations in inhomogeneous two-dimensional electron systems". *Sov. Phys. JETP* **67**, 1639–1653 (1988).

[227] P. Atkinson, "PhD Thesis". PhD thesis. Cavendish Laboratory, University of Cambridge, 2002.

[228] A. Ortiz-Conde, F. G. Sánchez, J. J. Liou, A. Cerdeira, M. Estrada, and Y. Yue, "A review of recent MOSFET threshold voltage extraction methods". *Microelectronics reliability* **42**, 583–596 (2002).

[229] L. Landau, "Diamagnetismus der Metalle". *Zeitschrift für Physik* **64**, 629–637 (1930).

[230] Л. Д. Ландау и Е. М. Лифшиц (L. D. Landau and E. M. Lifshitz), *Том 3: Квантовая механика, нерелятивистская теория (Volume 3: Quantum mechanics, non-relativistic theory)*, 1974, Publisher: *Наука (Nauka)*.

[231] W. Nolting, *Grundkurs Theoretische Physik 5/2: Quantenmechanik: Methoden und Anwendungen*, 7th ed. Springer, 2012.

[232] E. Teller, "Der Diamagnetismus von freien Elektronen". *Zeitschrift für Physik* **67**, 311–319 (1931).

[233] J. Furneaux and T. Reinecke, "Effects of interface charge on the quantum Hall effect". *Physical Review B* **33**, 6897 (1986).

[234] L. Shubnikov and W. de Haas, "Magnetische Widerstandsvergrösserung in Einkristallen von Wismut bei tiefen Temperaturen". *Proceedings of the Royal Netherlands Academy of Arts and Science* **33**, 130–133 (207a) (1930).

[235] R. Haug, K. v. Klitzing, and K. Ploog, "Analysis of the asymmetry in Shubnikov–de Haas oscillations of two-dimensional systems". *Physical Review B* **35**, 5933 (1987).

[236] P. Koenraad, F. Blom, P. Blom, C. Foxon, E. Frijns, J. Harris, G. Weimann, and J. Wolter, "Dependence of spin-asymmetry in the Shubnikov-de Haas resistance on back-gating, illumination and uniaxial stress". *Superlattices and microstructures* **5**, 519–522 (1989).

[237] W. Michailow, F. J. Schülein, B. Möller, E. Preciado, A. E. Nguyen, G. Von Son, J. Mann, A. L. Hörner, A. Wixforth, L. Bartels, and H. J. Krenner, "Combined electrical transport and capacitance spectroscopy of a MoS2-LiNbO3 field effect transistor". *Applied Physics Letters* **110**, 023505 (2017).

[238] D. Lang and R. Logan, "Large-lattice-relaxation model for persistent photoconductivity in compound semiconductors". *Physical Review Letters* **39**, 635 (1977).

[239] D. Lang, R. Logan, and M. Jaros, "Trapping characteristics and a donor-complex (DX) model for the persistent-photoconductivity trapping center in Te-doped $Al_xGa_{1-x}As$". *Physical Review B* **19**, 1015 (1979).

[240] A. Kastalsky and J. Hwang, "Study of persistent photoconductivity effect in n-type selectively doped AlGaAs/GaAs heterojunction". *Solid state communications* **51**, 317–322 (1984).

[241] P. Mooney, "Electrical properties of DX centers in GaAs and AlGaAs". *Radiation Effects and Defects in Solids* **111**, 281–298 (1989).

[242] P. Mooney, "Deep donor levels (DX centers) in III-V semiconductors". *Journal of Applied Physics* **67**, R1–R26 (1990).

[243] D. Chadi and K. Chang, "Energetics of DX-center formation in GaAs and $Al_xGa_{1-x}As$ alloys". *Phys. Rev. B* **39**, 10063–10074 (1989).

[244] A. Baraldi, P. Frigeri, C. Ghezzi, A. Parisini, A. Bosacchi, S. Franchi, E. Gombia, and R. Mosca, "Coexistence of the DX center with nonmetastable states of the donor impurity in Si-doped $Al_xGa_{1-x}As$: Effects on the low-temperature electron mobility". *Physical Review B* **53**, 10715 (1996).

[245] C. Falt, C. Hurd, S. McAlister, W. McKinnon, D. Day, and A. S. Thorpe, "Photo-excited carriers in GaAs/AlGaAs/$Al_xGa_{1-x}As$ heterostructures". *Semiconductor science and technology* **2**, 513 (1987).

[246] H. Störmer, A. Gossard, and W. Wiegmann, "Observation of intersubband scattering in a 2-dimensional electron system". *Solid State Communications* **41**, 707–709 (1982).

[247] R. Fletcher, E. Zaremba, M. D'iorio, C. Foxon, and J. Harris, "Evidence of a mobility edge in the second subband of an $Al_{0.33}Ga_{0.67}As$-GaAs heterojunction". *Physical Review B* **38**, 7866 (1988).

[248] S. Luryi and A. Kastalsky, "Anomalous photomagnetoresistance effect in modulation-doped AlGaAs/GaAs heterostructures". *Applied Physics Letters* **45**, 164–167 (1984).

[249] K. Hirakawa, H. Sakaki, and J. Yoshino, "Concentration of electrons in selectively doped GaAlAs/GaAs heterojunction and its dependence on spacer-layer thickness and gate electric field". *Applied Physics Letters* **45**, 253–255 (1984).

[250] H. Mizuta, K. Yamaguchi, M. Yamane, T. Tanoue, and S. Takahashi, "Two-dimensional numerical simulation of Fermi-level pinning phenomena due to DX centers in AlGaAs/GaAs HEMTs". *IEEE Transactions on Electron Devices* **36**, 2307–2314 (1989).

[251] B. J. Van Wees, H. Van Houten, C. W. J. Beenakker, J. G. Williamson, L. P. Kouwenhoven, D. Van der Marel, and C. T. Foxon, "Quantized conductance of point contacts in a two-dimensional electron gas". *Physical Review Letters* **60**, 848 (1988).

[252] D. A. Wharam, T. J. Thornton, R. Newbury, M. Pepper, H. Ahmed, J. E. F. Frost, D. G. Hasko, D. C. Peacock, D. A. Ritchie, and G. A. C. Jones, "One-dimensional transport and the quantisation of the ballistic resistance". *Journal of Physics C: Solid State Physics* **21**, L209 (1988).

[253] J. Waldrop, "Electrical properties of ideal metal contacts to GaAs: Schottky-barrier height". *Journal of Vacuum Science & Technology B: Microelectronics Processing and Phenomena* **2**, 445–448 (1984).

[254] V. L. Bonch-Bruevich and S. G. Kalashnikov, *Halbleiterphysik*. Springer Wien (Verlag), 1982.

[255] V. Gantmakher and Y. Levinson, *Carrier Scattering in Metals and Semiconductors*. Vol. 19. Elsevier, 1987.

[256] P. Lenard, "Über die lichtelektrische Wirkung". *Annalen der Physik* **313**, 149–198 (1902).

[257] A. Einstein, "Über einen die Erzeugung und Verwandlung des Lichtes betreffenden heuristischen Gesichtspunkt". *Annalen der Physik* **322**, 132–148 (1905).

[258] A. Perera, R. Sherriff, M. Francombe, and R. Devaty, "Far infrared photoelectric thresholds of extrinsic semiconductor photocathodes". *Applied Physics Letters* **60**, 3168–3170 (1992).

[259] Y.-F. Lao, A. U. Perera, L. Li, S. Khanna, E. Linfield, and H. Liu, "Tunable hot-carrier photodetection beyond the bandgap spectral limit". *Nature Photonics* **8**, 412–418 (2014).

[260] S. Matsik, M. Rinzan, A. Perera, H. Liu, Z. Wasilewski, and M. Buchanan, "Cutoff tailorability of heterojunction terahertz detectors". *Applied Physics Letters* **82**, 139–141 (2003).

[261] P. Bai, Y. Zhang, X. Guo, Z. Fu, J. Cao, and W. Shen, "Realization of the high-performance THz GaAs homojunction detector below the frequency of Reststrahlen band". *Applied Physics Letters* **113**, 241102 (2018).

[262] W.-Z. Shen, A. Perera, H.-C. Liu, M. Buchanan, and W. Schaff, "Bias effects in high performance GaAs homojunction far-infrared detectors". *Applied Physics Letters* **71**, 2677–2679 (1997).

[263] E. Haller, M. Hueschen, and P. Richards, "Ge:Ga photoconductors in low infrared backgrounds". *Applied Physics Letters* **34**, 495–497 (1979).

[264] G. Stacey, J. Beeman, E. Haller, N. Geis, A. Poglitsch, and M. Rumitz, "Stressed and unstressed Ge:Ga detector arrays for airborne astronomy". *International Journal of Infrared and Millimeter Waves* **13**, 1689–1707 (1992).

[265] C. N. Berglund and W. E. Spicer, "Photoemission studies of copper and silver: theory". *Physical Review* **136**, A1030 (1964).

[266] R. Broudy, "Vectorial photoelectric effect". *Physical Review B* **3**, 3641 (1971).

[267] E. O. Kane, "Theory of photoelectric emission from semiconductors". *Physical Review* **127**, 131 (1962).

[268] M. Rinzan, S. Matsik, and A. Perera, "Quantum mechanical effects in internal photoemission THz detectors". *Infrared physics & technology* **50**, 199–205 (2007).

[269] I. Tamm and S. Schubin, "Zur Theorie des Photoeffektes an Metallen". *Zeitschrift für Physik* **68**, 97–113 (1931).

[270] K. Mitchell, "The theory of the surface photoelectric effect in metals—I". *Proceedings of the Royal Society of London. Series A, containing papers of a mathematical and physical character* **146**, 442–464 (1934).

[271] J. Sass, "Evidence for an anisotropic volume photoelectric effect in polycrystalline nearly free electron metals". *Surface Science* **51**, 199–212 (1975).

[272] U. Gerhardt and E. Dietz, "Angular distribution of photoelectrons emitted from copper single crystals". *Physical Review Letters* **26**, 1477 (1971).

[273] K. Mitchell, "The theory of the surface photoelectric effect in metals—II". *Proceedings of the Royal Society of London. Series A-Mathematical and Physical Sciences* **153**, 513–533 (1936).

[274] J. Girardeau-Montaut, C. Girardeau-Montaut, S. Moustaizis, and C. Fotakis, "Dependence of femtosecond single-photon photoemission from gold on laser beam incidence and polarization". *Applied Physics Letters* **63**, 699–701 (1993).

[275] G. Hechenblaikner and T. Ziegler, "The vectorial photoelectric effect under solar irradiance and its application to sun sensing". *Measurement Science and Technology* **25**, 075103 (2014).

[276] W. Nolting, *Grundkurs Theoretische Physik 5/1: Quantenmechanik: Grundlagen*. Springer-Verlag, 2008.

[277] W. Michailow, P. Spencer, N. W. Almond, S. J. Kindness, R. Wallis, T. A. Mitchell, R. Degl'Innocenti, S. A. Mikhailov, H. E. Beere, and D. A. Ritchie, "An in-plane photoelectric effect in two-dimensional electron systems for terahertz detection". *arXiv preprint arXiv:2011.04177* (2020, submitted).

[278] Y. Hirayama, K. Muraki, and T. Saku, "Two-dimensional electron gas formed in a back-gated undoped heterostructure". *Applied Physics Letters* **72**, 1745–1747 (1998).

[279] V. Mokerov, Y. V. Fedorov, and A. Hook, "High density 2DEG in III-V semiconductor heterostructures and high-electron-mobility transistors based on them". *Semiconductors* **33**, 970–971 (1999).

[280] L. Lin, L. Liao, J. Yin, H. Peng, and Z. Liu, "Building graphene p–n junctions for next-generation photodetection". *Nano Today* **10**, 701–716 (2015).

[281] O. Gywat, H. J. Krenner, and J. Berezovsky, *Spins in optically active quantum dots: concepts and methods*. John Wiley & Sons, 2010. ISBN: 978-3-527-40806-1.

[282] D. Loss and D. P. DiVincenzo, "Quantum computation with quantum dots". *Physical Review A* **57**, 120 (1998).

[283] E. Zibik, T. Grange, B. Carpenter, N. Porter, R. Ferreira, G. Bastard, D. Stehr, S. Winnerl, M. Helm, H. Liu, et al., "Long lifetimes of quantum-dot intersublevel transitions in the terahertz range". *Nature Materials* **8**, 803–807 (2009).

[284] W. Michailow, "Electrical and Optical Properties of Hole Spin Storage Devices Based on InGaAs Self-assembled Quantum Dots". Master's Thesis. Walter Schottky Institute, Technical University of Munich, 2017.

[285] J. Cibert, P. Petroff, G. Dolan, S. Pearton, A. Gossard, and J. English, "Optically detected carrier confinement to one and zero dimension in GaAs quantum well wires and boxes". *Applied Physics Letters* **49**, 1275–1277 (1986).

[286] A. Zrenner, L. Butov, M. Hagn, G. Abstreiter, G. Böhm, and G. Weimann, "Quantum dots formed by interface fluctuations in AlAs/GaAs coupled quantum well structures". *Physical Review Letters* **72**, 3382 (1994).

[287] C. Murray, D. J. Norris, and M. G. Bawendi, "Synthesis and characterization of nearly monodisperse CdE (E= sulfur, selenium, tellurium) semiconductor nanocrystallites". *Journal of the American Chemical Society* **115**, 8706–8715 (1993).

[288] A. L. Efros and M. Rosen, "The electronic structure of semiconductor nanocrystals". *Annual Review of Materials Science* **30**, 475–521 (2000).

[289] R. Hanson, L. P. Kouwenhoven, J. R. Petta, S. Tarucha, and L. M. Vandersypen, "Spins in few-electron quantum dots". *Reviews of Modern Physics* **79**, 1217 (2007).

[290] G. Schedelbeck, W. Wegscheider, M. Bichler, and G. Abstreiter, "Coupled quantum dots fabricated by cleaved edge overgrowth: From artificial atoms to molecules". *Science* **278**, 1792–1795 (1997).

[291] D. Leonard, M. Krishnamurthy, C. Reaves, S. P. DenBaars, and P. M. Petroff, "Direct formation of quantum-sized dots from uniform coherent islands of InGaAs on GaAs surfaces". *Applied Physics Letters* **63**, 3203–3205 (1993).

[292] J.-Y. Marzin, J.-M. Gérard, A. Izraël, D. Barrier, and G. Bastard, "Photoluminescence of single InAs quantum dots obtained by self-organized growth on GaAs". *Physical Review Letters* **73**, 716 (1994).

[293] K. Barnham and D. Vvedensky, *Low-dimensional semiconductor structures: Fundamentals and device applications*. Cambridge University Press, 2008.

[294] J. Finley, P. Fry, A. Ashmore, A. Lemaître, A. Tartakovskii, R. Oulton, D. Mowbray, M. Skolnick, M. Hopkinson, P. D. Buckle, et al., "Observation of multicharged excitons and biexcitons in a single InGaAs quantum dot". *Physical Review B* **63**, 161305 (2001).

[295] M. Fox, *Quantum optics: an introduction*. Vol. 15. Oxford University Press, 2006.

[296] D. P. DiVincenzo, "The Physical Implementation of Quantum Computation". *Fortschritte der Physik* **48**, 771–783 (2000). ISSN: 1521-3978.

[297] A. Bechtold, D. Rauch, F. Li, T. Simmet, P.-L. Ardelt, A. Regler, K. Muller, N. A. Sinitsyn, and J. J. Finley, "Three-stage decoherence dynamics of an electron spin qubit in an optically active quantum dot". *Nature Physics* **11**, 1005–1008 (Dec. 2015). ISSN: 1745-2473.

[298] A. Bechtold, F. Li, K. Müller, T. Simmet, P.-L. Ardelt, J. J. Finley, and N. A. Sinitsyn, "Quantum effects in higher-order correlators of a quantum-dot spin qubit". *Physical Review Letters* **117**, 027402 (2016).

[299] P. W. Shor, "Quantum computing". *Documenta Mathematica* **1**, 467–486 (1998).

[300] K.-H. Han and J.-H. Kim, "Quantum-inspired evolutionary algorithm for a class of combinatorial optimization". *IEEE transactions on evolutionary computation* **6**, 580–593 (2002).

[301] P. W. Shor, "Algorithms for quantum computation: Discrete logarithms and factoring". *Foundations of Computer Science, 1994 Proceedings., 35th Annual Symposium on*. 1994, 124–134.

[302] L. K. Grover, "A fast quantum mechanical algorithm for database search". *Proceedings of the twenty-eighth annual ACM symposium on Theory of computing*. 1996, 212–219.

[303] L. K. Grover, "Quantum mechanical searching". *Evolutionary Computation, 1999. CEC 99. Proceedings of the 1999 Congress on*. Vol. 3. 1999, 2255–2261.

[304] P. Martyniuk and A. Rogalski, "Quantum-dot infrared photodetectors: Status and outlook". *Progress in Quantum Electronics* **32**, 89–120 (2008).

[305] J. Phillips, K. Kamath, and P. Bhattacharya, "Far-infrared photoconductivity in self-organized InAs quantum dots". *Applied Physics Letters* **72**, 2020–2022 (1998).

[306] Y. Zhang, K. Shibata, N. Nagai, C. Ndebeka-Bandou, G. Bastard, and K. Hirakawa, "Probing many-body quantum states in single InAs quantum dots: Terahertz and tunneling spectroscopy". *Physical Review B* **91**, 241301 (2015).

[307] Y. Zhang, K. Shibata, N. Nagai, C. Ndebeka-Bandou, G. Bastard, and K. Hirakawa, "Gate-controlled terahertz single electron photovoltaic effect in self-assembled InAs quantum dots". *Applied Physics Letters* **107**, 103103 (2015).

[308] Y. Zhang, K. Shibata, N. Nagai, C. Ndebeka-Bandou, G. Bastard, and K. Hirakawa, "Excited-state charging energies in quantum dots investigated by terahertz photocurrent spectroscopy". *Physical Review B* **93**, 235313 (2016).

[309] J. H. Prechtel, A. V. Kuhlmann, J. Houel, A. Ludwig, S. R. Valentin, A. D. Wieck, and R. J. Warburton, "Decoupling a hole spin qubit from the nuclear spins". *Nature Materials* **15**, 981–986 (Sept. 2016). ISSN: 1476-1122.

[310] D. A. Miller, D. Chemla, T. Damen, A. Gossard, W. Wiegmann, T. Wood, and C. Burrus, "Band-edge electroabsorption in quantum well structures: The quantum-confined Stark effect". *Physical Review Letters* **53**, 2173 (1984).

[311] P. W. Fry, I. E. Itskevich, D. J. Mowbray, M. S. Skolnick, J. J. Finley, J. A. Barker, E. P. O'Reilly, L. R. Wilson, I. A. Larkin, P. A. Maksym, M. Hopkinson, M. Al-Khafaji, J. P. R. David, A. G. Cullis, G. Hill, and J. C. Clark, "Inverted electron-hole alignment in InAs-GaAs self-assembled quantum dots". *Physical Review Letters* **84**, 733 (2000).

[312] J. J. Finley, M. Sabathil, P. Vogl, G. Abstreiter, R. Oulton, A. I. Tartakovskii, D. J. Mowbray, M. S. Skolnick, S. L. Liew, A. G. Cullis, and M. Hopkinson, "Quantum-confined Stark shifts of charged exciton complexes in quantum dots". *Physical Review B* **70**, 201308 (2004).

[313] R. Warburton, C. Schaflein, D. Haft, F. Bickel, A. Lorke, K. Karrai, J. Garcia, W. Schoenfeld, and P. Petroff, "Optical emission from a charge-tunable quantum ring". *Nature* **405**, 926–9 (2000). ISSN: 1476-4687.

[314] J. Finley, A. Ashmore, A. Lemaître, D. Mowbray, M. Skolnick, I. Itskevich, P. Maksym, M. Hopkinson, and T. Krauss, "Charged and neutral exciton complexes in individual self-assembled In (Ga) As quantum dots". *Physical Review B* **63**, 073307 (2001).

[315] P. Spencer, C. Chen, W. Michailow, H. Beere, and D. Ritchie, "Triggering InAs/GaAs Quantum Dot nucleation and growth rate determination by in-situ modulation of surface energy". *arXiv preprint arXiv:1906.05842* (2019).

[316] K. Müller, "Optical Control of Quantum States in Artificial Atoms and Molecules". Doctoral Thesis. Technical University of Munich, 2013.

[317] C. Heyn, A. Stemmann, A. Schramm, H. Welsch, W. Hansen, and Á. Nemcsics, "Faceting during GaAs quantum dot self-assembly by droplet epitaxy". *Applied Physics Letters* **90**, 203105 (2007).

[318] C. Heyn, A. Stemmann, and W. Hansen, "Dynamics of self-assembled droplet etching". *Applied Physics Letters* **95**, 173110 (2009).

[319] C. Heyn, A. Stemmann, T. Köppen, C. Strelow, T. Kipp, M. Grave, S. Mendach, and W. Hansen, "Highly uniform and strain-free GaAs quantum dots fabricated by filling of self-assembled nanoholes". *Applied Physics Letters* **94**, 183113 (2009).

[320] Z. M. Wang, K. Holmes, J. L. Shultz, and G. J. Salamo, "Self-assembly of GaAs holed nanostructures by droplet epitaxy". *Physica status solidi (a)* **202**, R85–R87 (2005).

[321] C. Heyn, A. Küster, A. Ungeheuer, A. Gräfenstein, and W. Hansen, "Excited-state indirect excitons in GaAs quantum dot molecules". *Physical Review B* **96**, 085408 (2017).

[322] Q. Xie, A. Madhukar, P. Chen, and N. P. Kobayashi, "Vertically self-organized InAs quantum box islands on GaAs (100)". *Physical Review Letters* **75**, 2542 (1995).

[323] H. J. Krenner, M. Sabathil, E. C. Clark, A. Kress, D. Schuh, M. Bichler, G. Abstreiter, and J. J. Finley, "Direct observation of controlled coupling in an individual quantum dot molecule". *Physical Review Letters* **94**, 057402 (2005).

[324] K. Müller, G. Reithmaier, E. C. Clark, V. Jovanov, M. Bichler, H. J. Krenner, M. Betz, G. Abstreiter, and J. J. Finley, "Excited state quantum couplings and optical switching of an artificial molecule". *Physical Review B* **84**, 081302 (2011).

[325] A. S. Bracker, M. Scheibner, M. F. Doty, E. A. Stinaff, I. V. Ponomarev, J. C. Kim, L. J. Whitman, T. L. Reinecke, and D. Gammon, "Engineering electron and hole tunneling with asymmetric InAs quantum dot molecules". *Applied Physics Letters* **89**, 233110 (2006).

[326] B. Lambert, J. Caulet, A. Regreny, M. Baudet, B. Deveaud, and A. Chomette, "Optical determination of the $Al_xGa_{1-x}As$ energy gap variation versus the Al concentration in MBE-grown samples". *Semiconductor Science and Technology* **2**, 491 (1987).

[327] K. Müller, A. Bechtold, C. Ruppert, C. Hautmann, J. Wildmann, T. Kaldewey, M. Bichler, H. J. Krenner, G. Abstreiter, M. Betz, and J. J. Finley, "High-fidelity optical preparation and coherent Larmor precession of a single hole in an (In,Ga)As quantum dot molecule". *Physical Review B* **85**, 241306 (2012).

[328] K. Müller, A. Bechtold, C. Ruppert, M. Zecherle, G. Reithmaier, M. Bichler, H. J. Krenner, G. Abstreiter, A. W. Holleitner, J. M. Villas-Boas, M. Betz, and J. J. Finley, "Electrical control of interdot electron tunneling in a double InGaAs quantum-dot nanostructure". *Physical Review Letters* **108**, 197402 (2012).

[329] L. Zhai, M. C. Löbl, G. N. Nguyen, J. Ritzmann, A. Javadi, C. Spinnler, A. D. Wieck, A. Ludwig, and R. J. Warburton, "Low-Noise GaAs Quantum Dots for Quantum Photonics". *Nature Communications* **11**, 4745 (2020).

[330] S. W. Hell and J. Wichmann, "Breaking the diffraction resolution limit by stimulated emission: stimulated-emission-depletion fluorescence microscopy". *Optics Letters* **19**, 780–782 (1994).